OPTICAL SCIENCES

Peter Günter
Jean-Pierre Huignard
(Eds.)

Photorefractive Materials and Their Applications 1

Basic Effects

Springer

Springer Series in

OPTICAL SCIENCES 113

founded by H.K.V. Lotsch

Springer Series in

OPTICAL SCIENCES

The Springer Series in Optical Sciences, under the leadership of Editor-in-Chief *William T. Rhodes*, Georgia Institute of Technology, USA, provides an expanding selection of research monographs in all major areas of optics: lasers and quantum optics, ultrafast phenomena, optical spectroscopy techniques, optoelectronics, quantum information, information optics, applied laser technology, industrial applications, and other topics of contemporary interest.
With this broad coverage of topics, the series is of use to all research scientists and engineers who need up-to-date reference books.

The editors encourage prospective authors to correspond with them in advance of submitting a manuscript. Submission of manuscripts should be made to the Editor-in-Chief or one of the Editors. See also http://springeronline.com/series/624

Peter Günter Jean-Pierre Huignard
(Editors)

Photorefractive Materials and Their Applications 1

Basic Effects

With 169 Illustrations

Springer

Peter Günter
Institute of Quantum Electronics
Nonlinear Optics Laboratory
Swiss Federal Institute of Technology
ETH Hoenggerberg HPF E 8
CH-8093 Zurich
Switzerland
Email: nlo@phys.ethz.ch

Jean-Pierre Huignard
Thales Research and Technology France
RD 128
91767 Palaiseau Cedex
France
Email: jean-pierre.huignard@thalesgroup.com

Library of Congress Control Number: 2005923809

ISBN-10: 0-387-25191-X e-ISBN 0-387-25192-8 Printed on acid-free paper.
ISBN-13: 978-0387-25191-2

Printed in the United States of America. (SPI/MVY)

9 8 7 6 5 4 3 2 1

springeronline.com

Preface

This is the first volume of a set of three within the *Springer Series in Optical Sciences*, and is devoted to photorefractive effects, photorefractive materials, and their applications. Since the publication of our first two Springer books on *Photorefractive Materials and Their Applications* (Topics in Applied Physics, Vols. 61 and 62) almost 20 years ago, a lot of research has been done in this area. New and often expected effects have been discovered, theoretical models developed, known effects finally explained, and novel applications proposed. We believe that the field has now reached a high level of maturity, even if research continues in all areas mentioned above and with new discoveries arriving quite regularly.

We therefore have decided to invite some of the top experts in the field to put together the state of the art in their respective fields. This after we had been encouraged to do so for more than ten years by the publisher, due to the fact that the former volumes were long out of print.

This first volume is devoted to the description of the basic effects leading to photoinduced refractive index changes in electro-optical materials. As is commonly known, this photorefractive effect was originally discovered as undesirable optical damage in nonlinear and electro-optical crystals. Light- induced changes of the refractive index limited the usefulness of crystals such as $LiNbO_3$ with large electro-optic and nonlinear optical coefficients, because the index changes give rise to decollimation and scattering of laser beams in devices such as modulators and frequency doublers. Subsequently, materials exhibiting such an optical damage effect—later called the photorefractive effect—were proposed as holographic materials and when faster recording materials became available as dynamic holographic materials used for beam amplification, real-time interferometry, optical phase conjugation, and image processing applications. This class of photoinduced mechanisms has contributed to establish the link between the fields of nonlinear optics and coherent Fourier optics.

The optically induced refractive index changes are generally explained in the following way: When light of a suitable wavelength is incident on a crystal, photoelectron holes or ions are generated, which then migrate in the lattice and are subsequently trapped at new sites. The resulting space charges give rise to

an electric field strength distribution in the material that changes the refractive index via the electro-optic effect.

This first volume gives a comprehensive treatment of several aspects of photorefractive effects. Besides the detailed description of the photoinduced refractive index changes observed in anisotropic media, newer effects such as the effects of photoinduced space charge waves, feedback controlled grating recording, the description of spatiotemporal instabilities, and self-organized optical pattern formation by self-induced refraction index gratings are covered. Special recording methods by band-to-band photorefraction or two-step recording are topics of two other chapters. The observation and theoretical description of dark and bright solitons induced by the photorefractive effect is another exciting, novel phenomena described in this volume. The status of research in thermally or electrically fixing photoinduced gratings by ionic charge transport and thermal treatment, or by domain reversal, is described in two chapters of this book.

The volume reviews the present understanding of the fundamental origins of the effect in a variety of materials from ferroelectrics, compound semiconductors to polar organic crystals and polymers. The parameters that enter into the design of optimized materials are described and these parameters will be further discussed in Volume 2, which will deal with 'materials.'

The different beam interactions, self-induced optical effects, grating fixing mechanisms, and so on that form the basis of the applications described in detail in Volume 3 are also treated.

The three volumes on photorefractive effects, materials, and applications have been prepared mainly for researchers in the field, but also for physics, engineering, and materials science students. Several chapters contain sufficient introductory material for those not so familiar with the topic to obtain a thorough understanding of the photorefractive effect. We hope that for researchers active in the field, these books should provide a useful reference source for their work.

We would like to thank all authors of chapters for their great efforts in presenting attractive overviews of the topics they present in this book. We are very much indebted to Mrs. Lotti Nötzli for her great administrative support. We also acknowledge the efforts of Dr. Hans Koelsch of Springer and his team who made a great effort in efficiently producing this first volume.

Zürich, Orsay, April 2005

Peter Günter
Jean-Pierre Huignard

Contents

Preface . . . . . **v**

Contributors . . . . . **xiii**

1 Introduction **1**

2 Light-Induced Dynamic Gratings and Photorefraction **7**

2.1 Introduction 7

2.2 Two-Beam Interference and Interference Gratings 8

2.3 Material Response: Amplitude and Phase Gratings 19

2.4 Grating Detection by Diffraction and Wave-Mixing 31

2.5 Conclusions 40

3 Fundamentals of Photorefractive Phenomena **43**

3.1 The Photorefractive Nonlinearity: Introductory Remarks . . 43

3.2 Physical Mechanisms: Standard Microscopic Model 46

3.3 Theoretical Modeling: Rate Equations 47

3.4 Photovoltaic Drift 48

3.5 Macroscopic Formulation 50

3.6 Low Intensities: Continuous Wave (CW) Regime 50

3.7 Quasi-Equilibrium (Adiabatic) Approximation 51

3.8 Perturbative Approach to the Nonlinear Equation 52

3.9 Sinusoidal Light Excitation at Low Modulation Linear Equation for the Field 52

3.10 Summary of Characteristic Times, Lengths and Fields 56

3.11 Grating Enhancement Methods 57

3.12 High-Contrast Effects 60
3.13 Space-Charge Waves 64
3.14 Complicating Features to the Standard Model 65
3.15 Localized Optical Beams 67
3.16 Transient and Quasi-Steady-State Effects 74
3.17 Conclusions 77

4 Space-Charge Driven Holograms in Anisotropic Media 83
4.1 Introduction 83
4.2 Basic Considerations 83
4.3 Light Diffraction at Thick Anisotropic Phase and Absorption Gratings 91
4.4 Two-Wave Mixing in Anisotropic Dichroic Media 102
4.5 Examples 110
4.6 Conclusions 116

5 Space-Charge Wave Effects in Photorefractive Materials 119
5.1 Overview 119
5.2 Space-Charge Wave Characteristics 123
5.3 Linear Excitation of Space-Charge Waves 131
5.4 Parametric Excitation of SCWs: Subharmonic Generation . . 134
5.5 High-Contrast Effects in Photorefractive Response 145
5.6 Joint Action of Material and Optical Nonlinearities 152
5.7 Conclusions 158

6 Feedback-Controlled Photorefractive Beam Coupling 163
6.1 Introduction 163
6.2 Operation Principle of the Feedback Setup 168

6.3 Basic Relations for Feedback-Controlled Beam Coupling . . 172
6.4 Periodic States 180
6.5 Feedback Operation in Reflection Geometry 194
6.6 Summary 198

7 Band-to-Band Photorefraction 203
7.1 Introduction 203
7.2 Interband Photorefraction with cw Recording Waves 204
7.3 Materials 212
7.4 Applications 221
7.5 Conclusions 226

8 Two-Step Recording in Photorefractive Crystals 231
8.1 Introduction 231
8.2 Early Experiments 232
8.3 Shallow Levels, Two-Level Models 234
8.4 Two-Step Excitations via Shallow Levels 237
8.5 Hologram Recording Utilizing Pyroelectric Fields 241
8.6 Lifetime of the Holograms 244
8.7 Advantages of Infrared Recording 247
8.8 Conclusions 248

9 Spatio-Temporal Instabilities and Self-Organization 253
9.1 Pattern Formation in Nonlinear Optics 254
9.2 Overview of Pattern Formation in Photorefractive Media . . 257
9.3 Spotlight: $KNbO_3$: Fe Single Feedback System 265
9.4 Controlling Pattern Formation 278

9.5 Summary and Outlook 282

10 Photorefractive Waveguides 289

10.1 Introduction 289

10.2 Fundamentals of Photorefractive Waveguides 289

10.3 Materials with Illmenite Structure 294

10.4 Materials with Perovscite Structure 302

10.5 Materials with Tungsten-Bronze Structure 305

10.6 Sillenites 307

10.7 Applications 307

10.8 Conclusions and Outlook 310

11 Photorefractive Solitons 317

11.1 Introduction 317

11.2 The Discovery of Solitons in Photorefractives 318

11.3 A Saturable Nonlinearity 322

11.4 Two-Dimensional Solitons 329

11.5 Temporal Effects and Quasi-Steady–State Dynamics 334

11.6 Various Photorefractive Mechanisms Supporting Self-Trapping 336

11.7 Alternative Photorefractive Materials 342

11.8 Soliton Interaction-Collisions 343

11.9 Vector and Composite Solitons 348

11.10 Incoherent Solitons: Self-trapping of Weakly-Correlated Wavepackets 351

11.11 Applications 353

11.12 New Ideas and Concluding Remarks 357
11.13 Acknowledgements 358

12 Thermal Fixing of Photoinduced Gratings 369
12.1 Introduction 369
12.2 The Thermal Fixing Technique 370
12.3 Mathematical Formulation of the Model 372
12.4 Experimental Aspects of Thermal Fixing 380
12.5 Fixing in Photorefractive Waveguides 388
12.6 Photorefractive Applications Using Thermal Fixing 391
12.7 Summary 393

13 Electrical Fixing of Photoinduced Gratings 397
13.1 Introduction 397
13.2 Electrical Properties 398
13.3 Domain Fixing Mechanisms 402
13.4 Fidelity of Fixed Holograms 413

Index 417

Contributors

Fernando Agulló-López, Departmento de Física de Materiales, C-IV
Universidad Autónoma de Madrid, 28049 Madrid, Spain

Luis Arizmendi, Departmento de Física de Materiales, C-IV
Universidad Autónoma de Madrid, 28049 Madrid, Spain

Karsten Buse, Institute of Physics, University of Bonn, D-53115 Bonn, Germany

Gabriel F. Calvo, Grup de Física Teòrica, Universitat Autònoma de Barcelona, 08193 Bellaterra (Barcelona), Spain

Mercedes Carrascosa, Departmento de Física de Materiales, C-IV
Universidad Autónoma de Madrid, 28049 Madrid, Spain

José M. Cabrera, Departmento de Física de Materiales, C-IV
Universidad Autónoma de Madrid, 28049 Madrid, Spain

Demetrios N. Christodoulides, School of Optics-CREOL
University of Central Florida, Orlando, FL 32816-2700, USA

Bruno Crosignani, Dipartimento di Fisica, Università dell'Aquila, 67040 L'Aquila, Italy
and
Instituto Nazionale Fisica della Materia, Università di Roma "La Sapienza", 00185 Roma, Italy

Roger S. Cudney, Departamento de Optica, CICESE, Ensenada, Mexico

Eugenio DelRe, Dipartimento di Ingegneria Electtrica e dell'Informazione, Università dell'Aquila, 67040 L'Aquila, Italy

Cornelia Denz, AG Nichtlineare Photonik, Institut für Angewandte Physik, Westfälische Wilhelms-Universität Münster, D-48149 Münster, Germany

Philipp Dittrich, Institute of Quantum Electronics, Nonlinear Optics Laboratory, Swiss Federal Institute of Technology Zurich, CH-8093 Zurich, Switzerland

Hans Joachim Eichler, Technische Universität Berlin, Institute of Optics, 10623 Berlin, Germany

Jan Fousek, International Center for Piezoelectric Research,
Faculty of Mechatronics, Technical University of Liberec, CZ – 460 17 Liberec Czech Republic

Maxim V. Gorkunov, Department of Physics, University of Osnabrück, D-49069 Osnabrück, Germany

Peter Günter, Institute of Quantum Electronics, Nonlinear Optics Laboratory, Swiss Federal Institute of Technology Zurich, CH-8093 Zurich, Switzerland

Andreas Hermerschmidt, Technische Universität Berlin, Institute of Optics, 10623 Berlin, Germany

Jean-Pierre Huignard, Thales Research and Technology France, RD 128, 91767 Palaiseau Cedex, France

Philip Jander, AG Nichtlineare Photonik, Institut für Angewandte Physik, Westfälische Wilhelms-Universität Münster, D-48149 Münster, Germany

Detlef Kip, Institute of Physics and Physical Technologies, Clausthal University of Technology, 38678 Clausthal-Zellerfeld, Germany

Eckhard Krätzig, Department of Physics, University of Osnabrück, D-49069 Osnabrück, Germany

Germano Montemezzani, Laboratoire Matériaux Optiques, Photonique et Systèmes, University of Metz and Supélec, 57070 Metz Cédex, France

Serguey G. Odoulov, Institute of Physics, National Academy of Science, 252650 Kiev, Ukraine

Evgeny V. Podivilov, International Institute for Nonlinear Studies, Institute of Automation and Electrometry, 630090 Novosibirsk, Russia

Greg Salamo, Physics Department, University of Arkansas, Fayetteville, AR 72703, USA

Mordechai (Moti) Segev, Physics Department, Technion – Israel Institute of Technology, Haifa, Israel

Boris I. Sturman, International Institute for Nonlinear Studies, Institute of Automation and Electrometry, 630090 Novosibirsk, Russia

Monika Wesner, Department of Physics, University of Osnabrück, D-49069 Osnabrück, Germany

Marko Zgonik, Faculty of Mathematics and Physics, University of Ljubljana and Jozef Stefan Institute, Ljubljana, Slovenia

1

Introduction

P. Günter and J.P. Huignard

The research and developments in laser physics and nonlinear optics rapidly expanded over the last twenty years, and many applications of photonics are now relevant to the industrial or consumer markets. Also, it is expected that photonics will disseminate in the near future in new, important areas like medicine, biology, or nano technologies. A major factor behind such impressive growth is the advent of high powered and efficient solid state lasers in combination with the use of materials that exhibit large second or third order nonlinearities. In such conditions, nonlinear optics is becoming an important technology in the design of new laser sources emitting in the visible or near IR. Nonlinear optics also enables the attainment of new functionalities in laser systems and optoelectronic signal transmission and processing. The class of nonlinear phenomena based on the photorefractive effects in electro-optic crystals will undoubtly play a major role for these different applications of laser photonics.

To briefly introduce this particular field of nonlinear optics, let us recall in the following the basic of the physical mechanisms and main characteristics: when coherent laser beams interfere in the volume of the material, it generates a photoinduced space charge field which modulates the crystal or polymer refractive index through the linear electro-optic effects. In other words, photorefractive materials are very well suited to record dynamic holograms using two-wave or four-wave mixing interactions involving continuous wave or pulsed lasers. The magnitude of the hologram recording slope is proportional to the absorbed incident energy and there is a trade-off between response time and material saturation efficiency.

The result is that, in general, a photorefractive mechanism is not as fast as other nonlinear effects such as Kerr, Raman, or Brillouin, but it can present a dark storage time that provides attractive capabilities for memory applications. Consequently, this particular type of optical nonlinearity exhibits very specific properties that will be developed in the different chapters of this volume and which have opened new advances in optical sciences.

Nonlinear photorefractive optics is now well established and it has reached scientific maturity. It contributes to stimulate basic research in solid state

physics to investigate with details the mechanisms of charge transport in different types of ferroelectric or semiconductor crystals. It thus results in great interest to grow new doped crystals whose photorefractive properties can be tailored to the applications, encompassing materials that have no photorefraction to materials that can exhibit large photoinduced index modulations.

Another important aspect of the photorefractive materials is their ability to perform efficient energy transfer between pump and probe waves interfering in the volume of the crystal. This remarkable property opens a wide range of applications, including image amplification, optical phase conjugation with gain, or self pumped optical cavities. The amplitude of the energy transfer is governed by the nonlinear photorefractive gain coefficient whose value is deduced from the intrinsic values of the electro-optic and charge transport parameters of the material. The importance of this parameter is outlined in the chapters of this volume in order to evaluate and compare material performances. All the remarkable properties of photorefractive materials are challenging a lot of innovative beam interactions, even at very low power levels, and permit the demonstration of unconventional optical functions and devices. A fascinating example is the self pumped phase conjugate mirror, which restores excellent images when the beam propagates through a phase disturbing media. A photorefractive phase conjugate mirror has the ability to realize a dynamic compensation of the thermal lensing effects and aberrations that occur in laser cavities. The solid state laser source can now operate at high power with a diffraction limited beam quality and optimum brightness. These few examples clearly outline the importance of the nonlinear photorefractive mechanisms to introduce new optical performances beyond traditional limits. As it often occurs in nonlinear optics, the choice of the material is a critical issue due to the diversity of parameters and material properties that are involved in the interactions of the crystal with the incident optical field. It is the objective of these new volumes to status on the most recent progress of the field, covering both the fundamental and applied aspects relevant to solid state physics and beam interactions or propagation in these complex media.

When we published the first edition on photorefractive materials and applications in 1987, it was the result of very intense research activity in the field, as well as in other closely related subjects on optical phase conjugation and information processing. These volumes remain a very good source of comprehensive coverage of the domain. Starting from the discovery of the effects in lithium niobate at Bell Labs in the mid 60s, the book chapters already developed a first extensive analysis of the nonlinear mechanisms and applications in materials like $LiNbO_3$, $BaTiO_3$, $KNbO_3$, $Bi_{12}\,SiO_{20}$, or GaAs. The basic of the early works on the charge transport models and beam coupling phenomena in these materials were investigated with details. Several chapters also highlighted early demonstrations of high reflectivity phase conjugate mirrors using photorefractive crystals as well as image amplification through dynamic holography. The capability of achieving high gain at low power levels in most

materials was already well developed by analyzing and demonstrating several types of selfinduced optical cavities. It was often outlined in these articles that a critical issue is to identify and select the material having the required characteristics. So it is now important to review the research works that have significantly contributed to new advances during the last decade. An important objective is thus to show that the discovery of new effects or continuing an extended analysis of the physical phenomena lead to a better control of material properties for further development of attractive applications.

This first volume reviews the basic effects of photorefractive nonlinear optics. Chapters 2 and 3 develop the fundamental aspects of photoinduced dynamic gratings and clearly present the major physical mechanisms as well as the space charge field solutions relevant to different types of recording conditions and beam configurations. The authors also review the effects of beam coupling due to dynamic interaction of the two interfering beams with the photoinduced phase shifted grating. Chapter 4 analyzes the anisotropic responses of the photorefractive media. It thus includes the contribution of the light polarization, dielectric, electro-optic, and piezo-electric tensor coefficients that play a role in the amplitude of the photoinduced index modulation. Chapter 4 also takes account of the anisotropy of the photocarrier mobility. This work leads to an optimization of the gain coefficient and diffraction efficiency in media that exhibits a complex anisotropic response. Chapter 5 provides a description of the basic properties of low frequency space charge waves. They are characterized by intrinsic parameters such as the wave vector, the eigen frequency, and the damping coefficient. The conditions on material properties to ensure propagation of the space charge waves are presented. Due to their resonant character, space charge waves contribute to enhance the index modulation in moving grating recording with a large applied field and to the generation of spatial subharmonics in nearly degenerate two-wave mixing. In the Chapter 6, the authors outline the interest of implementing an electronic feedback loop to stabilize the experimental setups against phase fluctuations and shape the characteristics of grating recording and beam coupling. These effects are modeled by the introduction of the feedback term in the dynamic coupled wave amplitude equations. The nonlinear feedback control opens attractive capabilities for beam intensity and phase stabilizations over very long time periods.

Chapter 7 deals with band-to-band photorefraction. The mechanism provides an efficient way to highly improve the response speed as well as the robustness for long time storage and readout. These properties, which are specific to interband photorefraction, open very attractive perspectives for the processing and manipulation of visible laser beams when illuminating the crystal with UV light. The experimental results are clearly supported by a complete modeling of the UV recording process where the incident wavelength is strongly absorbed and induces a large photoconductivity effect. In Chapter 8, the authors develop the mechanisms of two-step recording in photorefractive crystals like $LiNbO_3$ or $LiTaO_3$. The technique has been early used for storage

applications but the recent research results reported in Chapter 8 provide a complete understanding and control of the mechanisms. Two-step recording provides the capability of sensitizing the crystal with near IR wavelengths, thus ensuring nearly nondestructive read-out of the stored information. The doping of the material with ions that exhibit real intermediate energy levels with long lifetime permit a reduction of the peak intensity required for recording. Several experimental results clearly illustrate this capability. A further approach is based on the pyroelectric effect combined with an excitation of visible light. Most of the interactions considered in this volume are relevant to free space propagation in the bulk of the nonlinear crystal. However, as shown in Chapter 9, both dynamic wave mixing and permanent gratings are of interest for the development of new integrated optics components. Different types of optical waveguides are considered, including the technology for their realization. Demonstrations are shown with materials like sillenites and ferroelectrics, and applications are considered on some examples. Like with other nonlinear phenomena, spatio-temporal instabilities can also be obtained with the photorefractive effects. These mechanisms, as well as self-organizations and pattern formations, are developed in Chapter 10. Pattern formation can be observed due to a transverse coupling between spatial regions of the nonlinear crystal. The conditions for pattern control, selection and stabilization are also presented.

Chapter 11 address a new subject, the photorefractive spatial solitons, which has led to very active original research in the field of nonlinear optics. The diversity of photorefractive effects allows the investigation of a large variety of new soliton phenomena and many of them have been firstly observed and interpreted in photorefractive crystals. It concerns, for example, coherent or incoherent solitons interactions, effect of solitons spiraling, fission, and annihilation, or multimode solitons propagation. Besides the fundamental aspects and their experimental demonstrations, the chapter also introduces applications to new active and passive electro-optic devices. Due to the rich new phenomena of underlying solitons formation in various nonlinear media, it is expected that the properties can be carefully controlled for further important developments of this domains.

The long-term fixing of the recorded holographic information in a photorefractive crystal is an important objective, which is developed in Chapters 12 and 13. Since read-out of the volume hologram is done at the same wavelength as that used for recording, the holographic information is erased due to space charge field relaxation under uniform illumination. It was early proposed that two techniques could be used to get quasi nondestructive readout: respectively, thermal and electrical fixing. These two chapters provide an extended analysis of the physical mechanisms involved for space charge field compensation, or domain switching in different types of ferroelectric crystals. Experimental results support the physical analysis and open attractive capabilities for memory applications.

In conclusion, this collection of chapters provides a broad survey of the most advanced research developments relevant to the basics of photorefractive

nonlinear optics. The chapters deal with a large overview of the physical phenomena, and many of them contribute to establish the link with other well-known nonlinear mechanisms used in laser physics. The authors of this volume are major scientists in the field and their contributions bring a full complement research efforts in material sciences, dynamic holography, and applications. The volume should serve the needs of the scientific and engineering communities interested in multidisciplinary aspects of photorefractive nonlinear optics.

The editors of this volume express their warm regards to all the authors for their outstanding contributions and very fruitful cooperation for the preparation of the book volume, which should contribute to stimulate further developments of the field. We also thank Mrs. Lotti Nötzli for her valuable secretarial support.

2

Light-Induced Dynamic Gratings and Photorefraction

Hans Joachim Eichler and Andreas Hermerschmidt

TU Berlin, Institute of Optics, Straße des 17. Juni 135, 10623 Berlin, Germany
eichler@physik.tu-berlin.de

2.1 Introduction

The spatial superposition of two or more coherent light waves yields a spatially modulated distribution of the energy density, and the interaction with the material leads to the creation of light-induced dynamic gratings. Many interesting effects and applications are based on such gratings. In some applications, e.g. when using dynamic gratings for holographic storage applications [1, 2] or the nanofabrication of three-dimensional photonic crystals by holographic lithography [3], the superposition of the beams defines the spatial structure of the grating. In other applications like using Stimulated Brillouin Scattering (SBS) for the creation of phase-conjugating mirrors for high-power laser systems [4, 5], the superposition of the laser beam with initially randomly scattered beam components eventually leads to the build-up of a dynamic grating acting as a phase-conjugating mirror.

The photorefractive effect, which is the topic of this volume, is as well based on dynamic light-induced gratings and has many applications and very interesting properties. For example, phase-conjugating mirrors based on Four-Wave Mixing in photorefractive materials do not have a distinct threshold in terms of laser intensity due to the entirely different physical process of the grating creation [6, 7] in contrast to the previously mentioned case of mirrors based on SBS. However, it is interesting that beam fanning as a driving effect for the build-up of such a photorefractive mirror [8] is again based on the transient evolution of scattered beam components, like in the SBS case.

Following a similar approach to the topic as used in [9] in this chapter, we will first recapitulate some basic properties of coherent light fields, which are usually derived from lasers [10], and discuss two-beam interference leading to interference gratings. In Section 2.3, we will discuss how the material response leads to changes in the absorption and the refraction of the material, which are described as amplitude and phase gratings. The diffraction of light at the gratings and wave mixing effects are described in Section 2.4.

2.2 Two-Beam Interference and Interference Gratings

Many properties of laser beams related to dynamic grating physics and applications can be described by a plane-wave approximation of the light field. The propagation of light in different types of media, the interference of light fields, and the diffraction of light at periodic structures are also often described using plane waves as a representation of the light field [11–13]. We will mainly follow the same approach, but we will also discuss some deviations of real laser beams from ideal plane waves, e.g., with respect to their limited size, duration, and coherence.

2.2.1 Plane Waves and Gaussian Laser Beams

In many experimental configurations, a Gaussian beam corresponding to the fundamental TEM_{00} mode of a laser resonator is used, which comes close to the ideal plane wave,

$$\mathbf{E}(\boldsymbol{r}, t) = \boldsymbol{A} \exp\left[\mathrm{i}(\boldsymbol{k} \cdot \boldsymbol{r} - \omega t + \phi)\right]. \tag{2.1}$$

Here $\boldsymbol{E}$ is the complex electric field vector dependent on the spatial coordinate $\boldsymbol{r}$ and time t, $\boldsymbol{A}$ the real-valued wave amplitude, $\boldsymbol{k}$ its wave vector, $\omega = 2\pi f$ its angular frequency, and ϕ a constant phase offset. The electric field $\boldsymbol{E}^r$ is given by

$$\boldsymbol{E}^r(\boldsymbol{r}, t) = \frac{1}{2}(\boldsymbol{E}(\boldsymbol{r}, t) + \boldsymbol{E}^*(\boldsymbol{r}, t)) = \boldsymbol{A} \cos(\boldsymbol{k} \cdot \boldsymbol{r} - \omega t + \phi), \tag{2.2}$$

and can only take real values in order to retain its physical meaning [14]. For many computations, however, it is convenient to use the complex-valued field $\boldsymbol{E}$ (i.e., without adding the c.c.), but by doing so, the formulas for the relevant quantities can be slightly different from the familiar form.

The time-averaged Poynting vector $\boldsymbol{S}$ of a plane wave using complex-valued fields is given by [12]

$$\boldsymbol{S} = \frac{1}{2}\mathrm{Re}(\boldsymbol{E} \times \boldsymbol{H}^*). \tag{2.3}$$

For the intensity I of this plane wave at point $\boldsymbol{r}$, time t, given by the time average of the absolute value of the Poynting vector, we obtain

$$I(\boldsymbol{r}, t) = \overline{|\boldsymbol{S}|} = \frac{\varepsilon_0 c n}{2}|\boldsymbol{E}(\boldsymbol{r}, t)|^2 = \frac{1}{2Z}|\boldsymbol{E}(\boldsymbol{r}, t)|^2, \tag{2.4}$$

where c is the velocity of light, ε_0 the vacuum permittivity, n the refractive index, and $Z = \sqrt{\mu_r \mu_0 / \varepsilon_r \varepsilon_0}$ the corresponding wave resistance of the material. For most materials relevant in optics, the relative magnetic permeability μ_r is

given by $\mu_r \approx 1$, and the material properties are determined by the electric permittivity $\varepsilon = \varepsilon_0 \varepsilon_r$. To account for absorption and dispersion effects in isotropic materials with one quantity, the complex permittivity

$$\varepsilon_r = \varepsilon' + \mathrm{i}\varepsilon''. \tag{2.5}$$

is introduced. Assuming weak absorption ($\varepsilon'' \ll \varepsilon'$), the complex-valued refractive index $\hat{n}$ is given by

$$\hat{n} = \sqrt{\varepsilon_r} \approx \sqrt{\varepsilon'} + \mathrm{i}\frac{\varepsilon''}{2\sqrt{\varepsilon'}}. \tag{2.6}$$

The absorption coefficient α is introduced as

$$\alpha = \frac{2\omega}{c}\mathrm{Im}(\hat{n}) \approx \frac{\omega\varepsilon''}{nc}, \tag{2.7}$$

where $n = \mathrm{Re}(\hat{n})$ is the familiar real refractive index used in Eq. 2.4.

The electromagnetic energy density associated with the electric field $\boldsymbol{E}$ is given by

$$w(\boldsymbol{r}, t) = \frac{1}{2}\varepsilon_0 \varepsilon' \boldsymbol{E}(\boldsymbol{r}, t) \cdot \boldsymbol{E}^*(\boldsymbol{r}, t). \tag{2.8}$$

Often, the interaction of the field with the material (i.e., the creation of a material excitation grating, see Section 2.3) is related to the rate of the dissipated energy density of the field that is given by [15]

$$W_f(\boldsymbol{r}, t) = \frac{\varepsilon_0 \varepsilon'' \omega}{2} \boldsymbol{E}(\boldsymbol{r}, t) \cdot \boldsymbol{E}^*(\boldsymbol{r}, t). \tag{2.9}$$

For a plane wave and in isotropic materials, the rate of the dissipated energy density W_f and also the energy density w are directly proportional to the intensity as defined in Eq. 2.4

$$W_f(\boldsymbol{r}, t) = \frac{\varepsilon_0 cn\alpha}{2} |\boldsymbol{E}(\boldsymbol{r}, t)|^2 = \alpha I(\boldsymbol{r}, t). \tag{2.10}$$

Please note that while the left part of this equation is a general expression for weakly absorbing isotropic media, the right part obtained using Eq. 2.4 is valid for plane waves, but does not hold always in the general case.

In anisotropic materials, the permittivity of the material is described by introduction of the permittivity tensor ε_r. The resulting anisotropy of the refractive index is referred to as birefringence and in the case of uniaxial optical materials the propagation can be described using polarization-dependent refractive indices n_e and n_o for a given direction of the wave vector of the light. In some materials the anisotropy of the energy dissipation (referred to as dichroism) is also relevant.

The most relevant quantities describing the field in vacuum and within weakly absorbing materials are summarized in the Table 2.1. The expressions for the intensity are obtained for a single plane wave, while the other expressions are valid for general fields as well. In anisotropic materials, $\varepsilon_r, \varepsilon'$ and ε'' are tensor quantities. For the description of some effects, more sophisticated quantities may be needed to cover material properties like e.g., the polarization dependent quantum efficiency of the excitation processes involved [16].

In contrast to a plane wave, the amplitude of a field describing a laser beam is not constant within the plane of a wave front. A TEM_{00} mode has a Gaussian rotationally symmetric amplitude distribution

$$\boldsymbol{A}(\rho) = \boldsymbol{A}_0 \exp[-\rho^2/\rho_0^2], \tag{2.11}$$

where ρ is the cylindrical coordinate perpendicular to the direction of propagation z and ρ_0 is called the spot radius. The intensity distribution of a Gaussian beam is given by

$$I(\rho) = I_0 \exp[-2\rho^2/\rho_0^2]. \tag{2.12}$$

At $\rho = \rho_0$, the electric field drops to $1/e \cong 37\%$ of its maximum value $\boldsymbol{A}_0$ while the intensity is reduced to $1/e^2 \cong 14\%$ of I_0. The total power or light flux P_t of a TEM_{00} beam is

$$P_t = 2\pi \int_0^\infty I(\rho)\rho d\rho = \frac{\pi}{2}\rho_0^2 I_0. \tag{2.13}$$

About 86.5% of this flux is contained within a radius equal to the spot radius ρ_0. The laser beam diameter changes during propagation. Thus, except when going through a focus, the wavefronts are not perfectly plane and the spot radius is not constant but a function of z. Since the divergence is inversely proportional to the beam diameter, a sufficiently large spot radius $\rho_0 \gg \lambda$ is a necessary requirement for plane-wave-like behavior.

Short laser pulses are frequently used for grating excitation and detection. If their duration t_p is sufficiently small, the total pulse energy per unit area F, i.e., the exposure or fluence

$$F = \int_{-\infty}^{\infty} I(t)dt \tag{2.14}$$

TABLE 2.1 Physical quantities used for the description of optical fields

	Vacuum	Isotropic material	Anisotropic material
intensity I (plane wave)	$\frac{1}{2}\varepsilon_0 c\lvert\boldsymbol{E}\rvert^2$	$\frac{1}{2}\varepsilon_0 cn\lvert\boldsymbol{E}\rvert^2$	$\frac{1}{\mu_0\omega}\boldsymbol{E}\times(\boldsymbol{k}\times\boldsymbol{E})$
energy density w	$\frac{1}{2}\varepsilon_0\lvert\boldsymbol{E}\rvert^2$	$\frac{1}{2}\varepsilon_0\varepsilon'\lvert\boldsymbol{E}\rvert^2$	$\frac{1}{2}\varepsilon_0(\boldsymbol{E}\cdot\varepsilon'\boldsymbol{E}^*)$
energy dissipation rate W_f	0	$\frac{1}{2}\varepsilon_0\varepsilon''\omega\lvert\boldsymbol{E}\rvert^2$	$\frac{1}{2}\varepsilon_0\omega(\boldsymbol{E}\cdot\varepsilon''\boldsymbol{E}^*)$

and the total laser pulse energy

$$W = 2\pi \int_0^\infty F(\rho)\rho d\rho = \int_{-\infty}^{\infty} P_t(t)dt \tag{2.15}$$

are more relevant parameters than the instantaneous quantities intensity and flux.

2.2.2 Superposition of Two Plane Waves

Two-beam interference produces a spatially modulated light field, which is called an interference grating. In many cases, the quantity used for the description of effects related to interference and the interaction with the material is the intensity I. However, in other cases, for a feasible description of the interaction of the interference pattern with the material, the energy density w, or the energy dissipation of the field W_f as introduced in Eq. (2.9) should be used instead [17]. Still in many relevant cases the approximation of the tensor ε'' by a scalar and the assumption of weak absorption are justified, and the three mentioned quantities are proportional to $|\boldsymbol{E}|^2$ (see Table 2.1).

The principal experimental arrangement for the production of laser-induced gratings is shown in Fig. 2.1. Light from a more-or-less powerful pump laser is split into two beams, A and B, with wave vectors $\boldsymbol{k}_A$, $\boldsymbol{k}_B$ and electric field amplitudes $\boldsymbol{A}_A$, $\boldsymbol{A}_B$. The field amplitudes can be written using the polarization vectors $\boldsymbol{p}_A$, $\boldsymbol{p}_B$ as $\boldsymbol{A}_A = A_A\boldsymbol{p}_A$ and $\boldsymbol{A}_B = A_B\boldsymbol{p}_B$. The two beams intersect at an angle 2θ at the sample and create an interference pattern with an electric field given by

$$\boldsymbol{E}(\boldsymbol{r},\ t) = \exp(-\mathrm{i}\omega t)(\boldsymbol{A}_A \exp[\mathrm{i}(\boldsymbol{k}_A \cdot \boldsymbol{r} + \phi_A)] + \boldsymbol{A}_B \exp[\mathrm{i}(\boldsymbol{k}_B \cdot \boldsymbol{r} + \phi_B)]). \tag{2.16}$$

Thus,

$$|\boldsymbol{E}(\boldsymbol{r},\ t)|^2 = \boldsymbol{A}_A^2 + \boldsymbol{A}_B^2 + 2\boldsymbol{A}_A \cdot \boldsymbol{A}_B \cos(\boldsymbol{K} \cdot \boldsymbol{r} + \Delta\phi) \tag{2.17}$$

where the grating vector $\boldsymbol{K}$ and the phase difference $\Delta\phi$ have been introduced, which are given by

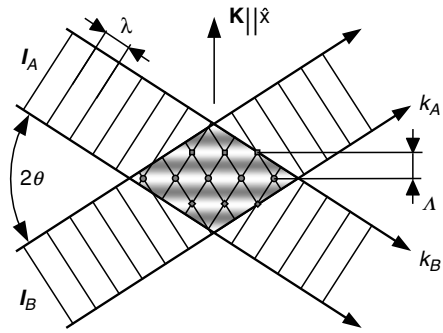

FIGURE 2.1. Interference grating produced by interference of two incident light waves with intensities I_A, I_B and wave vectors $\boldsymbol{k}_A$, $\boldsymbol{k}_B$. For simplicity, we have chosen $\boldsymbol{K} \parallel \hat{\boldsymbol{x}}$.

$$\begin{aligned} \boldsymbol{K} &= \pm(\boldsymbol{k}_A - \boldsymbol{k}_B) \\ \Delta\phi &= \pm(\phi_A - \phi_B) \end{aligned} \tag{2.18}$$

The energy density of the field in the material is therefore given by

$$w = (w_A + w_B)\left(1 + \frac{\Delta w}{w_A + w_B}\cos(\boldsymbol{K}\cdot\boldsymbol{r} + \Delta\phi)\right) \tag{2.19}$$

where

$$\Delta w = \varepsilon_0 \varepsilon'(\boldsymbol{A}_A \cdot \boldsymbol{A}_B) \tag{2.20}$$

is the spatial modulation amplitude of the field energy density and w_A and w_B denote the energy densities associated with the incident beams A and B, respectively. To simplify the analysis, we will in the following choose the coordinate system with respect to the grating so that $\boldsymbol{K} \parallel \hat{x}$ and $\phi_A = \phi_B$.

The spatial period of the intensity grating is referred to as Λ and given by

$$\Lambda = 2\pi/K \tag{2.21}$$

where $K = |\boldsymbol{K}|$. Λ can be expressed in terms of the pump wavelength λ and the angle θ.

$$\Lambda = \frac{\lambda}{2\sin\theta}. \tag{2.22}$$

For small angles $\theta \ll 1$, the grating period is approximately

$$\Lambda \approx \lambda/2\theta. \tag{2.23}$$

Note that, up to now, the wave vectors $\boldsymbol{k}_A$, $\boldsymbol{k}_B$, the wavelength λ and intersection angle 2θ are measured in the material with refractive index n. For nearly normal incidence, Eq. 2.23 is also approximately valid if the wavelength $\lambda_0 = n\lambda$ and the intersection angle $\theta_0 \approx n\theta$ are measured outside the sample, so that $\Lambda = \lambda_0/2\theta_0$ is obtained as long as $\theta_0 \ll 1$ is satisfied. This means that by varying the intersection angle θ_0, the grating period Λ can be changed. The maximum value of Λ is limited by the diameter of the laser beam inducing the grating. Experimentally, values up to approximately 100μm have been used. The smallest grating-period values are achieved when the two excitation beams are antiparallel with $2\theta = 180^\circ$, giving a minimum value of $\Lambda = \lambda/2 = \lambda_0/(2n)$. Using a visible laser and highly refractive material, the grating period may be smaller than 100 nm.

2.2.3 *Superposition of Beams with Different Polarizations*

In many textbooks, interference of two plane light waves with parallel polarization is considered [13]. However, excitation of dynamic gratings is also

possible by interfering beams with different, e.g, perpendicular polarization. Therefore, the general case of superposition of beams with different polarization is treated here. This leads to an interference grating with an amplitude described by a tensor.

In most cases, the modulation amplitude of the energy density Δw or the energy dissipation rate ΔW_f are the significant parameters for optical grating creation if both sample and interaction mechanism are isotropic. In anisotropic media, however, or with anisotropic interaction, gratings may also be induced if $\boldsymbol{p}_A \perp \boldsymbol{p}_B$ or $\Delta W_f = 0$. To account for such a situation, we introduce the *interference tensor* Δm, that is defined as

$$\Delta m_{ij} = \frac{2A_A A_B}{A_A^2 + A_B^2} p_{A,i}\, p_{B,j}, \tag{2.24}$$

where $p_{A,i}$ and $p_{B,j}$ with $i,\ j = x,\ y,\ z$ are the components of the polarization vectors of the incident fields. We can obtain Δw and ΔW_f by evaluating the absolute value of the trace of Δm, e.g.,

$$\Delta w = w_0 |\mathrm{tr}\{\Delta m\}|, \tag{2.25}$$

where $w_0 = w_A + w_B$ is the spatially unmodulated contribution to the field density, so that the spatially dependent field density is then given by

$$w = w_0(1 + |\mathrm{tr}\{\Delta m\}| \cos(Kx)). \tag{2.26}$$

We discuss four important special cases here, which are illustrated in Fig. 2.2:

(a) *s polarization*: $\boldsymbol{p}_A \parallel \boldsymbol{p}_B \parallel \hat{\boldsymbol{y}}$. This is probably the most frequently used experimental situation and also the simplest one. Δm degenerates into the one-element tensor

$$\Delta m = \frac{2A_A A_B}{A_A^2 + A_B^2} \begin{pmatrix} 0 & 0 & 0 \\ 0 & 1 & 0 \\ 0 & 0 & 0 \end{pmatrix}, \tag{2.27}$$

so that in this case, $\Delta w = 2\sqrt{w_A w_B}$. If, in addition, $A_A = A_B$ then $\Delta w = w_0 = 2w_A$ and

$$w = w_0(1 + \cos Kx). \tag{2.28}$$

Thus, the energy density is fully modulated, varying between zero and four times the value for a single beam.

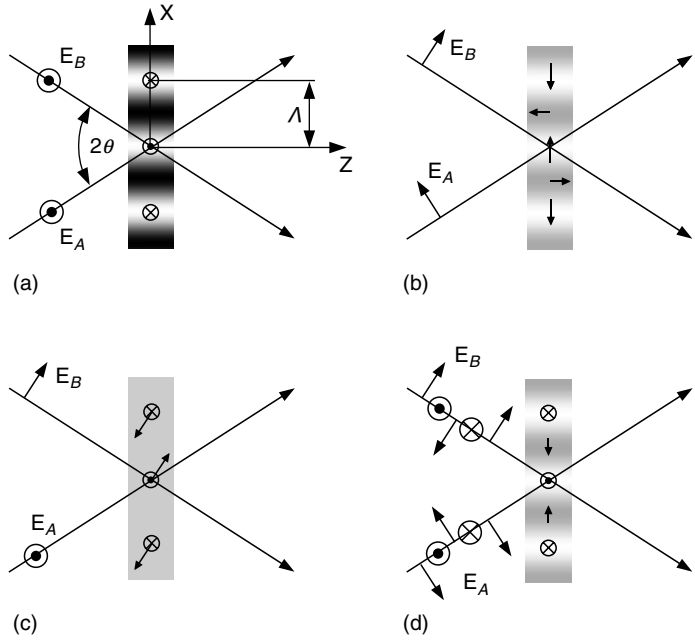

FIGURE 2.2. The four arrangement of pump beam polarizations as discussed in the text. As usual, $\odot$ and $\otimes$ indicate positive and negative directions normal to the paper surface, respectively. The grayscale images illustrate the spatial dependence of the energy density, and the symbols inside indicate the corresponding polarization directions. In (c), the composite symbols indicate vectors that are given by the sum of the two vectors indicated by the individual symbols.

(b) *p polarization*: $\boldsymbol{p}_A \perp \hat{\boldsymbol{y}}$ and $\boldsymbol{p}_B \perp \hat{\boldsymbol{y}}$. In this case, $\boldsymbol{A}_A$ and $\boldsymbol{A}_B$ are in the xz-plane and the interference tensor is given by

$$\Delta m = \frac{2A_A A_B}{A_A^2 + A_B^2} \begin{pmatrix} p_{Ax}p_{Bx} & 0 & p_{Ax}p_{Bz} \\ 0 & 0 & 0 \\ p_{Az}p_{Bx} & 0 & p_{Az}p_{Bz} \end{pmatrix}, \tag{2.29}$$

which can be written as

$$\Delta m = \frac{2A_A A_B}{A_A^2 + A_B^2} \begin{pmatrix} \cos^2\theta & 0 & \frac{1}{2}\sin(2\theta) \\ 0 & 0 & 0 \\ -\frac{1}{2}\sin(2\theta) & 0 & -\sin^2\theta \end{pmatrix}, \tag{2.30}$$

where 2θ is the angle between the writing beams (see Fig. 2.1), and corresponds to an energy density modulation

$$\Delta w = w_0 |\mathrm{tr}\{\Delta m\}| = 2\sqrt{w_A w_B}(\cos^2\theta - \sin^2\theta). \tag{2.31}$$

The physical interpretation of Δm is as follows: Depending on the relative phase Kx of the two pump beams along x, the superposition of $\boldsymbol{A}_A$ and $\boldsymbol{A}_B$ results in a polarization varying between linear (for $Kx = 0$ and $Kx = \pi$) and elliptic. At $2\theta = 90^\circ$, the intensity modulation disappears completely since $\boldsymbol{p}_A \perp \boldsymbol{p}_B$ in this case. The interference field polarization is particularly interesting if, in addition, $A_A = A_B$. It points into the x-direction for $Kx = 0$, becomes circular at $Kx = \pi/2$, and finally, at $Kx = \pi$, it is linear in the z-direction, i.e., a longitudinal field with respect to the interference pattern (see Fig. 2.2(b)). Interestingly, the polarization interference pattern can be made visible by placing a dichroic medium such as a polaroid foil into the zone of interaction. Thus, for the investigation of optically anisotropic media, perpendicular polarization can be of interest.

(c) *Mixed linear polarization*: $\boldsymbol{p}_A \parallel \hat{\boldsymbol{y}}, \boldsymbol{p}_B \perp \hat{\boldsymbol{y}}$. In this case, the electric fields of the excitation beams are perpendicular ($\boldsymbol{A}_A \perp \boldsymbol{A}_B$) for any value of θ. The interference tensor is

$$\Delta m = \frac{2A_A A_B}{A_A^2 + A_B^2} \begin{pmatrix} 0 & 0 & 0 \\ p_A p_{Bx} & 0 & p_A p_{Bz} \\ 0 & 0 & 0 \end{pmatrix}. \tag{2.32}$$

No energy density modulation exists. The field amplitude undergoes periodic changes between linear and elliptic polarizations dependent on the relative phase Kx similar to the case of two p_polarized beams with $2\theta = 90^\circ$ discussed before.

(d) *Opposite circular polarization with equal amplitudes*: In this case, we have $A_A = A_B$ and the polarization vectors of the two beams are given by

$$\boldsymbol{p}_{A,B} = \frac{1}{\sqrt{2}}(\pm \cos\theta \hat{\boldsymbol{x}} + \mathrm{i}\hat{\boldsymbol{y}} + \sin\theta \hat{z}). \tag{2.33}$$

The interference tensor is

$$\Delta m = \begin{pmatrix} -\cos^2\theta & \mathrm{i}\cos\theta & \frac{1}{2}\sin(2\theta) \\ -\mathrm{i}\cos\theta & -1 & \mathrm{i}\sin\theta \\ -\frac{1}{2}\sin(2\theta) & \mathrm{i}\sin\theta & \sin^2\theta \end{pmatrix}, \tag{2.34}$$

The modulation of the energy density is then

$$\Delta w = 2w_0 \sin^2\theta \tag{2.35}$$

which becomes vanishingly small for $\theta \to 0$, while the polarization tends to become linearly polarized and rotating with the grating period Λ across the grating structure, as indicated in Fig. 2.2(d). This choice of polarization is favorable for studying optically active interactions or media because circular polarization is preserved when a laser beam propagates there.

2.2.4 Superposition of Short Pulses

Present-day mode-locked lasers provide pulses of very short duration, ranging down to the fs regime [18], equivalent to a physical lengths smaller than 0.1 mm. In order to make the beams overlap, sophisticated experimental arrangements have been devoleped [19, 20] The interference of two beams derived from such a source depends on the delay between the pulse fractions traveling along paths A and B. The time dependence of such pulses is close to Gaussian with half width t_p

$$I_{A,B}(t) = \hat{I}_{A,B} \exp\left\{ -\left[\frac{t \pm \tau/2}{t_p}\right]^2 \right\}, \tag{2.36}$$

where τ is the delay of pulse B with regard to A, and $\hat{I}_{A,B} = \frac{1}{2} nc\varepsilon_0 \hat{A}^2_{A,B}$ are the peak intensities of the two pulses. The magnitude of the interference tensor in this case also depends on the overlap of the two pulses given by the ratio τ/t_p, i.e.,

$$\Delta m_{ij} = \frac{2A_A A_B}{A_A^2 + A_B^2} p_{A,i} p_{B,j} \exp\left\{ -\left[\frac{\tau}{2t_p}\right]^2 \right\} \exp\left\{ -\left[\frac{t}{t_p}\right]^2 \right\}. \tag{2.37}$$

Thus, the temporal behavior of $\Delta m(t)$ is the same as that of the original pulse(s), but its amplitude decreases in proportion to $\exp\{-[\tau/2t_p]^2\}$.

2.2.5 Influence of Coherence Properties

Interference of light beams will only be observed as long as the light beams are mutually coherent. Coherence corresponds to the correlation properties between quantities describing the optical field. The temporal coherence function $\Gamma(\tau)$ of a light wave (or light pulse) is defined as the autocorrelation function of the complex field amplitude $\boldsymbol{E}$

$$\Gamma(\tau) = \int_{-\infty}^{\infty} \mathbf{E}^*(t)\mathbf{E}(t+\tau)dt. \tag{2.38}$$

The normalized coherence function given by

$$\gamma(\tau) = \frac{\Gamma(\tau)}{\Gamma(0)} \tag{2.39}$$

is used to determine the coherence $|\gamma(\tau)|$ of a laser beam. For an ideal plane wave of monochromatic light, a value of 1 is obtained for all values of τ. For real light sources, the coherence will decrease with increasing $|\tau|$, and the optical coherence length is defined by the width of the coherence function $|\gamma(\tau)|$. The power spectrum of the light $G\ (f)$ and the absolute value of the coherence

function are related by a Fourier transform relationship, the Wiener–Khintchine theorem [13]

$$G(f) = \int_{-\infty}^{\infty} \gamma(\tau) \exp(\mathrm{i}2\pi f\tau) d\tau. \tag{2.40}$$

For a single longitudinal mode laser with Gaussian line shape, the coherence function is given by a Gaussian distribution with its width being inversely proportional to the laser linewidth. For laser light sources with discrete emission frequencies like, e.g., diode lasers in longitudinal multimode operation, the coherence function is more complicated. It is given by a Gaussian envelope with a width determined by the linewidth of a single longitudinal mode, containing oscillations with a spacing inversely dependent on the frequency spacing between the longitudinal laser modes.

It is possible to determine the absolute value $|\gamma(\tau)|$ by measurement of the interference fringe modulation, e.g., using photorefractive index gratings induced by pump and signal beam from the same source and variable optical path delay τ [21]. For the excitation of laser-induced gratings, the optical path length difference of the involved beams must be adapted to the coherence function of the used laser source.

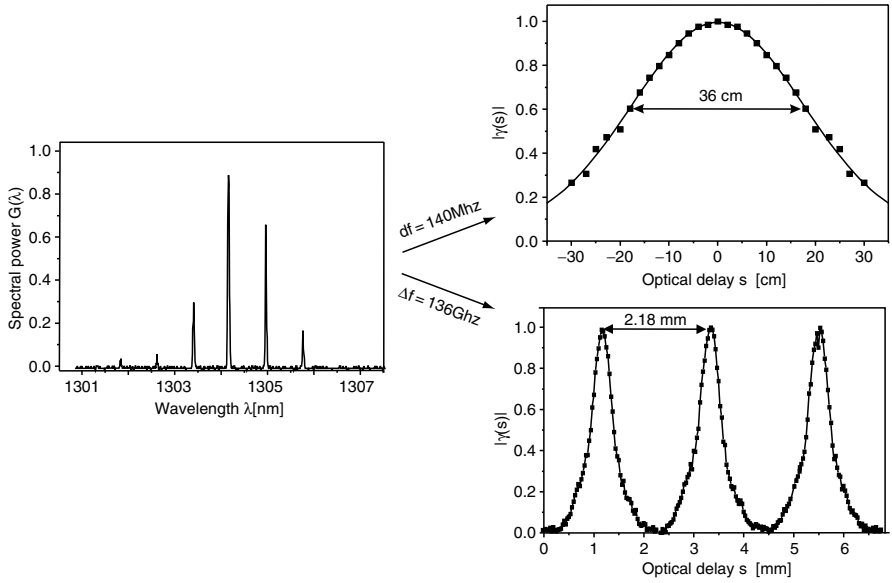

FIGURE 2.3. Relationship between power spectrum (left curve) and coherence function (right curves) of a diode laser. The upper right curve shows the envelope of the coherence function, its width given by the line width of a single longitudinal laser mode $df = 140$ MHz.The lower right curve shows the modulation contained in the envelope. Spatial periodicity of 2.18 mm corresponds to longitudinal mode spacing of $\Delta\lambda = 0.77$ nm, equivalent to $\Delta f = 136$ GHz. [21]

Note also that the spatial coherence of a laser beam can be determined by diffraction at laser-induced gratings [22]. The spatial coherence function of a Gaussian laser beam with waist ρ_0 is given by

$$\frac{\Gamma(s)}{\Gamma(0)} = \exp\frac{-s^2}{2\rho_0^2}\exp\frac{-\phi_0^2(s)}{2}, \tag{2.41}$$

where $\phi_0^2(s)$ is the mean square change of the phase difference $\Delta\phi$ between two points P_1 and P_2 in a plane normal to the direction of propagation. For a linear dependence $\phi_0^2(s)$, the spatial coherence is also given by a Gaussian function that was indeed observed in the diffraction experiment.

2.2.6 Finite Size Effects

The finite cross-section of the pump-laser beams limits the lateral extent of the interference zone. Hence, the electric-field amplitudes and intensities in Eqs. 2.17–2.20 are slowly varying functions of all spatial coordinates x, y, and z in addition to the modulation with respect to the x-direction. Calculation of the spatial variation is straightforward assuming TEM_{00} beams, but involves a lengthy notation. The interference between two TEM_{00} beams will obviously come close to an ideal plane grating if the following three conditions can be met:

1. The minimum width w of the interaction zone must be large compared to the grating period, i.e.,

$$Kw \gg 1. \tag{2.42}$$

2. The overlap length z_0 of the two beams in z-direction must be large compared to the sample thickness d,

$$z_0/d \gg 1. \tag{2.43}$$

3. The attenuation of the exciting beams must be negligible within the sample, i.e.,

$$\alpha d \ll 1, \tag{2.44}$$

where α is the absorption constant of the material at wavelength λ.

The first condition puts a limit on focusing of the pump beams to increase intensity; the second puts a limit on the angle 2θ between the beams; and the third puts a limit on pump beam utilization by absorption.

The description of a laser-induced grating is particularly straightforward if the above three conditions are satisfied experimentally. In the following discussion, we shall assume this to be the case unless mentioned otherwise.

Note that the results stay qualitatively correct even if one or several of the conditions are satisfied marginally only.

Extremely large values of Λ would require inconveniently small angular beam separations 2θ. Under such circumstances, it is possible to use one pump beam only, and to produce the grating by insertion of a comb-like aperture. Values of Λ up to 4 mm were obtained in this way [23]. There is no obvious upper limit to the period of gratings produced in this manner—except that the laser beam's cross-section has to be increased proportionally, thus lowering the intensity available for the pumping process.

2.2.7 *Frequency Offset Effects*

The grating is stationary in position when the two beams have the same frequency. When the two excitation beams have slightly different frequencies $\omega_A \neq \omega_B$ and wave vectors $\boldsymbol{k}_A$ and $\boldsymbol{k}_B$, they can be described by the fields

$$\boldsymbol{E}_i = \boldsymbol{A}_i \exp[\mathrm{i}(\boldsymbol{k}_i \cdot \boldsymbol{r} - \omega_i t], \qquad i = A, B, \tag{2.45}$$

where $\boldsymbol{A}_A$ and $\boldsymbol{A}_B$ are the amplitude vectors of the beams, which for simplicity assumed to be parallel. In a region where the beams intersect, an energy density

$$w = \frac{1}{2}\varepsilon_0 \varepsilon'(A_A^2 + A_B^2 + A_A A_B \exp\{\mathrm{i}[(\boldsymbol{k}_A - \boldsymbol{k}_B) \cdot \boldsymbol{r} - (\omega_A - \omega_B)t]\}) \tag{2.46}$$

will be created. When deriving this equation, averaging has been performed over times that are long compared to the optical periods of the light fields $2\pi/\omega_A$ and $2\pi/\omega_B$, but short compared to the period $2\pi/(\omega_A - \omega_B)$ corresponding to the difference frequency.

The field energy density w exhibits a wavelike modulation with a grating vector $\boldsymbol{K}$ and a frequency Ω given by

$$\boldsymbol{K} = \boldsymbol{k}_A - \boldsymbol{k}_B \tag{2.47}$$

$$\Omega = |\omega_A - \omega_B|. \tag{2.48}$$

The direction wave vector $\boldsymbol{K}$ is given without the ambiguity that exists in the case of stationary interference patterns. If the material response is fast enough, the frequency offset Ω between the two writing beams will cause traveling grating structures in the material.

2.3 Material Response: Amplitude and Phase Gratings

The mechanisms of light-induced changes of optical materials properties are often described as having two steps. First, the light produces some material excitation, which then leads to a change of the optical properties. In the simplest case, the absorption and the refraction of the material are changed, resulting in amplitude and phase gratings.

Light-induced refractive index changes can in general be referred to as photorefraction. However, the term ''photorefractive effect'' is often used in a more restricted way, describing refractive index changes due to electrooptic effects generated by electric space charge distributions, which are caused by inhomogenous light irradiation, as will be discussed in Section 2.3.6.

2.3.1 Material Excitation Gratings

When a material is placed into the interference region of the pump waves, some light–matter interaction such as absorption creates a corresponding spatial modulation (grating) of some material property [9], e.g., the population of an excited electronic state, the conduction electron density (in a semiconductor [24]), the space charges and their accompanying fields (in photorefractive materials [25]), or the temperature [26] , the molecular orientation (of liquid crystals [27]), or the concentration (in polymer mixtures) [28].

Many of these changes can be described by the population of one, several, or a whole continuum of excited (e.g., electronic or phonon) states of the sample material. Hence, the corresponding gratings can also be considered population gratings in a generalized sense.

The description in terms of excited-state populations is necessary if the local population density is out of thermal equilibrium. This is usually the case if the excited-state energy is far above the thermal energy $k_B T$, which at room temperature is about 25 meV. Strong deviations from thermal distribution can also occur during radiationless decay from the primarily excited electronic state. In solids, the energy freed during such a process may create hot phonons which, in turn, decay into cooler ones until thermal energies are reached. This process is very fast because hot-phonon lifetimes are on the subpicosecond scale. Since today's mode-locked lasers provide pulses down to femtosecond duration such transient effects can play a role in experiments with extremely high-time resolution. In other materials, it is also possible that long-lived intermediate states of different nature get populated during the decay, particularly at low temperatures. This can considerably slow down the thermalization process, giving rise to secondary grating structures with their own characteristic properties and decay times.

Once the absorbed energy is thermalized locally, the description of the resulting grating in terms of the usual thermodynamic variables, temperature concentration, etc., is appropriate and convenient (compare Fig. 2.4). The sample as a whole is not in equilibrium as long as these quantities still vary spatially. Their equilibration requires transport of heat, matter, etc., which usually occurs by diffusion. Thus, their decay time depends on the magnitude of the excitation gradients, and hence, the $\boldsymbol{K}$ vector of the grating.

Note that a diffusion process, in general, does not change the center position of the excited region but tends to smear out its spatial profile. Hence, a grating stays stationary during diffusive decay, i.e., its phase stays constant while its amplitude decreases monotonically.

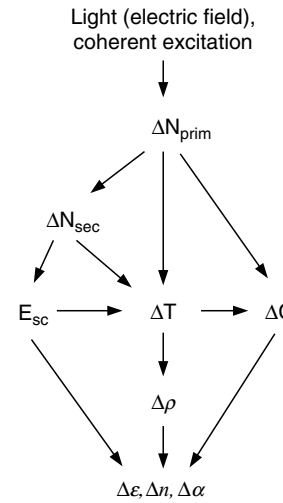

FIGURE 2.4. Possible sequences of material excitations produced by a short laser pulse. N_{prim}, N_{sec}: primary and secondary population density of excited electronic levels, E_{sc}: space charge field, ΔT: temperature change, ΔC: concentration change, $\Delta\rho$: density change, $\Delta\varepsilon$: permittivity change, Δn: refractive index change, and $\Delta\alpha$: absorption change.

The dependence of the material excitation on the light intensity or energy density depends on its dynamics and cannot generally be expressed by a simple function. The time dependence of the material excitation is often described by a differential equation with the pump light intensity as a source term.

Under stationary conditions, the material excitation amplitude ΔX is proportional to the modulated energy density amplitude Δw in the simplest case

$$\Delta X = g^P(\lambda)\Delta w(\lambda), \tag{2.49}$$

where g^P is a coupling coefficient, which depends on the type of material excitation and the pump wavelength λ. The right-hand side may be considered as the first term of a power series describing the general relations between ΔX and Δw. Depending on the nature of excitation, ΔX can be a scalar (temperature, etc.), vector (electric field, flow velocity), or tensor (stress, strain, orientational distribution of excited molecules). Thus, it is convenient for further discussions to rewrite Eq. 2.49 in tensorial form and use the interference modulation tensor Δm

$$\Delta X_{ij} = \sum_{k,l} g^p_{ijkl}\Delta m_{kl}. \tag{2.50}$$

Here i, j, k, l stand for the spatial coordinates x, y, and z. In general, g^p_{ijkl} is a fourth-rank tensor. Note that the tensorial product in Eq. 2.50 allows for a nonvanishing ΔX_{ij} even if $\boldsymbol{p}_A \perp \boldsymbol{p}_B$, i.e., vanishing intensity modulation. Such odd contributions to ΔX_{ij} are needed to account for polarization dependent interactions such as the dichroic bleaching of a dye.

2.3.2 Refractive Index and Absorption Gratings

The material excitation, in general, couples to the refractive index and absorption coefficient, which then also exhibit a grating-like modulation with ampli-

tudes $\Delta n(\lambda)$ and $\Delta\alpha(\lambda)$. Both Δn and $\Delta\alpha$ are, of course, functions of the probe wavelength λ. The refractive-index modulation caused by a temperature grating, for example, is $\Delta n = (\partial n/\partial T) \cdot \Delta T$, where ΔT is the temperature amplitude and $(\partial n/\partial T)$ the thermo-optic coefficient. Generally speaking, any modulation of a material property with amplitude ΔX inside a medium will be accompanied by an optical grating with amplitudes

$$\Delta\alpha = (\partial\alpha/\partial X)\Delta X, \tag{2.51}$$

$$\Delta n = (\partial n/\partial X)\Delta X, \tag{2.52}$$

where the tensor character of ΔX has been ignored for the moment. Quite frequently, one of the coupling constants $(\partial n/\partial X)$ and $(\partial\alpha/\partial X)$ is very small; the grating is then either of the phase or the amplitude type.

Using the complex refractive index $\hat{n}$, the more general expression

$$\Delta\hat{n} = (\partial\hat{n}/\partial X)\Delta X \tag{2.53}$$

is obtained. The complex refractive index $\hat{n}$ is related to the complex optical frequency dielectric constant ε_r and the susceptibility χ by

$$\hat{n} = \sqrt{\varepsilon}_r = \sqrt{1+\chi} \tag{2.54}$$

$$\Delta\hat{n} = \frac{\Delta\varepsilon_r}{2\sqrt{\varepsilon}_r} = \frac{\Delta\chi}{2\sqrt{1+\chi}}. \tag{2.55}$$

Thus, an optical grating corresponds to a spatial modulation of any of the quantities $\hat{n}$, ε_r, or χ. Following Eqs. 2.6 and 2.7, the relation to the refractive index and absorption properties is given by

$$\Delta\varepsilon_r = \Delta\chi = \Delta(\hat{n}^2) = 2n\Delta n + \frac{c^2}{2\omega^2}\alpha\Delta\alpha + \mathrm{i}\frac{c}{\omega}(\alpha\Delta n + n\Delta\alpha). \tag{2.56}$$

In many cases, the absorption of the material is weak ($\alpha \ll 2\omega/c$) and the two addends directly proportional to α may be neglected.

2.3.3 Tensor Gratings

It is important that ε_r and χ are tensors, in general, while $\hat{n}$ is not. Therefore, if anisotropic interaction is important, susceptibilities should be used for general description. Specifically, the susceptibility component χ_{ij} connects the electric-field component E_j, with the polarization density component P_i (where again $i, j = x, y, z$) by means of

$$P_i = \varepsilon_0\chi_{ij}E_j \tag{2.57}$$

$$\Delta P_i = \varepsilon_0\Delta\chi_{ij}E_j. \tag{2.58}$$

The tensorial character of $\Delta\chi_{ij}$ includes induced birefringence and dichroism, i.e., a polarization-dependent refractive index and absorption coefficient. Because both ΔX and $\Delta\chi$ are generally tensors of rank 2, the coupling constant between them is of rank 4, namely,

$$\Delta\chi_{ij} = \sum_{k,l} (\partial\chi_{ij}/\partial X_{kl})\Delta X_{kl}. \tag{2.59}$$

χ_{ij}, $\Delta_{\chi ij}$, and $(\partial_{\chi ij}/\partial X_{kl})$ are generally complex numbers to account for both index of refraction and absorption. Eq. 2.59 shows that the anisotropy of $\Delta\chi_{ij}$ may be either due to the sample medium itself (crystals, external forces, flow), or be induced by the grating formation process. Even in an isotropic solid, anisotropy may be introduced by, e.g., thermal expansion, and namely strain along the direction of $\boldsymbol{K}$ but stress in the planes perpendicular to $\boldsymbol{K}$. Eq. 2.59 can be combined with Eq. 2.50 to connect the optical grating amplitude directly with the pump field under stationary conditions

$$\Delta\chi_{ij} = \sum_{k,l} f_{ijkl}\Delta m_{kl}, \text{ where} \tag{2.60}$$

$$f_{ijkl} \equiv \sum_{k',l'} (\partial\chi_{ij}/\partial X_{k'l'}) \cdot g^{p}_{k'l'kl}. \tag{2.61}$$

2.3.4 Population Density Gratings in Solids and Liquids

If an atomic system is excited from the ground to an upper state, the absorption coefficient and refractive index change, which can be observed in a grating experiment. In the following, we shall outline some basic equations connecting the intensity of the exciting light field to the change of the optical properties that determine the diffraction properties of the corresponding grating.

Light-induced changes of level population. We will consider simplified atomic systems where the incident light couples only two electronic-energy levels with population densities N_a of the lower level and N_b of the upper level, respectively. The quantity $\Delta N = N_a - N_b$ can be determined by solving the rate equation

$$\frac{\partial N_a}{\partial t} = \frac{N_b}{\tau} - \frac{\sigma wc}{\hbar\omega_0}(N_a - N_b), \tag{2.62}$$

where τ denotes the lifetime of the upper level, σ the absorption cross section, and $\hbar\omega_0$ the energy difference between the involved levels. Note that the product wc corresponds to the intensity I in many cases.

Most of the relevant materials, however, are better described as 3-level-systems in which only two levels are strongly populated. Excitation from the ground state with population density N_0 will create a small population in an intermediate state, that rapidly decays into state with slightly lower energy, having a population density N_1 and a lifetime τ. The rate equation is then

$$\frac{\partial N_0}{\partial t} = \frac{N_1}{\tau} - \frac{\sigma w c}{\hbar \omega_0} N_0. \tag{2.63}$$

In the steady state,

$$\Delta N = N \frac{w/w_s}{1 + w/w_s} \text{ with } w_s = \frac{\hbar \omega_0}{\sigma \tau c}. \tag{2.64}$$

Note that the quantity ΔN will vary spatially with a spatially dependent energy density w, leading to the creation of optical gratings.

Change of optical properties of the material. The 2-level system with transition frequency ω_0 and a half width $1/\tau_{pd}$ of the absorption curve will lead to a polarization density of the material corresponding to a susceptibility [11]

$$\chi = \frac{\mu^2}{\hbar \varepsilon_0} \frac{(N_a - N_b)}{(\omega_0 - \omega) + (\mathrm{i}/\tau_{pd})}, \tag{2.65}$$

where τ_{pd} is referred to as polarization decay time or phase relaxation time, and μ denotes the dipole matrix element of the transition. Depending on the ratio $q = (1/\tau_{pd})/|\omega - \omega_0|$, the grating can be approximated by a pure phase grating ($q \gg 1$) or a pure amplitude grating ($q \ll 1$).

Population density gratings have been investigated experimentally in doped crystals (e.g., Cr ions in ruby, Nd ions in YAG) and also in dye solutions [9]. Spatial holes burnt into the upper-level population of laser materials and carrier distribution gratings in semiconductors can also be considered population density gratings. In semiconductors, however, the effects need to be described using spatially dependent equations as transport mechanisms for the carriers need to be taken into account.

2.3.5 Gratings in Semiconductors

In solid state crystals like semiconductors, the electronic-energy levels are not discrete with respect to their energy like in single atoms. Instead these levels are contained in several energy bands, and their density within these bands, referred to as density of states ρ, is dependent on their associated energy E. Most relevant to the description of the optical properties of semiconductors are the valence band and the conduction band, which are separated by a band gap energy $E_g = E_c - E_v$, where E_c is the lowest and E_v the highest possible energy in the respective bands. Close to this band gap, the density of states for electrons in the conduction band can be approximated by

$$\rho_c(E) = \frac{(2m_c)^{3/2}}{2\pi^2 \hbar^3} \sqrt{E - E_C}, \tag{2.66}$$

where m_c denotes the effective mass of an electron in the conduction band when moving within the lattice. Please note that here and throughout this section, similar expressions are obtained for the quantities related to the valence band, but will be omitted as the relationships for the conduction band are sufficient to understand the concepts of the model. If needed, quantities related to the valence band will be denoted using the subscript v rather than c for the conduction band without further notice.

In thermal equilibrium, the probability that an electronic state is actually taken by an electron is given by the Fermi function f_c of the conduction band

$$f_c(E) = \frac{1}{\exp[(E - F_c)/k_B T] + 1}, \tag{2.67}$$

where k_B denotes the Boltzmann number and F_c denotes the Fermi energy of the conduction band. This Fermi energy determines the electron density in the conduction band N_c by the integral

$$N_c = \int_{E_c}^{\infty} \rho_c(E) f_c(E) dE, \tag{2.68}$$

and vice versa.

Each electronic state given by a certain wave function is also associated with a certain momentum $\hbar k$. While in general the relation between the associated energy and wave number k of a state can be quite complicated; we will limit our discussion to electronic states close to the band gap where the relationship

$$\hbar k = \sqrt{2m_c(E - E_c)} \tag{2.69}$$

holds. The density of states is approximately given by $\rho(k) = k^2/\pi^2$ in both the valence and conduction bands. The conservation of momentum $\hbar k$ needs to be considered in processes like optical transitions.

Optical transitions in semiconductors. Absorption of light leads to transitions of the electrons so that excited states are populated. The polarizability of the excited electrons is different from the ground-state polarizability, similar to the situation described in Section 2.3.4. In semiconductors, the transitions may take place from the valence to the conduction band (interband transitions) or within a band (intraband transitions).

The density of systems N_b in the excited state can be obtained from solving a suitable rate equation describing the generation and recombination processes

$$\frac{\partial N_b}{\partial t} = \frac{\sigma w c}{\hbar \omega}(N_a - N_b) - \frac{N_b}{\tau}. \tag{2.70}$$

Here τ is the recombination time, σ the absorption cross-section of the transition, and N_a the density of systems in the ground state. Note that there may be several decay mechanisms involved that can make it necessary to replace the

recombination rate N_b/τ by a more complicated relationship, like a Taylor expansion $AN_b + BN_b^2 + CN_b^3 + \ldots$, where the coefficients *A, B, C* are attributed to different decay mechanisms, e.g., intraband relaxations. For small light intensities, the density of excited electrons is obtained as

$$\frac{N_b}{N_a + N_b} = \frac{\sigma \tau w c}{\hbar \omega}. \tag{2.71}$$

In semiconductors, there are also grating decay mechanisms, that may not be described solely by time-dependent equations. Diffusion of the carriers involved will cause a spatially dependent current density $\boldsymbol{J}_{\text{diff}}$, that may significantly contribute to the carrier grating that is eventually obtained and, especially in experiments with pulsed laser sources, its lifetime.

Carrier diffusion. Because of the spatial gradient of the electron density, diffusion processes will occur and create a current density of the electrons

$$\boldsymbol{J}_{\text{diff}} = qD\nabla N_c, \tag{2.72}$$

where D is the diffusion constant of the material, which in general is a tensor quantity, and $q = \pm e$ the charge of the carrier. The holes will create a corresponding diffusion current. The spatially dependent rate equation is then

$$\frac{\partial N_b(x,\ t)}{\partial t} = \frac{\sigma c w(x,\ t)}{\hbar \omega}\ (N_a - N_b) - \frac{N_b(x,\ t)}{\tau} + \frac{1}{q}\nabla \cdot \boldsymbol{J}_{\text{diff}}(x,\ t). \tag{2.73}$$

Note that in this case, it becomes possible that the maximum of the light field modulation will be spatially separated from the maximum number of excited carriers. We will discuss such effects in Section 2.3.6.

The modulated carrier densities lead to corresponding changes of the optical properties, thereby forming a grating. We will limit our discussion of the grating creation to two effects: the bleaching of the interband absorption and the absorption caused by free carriers in the bands.

Bleaching of the interband absorption. In direct semiconductors, interband transitions lead to a depletion of the absorbing electrons in the valence band. In addition, the density of the unpopulated energy states in the conduction band is reduced. The wave number of the electronic states is determined by the conservation of momentum and by the band structure as

$$\hbar k(\omega_0) = \sqrt{2m_r(\hbar\omega_0 - E_g)}\ , \tag{2.74}$$

where ω_0 is the frequency of the light wave, and $m_r = (1/m_c + 1/m_v)^{-1}$ is the reduced effective mass of the electron-hole pair (see Fig. 2.5). Electrons within an interval of width Δk around this wave number may be involved in the transition, because the energy of the involved states is also known within a certain interval only (due to the uncertainty principle). This energy interval is determined by intraband relaxation processes as $\Delta E = \hbar/\tau_{relax}$.

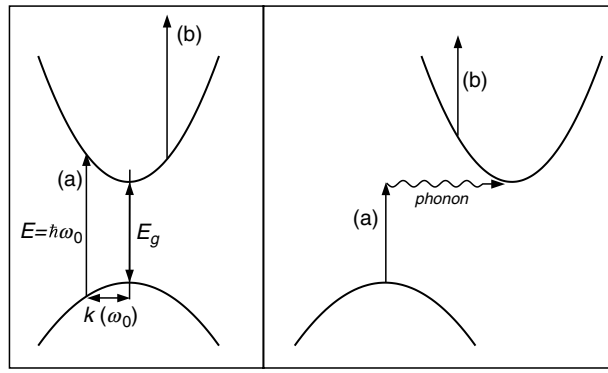

FIGURE 2.5. Optical transitions in direct (left image) and indirect (right image) semiconductors. The curves shown indicate the electron energy of the valence band (lower curve) and conduction band, respectively, as a function of the wavenumber k. Interband transitions (denoted with letter (a)) can take place if $\Delta k = 0$ in the direct semiconductor, or involving a phonon in the indirect semiconductor material. Intraband absorption of free carriers is denoted with letter (b).

The density of the states for each of the levels involved may be expressed as

$$N = \rho(k) f(k) \Delta k \tag{2.75}$$

so that the difference $(N_a - N_b)$ of the populations of the two states with their respective energies $E_a,\ E_b$ can be expressed as

$$N_a - N_b = \frac{(2m_r)^{3/2}}{\pi \hbar^2 \tau_{relax}} \sqrt{\hbar\omega - E_g}\,(f_c(E_b) - f_v(E_a)) \tag{2.76}$$

and the change of the absorption constant $\Delta\alpha(\omega) = \sigma(N_a - N_b)$ can be calculated.

The change of the absorption coefficient is accompanied by a change of the refractive index Δn. It is possible to estimate Δn using the Kramers–Kronig relation [29].

$$\Delta n = \frac{c}{\pi} \int_0^\infty \frac{\Delta\alpha(\omega')}{\omega'^2 - \omega^2} d\omega'. \tag{2.77}$$

The change of the absorption coefficient and the refractive index can be combined to express a change of the complex susceptibility. From Eq. 2.56 with $\alpha \ll 2\omega/c$, we obtain

$$\Delta\varepsilon_r(\omega) = 2n\Delta n + i\frac{nc}{\omega}\Delta\alpha. \tag{2.78}$$

Free-carrier absorption. In indirect band-gap semiconductors like silicon, the absorption of radiation at a frequency corresponding to the band-gap energy does not lead to absorption bleaching. On the contrary, the absorption increases due to transitions within the conduction and valence bands. The frequency dependence of the corresponding change of the permittivity ε_r may be approximately described by the classical Drude model that treats the electrons and holes as quasifree carriers oscillating in the light field [30]

$$\Delta\varepsilon_r(\omega) = \frac{Ne^2}{\varepsilon_o m_r \omega(\omega + \mathrm{i}/\tau_{\mathrm{relax}})^2}. \tag{2.79}$$

Here N is the population density of the optically excited electron–hole pairs and τ_{relax} is the relaxation time.

2.3.6 Photorefractive Gratings in Electro-Optic Crystals

The photorefractive effect is caused by free carriers, which are released due to ionization of donors or acceptors in electro-optic materials. The light driving the effect has an optical frequency ω smaller than $E_g/\hbar$, because the energy of these so-called photorefractive centers is situated within the band-gap. Important examples for photorefractive electro-optic crystals are $LiNbO_3$, $BaTiO_3$, KNSBN, or $Sn_2P_2S_6$. We will limit our discussion to a single center model, with a single trap level, acting as a donor, and electrons as carriers. For deeper understanding of many photorefractive materials, more sophisticated models are needed [31].

Like in semiconductors, a spatially dependent carrier distribution is created by the light field. The corresponding space charge ρ creates an electric field E_{sc}. Apart from its influence to carrier transport processes, this field is responsible for the change of the ε_r tensor by means of the electro-optic effect.

2.3.6.1 Generation and Recombination Processes

The generation and recombination processes are described by the densities N_D and N_D^+ of the donor atoms and the ionized donor atoms, respectively, and by the density of the electrons in the conduction band N_c by the rate equation

$$\frac{\partial N_D^+}{\partial t} = \left(\frac{\sigma c w(x,\ t)}{\hbar\omega} + \beta\right)(N_D - N_D^+) - \gamma_R N_c N_D^+, \tag{2.80}$$

where β is a rate constant describing the thermal excitation, and γ_R denotes the recombination constant. Note that the ionized donors cannot change positions, while the electrons will create a current density $\boldsymbol{J}$, so that the rate equation for the electron density is

$$\frac{\partial N_c}{\partial t} = \frac{\partial N_D^+}{\partial t} + \frac{1}{e}\nabla \cdot \boldsymbol{J}. \tag{2.81}$$

2.3.6.2 Transport Phenomena

The current density $\boldsymbol{J}$ consists of three important contributions. The creation of a diffusion current density $\boldsymbol{J}_{\text{diff}}$ has already been discussed in Section 2.3.5. Here, we have two other important contributions: drift currents induced by an electric field obtained as the sum of an initrinsic space charge field, and an external electric field applied to the material and photovoltaic currents.

Drift. The spatially dependent carrier concentration causes a space charge field $\boldsymbol{E}_{sc}$. This intrinsic electric field and a possibly externally applied field $\boldsymbol{E}_{ext}$ will add up, and create a current density

$$\boldsymbol{J}_{\text{drift}} = qN_c\mu_c(\boldsymbol{E}_{sc} + \boldsymbol{E}_{ext}), \tag{2.82}$$

where μ_c denotes the mobility of the electrons. For the holes, an equivalent correlation applies. The diffusion constant and the mobility are related by $D = \mu_c k_B T/q$.

Photovoltaic effect. In piezoelectric materials, photoelectrons are excited into the charge transfer band with a preferential direction of the velocity along the direction of the polar axis. Additional current contributions due to anisotropic electron trapping and ion displacement are also possible. The current density is given by

$$\boldsymbol{J}_{\text{ph}} = -\beta_{ijk}E_jE_k^*. \tag{2.83}$$

The overall current density is given by $\boldsymbol{J} = \boldsymbol{J}_{\text{diff}} + \boldsymbol{J}_{\text{drift}} + \boldsymbol{J}_{\text{ph}}$.

2.3.6.3 Space Charge Field and Electro-Optic Effect

The space charge field induced by the carrier distribution will satisfy Maxwell's equation

$$\nabla \cdot (\varepsilon \boldsymbol{E}) = \rho \tag{2.84}$$

and can be determined from the space charge distribution using the Coulomb law for anisotropic media [32]. For $\rho = \rho_0 \cos(\boldsymbol{K} \cdot \boldsymbol{r})$ as the first harmonic component of the space charge distribution induced by the energy density modulation in the material created by the incident light waves, the integration leads to [6]

$$\boldsymbol{E}_{sc} = \rho_0 \frac{\boldsymbol{K}}{\boldsymbol{K} \cdot \varepsilon \boldsymbol{K}} \sin(\boldsymbol{K} \cdot \boldsymbol{r}) = \boldsymbol{E}_1 \cos(\boldsymbol{K} \cdot \boldsymbol{r} - \pi/2), \tag{2.85}$$

where $\boldsymbol{E}_1 \parallel \boldsymbol{K}$ has been introduced as the amplitude of the space charge field. The phase shift of $\pi/2$ means that the space charge field is spatially shifted by $\Lambda/4$ with respect to the energy density modulation, as indicated in Fig. 2.6. When no external field is applied to the material (diffusion-driven effect), the

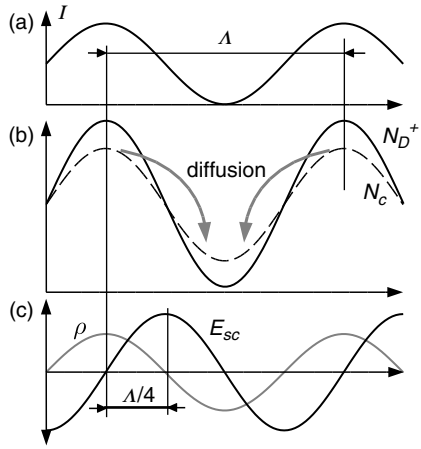

FIGURE 2.6. Photorefractive grating build-up: (a) the stationary intensity pattern with grating constant Λ, (b) distribution of ionized donors N_D^+ and electrons N_c. The latter distribute by diffusion. (c) The resulting space charge distribution ρ induces a space charge field E_{sc}, spatially shifted by $\Lambda/4$.

amplitude E_1 of the electric field can be obtained [6], using the interference tensor Δm as

$$E_1 = \frac{2\pi}{\Lambda}\frac{k_B T}{q}\left(1+\frac{l_D^2}{\Lambda^2}\right)^{-1}|\mathrm{tr}\{\Delta m\}|, \tag{2.86}$$

where l_D denotes the Debye screening length of the material.

The modulation of the dielectric tensor caused by the electro-optic effect caused by an electric field $\boldsymbol{E}$ can be written as

$$(\Delta\varepsilon_r)_{ij} = -n_i^2 n_j^2 (r_{ijk}E_k + s_{ijkm}E_k E_m) \tag{2.87}$$

where r_{ijk} and s_{ijkm} denote the components of the tensor quantities describing the material properties for the first-order and second-order electro-optic effect, and E_k and E_m denote components of $\boldsymbol{E}$. The magnitude of the components of these tensors for a single material may vary significantly, which implies that the strength of the photorefractive effect can vary considerably with the orientation of the grating vector $\boldsymbol{K}$, e.g., in $BaTi0_3$ (and other crystals with the same point group symmetry, 4 *mm*) the modulation of the permittivity change due to the electric field $\boldsymbol{E}_1$ is given by

$$\Delta\varepsilon_r(\boldsymbol{E}_1) \equiv \varepsilon_1 = -\begin{pmatrix} n_o^4 r_{13}E_{1z} & 0 & n_o^2 n_e^2 r_{42}E_{1x} \\ 0 & n_o^4 r_{13}E_{1z} & n_o^2 n_e^2 r_{42}E_{1y} \\ n_o^2 n_e^2 r_{42}E_{1x} & n_o^2 n_e^2 r_{42}E_{1y} & n_e^4 r_{33}E_{1z} \end{pmatrix} \tag{2.88}$$

where n_o and n_e are the ordinary and extraordinary indices of refraction, and the r_{ij} correspond to the material coefficients r_{ijk} used in Eq. 2.87 in a shortened notation. For the equation above, we have chosen that the crystal

axis (also referred to as the c axis) is parallel to the z direction. As the coefficient r_{42} is by far the largest in $BaTi0_3$, the effect is strongly anisotropic and because the grating vector $\boldsymbol{K}$ and therefore also the vector $\boldsymbol{E}_1$ are in the x–z-plane, the field component E_{1x} is the most significant one.

2.4 Grating Detection by Diffraction and Wave-Mixing

Diffraction at dynamic or permanent gratings is a special problem in the more general context of light-matter interaction. It can be treated by different theoretical descriptions with varying levels of sophistication, in which certain assumptions simplifying the problem are made. For example, it is possible to predict the diffraction angles correctly using simple geometrical considerations about the constructive or destructive interference of partial waves created by the gratings (see Section 2.4.1). In order to obtain information about the amplitudes of the diffracted waves, solutions of the wave equation are obtained for special cases by the Fraunhofer Diffraction theory or the Coupled Mode Theory (see Section 2.4.2). Effects causing energy transfer between the involved partial waves are referred to as wave mixing, where the probably most important examples are Two-Wave Mixing (discussed in Section 2.4.3), and Four-Wave mixing that can lead to the creation of optical gratings acting as a phase-conjugate mirror.

2.4.1 Diffraction Angles

Gratings are usually divided into several subclasses. Probably, the most important distinction is between thin and thick gratings. The latter are often also referred to as volume gratings.

Thin gratings. A light-wave incident at a thin periodical structure (a thin grating) will produce a number of partial waves that may at a certain distance from the grating interfere in a constructive or destructive manner, dependent on the difference between their respective optical path lengths.

From geometrical considerations (see Fig. 2.7(a)), the familiar condition for the directions of constructive interference, given by the diffraction angles φ_m

$$\Lambda[\sin(\theta + \varphi_m) - \sin(\theta)] = m\lambda, \quad m = 0, \pm 1, \pm 2, \ldots \tag{2.89}$$

is obtained, where θ denotes the angle of incidence, λ the wavelength of the light, and Λ the spatial period of the grating. For sufficiently small angles θ, φ_m, the angle of mth order of diffraction is given by

$$\varphi_m = m\frac{\lambda}{\Lambda} \tag{2.90}$$

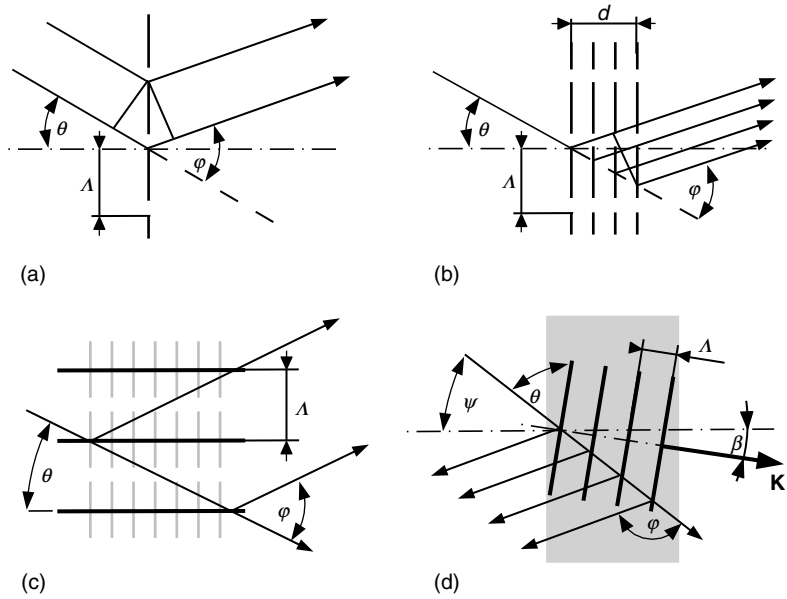

FIGURE 2.7. Diffraction at a single thin grating (a), at a series of thin gratings (b), at a thick (volume) transmission grating (c), and at a reflection volume grating (d). Incidence angle is denoted as θ, diffraction angle as φ and grating period as Λ.

and, there, the angular separation between two adjacent diffraction orders is approximately constant at a value λ/Λ. For $\boldsymbol{K} \parallel \hat{x}$, the x-component of the wave vectors k_m of the diffraction orders are given by

$$k_{m,x} - k_x = mK \quad m = 0, \pm 1, \pm 2, \ldots, \tag{2.91}$$

where k_x denotes the x-component of the wave vector of the incident wave.

When the diffracting structure is thicker than a certain value, partial waves created within different depths have to be in phase as well in order to observe constructive interference. To estimate up to which thickness existing phase differences may be neglected, the structure may be described as a succession of a number of thin-grating structures (see Fig. 2.7(b))

The optical path difference Δs between partial waves originating from thin-grating elements separated by a thickness d is given by

$$\Delta s = d(1 - \cos\varphi)/\cos\theta. \tag{2.92}$$

For small angles θ and φ that satisfy Eq. 2.90, the corresponding phase difference $\Delta\phi$ is given by

$$\Delta\phi = 2\pi \frac{\lambda d}{\Lambda^2 n(1 - \theta^2)}. \tag{2.93}$$

This means that at normal incidence, the phase difference will be sufficiently small ($\Delta\phi \ll 1$), if the grating thickness satisfies

$$d \ll \frac{\Lambda^2 n}{2\pi\lambda}. \tag{2.94}$$

Thick gratings. If the condition for a thin grating given by Eq. 2.94 is not satisfied, the partial waves that are diffracted at angles according to Eq. 2.89 at different depths must be exactly in phase in order to interfere constructively. This leads to a condition for the incidence angles at which diffracted beams can be observed. Deriving Eq. 2.94, we have neglected that every partial beam is diffracted at a subgrating that appears to be spatially shifted by a distance $\Delta x = d\tan\theta$. The Fourier transform diffraction theory for thin gratings (see Section 2.4.2) shows that the diffracted beam will have a phase shift $\Delta\phi = 2\pi\Delta x/\Lambda$ with respect to a beam diffracted at the untranslated grating. Following Eq. 2.92, the resulting phase difference is then given by

$$\Delta\phi = 2\pi\frac{d\tan\theta}{\Lambda} - \frac{d(1-\cos\varphi)}{\cos\theta}\frac{2\pi}{m\lambda}. \tag{2.95}$$

The condition $\Delta\phi = 0$ and Eq. 2.89 describing the diffraction at the thin subgratings can only be simultaneously fulfilled if $\varphi = -2\theta$ and, therefore

$$2\sin\theta = 2\sin\left(-\frac{\varphi_m}{2}\right) = \frac{m\lambda}{\Lambda}, \quad m = 0, \pm 1, \pm 2, \ldots \tag{2.96}$$

This equation is referred to as the *Bragg condition*, and indeed in the experiment it can be verified that only one diffraction order is created from a volume grating, and only if the incidence angle is chosen according to Eq. 2.96. Note that the condition $\varphi = -2\theta$ is also obtained if the diffracted waves are interpreted as reflections at planes formed by the structures of the thin subgratings, as is illustrated in Fig. 2.7(c).

Using the wave vectors of the incident and the diffracted light waves, the Bragg condition may be expressed as

$$\boldsymbol{k}_m - \boldsymbol{k} = m\boldsymbol{K}, \quad m = 0, \pm 1, \pm 2, \ldots. \tag{2.97}$$

Diffraction at a thick grating requires that all components of the wave vectors involved satisfy conditions, in contrast to a thin grating, where only one component of the wave vector is determined by the diffraction (compare Eq. 2.91). The configuration shown in Fig. 2.7(c) is referred to as a *transmission volume grating*. When the incidence angle θ exceeds $\pi/4$ as shown in Fig. 2.7(d), the grating is called a *reflection volume grating*. Here the grating vector $\boldsymbol{K}$ has a slant angle β with respect to the z-axis. Note that the Bragg condition is valid for the angle $\theta = (\pi/2 - (\psi - \beta))$ for this configuration.

2.4.2 Diffraction Amplitudes and Efficiencies

In order to gain information about the amplitudes of the diffracted waves, solutions to the Helmholtz equation

$$\nabla^2 \boldsymbol{E}(x,z) + k^2 \varepsilon_r(x,z)\boldsymbol{E}(x,z) = 0, \tag{2.98}$$

where we have restricted our analysis to the x–z-plane, can be found using different approaches. For thin gratings, the well-known classical boundary-value approach of Huyghens and Kirchhoff may be used. For thick gratings, the wave propagation inside the material has to be considered. For weakly modulated gratings, a suitable approach is the coupled-wave theory in the two-wave approximation as described by Kogelnik [33].

Fourier transform diffraction theory for thin gratings. Based on the assumption that the light is linearly polarized, Eq. 2.98 is reduced to a scalar equation for the one-dimensional field amplitude E. The thin grating will change the incident wave

$$E^{(i)} = A^{(i)} \exp\left[\mathrm{i}(\omega t - kz)\right] \tag{2.99}$$

into the following wave by means of its transmittance $t(x)$

$$E(z=0) = A^{(i)} t(x) \exp\left[\mathrm{i}(\omega t)\right], \tag{2.100}$$

where, for simplicity, normal incidence has been assumed. The transmittance can be calculated from the spatially modulated permittivity ε_r. The wave behind the grating is described by a superposition of plane waves with amplitudes A_m as

$$E = \sum_m A_m \exp\left[\mathrm{i}(\omega t - k_m x - \sqrt{k^2 - k_m^2}\, z)\right]. \tag{2.101}$$

Substituting Eq. 2.91 into this equation we obtain

$$A_m = \frac{A^{(i)}}{\Lambda} \int_0^{\Lambda} t(x) \exp\left(\mathrm{i}2\pi \frac{mx}{\Lambda}\right) \mathrm{d}x \tag{2.102}$$

which means that the wave amplitudes A_m are given by the Fourier coefficients of the transmittance $t(x)$. The diffraction efficiency for the mth diffraction order is given by $\eta_d = (A_m/A^{(i)})^2$.

For the case of a sinusoidal refractive index grating, the transmission function can be written as

$$t(x) = \exp\left[\mathrm{i}\phi \cos\left(2\pi x/\Lambda\right)\right], \tag{2.103}$$

where $\phi = 2\pi\Delta\hat{n}d/\lambda$ is determined by the modulation amplitude $\Delta\hat{n}$ of the refractive index grating. For a pure amplitude transmittance grating (i.e., $\mathrm{Re}(\hat{n}) = 0$), only the three central diffraction orders (corresponding to $m = 0, \pm 1$) are observed [34], and a maximum diffraction efficiency of $\eta_d = 6.25\%$ is obtained for the first order $m = \pm 1$. In contrast, a pure phase grating will diffract into higher orders as well. The maximum diffraction efficiency for the first order is $\eta_d = 33.8\%$ for a value of the grating amplitude $\phi \approx 1.8$.

Coupled-wave theory for volume gratings. For a volume grating with slant angle β between grating wave vector $\boldsymbol{K}$ and the surface normal of the material (compare Fig. 2.7(d)), the spatial modulation of material properties may be written as

$$\varepsilon_r(x,\ z) = \varepsilon_c + \varepsilon_1 \cos\left(K(x\sin\beta + z\cos\beta)\right) \tag{2.104}$$

A slant angle $\beta = 0$ corresponds to an unslanted reflection grating, $\beta = \pi/2$ to an unslanted transmission grating. We can substitute

$$E = \sum_m A_m \exp\left[\mathrm{i}(\boldsymbol{k}_i - m\mathbf{K})\cdot\mathbf{r}\right] \tag{2.105}$$

into the wave equation, and applying the approximation of weak absorption ($\varepsilon_r - n^2 \approx in\alpha/k$) and neglecting the second-order derivative d^2A_m/dz^2 (which is known as the slowly varying envelope (SVE) approximation), we obtain the rigorous coupled-wave equations [9]

$$\begin{aligned}\mathrm{i}\left(\cos\psi - \frac{m\lambda\cos\beta}{n\Lambda}\right)\frac{dA_m}{dz} + m\frac{\pi}{\Lambda^2}\left(2\Lambda\cos(\psi-\beta) - m\frac{\lambda}{n}\right)A_m \\ + \mathrm{i}\frac{\alpha}{2n}A_m + \frac{\pi n\varepsilon_1}{2\lambda}(A_{m+1} + A_{m-1}) = 0\end{aligned} \tag{2.106}$$

which is an infinite set of coupled differential equations. The real-valued coefficient of the first addend proportional to A_m will vanish only for the transmitted wave $m = 0$ and the one mth partial wave that satisfies the Bragg condition given in Eq. 2.96. For all other waves, the nonvanishing coefficient leads to oscillatory behavior with respect to the propagation direction z, a continuous build-up of the amplitude A_m is not possible. This corresponds to the statement that (if any) only one diffracted-wave may be generated efficiently by a volume grating. We will therefore reduce the coupled-wave equations in Eq. 2.106 to only two equations, for the two waves given by amplitudes A_0 and A_1. In this two-wave approximation, using the definitions

$$\kappa = \frac{\pi\varepsilon_1}{2n\lambda\cos\psi} \tag{2.107}$$

$$\delta = \frac{\alpha}{2\cos\psi} \tag{2.108}$$

we obtain the equations

$$\begin{aligned} \frac{dA_0}{dz} &= -\delta A_0 + \mathrm{i}\kappa A_1 \\ \pm\frac{dA_1}{dz} &= -\delta A_1 + \mathrm{i}\kappa A_0. \end{aligned} \tag{2.109}$$

These equations cover two cases: the plus sign in the second equation corresponds to the unslanted transmission grating case ($\beta = \pi/2$). For an unslanted reflection grating ($\beta = 0$), the minus sign applies. The quantity κ used in the equations is referred to as the coupling constant. It will take a slightly different form when the coupling between waves of different polarization is to be described.

Let the polarization of two waves be given by the two polarization vectors $\boldsymbol{p}_1, \boldsymbol{p}_2$, and the amplitude of the spatial modulation of the permittivity be given by the tensor quantity ε_1 to account for anisotropy, the coupling constant takes the form [6]

$$\kappa_{ij} = \frac{\pi}{2n_i\lambda\cos\psi_i\varepsilon_0}\boldsymbol{p}_i \cdot \varepsilon_1 \boldsymbol{p}_j, \tag{2.110}$$

where $i,j = 1,2$. Note that two waves that are both polarized within the plane of incidence have different polarization vectors and Eq. 2.110 needs to be used rather than Eq. 2.107 obtained from the scalar wave equation [33].

Transmission volume gratings. The initial condition for solving the Eqs. (2.109) for a transmission grating is given by the amplitudes $A_0(0)$ and $A_1(0)$ when entering the interaction region, and the solution is given by

$$\begin{aligned} A_0(z) &= (A_0(0)\cos(\kappa z) + \mathrm{i}A_1(0)\sin(\kappa z))\exp(-\delta z) \\ A_1(z) &= (A_1(0)\cos(\kappa z) + \mathrm{i}A_0(0)\sin(\kappa z))\exp(-\delta z). \end{aligned} \tag{2.111}$$

When a single beam is incident on the grating, the initial conditions are $A_0(0) = A^{(i)}$ and $A_1(0) = 0$. The dependence of the intensities on the position is depicted in Fig. 2.8. Because the absorption of the material is considered to be weak, we may then use Eq. 2.78 to compute the amplitude and phase grating amplitudes, and the diffraction efficiency of a grating of thickness d is obtained as

$$\eta_d(d) = \frac{I_1}{I^{(i)}} = \left(\sin^2\frac{\pi\Delta n d}{\lambda\cos\psi} + \sinh^2\frac{\Delta\alpha d}{4\cos\psi}\right)\exp[-2\delta d]. \tag{2.112}$$

Reflection volume gratings. In the reflection case, the Bragg condition causes the diffracted wave to travel into the region in front of the grating, while behind the grating region, only the transmitted beam corresponding to diffraction order $m = 0$ is observed. Therefore, the diffracted beam is often referred to as a reflected beam.

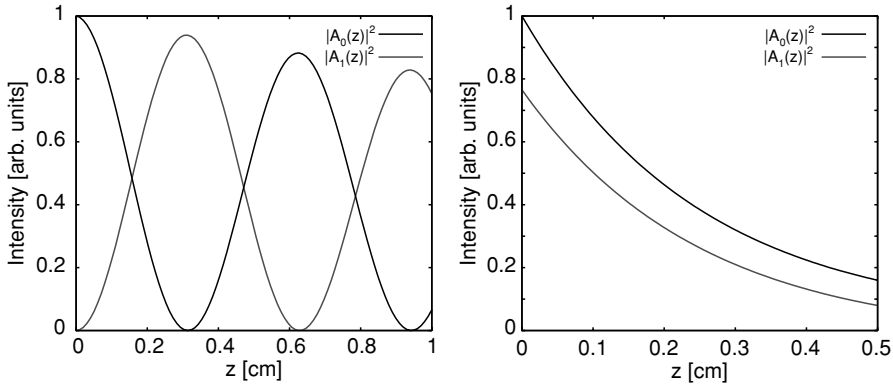

FIGURE 2.8. Diffraction at volume gratings: Calculated normalized field densities for an incidence angle $\psi = 10^\circ$, assuming an absorption coefficient $\alpha = 0.5\,\mathrm{cm}^{-1}$ and a phase-only transmission grating with $\kappa = 4\,\mathrm{cm}^{-1}$ (left figure) and a reflection grating with $\kappa = 2\,\mathrm{cm}^{-1}$ (right figure), respectively.

Assuming a volume grating of thickness d, the initial conditions are determined by the wave amplitudes $A_0(0)$ and $A_1(d)$ as the beams enter the interaction region from opposite directions. The solutions in this case are obtained as

$$A_0(z) = A_0(0)\left(\cosh(\zeta z) - \frac{\delta}{\zeta}\sinh(\zeta z)\right) + \mathrm{i}B\frac{\kappa}{\zeta}\sinh(\zeta z) \tag{2.113}$$

$$A_1(z) = B\left(\cosh(\zeta z) + \frac{\delta}{\zeta}\sinh(\zeta z)\right) - \mathrm{i}A_0(0)\frac{\kappa}{\zeta}\sinh(\zeta z) \tag{2.114}$$

where we have introduced ζ and B as

$$\zeta = \sqrt{\kappa^2 + \delta^2}, \tag{2.115}$$

$$B \equiv A_1(0) = \frac{\mathrm{i}A_0(0)\kappa\sinh(\zeta d) + \zeta A_1(d)}{\zeta\cosh(\zeta d) + \delta\sinh(\zeta d)} \tag{2.116}$$

and identified the quantity B as the amplitude of the reflected wave at the boundary $z = 0$. For a single wave incident on the grating $A_1(d) = 0$ and neglecting the bulk material absorption ($\alpha = 0$), we obtain the diffraction efficiency η_d of a pure phase grating ($\Delta\alpha = 0$) as

$$\eta_d = \tan\mathrm{h}^2\frac{\pi\Delta n d}{\lambda\cos\psi}. \tag{2.117}$$

2.4.3 Two-Wave Mixing in Electro-Optic Crystals

In this section, we will discuss the interaction of laser beams with the grating that has been induced in a material due to the spatial modulation of their intensity I, energy density w, or energy dissipation rate W_f, using the two-wave mixing in electro-optic crystals as an example. At a light-induced grating written by two writing beams A and B, each of the beams will be partially transmitted (with amplitudes $\boldsymbol{A}_{A,0}$ and $\boldsymbol{A}_{B,0}$) and partially diffracted (with amplitudes $\boldsymbol{A}_{A,1}$ and $\boldsymbol{A}_{B,1}$). The transmitted part of one beam happens to be collinear with the diffracted part of the other beam and vice versa. As the beams A and B are coherent (for simplicity we will assume ideal coherence here), the field amplitudes of the respective transmitted and diffracted beams will add up.

Depending on the material, the light field will produce a material excitation and produce a modulation of the permittivity that can be approximately described by

$$\varepsilon_r(x,\ z) = \varepsilon_c + \varepsilon_1 \cos(\boldsymbol{K}\cdot\boldsymbol{r} + \phi), \tag{2.118}$$

where ϕ describes a spatial shift between the stationary field modulation and the induced optical grating that can be caused by the physical mechanism of grating creation. In a diffusion-driven photorefractive material without external field, we have $\phi = \pi/2$ as obtained in Eq. 2.85.

The modulation amplitude ε_1 of the dielectric tensor is dependent on the interference tensor of the incident writing beams, i.e.,

$$\varepsilon_1 = |\mathrm{tr}\{\Delta m\}|\tilde{\varepsilon}_1 \tag{2.119}$$

as can be seen from Eqs. 2.86 and 2.88 for the case of electro-optic crystals. As diffraction will change the amplitudes of the writing beams (and consequentially the interference tensor Δm) while they propagate through the material, following the discussion of transmission volume gratings in Section 2.4.2 and Eq. 2.24, the case of codirectional two-wave mixing can be described by a set of coupled differential equations for the beam intensities I_A and I_B

$$\begin{aligned}\frac{dI_A}{dz} &= \gamma\frac{I_A I_B}{I_A + I_B} - \delta I_A\\ \frac{dI_B}{dz} &= -\gamma\frac{I_A I_B}{I_A + I_B} - \delta I_B,\end{aligned} \tag{2.120}$$

where the coupling constant

$$\gamma = \frac{\pi \boldsymbol{p}_A\cdot\boldsymbol{p}_B}{n\lambda\cos\psi\varepsilon_0}(\boldsymbol{p}_A\cdot\tilde{\boldsymbol{\varepsilon}}_1\boldsymbol{p}_B)\sin\phi \tag{2.121}$$

has been introduced. When there is no spatial shift between the stationary field modulation and the induced optical grating (i.e., $\phi = 0$), the coupling coefficient is zero, while it reaches a maximum for $\phi = \pm\pi/2$. As can be seen from its definition, the orientation of the polarization vectors of the beams with respect to each other and to the crystal axes is significant for the magnitude of γ. Following Eq. 2.88, we obtain for a wave mixing of beams with polarization vectors $\boldsymbol{p}_A = (p_{Ax},\ p_{Ay},\ p_{Az})$ and $\boldsymbol{p}_B = (p_{Bx},\ p_{By},\ p_{Bz})$ in $BaTiO_3$

$$(\boldsymbol{p}_A \cdot \tilde{\boldsymbol{\varepsilon}}_1 \boldsymbol{p}_B) \propto r_{42} \sin\xi (p_{Ax} p_{Bz} + p_{Az} p_{Bx}), \tag{2.122}$$

where the c-axis of the crystal is again assumed to be parallel to the z direction, and the $\boldsymbol{K}$ vector of the grating is contained in the x–z-plane with an angle ξ to the c axis. In Eq. 2.122, we have only considered the contribution of the dominant nonlinear coefficient r_{42}, and it can be seen that only beams with a polarization parallel to the x–z-plane (i.e., e–o polarized beams in this case) will create a significant coupling coefficient γ. In order to determine the incidence angles so that the largest value of γ can be obtained, the influence of material parameters (e.g., the Debye screening length, compare Eq. 2.86) as well as the limit to the interference contrast given by $\boldsymbol{p}_A \cdot \boldsymbol{p}_B$ need to be considered.

The solution of Eq. 2.120 is found as

$$\begin{aligned} I_A(z) &= I_A(0) \frac{1 + m^{-1}}{1 + m^{-1} \exp(\gamma z)} \exp(-\delta z) \\ I_B(z) &= I_B(0) \frac{1 + m}{1 + m \exp(-\gamma z)} \exp(-\delta z), \end{aligned} \tag{2.123}$$

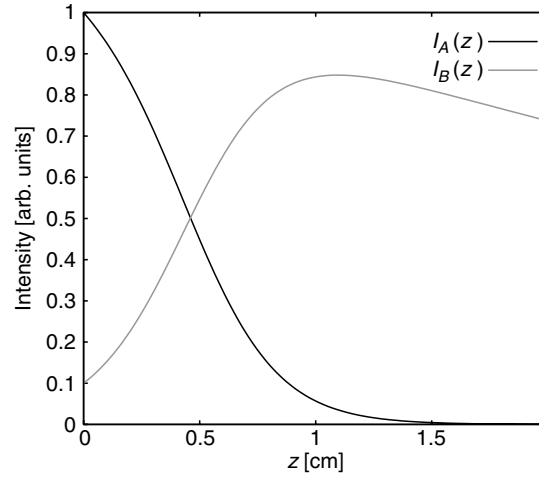

FIGURE 2.9. Calculated intensities of the writing beams in the interaction region of a two-wave mixing process assuming $m = 10$, $\gamma = 5\,\mathrm{cm}^{-1}$ and $\delta = 0.2\,\mathrm{cm}^{-1}$. After an interaction length of 1 cm, beam B has reached maximum intensity.

where $m = I_A(0)/I_B(0)$ denotes the input intensity ratio of the two beams. In Fig. 2.9, it can be seen that the intensity of one of the beams may be almost fully transferred into the other beam, only limited by the material absorption.

2.5 Conclusions

Dynamic gratings can be induced by interfering laser beams in almost any optical material. Some selected works related to laser-induced gratings have been used as references of this chapter, but inevitable these publications cover only a small fraction of the research activities in this widespread field. There are certainly many other important contributions that we could not include here. The following chapters of this volume are devoted to the photorefractive materials and will provide a detailed review of the effects related to this important class of materials, in particular, of the effects related to laser-induced gratings in photorefractive materials.

Acknowledgments

We would like to thank Prof. G. Montemezzani from the University of Metz, France and some unknown referee for review and fruitful discussion of this chapter.

References

1. H.J. Coufal, D. Psaltis, and G.T. Sincerbox, eds.: *Holographic data storage*, Vol. 76 of *Springer Series in Optical Sciences*, Springer, New York (2000).
2. H.J. Eichler, P. Kuemmel, S. Orlic, and A. Wappelt: High density disk storage by multiplexed microholograms, *IEEE J. Selected Topics Quantum Electron.* **4**(5), 840–848 (1998).
3. D.C. Meisel, M. Wegener, and K. Busch: Three-dimensional photonic crystals by holographic lithography using the umbrella configuration: Symmetries and complete photonic band gaps, *Phys. Rev. B*, 70, 165104 (2004).
4. A. Brignon and J.-P. Huignard, eds.: *Phase conjugated laser optics*, John Wiley & Sons (2004).
5. T. Riesbeck, E. Risse, and H.J. Eichler: Pulsed solid-state laser systems with high brightness by fiber phase conjugation, *Proc. SPIE* **5120**, pp. 494–499, Nov. 2003.
6. P. Yeh, *Introduction to photorefractive nonlinear optics*, Wiley 1993.
7. L. Solymar, DJ. Webb, and A. Grunnet-Jepson: *The physics and applications of photorefractive materials*, Oxford University Press (1996).
8. A.A. Zozulya: Propagation of light beams in photorefractive media: Fanning, self-bending and formation of self-pumped four-wave-mixing phase conjugation geometries, *Phys. Rev Lett.* 73 (6), 818–825 (1994).

9. H.J. Eichler, P. Günter, and D.W. Pohl: *Laser-induced dynamic gratings*, Springer-Verlag, Berlin (1986).
10. O. Svelto: *Principles of lasers*, Kluwer Academic/Plenum Publishers (1998).
11. A. Yariv: *Quantum electronics*, John Wiley & Sons, 3rd edn (1989).
12. A. Yariv and P. Yeh: *Optical waves in crystals*, John Wiley & Sons (1984).
13. M. Born and E. Wolf: *Principles of optics*, Cambridge University Press, 7th edn. (1999).
14. L. Bergmann and C. Schäfer: *Optics of waves and particles*, De Gruyter (1999).
15. G.N. Ramachandran and S. Ramaseshan: *Crystal optics*, Vol. XXV/1 of *Handbuch der Physik*, Springer-Verlag, Berlin (1961).
16. P. Günter, ed.: *Nonlinear optical effects and materials*, Vol. 72 of Springer Series in Optical Sciences. Springer, Berlin (2000).
17. G. Montemezzani, C. Medrano, and M. Zgonik: Charge carrier photoexcitation and two-wave mixing in dichroic materials, *Phys. Rev. Lett.* **97**, 3403–3406 (1997).
18. M. Nisoli, S.D. Silvestri, R. Scipocs, K. Ferencz, C. Spielmann, S. Sartania, and F. Krausz: Compression of high-energy laser pulses below 5fs, *Opt. Lett.* **22**(8), 522(1997).
19. A.A. Mahznev, T.F. Crimmins, and K.A. Nelson: How to make femtosecond pulses overlap, *Opt. Lett.* **23** (17), 1378–1380 (1998).
20. I.Z. Kozma and J. Hebling: Comparative analysis of optical setups for excitation of dynamic gratings by ultrashort light pulses, *Opt. Commun.* **199**, 407–415 (2001).
21. P. Pogany, A. Hermerschmidt, S.X. Dou, and H. J. Eichler: Simple measurement of the temporal coherence function of cw diode lasers by a photorefractive grating method, in *5th International Workshop on Laser Beam and Optics Characterization*, H. Weber and H. Laabs, eds., pp. 71–78, March 2000.
22. H.J. Eichler, G. Enterlein, and D. Langhans: Investigation of the spatial coherence of a laser beam by a laser-induced grating method, *Appl. Phys.* **23**, 299–302 (1980).
23. C. Allain, H.Z. Cummins, and P. Lallemand: Critical slowing down near the Rayleigh–Benard convective instability, *J. Physique Lett.* **39**, L475–L479 (1978).
24. T. Sjodin, H. Petek, and H.-L. Dai: Ultrafast carrier dynamics in silicon: A two-color transient reflection grating study on a (111) surface, *Phys. Rev Lett.* **81** (25) 5664–5667 (1998).
25. M. Sudzius, R. Aleksiejunas, K. Jarasiunas, D. Verstraeten, and J.C. Launay: Investigation of nonequilibrium carrier transport in vanadium-doped CdTe and CdZnTe crystals using the time-resolved four-wave mixing technique, *Semicond. Sci. Technol.* **18** (4), 367–76 (2003).
26. P.F. Barker, J.H. Grinstead and R.B. Miles: Single-pulse temperature measurement in supersonic air flow with predissociated laser-induced thermal gratings, *Opt. Commun.* 168, 177–182 (1999).
27. M. Jazbinšek, I.D. Olenik, M. Zgonik, A.K. Fontecchio, and G.P. Crawford: Characterization of holographic polymer dispersed liquid crystal transmission gratings, *J. Appl. Phys.* **90** (8), 3831–3837 (2001).
28. M.J. Escuti, J. Qi, and G.P. Crawford: Two-dimensional tunable photonic crystal formed in a liquid–crystal/polymer composite. Threshold behavior and morphology, *Appl. Phys. Lett.* **83** (7) 1331–1333 (2003).
29. E. Garmire and A. Kost, eds: *Nonlinear optics in semiconductors* I, Vol. 58 of *Semiconductors and Semimetals*, Academic Press, San Diego (1999).
30. T. Numai: *Fundamentals of semiconductor lasers*, Vol. 93 of Springer Series in Optical Sciences. Springer, New York (2004).

31. K. Buse: Light-induced charge transport processes in photorefractive crystals, I: Models and experimental methods, II: Materials, *Appl. Phys. B* **64**, 273–291, 391–407 (1997).
32. B. Jancewicz: A variable metric electrodynamics. The Coulomb and Biot-Savart laws in anisotropic media, *Ann. Phys.* **245**, 227–274 (1996).
33. H. Kogelnik: Coupled-wave theory for thick hologram gratings, *Bell Syst. Tech. J.* **48**, 2909–2948 (1969).
34. J.W. Goodman, Introduction to Fourier optics, McGraw-Hill, 2nd ed. (1996).

3

Fundamentals of Photorefractive Phenomena

F. Agulló-López[1], G.F. Calvo[2], and M. Carrascosa[1]

[1] Departamento de Física de Materiales, C-IV, Universidad Autónoma de Madrid, 28049 Madrid, Spain.
[2] Grup de Física Teòrica, Universitat Autònoma de Barcelona, 08193 Bellaterra (Barcelona), Spain.
gfernand@ifae.es

In this chapter, the standard model accounting for the photorefractive nonlinearity in a material is presented. The mathematical formalism of the rate equations has been introduced and developed under the adiabatic approximation. Through a perturbative treatment, it leads to a single nonlinear equation relating the general space-charge field to light intensity. Steady-state and transient solutions are discussed in certain detail for the particular case of sinusoidal (harmonic) light excitation at low modulation. The analysis includes the effect of a running interference pattern (dc frequency detuning) as well as dc and ac fields. Subsequently, the consequences of high light modulation such as cross-talk, subharmonic and combination grating generation, as well as parametric oscillation are summarily described. Some complicating features to the standard model are briefly touched upon. A second part of the chapter is devoted to the relevant case of the photorefractive response under localized optical beams which constitutes the basis to further describe in later chapters of the book soliton behavior. Both 1D and 2D approaches within the strong nonlinear regime (high contrast) are presented. For the 1D case, steady-state solutions for the different transport regimes are worked out. Moreover, the singular features associated to the presence of an ac-field are described.

3.1. The Photorefractive Nonlinearity: Introductory Remarks

Electro-optic photoconductive materials present a very interesting phenomenom, known as *photorefractive effect*, with a variety of applications in photonics and optoelectronics [1–10]. The effect was discovered by Ashkin and coworkers [11] in 1966, as degradation of a linearly polarized laser beam

traversing a plate of $LiNbO_3$ whose large faces contained the trigonal **c**-axis of the crystal (see Fig. 3.1). For beams polarized along a direction orthogonal to the **c**-axis (*ordinary waves*), no degradation was observed. However, beams polarized along a direction parallel to the **c**-axis (*extraordinary waves*) exhibited a spreading along this axis and gave rise to an elongated light spot on an observation screen. It was proposed by these authors, and it is now generally accepted, that the phenomenon involves a light-induced modification of the refractive index. The recorded index profile, measured by a compensator technique, is illustrated in Fig. 3.2. It was obtained for $LiNbO_3$ excited with a He-Ne laser beam (power density $\simeq 50\,\mathrm{mW/cm^2}$). The index change Δn became negative at the illuminated spot and reached a value of $|\Delta n| \simeq 5 \cdot 10^{-5}$. The authors explained the observed degradation of the beam as its self-diffraction by the refractive index pattern generated during light propagation. One should

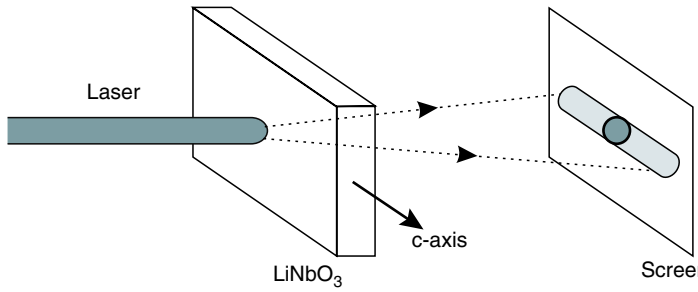

FIGURE 3.1. Distortion of a collimated laser beam across a $LiNbO_3$ plate caused by the photorefractive effect.

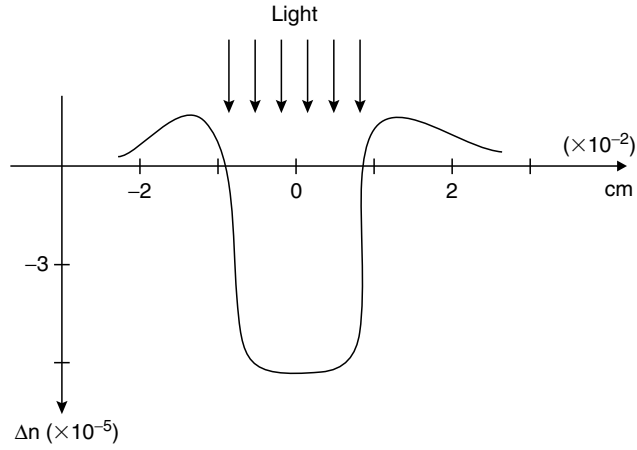

FIGURE 3.2. Change in the extraordinary refractive index profile induced by a localized optical beam in $LiNbO_3$.

make clear that the light-induced change of refractive index (and not the beam degradation) constitutes the photorefractive (PR) effect, although the two phenomena (index and light distortions) are intimately coupled.

Before a more thorough discussion, one should mention here that the PR effect is an optical nonlinearity mediated by transport of the electronic charge carriers generated by the light and the build-up of a space-charge field in the material. Therefore, it cannot be properly described by a power expansion of the polarization in terms of the field and so by any m-order susceptibility $\chi^{(m)}$. Some effective susceptibility can be introduced [12], although it has a limited practical significance. Then, its magnitude is largely determined by the values of the electro-optic coefficients that convert that field into a refractive index change. This basic mechanism is responsible for the very high sensitivity of the effect to the nature and concentration of defects and impurities present in the material acting as donor centers or traps for the carriers. Under suitable conditions, it leads to observable effects for intensities down to $\mathrm{mW/cm^2}$. On the other hand, the response time is determined by the time needed to build up the space-charge field and so is related to light intensity and carrier mobility. At room temperature, the induced PR damage has a persistence in the dark ranging from microseconds or less for semiconductors to months or even years for $LiNbO_3$. However, the effect is reversible and can be erased by intense uniform illumination.

The theoretical description of the effect is based on a rather simple kinetic model initially put forward by the Kiev's group [13]. It leads to a set of nonlinear rate equations that are commonly solved under a linearized approximation. This linear treatment accounts for a large body of experimental information. However, it is becoming more and more interesting to exploit the consequences of the nonlinear terms and the coupling to the wave equation to account for exciting effects such as propagation of spatial solitons [10,14], beam break-up, filamentation, and collapse [15–18], surface waves [19], modulation instability [20], pattern formation [21], subharmonic generation [7,22], parametric instabilities [23,24] and scattering [25], space-charge singularities [26], critical enhancement [27], and cross-talk [28]. Most of these effects were developed after the publication of the first Springer review books [1,2] and so here they will deserve special attention. In particular, the final part of our treatment is devoted to the PR effect associated to localized optical fields in the large contrast regime. This analysis, particularly in the case of two dimensions (2D), is of key relevance to study beam propagation effects and soliton behavior. On the other hand, since some of the topics constitute the objective of special chapters in this book, we will only mention them or provide a short description to maintain the coherence of the text. In particular, we will concentrate exclusively on the PR effect leaving aside the consequences on light propagation (discussed in Chapters 2, 4, 11, and 12).

We can now anticipate a summary of the main distinctive features of the PR nonlinearity:

a) *Critically dependent on material imperfections and so on intentional doping.*
b) *High sensitivity making the effect observable down to* $\mathrm{mW/cm^2}$ *intensities.*

c) *Noninstantaneous: Relatively slow response (dependent on light intensity and carrier mobility).*
d) *Nonlocal effect: Phase shift between light and index patterns leading to wave coupling effects (amplification).*
e) *Low or high persistence in the dark depending on the material.*
f) *Erasable by homogeneous illumination.*

3.2 Physical Mechanisms: Standard Microscopic Model

Leaving aside some old models of historical interest, the physical mechanism generally accepted to discuss the PR effect is illustrated in Fig. 3.3. The electro-optic material has both donor and acceptor centers N_D and N_A, respectively, which may correspond, for instance, to two valence states of the same impurity (or defect), such as Fe^{2+} (donor) and Fe^{3+} (acceptor). Nonuniform illumination with light of suitable wavelength ionizes the donors and generates free carriers (either electrons or holes or both). They move through the conduction and/or valence band and are finally trapped at acceptors. As a result, a charge redistribution between the illuminated and dark areas is induced. The associated electric field causes a refractive index pattern via the electro-optic effect [5,29]. Although most experiments rely on the linear (Pockels) effect, the role of the quadratic (Kerr) effect has also been demonstrated (e.g., in the paraelectric phase of some ferroelectric PR materials such as potassium lithium tantalate niobate, in transparent electro-optic ceramics, and multiple-quantum-well semiconductor structures).

For the most common Pockels case, the local change in the refractive index can be written as

$$\Delta\left(\frac{1}{n^2}\right)_{ij} = r_{ijk}E_k, \tag{3.1}$$

where $\mathbf{E}$ is the space-charge electric field and r_{ijk} the Pockels electro-optic coefficients. In contracted notation, i.e., using a single index m (from $m = 1$

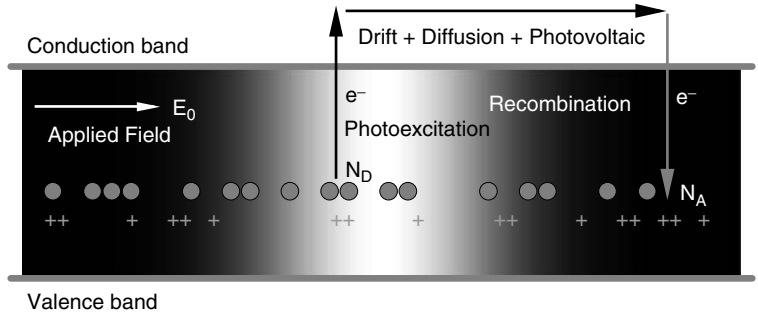

FIGURE 3.3. Band diagram for the standard PR *one-center model.*

to $m = 6$) for the 6 nonequivalent i, j pairs, (3.1) can be equivalently expressed as,

$$\Delta\left(\frac{1}{n^2}\right)_m = r_{mk} E_k. \tag{3.2}$$

The tensorial character of the electro-optic effect is a main factor accounting for the strong anisotropy of the PR response.

Note: The electro-optic coefficients to be used in (3.1) are those corresponding to a zero frequency (*static*). However, the question of whether clamped or free (*unclamped*) coefficients apply is not trivial. The solution, a combination of them, has been provided by P. Günter and M. Zgonic [30].

3.3 Theoretical Modeling: Rate Equations

The above physical model for the PR effect can be easily translated into mathematical equations. For simplicity, we will consider one single type of free charge carrier having concentration n (i.e., monopolar transport), as well as a single impurity center. Let N be the concentration of those active centers presenting two valence (charge) states acting as either donors (concentration N_D) or acceptors (concentration N_A) for the carriers, so that $N = N_D + N_A$ is a constant independent of the presence of light. The rate equations governing the evolution of the system under a nonuniform photon flux $I(r,t)$ ($\hbar\omega I$ is the light intensity pattern) write [13],

$$\frac{\partial n}{\partial t} = sIN_D - \gamma n N_A - \frac{1}{q}\nabla \cdot \mathbf{J}, \tag{3.3a}$$

$$\frac{\partial N_D}{\partial t} = -\frac{\partial N_A}{\partial t} = -sIN_D + \gamma n N_A, \tag{3.3b}$$

$$\mathbf{J} = q\mu n\mathbf{E} - qD\nabla n + qsIN_D L_{\mathrm{PV}}\mathbf{u}_{\mathrm{PV}}, \tag{3.3c}$$

where q is the charge of the carrier ($-e$ for electrons and $+e$ for holes, e being the elementary charge), s the photoionization cross-section, γ the recombination constant, μ the mobility, $D = \mu k_B T/q$ the diffusion coefficient, k_B Boltzmann constant, T the absolute temperature, L_{PV} the photovoltaic transport length (see the next section), and $\mathbf{u}_{\mathrm{PV}}$ the unit vector in the direction of the polar axis. The expression (3.3c) for the current density $\mathbf{J}$ includes the drift, diffusion and photovoltaic contributions. $\mathbf{E}$ is the total electric field including the one externally applied and that associated to the generated space charge. For simplicity, we have ignored the thermal ionization of donors in (3.3a) and (3.3b)[1].

[1] If thermal ionization of donors is taken into account, then the first terms in the right-hand sides of (3.3a) and (3.3b) should be replaced by $(\beta_T + sI)N_D$, with β_T being the thermal generation rate (see more on this in Section 3.15).

Regarding the space-charge field, it obeys the Poisson equation

$$\nabla \cdot (\varepsilon_0 \varepsilon \mathbf{E}) = q(n + N_D - N_D(0)) = q(n - N_A + N_A(0)), \tag{3.4}$$

where ε_0 is the electric permeability of vacuum, ε the relative static dielectric constant. Here, $N_D(0)$ and $N_A(0)$ are the corresponding constant donor and acceptor concentrations in the absence of illumination.

By adding (3.3a) and (3.3b), one obtains the continuity equation

$$\frac{\partial(N_D + n)}{\partial t} = -\frac{1}{q}\nabla \cdot \mathbf{J}. \tag{3.5}$$

Differentiation of (3.4) with respect to time, and using (3.5), yields

$$\nabla \cdot \left(\varepsilon_0 \varepsilon \frac{\partial \mathbf{E}}{\partial t} + \mathbf{J}\right) = 0. \tag{3.6}$$

Then, from (3.5) and (3.6), one arrives at

$$\frac{\partial(N_D + n)}{\partial t} = -\frac{1}{q}\nabla \cdot \mathbf{J} = \frac{1}{q}\nabla \cdot \left(\varepsilon_0 \varepsilon \frac{\partial \mathbf{E}}{\partial t}\right). \tag{3.7}$$

Eqs. (3.3b), (3.3c), and (3.7) constitute the starting point for the subsequent analysis.

Note 1: The above rate equations are valid for both electrons and holes if the corresponding sign of q and μ is properly taken into account (μ is negative for electrons). Notice that D is positive for both electrons and holes.

Note 2: In many studies of the PR effect, a different notation is used for the trap (acceptor and donor) centers. The equivalence is as follows: N_D is used instead of N, N_D^+ in place of N_A, and N_A replaces $N_A(0)$.

3.4 Photovoltaic Drift

The photovoltaic (PV) effect is a peculiar drift mechanism [3,7] operating in some non-centrosymmetric crystals, such as $LiNbO_3$, $KNbO_3$, $BaTiO_3$, and $LiTaO_3$. It involves an asymmetric excitation of carriers that, for the one dimensional (1D) case (see Fig. 3.4), gives rise to a current density

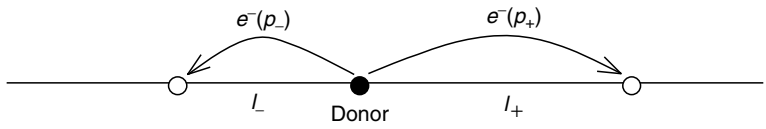

FIGURE 3.4. Simple scheme for the PV effect in a one-dimensional system.

$$J_{\mathrm{PV}} = qsN_D L_{\mathrm{PV}} I = q\alpha L_{\mathrm{PV}} I, \tag{3.8}$$

where $\alpha = sN_D$ is the absorption coefficient. The characteristic parameter $L_{\mathrm{PV}} = p_+ l_+ - p_- l_-$ is the photovoltaic transport length (around 5 $\mathring{A}$ for $LiNbO_3$), which can be written in terms of the excitation probabilities $p_{+(-)}$ and drift lengths $l_{+(-)}$ for positive and negative carrier displacement, respectively. Rigorously, the PV effect is described by a third-rank tensor $\beta_{ijk} = \beta^*_{ikj}$ through $\mathbf{J}_{PV} \equiv J_i = \beta_{ijk} E_j E^*_k$, where $\mathbf{E}$ is the complex amplitude of the polarization state of the light field. For linearly polarized light, only the real part of β_{ijk} contributes to J_i and therefore the corresponding tensor is symmetric in the j, k indices (*linear photovoltaic effect* or LPV). In contracted notation, the LPV tensor for $LiNbO_3$ writes

$$\beta_{im} = \begin{pmatrix} 0 & 0 & 0 & 0 & \beta_{15} & -\beta_{22} \\ -\beta_{22} & \beta_{22} & 0 & \beta_{15} & 0 & 0 \\ \beta_{31} & \beta_{31} & \beta_{33} & 0 & 0 & 0 \end{pmatrix}. \tag{3.9}$$

Let us now consider linearly polarized light propagation in the XY plane. For o-polarization:

$$J_x = 0,\ J_y = -\beta_{22} I,\ J_z = \beta_{31} I, \quad \text{for } \mathbf{k} \parallel Y \text{ and } \mathbf{E} \parallel X, \tag{3.10a}$$

$$J_x = 0,\ J_y = \beta_{22} I,\ J_z = \beta_{31} I, \quad \text{for } \mathbf{k} \parallel X \text{ and } \mathbf{E} \parallel Y. \tag{3.10b}$$

For e-polarization:

$$J_x = 0,\ J_y = 0,\ J_z = \beta_{33} I, \text{ for } \mathbf{k} \parallel X \text{ or } Y \text{ and } \mathbf{E} \parallel Z. \tag{3.10c}$$

For $LiNbO_3$: Fe, $\beta_{33} \approx \beta_{31} \gg \beta_{22},\ \beta_{15}$ and so the PV current is in all cases mostly along the Z or photovoltaic axis. Comparing the current density for e-polarization with the microscopic expression, one obtains $\beta_{33} = sqN_D L_{\mathrm{PV}}$, and one may define an equivalent PV field as

$$E_{\mathrm{PV}} = \frac{J_{\mathrm{PV}}}{q\mu n} = \frac{sIN_D L_{\mathrm{PV}}}{\mu n} \tag{3.11}$$

which is characteristic of the material and doping.

One curious feature of the PV drift is that it may give rise to a modulated J_{PV} (i.e., to a PR effect) even if the crystal is subjected to a uniform light intensity. In fact, the effect is associated to a modulation of the polarization. Let us consider two linearly polarized waves propagating in the XY plane (one o-polarized with $\mathbf{E}$ along X and another one e-polarized with $\mathbf{E}$ along Z). The total amplitude of the wave field is

$$\mathbf{E}_T = E_{0x}\mathbf{u}_x e^{i\mathbf{k}\cdot\mathbf{r}} + E_{0z}\mathbf{u}_z e^{i\mathbf{k}'\cdot\mathbf{r}}, \tag{3.12}$$

which gives rise to a nonmodulated light intensity. However, the three components of the LPV current density are

$$J_x = \beta_{15} E_{0x} E_{0z}^* e^{i(\mathbf{k}-\mathbf{k}')\cdot\mathbf{r}} + \text{c.c.}, \tag{3.13a}$$

$$J_y = -\beta_{22} I, \tag{3.13b}$$

$$J_z = \beta_{33} I, \tag{3.13c}$$

i.e., the x-component is modulated with a grating vector $\mathbf{k} - \mathbf{k}'$. In other words, an index grating is formed even if there is no interference light-intensity pattern.

3.5 Macroscopic Formulation

For a considerable range of phenomena, a more general and simpler phenomenological description exists that only relies on the spatial symmetry of the medium and is free of the assumptions associated to any particular microscopic model [31]. The key point of the macroscopic model is the expression that links the current density **J** to the field **E** and light intensity I. The explicit answer for 1D (x variable) is

$$J = \sigma E + \beta I + \xi \frac{\partial I}{\partial x}. \tag{3.14}$$

The first term describes the ohmic conduction, σ being the electrical conductivity. The second term stands for the photovoltaic drift and the third one represents the effect of the inhomogeneity of the light pattern (carrier diffusion). The macroscopic parameter ξ is related to the diffusion coefficient through $\xi \partial I/\partial x = qD\partial n/\partial x$. By adding the Poisson and the continuity equations, one has the basic equations for the macroscopic model. Together with the boundary conditions, they allow the solution for the space-charge field if the macroscopic parameters σ, β, and ξ are known. Of course, the microscopic models are the ones capable of giving physical meaning to the macroscopic parameters and so providing a full understanding of the involved physical processes.

3.6 Low Intensities: Continuous Wave (CW) Regime

Since the space-charge field **E** is the key quantity to describe the PR response, our first aim is to reduce the set of rate equations to one single equation involving **E** and the light intensity I. From (3.3a) and (3.7), one finds

$$N_A = \frac{sNI + \dfrac{\varepsilon_0 \varepsilon}{q} \dfrac{\partial \nabla \cdot \mathbf{E}}{\partial t} - \dfrac{\partial n}{\partial t}}{sI + \gamma n}. \tag{3.15}$$

Many practical situations involve the use of CW illumination. For this regime and low intensity levels, the inequalities $n \ll N_A - N_A(0),\ N_D - N_D(0)$ hold. Therefore, (3.4) reduces to

$$\frac{\varepsilon_0 \varepsilon}{q} \nabla \cdot \mathbf{E} + \frac{sNI + \dfrac{\varepsilon_0 \varepsilon}{q} \dfrac{\partial \nabla \cdot \mathbf{E}}{\partial t} - \dfrac{\partial n}{\partial t}}{sI + \gamma n} - N_A(0) = 0, \tag{3.16}$$

which is equivalent to

$$\frac{\partial n}{\partial t} = s\left[N_D(0) + \frac{\varepsilon_0 \varepsilon}{q} \nabla \cdot \mathbf{E}\right] I + \frac{\varepsilon_0 \varepsilon}{q} \frac{\partial \nabla \cdot \mathbf{E}}{\partial t} + \gamma \left[\frac{\varepsilon_0 \varepsilon}{q} \nabla \cdot \mathbf{E} - N_A(0)\right] n. \tag{3.17}$$

On the other hand, combining (3.3c), (3.6), and (3.15), one derives

$$\frac{\varepsilon_0 \varepsilon}{q} \frac{\partial \mathbf{E}}{\partial t} + \mu \left(n\mathbf{E} - \frac{k_B T}{q} \nabla n\right) + \frac{sL_{\mathrm{PV}} \left[\gamma N n - \dfrac{\varepsilon_0 \varepsilon}{q} \dfrac{\partial \nabla \cdot \mathbf{E}}{\partial t} + \dfrac{\partial n}{\partial t}\right] I \mathbf{u}_{\mathrm{PV}}}{sI + \gamma n} = \frac{\mathbf{J}_{\mathrm{Tot}}}{q}, \tag{3.18}$$

where it has been assumed that the photovoltaic current is only significant along the polar axis. The value of the total current density $\mathbf{J}_{\mathrm{Tot}}$ has to be determined from the appropriate boundary conditions.

3.7 Quasi-Equilibrium (Adiabatic) Approximation: Nonlinear Equation for the Field

Except for the neglect of the carrier density in the expression for the charge density, (3.17) and (3.18) constitute an exact reduction of the starting set of rate equations, though, still a quite intractable one for the objective of obtaining a single nonlinear equation for the field. To this end, it is useful to make a further approximation. In many materials under normal conditions the relaxation time of electrons, i.e., the recombination time τ_{R}, is much shorter than the characteristic time scale for the variation of $\mathbf{E}$, which is also referred to as dielectric relaxation time τ_{D}. Consequently one can assume that $\partial n/\partial t = 0$, which implies that electrons are at any time in equilibrium (quasi-equilibrium) with the trap distribution. Then, (3.17) reduces to

$$n = \frac{s\left[N_D(0) + \dfrac{\varepsilon_0 \varepsilon}{q} \nabla \cdot \mathbf{E}\right] I + \dfrac{\varepsilon_0 \varepsilon}{q} \dfrac{\partial \nabla \cdot \mathbf{E}}{\partial t}}{\gamma \left[N_A(0) - \dfrac{\varepsilon_0 \varepsilon}{q} \nabla \cdot \mathbf{E}\right]}. \tag{3.19}$$

This expression can be now substituted into (3.18) and one may obtain the general nonlinear equation for the electric field. We will explicitly write it for a particular approximation (see next section).

3.8 Perturbative Approach to the Nonlinear Equation

The procedure to arrive at the nonlinear equation for the field is a complicated task and requires some approximation techniques. In many cases, such as in holographic recording experiments, one may use a perturbative scheme. It considers that the dynamic variables are decomposed into a constant spatially uniform average term (labeled with superscript 0) and a time-dependent spatially modulated term (with superscript 1), i.e., $X(r,\ t) = X^{(0)} + X^{(1)}(r,\ t)$. Under the adiabatic approximation and small light intensity (see previous sections), a useful equation has been obtained by Pedersen and Johansen for the modulated space charge field in non-photovoltaic materials [24]. It writes

$$
\begin{aligned}
&-\mathbf{E}^{(0)}\frac{\partial\nabla\cdot\mathbf{E}^{(1)}}{\partial t}+\frac{k_BT}{q}\frac{\partial\nabla^2\mathbf{E}^{(1)}}{\partial t}-\varpi_0\mathbf{E}^{(0)}(\nabla\cdot\mathbf{E}^{(1)})+\frac{k_BT}{q}\varpi_0\nabla^2\mathbf{E}^{(1)}\\
&-\varsigma I^{(0)}\mathbf{E}^{(1)}-\frac{\gamma N_A^{(0)}}{\mu}\frac{\partial\mathbf{E}^{(1)}}{\partial t}=\varsigma I^{(1)}\mathbf{E}^{(0)}-\frac{k_BT}{q}\varsigma\nabla I^{(1)}+\varpi_0\mathbf{E}^{(1)}(\nabla\cdot\mathbf{E}^{(1)})\\
&+\mathbf{E}^{(1)}\frac{\partial\nabla\cdot\mathbf{E}^{(1)}}{\partial t}
\end{aligned}
\tag{3.20}
$$

where $\varpi_0 = sI_0N/N_A^{(0)}$ and $\varsigma = sqN/\varepsilon_0\varepsilon$. This expression also uses an additional restriction $N_A^{(0)} \ll N_D^{(0)} \simeq N$. The left-hand side of the equation is linear in $\mathbf{E}^{(1)}$. The first two terms on the right-hand side represent the driving force due to light excitation, and the two last terms are the nonlinear terms responsible for the nonlinear coupling. Note also that the equation is first-order with respect to time and higher-order with respect to space. The same or similar equation has been used in several works [32–34]. Then, in order to further exploit the perturbative scheme, one assumes that the modulated values are small in comparison to the constant ones. The first-order approximation is discussed in the next section.

3.9 Sinusoidal Light Excitation at Low Modulation Linear Equation for the Field

A large number of experiments can be described within a linear approximation to Eq. (3.20) that accounts for the key features of the PR response. In what follows, we will consider, for simplicity, a 1D sinusoidal light pattern along the X axis, i.e., the real part of the complex expression $I = I_0(1 + me^{iKx})$, where the modulation m is defined by $m = (I_{\max} - I_{\min})/(I_{\max} + I_{\min})$ with $I_{\max}$ and $I_{\min}$ being the maximum and minimum values of I, respectively. This is the situation that applies to the experiments using an holographic set-up. If m is small, all

variables are expected to write $X(t) = X^{(0)} + X^{(1)}(t)e^{iKx}$ ($X \equiv n,\ N_D,\ N_A,\ E$), where $X^{(1)}$ stands for the amplitude of the sinusoidal component[2]. Then, substituting those sinusoidal expressions into equation (3.20) and neglecting all terms involving products of the modulated variables, one obtains a simple linear equation for the amplitude of the modulated space-charge field [35]

$$\frac{\partial E^{(1)}}{\partial t} + pE^{(1)} = mh, \tag{3.21}$$

where

$$p = \frac{E_q + E_D + i(E_0 + rE_{PV})}{E_q H}, \tag{3.22a}$$

$$h = i\frac{E_D + i(E_0 + E_{PV})}{H}, \tag{3.22b}$$

$$H = \tau_D\left[1 + \frac{E_D + iE_0}{E_M}\right], \tag{3.22c}$$

$\tau_D = \varepsilon\varepsilon_0/e\mu n^{(0)}$ being the dielectric relaxation time corresponding to a carrier concentration $n^{(0)} = sI_0N_D^{(0)}/\gamma N_A^{(0)}$ and $r = N_A^{(0)}/N$ is an oxidation/reduction ratio. Also, for convenience, we have set $E_0 \equiv E^{(0)}$ as the applied field. The characteristic fields in (3.22) are defined as

$$E_D = \frac{k_B KT}{q},\ E_M = \frac{\gamma N_A^{(0)}}{\mu K},\ E_q = \frac{qN_D^{(0)}r}{\varepsilon\varepsilon_0 K},\ E_{PV} = \frac{L_{PV}}{\tau_R \mu}, \tag{3.23}$$

where $\tau_R = 1/\gamma N_A^{(0)}$ is the carrier recombination time. These characteristic fields play a crucial role in the possible charge transport regimes under sinusoidal light excitation. Their physical meaning is given in Section 3.10.

3.9.1 Steady-State Solution

By making $\partial E^{(1)}/\partial t = 0$, one immediately obtains from (3.21) the steady-state amplitude $E^{(1)}$ of the modulated space-charge field,

$$E^{(1)} = m\frac{h}{p} = im\frac{E_D + i(E_0 + E_{PV})}{1 + \dfrac{E_D + i(E_0 + rE_{PV})}{E_q}}. \tag{3.24}$$

One should note that, within our linearized standard model, the steady-state space-charge field is *independent* of the average light intensity and *proportional* to the modulation depth (index).

---

[2] Note that for high light intensities, $N_D^{(0)}$ and $N_A^{(0)}$ may not coincide with $N_D(t = 0)$ and $N_A(t = 0)$, respectively.

If $E_0 = 0$, $E_{PV} = 0$, so that *diffusion* is the only operative transport mechanism, and assuming $E_D \ll E_q$ (valid in many cases) then

$$E^{(1)} = im\frac{E_D}{1 + (E_D/E_q)} \cong imE_D, \tag{3.25}$$

i.e., a phase-mismatch $\phi = \pi/2$ appears between the light and space-charge field gratings. Eq. (3.25) may also be written as,

$$E^{(1)} \cong \frac{E_D}{K}\frac{1}{I_0}\frac{\partial I}{\partial x} = \frac{k_B T}{q}\frac{1}{I_0}\frac{\partial I}{\partial x}, \tag{3.26}$$

i.e., the response is proportional to the gradient of the light intensity (*gradient response*).

When diffusion is negligible and the material is not photovoltaic (e.g., under common experimental situation in $Bi_{12}SiO_{20}$), $E_D \ll E_0$, E_q, the steady-state solution is

$$E^{(1)} \simeq -m\frac{E_0}{1 + (iE_0/E_q)}. \tag{3.27}$$

For moderate applied fields, ($E_0 \ll E_q$). $E^{(1)} \simeq -mE_0$, indicating that the field is approximately in phase with the light, as expected for a local response.

For a PV material such as $LiNbO_3$($E_{PV} \gg E_D$), in absence of applied field, one has

$$E^{(1)} = -m\frac{E_{PV}}{1 + \frac{irE_{PV}}{E_q}}, \tag{3.28}$$

i.e., the generated phase-shift depends on the ratio E_{PV}/E_q ($\phi = 0$ or $\phi = \pi$ for $E_{PV} \ll E_q$, $\phi = \pm\pi/2$ for $E_{PV} \gg E_q$). Moreover, when $E_{PV} \ll E_q$, $E^{(1)} = -mE_{PV}$.

3.9.2 Transient Response

a) Recording of a Grating

Assuming that the initial condition for the fundamental component of the space-charge field is $E^{(1)}(t = 0) = 0$, the general time-dependent solution of Eq. 3.21 is,

$$E^{(1)}(t) = E^{(1)}(1 - e^{-pt}). \tag{3.29}$$

If p is real, the recording curve is a (monotonic) exponential. However, the imaginary part of p, which is associated to the motion of the index fringes, may introduce oscillations in the transient response. In order to clearly observe these oscillations, $\mathrm{Im}(p) > \mathrm{Re}(p)$.

For nonphotovoltaic materials,

$$p \simeq \frac{1}{\tau_D} \frac{1 + (iE_0/E_q)}{1 + (iE_0/E_M)}. \tag{3.30}$$

In the case of $Bi_{12}SiO_{20}$, oscillations have been predicted [36,37] and observed for a certain range of characteristic fields [38]. On the other hand, for photovoltaic materials such as $LiNbO_3$ oscillations have been also reported [39–41].

The rise time, defined as the reciprocal of the initial growth rate, is

$$\tau = \frac{1}{\mathrm{Re}(p)}, \tag{3.31}$$

and so it is of the order of the dielectric relaxation time (both are proportional to the light intensity). However, remarkable differences between τ and τ_D appear, depending on the material and the recording conditions (applied field and grating period). For a PV material, like $LiNbO_3$, where E_{PV} and E_M are large, the parameter p is (for $E_0 = 0$),

$$p = \frac{1}{\tau_D}\left(1 + i\frac{rE_{PV}}{E_q}\right) \tag{3.32}$$

and so $\tau = \tau_D$. For a nonphotovoltaic material ($E_{PV} = 0$) and assuming $E_D \ll E_0$, it yields

$$\tau = \tau_D \frac{1 + \dfrac{E_0^2}{E_M^2}}{1 + \dfrac{E_0^2}{E_q E_M}}. \tag{3.33}$$

Then, if $E_q > E_M$ (e.g., $Bi_{12}SiO_{20}$), $\tau > \tau_D$. If $E_q < E_M$ (e.g., $BaTiO_3$ or SBN), $\tau < \tau_D$.

b) Initial Recording (Short-Time Limit)

The short-time solution for the fundamental component is

$$E^{(1)} = im \frac{E_M[E_D + i(E_0 + E_{PV})]}{E_M + E_D + iE_0} \frac{t}{\tau_D}. \tag{3.34}$$

For common experimental situations in sillenites, $E_0 > E_M > E_D$ and $E_{PV} = 0$. Then,

$$E^{(1)} \approx im \frac{E_M t}{\tau_D} = im \frac{q\alpha I_0}{\varepsilon\varepsilon_0 K} t. \tag{3.35}$$

The initial rate increases on increasing absorption ($\alpha = sN_D^{(0)}$) due to enhanced ionization cross-section and on decreasing dielectric constant due to reduced screening.

We have now the ingredients to obtain the sensitivity S of a PR material, which is defined as the energy required to produce a given refractive index change (or diffraction efficiency). For $m = 1$

$$S = \frac{|\Delta n|}{tI_0} = \frac{1}{2}\frac{n^3 r_{\text{eff}}|E^{(1)}|}{I_0 t} = \frac{1}{2}\frac{e\alpha n^3 r_{\text{eff}}}{\varepsilon\varepsilon_0 K}, \tag{3.36}$$

where r_{eff} is the effective electro-optic component. Eq. (3.36) illustrates that $n^3 r_{\text{eff}}/\varepsilon$ is an appropriate figure of merit for the PR sensitivity.

c) Dark and Light-Induced Erasure

Under homogeneous illumination or in the dark (due to homogeneous thermal ionization), the photorefractive gratings fade out. The decay for the complex amplitude of the space-charge field is described by

$$E^{(1)} = E^{(1)}(0)e^{-\text{Re}(p)t}e^{-i\text{Im}(p)t}. \tag{3.37}$$

Therefore [42], the decay is exponential with a time constant $\tau = 1/\text{Re}(p)$ as for the case of recording. It is easy to show that $\tau \propto 1 + CK^2$, where C is a constant. On the other hand, fringes move during erasure at aconstant velocity $v = \text{Im}(p)/K$.

3.10 Summary of Characteristic Times, Lengths and Fields

Here we summarize a number of characteristic parameters used in the semiconductor literature and that determine the PR response.

a) Characteristic Times

Recombination time or carrier life-time: $\tau_{\text{R}} = 1/\gamma N_A^{(0)}$.

Dielectric relaxation time: $\tau_{\text{D}} = \varepsilon_0\varepsilon/(e\mu n^{(0)}) = \varepsilon_0\varepsilon/\sigma$, or time needed to screen a given (arbitrary) field in the medium (only depends on the conductivity and dielectric constant of the medium).

b) Characteristic lengths

Diffusion length: $l_{\text{Diff}} = (D\tau_{\text{R}})^{1/2} = \sqrt{\mu k_B T \tau_{\text{R}}/e}$, is the average forward distance traveled by a carrier during its life time.

Drift length: $l_0 = \mu E_0 \tau_{\text{R}}$, is the drift distance traveled by the carrier under the field E_0 before recombination.

Debye screening length: $l_D = (D\tau_D)^{1/2} = \sqrt{k_B T \varepsilon_0 \varepsilon / e^2 N_A^{(0)}}$, is the distance needed to screen a charge or field perturbation in the medium.

Photovoltaic length: L_{PV} is the average distance traveled by a carrier on photoexcitation.

c) Characteristic Fields

Diffusion field: $E_D = K k_B T/q$. For a sinusoidal carrier grating is the field amplitude causing the same currents as diffusion or, equivalently, the one that exactly balances the diffusion current. It is also the maximum field that can be achieved by carrier diffusion. For a localized beam of transversal size d_s (see Section 3.15), the equivalent diffusion field would correspond to $K = 1/d_s$, i.e. $E_D = k_B T/q d_s$.

Characteristic field $E_M = \gamma N_A^{(0)}/\mu K = 1/\tau_R \mu K$ is the electric field that moves a carrier a distance $1/K = \Lambda/2\pi$ during its lifetime.

Limiting or saturation field: $E_q = q r N_D^{(0)}/(K\varepsilon\varepsilon_0)$. If $N_A^{(0)} \ll N_D^{(0)}$ (e.g., sillenites), it reduces to $E_q = N_A^{(0)} q/K\varepsilon\varepsilon_0$ and represents the maximum field that can be obtained when all traps are used (saturation limit). For a localized beam of transversal size d_s (also in sillenites), the limiting field writes $E_q = q d_s N_A^{(0)}/\varepsilon\varepsilon_0$. One notes that for a grating with period $\Lambda = 2\pi l_D$ ($K = 1/l_D$) or a beam of transversal size l_D, $E_D = E_q = E_L$. On the other hand, for an applied field E_0, the transversal size of a localized beam whose saturation field $E_q = E_0$ is designated as the *saturation length* $l_s = \varepsilon_0 \varepsilon E_0/(eN_A(0))$.

3.11 Grating Enhancement Methods

Fast photorefractive materials such as sillenites and semiconductors show a small electro-optic coefficient and so, also, a weak response. There are two main techniques for enhancing the refractive index change in these materials. The first method involves detuning the frequency of the interfering optical beams while a dc field is maintained across the crystal [35]. The appropriate choice of the detuning frequency leads to resonant coupling between the induced drift of charges and the motion of the optical interference pattern. The other method involves the use of an ac field with frequency much higher than the dielectric relaxation frequency [43,44,58]. The two methods are now briefly analyzed.

3.11.1 Applied dc *Field plus Light Frequency Detuning*

Here we impose on the crystal a dc field along the X-axis and a traveling interference pattern generated by two monochromatic waves with close frequencies ω_1, ω_2, so that $(\omega_2 - \omega_1)/\omega_1 \ll 1$, i.e.,

$$E(x,\ t) = E_1 e^{i(\mathbf{k}_1 \mathbf{r} - \omega_1 t)} + E_2 e^{i(\mathbf{k}_2 \mathbf{r} - \omega_2 t)}. \tag{3.38}$$

The light intensity pattern writes,

$$I(x,\ t) \propto |EE^*| = \mathrm{Re}\left\{I_0\left[1 + me^{i(\mathbf{Kr}-\Omega t)}\right]\right\}, \tag{3.39}$$

with $I_0 = |E_1|^2 + |E_2|^2$, $m = 2|E_1E_2|/I_0$, the *detuning* $\Omega = \omega_2 - \omega_1$ and $K = k_2 - k_1$. The grating vector K is assumed to be parallel to the field and so $K = K_x$. Eq. (3.39) represents a grating of wave vector K moving at a constant speed $v = \Omega/K$. The differential equation for the amplitude of the modulated field is still (3.21) after substituting $mhe^{-i\Omega t}$ for mh. Therefore, assuming a solution $E^{(1)}(t) = E^{(1)}(\Omega)e^{-i\Omega t}$, one obtains

$$E^{(1)}(\Omega) = \frac{mh}{p - i\Omega}. \tag{3.40}$$

Resonance conditions and, thus, enhancement of the response, will occur for $\Omega_R = \mathrm{Im}(p)$. In the conditions usually prevailing for $Bi_{12}SiO_{20}$,

$$\Omega_R = \frac{-E_\mathrm{M}}{\tau_\mathrm{D}E_0}. \tag{3.41}$$

For $Bi_{12}SiO_{20}$, Ω_R is around $0.1 - 1.0\Omega_D$ ($\Omega_D = 2\pi/\tau_\mathrm{D}$) and the corresponding space-charge field will be

$$E^{(1)}(\Omega_R) = imE_\mathrm{q}, \tag{3.42}$$

i.e., one produces a traveling space-charge wave moving at the same velocity as the light pattern but having a $\pi/2$ phase shift. So, the response is diffusion-like but markedly enhanced with regard to the pure diffusion case since usually $E_\mathrm{q} \gg E_\mathrm{D}$.

One may also calculate the enhancement factor

$$R = \frac{E^{(1)}(\Omega)}{E^{(1)}(0)} = \frac{p}{p - i\Omega}, \tag{3.43}$$

which, in the case of optimum detuning $\Omega = \Omega_R = \mathrm{Im}(p)$, yields

$$R(\Omega_R) = \frac{p}{\mathrm{Re}(p)} = \sqrt{1 + \frac{E_\mathrm{q}^2}{E_0^2}} \sim \frac{E_\mathrm{q}}{E_0}. \tag{3.44}$$

for $E_\mathrm{M} \ll E_0 \ll E_\mathrm{q}$. Enhancement of about one order of magnitude can be readly achieved.

3.11.2 Application of an ac Field

Let us assume a fixed light grating $I = I_0(1 + me^{iKx})$. We can use the first-order equation (3.21) with a total field $E(x,\ t) = E^{(0)}(t) + E^{(1)}e^{iKx}$ applied along the K vector (X-axis). Then,

$$\frac{\partial E^{(1)}}{\partial t} + p(t)E^{(1)} = mh(t), \tag{3.45}$$

where

$$p(t) = \frac{1}{\tau_D}\frac{1 + (E_D/E_q) + (iE_0(t)/E_q)}{1 + (E_D/E_M) + (iE_0(t)/E_M)}, \tag{3.46}$$

and

$$h(t) = \frac{1}{\tau_D}\frac{-E_0(t) + iE_D}{1 + (E_D/E_M) + (iE_0(t)/E_M)}. \tag{3.47}$$

A simple approximate method to solve Eq. (3.45) is the averaging procedure developed by Stepanov and Petrov [43]. It is applicable when the temporal period of the applied field is much larger than the carrier recombination time and much shorter than the grating relaxation time. Under these conditions, $E^{(1)}$ can be considered constant in time and equal to $E^{(1)} = m\langle h\rangle/\langle p\rangle$. The solutions for two particular cases are as follows:

a) **Applied square-wave field**, $E_0 = E_{00}\text{sign}(\sin\Omega t)$. Then,

$$E^{(1)} = im\frac{E_D + \eta_{sq}E_{00}}{2(1 + E_D/E_q + \eta_{sq}E_{00}/E_q)}. \tag{3.48}$$

with $\eta_{sq} = \xi = -E_{00}/(E_D + E_M)$. One sees that the field is exactly the same as for a diffusion nonlinearity after substituting $E_D + \eta_{sq}E_{00}$ for E_D, so it provides an enhanced gradient response.

b) **Applied sinusoidal wave field**, $E_0 = E_{00}\sin\Omega t$. One arrives at the same solution (3.48) with $\eta_{sq} = \left[\sqrt{1 + \xi^2} - 1\right]/\xi$, leading to a smaller enhancement than for case a). Again the response is diffusion-like as corresponds to the symmetry of the ac field without any privileged direction. A complete theoretical model describing the formation of the space-charge field in a PR material exposed to a sinusoidal *ac* field, *dc* field and a running light pattern that is valid for all time scales has been given in [45].

Enhancement factors under ac fields are similar to those obtained in the detuning method.

3.12 High-Contrast Effects

3.12.1 Higher Harmonics and Cross-Talk Effects

The linearized approximation requires a low light contrast ($m \ll 1$). When m approaches 1, the general rate equations (3.3) are no longer linear and have more complicated solutions exhibiting new features: i) the growth kinetics of the recorded (fundamental) grating is modified as well as its steady-state level; ii) other gratings with K vectors that are multiples of that of the fundamental grating develop and become important. A number of approximate treatments have been developed to deal with the solution of the *nonlinear* material (rate) equations [36,46–48]. As an illustrative example, we can quote the analytical (nonperturbative) method by Serrano et al. [48], valid for the diffusion regime. It gives for the steady-state amplitude of the fundamental component of the space-charge field

$$E^{(1)} = i\frac{mE_{\mathrm{D}}}{2}\left[1 + (m/2)^2 + 2(m/2)^4\right] + O(m^7). \tag{3.49}$$

One sees that the dependence of that amplitude on m is superlinear, in accordance with experiments as illustrated in Fig. 3.5. Note that for $m = 1$, the effect of the nonlinear terms is to increase by a factor 2 the value derived from the linear approximation. The same model yields the dependencies of the steady-state levels for the various harmonics of the fundamental grating. They

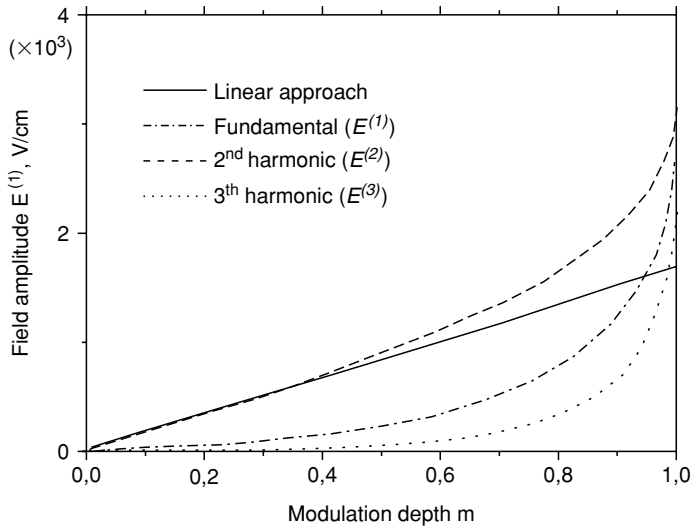

FIGURE 3.5. Dependence of the amplitude of the first three Fourier components of the field $E^{(1)}$, $E^{(2)}$, $E^{(3)}$ on the modulation depth m. The amplitude of the fundamental component correponding to the linear solution is displayed for comparison.

show an even steeper dependence on m. The lower order terms go as m^2 for the second harmonic, as m^3 for the third-harmonic and so on, as expected from the nonlinear mixing of the various harmonic gratings. Anyhow, the most useful way to discuss high-m effects is the use of numerical methods that have been applied to steady-state as well as transient situations [36,37,49].

The nonlinear terms in the rate equations are also responsible for the occurrence of combinatorial gratings and cross-talk effects when several light gratings are imposed on the material [28,50–53]. Figure 3.6 shows the combinatorial gratings, i.e., the ones having K vectors that are linear combinations of those of the light, when two holograms are sequentially recorded in $LiNbO_3$ [52]. Cross-talk effects have also been observed during simultaneous recording of two gratings in $Bi_{12}SiO_{20}$ [50,51] and $BaTiO_3$ [53]. A theoretical study of these effects, including a comparison between simultaneous and sequential recording (see Fig. 3.7), can be found in Ref. [28].

3.12.2 Grating Instabilities: Generation of Subharmonics

Under certain conditions, a $Bi_{12}SiO_{20}$ crystal (and other sillenites) exposed to a running light interference pattern generates secondary gratings with spacings that are two, three, or four times that of the fundamental grating [32,54,55]. Therefore, they are subharmonics of that grating with K-vectors equal to $K/2$, $K/3$, $K/4, \ldots$. The experiment is schematically illustrated in Fig. 3.8 for the first subharmonic ($K/2$). The same phenomenon was observed when the crystal is illuminated with a stationary light pattern under an ac field [56–58]. In other

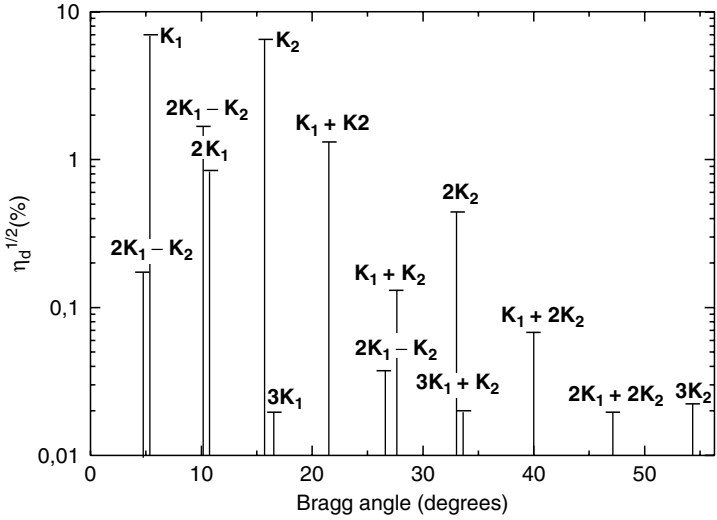

FIGURE 3.6. Square root of the diffraction efficiency of the observed gratings as a function of the grating's Bragg angles. The corresponding K vector of each grating is shown.

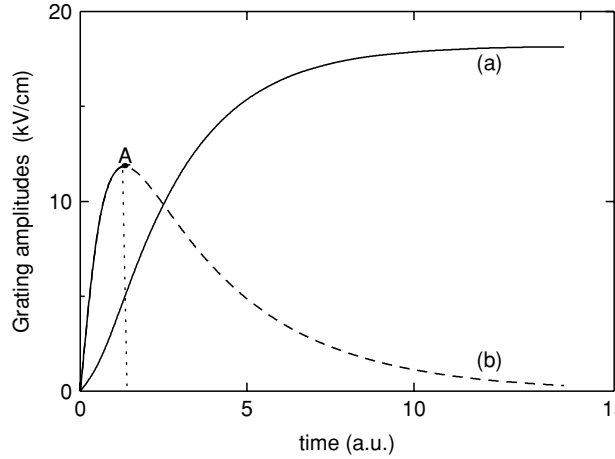

FIGURE 3.7. Time evolution of the combinational grating ($K_1 + K_2$) in simultaneous (a) and sequential (b) recording. For case (b), the time scale refers to the recording of the second grating. For applications, the recording of this second grating is stopped at point A where the two fundamental gratings reach the same amplitude.

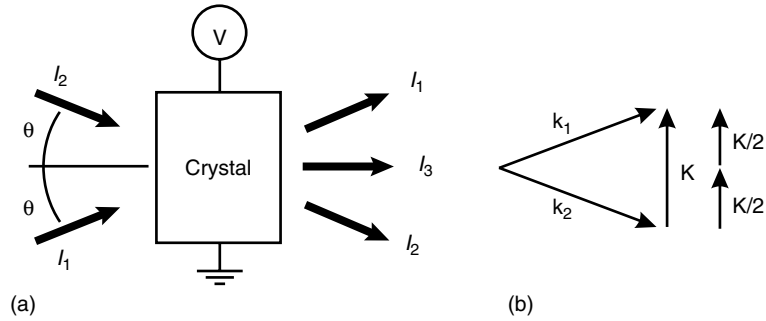

FIGURE 3.8. (a) Schematic set-up for the observation of subharmonic generation. (b) K-vector diagram.

words, the generation of subharmonics has been observed applying the two techniques used to enhance the PR response. It is now clear that the primary mechanism for the generation of subharmonics is the instability of the non-linear material equations.

The usual way to discuss the phenomenom is to propose an ansatz solution for the rate equations (including the nonlinear terms) or for the nonlinear field equation. It should consist of the fundamental grating and a seed for the subharmonic grating, i.e.,

$$E^{(1)}(x,\ t) = A^{(1)}(t)e^{iKx} + A^{(1/2)}(t)e^{iKx/2} + \text{c.c.} \tag{3.50}$$

For the purposes of an instability analysis, it is reasonable to assume that the subharmonic has no influence on the fundamental space-charge field grating that can therefore be independently calculated. In this way, one can obtain the region of physical parameters that lead to subharmonic generation. The analysis consists of monitoring the amplitude of the subharmonic grating and determine under which parameters this amplitude overcomes a certain threshold representative of the instability. The problem of obtaining the steady-state amplitude of the subharmonic grating is much harder [34,59].

We will, here, concentrate on the threshold determinations. Let us, first, consider the case of a running interference pattern $I_p = mI_0 \cos(Kx - \Omega t)$, with Ω being the detuning. Using a simplified version of the nonlinear equation (3.20) and applying the Routh-Hurwitz criterion for instability, one derives the condition

$$\frac{E_0}{E_M} = 2\left[2 \pm (m^2 - b^2)^{1/2}\right], \tag{3.51}$$

defining the boundary of the instability region. b is the detuning frequency normalized to $1/\tau_D$. It has a typical banana shape and so it is multivalued.

Now let us comment on the case where the recording is performed under an applied ac field $E_0(t) = E_{00} \cos bt$. One can assume that the light intensity pattern includes both the fundamental and a *seed* harmonic beam (in fact, this does not modify the results and can be neglected), i.e., $I = I_0[1 + m_1 \cos Kx + m_{1/2} \cos(Kx/2)]$. By substituting this expression into the approximate nonlinear equation (3.20), one obtains two coupled equations that can be solved numerically. So, one can determine the conditions leading to growth of the subharmonic amplitude. The boundary separating the stability and instability regions in a $E_{00} - m$ diagram is now single valued. The stability increases for a sinusoidal ac field in comparison to a square wave.

3.12.3 Grating Instabilities: Parametric Processes

Under certain conditions, the subharmonic gratings become also unstable and the fundamental grating splits into other secondary gratings [60,61]. In fact, a large diversity of instability schemes are possible. In [61], this problem is linked with the more familiar optical parametric oscillation (OPO) processes in the field of nonlinear optics. Here, the analogous schemes are termed parametric photorefractive oscillation (PPO) processes and refer to the instability of space-charge waves, which will be briefly introduced in the next section. Three different schemes are possible: degenerate, longitudinal, and transversal (see Fig. 3.9). In all cases, the phase-matching conditions

$$\mathbf{K}_1 + \mathbf{K}_2 = \mathbf{K}_p, \tag{3.52a}$$

$$\omega_1 + \omega_2 = \omega_p, \tag{3.52b}$$

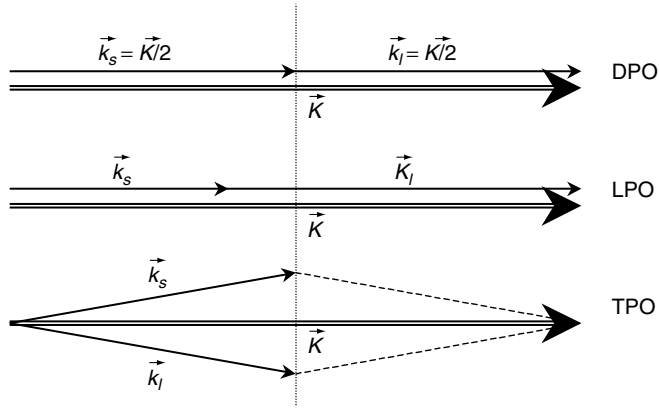

FIGURE 3.9. *K*-vector diagram for parametric processes. DPO stands for degenerate parametric oscillation or subharmonic generation. LPO and TPO respectively, represent longitudinal and transversal parametric oscillations.

should be obeyed, where $\mathbf{K}_p$ and ω_p correspond to the fundamental or light grating (*pump*) and $\mathbf{K}_i$, $\omega_i (i = 1, 2)$ to the parametrically generated gratings. The subharmonic generation refers to the particular case $\mathbf{K}_1 = \mathbf{K}_2 = \mathbf{K}_p/2$ and $\omega_1 = \omega_2 = \omega_p/2$.

3.13 Space-Charge Waves

In the case of a complex parameter p, the homogeneous equation $\partial E^{(1)}/\partial t + pE^{(1)} = 0$, under uniform illumination, presents damped wave-like solutions, $E^{(1)} \propto e^{-\mathrm{Re}(p)t} e^{i(Kx - \Omega_{\mathrm{scw}} t)}$, with $\Omega_{\mathrm{scw}} = \mathrm{Im}(p)$. They correspond to traveling waves, known as space-charge waves [7,59], moving at a speed $v_{scw} = \Omega_{\mathrm{scw}}/K$.

The concept of space-charge waves offers an adequate physical basis to discuss the gain enhancement techniques described in Section 3.11 as well as the instability of the recording grating versus a variety of parametric processes. One can use the space-charge waves formalism to study the recording of a PR grating under a running interference pattern or an ac field. Let us consider a running sinusoidal light pattern $I = I_0[1 + m\cos(Kx - \Omega t)]$ moving at a speed $v = \Omega/K$. Assuming that $Re(p)$ is negligible, the equation for the complex amplitude $A^{(1)}$ of the modulated field $E^{(1)} = A^{(1)} e^{i\Omega t}$ can be written as

$$\frac{dA^{(1)}}{dt} + i(\Omega_{\mathrm{scw}} - \Omega)A^{(1)} = mh, \tag{3.53}$$

which has the structure of a forced oscillator. The steady solution is

$$E^{(1)}(t) = \frac{mh}{i(\Omega_{scw} - \Omega)} e^{-i\Omega t}, \tag{3.54}$$

which provides a simple explanation of the enhancement of the grating amplitude as a resonance effect between the oscillating light excitation and the space-charge wave eigenmode. The space-charge waves formalism is also particularly adapted to understand grating instabilities and generation of subharmonics discussed in the previous sections. A detailed description of space-charge waves and their applications is offered in Chapter 5 of this volume.

3.14 Complicating Features to the Standard Model

Although the standard simple model described above has shown a very wide range of validity, there are experimental situations that demand some modifications. One of such situations arises when dealing with several active centers (see Subsection 3.14.1), or under bipolar transport, i.e., simultaneous electron and hole transport (see Subsection 3.14.2). Another example is provided by band-to-band transitions that can also cause bipolar photorefractivity (see Chapter 7 in this volume). In the case of PR polymers, field-dependent photoexcitation and transport parameters have to be introduced as well as additional molecular reorientation and birefringence effects. Moreover, when describing the response of semiconductors and multiple-quantum-well (MQW) structures at frequencies close to the band-gap, the electro-optic response is neither Pockels or Kerr-type, but it is mostly governed by the resonant Franz-Keldysh effect [5] (see Chapter 10, vol II).

3.14.1 Multiple Active Centers

Some experimental data have been obtained that are not consistent with the standard model and suggest that more than one type of trap may contribute to photorefraction. These effects have been observed in several crystals such as $Bi_{12}SiO_{20}$ [62], $KNbO_3$ [63,64], or in $LiNbO_3$ [64,65], to cite only a few examples. One may quote a strong dependence of the shape of the recording curve on light intensity and temperature. For example, maxima of the grating amplitude can appear before the steady-state is reached. Also, the decay curves in the dark or under illumination are not any longer exponential and present singular features. The theoretical description and some detailed computer simulations for recording and erasure are given in Refs. [66–68]. A particularly relevant case investigated in this reference is a material containing an optically active center and a thermal trap that appears to be a common situation [68]. More recently, some techniques applied to achieve long hologram lifetime have taken advantage of the existence of two photosensitive centers that are active at different wavelengths [69,70]. For instance, Buse et al. [69] report on a

permanent hologram written by IR excitation of a shallow photosensitive center, which is then stored in a deeper trap not affected by the recording wavelength. To initially fill the shallow traps, the sample has to be illuminated with visible light acting as a gate. For further details see also Chapter 8 of this book.

3.14.2 Bipolar Transport

Here, both electrons and holes simultaneously contribute to transport. A simple model leading to bipolar transport also involves donor and acceptor centers. However, under illumination, the donors can be ionized to generate holes (or trap holes) as well as electrons (or trap electrons), as illustrated in Fig. 3.10. Also, acceptors can trap electrons and holes. The rate equations should be slightly modified to include the new processes. For simplicity we will consider that diffusion is the only charge transport mechanism. Then, one easily arrives to the steady-state solution [6,7,71–73]

$$E^{(1)} = i\frac{m\xi(K)E_{\mathrm{D}}E_{\mathrm{q}}}{E_{\mathrm{D}} + E_{\mathrm{q}}}, \tag{3.55}$$

where $\xi(K) = (1 - C)/(1 + C)$ is the so-called *electron-hole competition factor*. The parameter C is given by

$$C = \frac{\tau_{\mathrm{D}e}(1 + \dfrac{E_{\mathrm{D}}}{E_{\mathrm{M}e}})}{\tau_{\mathrm{D}h}(1 + \dfrac{E_{\mathrm{D}}}{E_{\mathrm{Mh}}})}, \tag{3.56}$$

where $\tau_{\mathrm{D}e}$ and $\tau_{\mathrm{D}h}$ are the dielectric relaxation times corresponding to electrons and holes, respectively. It is easy to show that

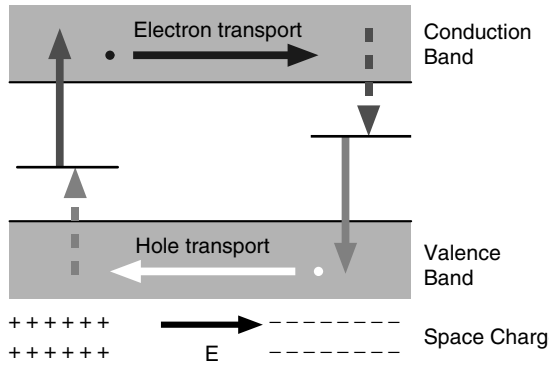

FIGURE 3.10. Illustration of the bipolar PR mechanism. Photoionization transitions are represented by solid gray arrows and recombination with dashed arrows.

$$\xi(K \to 0) = \frac{\sigma_e - \sigma_h}{\sigma_e + \sigma_h}, \tag{3.57a}$$

$$\xi(K \to \infty) = \frac{\alpha_e - \alpha_h}{\alpha_e + \alpha_h}, \tag{3.57b}$$

with $\sigma_{e(h)}$ and $\alpha_{e(h)}$ being the conductivity and absorption coefficients, respectively, associated to electron (hole) carriers and centers. The electron-hole competition factor gives rise to the following effects:

a) Reduces the space-charge field.
b) Leads to a variation of the relative contribution of electrons and holes depending on grating spacing.
c) The sign of the space-charge field depends on the difference between electron and hole photoconductivities (for $K \to 0$) or between absorption coefficients (for $K \to \infty$).

3.15 Localized Optical Beams

Another prolific research area in PR media has been that of localized optical beams (i.e., those having finite transversal width), mainly in connection with spatial solitons [10] (see Chapter 11 where the subject of PR solitons is covered in detail). Since their prediction by M. Segev and coworkers [74], several different types of PR solitons have been identified [15,18,75–78] and experimentally demonstrated [79–92], each exploiting distinct aspects of the charge transport mechanism. As for Kerr nonlinearities, spatial solitons refer to optical beams that preserve their transversal profile during propagation due to the balance between nonlinearity and diffraction.

The first aim here, as it occurred in the periodic case, is to reduce the set of rate equations (3.3) to a single equation involving the space-charge field **E** and the light intensity I. However, at variance with the former case, the expansion of all relevant variables in Fourier components does not provide, in general, an adequate theoretical framework. The main reason is that most applications exploit the strong saturation regime, where the spatial modulation of the light intensity is no longer a small quantity in comparison to its average value.

In order to deal with localized beams, it is convenient to express the rate equations in a suitable form. To this end, we normalize (3.3) by introducing the variables $\tau = t/\tau_B$ and $\nabla \equiv \nabla/d_s$, where d_s represents a characteristic spatial length for the variation of the light intensity profile. We assume that electrons are the sole charge carriers. Also, we use the Debye screening length $l_D = \sqrt{\varepsilon_0 \varepsilon k_B T / e^2 N_A(0)}$, the characteristic limiting field $E_L = k_B T / e l_D$ (e is the elementary charge), the impurity concentration ratio $r_N = N_D(0)/N_A(0)$, and the normalized electric field $\boldsymbol{\mathcal{E}} = \mathbf{E}/E_L$. Most of the values corresponding to these characteristic magnitudes are in the ranges $l_D \sim 0.01 - 0.4\,\mu\text{m}$, $E_L \sim 0.5 - 15\,\text{kVcm}^{-1}$, and $r_N \sim 10 - 10^3$ for many materials (an important exception is $LiNbO_3$ doped with Fe, where $r_N \sim 10^{-2} - 1$).

In applications with localized spatial light beams and solitons, it is very convenient to use an additional incoherent background illumination I_B (that may include the equivalent illumination level corresponding to the thermal emission of carriers) superimposed to the light intensity I [93]. Thus, one may introduce a *background dielectric relaxation time* $\tau_B = \varepsilon_0 \varepsilon \gamma / e\mu r_N s I_B$ associated to the background illumination, which will be used from here on.

With the help of the above definitions, the set of Eqs. (3.3) is transformed again into two equations. Within the adiabatic approximation ($\partial n/\partial t = 0$), the carrier density is governed by

$$\frac{n}{N_A(0)} = \frac{1}{2}\left[1 + \frac{l_D}{d_s}\nabla\cdot\boldsymbol{\mathcal{E}} + \frac{\tau_R \nu}{\tau_B r_N}(1+I)\right] \times \left\{-1 + \sqrt{1 + \frac{4\tau_R\left[\nu(1+I)\left(1 - \frac{l_D}{r_N d_s}\nabla\cdot\boldsymbol{\mathcal{E}}\right) - \frac{l_D}{d_s}\frac{\partial\nabla\cdot\boldsymbol{\mathcal{E}}}{\partial\tau}\right]}{\tau_B\left[1 + \frac{l_D}{d_s}\nabla\cdot\boldsymbol{\mathcal{E}} + \frac{\tau_R\nu}{\tau_B r_N}(1+I)\right]^2}}\right\}, \tag{3.58}$$

where $\nu = \varepsilon_0\varepsilon/e\mu\tau_R N_A(0)$, $I \equiv I/I_B$, and the space-charge field satisfies

$$\frac{\mathbf{J}_0}{e\mu N_A(0) E_L} = \frac{n}{N_A(0)}\boldsymbol{\mathcal{E}} + \frac{l_D}{N_A(0) d_s}\nabla n + \frac{\tau_R\nu}{\tau_B}\times\frac{\partial\boldsymbol{\mathcal{E}}}{\partial\tau} + \frac{\tau_R\nu}{\tau_B}\frac{E_{PV}}{E_L}\left[\frac{(1+\frac{1}{r_N})\frac{n}{N_A(0)} + \frac{\tau_R}{\tau_B r_N}\frac{l_D}{d_s}\frac{\partial\nabla\cdot\boldsymbol{\mathcal{E}}}{\partial\tau}}{\frac{n}{N_A(0)(1+I)} + \frac{\tau_R\nu}{\tau_B r_N}}\right]\mathbf{u}_{PV}, \tag{3.59}$$

with $\mathbf{J}_0$ being the boundary value of the current density and $E_{PV} = L_{PV}/\mu\tau_R$ a characteristic photovoltaic field that is measured across an open-circuited crystal. In photovoltaic crystals, typical values of $E_{PV} \simeq 10$–$50\,\mathrm{kVcm}^{-1}$.

We can now make some useful further approximations by taking into account that Eqs. (3.58) and (3.59) depend on the ratios $\tau_R\nu/\tau_B$ and l_D/d_s. Despite the large spread of τ_R/τ_B, (varying from 10^{-3} in sillenites to 10^{-12} in lithium niobate), the presence of ν makes the quotient $\tau_R\nu/\tau_B$ be typically around $10^{-5} - 10^{-7}$ for most PR materials. On the other hand, for spatial beams with characteristic widths $d_s \gtrsim 10\,\mu\mathrm{m}$, the ratio $l_D/d_s \gtrsim 10^{-2}$ is also satisfied. Therefore, Eq. (3.58) can be cast in the approximate form

$$\frac{n}{N_A(0)} = \frac{\tau_R\left[\nu(1+I)\left(1 - \frac{l_D}{r_N d_s}\nabla\cdot\boldsymbol{\mathcal{E}}\right) - \frac{l_D}{d_s}\frac{\partial\nabla\cdot\boldsymbol{\mathcal{E}}}{\partial\tau}\right]}{\tau_B\left[1 + \frac{l_D}{d_s}\nabla\cdot\boldsymbol{\mathcal{E}}\right]}. \tag{3.60}$$

Regarding Eq. (3.59), it is necessary to specify an experimental configuration to determine self-consistently the value of $\mathbf{J}_0$. In the overwhelming majority of

experiments involving the propagation of spatial light beams in PR materials, the experimental setup includes the scheme shown in Fig. 3.11. Denoting by V the terminal voltage (constant or time-dependent) between two electrodes placed at opposite faces of a crystal of thickness L, one has the line integral

$$\frac{V(t)}{E_{\mathrm{L}} d_s} = -\int_{-\mathrm{Electrode}}^{+\mathrm{Electrode}} \boldsymbol{\mathcal{E}} \cdot d\mathbf{l}, \tag{3.61}$$

where $\mathbf{l}$ denotes the normalized line element. In what follows, we shall briefly discuss the most often encountered scenarios.

3.15.1 Steady-State Solution

In steady-state under a time-constant voltage, the situation becomes simpler and it is possible to obtain, from Eqs. (3.59) and (3.60), a single nonlinear equation for the space-charge field

$$\boldsymbol{\mathcal{E}} = \left\{ \mathcal{J}_0 - \frac{l_{\mathrm{D}}}{d_s} \nabla \left[(1+I) \left[\frac{1 - \frac{l_{\mathrm{D}}}{r_N d_s} \nabla \cdot \boldsymbol{\mathcal{E}}]}{1 + \frac{l_{\mathrm{D}}}{d_s} \nabla \cdot \boldsymbol{\mathcal{E}}} \right] \right] \right\} \frac{\left[1 + \frac{l_{\mathrm{D}}}{d_s} \nabla \cdot \boldsymbol{\mathcal{E}}\right]}{(1+I)\left[1 - \frac{l_{\mathrm{D}}}{r_N d_s} \nabla \cdot \boldsymbol{\mathcal{E}}\right]}$$

$$- \frac{E_{\mathrm{PV}}}{E_{\mathrm{L}}} \left[1 + \frac{l_{\mathrm{D}}}{d_s} \nabla \cdot \boldsymbol{\mathcal{E}}\right] \mathbf{u}_{\mathrm{PV}}, \tag{3.62}$$

where $\mathcal{J}_0 = \tau_{\mathrm{B}} \mathbf{J}_0 / e\mu N_A(0) E_{\mathrm{L}} \tau_{\mathrm{R}} \nu$.

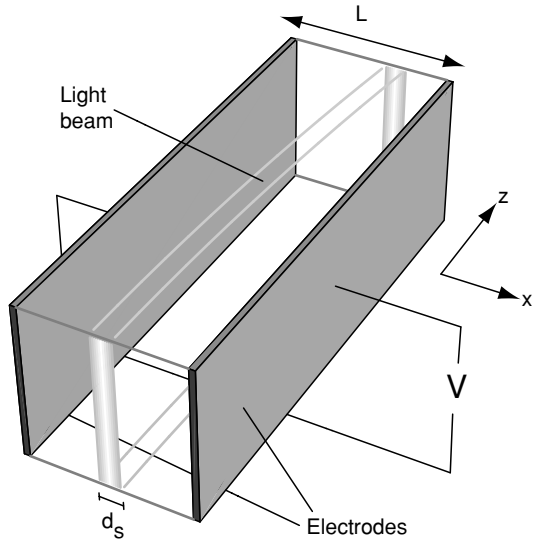

FIGURE 3.11. Simplified diagram of the experimental setup to study the propagation of a localized light beam through a PR crystal.

With appropriate approximations, Eq. (3.62) allows one to calculate $\mathcal{E} = \mathcal{E}(I)$. Let us first consider the one dimensional situation.

One Transverse Dimension

Let x be the only transverse coordinate and d_x the corresponding characteristic spatial length of the beam. Assuming $d_x \ll L$, one can consider that away from the central beam spot the light intensity approaches asymptotically a constant value I_∞. On the other hand, the field in this region also becomes independent of x so that $\mathcal{E} \to \mathcal{E}_0 = -V/E_L L$ and $\partial\mathcal{E}/\partial x = 0$. With these conditions and after some algebra, one finds from Eq. (3.62)

$$(1 + I_\infty)\mathcal{E}_0 = \mathcal{J}_0 - (\mathbf{u}_{PV} \cdot \mathbf{u}_x)\frac{\mathcal{E}_{PV}}{\mathcal{E}_L}(1 + I_\infty), \tag{3.63}$$

which allows us to obtain $\mathcal{J}_0$. For simplicity, let us ignore the photovoltaic contribution in Eqs. (3.62) and (3.63). Upon substitution of $\mathcal{J}_0$ into Eq. (3.62), one arrives at

$$\mathcal{E} = \frac{(1 + I_\infty)\left[1 + \frac{l_D}{d_x}\frac{\partial\mathcal{E}}{\partial x}\right]\mathcal{E}_0}{(1 + I)\left[1 - \frac{l_D}{r_N d_x}\frac{\partial\mathcal{E}}{\partial x}\right]} - \frac{l_D}{d_x}\frac{\partial}{\partial x}\ln\left[\frac{(1 + I)\left[1 - \frac{l_D}{r_N d_x}\frac{\partial\mathcal{E}}{\partial x}\right]}{1 + \frac{l_D}{d_x}\frac{\partial\mathcal{E}}{\partial x}}\right]. \tag{3.64}$$

In the above equation, one can distinguish the drift and diffusion contributions, represented by the first and the second terms, respectively. These regimes are strongly dependent not only on the particular material but on the boundary conditions: Open- or short-circuit conditions, applied external voltages, and so on. Diffusion is always present, but its effect on the global electric field profile is usually small under strong bias. Let us mention the main features of the particular regimes where diffusion and drift are the dominant transport mechanisms. To that end, the full Eq. (3.64) is solved numerically and we assume, for illustrative purposes, that the light intensity profile is described by a Gaussian beam of the form $I(x) = I_\infty + I_0 \exp(-4x^2/d_x^2)$, encompassing *bright* and *dark* Gaussian beams when $I_\infty = 0$ and $I_0 = -I_\infty$, respectively.

a) Diffusion Regime

In the diffusion regime, Eq. (3.64) reduces to

$$\mathcal{E} = -\frac{l_D}{d_x}\frac{\partial \ln(1 + I)}{\partial_x} + \left(\frac{l_D}{d_x}\right)^2 \frac{(1 + \frac{1}{r_N})\frac{\partial^2\mathcal{E}}{\partial x^2}}{\left[1 + \frac{l_D}{d_x}\frac{\partial\mathcal{E}}{\partial x}\right]\left[1 - \frac{l_D}{r_N d_x}\frac{\partial\mathcal{E}}{\partial_x}\right]}. \tag{3.65}$$

For the usual parameters found in many PR materials ($l_D/d_x \ll 1$ and $r_N > 1$), the field profile can be described accurately by

$$\mathcal{E} \simeq -\frac{l_D}{d_x}\frac{\partial \ln(1+I)}{\partial x}. \tag{3.66}$$

This nonlinear *gradient* dependence of the electric field with the light intensity is caused by the symmetric redistribution of acceptors, described by Poisson equation. Figure 3.12 depicts the profiles of $\mathcal{E}(x)$ induced by bright and dark Gaussian beams. If l_D/d_x becomes comparable to 1, the *strong diffusion* regime appears: The field exhibits a stronger steepening at the origin. The influence of r_N on the field profiles is only noticeable when $r_N < 1$ and reduces the maximum amplitude of $\mathcal{E}$.

b) Drift Regime

When a sufficiently strong field is applied, one expects that the tendency of carriers to move symmetrically owing to diffusion will be overcome by the the drift component of the current. Figure 3.13 shows representative profiles of the electric field induced by bright and dark Gaussian beams for $\mathcal{E}_0 l_D/d_x \ll 1$ and $r_N > 1$. One can see that $\mathcal{E}$ *essentially* follows a local dependence on the light beam intensity $I(x)$. This local behavior appears because the contribution of the terms $\frac{l_D}{d_x}\frac{\partial \mathcal{E}}{\partial x}$ (just as it happens in the diffusion regime for the usual parameters found in many materials) is small. This means that the electric field is given approximately by

$$\mathcal{E} \simeq \mathcal{E}_0 \frac{(1+I_\infty)}{(1+I)} - \frac{l_D}{d_x}\frac{\partial \ln(1+I)}{\partial x}\ , \tag{3.67}$$

where the first term corresponds to the well-known case of a *saturable nonlinearity* [75,77], with the diffusion term being a small correction.

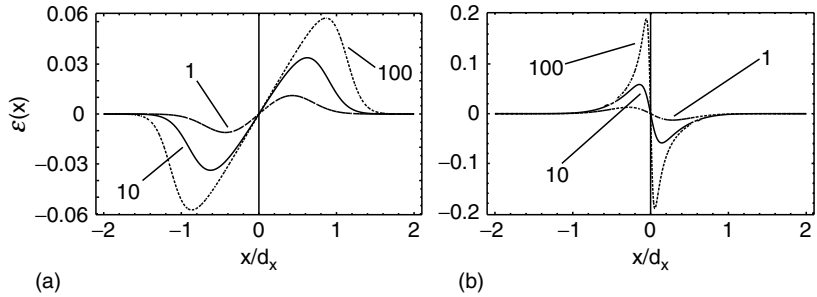

FIGURE 3.12. Diffusion regime. Normalized electric field $\mathcal{E}(x)$ induced by (a) a bright and (b) a dark Gaussian beam for $l_D/d_x = 0.01$ and $r_N = 100$. The numbers displayed correspond to the values of I_0 and I_∞, respectively.

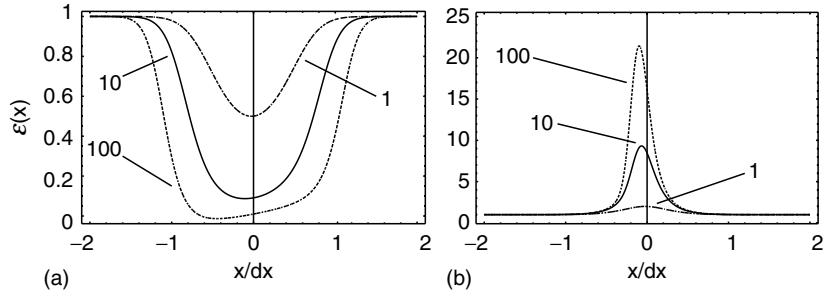

FIGURE 3.13. Drift regime. Normalized electric field $\mathcal{E}(x)$ induced by (a) a bright and (b) a dark Gaussian beam with $\mathcal{E}_0 l_D/d_x = 0.01$. The remaining parameters are as in Fig. 3.12.

Two Transverse Dimensions

We have seen that for the usual parameters encountered in most nonphotovoltaic PR materials, the light-induced electric field in one transverse dimension can be approximately represented as the sum of two *independent* contributions: A local drift term and a gradient diffusion component. Higher dimensionality introduces one key ingredient: *anisotropy* [94–100]. This is so because the applied field is oriented along one specific direction and so the response depends on the relative orientation of that direction with respect to the crystal axis.

For convenience, let us introduce the electrostatic potential ϕ through $\boldsymbol{\mathcal{E}} = \boldsymbol{\mathcal{E}}_0 - \nabla\phi$. The direction of the applied field $\mathcal{E}_0 = \mathcal{E}_0 \mathbf{u}_x$ is chosen along the x-axis. Therefore, we will be interested in the x-component of the light-induced electric field $\boldsymbol{\mathcal{E}}$, $\mathcal{E}^{(x)} \equiv \mathcal{E}$, and disregard the y-component whenever the associated value of the electro-optic coefficient to this direction is much smaller.

We focus our approach on the experimental configurations encountered in applications of $(2+1)$D PR screening solitons. This implies that the drift mechanism is the relevant contribution to charge transport, whereas diffusion is often small. Ferroelectric strontium barium niobate has been the most widely used crystal in applications to observe bright [96, 101–103] and dark [104] $(2+1)$D *needle* solitons because it fulfills such requirements. Typical values of the external field applied to generate needles, having characteristic widths d_s in the range $d_s \simeq 10 - 30\,\mu$m, vary between $1 - 2\,$kV/cm. In the case of bulk strontium barium niobate crystals, the characteristic Debye length l_D and field E_L are of the order of $l_D \simeq 0.3\,\mu$m and $E_L \simeq 1\,$kV/cm at room temperature. Hence the ratio $\mathcal{E}_0 l_D/d_s \simeq 0.03 \ll 1$. We may then neglect the terms $\frac{l_D}{d_s}\nabla\cdot\boldsymbol{\mathcal{E}}$ in Eq. (3.62) that are associated to the spatial modulation of N_A. Obviously, this implies that the values of the normalized light intensity I cannot be taken arbitrarily large in principle.

Taking into account the above assumptions, Eq. (3.62) reduces to

$$\nabla_{\perp}^{2}\phi+\nabla_{\perp}\ln(1+I)\cdot\nabla_{\perp}\phi-\boldsymbol{\mathcal{E}}_{0}\cdot\nabla\ln(1+I)= =\frac{l_{\mathrm{D}}}{d_{s}}\left\{\nabla_{\perp}^{2}\ln(1+I)+[\nabla_{\perp}\ln(1+I)]^{2}\right\}\cdot \tag{3.68}$$

Equation (3.68) has been employed in several numerical studies of (2 + 1)D propagation of solitons [89, 96, 98, 105–108] and it has shown a remarkable agreement with experiments [16, 89, 96, 98, 109] performed in cerium-doped SBN: 60. Notice that, in the one-dimensional case, Eq. (3.68) leads to an electric field represented by Eq. (3.67).

In order to show the new features arising in higher dimensionality, let us consider for simplicity a circular *flat-top hat* beam of radius R defined as

$$I(r,\ \varphi)=\begin{cases} I_{0} & \textit{if}\ \mathrm{r}\ \leq \mathrm{R}, \\ I_{\infty} & \textit{if}\ \mathrm{r} > \mathrm{R}. \end{cases} \tag{3.69}$$

For this particular case, the solution of Eq. (3.68) leads to [100]

$$\mathcal{E}(r,\ \varphi)=\begin{cases} \dfrac{2(1+I_{\infty})\mathcal{E}_{0}}{2+I_{0}+I_{\infty}} & \textit{if}\ \mathrm{r}\ \mathrm{le}\ \mathrm{R}, \\ \mathcal{E}_{0}+\dfrac{(I_{0}-I_{\infty})\mathcal{E}_{0}}{2+I_{0}+I_{\infty}}\dfrac{R^{2}\cos 2\varphi}{r^{2}} & \textit{if}\ \mathrm{r} > \mathrm{R}. \end{cases} \tag{3.70}$$

Equation (3.70), illustrated in Fig. 3.14, exhibits several interesting features. The constant value of $\mathcal{E}$ inside the beam perimeter differs from that obtained by using Eq. (3.67). That is, one expects a *fundamentally* different type of saturable dependence with the light intensity that deviates from the model $\mathcal{E}\propto(1+I)^{-1}$. Outside the beam perimeter, other features inherent of the higher spatial dimension arise as well: The electric field decays with the distance following a

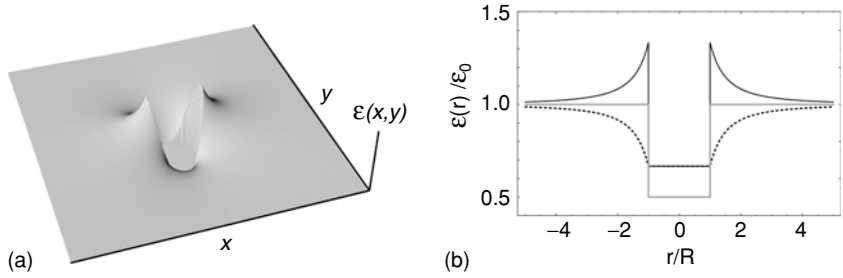

FIGURE 3.14. Electric field created by a circular flat-top light beam ($I_0 = 1,\ I_\infty = 0$): (a) two-dimensional distribution, (b) profiles along the x-axis (black solid curve), y-axis (dotted curve). The gray curve in (b) corresponds to the local case given by Eq. (3.67).

dependence of the form $\mathcal{E} \propto r^{-2}$ (nonlocality), and it is a function of the azimuthal angle φ (anisotropy). One may notice that the profile in Fig. 3.14 very closely resembles the experimental results depicted in Fig. 3.2. These nonlocal and anisotropic properties cannot be predicted by lifting the one-dimensional form given by Eq. (3.67) to two transverse dimensions. For a more detailed description of the form of the electric field in two transverse dimensions, see Ref. [99], where analytical solutions of Eq. (3.68), in the case of circularly symmetric beams, were found.

3.16 Transient and Quasi-Steady-State Effects

In the rest of the chapter, we touch on time-dependent and quasi-steady state situations. To simplify our analysis, we concentrate on a one dimensional case.

The temporal response of the electric field can be obtained by combining Eqs. (3.59) and (3.60). Here it is implicitly assumed that the beam intensity varies slowly in time in comparison with the temporal evolution of the electric field. Following a similar procedure as in steady-state conditions, the boundary condition for $\mathcal{J}_0(\tau)$ is

$$\mathcal{J}_0(\tau) = \frac{\tau_R \nu}{\tau_B}\left[(1+I_\infty)\mathcal{E}_0 + \frac{\partial \mathcal{E}_0}{\partial \tau} + \mathcal{E}_{PV}^{(x)}(I_\infty + I_B)\right], \tag{3.71}$$

where $\mathcal{E}_{PV}^{(x)} = (\mathbf{u}_{PV}\cdot\mathbf{u}_x)\mathcal{E}_{PV}$. Thus, the resulting equation for $\mathcal{E}$ is

$$\begin{aligned}&\frac{\partial \mathcal{E}}{\partial \tau} + \left[\mathcal{E} + \frac{l_D}{d_x}\frac{\partial}{\partial x}\right]\left[\frac{(1+I)\left(1 - \dfrac{l_D}{r_N d_x}\dfrac{\partial \mathcal{E}}{\partial x}\right) - \dfrac{l_D}{\nu d_x}\dfrac{\partial^2 \mathcal{E}}{\partial \tau \partial x}}{1 + \dfrac{l_D}{d_x}\dfrac{\partial \mathcal{E}}{\partial x}}\right] \\ &+ \mathcal{E}_{PV}^{(x)}\left(1 - \frac{l_D}{r_N d_x}\frac{\partial \mathcal{E}}{\partial x}\right)(1+I) = \frac{\partial \mathcal{E}_0}{\partial \tau} + (1+I_\infty)\mathcal{E}_0 + \mathcal{E}_{PV}^{(x)}(1+I_\infty)\cdot\end{aligned} \tag{3.72}$$

The left-hand side terms of Eq. (3.72) represent the displacement current, the drift, diffusion, and photovoltaic contributions, respectively, whereas those on the right-hand side are the corresponding boundary values. An accurate estimate of the boundary value of the electric field, $\mathcal{E}_0$, can be obtained if the characteristic length d_x of transverse variation of the beam is much smaller than the crystal thickness L. Then, from Eq. (3.61), it follows that $\mathcal{E}_0$ is given approximately by

$$\mathcal{E}_0(\tau) = -\frac{V(\tau)}{E_L L}, \tag{3.73}$$

where $V(\tau)$ is the voltage between the two electrodes that are in contact with the opposite faces of the crystal (perpendicular to the x-axis).

3.16.1 Transient Effects

Let us first consider the situation where $\mathcal{E}_0$ is independent of time (this implies by Eq. (3.71) that $\jmath_0(\tau)$ is a constant). In order to find the main features of the temporal dynamics of the electric field, we use analogous simplifying assumptions as under steady-state conditions. When the ratios $\mathcal{E}_0 l_D/d_x$, $\mathcal{E}_{PV} l_D/d_x \ll 1$ (together with $r_N > 1$), it is possible to neglect the derivative terms $|\frac{l_D}{d_x}\frac{\partial \mathcal{E}}{\partial x}|$, $|\frac{l_D}{r_N d_x}\frac{\partial \mathcal{E}}{\partial x}| \ll 1$. An additional approximation consists of neglecting the term $\frac{l_D}{\nu d_x}\frac{\partial^2 \mathcal{E}}{\partial \tau \partial x}$ as compared to $1 + I$. This last approximation is only justified for ferroelectric crystals but not for sillenites and semiconductors since the parameter $\nu \ll 1$ for the latter. The smallness of this parameter plays an important role in the electric field distribution of sillenites and semiconductors, and we defer its proper inclusion into the material equation when analyzing quasi-steady situations.

Therefore, taking into account the above-mentioned approximations, Eq. (3.72) reduces to

$$\frac{\partial \mathcal{E}}{\partial \tau} + (1+I)\mathcal{E} + \frac{l_D}{d_x}\frac{\partial (1+I)}{\partial x} + \mathcal{E}_{PV}^{(x)}(I - I_\infty) = (1 + I_\infty)\mathcal{E}_0, \tag{3.74}$$

whose solution is given by

$$\mathcal{E}(x,\ \tau) = \left[\mathcal{E}_0 \frac{(1+I_\infty)}{(1+I)} - \frac{l_D}{d_x}\frac{\partial \ln(1+I)}{\partial x} + \mathcal{E}_{PV}^{(x)}\frac{(I_\infty - I)}{(1+I)}\right]\left[1 - e^{-(1+I)\tau}\right] + \mathcal{E}(x,\ 0)e^{-(1+I)\tau}, \tag{3.75}$$

where $\mathcal{E}(x,\ 0)$ denotes the initial distribution of the electric field. Eq. (3.75) generalizes Eq. (3.67) to the temporal domain and includes the photovoltaic contribution. Notice also that the exponential factors depend on the local intensity I. This implies that the electric field build-up time constant is a function of the transverse spatial coordinate and is, in particular, shorter where the optical intensity is larger. A more detailed account of transient effects under constant applied fields can be found in Ref. [110].

3.16.2 Applied ac Fields

As already envisaged in Section 3.11.2, the application of ac fields during PR recording is a well-known method to markedly enhance the space-charge field and optical gain in fast materials such as sillenites ($Bi_{12}SiO_{20}$, $Bi_{12}TiO_{20}$, $Bi_{12}GeO_{20}$) and semiconductors (GaAs, CdTe, GaP, etc) [43,44,111]. We have shown there that under low contrast illumination, the PR nonlinearity is of gradient type, i.e., the induced space-charge field is proportional to the derivative of the light intensity profile. As mentioned in Section 3.12, high contrast illumination gives rise to some peculiar features in the PR recording as multiple

harmonics, cross-talk, and instabilities such as generation of subharmonics [57,59,112]. For localized beams [26], the main effects rely upon the occurrence of very strong and narrow peaks (so-called *singularities*) of the light-induced charge density coupled to abrupt changes (*discontinuities*) in the space-charge field distribution. This intriguing behavior was qualitatively in accordance with previous experiments performed on $Bi_{12}SiO_{20}$ in which there was some indication of the existence of high electric field gradients near to the peak of the light intensity [17].

Let us consider an optically isotropic bulk crystal subjected to an strong applied ac field $E_0(t) = E_0 p(t)$ parallel to the x-axis, with $p(t) = \pm 1$ a square-wave function of period T_0 having a temporal average $\langle p(t) \rangle_{T_0} = 0$. The main reason to employ an applied ac field having square-wave temporal form instead of other profiles (such as e.g., sinusoidal form or an exponential-edge form) is based on the mentioned fact that for periodic gratings, it provides the maximum enhancement for the imaginary component of the space-charge field (which governs the energy transfer between interfering plane waves), for a given peak voltage [44].

Two important characteristic length scales arise in our problem, the so-called *drift length* $l_0 = \mu \tau_R E_0$ and the *saturation length* $l_s = \varepsilon_0 \varepsilon E_0 / e N_A$. These two characteristic scales are related to parameter ν as the ratio $\nu = l_s / l_0$, and satisfy the inequality $l_s / l_0 \lesssim 10^{-2}$. Moreover, for sillenites we have the condition $r_N \gtrsim 10^3$ and for semiconductors $r_N \gtrsim 10$, and together with the fact that $l_D / d_x \ll 1$, we may neglect all terms $\frac{l_D}{r_N d_x} \frac{\partial \mathcal{E}}{\partial x}$. Now, in ac experiments, the usual values of the applied field are within the range $E_0 \sim 10 - 40\,\mathrm{kV/cm}$, so the inequality $E_0 \gg E_L$ is always fulfilled, since $E_L \simeq 2 - 3\,\mathrm{kV/cm}$ for most sillenites and semiconductors. This implies that the diffusion contribution can also be neglected. In the approach presented henceforth, we concentrate on bright beams.

Let us now set $\mathcal{E} = \mathcal{E}_S + \mathcal{E}_F$, where $\mathcal{E}_S$ and $\mathcal{E}_F$ are the slow and fast dimensionless components of the space-charge field, respectively. By averaging over the fast oscillations of the ac field, i.e., assuming that the period T_0 of the ac field is much smaller than τ_B, then, in the leading approximation in T_0 / τ_B, the following averages hold true $\langle \mathcal{E}_F(x, \tau) \rangle_{T_0} = 0$, $\langle \mathcal{E}_S(x, \tau) \rangle_{T_0} = \mathcal{E}_S(x)$, and $\mathcal{E}_F |(x, \tau)| \ll |\mathcal{E}_S(x, \tau)|$. Taking into account all the above conditions, the governing material equation in the quasi-steady state [26] reads as

$$\frac{\partial}{\partial x} \left[\frac{(1 + I)(1 - \mathcal{E}_S^2)}{1 + \dfrac{l_s}{d_x} \dfrac{\partial \mathcal{E}_S}{\partial_x}} \right] + \frac{d_x}{l_0} (1 + I) \mathcal{E}_S = 0. \tag{3.76}$$

Eq. (3.76) contains two nonlinear terms. The term $\mathcal{E}_S^2$ originates from the drift contribution, whereas the term $\frac{l_s}{d_x} \frac{\partial \mathcal{E}_S}{\partial x}$ in the denominator comes from the recombination product in the band transport equation and describes the saturation of aceptors. It can be larger than 1, but it is assumed to be much smaller than r_N. In other words, Eq. (3.76) includes situations where the modulation of acceptors $\delta N_A = N_A - N_A(0)$ is locally comparable to or even larger

than its average value (although it remains much smaller than N). When $\frac{l_s}{d_x}\frac{\partial \mathcal{E}_S}{\partial x} \gtrsim 1$, a strong localization of the charge density is produced (a singularity). The narrow central peak and the broad symmetric profile in Fig. 3.15(a) illustrate the relationship between the charge density and symmetric/asymmetric intensity distributions. The size of the charge singularity is dramatically smaller than the beam width. We see that the singularity is pinned exactly to the intensity maximum only under symmetric illumination. The central part of the charge distribution induced by a Gaussian beam is depicted in Fig. 3.15(b) for several values of I_0. The profile of the charge density exhibits a sech-type form and its size is of the order of l_s. By Gauss's Law, these charge density singularities are coupled to an strong steepening of the electric field placed at the maximum of the charge density distribution (formation of discontinuities, see Ref. [26]). The existence of such strong gradients in the field distribution (resembling shock waves) has a striking consequence on beam propagation and leads, under suitable conditions, to the formation and propagation of stable spatial solitons [18].

The generation of charge singularities with a characteristic width of the order of $l_s \sim 0.5\,\mu$m is a striking feature of the ac technique attractive for semiconductor and optical applications. This feature goes, in fact, beyond the scope of the PR effect because it has nothing to do with the linear electro-optic effect. For PR applications based on weak optical nonlinearities (like displacement sensing [111,113–115]), the steepening of the field profile is a positive effect because it increases the sensitivity of measurements.

3.17 Conclusions

Photorefractivity constitutes a rather special class of nonlinearity since, at variance with many other optical nonlinearities, it cannot be described by a nonlinear susceptibility. It occurs at low light-intensity levels and offers an

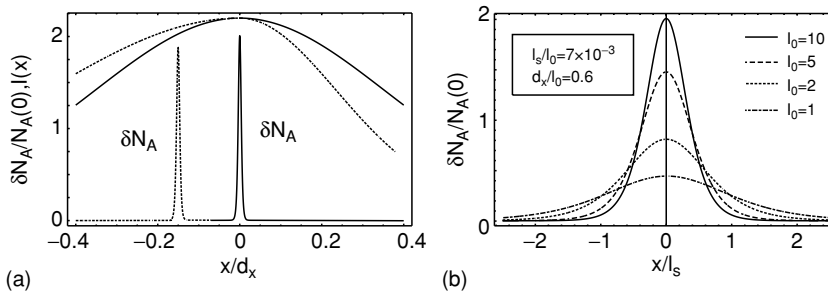

FIGURE 3.15. (a) Correspondence between space charge $\delta N_A = N_A - N_A(0)$ and intensity $I(x)$ profiles (a.u.). The dotted curves refer to an asymmetric light profile. (b) Core of the charge singularity for different peak intensities.

excellent scenario for the investigation of a rich variety of nonlinear physical processes. The main purpose of this chapter has been to show that the key ingredient in almost all photorefractive phenomena is the development of an electric space-charge field, via a non-instantaneous light-induced charge transport mechanism. The formation of this field has been described within the standard band transport model.

Although the basic "standard" model for photorefraction is well established, the area has markedly evolved in several directions during the last decades. The model has been thoroughly investigated beyond the linear (low-contrast) approximation and the consequences of the intrinsic nonlinearities in the rate equations have been largely exploited (high-contrast and nonlinear coupling effects). Extensions of the model to describe new physical situations (e.g., several traps and active centers) have been developed. Finally, 2D and 3D geometries, posing real theoretical challenges, have been analyzed in connection with beam propagation phenomena and soliton physics.

Further developments may be expected from novel experimental situations, such as new materials, high light intensities, short pulses, 2D geometries (optical waveguides and semiconductor nanostructures), composite media, and others. Moreover, the coalescence of photorefractivity with other emerging areas exhibiting new linear and nonlinear (and even genuine quantum) phenomena could eventually open the path to exciting theoretical and experimental advances in the realm of Optics.

References

1. P. Günter, J.P. Huignard (eds.), *Photorefractive Materials and their Applications* Vol. I, Springer, Berlin, 1988.
2. P. Günter, J.P. Huignard (eds.), *Photorefractive Materials and their Applications* Vol. II, Springer, Berlin, 1989.
3. B.I. Sturman, V.M. Fridkin, *The photovoltaic and photorefractive effects in noncentrosymmetric materials*, Gordon and Breach Science Publishers, Philadelphia, 1992.
4. P. Yeh, *Introduction to Photorefractive Non Linear Optics*, J. Wiley & Sons, New York, 1993.
5. F. Agulló-López, J.M. Cabrera, F. Agulló-Rueda, *Electrooptics: Phenomena, Materials and Applications*, Academic Press, San Diego, 1994.
6. D. Nolte (ed.), *Photorefractive Effects and Materials*, Kluwer Academic Publishers, Norwell, 1995.
7. L. Solymar, D.J. Webb, A. Grunnet-Jepsen, *The Physics and Applications of Photorefractive Materials*, Claredon Press, Oxford, 1996.
8. P. Günter (ed.), *Nonlinear Optical Effects and Materials*, Springer Series in Optical Sciences, Springer, Berlin, 2000.
9. H.J. Coufal, D. Psaltis, G.T. Sincerbox (eds.), *Holographic Data Storage*, Springer Series in Optical Sciences, Springer, Berlin, 2000.
10. S. Trillo, W. Torruellas (eds.), *Spatial Solitons*, Springer Series in Optical Sciences, Springer, Berlin, 2001.

11. A. Ashkin, G.D. Boyd, J.M. Dziedzic, R.G. Smith, A.A. Ballman, J.J. Levinstein, K. Nassau, Appl. Phys. Lett. **9**, 72 (1966).
12. M. Aguilar, M. Carrascosa, F. Agulló-López, Opt. Mat. **5**, 187 (1996).
13. N.V. Kukhtarev, V.B. Markov, S.G. Odulov, M.S. Soskin, V.L. Vinetskii, Ferroelectrics **22**, 949 (1979); *ibid*. **22**, 961 (1979).
14. Special Issue on Solitons, Opt. Photon. News **13**, 27 (2002).
15. D.N. Christodoulides, M.I. Carvalho, Opt. Lett. **19**, 1714 (1994).
16. A.V. Mamaev, M. Saffman, A.A. Zozulya, Europhys. Lett. **35**, 25 (1996).
17. C.A. Fuentes-Hernández, A.V. Khomenko, Phys. Rev. Lett. **83**, 1143 (1999).
18. G.F. Calvo, B. Sturman, F. Agulló-López, M. Carrascosa, Phys. Rev. Lett. **89**, 033902 (2002).
19. G.S. García-Quirino, J.J. Sánchez-Mondragón, S.I. Stepanov, Phys. Rev. A **51**, 1571 (1995); M. Cronin-Golomb, Opt. Lett. **20**, 2075 (1995); A.A. Kamshilin, E. Raita, A.V. Khomenko, J. Opt. Soc. Am. B **13**, 2536 (1996); A.V. Khomenko, E. Nippolainen, A.A. Kamshilin, A. Zúñiga Segundo, T. Jaaskelainen, Opt. Comm. **150**, 175 (1998).
20. D. Kip, M. Soljacic, M. Segev, E. Eugenieva, D. Christodoulides, Science **290**, 495 (2000); J. Klinger, H. Martin, Z. Chen, Opt. Lett. **26**, 271 (2000); H. Buljan, A. Siber, M. Soljacic, M. Segev, Phys. Rev. E **66**, 035601(R) (2002).
21. T. Honda, Opt. Lett. **18**, 598 (1993); A.V. Mamaev, M. Saffman, Phys. Rev. Lett. **80**, 3499 (1998); S.G. Odoulov, M.Yu. Goulkov, O.A. Shinkarenko, Phys. Rev. Lett. **83**, 3637 (1999).
22. T.E. McClelland et al, Phys. Rev. Lett. **73**, 3082 (1994); H.C. Pedersen, P.M. Johansen, Phys. Rev. Lett. **77**, 3106 (1996).
23. B.I. Sturman, M. Mann, J. Otten, K.H. Ringhofer, J. Opt. Soc. Am. B **10**, 1919 (1993).
24. H.C. Pedersen, P.M. Johansen, J. Opt. Soc. Am. B **12**, 1065 (1995).
25. B.I. Sturman, S.G. Odoulov, M.Yu. Goul'kov, Phys. Reports, **275**, 197 (1996); M. Goul'kov, S. Odoulov, I. Naumova, F. Agulló-López, G. Calvo, E. Podivilov, B. Sturman, V. Pruneri, Phys. Rev. Lett. **86**, 4021 (2001).
26. G.F. Calvo, B. Sturman, F. Agulló-López, M. Carrascosa, Phys. Rev. Lett. **84**, 3839 (2000).
27. E. Podivilov et al, Phys. Rev. Lett. **85**, 1867 (2000).
28. J. Limeres, M. Carrascosa, L. Arizmendi, F. Agulló-López, P.E. Andersen, Phys. Rev. B **65**, 195117 (2002).
29. A. García-Cabañes, J.M. Cabrera, F. Agulló-López, Chapter on "Electro-optic Inorganic Materials," in *Encyclopedia of Optical Engineering*, R.B. Johnson, R.G. Driggers (eds.). Marcel Dekker Inc., New York (2003).
30. P. Günter, M. Zgonic, Opt. Lett. **16**, 1826 (1991).
31. B. Sturman, F. Agulló-López, M. Carrascosa, L. Solymar, Appl. Phys. B **68**, 1013 (1999).
32. B.I. Sturman, M. Mann, K.H. Ringhofer, Appl. Phys. A **55**, 235 (1992); Opt. Lett. **18**, 702 (1993).
33. E.V. Podivilov, H.C. Pedersen, P.M. Johansen, B.I. Sturman, Phys. Rev. E **57**, 6112 (1998).
34. P.M. Johansen, H.C. Pedersen, E.V. Podivilov, B.I. Sturman, Phys. Rev. A **58**, 1601 (1998).
35. Ph. Refregier, L. Solymar, H. Rajbenbach, J.P. Huignard, J. Appl. Phys. **58**, 45 (1985).

36. G. A. Brost, Opt. Commun. **96**, 113 (1993).
37. E. Serrano, V. López, M. Carrascosa, F. Agulló-López, J. Opt. Soc. Am. B **11**, 670 (1994).
38. C. Soutar, W.A. Gillespie, C.M. Cartwright, Opt. Commun **90**, 329 (1992).
39. N.V. Kukhtarev, V.B. Markov, S. Odulov, Opt. Commun. **23**, 338 (1977).
40. F. Jariego, F. Agulló-López, Opt. Comm. **76**, 169 (1990).
41. E.M. de Miguel-Sanz, J. Limeres, M. Carrascosa, L. Arizmendi, J. Opt. Soc. Am. B **17**, 1140 (2000).
42. M. Carrascosa, F. Agulló-López, IEEE J. Quantum Electron. **22**, 1369 (1986).
43. S.I. Stepanov, M.P. Petrov, Opt. Comm. **53**, 292 (1985).
44. K. Walsh, A.K. Powell, C. Stace, T.J. Hall, J. Opt. Soc. Am. B **7**, 288 (1990).
45. P.M. Johansen, H.C. Pedersen, J. Opt. Soc. Am.B **15**, 1366 (1998).
46. T.J. Hall, R. Jaura, L.M. Connors, P.D. Foote, Prog. in Quantum Electron. **10**, 77 (1985).
47. A. Bledowski, J. Otten, K.H. Ringhofer, Opt. Lett **16**, 672 (1991).
48. E. Serrano, M. Carrascosa, F. Agulló-López, Opt. Lett. **20**, 1910 (1995); J. Opt. Soc. Am. B **13**, 2587 (1996).
49. E. Serrano, V. López, M. Carrascosa, F. Agulló-López, IEEE J. Quantum Electron. **30**, 875 (1994)
50. P.E. Andersen, P.M. Petersen, P. Buchhave, Appl. Phys. Lett. **65**, 271 (1994).
51. P.E. Andersen, P. Buchhave, P.M. Petersen, M.V. Vasnetsov, J. Opt. Soc. Am. B **12**, 1422 (1995).
52. E.M. de Miguel-Sanz, J. Limeres, L. Arizmendi, M. Carrascosa, J. Opt. Soc. Am. B **16**, 1658 (1999).
53. J. Limeres, M. Carrascosa, P.M. Petersen, P.E. Andersen, J. Appl. Phys. **88**, 5527 (2000).
54. S. Mallick, H. Imbert, H. Ducollet, J. P. Herriau, J.P. Huignard, J. Appl. Phys. **63**, 5660 (1988).
55. I. Richter, A. Grunnet-Jepsen, J. Takacs, L. Solymar, IEEE J. Quantum. Electron. **30**, 1645 (1994).
56. J. Takacs, L. Solymar, Opt. Lett. **17**, 247 (1992).
57. C.H. Kwak, M. Shamonin, J. Takacs, L. Solymar, Appl. Phys. Lett. **62**, 328 (1993).
58. A. Grunnet-Jepsen, C.H. Kwak, I. Richter, L. Solymar, J. Opt. Soc. Am. B **11**, 124 (1994).
59. B. I. Sturman, M. Aguilar, F. Agulló-López, K. H. Ringhofer, Phys. Rev. E **55**, 6072 (1997).
60. O.P. Nestiorkin, Ye.P. Shershakov, J. Opt. Soc. Am. B **10**, 1907 (1993).
61. H.C. Pedersen, P.M. Johansen, Phys. Rev. Lett. **76**, 4159 (1996).
62. J.A. Baquedano, L. Contreras, E. Dieguez, J.M. Cabrera, J. Appl. Phys. **66**, 5146 (1989).
63. P. Günter, F. Micheron, Ferroelectrics **18**, 27 (1978).
64. G. Montemezzani, M. Ingold, H. Looser, P. Günter, Ferroelectrics **92**, 281 (1989).
65. E. Jermann, J. Otten, J. Opt. Soc. Am. B **10**, 2085 (1993).
66. G.C. Valley, Appl. Opt. **22**, 3160 (1983).
67. M. Carrascosa, F. Agulló-López, Appl. Opt. **27**, 2851 (1988).
68. F. Jariego, F. Agulló-López, Appl. Opt. **33**, 4615 (1991).
69. K. Buse, A. Adibi, D. Psaltis, Nature **393**, 665 (1998).
70. L. Hesselink, S.S. Orlov, A. Liu, A. Akella, D. Lande, R.R. Neurgaonkar, Science **282**, 1089 (1998).

71. G.C. Valley, J. Appl. Phys. **59**, 3363 (1986).
72. F.P. Strohkendl, J. M. Jonathan, R. W. Hellwarth, Opt. Lett. **11**, 312 (1986).
73. L.M. Bernardo, J.C. Lopes, O.D. Soares, Appl. Opt. **29**, 12 (1990).
74. M. Segev, B. Crosignani, A. Yariv, B. Fischer, Phys. Rev. Lett. **68**, 923 (1992).
75. M. Segev, G.C. Valley, B. Crosignani, P. Di Porto, A. Yariv, Phys. Rev. Lett. **73**, 3211 (1994).
76. G.C. Valley, M. Segev, B. Crosignani, A. Yariv, M.M. Fejer, M.C. Bashaw, Phys. Rev. A **50**, R4457 (1994).
77. D.N. Christodoulides, M.I. Carvalho, J. Opt. Soc. Am. B **12**, 1628 (1995).
78. M. Segev, A.J. Agranat, Opt. Lett. **22**, 1299 (1997).
79. G.C. Duree, J.L. Shultz, G.J. Salamo, M. Segev, A. Yariv, B. Crosignani, P. Di Porto, E.J Sharp, R.R. Neurgaonkar, Phys. Rev. Lett. **71**, 533 (1993).
80. M.D. Iturbe Castillo, P.A. Marquez Aguilar, J.J. Sanchez-Mondragon, S. Stepanov, V. Vysloukh, Appl. Phys. Lett. **64**, 408 (1994).
81. G. Duree, M. Morin, G. Salamo, M. Segev, B. Crosignani, P. Di Porto, E. Sharp, A. Yariv, Phys. Rev. Lett. **74**, 1978 (1995).
82. M.-F. Shih, M. Segev, G.C. Valley, G. Salamo, B. Crosignani, P. Di Porto, Electron. Lett. **31**, 826 (1995).
83. M. Taya, M.C. Bashaw, M.M. Fejer, M. Segev, G.C. Valley, Phys. Rev. A **52**, 3095 (1995).
84. M.-F. Shih, P. Leach, M. Segev, M.H. Garrett, G. Salamo, G.C. Valley, Opt. Lett. **21**, 324 (1996).
85. Z.G. Chen, M. Mitchell, M.-F. Shih, M. Segev, M.H. Garrett, G.C. Valley, Opt. Lett. **21**, 629 (1996).
86. K. Kos. H. Meng, G. Salamo, M.-F. Shih, M. Segev, G.C. Valley, Phys. Rev. E **53**, R4330 (1996).
87. Z.G. Chen, M.F. Shih, M. Segev, D.W. Wilson, R.E. Muller, P.D. Maker, Opt. Lett. **22**, 1751 (1997).
88. M. Shih, M. Segev, G. Salamo, Phys. Rev. Lett. **78**, 2551 (1997).
89. W. Krolikowski, M. Saffman, B. Luther-Davis, C. Denz, Phys. Rev. Lett. **80**, 3240 (1998).
90. E. DelRe, B. Crosignani, M. Tamburrini, M. Segev, M. Mitchell, E. Refaeli, A.J. Agranat, Opt. Lett. **23**, 421 (1998).
91. E. DelRe, M. Tamburrini, M. Segev, E. Refaeli, A.J. Agranat, Appl. Phys. Lett. **73**, 16 (1998).
92. W. Krolikowski, E.A. Ostrovskaya, C. Weilnau, M. Geisser, G. McCarthy, Yu.S. Kivshar, C. Denz, B. Luther-Davis, Phys. Rev. Lett. **85**, 1424 (2000).
93. M. Segev, M.-F. Shih, G.C. Valley, J. Opt. Soc. Am. B **13**, 706 (1996).
94. A.A. Zozulya, D.Z. Anderson, Phys. Rev. A **51**, 1520 (1995).
95. N. Korneev, P.A. Márquez Aguilar, J.J. Sánchez Mondragón, S. Stepanov, M. Klein, B. Wechsler, J. Mod. Opt. **43**, 311 (1996).
96. A.A. Zozulya, D.Z. Anderson, A.V. Mamaev, M. Saffman, Europhys. Lett. **36**, 419 (1996).
97. B. Crosignani, P. Di Porto, A. Degasperis, M. Segev, S. Trillo, J. Opt. Soc. Am. B **14**, 3078 (1997).
98. A.A. Zozulya, D.Z. Anderson, A.V. Mamaev, M. Saffman, Phys. Rev. A **57**, 522 (1998).
99. G.F. Calvo, F. Agulló-López, M. Carrascosa, M.R. Belić, W. Królikowski, Europhys. Lett. **60**, 847 (2002).

100. G.F. Calvo, F. Agulló-López, M. Carrascosa, Opt. Comm. **233**, 439 (2004).
101. M.-F. Shih, M. Segev, G.C. Valley, G. Salamo, B. Crosignani, P. Di Porto, Electron. Lett. **31**, 826 (1995).
102. M.-F. Shih, P. Leach, M. Segev, M.H. Garrett, G. Salamo, G.C. Valley, Opt. Lett. **21**, 324 (1996).
103. H. Meng, G. Salamo, M. Segev, Opt. Lett. **23**, 897 (1998).
104. Z.G. Chen, M.F. Shih, M. Segev, D.W. Wilson, R.E. Muller, P.D. Maker, Opt. Lett. **22**, 1751 (1997).
105. M.R. Belić, A. Stepken, F. Kaiser, Phys. Rev. Lett. **82**, 544 (1999).
106. M.R. Belić, A. Stepken, F. Kaiser, Phys. Rev. Lett. **84**, 83 (2000).
107. M.R. Belić, D. Vujić, A. Stepken, F. Kaiser, G.F. Calvo, F. Agulló-López, M. Carrascosa, Phys. Rev. E **65** 066610 (2002).
108. G.F. Calvo, F. Agulló-López, M. Carrascosa, M.R. Belić, D. Vujić, Opt. Comm. **227**, 193 (2003).
109. D. Neshev, G. McCarthy, W. Królikowski, E.A. Ostrovskaya, Yu.S. Kivshar, G.F. Calvo, F. Agulló-López, Opt. Lett. **26**, 1185 (2001).
110. N. Fressengeas, J. Maufoy, G. Kugel, Phys. Rev. E **54**, 6866 (1996).
111. A.A. Kamshilin, Y. Iida, S. Ashihara, T. Shimura, Appl. Phys. Lett. **74**, 2575 (1999).
112. B.I. Sturman, M. Mann, K.H. Ringhofer, Opt. Lett. **17**, 1620 (1992).
113. A.A. Kamshilin, K. Paivasaari, A.V. Khomenko, C. Fuentes-Hernández, Opt. Lett. **24**, 832 (1999).
114. A.A. Kamshilin, K. Paivasaari, M. Klein, B. Pouet, Appl. Phys. Lett. **77**, 4098 (2000).
115. G.F. Calvo, B.I. Sturman, F. Agulló-López, M. Carrascosa, A.A. Kamshilin, K. Paivasaari, J. Opt. Soc. Am. B **19**, 1564 (2002).

4

Space-Charge Driven Holograms in Anisotropic Media

Germano Montemezzani[1] and Marko Zgonik[2]

[1] Nonlinear Optics Laboratory, Swiss Federal Institute of Technology, Zürich (Switzerland); Present address: Laboratoire Matériaux Optiques, Photoniques et Systèmes, University of Metz and Supélec, Metz (France)
germano.montemezzani@metz.supelec.fr

[2] Faculty of Mathematics and Physics, University of Ljubljana and Jozef Stefan Institute, Ljubljana (Slovenia)
marko.zgonik@fmf.uni-lj.si

4.1 Introduction

Most photorefractive materials treated in this book trilogy are anisotropic in nature. The anisotropies may involve the electro-optic and dielectric response, but also the transport and photoexcitation properties. In crystals, the perturbation induced by the locally periodic illumination fringes leads to a complex mechanical response of the material, which, on its turn, influences the dielectric and electro-optic responses being observed. On the other hand, the resulting space-charge field holograms can also be significantly affected by an anisotropy of the photoexcitation properties with respect to light polarization. Two-wave mixing amplification is influenced by such effects. This chapter summarizes the above mentioned effects as well as the main results of a coupled wave analysis of light diffraction at anisotropic volume phase and absorption gratings in anisotropic media, which extend the isotropic coupled wave theory of Kogelnik [1].

4.2 Basic Considerations

Space-charge holograms in photorefractive materials are characterized by an inhomogeneous charge density distribution in response to an inhomogeneous distribution of *photoexcited* charges that are mobile. The latter inhomogeneous distribution may be induced by an inhomogeneous light intensity of illumination. However, since in dichroic materials the photoexcitation cross-section can depend on the light polarization, in general, the photoexcited charge

density and the light intensity do not possess the same degree of modulation. Further, after photoexcitation, a carrier might have a different mobility in various directions. Therefore the grating formation time is influenced by the anisotropy of the carrier mobility tensor in the given material. The charge density distribution gives rise to a spatially modulated space-charge electric field and the functional dependence involves an effective dielectric constant. In anisotropic materials, the latter depends strongly on the direction of the charge density gradients (grating vector direction) and on mechanical deformation fields, which in their turn, depend on these directions again. Finally, in electro-optic materials, the resulting electric field produces a change of the optical properties that is proportional to an effective electro-optical coefficient. Unlike often assumed, the latter quantity cannot be determined by a simple projection of the (usually anisotropic) unclamped electro-optic tensor along the grating direction, but is influenced by the above mentioned mechanical deformations.

As evident from the above arguments, the formation of space-charge holograms is a complex process that involves a large amount of material properties, the vast majority of which are or can be anisotropic, that is tensorial in nature. As we will try to summarize in this section, the treatment of space-charge hologram formation and its optical response must take into account all these effects.

4.2.1 Photoexcitation

In doped photorefractive crystals, absorption is in general an extrinsic property of the material. It is not uncommon that the absorption constant differ for different polarization of the incident photons. Such a dichroism is expected to influence the formation of photorefractive gratings [2, 3]. For photorefraction, even more fundamental than the absorption constant is the probability for a carrier to be photoexcited to the conduction or valence band. It has been shown that if this photoexcitation process depends on light polarization, the complex amplitude $E_{sc,0}$ of the modulated photoinduced internal electric field is being strongly influenced and can differ significantly from what would be expected on the base of the light intensity distribution [4]. This is because it is the modulation m of the photoexcited free carriers and not the light intensity modulation that drives the formation of the space-charge field.

Let us consider a signal (S) and a pump wave (P) in the form of plane waves. The total complex amplitude of the electric field vector $\boldsymbol{\mathcal{E}}$ resulting from their coherent superposition may be written as

$$\boldsymbol{\mathcal{E}}(\boldsymbol{r}) = E_s(\boldsymbol{r})\hat{\boldsymbol{e}}_s e^{i\boldsymbol{k}_s \cdot \boldsymbol{r}} + E_p(\boldsymbol{r})\hat{\boldsymbol{e}}_p e^{i\boldsymbol{k}_p \cdot \boldsymbol{r}}, \tag{4.1}$$

where $\boldsymbol{r}$ is the position vector, $\hat{\boldsymbol{e}}_s$ and $\hat{\boldsymbol{e}}_p$ are unit vectors, and E_s and E_p are the scalar electric field amplitudes. In general, the wavevectors $\boldsymbol{k}_s$ and $\boldsymbol{k}_p$ can be assumed to be complex vectors with the imaginary part that possibly has a different direction from the real part [5].

$$\boldsymbol{k}_s = \boldsymbol{k}_{s,r} + i\boldsymbol{k}_{s,\,i} \tag{4.2a}$$

$$\boldsymbol{k}_p = \boldsymbol{k}_{p,r} + i\boldsymbol{k}_{p,\,i.} \tag{4.2b}$$

The real part, as usual, is related to the wavefront propagation direction for an eigenpolarization in the material, while the imaginary part is related to the linear absorption experienced by the waves, for instance, $\boldsymbol{k}_{s,i} \equiv \alpha_s \hat{\boldsymbol{\zeta}}$ and $\boldsymbol{k}_{p,i} \equiv \alpha_p \hat{\boldsymbol{\zeta}}$. In this case, it is assumed that the waves S and P enter the absorbing material through the same flat surface characterized by the normal unit vector $\hat{\boldsymbol{\zeta}}$ and the amplitude absorption parameters α_s and α_p are given along this direction [6]. Note that the magnitude of these absorption parameters depends on the direction of the real parts of the wavevectors $\boldsymbol{k}_s$ and $\boldsymbol{k}_p$, explicit expressions for α_s and α_p will be given in Section 4.3.2. It is important to notice that, in the sense given above, the complex amplitudes $E_s(\boldsymbol{r})$ and $E_p(\boldsymbol{r})$ are cleaned from the absorption contribution. This means that, even in presence of absorption, they are always constant in absence of coupling between the waves or of other nonlinear effects.

The interference of the two waves expressed by Eq. (4.1) leads to a plane-wave grating associated to the grating vector $\boldsymbol{K} = \boldsymbol{k}_{s,r} - \boldsymbol{k}_{p,r}$. The driving term for the photorefractive charge redistribution is given by what we may call the "usefully dissipated energy" w; that is, the optical energy that is locally dissipated for the generation of mobile charge carriers. It is defined as

$$w(\boldsymbol{r}) = \frac{1}{2}\varepsilon_0[\boldsymbol{\mathcal{E}}(\boldsymbol{r}) \cdot \kappa \cdot \boldsymbol{\mathcal{E}}^*(\boldsymbol{r})], \tag{4.3}$$

where ε_0 is the electric field-constant. The real second rank tensor κ describes the anisotropy of the photoexcitation process and is related to the absorptive part of the dielectric tensor, i.e., to the symmetric imaginary part ε'' of the complex dielectric tensor $\varepsilon = \varepsilon' + i\varepsilon''$ of the material. It is defined as

$$\kappa_{kl} \equiv \phi_{kl}(\varepsilon'')_{kl}, \tag{4.4}$$

where no summing over equal indices is performed. The quantities ϕ_{kl} describe the light polarization dependence of the quantum efficiency, that is, the probability that an absorbed photon of given polarization produces a photoexcited mobile carrier. With the combined wave (4.1) the "usefully dissipated energy" takes the form

$$w(\boldsymbol{r}) = w_0 \mathrm{Re}[1 + m\exp(i\boldsymbol{K} \cdot \boldsymbol{r})]. \tag{4.5}$$

The photorefractive space-charge electric field vector resulting from this modulation points in direction of the unit grating vector $\hat{\boldsymbol{K}} \equiv \boldsymbol{K}/|\boldsymbol{K}| \equiv \boldsymbol{K}/K$ and reads

$$\boldsymbol{E}_{sc}(\boldsymbol{r}) = \hat{\boldsymbol{K}} E_{sc,0} \exp(i\boldsymbol{K} \cdot \boldsymbol{r})] \tag{4.6}$$

Its amplitude $E_{sc,0}$ is determined by the (complex) modulation index m of w (4.5), which is expressed by [6]

$$m(\boldsymbol{r}) = \frac{2E_s(\boldsymbol{r})E_p^*(\boldsymbol{r})[\hat{e}_s \cdot \kappa \cdot \hat{e}_p]e^{-(\alpha_s+\alpha_p)\hat{\boldsymbol{\zeta}}\cdot\boldsymbol{r}}}{|E_p(\boldsymbol{r})|^2[\hat{e}_p \cdot \kappa \cdot \hat{e}_p]e^{-2\alpha_p\hat{\boldsymbol{\zeta}}\cdot\boldsymbol{r}} + |E_s(\boldsymbol{r})|^2[\hat{e}_s \cdot \kappa \cdot \hat{e}_s]e^{-2\alpha_s\hat{\boldsymbol{\zeta}}\cdot\boldsymbol{r}}}. \tag{4.7}$$

If the tensor κ is anisotropic, as might be expected in dichroic materials, the above modulation index (4.7) can be strongly different from the modulation amplitude of the light intensity fringes. As will be discussed in Section 4.4, this fact has important consequences for the strength of the resulting refractive index gratings as well as for the magnitude of the two-wave mixing gain coefficients. Examples will be given in Section 4.5.

4.2.2 Mechanical Response to Modulated Electric Field

As pointed out by several researchers [7, 8, 9, 10], the magnitude of the effective dielectric constant and effective electro-optic coefficient being active in a particular photorefractive experiment does not depend only on the primary tensor properties, but is also influenced by the mechanical state of the crystal. Let us consider specifically the case where the photorefractive medium is a piezoelectric crystal. Its response to external electrical and mechanical fields is described by the relationships [11]

$$T_{ij} = C^E_{ijkl}S_{kl} - e_{kij}E_k, \tag{4.8}$$

and

$$D_i = e_{ijk}S_{jk} + \varepsilon_0\varepsilon^S_{ij}E_j. \tag{4.9}$$

Here the Einstein summation convention over equal indices is used, and T_{ij} is the elastic stress tensor, C^E_{ijkl} is the elastic stiffness tensor at constant electric field, e_{ijk} is the piezoelectric stress tensor, ε^S_{ij} is the clamped static dielectric tensor, E_j is the electric field vector, D_i is the electric displacement vector, and

$$S_{kl} = \frac{1}{2}\left(\frac{\partial u_k}{\partial x_l} + \frac{\partial u_l}{\partial x_k}\right) \tag{4.10}$$

is the strain tensor corresponding to the symmetrized part of the displacement gradient matrix $\partial u_l/\partial x_k$.

The crystal response can be easily calculated in the case of a homogeneous field $\boldsymbol{E}$. In contrast, for a photorefractive periodic electric field of the form (4.6), the mechanical response is more complex. In order to determine the effective dielectric constant and electro-optic coefficient, it is therefore necessary to

calculate the modulated displacement vector field $\boldsymbol{u}(\boldsymbol{r})$ for this situation. Since the piezoelectric effect is linear, $\boldsymbol{u}$ must have the form

$$\boldsymbol{u}(\boldsymbol{r}) = \boldsymbol{u}_0 \mathrm{Re}[\exp\, i(\boldsymbol{K}\cdot\boldsymbol{r} - \pi/2)], \tag{4.11}$$

where the displacement amplitude vector $\boldsymbol{u}_0$ in general differs from the direction of the normalized grating vector $\hat{\boldsymbol{K}}$ with Cartesian components $\hat{K}_i$. In steady-state, the equation of motion for a crystal volume element leads to the equilibrium condition [11]

$$\frac{\partial T_{ij}}{\partial x_j} = 0 = C^E_{ijkl}\frac{\partial^2 u_k(\boldsymbol{r})}{\partial x_j \partial x_l} - e_{kij}\frac{\partial E_{sc,k}(\boldsymbol{r})}{\partial x_j}, \tag{4.12}$$

where $u_k(\boldsymbol{r})$ and $E_{sc,k}(\boldsymbol{r})$ are the k-th cartesian component of $\boldsymbol{u}(\boldsymbol{r})$ and $\boldsymbol{E}_{sc}(\boldsymbol{r})$, respectively. Eq. (4.12) can be rewritten as

$$C^E_{ijkl}\hat{K}_j\hat{K}_l u_{0,k} = \frac{E_{sc,0}}{K} e_{kij}\hat{K}_k\hat{K}_j, \tag{4.13}$$

or in the form $A_{ik}u_{0,k} = B_i(E_{sc,0}/K)$, which allows us to write the result as

$$u_{0,k} = A^{-1}_{ki}B_i(E_{sc,0}/K). \tag{4.14}$$

The matrix A_{ik} and the vector B_i are defined as [9],

$$A_{ik} \equiv C^E_{ijkl}\hat{K}_j\hat{K}_l, \tag{4.15}$$

$$B_i \equiv e_{kij}\hat{K}_k\hat{K}_j. \tag{4.16}$$

Fig. 4.1 shows schematically the periodic crystal deformations in the case of a crystal with point group symmetry $4mm$ such as $BaTiO_3$ at room temperature. The partial clamping of some deformation modes leads to complex displacement fields (see, for instance, case (d)).

4.2.3 *Effective Static Dielectric Constant*

The effective scalar static dielectric constant ε_{eff} that acts in a photorefractive experiment is the quantity connecting the space-charge field amplitude $E_{sc,0}$ to the modulation amplitude of the charge density $\rho_{sc,0}$ by means of the Gauss equation $\nabla\cdot\boldsymbol{D} = \rho$. By using this equation, the dielectric relationship (4.9) and the displacement field $\boldsymbol{u}$ determined above (4.14), one obtains [9]

$$\varepsilon_{eff} \equiv \frac{\rho_{sc,0}}{\varepsilon_0 K E_{sc,0}} = \hat{K}_i\hat{K}_j\left[\varepsilon^S_{ij} + \frac{1}{\varepsilon_0}e_{ijk}A^{-1}_{kl}B_l\right]. \tag{4.17}$$

The quantity in the square bracket represents a new second-rank tensor whose components depend on the direction $\hat{\boldsymbol{K}}$ of the grating vector. In general,

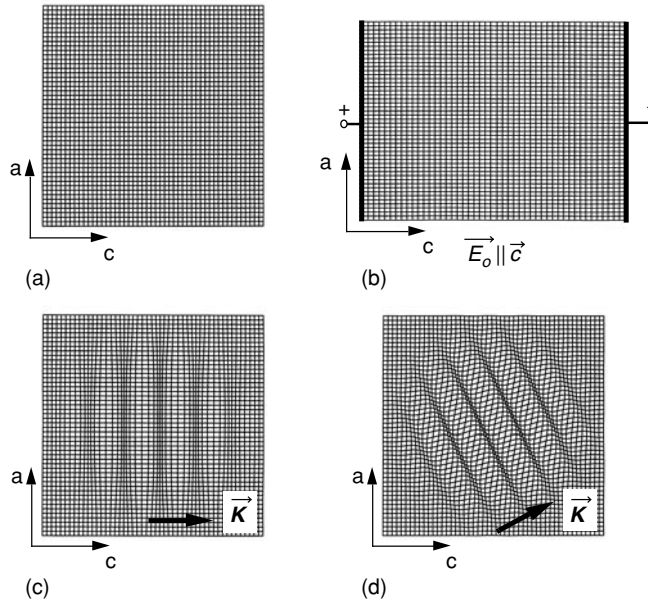

FIGURE 4.1. Elastic deformations of an ideal crystal belonging to the 4*mm* point group symmetry. (a) undisturbed crystal; (b) homogeneous strain induced by homogeneous electric field along the 4-fold *c*-axis; (c) periodic dilation/compression under the effect of a periodic space-charge field with grating $\boldsymbol{K}$-vector $\|$ *c*-axis. (d) same as (c), but for a $\boldsymbol{K}$-vector in the *ac* plane, the deformations are a combination of dilation/compression and shear deformations. The space-charge field in cases (c) and (d) is assumed to interest only the central part of the crystal. The deformation amplitudes are highly exaggerated.

even in the principal system of coordinates of the crystal, this tensor is no longer diagonal. It differs significantly from the unclamped (free) dielectric tensor ε_{ij}^{T} measured at constant stress. The latter can be expressed as [11]

$$\varepsilon_{ij}^{T} = \varepsilon_{ij}^{S} + \frac{1}{\varepsilon_0} e_{ilm} d_{jlm} \tag{4.18}$$

by using (4.9) and the relationship $S_{lm} = d_{jlm} E_j$ for the inverse piezoeffect, with d_{jlm} being the inverse piezoelectric tensor. Examples visualizing the consequence of Eq. (4.17) will be given in Section 4.5.

4.2.4 *Electro-Optic Response to Electric Field Grating*

Let us first consider a spatially homogeneous electric field $\boldsymbol{E}(\boldsymbol{r}, t) = \boldsymbol{E}_0(t)$ applied to an electro-optic crystal. In this case, the change of (t)he optical indicatrix due to the linear electro-optic effect is given by the well-known relationship

$$\Delta\left(\frac{1}{n^2}\right)_{ij} = r_{ijk}E_k, \tag{4.19}$$

where the third-rank electro-optic tensor r_{ijk} depends on the frequency ω of the applied field.

For a spatially inhomogeneous deformation (4.11) of the kind resulting in the presence of a periodic space-charge grating of the type (4.6) the situation is slightly more involved. The change of the indicatrix is then expressed as

$$\Delta\left(\frac{1}{n^2}\right)_{ij} = r^S_{ijk}E_k + p'^E_{ijkl}\frac{\partial u_k}{\partial x_l}, \tag{4.20}$$

where r^S_{ijk} is the clamped electro-optic tensor that contains the electronic as well as the optical phonon contributions, and p'^E_{ijkl} is the modified elasto-optic tensor at constant electric field. The latter tensor contains also the roto-optic contributions and has no symmetry upon interchange of the last two indices [12]. By inserting (4.14) and the space-charge field amplitude $E_{sc} = E_{sc,0}\hat{K}$ in the above equation, after a small index rearrangement, one obtains [9]

$$\Delta\left(\frac{1}{n^2}\right)_{ij} = E_{sc,0}\left[r^S_{ijk} + p'^E_{ijlk}A^{-1}_{lm}B_m\right]\hat{K}_k. \tag{4.21}$$

The expression in the square brackets represents an effective third-rank electro-optic tensor

$$r^{eff}_{ijk} \equiv r^S_{ijk} + p'^E_{ijlk}A^{-1}_{lm}B_m \tag{4.22}$$

and differs considerably from the expression

$$r^T_{ijk} \equiv r^S_{ijk} + p^E_{ijlm}d^T_{klm} \tag{4.23}$$

for the unclamped electro-optic tensor r^T_{ijk} calculated in analogy to (4.18) by starting from (4.20) and assuming a homogeneous electric field. Note that in the latter case, the tensor p'^E_{ijlk} is replaced by the conventional elasto-optic (Pockels) tensor $p^E_{ijlk} \equiv p^E_{ijkl}$ because for a homogeneous field, roto-optic contributions do not lead to a change in refractive index in a free crystal.

Due to the symmetry breaking brought about by the periodic field in direction $\hat{K}$ and the resulting mechanical response, the tensor r^{eff}_{ijk} may possess a lower symmetry than r^S_{ijk}, which is in full analogy with the above discussion in relation to the Eq (4.17) for the effective dielectric constant. The elastic, piezoelectric, and elasto-optic contributions contained in the second term on the right-hand side of (4.22) can have a dramatic influence on the photorefractive nonlinearity in several circumstances. Therefore, the full knowledge of the corresponding tensors C^E_{ijkl}, e_{ijk} and p'^E_{ijlk} is required for the correct evaluation of the electro-optic response.

Finally, we want to give an expression for the scalar electro-optic coefficient r_{eff}, which is active in a specific photorefractive geometry. This scalar coefficient enters the expressions describing light diffraction and two-wave mixing that will be presented in Sections 4.3 and 4.4. Let us consider a grating directed along the vector $\hat{\boldsymbol{K}}$ and the interaction of a pump wave P polarized along the unit vector $\hat{\boldsymbol{d}}^P$ (corresponding to the direction of the optical electric displacement vector) with a signal wave S polarized along $\hat{\boldsymbol{d}}^S$. The scalar effective electro-optic coefficient is then expressed by

$$r_{eff} \equiv \hat{d}_i^S \cdot \left(r_{ijk}^{eff} \hat{K}_k \right) \cdot \hat{d}_j^P . \tag{4.24}$$

Note that the expression in the brackets can also be summarized into an effective (photorefractive) second-rank electro-optic tensor, $r_{ij}^{eff} \equiv r_{ijk}^{eff} \hat{K}_k$ [13]. The use of the scalar quantity (4.24) will become clear later.

4.2.5 Mobility Anisotropy

Since the Maxwell dielectric time τ_{die} is inversely proportional to the carrier drift mobility, the latter is one of the principal quantities influencing the build-up time of the photorefractive space-charge grating. In general, in anisotropic materials, the carrier drift velocity vector $\boldsymbol{v}$ is not necessarily parallel to the electric field $\boldsymbol{E}$ driving the charges and the two quantities are related by a tensorial drift mobility $\boldsymbol{v} = \mu \cdot \boldsymbol{E}$. In the bulk of a photorefractive grating, any charge movement in a direction perpendicular to the grating vector $\hat{\boldsymbol{K}}$ does not lead to charge separation because the light energy is homogeneous along such directions. Therefore, one is interested only in the component of the drift velocity parallel to the modulated field $\boldsymbol{E}_{sc}$, i.e., parallel to $\hat{\boldsymbol{K}}$. The scalar (parallel) effective drift mobility $\mu_{\|}$ can then be easily calculated as

$$\mu_{\|} = \hat{\boldsymbol{K}} \cdot \mu \cdot \hat{\boldsymbol{K}}. \tag{4.25}$$

For a specific geometry where the grating wavevector is in the *ac*- or *bc*-plane of a crystal with a symmetry higher than orthorhomic and makes an angle θ with the *c*-axis, the above relationship can be rewritten as

$$\mu_{\|} = \mu_c(\cos^2\theta + \frac{\mu_{a,b}}{\mu_c}\sin^2\theta), \tag{4.26}$$

where $\mu_{a,b,c}$ are the principal mobilities along the three crystallographic axes.

It turns out that dynamic photorefractive holographic experiments are a very effective method for the contact-free determination of the ratio of mobilities and the shape of the mobility tensor, as performed for instance in [14, 15, 16] for $BaTiO_3$ and $KNbO_3$. Note also that, while the absolute values of the effectively observed mobility may be influenced by trapping effects and the

observation time scale, the ratio between the mobility in different directions is not.

4.3 Light Diffraction at Thick Anisotropic Phase and Absorption Gratings

Before discussing the consequences of material anisotropies on photorefractive two-wave mixing, we summarize in this section the main features of a coupled wave model applying to anisotropic gratings in anisotropic materials [6], which extends the results of the coupled-wave theory of Kogelnik [1]. Note that this model does not apply only to photorefractive gratings, but is relevant for any holographic materials having strong birefringence and/or containing gratings with strongly anisotropic properties, such as organic crystals [17], liquid crystals [18, 19], or polymer dispersed liquid crystals [20, 21, 22].

4.3.1 Coupled-Wave Equations

Let us consider a plane phase and/or amplitude grating in the form of a slab of thickness d. By whatever mechanism it might have been recorded, following Gaylord and Moharam [23], this grating (hologram) is considered to be thick if the following two conditions are fulfilled simultaneously:

$$Q' \equiv \frac{K^2 \lambda d}{2\pi n \cos\gamma} > 1 \tag{4.27}$$

and

$$\rho \equiv \frac{K^2 \lambda^2}{(2\pi)^2 n\sigma} \geq 10, \tag{4.28}$$

where $\sigma = \Delta n$ for dielectric gratings and $\sigma = \Delta\alpha\lambda/2\pi$ for absorption gratings. In our specific case of anisotropic materials, the (pseudo-scalar) refractive index change Δn and the absorption modulation $\Delta\alpha$ will be defined later. In (4.27) and (4.28), λ is the vacuum wavelength, n is the average refractive index of the medium, and γ is the angle between the incident wave and the fringe planes as measured inside the medium.

As shown by Kogelnik [1], the diffraction properties of thick gratings may be calculated by considering the propagation of only two plane waves P and S. Since we consider the general case of anisotropic materials, the waves P and S should represent eigenwaves of the medium and the coherent superposition of their electric fields was already given in Eq. (4.1). The combined wave expressed by (4.1) has to fulfill the time independent vector wave equation

$$\nabla \times (\nabla \times \boldsymbol{\mathcal{E}}) - k_0^2 \varepsilon \cdot \boldsymbol{\mathcal{E}} = 0, \tag{4.29}$$

where $\varepsilon = \varepsilon_{\mathbf{r}} + i\varepsilon_{\mathbf{i}}$ is the complex second rank dielectric tensor that includes the effects of the material refractive index and absorption [24], and $k_0 = 2\pi/\lambda$ is the free space wavenumber.

We treat a general case of plane hologram where a phase and an amplitude grating (with common grating vector) may coexist and are mutually phase shifted by a phase angle ϕ. The complex dielectric tensor ε can then be written as

$$\varepsilon = [\varepsilon_r^0 + \varepsilon_r^1 \cos(\boldsymbol{K} \cdot \boldsymbol{r})] + i[\varepsilon_i^0 + \varepsilon_i^1 \cos(\boldsymbol{K} \cdot \boldsymbol{r} + \phi)], \tag{4.30}$$

where the superscripts 0 and 1 denote the average value and the amplitude of the modulated component, respectively. The grating vector $\boldsymbol{K}$ can have an arbitrary direction with respect to the geometrical or crystallographic axes of the anisotropic medium. The phase grating is associated with the modulated term in the real part of (4.30), while the absorption grating is associated with the modulated term in the imaginary part.

One may choose the coordinate system to coincide with the main axes of the optical indicatrix so that the tensor ε_r^0 contains only diagonal elements. In contrast, the modulated part ε_r^1 of the real dielectric tensor is generally non-diagonal. That is

$$\varepsilon_r^0 = \begin{pmatrix} \varepsilon_{r,11}^0 & 0 & 0 \\ 0 & \varepsilon_{r,22}^0 & 0 \\ 0 & 0 & \varepsilon_{r,33}^0 \end{pmatrix}, \tag{4.31}$$

$$\varepsilon_r^1 = \begin{pmatrix} \varepsilon_{r,11}^1 & \varepsilon_{r,12}^1 & \varepsilon_{r,13}^1 \\ \varepsilon_{r,12}^1 & \varepsilon_{r,22}^1 & \varepsilon_{r,23}^1 \\ \varepsilon_{r,13}^1 & \varepsilon_{r,23}^1 & \varepsilon_{r,33}^1 \end{pmatrix}. \tag{4.32}$$

For example, nondiagonal elements can be produced by shear acoustic waves and by space-charge induced electro-optic effects. For crystalline materials with orthorhombic or higher symmetry, the main axes of the imaginary dielectric tensor coincide with those of the real one [24]. For these materials ε_i^0 and ε_i^1 also are diagonal tensors,

$$\varepsilon_i^0 = \begin{pmatrix} \varepsilon_{i,11}^0 & 0 & 0 \\ 0 & \varepsilon_{i,22}^0 & 0 \\ 0 & 0 & \varepsilon_{i,33}^0 \end{pmatrix}, \quad \varepsilon_i^1 = \begin{pmatrix} \varepsilon_{i,11}^1 & 0 & 0 \\ 0 & \varepsilon_{i,22}^1 & 0 \\ 0 & 0 & \varepsilon_{i,33}^1 \end{pmatrix}. \tag{4.33}$$

For crystals with lower symmetry, the main axes of the absorption ellipsoid may differ from those of the refractive index ellipsoid [25] and the tensors ε_i^0 and ε_i^1 may therefore also contain nondiagonal elements in our system of coordinates. Note that the formalism presented here can be used to describe

the behavior in gain media (negative absorption) as well, as long as the system remains in a non-oscillating regime.

One may consider a general holographic wave interaction geometry as the one depicted in Fig. 4.2(a). The medium input surface ($\perp \hat{\boldsymbol{\zeta}}$) does not need to contain any of the main axes of the optical indicatrix of the medium. The relative directions of some important vectors associated with the wave S are shown in Fig. 4.2(b).

By inserting (4.1) and (4.30) into the wave Eq. (4.29), after a rather lengthy but straightforward calculation [6], it is possible to obtain the coupled-wave equation applying to the anisotropic case. With $\boldsymbol{E}_s = E_s\hat{\boldsymbol{e}}_s$ and $\boldsymbol{E}_p = E_p\hat{\boldsymbol{e}}_p$, they read

$$\nabla E_s \cdot \hat{\boldsymbol{u}}_s = \frac{k_0}{4n_s g_s}[iA_r - A_i e^{i\phi}]E_p e^{i\Delta\boldsymbol{k}\cdot\boldsymbol{r}}, \tag{4.34a}$$

$$\nabla E_p \cdot \hat{\boldsymbol{u}}_p = \frac{k_0}{4n_p g_p}[iA_r - A_i e^{-i\phi}]E_s e^{-i\Delta\boldsymbol{k}\cdot\boldsymbol{r}}, \tag{4.34b}$$

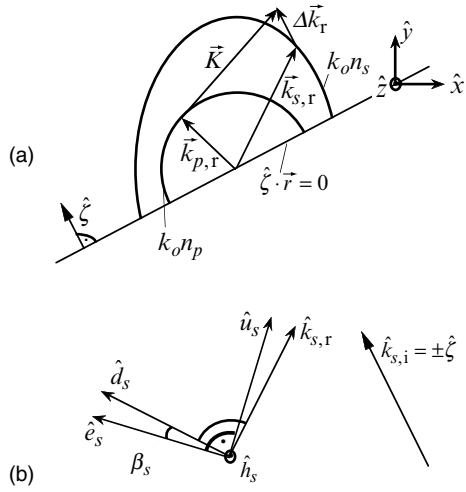

FIGURE 4.2. (a) General interaction geometry for coupled-wave theory. A projection of the wavevector diagram for the holographic interaction is schematically shown. The coordinate axes are parallel to the main axes of the optical indicatrix. The input surface plane $\hat{\boldsymbol{\zeta}}\cdot\boldsymbol{r} = 0$ does not necessarily contain the axis $\hat{z}$. The vectors $\boldsymbol{k}_{s,r}, \boldsymbol{k}_{p,r}, \boldsymbol{K}$ and $\Delta\boldsymbol{k}_r$ do not need to be all coplanar. (b) Schematics showing the relative orientation of important vectors associated with the signal wave S. The unit vectors in direction of the electric field ($\hat{e}_s$), the dielectric displacement ($\hat{d}_s$), the magnetic field ($\hat{h}_s$), the energy propagation ($\hat{u}_s$), and the real and imaginary component of the propagation vector ($\hat{k}_{s,r}$, $\hat{k}_{s,i}$) are shown. It holds that $\hat{e}_s \perp \hat{u}_s \perp \hat{h}_s$, $\hat{d}_s \perp \hat{k}_{s,r} \perp \hat{h}_s$, and $\hat{e}_s \cdot \hat{d}_s = \hat{u}_s \cdot \hat{k}_{s,r} = \cos\beta_s$.

where n_s and n_p are the unperturbed refractive indices seen by the signal and pump wave, respectively, $g_s = \hat{e}_s \cdot \hat{d}_s = \cos\beta_s$ and $g_p = \hat{e}_p \cdot \hat{d}_p = \cos\beta_p$ are the projection cosines between the electric field ($\hat{e}$) and the electric displacement vectors ($\hat{d}$) of the waves, and $\hat{u}_s$ and $\hat{u}_p$ are the Poynting vector directions. The scalar coupling constants A_r and A_i are defined as

$$A_r \equiv \hat{e}_s \cdot \varepsilon_r^1 \cdot \hat{e}_p = \hat{e}_p \cdot \varepsilon_r^1 \cdot \hat{e}_s, \tag{4.35}$$

and

$$A_i \equiv \hat{e}_s \cdot \varepsilon_i^1 \cdot \hat{e}_p = \hat{e}_p \cdot \varepsilon_i^1 \cdot \hat{e}_s, \tag{4.36}$$

where the second equalities are valid because the tensors ε_r^1 and ε_i^1 are symmetric. The coupling constant A_r reflects the effect of the phase grating, while A_i reflects the effect of the absorption or gain grating. The term $\exp(\pm i\Delta\boldsymbol{k}\cdot\boldsymbol{r})$ in (4.34a) and (4.34b) takes into account (small) deviations from the Bragg conditions as well as differences in absorption between the incident (pump) and diffracted (signal) wave. Note that in general, the wavevector mismatch $\Delta\boldsymbol{k}$ is a complex vector given as

$$\Delta\boldsymbol{k} \equiv \Delta\boldsymbol{k}_r + i\Delta\boldsymbol{k}_i = (\boldsymbol{k}_{p,r} - \boldsymbol{k}_{s,r} + \boldsymbol{K}) + i(\boldsymbol{k}_{p,i} - \boldsymbol{k}_{s,i}). \tag{4.37}$$

Eqs. (4.34a) and (4.34b) describe the coupling of two plane waves in any general geometry in anisotropic media containing phase and/or absorption gratings. It is important to notice that the coupling terms must describe the projection of the amplitude gradients along the Poynting vector direction $\hat{u}$ of the corresponding wave, and not along the wavevector direction $\hat{k}_r$.

For later use, it is useful to give at this point the form of the coupling constant A_r in the case where the grating is of photorefractive nature. It is easy to show that in this case

$$A_r = -\hat{e}_s \cdot \varepsilon_r^0 \cdot \left(r^{eff} \cdot \hat{\boldsymbol{K}}\right) \cdot \varepsilon_r^0 \cdot \hat{e}_p E_{sc,0}, \tag{4.38}$$

where the tensor r^{eff} is the third-rank effective electro-optic tensor defined in (4.22) and takes into account all mechanical coupling effects. Performing the tensor multiplications in the above expression leads to

$$A_r = -n_s^2 n_p^2 g_s g_p r_{eff}\ E_{sc,0}, \tag{4.39}$$

where r_{eff} is the scalar effective electro-optic coefficient defined in (4.24).

4.3.2 Diffraction Efficiency of Transmission Gratings

We apply the coupled wave theory developed above first to the case of transmission gratings. A transmission grating is characterized by the condition

$$\left(\hat{u}_p \cdot \hat{\zeta}\right)\left(\hat{u}_s \cdot \hat{\zeta}\right) \equiv \cos\theta_p \cos\theta_s > 0, \tag{4.40}$$

where θ_s and θ_p are the angles between the Poynting vectors and the normal $\hat{\boldsymbol{\zeta}}$ to the entrance surface. The boundary conditions corresponding to diffraction at such a grating are

$$E_s(\hat{\boldsymbol{\zeta}} \cdot \boldsymbol{r} = 0) = 0 \tag{4.41}$$

and

$$\nabla E_s \cdot \hat{\boldsymbol{u}}_s(\hat{\boldsymbol{\zeta}} \cdot \boldsymbol{r} = 0) = \frac{k_0}{4 n_s g_s}[iA_r - A_i e^{i\phi}]E_{p0} e^{i\Delta \boldsymbol{k} \cdot r}, \tag{4.42}$$

where $E_{p0} = E_p(\hat{\boldsymbol{\zeta}} \cdot \boldsymbol{r} = 0)$ is the pump wave amplitude at the entrance face of the anisotropic holographic medium. For a grating with infinite extent in the lateral direction, it can be shown that both the real and the imaginary part of the complex wavevector mismatch $\Delta \boldsymbol{k}$ have to be parallel to the surface normal $\hat{\boldsymbol{\zeta}}$, that is $\Delta \boldsymbol{k} = (\Delta \boldsymbol{k}_r + i\Delta \boldsymbol{k}_i)\hat{\boldsymbol{\zeta}}$. By using this and inserting the boundary conditions (4.41) and (4.42) into the coupled-wave equations (4.34a) and (4.34b), one can calculate the diffraction efficiency η as described in more detail in [6]. The diffraction efficiency is defined as the ratio of the output signal intensity to the incident pump intensity; that is,

$$\eta \equiv \frac{I_s(\hat{\boldsymbol{\zeta}} \cdot \boldsymbol{r} = d)}{I_p(\hat{\boldsymbol{\zeta}} \cdot \boldsymbol{r} = 0)} = \frac{E_s E_s^* n_s g_s}{E_{p0} E_{p0}^* n_p g_p} \frac{\cos \theta_s}{\cos \theta_p} e^{-2\boldsymbol{k}_{s,i} \cdot \boldsymbol{r}}, \tag{4.43}$$

where the factor $\cos \theta_s / \cos \theta_p$ is an obliquity term that assures consistent results in a general case when we are interested in the optical energy flow through the input and output surfaces of the medium. The existence of the term $n_s g_s / n_p g_p$ has been often overlooked in the literature. Neglecting this term is allowed only in isotropic materials or in anisotropic materials in the case of a configuration fully symmetric with respect to the axis $\hat{\boldsymbol{\zeta}}$ and the optical indicatrix.

Mixed Transmission Gratings

For a mixed grating as given by (4.30), consisting of a combination of a phase and absorption grating, the diffraction efficiency is expressed as [6]

$$\begin{aligned} \eta(\hat{\boldsymbol{\zeta}} \cdot \boldsymbol{r} = d) = {} & \frac{k_0^2}{16 n_s n_p g_s g_p \cos \theta_s \cos \theta_p} \frac{A_r^2 + A_i^2 - 2A_r A_i \sin \phi}{|W^2|} \\ & \times \{ \sin^2 (\mathrm{Re}[W]d) + \sinh^2(\mathrm{Im}[W]d) \} e^{-(\alpha_s + \alpha_p)d}, \end{aligned} \tag{4.44}$$

where the quantity W is a complex number found as the square root $(W = \sqrt{W^2})$ of

$$\begin{aligned} W^2 = {} & \left(\frac{\Delta \boldsymbol{k} \cdot \hat{\boldsymbol{u}}_p}{2 \cos \theta_p} \right)^2 + \frac{\boldsymbol{k}_o^2}{16 n_s n_p g_s g_p \cos \theta_s \cos \theta_p} \\ & \times (A_r^2 - A_i^2 + 2iA_r A_i \cos \phi), \end{aligned} \tag{4.45}$$

which depends itself on the coupling constants A_r and A_i defined in (4.35) and (4.36) and on the phase-shift angle ϕ. The quantities $\alpha_s = |\boldsymbol{k}_{s,i}|$ and $\alpha_p = |\boldsymbol{k}_{p,i}|$ in (4.44) are the effective amplitude absorption constants (in direction of the surface normal $\hat{\boldsymbol{\zeta}}$) experienced by the signal and pump wave, respectively. They are expressed as [6]

$$\alpha_s = \frac{k_0(\hat{e}_s \cdot \varepsilon_i^0 \cdot \hat{e}_s)}{2n_s g_s |\cos\theta_s|}, \quad \alpha_p = \frac{k_0(\hat{e}_p \cdot \varepsilon_i^0 \cdot \hat{e}_p)}{2n_p g_p |\cos\theta_p|}. \tag{4.46}$$

It should be noticed that the effective absorption constants for the waves S and P can differ from each other even in the case where the tensor ε_i^0 is isotropic. This is the case when the directions of propagation are not symmetric with respect to the surface normal.

Eq. (4.44) describes completely the diffraction at a mixed anisotropic phase and absorption transmission grating in anisotropic media. To give an example, we show in Fig. 4.3 that the total diffraction efficiency strongly depends on the phase- shift ϕ between the phase and absorption grating, which is in agreement with a previous analysis of mixed phase and absorption gratings in isotropic media [26]. This behavior is easily explained by the interference of the waves scattered off the phase and absorption grating, respectively, and leads to a nonreciprocal behavior of light-diffraction [27].

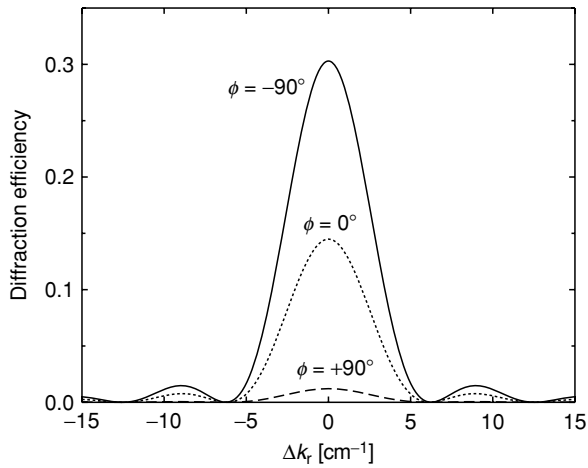

FIGURE 4.3. Diffraction efficiency at a mixed transmission grating vs. the real grating mismatch parameter Δk_r for three values of the phase-shift angle ϕ between phase and absorption grating. The parameters are: $A_r = 3 \times 10^{-5}$, $A_i = 2 \times 10^{-5}$, $\lambda = 633\,\text{nm}$, $d = 1\,\text{cm}$, $\alpha_s = 0.2\,\text{cm}^{-1}$, $\alpha_p = 0.3\,\text{cm}^{-1}$, $n_s = 2.2$, $n_p = 2.0$, $g_s = 0.98$, $g_p = 0.96, \theta_s = 20°$, and $\theta_p = -40°$.

Phase-Only Gratings

In most cases, a grating created by the photorefractive effect can be considered as a phase-only grating. Therefore, it is useful to look specifically at this case. In absence of absorption modulation, we have $A_i = 0$ and the quantity W^2 can be simplified and rewritten as

$$W^2 = \frac{1}{d^2}(\nu^2 + \xi^2 + i\chi^2), \tag{4.47}$$

where the real quantities ν^2, ξ^2 and χ^2 are defined as

$$\nu^2 = \frac{k_0^2 A_r^2}{16 n_s n_p g_s g_p \cos\theta_s \cos\theta_p} d^2, \tag{4.48}$$

$$\xi^2 = \frac{\Delta k_r^2 - \Delta k_i^2}{4} d^2 = \left[\frac{\Delta k_r^2}{4} - \frac{(\alpha_p - \alpha_s)^2}{4}\right] d^2, \tag{4.49}$$

$$\chi^2 = \frac{\Delta \boldsymbol{k}_r \cdot \Delta \boldsymbol{k}_i}{2} d^2 = \left[\frac{\Delta k_r (\alpha_p - \alpha_s)}{2}\right] d^2. \tag{4.50}$$

The diffraction efficiency of Eq. (4.44) reads then

$$\eta(d) = \frac{\nu^2}{\sqrt{(\nu^2 + \xi^2)^2 + \chi^4}} \left\{ \sin^2 \sqrt{\frac{(\nu^2 + \xi^2) + \sqrt{(\nu^2 + \xi^2)^2 + \chi^4}}{2}} \right.$$

$$\left. + \sinh^2 \sqrt{\frac{-(\nu^2 + \xi^2) + \sqrt{(\nu^2 + \xi^2)^2 + \chi^4}}{2}} \right\} e^{-(\alpha_s + \alpha_p)d}. \tag{4.51}$$

Note that the arguments of the $\sin^2$ and $\sinh^2$ functions are always real, although ξ^2 and χ^2 can be negative numbers. We notice also that the $\sinh^2$ term (second term in the curly bracket of (4.44)) survived even though there is no longer an absorption modulation. This term takes accurately into account the effect of different absorption constants for the pump and signal waves on the diffraction efficiency. Figure 4.4 shows the dependence of the diffraction efficiency on the Bragg mismatch Δk_r as calculated from (4.51). The behavior for different values of the amplitude absorption constants α_p and α_s of the two waves is shown. Note that at the minima, one has a complete destructive interference only when the absorption constants α_p and α_s are exactly equal. For a "given total" absorption $\alpha_p + \alpha_s$, the most favorable situation is found if the absorption values are as different as possible, in which case the peak diffraction efficiency is maximum.

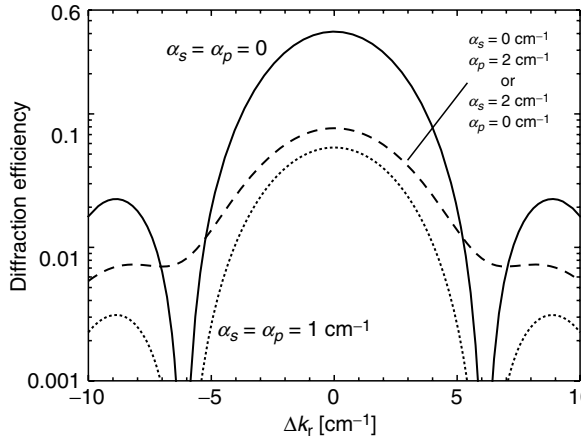

FIGURE 4.4. Effect of absorption on the diffraction efficiency and phase mismatch selectivity for diffraction at a phase-only transmission grating. Parameters: $A_r = 5 \times 10^{-5}$, $A_i = 0$, $\lambda = 633\,\text{nm}$, $d = 1\,\text{cm}$, $n_s = 2.2$, $n_p = 2.0$, $g_s = 1.0$, $g_p = 0.95$, $\theta_s = 10°$, and $\theta_p = -40°$.

This is accompanied by a certain broadening of the curve due to the fact that destructive interference at the minima is only partial.

The $\sinh^2$ term in (4.51) vanishes if the effective absorption constant seen by the two waves is the same ($\alpha_s = \alpha_p = \alpha, \chi^2 = 0$), in which case (4.51) simplifies further to

$$\eta(d) = \frac{\sin^2 \sqrt{\nu^2 + \xi^2}}{(1 + \xi^2/\nu^2)} e^{-2\alpha d}. \tag{4.52}$$

This equation has exactly the same form as Kogelnik's relationship (43) in [1]. However, here the quantities ν^2, ξ^2 and α are defined differently to take into account the effects of anisotropies. The quantity ξ^2 in this case reduces to

$$\xi^2 = \frac{\Delta k_r^2}{4} d^2, \tag{4.53}$$

ν^2 is redefined according to (4.48) and the effective amplitude absorption constant α is given by (4.46). Eq. (4.52) simplifies further in the case of perfect Bragg matching; that is, $\Delta k_r = 0$, $\xi^2 = 0$. One gets then

$$\eta(d) = \sin^2 \left(\frac{\pi A_r d}{2\lambda (n_s n_p g_s g_p \cos\theta_s \cos\theta_p)^{1/2}} \right) e^{-2\alpha d}, \tag{4.54}$$

where we recall that λ is the wavelength in vacuum. The argument of the sin function is of the form $(\pi \Delta n d/\lambda \cos\theta)$ in analogy with the well known expres-

sion (45) in Ref. [1]. In our description, the effective refractive index change Δn corresponds to

$$\Delta n = \frac{A_r}{2\sqrt{n_s n_p g_s g_p}} \tag{4.55}$$

and $\cos\theta = (\cos\theta_s \cos\theta_p)^{1/2}$. In nonabsorbing materials, the maximum possible diffraction efficiency is exactly 100% for phase-only gratings, regardless of whether isotropic or anisotropic diffraction processes are considered.

Even for a simple case where the refractive index change is treated as a scalar quantity, the effects of material birefringence contained in (4.54) can lead to substantial differences from Kogelnik's expression. This is shown in the example of Fig. 4.5, where the highly birefringent organic material 4-N,N-Dimethylamino- 4′-N-methyl-stilbazolium tosylate (DAST) [28] is being considered. The refractive indices of this material at $\lambda = 860\,\text{nm}$ are $n_1 = 2.315,\ n_2 = 1.660,\ n_3 = 1.604$ [4.29]. For a crystal cut along the dielectric principal axes ($x_1,\ x_2,\ x_3$) and pump and scattered signal beams with $\boldsymbol{k}$-vectors in the 1,3-plane and directed at $\pm 25^\circ$ to the x_3-axis, one obtains $n_p = n_s = 2.119$. The energy propagation vectors $\hat{\boldsymbol{u}}_p$ and $\hat{\boldsymbol{u}}_s$ are then directed at $\pm 44.2^\circ$ to the x_3-axis, giving a big walkoff angle of the order of 20° and

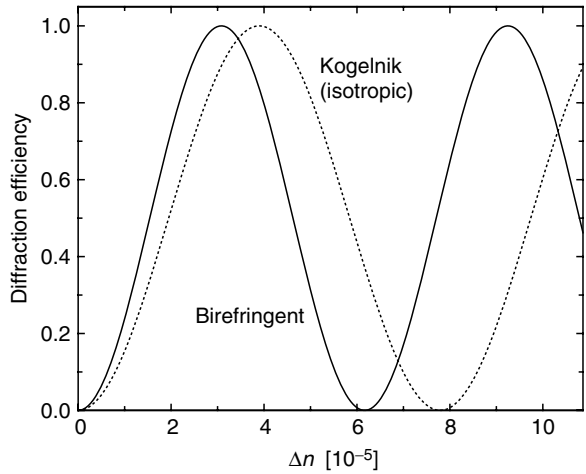

FIGURE 4.5. Diffraction efficiency vs. refractive index change Δn (4.55) predicted by the coupled wave theory for anisotropic materials described here (solid line) and the isotropic coupled wave theory of Kogelnik [1] (dotted line). The diffraction is modeled for the organic crystal 4-N,N-Dimethylamino-4′-N-methyl-stilbazolium tosylate (DAST) with symmetric p-polarized signal and pump wave propagating in the 1,3-plane ($\hat{\boldsymbol{\zeta}} = \hat{x}_3$) and the grating wavevector parallel to the 1-axis. The Bragg condition is fulfilled and the angle between the $\hat{\boldsymbol{k}}_p$ or $\hat{\boldsymbol{k}}_s$ vectors and the $\hat{x}_3$-axis is 25 degrees, which leads to $\theta_s = -\theta_p = 44.2^\circ$ and $n_s = n_p = 2.119,\ g_s = g_p = 0.945$. The other parameters are: $A_i = 0,\ \lambda = 860\,\text{nm},\ d = 1\,\text{cm}$, and $\alpha_s = \alpha_p = 0$.

$g_s = g_p = 0.945$. The curves in Fig. 4.5 show how in birefringent materials the use of the isotropic Kogelnik's expressions can lead to large errors even for fully symmetric beam geometries like the one considered here.

The above example applies to the case of an isotropic grating in an anisotropic material. As might be expected, the difference between the above relationships and Kogelnik's theory become even more important in the case where the grating itself is anisotropic. The latter situation is often encountered in photorefractive physics or acousto-optics and is also typical of gratings recorded in liquid crystals or polymer-dispersed liquid crystals. Since the diffraction properties are being strongly influenced, their detailed measurement allows the determination of the degree of grating anisotropy, as shown in the example of Fig. 4.6 for the case of a polymer filled with a nematic liquid crystal [21]. In this example, the Bragg angle was varied for a specific grating by changing the read-out wavelength. It is clearly seen that the isotropic theory fails to appropriately describe the measurements.

4.3.3 *Diffraction Efficiency of Phase-Only Reflection Gratings*

The case of reflection gratings is treated here in less detail and we concentrate uniquely on the solutions for lossless phase gratings. Solutions for the general case of mixed refractive index and absorption gratings are given in [6].

In analogy to (4.40), a reflection grating is characterized by the condition $\cos\theta_p \cos\theta_s < 0$. Let the pump wave P enter a parallel plate holographic

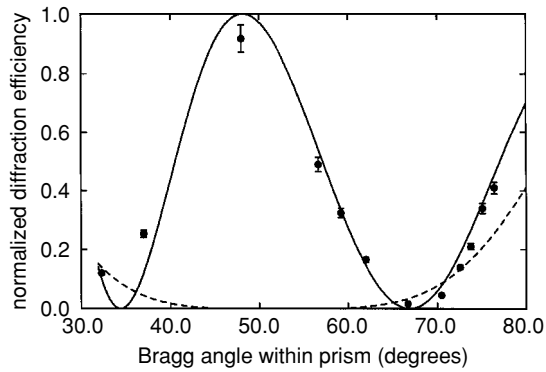

FIGURE 4.6. Comparison of anisotropic (solid line) and isotropic (dashed line) coupled-wave theory for the description of light diffraction at a grating recorded in a photopolymer filled with nematic liquid crystals. See Ref. [21] for details. The best parameters for the solid-line are $\varepsilon^0_{r,11} = \varepsilon^0_{r,33} = 2.56; \varepsilon^1_{r,11} = 0.22$ and $\varepsilon^1_{r,33} = 0.07$. (Reprinted with permission from [21], © Optical Society of America.)

medium from the face defined by $\hat{\boldsymbol{\zeta}} \cdot \boldsymbol{r} = 0$. The only change with respect to the case of transmission gratings are the boundary conditions, which are now

$$E_s\left(\hat{\boldsymbol{\zeta}} \cdot \boldsymbol{r} = d\right) = 0 \tag{4.56}$$

and

$$\boldsymbol{\nabla} E_s \cdot \hat{\boldsymbol{u}}_s(\hat{\boldsymbol{\zeta}} \cdot \boldsymbol{r} = 0) = \frac{k_0}{4 n_s g_s}[iA_r]E_{p0}e^{i\Delta \boldsymbol{k}\cdot\boldsymbol{r}}, \tag{4.57}$$

where $E_{p0} = E_p(\hat{\boldsymbol{\zeta}} \cdot \boldsymbol{r} = 0)$. The diffraction efficiency is now defined as

$$\eta = \frac{I_s(\hat{\boldsymbol{\zeta}} \cdot \boldsymbol{r} = 0)}{I_p(\hat{\boldsymbol{\zeta}} \cdot \boldsymbol{r} = 0)} = \frac{E_s E_s^* n_s g_s}{E_{p0} E_{p0}^* n_p g_p}\left|\frac{\cos\theta_s}{\cos\theta_p}\right|, \tag{4.58}$$

where, as in (4.43), an obliquity factor $\cos\theta_s/\cos\theta_p$ is introduced in the definition.

For lossless materials ($\alpha_s = \alpha_p = 0$), one finds for the diffraction efficiency

$$\eta = \frac{-\nu^2}{\xi^2 + (\nu^2 + \xi^2)\cot^2\sqrt{\nu^2 + \xi^2}}, \tag{4.59}$$

where ν^2 is still given by (4.48) and is now a *negative* real number. Note that with (4.55), one has the equivalence $\nu^2 = (\pi \Delta n d/\lambda\sqrt{\cos\theta_s \cos\theta_p})^2$. The quantity ξ^2, on the other hand is given by (4.53) in the present limit. Since for small values of ξ^2 the argument of the cotangent function in (4.59) is purely imaginary, for perfect Bragg matching ($\xi = 0$), one retrieves the well known expression

$$\eta = \tanh^2(|\nu|). \tag{4.60}$$

Dielectric reflection gratings are interesting, for instance, for applications as sharp wavelength filters. Therefore, we will soon discuss the Bragg selectivity of such gratings. Let us note first that, if the wavevector mismatch Δk_r is due uniquely by a mismatch $\Delta\lambda$ in the read-out wavelength λ, the relation between these two quantities is given as

$$\Delta\lambda \cong \Delta k_r \lambda^2/(4\pi n). \tag{4.61}$$

Fig. 4.7 shows the reflectivity of a grating as obtained from (4.59). The curves are given as a function of the wavevector mismatch Δk_r for different values of the coupling constant A_r and of the grating thickness d. For fixed d, besides the increase of the peak diffraction efficiency, there is also a broadening of the Bragg selectivity with increasing coupling constant A_r (Fig. 4.7(a)). Ultimately, for large enough values of A_r, this leads to the formation of a stop band with reflectivity equal to 1 for a broad range of wavelengths around the perfectly

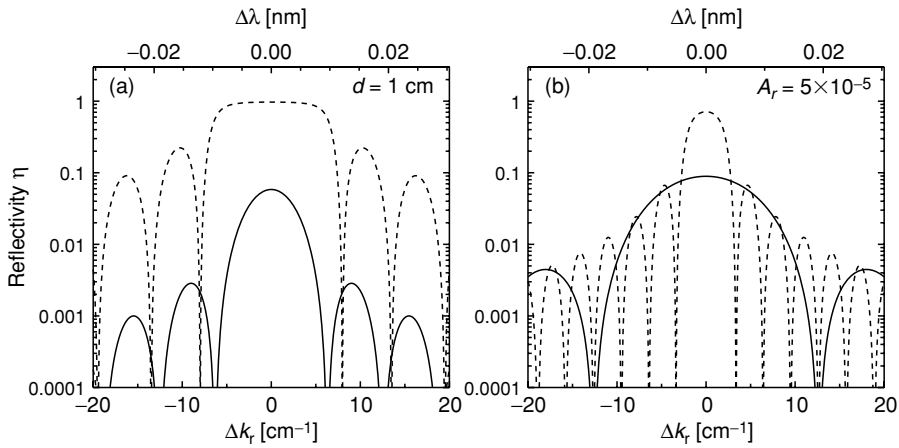

FIGURE 4.7. Diffraction efficiency (reflectivity) of a phase-only reflection grating as a function of the phase mismatch parameter Δk_r as obtained from (4.59). (a) $d = 1\,\text{cm}$, $A_r = 2 \times 10^{-5}$ (solid curve), $A_r = 2 \times 10^{-4}$ (dashed curve); (b) $A_r = 5 \times 10^{-5}$, $d = 0.5\,\text{cm}$ (solid curve), $d = 2\,\text{cm}$ (dashed curve); The other parameters are: $\lambda = 633\,\text{nm}$, $\alpha_s = \alpha_p = 0$, $n_s = 2.2$, $n_p = 2.0$, $g_s = 1.0$, $g_p = 0.95$, $\theta_s = 10°$, $\theta_p = 170°$.

phase matched one. One may eventually speak about one dimensional photonic band-gap structures in this context. The broadening of the selectivity curve for larger A_r is physically due to a shorter average distance traveled by the pump wave inside the grating structure (smaller effective thickness). The effect of the thickness on the Bragg selectivity can be seen explicitly on Fig. 4.7(b). Evidently, thicker gratings lead to sharper reflection filters, however, this is true only as far as the refractive index change ($\propto A_r$) is not too large. Therefore, the simultaneous optimization of the grating reflectivity and reflected bandwidth requires a careful balance between the grating thickness and the amplitude of the refractive index modulation.

4.4 Two-Wave Mixing in Anisotropic Dichroic Media

The gratings considered in the previous section are assumed to be unaffected by the read-out wave and can therefore be considered as being "pre-existing" in the material. In contrast, in the case of photorefractive two-wave mixing, the grating responsible for the coupling between light waves is a dynamic grating being recorded by the interacting waves themselves. Such a grating can adapt with a case-specific time constant to modifications in the shape and phases of the input waves.

In order to treat two-wave mixing in anisotropic photorefractive media, one can take advantage of much of the formalism developed in the previous section.

By using the fact that for two-wave mixing the Bragg condition is fulfilled automatically ($\Delta k_r = 0$), the coupled wave Eqs. (4.34a) and (4.34b) become

$$\nabla E_s \cdot \hat{u}_s = \frac{k_0}{4 n_s g_s}\left[-iRmE_p \tilde{E}_{sc} e^{(\alpha_s - \alpha_p)\hat{\zeta}\cdot r}\right], \tag{4.62a}$$

$$\nabla E_p \cdot \hat{u}_p = \frac{k_0}{4 n_p g_p}\left[-iRm^* E_s \tilde{E}^*_{sc} e^{(\alpha_p - \alpha_s)\hat{\zeta}\cdot r}\right], \tag{4.62b}$$

where $R \equiv n_s^2 n_p^2 g_s g_p r_{eff}$, and r_{eff} is given by (4.24). We recall that $\hat{u}_s$ and $\hat{u}_p$ are unit vectors in direction of the Poynting vectors of the waves S and P, respectively. The quantity

$$\tilde{E}_{sc} \equiv E_{sc,0}/m \equiv \tilde{E}_{sc,r} + i\tilde{E}_{sc,i} \tag{4.63}$$

is the complex amplitude of the first Fourier component of the internal space-charge field normalized by the complex modulation m given in (4.7). Its real part $\tilde{E}_{sc,r}$ corresponds to the component of the space-charge field being in phase with the energy density distribution (4.5), while the imaginary part $\tilde{E}_{sc,i}$ is the $\pi/2$ out-of-phase component. The latter predominates in the case where the charge redistribution is ruled by charge diffusion.

4.4.1 Undepleted Pump Approximation

In the regime where the pump wave is not significantly depleted by the interaction, its energy is always much larger than the one of the signal wave everywhere in the crystal, i.e., $|E_p|^2[\hat{e}_p \cdot \kappa \cdot \hat{e}_p]\ \exp(-2\alpha_p \hat{\zeta}\cdot r) \gg |E_s|^2 [\hat{e}_s \cdot \kappa \cdot \hat{e}_s]\exp(-2\alpha_s \hat{\zeta}\cdot r)$ in (4.7). In this case, Eqs. (4.62a) describing the evolution of the signal wave amplitude transforms to

$$\nabla E_s \cdot \hat{u}_s = \frac{k_0 R}{2 n_s g_s}\left(\frac{\hat{e}_s \cdot \kappa \cdot \hat{e}_p}{\hat{e}_p \cdot \kappa \cdot \hat{e}_p}\right)\left[\tilde{E}_{sc,i} - i\tilde{E}_{sc,r}\right]E_s, \tag{4.64}$$

which can be easily solved for E_s leading to

$$E_s(\hat{\zeta}\cdot \mathbf{r} = d) = E_{s0}\exp((\Gamma/2)d)\exp(i\delta d). \tag{4.65}$$

With (4.1) and (4.2a), this corresponds to

$$|\mathcal{E}_s|(\hat{\zeta}\cdot \mathbf{r} = d) = |\mathcal{E}_{s0}|\exp((\Gamma/2 - \alpha_s)d), \tag{4.66}$$

where $\mathcal{E}_s$ is the part of Eq. (4.1) associated with the signal wave S and E_{s0} and $\mathcal{E}_{s0}$ are incident amplitudes at the entrance surface $\hat{\zeta}\cdot \mathbf{r} = 0$. The two-wave mixing exponential gain Γ and the phase coupling factor δ in (4.65) are given by

$$\Gamma = \frac{2\pi}{\lambda}\frac{n_s n_p^2}{\cos\theta_s} g_p \left(\frac{\hat{e}_s \cdot \kappa \cdot \hat{e}_p}{\hat{e}_p \cdot \kappa \cdot \hat{e}_p}\right) r_{eff}\tilde{E}_{sc,i}, \tag{4.67}$$

and

$$\delta = -\frac{\pi}{\lambda}\frac{n_s n_p^2}{\cos\theta_s} g_p \left(\frac{\hat{e}_s \cdot \kappa \cdot \hat{e}_p}{\hat{e}_p \cdot \kappa \cdot \hat{e}_p}\right) r_{eff} \tilde{E}_{sc,r}. \tag{4.68}$$

The most important fact to notice in (4.67) is that the exponential gain depends on the photoexcitation anisotropy through the factor $(\hat{e}_s \cdot \kappa \cdot \hat{e}_p / \hat{e}_p \cdot \kappa \cdot \hat{e}_p)$. If the tensor κ is sufficiently anisotropic, by choosing appropriate geometries, this factor can become very large with respect to 1, thus giving an enhancement of the two-wave mixing gain. Experimental evidence for the influence of this factor will be given later in this chapter. Note that for the isotropic case, the above factor transforms to $(\hat{e}_s \cdot \hat{e}_p)$, which can be derived using the light intensity as the driving term for the photoexcitation.

In order to predict the magnitude of Γ and δ in a particular geometry, the knowledge of the values of $\tilde{E}_{sc,i}$ and $\tilde{E}_{sc,r}$ is necessary. In the undepleted pump approximation, the modulation m is always small and the space-charge field amplitude is linearly proportional to m. Therefore, the normalized amplitudes $\tilde{E}_{sc,i}$ and $\tilde{E}_{sc,r}$ do not depend at all on m in this regime. Here we limit our considerations to the predictions of the simplest photorefractive model that considers a single defect level and a single carrier type [30]. More involved models involving additional charge redistribution channels are described in several chapters of this book. In absence of photogalvanic effects [31] and of externally applied fields, for the simplest model, the normalized space-charge field amplitude $\tilde{E}_{sc}$ reads

$$\tilde{E}_{sc} = \pm i \frac{E_q E_D}{E_q + E_D}, \tag{4.69}$$

and therefore, $\tilde{E}_{sc,r} = 0$ under these assumptions. The + sign in the above equation holds for hole conduction and the − sign holds for electron charge transport. The trap-limited field E_q and the diffusion field E_D are described in the previous chapter of this book. The latter field is directly proportional to the grating vector magnitude K, while the former is inversely proportional to K and to the effective dielectric constant ε_{eff} in (4.17).

The implications of the photoexcitation anisotropy and other material anisotropies on the photorefractive gain were discussed in detail in [32] with specific examples related to the crystals $KNbO_3$ and $BaTiO_3$. In Fig. 4.8 we visualize by means of contour plots the gain landscape for all possible interaction geometries of two p-polarized waves propagating in the ac-plane of $BaTiO_3$, which is the plane of maximum nonlinearity. Note that, since the related information would be redundant (see [32] for details), we choose a representation where the pump (ϑ_p) and signal (ϑ_s) angles span a range of solely 180 degrees instead of 360. The plots are obtained using (4.67) and (4.69) by using the complete set of material parameters determined in [33], which are necessary for determining the quantities such as ε_{eff} (4.17) and r_{eff} (4.24) for

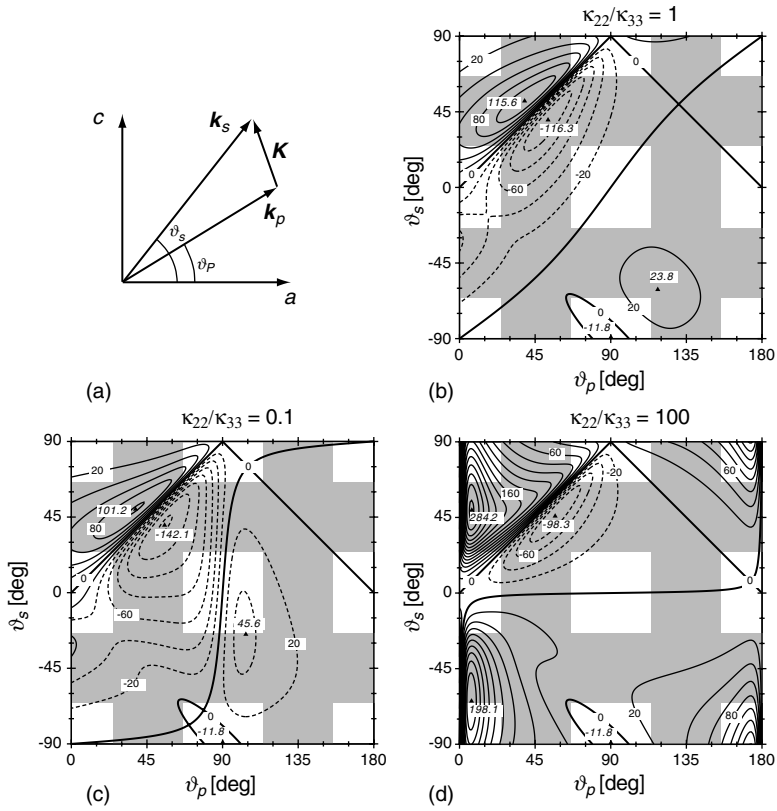

FIGURE 4.8. Contour plot of the exponential gain $\Gamma \cos\theta_s$ (Eq. (4.67)) for p-polarized beams in the ac-plane of $BaTiO_3$. (a) Angle convention, all angles are measured inside the medium; (b) Isotropic photoexcitation, $\kappa_{22}/\kappa_{33} = 1$; (c) Anisotropic photoexcitation $\kappa_{22}/\kappa_{33} = 0.1$; (d) $\kappa_{22}/\kappa_{33} = 100$. Contour line distance $= 20\,\mathrm{cm}^{-1}$. Effective density of traps $N_{eff} = 10^{17}\,\mathrm{cm}^{-3}$. For the meaning of shadows and special symbols, see text.

each individual geometry. The cases of isotropic ($\kappa_{22}/\kappa_{33} = 1$) as well as anisotropic photoexcitation are considered. Note that the gain is given along the Poynting vector direction; that is, it corresponds to $\Gamma \cos\theta_s$ (see (4.67)). In this way the representation becomes independent from a specific crystal cut. The thick lines in the graphs connect points where the gain is zero, positions of the peak values are indicated by triangles. The shadowed areas indicate angular regions which, as a result of Snell law, cannot be directly accessed from air in a crystal with the surfaces cut perpendicular to the crystallographic a- and c-axes. However, these regions may be accessed for other crystal cuts or by using external wedges.

It appears evident from Fig. 4.8 that the gain landscape is dramatically modified by the anisotropy of the photoexcitation constant. The position of

the maximum gain in the diagram moves by changing the parameter κ_{22}/κ_{33}: Some of the mountains grow, while others decrease in height. For $\kappa_{22}/\kappa_{33} \gg 1$, the optimum condition is found for a pump beam propagating under an angle ϑ_p close to 0: that is, nearly perpendicular to the c-axis. In contrast, for $\kappa_{22}/\kappa_{33} \ll 1$, the optimum is for a pump beam nearly parallel to c. Provided that the photoexcitation is sufficiently anisotropic, a significant gain Γ can be observed also for geometries along the main diagonal ($\vartheta_s = \vartheta_p - 90$) for which the $\boldsymbol{k}$-vectors of the two waves cross at right angles and the gain almost vanishes for $\kappa_{22}/\kappa_{33} = 1$. Such geometries are interesting because of a reduced linear scattering. It is also interesting to notice that the case where the tensor κ is isotropic constitutes, in general, a worst case scenario for the maximum gain that can be obtained in a given crystal. As discussed in [32], any asymmetry in the tensor elements of κ leads to an increase of the maximum achievable gain.

4.4.2 Pump Depletion

For large gain-length product Γd and low enough initial pump-to-signal intensity ratio, the pump wave can be significantly depleted during the interaction. This situation is more complex than the one found in the weak signal regime. In order to determine the spatial evolution of the signal and pump waves, one has then to rely in most cases to a numerical integration of the coupled Eqs. (4.62a) and (4.62b). This is necessary, for instance, if the two beams enter the crystal from surfaces that are not parallel to each other, in which case the surface normal vectors differ ($\hat{\boldsymbol{\zeta}}_s \neq \hat{\boldsymbol{\zeta}}_p$) and the waves S and P are no longer homogeneous in a direction perpendicular to the corresponding surface normal. It should also be remarked that for a general geometry, the absorption constants α_s and α_p for the two waves usually differ from each other (this statement is true even in fully isotropic materials for asymmetric geometries). Therefore, in this case, the coupled wave equations may be integrated numerically.

For simplicity, we consider here only cases where the two waves enter the crystal from a common surface or from opposite parallel surfaces. The $+z$ direction is defined as being parallel to the direction of the normal to the incidence surface for the S wave ($\hat{\boldsymbol{\zeta}} \equiv \hat{\boldsymbol{\zeta}}_s = (0, 0, 1)$). Furthermore, the absorption is assumed to be moderate ($\alpha_s d \approx 0,\ \alpha_p d \approx 0$ with d being the interaction length), so that we can neglect the absorption terms in the coupled wave equations (4.62a) and (4.62b).

Transmission Gratings

In this case, by multiplying (4.62a) by $E_s^* n_s g_s$ and (4.62b) by $E_p^* n_p g_p$ and inserting the modulation ratio (4.7), one obtains the coupled equations in the form

$$\frac{d}{dz}\tilde{I}_s = \Gamma \frac{\tilde{I}_s \tilde{I}_p}{G\tilde{I}_s + \tilde{I}_p,} \tag{4.70a}$$

$$\frac{d}{dz}\tilde{I}_p = -\Gamma \frac{\tilde{I}_s \tilde{I}_p}{G\tilde{I}_s + \tilde{I}_p}, \tag{4.70b}$$

where it was assumed that the space-charge field contains only the $\pi/2$ phase shifted component ($E_{sc} = iE_{sc,i}$). The quantity Γ is the same exponential gain constant given in (4.67). We recall that the light intensities for the waves are proportional to the product EE^*ng, with n and g being the refractive index and the projection cosine of the appropriate wave. The intensities $\tilde{I}_s \equiv I_s \cos\theta_s$ and $\tilde{I}_p \equiv I_p \cos\theta_p$ appearing in (4.70a) and (4.70b) correspond to the projections of the Poynting vectors along the surface normal $\hat{\zeta}$ and give the energy flow per unit area through a surface parallel to the input surface. The constant G is a kind of anisotropy parameter and depends on the geometry of interaction and on the shape of the photoexcitation tensor κ. It is is defined as

$$G \equiv \frac{n_p g_p \cos\theta_p}{n_s g_s \cos\theta_s} \frac{(\hat{e}_s \cdot \kappa \cdot \hat{e}_s)}{(\hat{e}_p \cdot \kappa \cdot \hat{e}_p)}. \tag{4.71}$$

For isotropic photoexcitation and symmetric configurations, one has $G = 1$ and the above coupled equations reduce to the commonly used ones [34]. The total projected energy flow $\tilde{I}_0 \equiv \tilde{I}_s + \tilde{I}_p$ is conserved, as can be verified by summing (4.70a) and (4.70b). Using this, one obtains the differential equation $d\tilde{I}_s/\tilde{I}_s + [G/(\tilde{I}_0 - \tilde{I}_s)]d\tilde{I}_s = \Gamma dz$, which can be integrated with the boundary conditions $\tilde{I}_s(z=0) = \tilde{I}_{s0}, \tilde{I}_p(z=0) = \tilde{I}_{p0}$ proper of transmission gratings and leads to the simple solution

$$\chi(z) = \chi_0 \exp(\Gamma z), \tag{4.72}$$

where

$$\chi(z) \equiv \frac{\tilde{I}_s(z)}{\left[\tilde{I}_p(z)\right]^G} \equiv \beta(z)\left[\tilde{I}_p(z)\right]^{1-G} \tag{4.73}$$

and

$$\chi_0 = \chi(z=0) = \left(\tilde{I}_{s0}/\tilde{I}_{p0}\right)\tilde{I}_{p0}^{1-G} \equiv \beta_0 \tilde{I}_{p0}^{1-G}. \tag{4.74}$$

Therefore, χ is a modified intensity ratio which for $G = 1$ reduces to the conventional intensity ratio $\beta = \tilde{I}_s/\tilde{I}_p$. The evolution of the signal and pump wave intensities can thus be expressed as

$$\tilde{I}_s(z) = \tilde{I}_{s0} \frac{1 + \beta_0^{-1}}{1 + \beta_0^{-1}\left(\tilde{I}_p/\tilde{I}_{p0}\right)^{1-G} \exp(-\Gamma z)}, \tag{4.75}$$

and

$$\tilde{I}_p(z) = \tilde{I}_{p0} \frac{1 + \beta_0}{1 + \beta_0\left(\tilde{I}_p/\tilde{I}_{p0}\right)^{G-1} \exp(\Gamma z)}. \tag{4.76}$$

In absence of photoexcitation anisotropy and for nearly symmetric incidence of signal and pump beams, the factor G is always very close to 1. For $G = 1$, the above expressions reduce to the well known ones derived by Kukhtarev and coworkers [35]; that is,

$$\tilde{I}_s(z) = \tilde{I}_{s0} \frac{1 + \beta_0^{-1}}{1 + \beta_0^{-1} \exp(-\Gamma z)}, \tag{4.77}$$

and

$$\tilde{I}_p(z) = \tilde{I}_{p0} \frac{1 + \beta_0}{1 + \beta_0 \exp(\Gamma z)}. \tag{4.78}$$

It should be noted that for the case of transmission gratings considered here, the factor G is bound to be positive because the tensor κ contains only positive elements. Although for strong anisotropies the factor G may depart significantly from 1, in (4.75) and (4.76), the influence of the term $(\tilde{I}_p/\tilde{I}_{p0})^{\pm(1-G)}$ on the beam intensities is still weaker than the one given by the exponential term. However, the corrections brought about by this term are not negligible. The saturation of the amplified signal beam to its maximum value is slower for $G > 1$, and faster for $G < 1$ than for the case $G = 1$. This can be seen in Fig. 4.9 where $\tilde{I}_s(z)/(\tilde{I}_{s0} + \tilde{I}_{p0})$ and $\tilde{I}_p(z)/(\tilde{I}_{s0} + \tilde{I}_{p0})$ are plotted for different values of G and for a common value of the gain Γ. It is worth noticing that in the saturation region the depleted pump wave intensity decreases as $\tilde{I}_p(z + \Delta z)$

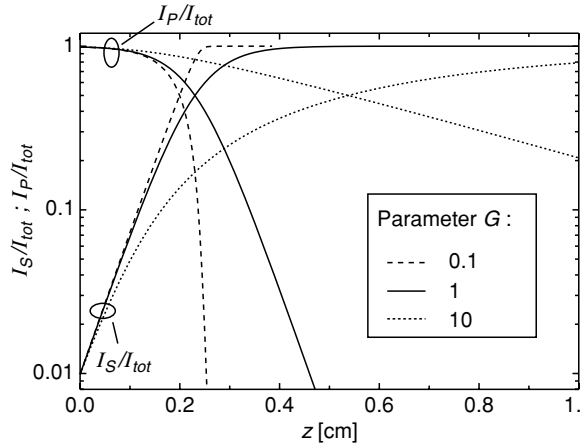

FIGURE 4.9. Signal wave amplification and pump wave depletion as a function of the propagation distance z in transmission geometry. The normalized intensities $\tilde{I}_s(z)/(\tilde{I}_{s0} + \tilde{I}_{p0})$ and $\tilde{I}_p(z)/(\tilde{I}_{s0} + \tilde{I}_{p0})$ are plotted according to (4.75) and (4.76) for $\Gamma = 20\,\mathrm{cm}^{-1}$. The factor G used as parameter is defined in (4.71).

$= \tilde{I}_p(z) \exp(-\Gamma \Delta z/G)$, as can be clearly recognized in Fig. 4.9. In order to get an impression of the possible range for the quantity G in a typical transmission geometry, let us take the example of a $BaTiO_3$ cut along the crystallographic axes and with both interacting beams entering the sample from air through the a-face of the crystal. Considering all possible two-beams interaction geometries in such a configuration, we have $0.936 < G < 1.07$ for $\kappa_{22}/\kappa_{33} = 1$, $0.944 < G < 1.06$ for $\kappa_{22}/\kappa_{33} = 0.1$, and $0.43 < G < 2.30$ for $\kappa_{22}/\kappa_{33} = 10$. The ranges for $KNbO_3$ in the same kind of geometry are very similar. For crystals cut under 45 degrees to the crystallographic axes, G varies between $G_{\min} \approx 0.25$ and $G_{\max} \approx 4$ for both $\kappa_{22}/\kappa_{33} = 0.1$ and $\kappa_{22}/\kappa_{33} = 10$.

Reflection Gratings

In this case, the signal and pump wave enter from opposite surfaces and one has $\cos\theta_s \cos\theta_p < 0$. The coupled wave equations (4.62a) and (4.62a) can be brought again exactly in the form of (4.70a) and (4.70b) if one allows one of the two projected intensities to take negative values. If we choose the signal wave to propagate toward positive z and the pump wave to propagate toward the negative z axis, then $\tilde{I}_s(z) > 0$ and $\tilde{I}_p(z) < 0$. Such a negative intensity value reflects the fact that the energy flow for the pump wave is in a direction that is opposite with respect to the considered surface orientation (vector $\hat{\zeta}$). Therefore, as in the above case of transmission gratings, the conserved quantity is still the sum of the (this time signed) intensities and the solution of the coupled equations (4.70a) and (4.70b) is still of the form given by (4.72) and (4.73). However, the exponent G (still defined by (4.71)) is now bound to be a negative number. For a plate of thickness d, the boundary values are now given at $z = 0$ for the signal wave, and at $z = d$ for the pump wave. Using these boundary values in (4.72) and (4.73) and reintroducing a positive intensity $|\tilde{I}_p(z)| = -\tilde{I}_p(z)$ for the pump wave, one can easily find the expressions for the transmitted intensities $\tilde{I}_s(z = d)$ and $|\tilde{I}_p(z = 0)|$; that is,

$$\tilde{I}_s(d) = \tilde{I}_s(0) \frac{1 + |\beta_0|^{-1}}{1 + |\beta_0|^{-1} |\tilde{I}_p(0)/\tilde{I}_p(d)|^{1-|G|} \exp(-\Gamma d)}, \tag{4.79}$$

and

$$\tilde{I}_p(0) = \tilde{I}_p(d) \frac{1 + |\beta_0|}{1 + |\beta_0| |\tilde{I}_p(0)/\tilde{I}_p(d)|^{|G|-1} \exp(\Gamma d)}, \tag{4.80}$$

which are in full analogy to (4.75) and (4.76). The intensity ratio $|\beta_0|$ is defined here as $|\beta_0| \equiv \tilde{I}_s(0)/|\tilde{I}_p|(d)$ and differs from the definition used for transmission gratings. For samples cut along the dielectric axes, symmetric interaction geometries and in absence of photoexcitation anisotropy, we have $G = -1$. In this case, the two above expressions reduce to the well known conventional relationships [36]. The new correcting factor $|\tilde{I}_p(0)/\tilde{I}_p(d)|^{\pm(1-|G|)}$ brings about a

similar influence on the output intensities as in the case of transmission gratings discussed above. Fig. 4.10 shows an example of the G-dependence of the signal and pump output intensities as obtained by solving the above transcendent equations. As in the case of transmission gratings, for a fixed value of the gain coefficient Γ, the saturation of the signal intensity is the faster the closer the exponent G is to zero.

4.5 Examples

In this section, we give a few additional examples that illustrate the consequences of some of the relationships given in the previous sections.

4.5.1 Effective Dielectric Constant and Mobility

We start by showing the effect of Eq. (4.17) for the effective dielectric constant that is active in a photorefractive experiment. The quantity ε_{eff} depends obviously only on the direction of the grating vector $\hat{\boldsymbol{K}}$, and not on the individual polarization vectors of the two interacting waves. Therefore, in a contour plot diagram such as the one of Fig. 4.8, except for small corrections due to birefringence, the contour lines for ε_{eff} are all essentially parallel to the diagonal, going from top-left to bottom-right. Keeping that in mind, we choose to plot the values of ε_{eff} in a conventional diagram while we move solely along the main diagonal (from left-bottom to top-right) in Fig. 4.8. This is shown in Fig.

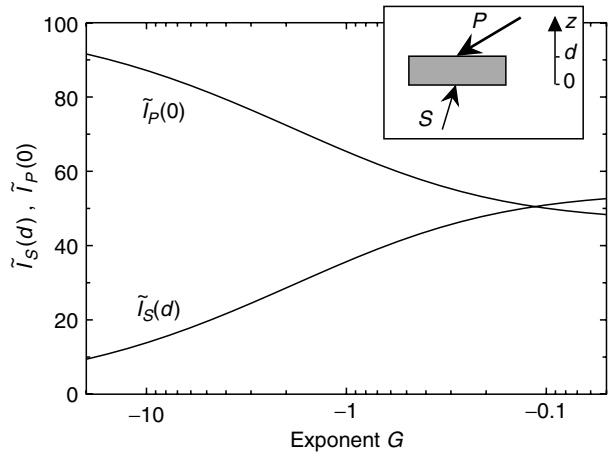

FIGURE 4.10. Transmitted signal $[\tilde{I}_s(d)]$ and pump intensity $[\tilde{I}_p(0)]$ for reflection grating two-wave mixing as a function of the exponent G. A value $G = -1$ corresponds to a fully symmetric and isotropic geometry. Parameters: gain coefficient $\Gamma = 20\,\mathrm{cm}^{-1}$; sample thickness $L = 0.2\,\mathrm{cm}$; input intensities $\tilde{I}_s(0) = 1$, $\tilde{I}_p(d) = 100$.

4.11 for the cases of $KNbO_3$ and $BaTiO_3$ crystals and beam interaction in the *bc*- and *ac*- plane, respectively. The plots use the parameter sets determined in [33] and [13], respectively. An extremely strong dependence of the dielectric constant on the interaction geometry as well as the deviation of ε_{eff} from both ε^T and ε^S are evident. Note that, for completeness, the top axes in Fig. 4.11 also give the angular direction θ of the corresponding grating vector $\hat{\boldsymbol{K}}$, these axes are slightly nonlinear with respect to the bottom one as a result of the material birefringence.

The dielectric constant does not influence only the magnitude of the space-charge field gratings, but also the grating response dynamics. If an experiment is performed at small beam crossing angle (large grating spacing) the build-up or erasure times are given by the dielectric relaxation time τ_{die}, which is directly proportional to the effective dielectric constant ε_{eff} and inversely proportional to the mobility $\mu_{\|}$ given in (4.25). Therefore, provided that the behavior of the dielectric constant has been determined by other means, grating erasure measurements as a function of the grating direction can give information on the form of the mobility tensor. Fig. 4.12 shows an example for hole conducting $BaTiO_3$ as reported in [16]. Unlike for the case analyzed in Fig. 4.8, here the

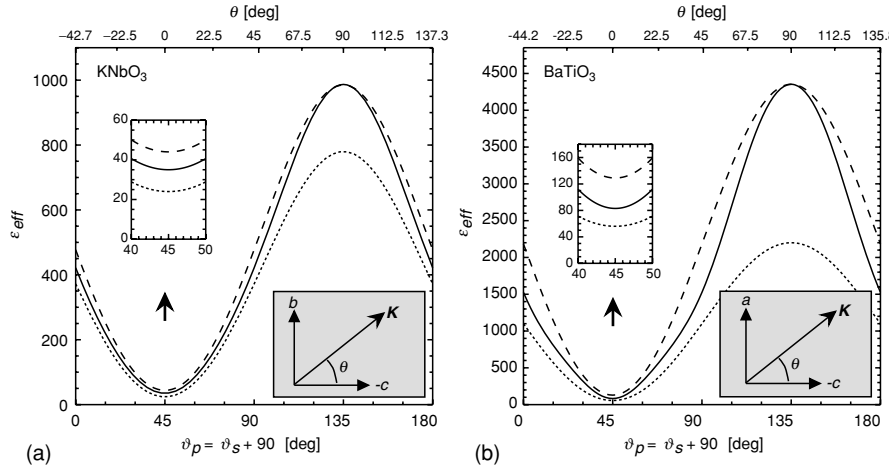

FIGURE 4.11. Effective dielectric constant ε_{eff} (solid curves) calculates according to (4.17) for $KNbO_3$ (a) and $BaTiO_3$ (b) and the material parameters determined in [13] and [33]. The values are given for geometries corresponding to the main diagonal (bottom-left to top-right) of a diagram such as the one of Fig. 4.8, with the *a* axis replaced by the *b* axis for $KNbO_3$ (Fig. 4.8(a)). The behaviour expected by erroneously using the unclamped ($\hat{K}_i \varepsilon_{ij}^T \hat{K}_j$, dashed curves) or clamped ($\hat{K}_i \varepsilon_{ij}^S \hat{K}_j$, dotted curves) dielectric constants are also shown for comparison. Note that in a representation such as in Fig. 4.8, the values of ε_{eff} remain essentially constant by moving away from the main diagonal in the normal direction (i.e., $\varepsilon_{eff}(\vartheta_p \pm \beta, \vartheta_s \mp \beta) \simeq \varepsilon_{eff}(\vartheta_p, \vartheta_s)$). The top axis shows the grating angle θ defined in the inset.

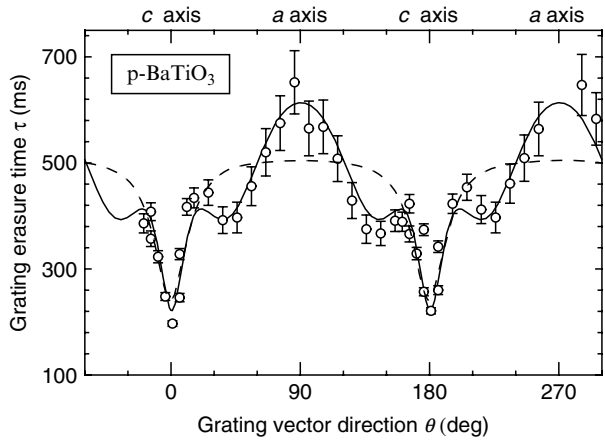

FIGURE 4.12. Erasure time of photorefractive gratings written in nominally pure *p*-type $BaTiO_3$ as a function of the angle θ between the grating vector K and the *c*-axis of the crystal. The solid curve represents the fit using (4.25) and the correct form for the effective dielectric constant ε_{eff} given by (4.17) and leads to a mobility anisotropy $\mu_a/\mu_c = 19.6 \pm 0.6$. The dashed line is the fit obtained when using the uncorrected clamped or unclamped dielectric constants. (Adapted from [16].)

grating vector $\boldsymbol{K}$ lies parallel to the entrance surface of the medium and the angle θ between $\boldsymbol{K}$ and the *c*-axis is changed by rotating the crystal around the *b*-axis. Such a measurement permits to determine the ratio μ_a/μ_c among the elements of the mobility tensor, which is found to be $\mu_a/\mu_c = 19.6 \pm 0.6$ for *p*-type $BaTiO_3$ [16]. The measurements shown in Fig. 4.12 also give clear evidence for the deviation of the photorefractively active effective dielectric constant from the clamped or unclamped value. While the solid line is drawn using ε_{eff} obtained from (4.17), the dashed line is fitted with the help of the clamped (ε^S) or unclamped (ε^T) dielectric constant, and clearly fails to describe the experimental data accurately.

4.5.2 *Effective Electro-Optic Coefficient*

In order to illustrate some of the consequences of Eqs. (4.22) and (4.24) for the effective scalar electro-optic coefficient, we keep with the example of $BaTiO_3$. Fig. 4.13(a) shows a contour plot diagram similar to the one in Fig. 4.8. Here the quantity being plotted is r_{eff} for every interaction of *p*-polarized waves in the *ac*-plane of $BaTiO_3$. A scalar electro-optic coefficient of the order of 800 pm/V can be accessed even for conventional crystal cuts. Fig. 4.13(b) shows the magnitude of r_{eff} if the electro-optic response is incorrectly calculated using the unclamped electro-optic tensor r^T_{ijk} (4.23) to insert in (4.24). As seen by comparison with Fig. 4.13(a), the shape of the contour lines differ significantly from the case where the mechanical coupling is correctly considered. By using

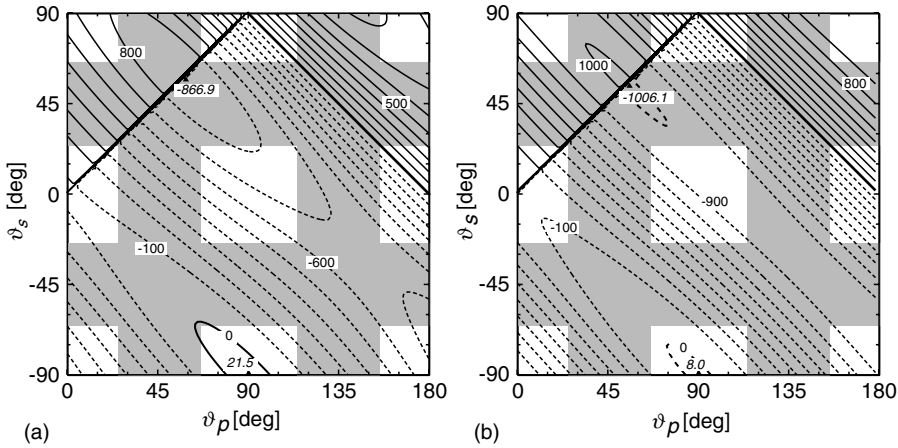

FIGURE 4.13. Contour plot of the scalar effective electro-optic coefficient r_{eff} (4.24) for each possible two-wave interaction geometry $(\vartheta_p, \vartheta_s)$ in the *ac*-plane (see Fig. 4.8) of $BaTiO_3$. Contour line distance = 100 pm/V. (a) Correct values obtained by considering mechanical coupling according to (4.22). (b) Incorrect values obtained by using r^T_{ijk} instead of r^{eff}_{ijk} in (4.24).

the correct expressions, for most of the geometries the effective electro-optic coefficient is somehow smaller with respect to what would be expected on the base of r^T_{ijk}.

In $BaTiO_3$, the discrepancy between r^{eff}_{ijk} and r^T_{ijk} is even stronger if one considers wave interactions outside the *ac* crystallographic plane. Fig. 4.14(a) shows a photograph of the far field light fanning distribution as observed on the backside of a $BaTiO_3$ crystal illuminated with a single *c*-polarized laser beam ($\lambda = 514\,\text{nm}$) propagating parallel to the crystal *a*-axis [37]. Fanning can be viewed as photorefractively amplified broadband light scattering. Therefore, in this configuration, its distribution depends primarily on the symmetry of the electro-optic tensor. On the base of the conventional electro-optic tensor r^T_{ijk}, the upper and lower fanning lobes are not predicted to exist. However, their existence can be fully understood with the help of the tensor r^{eff}_{ijk} (4.22) resulting from the mechanical coupling [37]. Fig. 4.14(b) shows the expected far field intensity distribution using (4.24) and the wave mixing expressions of section 4.4, which evidences an excellent agreement with the observations.

4.5.3 Photoexcitation Anisotropy

Finally, we want to illustrate the influence of a photoexcitation anisotropy on two-wave mixing (Eq. (4.67)) with the help of the example of dichroic $KNbO_3$ crystals doped by 3000 ppm Ni. Grating photoerasure experiments as a function of light polarization permit to independently determine the ratio κ_{22}/κ_{33} between the elements of the photoexcitation tensor to be $\kappa_{22}/\kappa_{33} = 3.4 \pm 0.1$

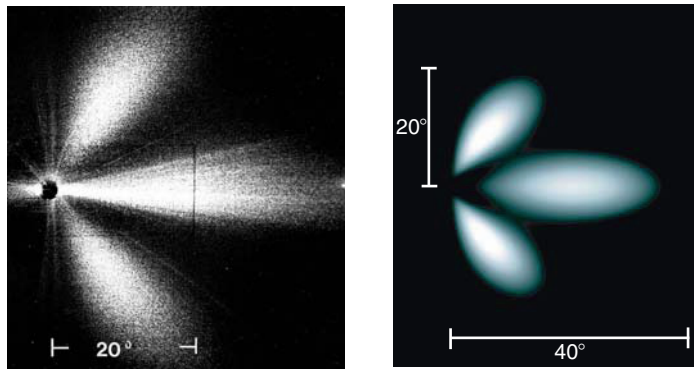

FIGURE 4.14. (a) Experimentally observed far field distribution of amplified scattered light (fanning) for a pump beam ($\lambda = 514\,\text{nm}$) propagating along the a-axis of $BaTiO_3$. Both the pump and the fanning have extraordinary polarization. The crystal c axis points to the right. After the crystal, the pump beam is blocked by the dark spot in the middle. (b) Corresponding theoretical far-field light fanning distribution calculated with the help of the photorefractively active electro-optic tensor r_{ijk}^{eff} (4.22). The clamped or unclamped electro-optic tensors do not predict the upper and lower lobes. The angles are outside the crystal and the initial noise is assumed to have a cylindrical symmetric Gaussian distribution around the incoming beam in wavevector space with a characteristic divergence of 24°. (Adapted from [37].)

[4]. The important effect of such an anisotropy is better proved by using a geometry such as the one depicted in Fig. 4.15(a), where the signal and pump wave cross at large angles.

Two sets of experiments were performed in this kind of geometry. In the first set, the angle γ between the two beams was kept constant while the angles α and β were changed simultaneously by rotating the crystal sample. For this case, the angles ϑ_p and ϑ_s for the pump and signal wave in the crystalline coordinate system move along the trajectory given by the bended arrow pointing toward the bottom left of the contour plot diagram in Fig. 4.15(b). In the second set of experiments, only the pump beam angle was changed while the crystal orientation and the direction of the signal beam were left fixed, which corresponds to the arrow pointing to the right in Fig. 4.15(b). The results of the two experiments are shown in Fig. 4.15(c) and Fig. 4.15(d), respectively. The solid curves are plotted using (4.67), with the independently determined anisotropy $\kappa_{22}/\kappa_{33} = 3.4$, and with the value of the space-charge electric field $E_{sc,i}$ calculated using the known material properties, i.e., the effective number of traps $N_{eff} = 5.3 \times 10^{16}\,\text{cm}^{-3}$, determined independently for this crystal [38]. No parameters were adjusted to plot the solid curves, which describe the measurements very well. The dotted curves, in contrast, are plotted using conventional photorefractive theory, which neglects the

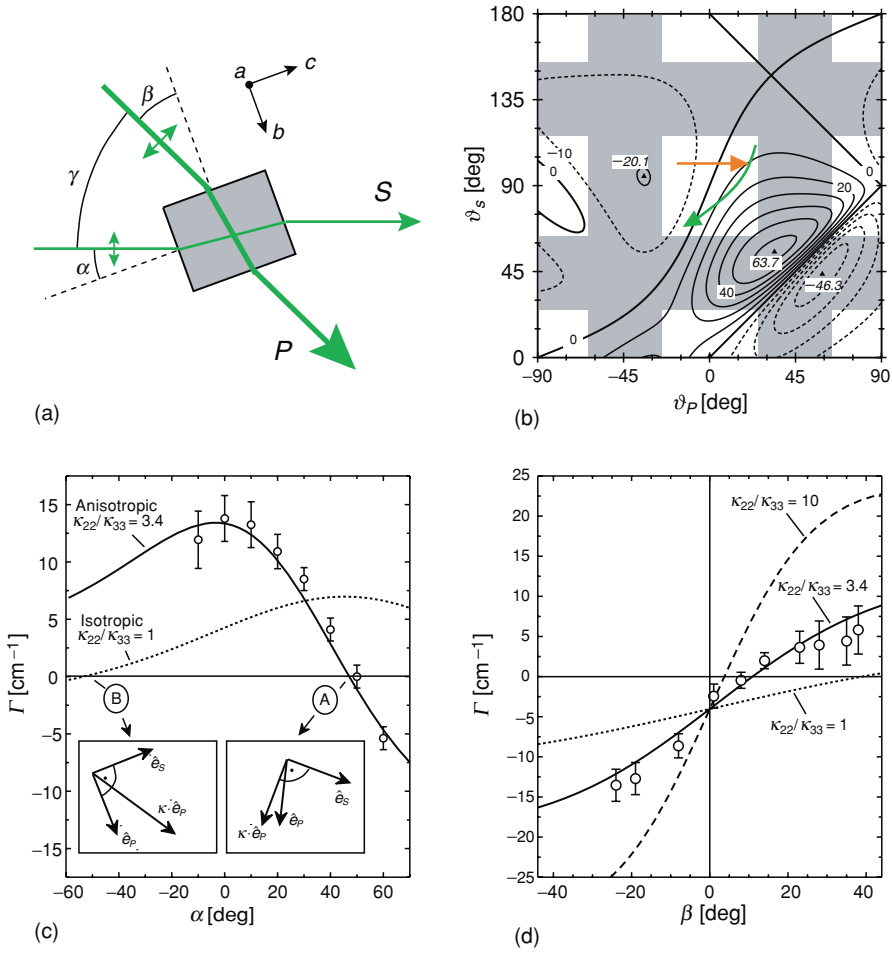

FIGURE 4.15. (a) Experimental configuration for two-wave mixing in dichroic $KNbO_3$. The pump wave P amplifies the signal wave S. As drawn here, the angles α, β and γ are taken to be all positive so that $\alpha + \beta + \gamma = 90°$. (b) Contour plots of the exponential gain Γ for dichroic Ni-doped $KNbO_3$. The experiments of (c) and (d) correspond to the trajectories shown by the arrows pointing to the bottom left and to the right, respectively. Parameters: $\kappa_{22}/\kappa_{33} = 3.4$, $N_{eff} = 5.3 \times 10^{16}\,\mathrm{cm}^{-3}$. The angle convention is the same as in Fig. 4.8(a). (c) Measured gain Γ (circles) upon variation of the angle α for $\gamma = 60°$. The insets show the orientations of the relevant vectors (all in the same plane) for the two gain zero-crossing points A and B. (d) Gain Γ (circles) as a function of β for $\alpha = -30°$. The upper theoretical curve for $\kappa_{22}/\kappa_{33} = 10$ (dashed line) evidences the possible gain enhancement for larger anisotropy. (See [4].)

effects of a photoexcitation anisotropy, and clearly fail to describe the measurements accurately. This corresponds to the case $\kappa_{22}/\kappa_{33} = 1$ in (4.67) and therefore to the replacement of the ratio inside the bracket in (4.67) by the simple scalar product $\hat{e}_s \cdot \hat{e}_p$.

The kind of geometry used for the measurements in Fig. 4.15 is particularly interesting from a technological point of view because, due to the large angle between pump and signal wave, scattering and fanning noise in direction of the signal wave are strongly reduced. For crystal characterization pourposes, however, one usually employs a geometry with both beams entering the sample from the same surface (transmission geometry). In this case, the photoexcitation anisotropy brings about quantitative but not qualitative differences with respect to the fully isotropic case, which may lead to overlooking its effect. Let us assume that the above crystal is operated in a symmetric transmission geometry with interference fringes having a grating spacing of $\Lambda = 0.4\,\mu$m for which the gain is close to a maximum. If the beams enter through the b crystal face, the grating vector is directed along the c-axis, and both beams are p-polarized, the gain coefficient is *reduced* by about 37% for $\kappa_{22}/\kappa_{33} = 3.4$ with respect to the isotropic case ($\kappa_{22}/\kappa_{33} = 1$). This reduction factor changes only slowly with the beam interaction angle. It is well known that in general, other effects also can lead to a reduction of the measured gain coefficients, such as electron-hole competition [39, 40], incomplete crystal poling, bad surfaces or bulk scattering effect leading to a reduction of light fringes modulation [41], or partial grating erasure due to surface reflections [42]. A discrimination between all these effects is difficult in symmetric transmission geometries.

4.6 Conclusions

In this chapter, we summarized the effects of the various anisotropic material properties on light diffraction, space-charge field formation, and photorefractive two-wave mixing interactions. These properties include the birefringence, the dielectric constants, the dichroism, the electro-optic constants, the elastic and photoelastic constants, the piezoelectric constants, the mobility tensor, and the cross-sections for free carrier photoexcitation. All these material properties have a substantial influence on the observable quantities. In particular, the role played in photorefractive materials by an anisotropy of the photoexcitation process with respect to light polarization, often over-looked, was discussed in detail here. Also, light diffraction in anisotropic media was treated in deeper detail. While the coupled wave model presented in Section 4.3 does apply to photorefractive volume gratings, it is equally important for any holographic materials having strong birefringence and/or containing volume gratings with strongly anisotropic properties.

References

1. H. Kogelnik: Bell Syst. Tech. J. **48**, 2909 (1969).
2. R.S. Cudney, R.M. Pierce, G.D. Bacher, and J. Feinberg: J. Opt. Soc. Am. B **8**, 1326 (1991).
3. B.I. Sturman, S.G. Odoulov, and M. Yu. Goulkov: Phys. Rep. **275**, 197 (1996)
4. G. Montemezzani, C. Medrano, P. Günter, and M. Zgonik: Phys. Rev. Lett. **79**, 3403 (1997).
5. V.M. Agranovich and V.L. Ginzburg, in *Crystal optics with spatial dispersion, and excitons, Springer Series in Solid-State Sciences 42*, 2 edn., edited by H. J. Queisser, Springer, Berlin (1984).
6. G. Montemezzani and M. Zgonik: Phys. Rev. E **35**, 1035 (1997).
7. A.A. Izvanov, A.E. Mandel, N.D. Khatkov, and S.M. Shandarov: Optoel. Data Proc. Instr. **2**, 80 (1986).
8. S.I. Stepanov, S.M. Shandarov, and N.D. Khatkov: Sov. Phys. Solid State **29**, 1754 (1987).
9. P. Günter and M. Zgonik: Opt. Lett. **16**, 1826 (1991).
10. G. Pauliat, M. Mathey, and G. Roosen: J. Opt. Soc. Am. B **8**, 1942 (1991).
11. J.F. Nye, *Physical properties of crystals*, Clarendon Press, Oxford (1985).
12. D.F. Nelson and M. Lax: Phys. Rev. Lett. **24**, 1187 (1970).
13. M. Zgonik, R. Schlesser, I. Biaggio, E. Voit, J. Tscherry, and P. Günter: J. Appl. Phys. **74**, 1287 (1993).
14. C.P. Tzou, T.Y. Chang, and R.W. Hellwarth: Proc. SPIE **613**, 58 (1986).
15. D. Mahgerefteh, D. Kirillov, R.S. Cudney, G.D. Bacher, R.M. Pierce, and J. Feinberg: Phys. Rev. B **53**, 7094 (1996).
16. P. Bernasconi, I. Biaggio, M. Zgonik, and P. Günter: Phys. Rev. Lett. **78**, 106 (1997).
17. S. Follonier, C. Bosshard, F. Pan, and P. Günter: Opt. Lett. **21**, 1655 (1996).
18. E.V. Rudenko and A.V. Sukhov: JETP **78**, 875 (1994).
19. I.C. Khoo, M.Y. Shih, M.V. Wood, B.D. Guenther, P.H. Chen, F. Simoni, S.S. Slussarenko, O. Francescangeli, and L. Lucchetti: Proc. IEEE **87**, 1897 (1999).
20. A. Golemme, B. Kippelen, and N. Peyghambarian: Chem. Phys. Lett. **319**, 655 (2000).
21. J.J. Butler and M.S. Malcuit: Opt. Lett. **25**, 420 (2000).
22. M. Jazbinsek, I. Drevensek-Olenik, M. Zgonik, A.K. Fontecchio and G.P. Crawford: J. Appl. Phys. **90**, 3831 (2001).
23. T.K. Gaylord and M.G. Moharam: Appl. Opt. **20**, 3271 (1981).
24. M. Born and E. Wolf, *Principles of optics*, 6 edn., Pergamon Press, Oxford (1980).
25. G.N. Ramachandran and S. Ramaseshan, in *Handbuch der Physik*, edited by S. Flügge Vol. 25/1, pp. 85–96. Springer, Berlin (1961).
26. E. Guibelalde: Opt. Quantum Electr. **16**, 173 (1984).
27. R. Birabassov, A. Yesayan, and T.V. Galtsyan: Opt. Lett. **24**, 1669 (1999).
28. S.R. Marder, J.W. Perry, and C.P. Yakymyshyn: Chem. Mater. **6**, 1137 (1994).
29. F. Pan, G. Knöpfle, C. Bosshard, S. Follonier, R. Spreiter, M.S. Wong, and P. Günter: Appl. Phys. Lett. **69**, 13 (1996).
30. N.V. Kukhtarev, V.B. Markov, S.G. Odulov, M.S. Soskin, and V.L. Vinetskii: Ferroelectrics **22**, 949 (1979).

31. A.M. Glass, D. VonderLinde, and T.J. Negran: Appl. Phys. Lett. **25**, 233 (1974).
32. G. Montemezzani: Phys. Rev. A **62**, 053803 (2000).
33. M. Zgonik, P. Bernasconi, M. Duelli, R. Schlesser, P. Günter, M.H. Garrett, D. Rytz, Y. Zhu, and X. Wu: Phys. Rev. B **50**, 5941 (1994).
34. P. Yeh, *Introduction to photorefractive nonlinear optics, Wiley series in pure and applied optics*, Wiley, New York (1993).
35. N.V. Kukhtarev, V.B. Markov, S.G. Odulov, M.S. Soskin, and V.L. Vinetskii: Ferroelectrics **22**, 961 (1979).
36. P. Yeh: Opt. Commun. **45**, 323 (1983).
37. G. Montemezzani, A.A. Zozulya, L. Czaia, D.Z. Anderson, M. Zgonik, and P. Günter: Phys. Rev. A **52**, 1791 (1995).
38. C. Medrano, M. Zgonik, I. Liakatas, and P. Günter: J. Opt. Soc. Am. B **13**, 2657 (1996).
39. G.C. Valley: J. Appl. Phys. **59**, 3363 (1986).
40. F.P. Strohkendl, J.M.C. Jonathan, and R.W. Hellwarth: Opt. Lett. **11**, 312 (1986).
41. U. van Stevendaal, K. Buse, H. Malz, H. Veenhuis, and E. Kratzig: J. Opt. Soc. Am. B **15**, 2868 (1998).
42. K.R. MacDonald, J. Feinberg, M.Z. Zha, and P. Günter: Opt. Commun. **50**, 146 (1984).

5

Space-Charge Wave Effects in Photorefractive Materials

Boris I. Sturman

Institute of Automation and Electrometry, 630090 Novosibirsk, Russia
sturman@iae.nsk.su

This chapter provides the first systematic description of the basic properties of low-frequency space-charge waves (SCWs) in photorefractive materials, and the effects caused by these weakly damped eigen-modes. The basic properties incorporate the dependences of the wave frequency and damping on the wavevector, and the restrictions on the material parameters necessary to ensure weakness of the wave damping. The unifying feature of the SCW effects is their resonant character. These effects include the known DC and AC enhancement of the photorefractive response (treated as the linear resonance), the subharmonic generation (treated as parametric excitation of SCWs), the low-frequency peculiarities of the nonlinear response, and also a number of effects caused by the joint action of the optical and material nonlinearities. While an exposition of the concepts lies at the center of this chapter, it also gives a review of experimental studies relevant to the subject matter and a historical sketch.

5.1 Overview

5.1.1 What Are Space-Charge Waves?

The subject of this chapter is low-frequency space-charge waves and the effects caused by these waves in photorefractive (PR) materials. By waves, we mean weakly-damped eigen-modes that can be characterized by the wavevector $\mathbf{k}$, eigen-frequency $\omega_{\mathbf{k}}$, damping $\gamma_{\mathbf{k}}$, and also by the amplitude, phase, and group velocity. These terms are common for waves of any nature: light waves, sound waves, and so on. Weakness of the damping means that $\gamma_{\mathbf{k}} \ll |\omega_{\mathbf{k}}|$. This condition allows waves to propagate over distances larger than the wave length $2\pi/k$; it is responsible for various resonant wave effects.

It is assumed that a uniform illumination excites free carriers—electrons or/and holes—and makes the medium conductive. Furthermore, a uniform electric field E_{ex} is applied in the general case (see Fig. 5.1a). Then, under certain additional

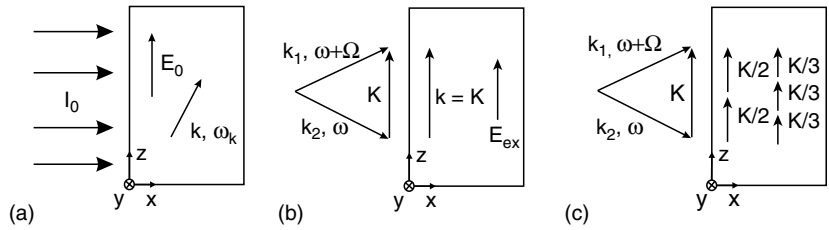

FIGURE 5.1. Diagrams illustrating SCW propagation (a), grating recording (b), and subharmonie generation (c). The external field $\mathbf{E}_{ex}$ can be constant ($\mathbf{E}_0$) or alternating. The difference between cases (b) and (c) can be in the value of the frequency detuning Ω and in the input intensity ratio.

conditions, the density of space charge ρ experiences spatio-temporal oscillations in the form of wave,

$$\rho = \mathrm{Re}\,[\rho_{\mathbf{k}} \exp(i\,\mathbf{k}\cdot\mathbf{r} - i\omega_{\mathbf{k}} t - \gamma_{\mathbf{k}} t)]. \tag{5.1}$$

The absolute value of the complex amplitude $\rho_{\mathbf{k}}$ characterizes the wave strength, while $\arg(\rho_{\mathbf{k}})$ represents the wave phase. The frequency $\omega_{\mathbf{k}}$ and damping $\gamma_{\mathbf{k}}$ do not depend on the wave amplitude for its sufficiently low values. The dependence of the eigen-frequency on the wavevector $\mathbf{k}$ is referred to as the dispersion law.

The space charge induces the space-charge field $\mathbf{E}_{sc}$, which is of prime importance for PR phenomena. Since the actual values of $\omega_{\mathbf{k}}$ are very small, this field can be treated as static. In other words, it possesses an electrostatic potential and its direction is parallel to the wavevector, $\mathbf{E}_{sc} = (\mathbf{k}/k)E_{sc}$. The spatio-temporal dependences of E_{sc} and ρ are similar. The complex field amplitude $E_{\mathbf{k}}$ is coupled with $\rho_{\mathbf{k}}$ through Poisson's equation.

To link the concept of space-charge waves with the photorefractive concepts, one can imagine that a space-charge grating with the grating vector $\mathbf{K}$ equal to the light wavevector difference is recorded by a pair of coherent light beams (see Fig. 5.1b). This grating vector represents a particular choice of the variable $\mathbf{k}$. When one of the recording beams is blocked, the grating decays under uniform illumination. If it is moving during the relaxation and propagating over the distances that are larger than the period $2\pi/K$, we are dealing with the eigen-mode.

The characteristics of space-charge waves (SCWs) are determined by the charge transport properties under illumination. The charge transport is always accompanied by energy dissipation. In this connection, the situations when $|\omega_{\mathbf{k}}| \gg \gamma_{\mathbf{k}}$ are not common. In reality, weakly-damped SCWs occur only under certain restrictions on the material parameters and only within limited ranges of the wavevectors. Even then, the ratio $Q_{\mathbf{k}} = |\omega_{\mathbf{k}}|/\gamma_{\mathbf{k}}$, referred to as the quality factor, can seldom exceed ten. One more distinctive feature of SCWs is the absence of general macroscopic equations for their description. The use of particular microscopic models of charge transport has no alternative here.

In contrast to photorefraction, the space-charge waves are not restricted to media possessing the linear electro-optic effect. They can exist in both noncentro- and centro-symmetric materials. However, the importance of SCWs and the breakthrough in the studies of the relevant effects are inextricably linked with PR phenomena. And we need to answer the question why:

First, the presence of the linear electro-optic effect allows us to visualize SCWs via Bragg diffraction on the corresponding refractive index grating. This gives a versatile tool for investigation of space-charge-wave effects.

Second, an extensive experience (experimental and theoretical) accumulated in the studies of PR phenomena is largely the experience in the excitation and description of space-charge fields. It allows us to sort out numerous factors relevant to SCWs in a wide range of materials.

Third, SCWs are closely involved in numerous and important PR effects. The root of this involvement lies in the general phenomenon of resonance.

5.1.2 Historical Sketch

To the best of our knowledge, the studies of SCWs date back to 1972–73 [1]. The authors considered the simplest semiconductor model (the one-species model) in the absence of illumination, derived a dispersion relation for two branches of space-charge waves (trap recharging waves), and analyzed some cases relevant to semiconductors. It was predicted that these eigen-modes result in oscillations of the impedance of semiconductors. These oscillations were found in 1978 in experiments with Ge:Au crystals [2]. The mentioned papers remained practically unknown in the PR domain until 1992–93.

In 1981–82, the so-called DC enhancement of holograms (of space-charge field) during two-wave mixing, see Fig. 5.1b, was detected in $Bi_{12}SiO_{20}$ crystals [3, 4]. The interpretation of this phenomenon, given in [4] in the PR terms, can nowadays be easily recognized as the linear excitation of weakly damped SCWs predicted in [1]. However, in the subsequent numerous publications on the DC enhancement, see, e.g., [5–7], it was not treated as an SCW effect. The same is valid with respect to the AC enhancement of the PR response [8, 9], which is also caused by the presence of weakly damped SCWs and requires application of an alternative electric field. The lack of recognition of the role of SCWs in the enhancement phenomena had no visible negative consequences for practice. The basic relations of the DC and AC enhancement techniques, expressed in the conventional PR terms, were fully correct.

The turning point in the studies of nonlinear SCW effects was the discovery of the subharmonic generation (i.e., generation of fractional spatial frequencies, $\mathbf{K}/2$, $\mathbf{K}/3$ etc. (see Fig. 5.1c) in two-beam coupling experiments with $Bi_{12}SiO_{20}$ crystals in 1988 [10]. As was proven experimentally in 1990–93, this effect is of a general nature; it is inherent in the whole family of sillenite crystals ($Bi_{12}SiO_{20}$, $Bi_{12}TiO_{20}$, $Bi_{12}GeO_{20}$) as well as in both DC and AC excitation techniques [11–17].

The initial attempts [18–20] to explain the major features of this effect by PR beam coupling were not successful. Along with them, it was suggested [12, 21]

that the subharmonic generation can be caused by the material nonlinearity. Independent efforts to describe the subharmonic instability on the basis of nonlinear material equations have been made in [22] and [23] in 1991. They resulted in 1992–93 in the development of a theory of parametric excitation of SCWs in fast PR crystals [24–31]. This theory includes the basic properties of the eigen-modes, the thresholds and increments of the instability for the DC and AC excitation methods, as well as explanation of the main experimental facts. Its most advanced version is presented in [28, 31]. The link to the early semiconductor papers, including the one relevant to the parametric excitation [32], was also established at this time.

In 1994, using a special experimental arrangement, it was proven unambiguously that the subharmonic generation occurs even in the absence of PR beam coupling [33]. Importance of the effects of material nonlinearity in the sillenite crystals was widely recognized since then. Furthermore, the use of the above "non-coupling" geometry has opened the possibility to separate experimentally the effects of optical and material nonlinearity [34–36].

After 1993–94, the studies of SCW effects are typically marked by the feedback between theory and experiment. Knowledge of the subject was greatly extended and refined. The burst of publications concerned at first with the subharmonic generation [37–61]. New materials, including the semiconductor CdTe, were used. A number of new features were found and explained. Many results were multiply reproduced. Several wrong calculations were made. Some of experimental findings still remain unclear and some of predictions still have no experimental confirmation.

Several new lines have appeared in the studies of SCW effects:

- It was realized in 1995 that weakly-damped SCWs are possible not only in fast but also in slow PR materials, typically ferroelectrics [62]. Their properties and the relevant SCW effects are expected to be strongly different from those typical of the sillenites. First experimental steps in this direction have been recently made [63].
- The factors limiting SCW effects in photorefractive GaAs crystals, as well as the prospects for detection of these effects, have been analyzed in [64, 65].
- Various high-contrast effects in the PR response have been investigated theoretically and experimentally in crystals of the sillenite family [66–71].
- Formation of light-induced discontinuities of the refractive index and their impact on the nonlinear beam propagation in AC-biased sillenite crystals were predicted in 1999–2001 [72–75].
- The effect of critical enhancement of PR beam coupling near the threshold of subharmonic generation was presented in 2000–02 [76–78].
- The effects of temporal and spatial rectification of SCWs in the sillenites have been investigated recently in [79, 80].

Note also that special efforts have been made to measure the fundamental characteristics of SCWs—the quality factor $Q_{\mathbf{k}}$ and the dependence of the

eigen-frequency $\omega_{\mathbf{k}}$ on the light intensity, applied field, and wavevector. The corresponding data can be found in [34, 63, 81, 82].

5.2 Space-Charge Wave Characteristics

The analysis made in [1] is not sufficient for PR materials. To a lesser degree, this is due to the necessity to take into account a uniform illumination, to distinguish between the low- and high-frequency waves, and to consider the general case when the wavevector $\mathbf{k}$ is not parallel to $\mathbf{E}_{ex}$. To a greater extent, this is caused by the fact that the possibility and conditions for the existence of two kinds of low-frequency SCWs (relevant to fast and slow PR materials) were not revealed.

5.2.1 Basic Equations

We consider first the space-charge wave characteristics within the simplest one-species model of charge transport (see Fig. 5.2a). The photoexcited charge carriers are supposed to be electrons. While the corresponding set of equations for the space-charge field $\mathbf{E}_{sc}$, the density of ionized traps N^+, the density of non-ionized traps N, and the electron concentration n is well known [7, 9, 83], we write it out to have a reference point for the subsequent considerations:

$$\boldsymbol{\nabla} \cdot \mathbf{E}_{sc} = \frac{q}{\epsilon\epsilon_0}(N^+ - N_A) \tag{5.2}$$

$$\frac{\partial N^+}{\partial t} = s_i I N - s_r n N^+ \tag{5.3}$$

$$= -\boldsymbol{\nabla} \cdot (\mu n \mathbf{E} + D\boldsymbol{\nabla} n + \beta N I \mathbf{z}). \tag{5.4}$$

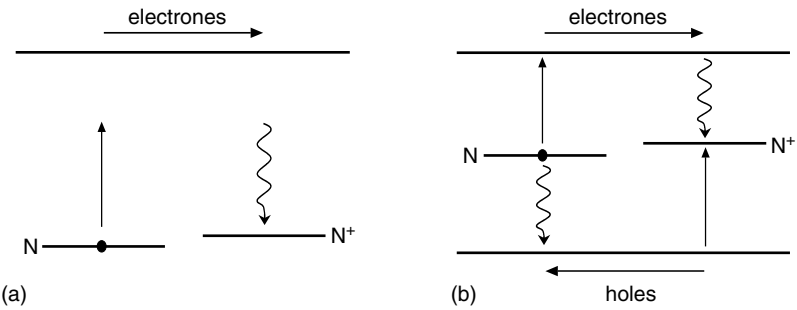

FIGURE 5.2. Diagrams of charge transfer for the simplest one-band (a) and two-band (b) models.

Here q is the elementary charge, $\epsilon\epsilon_0$ is the static dielectric constant, N_A is the concentration of compensating centers (acceptors), s_i and s_r are the ionization and recombination constants, and I is the light intensity. The total concentration of the active centers, $N_0 = N^+ + N$, is constant. The bracket in (5.4) represents the current density divided by q. Correspondingly, $\mathbf{E} = \mathbf{E}_{ex} + \mathbf{E}_{sc}$ is the total electric field, μ is the mobility of electrons, $D = \mu k_B T/q$ is their diffusion coefficient with k_B and T being the Boltzmann constant and the absolute temperature. The last term in the current density accounts for the photovoltaic contribution [84, 85]; β is the photovoltaic constant and $\mathbf{z}$ is a unit vector along the polar axis (if it is present in the medium). This term is important for ferroelectrics $LiNbO_3$ and $LiTaO_3$.

The coefficients entering the set (5.2)–(5.4) are coupled with simple characteristics of the system: The light absorption coefficient $\alpha = s_i N/\hbar\omega$, where ω is the energy of the light quantum; the electron lifetime $\tau = 1/s_r N^+$, and the photovoltaic field $E_{pv} = -\beta/s_i\mu\tau$.

The following general approximations have been used: The electrons' contribution to the total charge density, $\rho = q(N^+ - N_A - n)$, is neglected as compared to the ionic one and the derivative $\partial n/\partial t$ is neglected as compared to n/τ. We have also ignored the thermal excitation of electrons; this is justified for most of PR materials.

The set (5.2)–(5.4) can be applied to three different situations:

- Three-dimensional (3D) wave effects in optically isotropic materials including the crystals of the sillenite family ($Bi_{12}SiO_{20}$, $Bi_{12}TiO_{20}$, $Bi_{12}GeO_{20}$) and semiconductors GaAs, GaP, etc. The photovoltaic contribution is negligible here and the z-axis is parallel to the applied field.
- Three-dimensional propagation in ferroelectrics $LiNbO_3$ and $LiTaO_3$ under the condition that the applied field is directed along the polar axis, $\mathbf{E}_0 = E_0\mathbf{z}$.
- One-dimensional propagation in materials possessing strong optical anisotrophy, like $BaTiO_3$ and SBN, when the applied field is parallel to one of the principal crystal axes.

By considering the 3D-case, it is useful to express the space-charge field by the scalar electrostatic potential φ, $\mathbf{E}_{sc} = -\boldsymbol{\nabla}\varphi$.

5.2.2 Dispersion Relation for Space-Charge Waves

By setting $I = I_0 = const$ in (5.2)–(5.4), one can easily find the steady-state uniform concentration of electrons, $\bar{n} \simeq \alpha I_0 \tau/\hbar\omega$. For moderate light intensities, it is very small as compared to the nonperturbed ion densities. The space-charge field is zero in this spatially uniform background state.

To find a solution in the form of free waves, it is necessary to linearize the set (5.2)–(5.4) with respect to small perturbations $\delta N^+ = -\delta N$, δn, and φ. Assuming them to be proportional to $\exp(i\,\mathbf{k}\cdot\mathbf{r} - i\omega_{\mathbf{k}} t - \gamma_{\mathbf{k}} t)$, one arrives at a linear uniform set of algebraic equations for the perturbations. The condition of solvability of this set—the equality of its determinant to zero—gives the

necessary dispersion relation for the eigen-frequency and damping. By setting $\mathbf{E}_{ex} = E_0\mathbf{z}$ with $E_0 = const$, one can obtain for the above specified 3D-cases:

$$\frac{\omega_{\mathbf{k}} - i\gamma_{\mathbf{k}}}{\omega_0} = \frac{E_q + E_D - i(E_0 - N^+ N_0^{-1} E_{pv})}{E_0 + i(E_D + E_M)}. \tag{5.5}$$

Here $\omega_0 = \alpha I_0/\hbar\omega N_E$ is the characteristic frequency, $N_E = NN^+/N_0$ is the effective trap concentration, while E_q, E_D, and E_M are the characteristic saturation, diffusion, and drift fields, respectively,

$$E_q = \frac{qN_E}{k_z \epsilon\epsilon_0},\ E_D = \frac{k^2 k_B T}{qk_z},\ E_M = \frac{1}{k_z \mu\tau}. \tag{5.6}$$

The characteristic frequency ω_0 is proportional to the light intensity I_0 and independent of the wavevector $\mathbf{k}$. The characteristic fields E_q, E_D, and E_M depend on the wavevector, but do not depend on I_0. In the 3D-case, when the wavevector possesses not only the longitudinal (k_z) but also a nonzero transverse component $\mathbf{k}_\perp = (k_x, k_y)$, our notation for the characteristic fields differs slightly from the standard one [7, 83]. In the 1D-case, where $\mathbf{k}_\perp = 0$ and $k_z = k$, the difference disappears. By dealing in the 1D-case with strongly anisotropic crystals, like $BaTiO_3$ and SBN, we have to assume that the values of μ and ϵ correspond to the chosen propagation direction.

As seen from (5.5), there are only two possibilities to fulfill the inequality $\gamma_{\mathbf{k}} \ll |\omega_{\mathbf{k}}|$. They correspond to the dominating real and imaginary parts of both numerator and denominator. Physically, they are relevant to the fast and slow PR materials. We consider these important cases separately.

5.2.3 Fast Photorefractive Materials

In the fast materials the photovoltaic effect is negligible and we can set $E_{pv} = 0$ in (5.5). It is evident then that the inequalities

$$E_q \gg E_0, \quad E_0 \gg E_M, \quad E_0 \gg E_D \tag{5.7}$$

ensure the presence of weakly damped SCWs. The eigen-frequency and damping obey the relations [28, 31]

$$\omega_{\mathbf{k}} = \omega_0 \frac{E_q}{E_0} \equiv \frac{q}{\epsilon\epsilon_0 E_0} \frac{\alpha I_0}{\hbar\omega} \frac{1}{k_z} \tag{5.8}$$

$$\gamma_{\mathbf{k}} = \omega_0 \left(1 + \frac{E_q E_M}{E_0^2} + \frac{E_D E_q}{E_0^2}\right). \tag{5.9}$$

$$\equiv \frac{\alpha I_0}{\hbar\omega} \left(\frac{1}{N_E} + \frac{q}{\epsilon\epsilon_0 E_0^2 \mu\tau} \frac{1}{k_z^2} + \frac{k_{\mathbf{B}} T}{\epsilon\epsilon_0 E_0^2} \frac{k^2}{k_z^2}\right).$$

Several remarkable features follow from here: The damping is positive, $\gamma_{\mathbf{k}} > 0$, it is an even function of $\mathbf{k}$ and E_0. In contrast, the eigen-frequency is

an odd function of $\mathbf{k}$ and E_0, it can be as positive as negative. The expression for $\omega_\mathbf{k}$ includes only well defined material and experimental parameters. Both $\omega_\mathbf{k}$ and $\gamma_\mathbf{k}$ are proportional to the light intensity I_0.

In the case when holes are the photoexcited charge carriers, the expression for $\omega_\mathbf{k}$ changes its sign. The expression for $\gamma_\mathbf{k}$ experiences no changes.

The dispersion law of SCWs, predicted first in [1], is rather special, $\omega_\mathbf{k} \propto k_z^{-1}$. The group velocity $\mathbf{v}_g = \boldsymbol{\nabla}_\mathbf{k}\omega_\mathbf{k}$ is anti-parallel to the applied field and does not depend on the sign of k_z. The free path length $l_\mathbf{k} \equiv |v_\mathbf{k}|/\gamma_\mathbf{k} = Q_\mathbf{k}/|k_z|$, where $Q_\mathbf{k} = |\omega_\mathbf{k}|/\gamma_\mathbf{k}$ is the quality factor.

The expression for the damping $\gamma_\mathbf{k}$ consists of three positive contributions that are due to recombination, drift, and diffusion of photo-electrons. Only the last (diffusion) contribution depends on the transverse component of the wave-vector; it grows with increasing $k_\perp \equiv (k_x^2 + k_y^2)^{1/2}$.

The quality factor does not depend on the light intensity; it can be represented as

$$Q_\mathbf{k} = (|E_0/E_q| + |E_M/E_0| + |E_D/E_0|)^{-1}. \tag{5.10}$$

According to (5.7), each of three contributions to $Q_\mathbf{k}^{-1}$ is small; this ensures the inequality $Q_\mathbf{k} \gg 1$.

Consider the quality factor as a function of $k_z, k_\perp$, and E_0. Since $E_D \propto k_z^2 + k_\perp^2$, it is evident that Q decreases with growing $k_\perp$. By setting $k_\perp = 0, k_z = k$, we analyze now the dependence $Q(k, E_0)$. For a fixed value of E_0, the function $Q(k)$ possesses a maximum. The corresponding peak values are given by

$$Q^p(E_0) = \frac{Q_{max}|E_0|}{(E_0^2 + E_c^2)^{1/2}}, \quad \frac{1}{k^p(E_0)} = \left[\frac{\mu\tau k_B T}{q}\left(1 + \frac{E_0^2}{E_c^2}\right)\right]^{1/2}, \tag{5.11}$$

where

$$Q_{max} = (qN_E\mu\tau/4\epsilon\epsilon_0)^{1/2}, \quad E_c = (N_E k_B T/\epsilon\epsilon_0)^{1/2}. \tag{5.12}$$

These relations exhibit important properties of SCWs: The optimum period $2\pi/k^p$ grows monotonously with E_0 with no saturation. The optimized (with respect to k) value of the quality factor increases monotonously with $|E_0|$ and experiences a saturation for $|E_0| \gg E_c$. The quantity Q_{max} is the maximum value of $Q_\mathbf{k}$ achievable in a particular material. The inequality

$$qN_E\mu\tau/4\epsilon\epsilon_0 \gg 1 \tag{5.13}$$

is the criterion for the existence of weakly damped SCWs in fast PR materials. The major material parameter entering this criterion is the mobility-lifetime product $\mu\tau$. To approach closely the value of Q_{max}, it is sufficient to apply an electric field that exceeds the characteristic field E_c by a factor of 2–3; further increase of E_0 is inefficient. In the region $|E_0| \gg E_c$, the diffusion contribution to $Q_\mathbf{k}$ is negligible and the contributions related to the drift and saturation are equal to each other at $k = k^p$.

Table 5.1 represents the values of ϵ, N_E, $\mu\tau$, Q_{max}, E_c, and $\Lambda_c = 2\pi/k^p(E_c)$ for a number of PR materials meeting (5.13). They all are fast PR crystals distinguished by fairly high values of $\mu\tau$. Furthermore, they are isotropic so that the above relations are fully applicable to the 3D-case. The value of the eigen-frequency ω_{k} is typically within the range 10^2–$10^3 \mathrm{s}^{-1}$ in continuous-wave experiments with the fast materials.

Fig. 5.3a shows the dependence $Q(k, E_0)$ for $k_\perp = 0$ and representative parameters of $Bi_{12}SiO_{20}$ crystals. For modestly high values of E_0, weakly damped SCWs exist in a wide range of the wavelength $\Lambda = 2\pi/k$. The saturation of $Q^p(E_0)$ is clearly seen for $E_0 \gtrsim 6\,\mathrm{kV/cm}$. The values of the quality factor in this range are close to $Q_{max} \simeq 7$.

The linearized equations for the perturbations give not only (5.8) and (5.9) but also relations for the amplitudes $\varphi_{\mathbf{k}}$, $\delta N_{\mathbf{k}}^+$, $\delta n_{\mathbf{k}}$. They look especially simple when the small terms relevant to the wave damping are omitted,

$$k^2\varphi_{\mathbf{k}} = q\delta N_{\mathbf{k}}^+/\epsilon\epsilon_0, \qquad \delta n_{\mathbf{k}} = i\omega_{\mathbf{k}}\tau\delta N_{\mathbf{k}}^+. \tag{5.14}$$

Relations (5.14) are important for analysis of nonlinear SCW effects because they allow us to compare different nonlinear terms in the basic Eqs. (5.2)–(5.4). The second relation shows also that the inequality $\delta n_{\mathbf{k}} \ll \delta N_{\mathbf{k}}^+$, used earlier, is valid for $\omega_{\mathbf{k}}\tau \ll 1$, i.e., in the low-intensity range.

TABLE 5.1. Representative parameters of some fast cubic PR crystals [7, 9, 83].

Material	ϵ	$N_E\left[\frac{1}{\mathrm{cm}^3}\right]$	$\mu\tau\left[\frac{\mathrm{cm}^2}{V}\right]$	Q_{max}	$E_c\left[\frac{\mathrm{kV}}{cm}\right]$	$\Lambda_c[\mu\mathrm{m}]$
Sillenites	40–56	$\sim 10^{16}$	$10^{-6} - 10^{-7}$	$\sim 10^1$	≈ 3	≈ 10
GaAs	13	$\sim 10^{15}$	$10^{-4} - 10^{-5}$	$\sim 10^2$	≈ 2	≈ 100
CdTe	9.5	$\sim 10^{15}$	$10^{-5} - 10^{-6}$	$\sim 10^1$	≈ 2	≈ 30

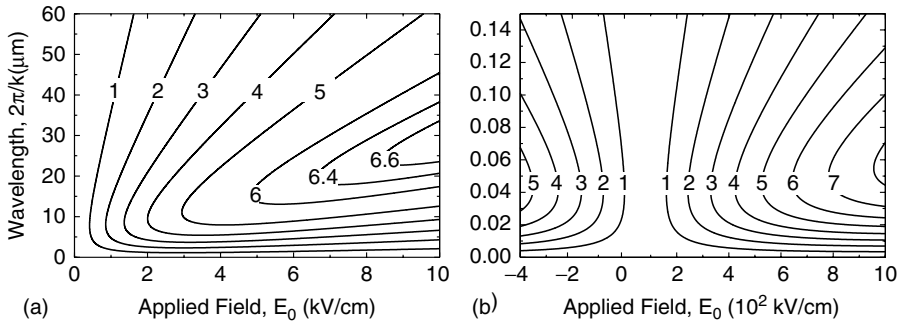

FIGURE 5.3. Contour lines $Q(E_0, 2\pi/k) = 1, 2, \ldots$ for $Bi_{12}SiO_{20}$ (a) and $LiNbO_3$: Fe (b) crystals. In the case (a) $\mu\tau = 6 \times 10^{-7}\,\mathrm{cm}^2/\mathrm{V}$, $N_E = 10^{16}\,\mathrm{cm}^{-3}$, $\epsilon = 56$ and in the case (b) $\mu\tau = 0.25 \times 10^{-13}\,\mathrm{cm}^2/\mathrm{V}$, $N_E = 10^{18}\,\mathrm{cm}^{-3}$, $\epsilon_\parallel = 30$, $E_{pv} = 80\,\mathrm{kV/cm}$.

Experimental evidences of the dependence $\omega_k \propto I_0/E_0 k$ for the sillenites can be found in [5, 34, 82] and other papers. They are obtained with the use of different excitation methods, see Section 5.3. Measurements of the quality factor Q_k have been performed in [81]; estimates of this parameter can also be made on the basis of the data on the subharmonic generation, see Section 5.4.

5.2.4 Slow Photorefractive Materials

Leaving provisionally aside $LiNbO_3$ and $LiTaO_3$ crystals, we set $E_{pv} = 0$ and consider the case when the imaginary parts are dominating in the numerator and denominator of (5.5). This bring us to the inequalities

$$E_M \gg E_0, \quad E_0 \gg E_q, \quad E_0 \gg E_D, \tag{5.15}$$

which differ strongly from the inequalities (5.7). Here we have [62]:

$$\omega_{\mathbf{k}} = -\omega_0 l_0 k_z, \quad \gamma_{\mathbf{k}} = t_d^{-1} + \omega_0 (l_0^2 k_z^2 + k^2 l_D^2), \tag{5.16}$$

where $t_d = \epsilon\epsilon_0/q\mu\bar{n}$ is the dielectric relaxation time, $l_0 = \mu\tau|E_0|$ is the drift length, and $l_D = (D\tau)^{1/2}$ is the diffusion length of photoelectrons. Again, the eigen-frequency and damping are even and odd functions of $\mathbf{k}$, E_0 and $\gamma_{\mathbf{k}}$ is positive and growing with $k_\perp$. The dispersion law is, however, completely new, $\omega_{\mathbf{k}} \propto E_0 k_z$. The group velocity is constant here and directed against the applied field vector. Switching from photoelectrons to photo-holes results in the changing sign of the eigen-frequency.

The expression for the quality factor has the form:

$$Q_{\mathbf{k}} = (|E_0/E_M| + |E_q/E_0| + |E_D/E_0|)^{-1}. \tag{5.17}$$

The inequalities (5.15) ensure that $Q_{\mathbf{k}} \gg 1$. The maximum of $Q(k_\perp)$ occurs at $k_\perp = 0$; it corresponds indeed to the longitudinal wave propagation.

By setting $k_\perp = 0$, $k_z = k$, we consider again the dependence $Q(k)$ for a fixed value of E_0. The corresponding peak values k^p and Q^p are given by

$$\frac{1}{k^p(E_0)} = \sqrt{(l_0^2 + l_D^2)\omega_0 t_d}, \quad Q^p(E_0) = \frac{l_0}{2}\sqrt{\frac{\omega_0 t_d}{l_0^2 + l_D^2}}. \tag{5.18}$$

The value of Q^p grows monotonously with $|E_0|$ and for $|E_0| \gg E_c = (k_B T/q\mu\tau)^{1/2}$ saturates on the level of

$$Q_{max} = (\epsilon\epsilon_0/4qN_E\mu\tau)^{1/2}. \tag{5.19}$$

This is the maximum possible value for the case considered. The inequality

$$\epsilon\epsilon_0/4qN_E\ \mu\tau \gg 1 \tag{5.20}$$

is the criterion for the presence of weakly damped SCWs in slow materials [62]. In contrast to (5.13), it requires small values of the mobility-lifetime product.

Note that the inequalities (5.13) and (5.20) are not exactly opposite; for the combination $qN_E\mu\tau/\epsilon\epsilon_0$, there is a gap from $\approx 1/4$ to ≈ 4 where weakly damped SCWs cannot exist. Quite a lot of PR materials belong to this gap.

The literature data evidence [9, 83] that the effective trap concentration ranges within roughly two orders of magnitude, from $\sim 10^{16}$to $\sim 10^{18}\,\mathrm{cm}^{-3}$. The mobility-lifetime product ranges within much wider limits, from $\sim 10^{-5}$to $\sim 10^{-13}\,\mathrm{cm}^2/\mathrm{V}$. This is why PR materials with low values of $\mu\tau$ are indispensable for the SCWs in question. Typically, such materials are ferroelectrics. High values of the dielectric constant, which are typical of them, favor large values of $Q_{\mathbf{k}}$. Furthermore, many ferroelectrics are strongly anisotropic; the longitudinal ($\|$) and transverse ($\perp$) values of ϵ and μ can be strongly different. If so, our theory can be applied only to the 1D-case.

Table 5.2 lists the relevant material parameters, the values of Q_{max}, E_c, and $\Lambda_c = 2\pi/k^p(E_c)$ for a number of ferroelectrics. Fairly high values of Q can potentially be achieved here.

Note that the condition (5.20) can be insufficient to employ SCW effects because of unrealistically high values of E_0. The characteristic field $E_c = (k_BT/q\mu\tau)^{1/2}$, which has to be exceeded to approach Q_{max}, can seldom be smaller than 10 kV/cm for the listed materials. The best candidate seems to be SBN:75.

One more distinctive feature of the slow materials is relatively small values of the wavelength $\Lambda_c = 2\pi/k^p(E_c) \approx 2\pi r_d$, where $r_d = (\epsilon\epsilon_0 k_BT/N_Eq^2)^{1/2}$ is the Debye screening length. The wavelength Λ_c does not typically exceed (1–2) μm. In SBN:75 crystals, it is expected to be relatively large.

Since the parameters $\mu\tau$ and Λ_c vary strongly over the slow materials, the range of variations of the eigen-frequency is also expected to be big.

Consider now the case of $LiNbO_3$ and $LiTaO_3$ crystals with dominating photovoltaic charge transport [84, 85]. The upper limit of the photovoltaic field E_{pv} is here around 100 kV/cm and the values of the mobility-lifetime product are extremely low, $\mu\tau \lesssim 10^{-13}\,\mathrm{cm}^2/\mathrm{V}$. Furthermore anisotropy of the dielectric permittivity and mobility is not high and can often be neglected.

It is important that the simplest one-species model is well justified for $LiNbO_3$ and $LiTaO_3$ crystals doped with Fe (or Cu) within a fairly wide range of concentrations [83, 86]. The Fe^{2+} (Cu^+) ions serve as donors and the Fe^{3+} (Cu^{2+}) centers as acceptors. The total concentration N_0 and the ratio

TABLE. 5.2. Representative parameters of some slow ferroelectric PR crystals [9, 62, 83].

Material	$\epsilon_\|$	$N_E[\frac{1}{\mathrm{cm}^3}]$	$\mu\tau\left[\frac{\mathrm{cm}^2}{V}\right]$	$Q^\|_{max}$	$E_c\left[\frac{\mathrm{kV}}{cm}\right]$	$\Lambda_c[\mu\mathrm{m}]$
$BaTiO_3$: h	135	$\sim 3\times10^{16}$	$\sim 3\times10^{-12}$	~ 25	$\sim 10^2$	~ 0.5
SBN:75	3400	$\sim 5\times10^{15}$	$\sim 5\times10^{-10}$	~ 25	~ 7	~ 6
SBN:60	880	$\sim 10^{16}$	$\sim 3\times10^{-10}$	~ 10	~ 10	~ 2
$KNbO_3$	50	$\sim 10^{16}$	$\sim 3\times10^{-11}$	~ 8	~ 30	~ 0.5
$LiNbO_3$: Fe	30	$\sim 10^{18}$	$\sim 3\times10^{-14}$	~ 20	$\sim 10^3$	~ 0.05

N^+/N can be controlled in experiment and the major model parameters are known. Typically, $N_E \simeq N_A \ll N_0$ and the effective trap concentration N_E ranges from $\sim 3\times 10^{17}$to $\sim 3\times 10^{18}\,\mathrm{cm}^{-3}$. Larger values of N_E lead to a strong light absorption while for smaller values, the influence of residual defects cannot be excluded. The photovoltaic field E_{pv} does not depend on N_E for $N_A \ll N_0$.

With these preliminaries, one can find from (5.5) that the inequality $\gamma_\mathrm{k} \ll |\omega_\mathrm{k}|$ is fulfilled under the conditions

$$|E_0 - N^+ N_0^{-1} E_{pv}| \gg E_q,\ E_D, \qquad E_M \gg E_0. \tag{5.21}$$

For the eigen-frequency and damping we get, compare with (16):

$$\omega_\mathrm{k} = -\omega_0 l_0^* k_z, \qquad \gamma_\mathrm{k} = t_d^{-1} + \omega_0 (l_0 l_0^* k_z^2 + k^2 l_D^2), \tag{5.22}$$

where $l_0^* = \mu\tau(E_0 - N^+ N_0^{-1} E_{pv})$.

Since l_0 and l_0^* can be opposite in sign, one can suspect that the damping γ_k can be negative in a range of E_0. This would mean an exponential grows of SCWs, i.e., instability of the medium. In reality, γ_k is always positive. To explain it, we point out that the necessary condition for the instability is the inequality $l_{pv} \equiv \mu\tau|E_{pv}| > 2l_D$. However, both experiment and theory evidence [85] that the photovoltaic length l_{pv} is smaller than l_D. Prediction of the instability of SCWs in $LiNbO_3$ made in [87, 88] is groundless.

The possibility to realize weakly damped SCWs without applied fields (owing to the photovoltaic effect) is slim [62]. To ensure the values $Q_\mathrm{k} \gg 1$, it is profitable to apply an electric field that is larger than E_{pv} but smaller than $E_c \sim 10^3\,\mathrm{kV/cm}$. In this case, $l_0^* \simeq l_0$, $k^p \simeq r_d^{-1}$, and $Q^p \simeq E_0(\epsilon\epsilon_0/4k_B T N_E)^{1/2}$. The possibility to apply fields up to 650 kV/cm to $LiNbO_3$: Fe crystals has been shown recently [89]. Thus one can obtain the values of the quality factor $Q \approx 5-6$ (see also Fig. 5.3b). The corresponding SCW wavelengths are comparable with (or smaller than) a typical light wavelength inside the crystal and the typical values of ω_k can be estimated as $10^{-2} - 10^{-1}\mathrm{s}^{-1}$. The dependence of the quality factor on E_0 is not even here owing to the photovoltaic effect. The use of strong "negative" fields, whose direction is antiparallel to the spontaneous polarization, is hardly possible because of the domain reversal. Experimental evidences of the dependence $\omega_\mathrm{k} \propto I_0 E_0$ for $LiNbO_3$: Fe crystals can be found in [63].

5.2.5 Two Generalizations

Two generalizations of the above results are worth mentioning. The first one is taking into account the electron-hole competition within the simplest two-band model (see Fig. 5.2b). The major effect of this competition is subtraction of the partial contributions to $\omega_\mathbf{k}$ and addition of the contributions to $\gamma_\mathbf{k}$ [62]. Thus, the $e-h$ competition is harmful for SCWs. This is in line with $e-h$ models of the DC enhancement [90].

The aims of the second generalization are to explain why the SCW characteristics of a promising fast PR material—GaAs:*EL*2 crystals—are much worse than the expected ones, and to see how to improve these characteristics.

Optical and photoelectrical characteristics of semiconductor GaAs:*EL*2 have been studied in many details [83, 91, 92]. The native defect *EL*2 with the concentration $N_0 = (1-3) \times 10^{16}\,\mathrm{cm}^{-3}$ is the main local center for undoped GaAs crystals. At room temperature it exists in the ionized and neutral states. Within the infrared wavelength range $(0.8-1.6)\,\mu$m, the model depicted in Fig. 5.2b works well and the main transport parameters are known. The hole and electron transport dominate for the low- and high-energy parts of the spectral range. The values $\mu\tau = 7$ and $80 \times 10^{-5}\,\mathrm{cm}^2/\mathrm{V}$ can be taken as representative for electrons and holes, respectively. This gives $Q_{max} \approx 90$ and 300. The same have to be the amplification factors for the space-charge field with the use of the DC and AC enhancement techniques, see Section 5.3. However, the experiments carried out with GaAs:*EL*2 crystals show neither large enhancement of the PR response nor the subharmonic generation [93, 94]. A similar situation takes place in GaAs:Cr crystals [95].

The most probable reason for the unexpectedly low values of the quality factor of SCWs is nonlinearity of charge transport [94]. This argument originates from the measurements of the electron-capture cross-section in high ($> 10\,\mathrm{kV/cm}$) applied fields [96]. The detected strong increase of this parameter, caused presumably by high values of the drift mobility μ, has to lead to a sharp decrease of the carrier lifetime and to the negative differential resistance of the crystal. In turn, this leads to the field instability for $E_0 > E_c$ [64, 65], which is similar to the well-known Gunn instability. In n-GaAs crystals, the critical field E_c is expected to be about 1 kV/cm.

Modeling of the nonlinear charge transport in n-GaAs has shown [64] that weakly damped SCWs have to exist only for moderate fields, $E_0 < E_c$, and light wavelengths $\lambda < 1.2\,\mu$m. The quality factor peaks at $E_0 \approx E_c/2$ and $2\pi/k = (100-200)\mu$m, here $Q_{max} \sim 10$. Pronounced SCW effects are expected in the indicated range of parameters.

5.3 Linear Excitation of Space-Charge Waves: Enhancement of Photorefractive Response

5.3.1 General Features

The simplest way of excitation of SCWs has much in common with recording of elementary PR gratings. Let two coherent light beams interfere in a PR medium (see Fig. 1b). The light intensity pattern $I(\mathbf{r}, t)$ has generally the form of a running grating,

$$I = I_0 [1 + m \cos(\mathbf{K} \cdot \mathbf{r} - \Omega t)], \tag{5.23}$$

where $\mathbf{K}$ and Ω are the differences of the light wavevectors and frequencies (referred to as the grating vector and frequency detuning), I_0 is the total intensity, and m is the light contrast. Correspondingly, a running grating of space-charge field is induced.

Within the linear approximation in m, only the spatial frequency $\mathbf{K}$ is present in medium response and the space-charge field can be expressed as

$$E_{sc}(\mathbf{r}, t) = \frac{1}{2} E_{\mathbf{K}}(t) \exp(i\,\mathbf{K} \cdot \mathbf{r}) + c.c. \tag{5.24}$$

The complex grating amplitude $E_{\mathbf{k}}$ obeys then the differential equation

$$\left(\frac{d}{dt} + i\omega_{\mathbf{K}} + \gamma_{\mathbf{K}}\right) E_{\mathbf{K}} = mF_{\mathbf{K}} \exp(-i\Omega t), \tag{5.25}$$

where the complex quantity F_{K} is an effective driving force. The structure of this equation is quite general while the parameters $\omega_{\mathbf{K}}$, $\gamma_{\mathbf{K}}$, and F_{K} are model-dependent. Within the basic one-species model $\omega_{\mathbf{k}}$ and $\gamma_{\mathbf{k}}$ obey the dispersion relation (5.5) and the ratio $|\omega_{\mathbf{k}}|/\gamma_{\mathbf{k}}$ is not necessarily large. In other words, the structure of (5.25) carries no special features relevant to SCWs. It describes buildup of the fundamental grating within the linear-contrast approximation and decay of this grating under a uniform illumination ($m = 0$). Recall lastly that the uniform applied field $\mathbf{E}_{ex}$ is generally time-dependent.

Suppose now that $\mathbf{E}_{ex} = \mathbf{E}_0 = const$, $|\omega_{\mathbf{K}}| \gg \gamma_{\mathbf{K}}$, and $\Omega \approx \omega_{\mathbf{K}}$, i.e., the resonance between the driving-force frequency Ω and the eigen-frequency $\omega_{\mathbf{K}}$ takes place. Eq. (5.25) gives then in steady state:

$$E_{\mathbf{K}} = \frac{mF_{\mathbf{K}}}{\gamma_{\mathbf{K}} + i(\omega_{\mathbf{K}} - \Omega)} \exp(-i\Omega t). \tag{5.26}$$

The grating amplitude experiences an obvious resonant enhancement when Ω approaches $\omega_{\mathbf{K}}$. The half-width of the resonant profile $|E_{\mathbf{K}}(\Omega)|^2$ is the damping γ_{K} and the enhancement factor for $|E_{\mathbf{K}}|$ at the resonance center (as compared to the case $\Omega = 0$) is the quality factor $Q_{\mathbf{K}}$. The argument of the ratio $F_{\mathbf{K}}/(\gamma_{\mathbf{K}} + i\omega_{\mathbf{K}} - i\Omega)$ is the phase shift between the field and intensity gratings; it is an important characteristic of the PR response. Switching Ω from 0 to $\omega_{\mathbf{K}}$ produces a $\approx 90^\circ$ change of the phase shift. The resonant excitation thus modifies the type of the response in addition to its enhancement.

In short, the place of the DC enhancement in the SCW concept can be commented as follows: Only one spatial frequency $\mathbf{k} = \mathbf{K}$ is selected from the whole spectrum of the wavevectors in the presence of the low-contrast intensity pattern. So we are dealing with the excitation of an elementary weakly damped oscillator by a periodic driving force.

Instead of the running grating technique, a phase-modulation technique can also be used for the excitation of SCWs in the DC case. If the phase of one of the pump beams is modulated as $\theta \cos \Omega t$, the light intensity is $I = I_0 [1 + m \cos(Kz - \theta \cos \Omega t)]$, i.e., the positions of the light fringes are oscillating

in time. The Fourier spectrum of $\delta I(t)$ is more complicated now; it includes the harmonics $0, \ \pm\Omega, \ \pm 2\Omega, \ldots$ The modulation method is useful for the studies of the linear and nonlinear SCW effects in the low-contrast-low-modulation range, see Section 5.5.2. For $m, \ \theta \ll 1$, the intensity components $I_0 m \cos(Kz)$ and $I_0(m\theta/2)\sin(Kz \pm \Omega t)$ are of prime importance. At $\Omega \simeq \pm\omega_{\mathbf{K}}$, we have again the resonant DC enhancement.

Consider now the AC enhancement. To make it, we set $\Omega = 0$ (static light pattern) and $\mathbf{E}_{ex}(t) = p\mathbf{E}_0$, where $p(t) = \pm 1$ is a periodically alternating function whose period is much shorter than the decay time $\gamma_{\mathbf{K}}^{-1}$. As soon as $|\omega_{\mathbf{K}}| \gg \gamma_{\mathbf{K}}$, the eigen-frequency is an odd function of $\mathbf{E}_{ex}$; it rapidly changes its sign. As for γ_{K}, it remains unchanged. Quickly alternating term $\omega_{\mathbf{K}} E_{\mathbf{K}}$ can be removed from the left-hand side of (5.25) and the major question is now whether the driving force $F_{\mathbf{K}}$ is alternating in time. If so, the AC enhancement is impossible. If $F_{\mathbf{K}}(t) \simeq const$, we have in steady state:

$$E_{\mathbf{K}} = mF_{\mathbf{K}}/\gamma_{\mathbf{K}}. \tag{5.27}$$

Again, the enhancement factor for $|E_{\mathbf{K}}|$ (as compared to the case $\Omega = 0$, $\mathbf{E}_{ex} = \mathbf{E}_0$) is $Q_{\mathbf{K}}$ and an almost 90° change of the phase shift between the field and intensity gratings takes place.

The strongest enhancement occurs indeed for $\mathbf{K} \parallel \mathbf{Eex}$. In what follows, we restrict ourselves to this most interesting situation.

5.3.2 Particular Cases

Fast materials: Here the driving force $F_K \simeq -i\omega_K E_{ex}$ for sufficiently strong applied fields (when $Q_K \gg 1$). Since $\omega_K \propto E_{ex}^{-1}$, it does not depend on E_{ex}. The DC and AC enhancement techniques give here the same result. For $\Omega = 0$ and $E_{ex} = E_0$, the phase shift between the field and light fringes is close to 0 or π (the local PR response) and the energy exchange between the light beams is weak. Under the DC or AC enhancement conditions, the phase shift is almost $\pm\pi/2$ (the nonlocal response) and the rate of energy transfer is high. Since 1985 both DC and AC techniques have been successfully used for a number of fast materials (predominantly for crystals of the sillenite family) [7, 9]. It was proven also that the square-wave shape of the applied electric field provides the best AC enhancement [9, 97]. Experimental dependences of the resonant detuning ($\Omega \simeq \omega_K$) on I_0, E_0, and K, obtained for the sillenites in the DC case, show that the eigen-frequency ω_K is proportional to I_0 and inversely proportional to E_0 and K [5, 34, 82].

While the mentioned characteristics of the DC and AC enhancement techniques are the same, there are essential differences. The DC method requires a precise adjustment of Ω to the resonant frequency $\omega_K \propto I_0$. If, as often happens, the intensity I_0 noticeably decreases across the sample because of light absorption, the nonuniform broadening of the resonance takes place and the efficiency of the DC enhancement falls down. The AC technique requires no adjustment to the resonance; it is robust in the nonuniform environment.

Furthermore, the highest applied fields (up to 60 kV/cm) have been used in AC experiments [98]; in the DC case, the field E_0 did not exceed 15 kV/cm.

One more difference concerns the field of applicability of the linear-contrast approximation. In the DC case, Eq. (5.25) is valid for $m \lesssim Q_K^{-1}$ if the detuning Ω is close to ω_K. For larger values of m, excitation of the higher spatial harmonics, E_{2K}, $E_{3K}, \ldots$ becomes important and the function $|E_K|(m)$ experiences a saturation on the level of E_0. In the AC case, the field of applicability is even narrower, $m \lesssim Q_K^{-2}$ (see Section 5.5.2 for more detail.)

Slow materials: In this case, the driving force $F_K \simeq \omega_K E_q \propto E_{ex}$ so that only DC enhancement is possible. At the resonance ($\Omega \simeq \omega_K$), the absolute value of the fundamental grating amplitude is $|E_K| \simeq m E_q Q_K$ and the enhanced PR response is local in contrast to the previous case.

Since the space-charge field cannot exceed the saturation field, applicability of the linear-contrast approximation is also restricted by the inequality $m \lesssim Q_K^{-1}$ at the resonance. The use of larger values of m results in saturation of the dependence $E_K(m)$ and broadening of the frequency dependence $|E_K(\Omega)|$ because of excitation of the higher harmonics [62].

Experimental conditions necessary to employ the resonant excitation in slow materials are rather tough. A reflection geometry should be used to meet the requirement of high spatial frequencies. The applied field has to be fairly strong ($E_0 \gg 10^2$ kV/cm for lithium niobate). Finally, the resonant detuning is expected to be small and the necessary waiting time rather long.

Despite the difficulties, the resonant excitation has been realized recently in $LiNbO_3$:Fe crystals [63]. The light beams were counter-propagating, the applied field ranged from 0 to 650 kV/cm, and the stabilization was achieved with the help of a feedback loop. By maximizing the diffraction efficiency of the recorded grating, this feedback introduced a detuning Ω, minimizing the energy exchange. This detuning was growing linearly with E_0 and identified as the eigen-frequency of SCWs. The quality factor was estimated as $Q_K \approx 5$.

5.4 Parametric Excitation of SCWs: Subharmonic Generation

5.4.1 Main Experimental Facts

Discovery of the effect of subharmonic generation in 1988 was the turning point in the studies of SCWs. Initially the subharmonic generation was observed in a $Bi_{12}SiO_{20}$ crystal during experiments on DC enhancement of the PR response [10]. Numerous subsequent DC and AC experiments with fast materials ($Bi_{12}SiO_{20}$, $Bi_{12}TiO_{20}$, $Bi_{12}GeO_{20}$, and CdTe) have revealed a number of apparent features of this general phenomenon [11–17, 41, 47–49, 52, 61]:

- If the frequency detuning Ω is increasing, an additional central light beam emerges spontaneously at the output at a certain value Ω_m. This beam is due

to diffraction of the pump from the subharmonic grating (the main subharmonic) with the spatial frequency $\mathbf{K}/2$ (see also Fig. 5.1c).

- Further increase of Ω results in the longitudinal (along $\mathbf{K}$) split of the central beam, progressing angular separation of its parts, and their decreasing intensity. For sufficiently high values of Ω, the additional light beams disappear. The spatial frequencies of the gratings responsible for the outgoing beams are sometimes close to $\mathbf{K}/3$ and $\mathbf{K}/4$.
- The described regularities take place only for sufficiently large values of the light contrast (the threshold value m_{th} ranges from ≈ 0.6 to 1), for sufficiently high applied fields, and within a restricted interval of $|\mathbf{K}|$.
- Reversal of the sign of $\mathbf{E}_0$ (or Ω) eliminates the subharmonic generation.
- The above restrictions on the light contrast, the value of the applied field, and the spatial frequency hold true as applied to the AC case.

There are also a number of other remarkable features of the effect that are relevant to particular experiments. Probably, the most exciting among them is the transverse subharmonic split—the non-planar ($\perp \mathbf{K}$) angular separation of the central beam—observed in some DC experiments with $Bi_{12}SiO_{20}$ crystals [41, 48, 100]. Below, we consider the main elements of theory that is capable of explaining the main observations.

5.4.2 Phase-Matching Conditions for Parametric Excitation

Phase-matching conditions, which are the conditions of the spatio-temporal resonances, are the most general tools for classification and characterization of various nonlinear wave processes [99]. Let $\mathbf{K}$ and Ω be the fundamental grating vector and the frequency detuning relevant to the DC excitation technique. Then the phase-matching conditions for the parametric excitation of a pair SCWs with wavevectors $k_{1,2}$ are [28, 31]:

$$\mathbf{K} = \mathbf{k}_1 + \mathbf{k}_2, \qquad \Omega = \omega_{\mathbf{k}_1} + \omega_{\mathbf{k}_2}. \tag{5.28}$$

They can be considered as the conditions for decay of the fundamental grating into two eigen-modes.

The tips of the vectors $\mathbf{k}_{1,\,2}$ fill a surface in the space of SCW wavevectors (the resonant surface). Each vector $\mathbf{k}_1$ is uniquely related to a vector $\mathbf{k}_2$. Assuming that $\mathbf{K} \parallel \mathbf{E}_0$, which is the case of the subharmonic experiments, and recalling that $\omega_{\mathbf{k}} \propto k_z^{-1}$, we obtain that $\mathbf{k}_{1\perp} = -\mathbf{k}_{2\perp}$ and

$$k_{1z} = \frac{K}{2}\left(1 \mp \sqrt{1 - \frac{4\omega_K}{\Omega}}\right), \; k_{2z} = \frac{K}{2}\left(1 \pm \sqrt{1 - \frac{4\omega_K}{\Omega}}\right). \tag{5.29}$$

The presence of the double signs in (5.29) expresses the symmetry with respect to the interchange of $\mathbf{k}_1$ and $\mathbf{k}_2$. It is sufficient to find the allowed values of $\mathbf{k}_1$ for the upper sign. We see that the longitudinal component k_{1z} is fixed

while there is no restriction on the transverse component $\mathbf{k}_{1\perp}$. Thus the resonant surface consists of two plains perpendicular to $\mathbf{K}$, see Fig. 5.4a.

The phase-matching conditions can be fulfilled only for sufficiently large values of the frequency detuning, $\Omega \geq 4\omega_K$. The minimum value, $\Omega_m = 4\omega_K$, exceeds the resonant one by a factor of four. In the 1D case, it corresponds to the excitation of the subharmonic $K/2$. With Ω increasing from Ω_m to ∞, the components k_{1z} and k_{2z} are changing from $K/2$ to 0 and K (see Fig. 5.4b). The found features are closely related to the dispersion law $\omega_{\mathbf{k}} \propto k_z^{-1}$.

Each resonance has indeed a finite width. Therefore the waves whose wavevectors lie in the close vicinity of the resonant surface can also be excited. Besides, the parametric excitation cannot die immediately for $\Omega > \Omega_m$.

The described consequences of the phase-matching conditions already allow us to understand some of the above-listed experimental facts on the subharmonic generation.

In the case of AC excitation, the only remaining phase-matching condition is $\mathbf{k}_1 + \mathbf{k}_2 = \mathbf{K}$; it does not fix the longitudinal components of the wavevectors. A wide spectrum of the longitudinal spatial frequencies can be excited here.

5.4.3 Simplified Nonlinear Equation

To exhibit and investigate the instability of the fundamental grating against parametric excitation of SCWs, we use the set of basic Eqs. (5.2)–(5.4). It can be considerably simplified and reduced to a single equation for the electrostatic potential φ if we assume that the inequalities (5.7) hold true.

The basic equations include linear and nonlinear terms with respect to the spatially-oscillating perturbations δn, δN^+, and φ. The linear terms are responsible for SCW propagation. The biggest of them in (5.3) and (5.4) are δN_t^+, $\delta n/\tau$ and $E_{ex}\delta n_z$, $\bar{n}\Delta\varphi$, respectively, with the subscripts z and t denoting differentiation. Retaining these terms leads to propagation without damping. The biggest nonlinear term is $\mu\boldsymbol{\nabla}\cdot(\delta n\mathbf{E}_{sc})$; it corresponds to the drift nonlinearity. The

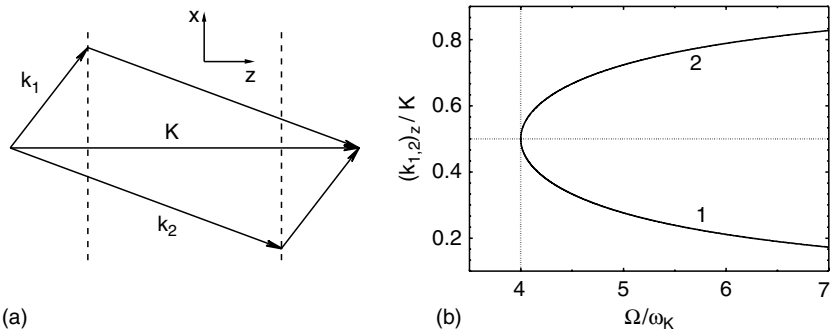

FIGURE 5.4. (a): Geometric scheme for the phase-matching conditions (28). (b) Dependence of the allowed values of $(k_{1,2})_z$ on Ω/ω_K.

nonlinear recombination term $s_r \delta n \delta N^+$ in (5.3) can be neglected. To see it, one can compare the nonlinear and the major linear terms using (5.14). Expressing algebraically δn and δN^+ by φ, we obtain finally [31]:

$$\begin{aligned} &\Delta\varphi_{zt} - \frac{\omega_0}{l_s}\Delta\varphi + \omega_0 \Delta\varphi_z - \frac{1}{l_0}\Delta\varphi_t + \frac{l_D^2}{l_0}\Delta^2\varphi_t \\ &= -\frac{q}{\epsilon\epsilon_0}\frac{\alpha\delta I_z}{\hbar\omega} + \frac{q}{\epsilon\epsilon_0}\frac{\alpha}{\hbar\omega}\frac{1}{E_{ex}}\nabla\cdot(\delta I\nabla\varphi) + \frac{1}{E_{ex}}\nabla\cdot(\Delta\varphi_t\nabla\varphi). \end{aligned} \tag{5.30}$$

Here $\Delta = \nabla^2$, $\delta I = I_0 \cos(Kz - \Omega t)$ is the nonuniform part of the light intensity, and $l_s = \epsilon\epsilon_o E_{ex}/qN_E$. The field E_{ex} can be constant, E_0, or alternating, $\pm E_0$.

Eq. (5.30) includes all linear and nonlinear terms relevant to SCW effects in the fast materials. It is applicable to the DC and AC cases in the whole range of light contrast. Two first terms of the left-hand side correspond to lossless wave propagation, while the subsequent three terms describe wave damping. The first term on the right-hand side is the effective driving force for SCWs caused by the spatial modulation of the light intensity. The next term describes coupling between δI and φ. The last term describes the intrinsic nonlinear wave coupling. Often the last two terms partially compensate each other. In the 1D case, Eq. (5.30) undergoes additional simplifications [31].

5.4.4 Thresholds and Increments of Parametric Instability

To consider the DC-case, we set $E_{ex} = E_0$ and use the ansatz:

$$\varphi = \varphi_K \exp(iKz) + \varphi_1 \exp(i\,\mathbf{k}_1\cdot\mathbf{r}) + \varphi_2 \exp(i\,\mathbf{k}_2\cdot\mathbf{r}), \tag{5.31}$$

where $\varphi_K = iE_K/K \propto \exp(-i\Omega t)$ is the amplitude of the electrostatic potential for the moving fundamental grating and $\varphi_{1,2}$ are small amplitudes of SCWs 1 and 2 whose wavevectors meet (5.28). By substituting it in (5.30) and keeping in mind that the derivatives of $(\varphi_{1,2})_t$ in the nonlinear terms have to be equalized to $-i\omega_{\mathbf{k}_{1,2}}\varphi_{1,2}$ within the leading approximation, we obtain, after separation of the spatial harmonics:

$$\left(\frac{d}{dt} + i\omega_{\mathbf{k}_1} + \gamma_{\mathbf{k}_1}\right)\varphi_1 = -i\,\frac{\omega_0}{l_s} f_{12}\frac{E_K}{E_0}\varphi_2^* \tag{5.32}$$

$$\left(\frac{d}{dt} - i\omega_{\mathbf{k}_2} + \gamma_{\mathbf{k}_2}\right)\varphi_2^* = i\,\frac{\omega_0}{l_s} f_{21}\frac{E_K^*}{E_0}\varphi_1, \tag{5.33}$$

where $f_{12} = [2k_{1z}k_{2z}^2 + k_\perp^2(k_{1z} - k_{2z})]/2k_{1z}k_{2z}k_1^2$. The contributions to f_{12} come from two last terms in (5.30).

The structure of (5.32), (5.33) is generic for the parametric wave processes. The left-hand sides express the resonant properties of the eigen-modes. The right-hand sides can be considered as the driving forces caused by the presence of quadratic nonlinear terms; these forces are proportional to the wave

amplitudes and the amplitude of the fundamental grating. If the phase-matching conditions are fulfilled, the forces are in resonance with the eigen-modes.

By setting $\varphi_1 \propto \exp(-i\omega_{\mathbf{k}_1} t + \Gamma t)$, $\varphi_2^* \propto \exp(i\omega_{\mathbf{k}_2} t + \Gamma t)$, we obtain for the increment Γ:

$$\Gamma = -\frac{1}{2}(\gamma_{\mathbf{k}_1} + \gamma_{\mathbf{k}_2}) \pm \sqrt{\frac{1}{4}(\gamma_{\mathbf{k}_1} - \gamma_{\mathbf{k}_2})^2 + \Gamma_0^2}, \tag{5.34}$$

where

$$\Gamma_0 = \frac{m\omega_K}{2(1-\varepsilon)} F(\varepsilon, k_\perp^2/K^2); \quad F(\varepsilon,\ x) = \sqrt{\frac{4\varepsilon^3 + (4\varepsilon - 1)x(x - 2\varepsilon)}{\varepsilon^2 + (1 - 2\varepsilon)x + x^2}}, \tag{5.35}$$

and $\varepsilon = \omega_K/\Omega$. The values of ϵ compatible with the phase-matching conditions range from 1/4 to 0. The positive values of Γ correspond to instability of the fundamental grating; they occur only for the upper sign in (5.34).

The threshold condition for the excitation of a pair of SCWs with wavevectors $k_{1,2}$, which corresponds to the equality $\Gamma = 0$, looks especially simple,

$$\Gamma_0^2 = \gamma_{\mathbf{k}_1}\gamma_{\mathbf{k}_2}. \tag{5.36}$$

It is evident that (5.36) can be satisfied only for sufficiently large values of the contrast m. It can be checked furthermore that the function $F(\varepsilon, k_\perp^2/K^2)$ is decreasing with increasing $k_\perp^2$ for any allowed value of ε. Since $\gamma_{k_{1,2}}$ are growing with $k_\perp^2$, we conclude that for any Ω, the lowest threshold value of the light contrast occurs in the 1D case, $k_\perp = 0$. Here

$$m_{th} = \frac{\Omega - \omega_K}{\omega_K (Q_{k_1} Q_{k_2})^{1/2}}, \tag{5.37}$$

where $k_1 = k_{1z}$ and $k_2 = k_{2z}$ are expressed by Ω/ω_K and K through (5.29).

The minimum threshold value,

$$m_{th}^{min} = 3/Q_{K/2}, \tag{5.38}$$

takes place at $\Omega = 4\omega_K(\varepsilon = 1/4)$; it corresponds to the excitation of the main subharmonic $K/2$. This is an important corollary of the theory. Above the threshold, the biggest value of $\Gamma(\Omega)$ also corresponds to the generation of the main subharmonic. The minimum value of the quality factor $Q_{K/2}$ necessary for the subharmonic generation is 3. The requirement $Q_{K/2} > 3$ can be fulfilled in a wide range of K and E_0, see Fig. 5.3a. With $Q_{K/2} \approx 6$, the threshold value $m_{th}(\Omega)$ reaches 1 for $\Omega = (6-7)\omega_K$.

Consider now the AC case. This can also be done with the help of (5.32), (5.33) if we replace the E_0 by $E_{ex} = p(t)E_0$ and use the relation $E_K = -im\omega_{\boldsymbol{K}}(E_{ex})\, E_{ex}/\gamma_K$ for the fundamental amplitude (see Section 5.3). The only parameters changing their signs at the AC switching are $\omega_{\mathbf{k}_{1,2}} \propto E_{ex}^{-1}$. The corresponding terms can be removed when the period of the AC oscillations is much

shorter than the response time γ_K^{-1}. Using the ansatz (5.31) and restricting ourselves to the 1D case, we proceed to (5.34) with $\Gamma_0 = (\omega_{k_1}\omega_{k_2})^{1/2}|E_K/E_0|$. Exactly the same expression for Γ_0 is valid in the DC case. However, the ratio $|E_K/E_0|$ is the highest in the AC case because the requirement $\Omega \geq 4\omega_K$ excludes the resonant enhancement of E_K in the DC case Correspondingly, the threshold value of the contrast is lowest in the AC-case,

$$m_{th} = Q_K^{-1}(Q_{k_1}Q_{k_2})^{-1/2}, \tag{5.39}$$

where $k_1 + k_2 = K$. The minimum threshold value, $m_{th}^{min} = 1/Q_K Q_{K/2}$, corresponds again to the excitation of the main subharmonic. The results obtained in the limit of quickly oscillating AC field admit a generalization on the case of an arbitrary alternation period [31]. The instability is getting weaker and disappears with increasing this period.

Recalling that the expression $E_K = -iQ_K E_0$ for the fundamental amplitude is valid for $m \lesssim Q_K^{-2}$ in the AC case, one can expect that taking into account the higher spatial harmonics, $E_{2K}, E_{3K}, \ldots$, can modify (5.39). An analysis shows [60] that this modification is reduced to an increase of m_{th} by a factor of 2–3. For moderate values of the quality factors, the threshold values of the light contrast can be comparable in the DC and AC cases.

5.4.5 Further Developments of Subharmonic Theory

Several important issues have been analyzed in addition to the above considered within the simplest one-species model:

An attempt to explain the transverse subharmonic split was made in [48, 54]. The authors analyzed stability of the fundamental grating in the DC case for $m \approx 1$ and $\Omega \approx \omega_K$ using an expression for E_K which is valid in the low-contrast approximation, i.e., skipping the high-contrast effects. Within this oversimplified model, the strongest instability took place for $(k_{1,2})_z = K/2$ and $k_\perp \neq 0$. The reason of this is simple: The postulated sharp increase of $E_K(\Omega)$ with Ω approaching ω_K compensates the growing distance from the parametric resonance and destroys the compensation of nonlinear terms.

The influence of the higher spatial harmonics ($2K, \ldots 20K$) on the parametric instability was analyzed in [55] by combining analytical and numerical methods. A new region of the instability, found for $\Omega \approx 2.5\omega_K$ and $m \approx 1$, corresponded to the excitation of the split subharmonic.

However, it was later found that this result is the consequence of a numerical error. Using the same method, it was shown later [57, 59] that the high-contrast effects modestly modify the initial results but lead neither to a new (in Ω) region of the instability nor to the transverse subharmonic split. This complies with the numerical 1D analysis of the influence of the higher spatial harmonics on the subharmonic instability [42]. Thus, the transverse subharmonic split is not consistent with the basic equations.

The major effect of the higher harmonics for $m \approx 1$ is as follows: The minimum value of the frequency detuning, Ω_m, is shifted from $4\omega_K$ to $\approx 3\omega_K$. Within the interval $\Omega_m < \Omega < 4.3\omega_K$, the excitation of the main subharmonic $K/2$ takes place. Further increase of the detuning frequency results in the longitudinal split in accordance with the phase-matching conditions.

The next issue to deal with is the problem of stability of the DC enhanced fundamental grating. It was expected first that this grating is unstable via the following mechanism [66]: At $\Omega \simeq \omega_K$, the second harmonic, $E_{2K} \simeq -E_K^2/E_0 \simeq Q_K^2 m^2 E_0$, is excited. This harmonic becomes unstable owing to the allowed parametric process defined by the phase-matching condition $2\omega_{\mathbf{K}} = \omega_{\mathbf{k}} + \omega_{\mathbf{K}-\mathbf{k}}$. The threshold value of contrast was estimated as $\sqrt{6}Q_K^{-3/2}$ and the wavevectors of the excited SCWs were expected to be close to $\mathbf{K}$ (modulation instability). However, the subsequent more accurate analysis has shown that the fundamental grating remains stable in the sillenites for any realistic values of the material parameters [71].

Several attempts have been made to describe the final state of the system above the threshold [25, 51, 56, 58]. It is shown that the nonlinear frequency shifts for SCWs are important in the saturated state. The mode of excitation seems to be "soft", i.e., the subharmonic amplitude follows the law $|E_{K/2}| \propto \sqrt{m - m_{th}}$ above the threshold. Build-up of the subharmonics should result in the back action on the fundamental amplitude E_K; it decreases in the absolute value and acquires an additional imaginary component leading to an energy exchange between the pump beams. Fine details of the final wave state can be complicated and superimposed by fluctuations typical of critical phenomena.

Very little is known about nonlinear SCW effects in the slow materials [62]. Owing to the linear dispersion law, there is little likelihood that effects similar to the subharmonic generation may occur here.

5.4.6 *Experimental Data and Comparison with Theory*

To understand properly the experimental situation, one should keep in mind that the data of initial subharmonic experiments, performed in the coupling configurations, were strongly affected by the optical nonlinearity and the spatial inhomogeneity. The sillenite crystals were typically thick, $d \sim 1\,\mathrm{cm}$, and the light absorption was fairly strong, $\alpha d > 1$. Under these conditions, the light contrast was changing considerably because of beam coupling and the intensity I_0 decreased substantially towards the output crystal face. Furthermore, the beam coupling in the sillenite crystals is vectorial: The changes of the light intensities are inseparable here from the polarization changes (see [101] and references therein). Despite the complicating circumstances, there is a qualitative agreement between the apparent features of the subharmonic generation, described in the beginning of this section, and the above theory.

This agreement becomes even more convincing with the use of the non-coupling experimental arrangement depicted in Fig. 5.5. The electro-optic

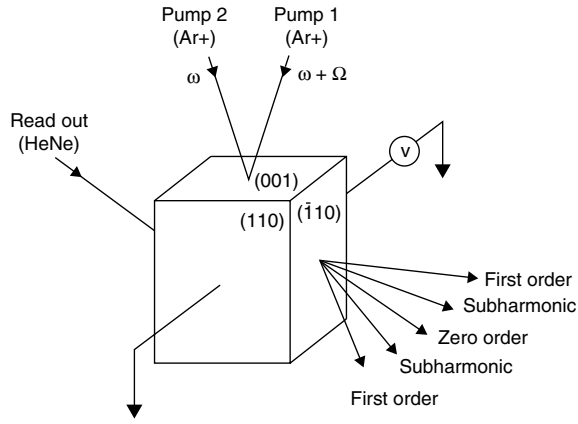

FIGURE 5.5. The noncoupling geometry. Two pump beams, 1 and 2, are propagating near the [001] axis and the read-out beam, incident onto the ($\bar{1}10$)-face, can be Bragg-matched to the fundamental and subharmonic gratings [33].

coefficient is zero here for the pump beams. They excite the space-charge field but cannot diffract from the induced gratings. Optical activity (of the sillenites) does not influence the intensity distribution and the pump contrast remains constant across the sample. Only the total pump intensity I_0 is decreasing during propagation because of light absorption. A narrow nondisturbing Bragg-matched read-out beam propagates perpendicular to the [001] axis passing through the area of an almost constant pump intensity I_0. The electro-optic coefficient is not zero here and the diffracted beam carries information about the value of the space-charge field at the relevant spatial frequency, **K**, **K**/2, etc. The influence of optical activity, polarization degrees of freedom, and light absorption on the diffraction efficiency can be taken into account [101, 102]. The degree of influence of the effects of nonuniform broadening is determined by the transverse size of the read-out beam and, possibly, by the degree of inhomogeneity of the applied field.

Turn now to the first experiments performed in the noncoupling geometry [33, 34]. The used $Bi_{12}SiO_{20}$ crystal had dimensions $10 \times 11 \times 5\,mm^3$ along the [$\bar{1}$10], [110], [001] axes, respectively. Its absorption coefficient $\alpha \simeq 1.1\,cm^{-1}$ at the pump wavelength 514 nm. The grating vector **K** was parallel to the [110] axis and the period $2\pi/K \simeq 20\,\mu m$. A DC field, applied parallel to **K**, ranged from 0 to 7 kV/cm. The input pump intensity was varied from 15 to $70\,mW/cm^2$. A read-out beam ($\lambda_r = 632.8\,nm$) had a diameter of 3 mm and an intensity of $1.5\,mW/cm^2$. The distance between the read-out beams and the input pump plane was a variable parameter.

With this arrangement it was not possible to see any sign of beam coupling involving the pump beams and no additional beams appeared between them. Nevertheless, the presence of the fundamental and subharmonic gratings was easily detected with the use of the read-out beam. This excludes the possibility that the optical nonlinearity contributes to the subharmonic grating and conclusively demonstrates the prime role of the material nonlinearity.

Fig. 5.6a,b show the diffraction efficiencies η_f and η_s for the K and $K/2$ gratings versus the detuning frequency. The found dependences represent two neat peaks centered at $\Omega_f \approx 115$ and $\Omega_s \approx 350\,\mathrm{s}^{-1} \simeq 3\Omega_f$. In contrast to the fundamental grating, the subharmonic exists in a limited range of Ω. The subharmonic grating near its maximum exceeds the fundamental one; the peak value of η_s is, however, smaller than that of η_f.

The optimum detunings $\Omega_{f,s}$ depend on I_0 and E_0. The corresponding data are presented in Figs. 5.7a,b. One sees that in the whole range both Ω_f and Ω_s

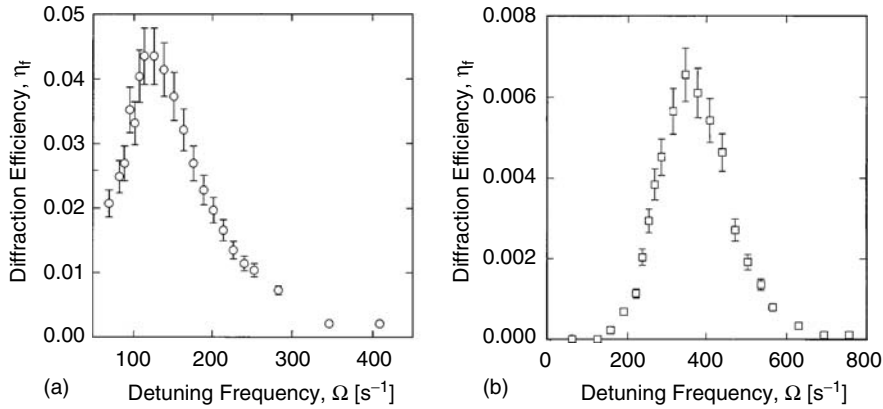

FIGURE 5.6. Frequency dependence of the diffraction efficiency η for the fundamental (a) and subharmonic (b) gratings [34].

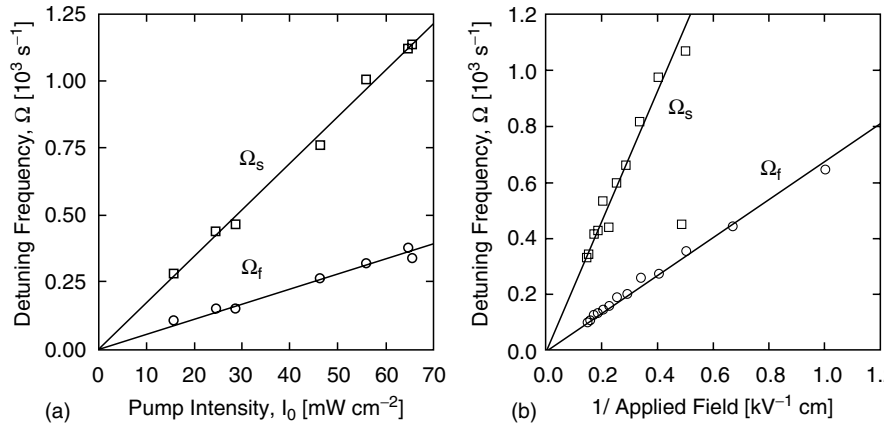

FIGURE 5.7. Dependence of the peak values of the frequency detunings, $\Omega_{f,s}$, on the total pump intensity (a) and applied field (b) [34].

are very accurately proportional to I_0 and E_0^{-1}. The ratio Ω_s/Ω_f is close to 3. For $E_0 < 2\,\mathrm{kV/cm}$, the subharmonic is not excited. It has been found also [34] that the values of $\Omega_{f,s}$ are decreasing by a factor of ≈ 2 with increasing distance between the read-out beam and the input pump plane. This shows the degree of spatial inhomogeneity caused by light absorption.

The effect of varying the pump ratio (light contrast) on the subharmonic excitation is shown in Fig. 5.8. The peak value of $\eta_s(\Omega)$ is decreasing monotonously with the reduction of m turning to zero at $m_{th} \simeq 0.8$. The peak position and width remain approximately constant. The situation with the peak value $\Omega_f(\mathrm{m})$ is different. When m is decreasing from 1 to 0.23, the optimum detuning Ω_f decreases by a factor of ≈ 1.4. This is the evidence of the nonlinear frequency shift, see also Section 5.5.2.

The angular distribution of SCWs excited in the DC case is also investigated in the noncoupling geometry [36]. The main finding in steady state are as follows (see Fig. 5.9): The main subharmonic $\mathbf{K}/2$ appears first when the detuning Ω exceeds a certain minimum value $\Omega_m \approx 2\Omega_f$. Its amplitude grows gradually with increasing Ω to reach a maximum at $\Omega \approx 4\omega_K$. Further increase of the detuning frequency leads to decreasing amplitude of the main

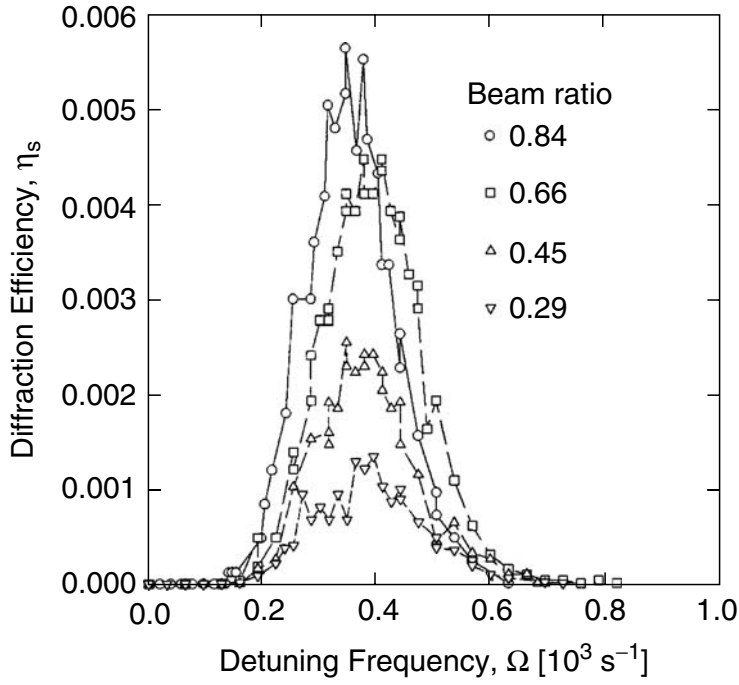

FIGURE 5.8. Dependence of the diffraction efficiency of the subharmonic grating η_s on the detuning frequency Ω for different values of the input pump ratio [34]. The indicated numbers correspond to the contrast values $m \simeq 0.99$, 0.98, 0.92, and 0.83.

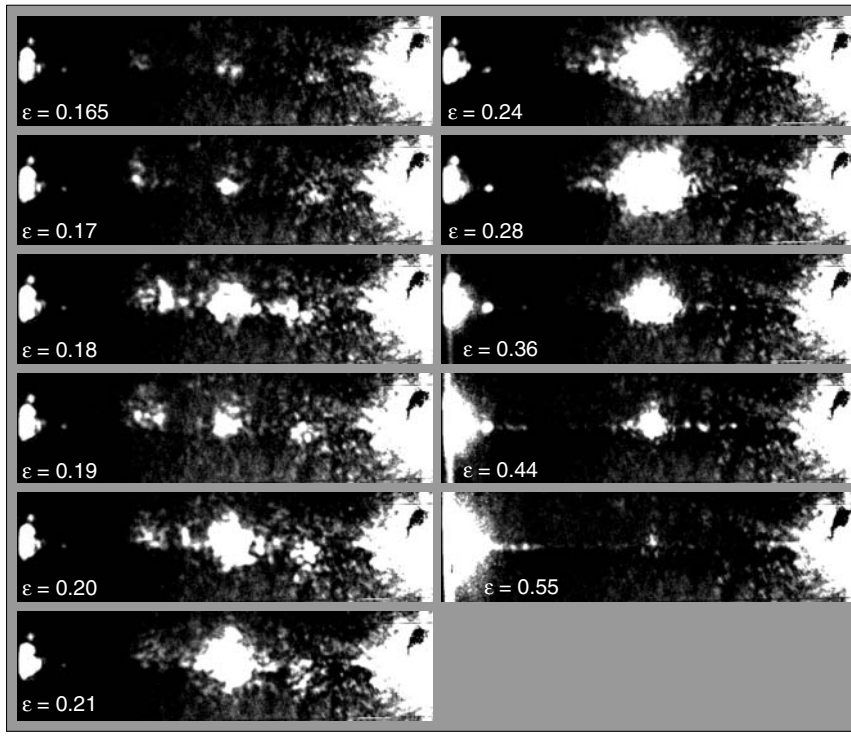

FIGURE 5.9. Intensity distributions on the observation screen for successfully decreasing values of $\varepsilon = \omega_K/\Omega$ (increasing detuning). The bright areas on the left and right sides correspond to diffraction of the read-out beam, Bragg-matched to the main subharmonic, from the fundamental grating [36].

subharmonic and its noticeable longitudinal broadening and split. The longitudinal component of the wavevector of the excited SCWs, k_z, ranges here from $\approx K/3$ to $\approx 2K/3$. For sufficiently large Ω, the instability disappears. It is remarkable that the transverse subharmonic split, observed in the coupling geometry [41, 48], is absent in the noncoupling configuration in agreement with theory. Most probably, this split is caused by the optical nonlinearity.

Comparison of the subharmonic characteristics for the coupling and noncoupling configurations has also been performed in the AC case [35]. With no coupling, a wide spectrum of longitudinal spatial frequencies is excited within a wide interval of light contrast, $0.1 \lesssim m < 1$. In the coupling geometry, the output characteristics are different. This shows that optical coupling strongly affects the subharmonic generation in the AC case. This is not surprising because the effects of optical nonlinearity are especially strong here.

A number of other features relevant to the subharmonic generation, which are found in the coupling configurations, are worthy of attention:

- The expected region of the subharmonic instability on the E_0, Ω-plane corresponds to the observations [39]. It is located nearby the curve $\Omega = const/E_0$ in agreement with the property $\omega_k \propto E_0^{-1}$.
- Characteristics of the subharmonic generation in CdTe crystals (the only semiconductor where this effect is found to date) show a good agreement with the theoretical predictions [61].
- The space-charge field distribution shows the presence of subharmonic domains distinguished by the opposite signs of $E_{K/2}$ [17, 49], which is fully consistent with the symmetry considerations. The boundaries of these domains are moving with the group velocity of SCWs.
- The fine structure of the light beams diffracted from the subharmonic gratings is much more noisy as compared to the structure related to the fundamental grating [46]. This evidences that space-charge fluctuations serve as the seed for the subharmonic instability.

One more interesting point is to estimate the values of the quality factor from the subharmonic experiments using the threshold relations. The data of [12, 39, 52, 100] allow us to estimate the maximum achieved value of $Q_{K/2}$ as (7–9), which is in a good agreement with the expectations. Special measurements of Q_K made in the noncoupling geometry gave the numbers (4–5) [81]. A claim about the values $Q_K \approx 10^2$ has been made on the basis of an observation of anomalously long relaxation of SCWs [103]. This fact was explained later (with moderate values of Q_K) by the critical slowing down near the threshold of an optical oscillation [104].

5.5 High-Contrast Effects in Photorefractive Response

In this section, we set aside the subharmonic generation and consider nonlinear SCW effects in the fast materials that are beyond the linear-contrast approximation. The DC and AC cases will be treated separately. We restrict ourselves to the 1D case when $\mathbf{E}_{ex}$ and $\mathbf{E}_{sc}$ are parallel to the z-axis.

5.5.1 Low-Frequency Peculiarities in the DC-Case

As follows from Sections 5.3 and 5.4, the ranges $\Omega \approx \omega_K$ and $\Omega \gtrsim 4\omega_K$ are relevant to the resonant and parametric excitation of SCWs in the fast PR materials. However, this classification of SCW effects would be incomplete if we ignore the low-frequency range $\Omega \lesssim \omega_K$. New nonlinear resonant phenomena and apparent peculiarities of the PR response occur here.

New nonlinear wave processes can be qualified as confluence processes; they lead to an effective excitation of higher spatial harmonics, $2K$, $3K$, etc. The phase-matching condition for the excitation of the n-th harmonic is $n\Omega = \omega_{nK}$. The frequency $n\Omega$ should be attributed to a driving force whose amplitude is proportional to m^n in the low-contrast region. The presence of such a force

is due to nonlinearity of the material equations. The confluence processes are not expected to be accompanied by instabilities.

Since $\omega_{nK} \propto 1/nK$, we have for the resonant detuning Ω_n,

$$\Omega_n = \omega_K/n^2. \tag{5.40}$$

Thus, there is a sequence of nonlinear resonances, $\omega_K/4$, $\omega_K/9, \ldots$ Zero detuning frequency is the point of accumulation of them. The effects of damping and nonlinear coupling lead to broadening and shifting the resonances, so that the neighboring frequency peaks may overlap. Furthermore, the quality factor Q_{nK} sooner or later becomes small with increasing n and the concept of resonant excitation fails.

Turn now to numerical results for the frequency dependence of the first three Fourier harmonics of space-charge field, E_K, E_{2K}, and E_{3K}, obtained within the basic model [67, 68]. The parameters used are typical for the sillenites: $N_E = 10^{16}\,\mathrm{cm}^{-1}$ and $\mu\tau = 3.75 \times 10^{-7}\,\mathrm{cm}^2/\mathrm{V}$. Thirty spatial harmonics of the space-charge field were taken into account to ensure correct results for arbitrary detuning Ω and light contrast m. For convenience, we use below the normalized quantities $e_n = E_{nK}/E_0$.

Figs. 5.10a–c show what happens with the spectral dependences with increasing m. At $m = 0.05$ the function $|e_1(\Omega)|$ is characterized by a pronounced maximum at $\Omega = \omega_K$. The peak value and width fit well the results obtained in the linear-contrast approximation. The resonant enhancement of the fundamental harmonic leads (owing to nonlinear coupling) to the corresponding peaks for $|e_{2,3}(\Omega)|$. These peaks are relatively weak because they correspond to forced oscillations driven far from resonance. Besides, one sees from Fig. 5.11a that for $\Omega \simeq \omega_K/4$, there is an additional peak for $|e_2(\Omega)|$. It corresponds to the resonant amplification of the second harmonic under the action of a very weak driving force with frequency 2Ω. Remarkable changes occur at $m = 0.5$, Fig. 5.10b. The fundamental peak of $|e_1(\Omega)|$ is wider now, it is displaced to the right and clearly asymmetric. The peak value is considerably smaller than mQ_K. The displacement and asymmetry are manifestations of the positive nonlinear frequency shift of the eigen-frequency ω_K mentioned in the previous section. In the vicinity of zero, one can see an additional narrow and structured peak in the dependence $|e_1(\Omega)|$. It arises because of the nonlinear nonresonant coupling with the higher harmonics. The function $|e_3(\Omega)|$ peaks near the eigen-frequency $\omega_K/4$. The peak of $|e_3(\Omega)|$ looks rather complicated because of an overlap between the eigen and forced oscillations. The values of second and third harmonics remain fairly small yet.

For $m = 1$, the nonlinear effects are most pronounced, see Fig. 5.10c. The fundamental peak of $|e_1(\Omega)|$ now looks as a broad shoulder of the main peak, which is situated at $\Omega = 0$. This new zero peak is fairly narrow; it has a substructure. The second and third harmonics are also characterized by sharp zero peaks; the corresponding peak values are comparable with the maximum value of $|e_1(\Omega)|$. For $\Omega \gtrsim 3\omega_K$, the higher harmonics are negligibly small.

How many harmonics are effectively excited at $m = 1$? The answer depends strongly on the value of Ω. Fig. 5.11 shows the dependence $|e_n|$ for three

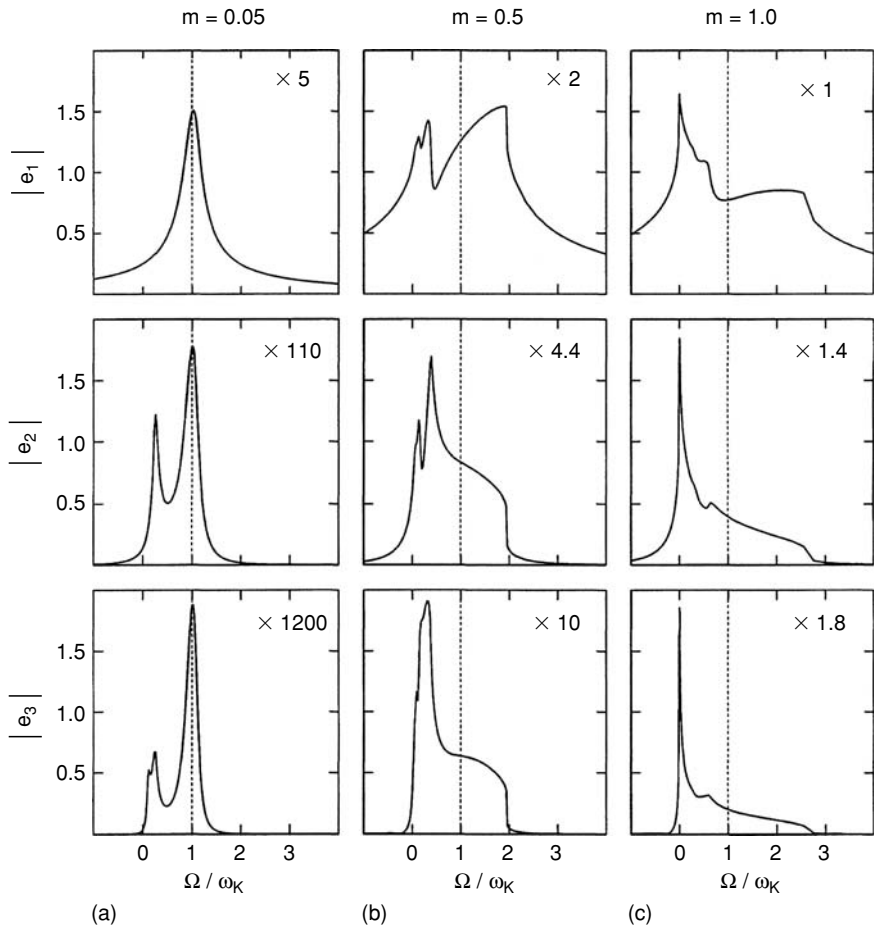

FIGURE 5.10. Absolute values of the normalized amplitudes $|e_{1,2,3}|$ versus the ratio Ω/ω_K for $m = 0.05$ (a), 0.5 (b), and 1 (c) [68]. Note the use of different scaling factors in the subfigures.

representative values of the detuning. For $\Omega = 0$, the decrease of $|e_n|$ with growing n is very slow, about one order of magnitude for 10 numbers. For $\Omega = 2\omega_K$, which corresponds roughly to the middle of the shoulder, a few harmonics are excited. Lastly, for $\Omega = 4\omega_K$, which belongs the subharmonic region, the higher harmonics are not important at all.

One more feature of the spectral dependences is worth mentioning. The positive nonlinear shift of the eigen-frequency ω_K may result not only in asymmetry and steepening of the fundamental peak, but also in ambiguity of the dependence $e_1(\Omega)$. For $\mu\tau \gtrsim 4 \times 10^{-7}\,\mathrm{V/cm^2}$ and $m \geq 0.3$, bistability of the fundamental grating takes place within a certain narrow interval of Ω located

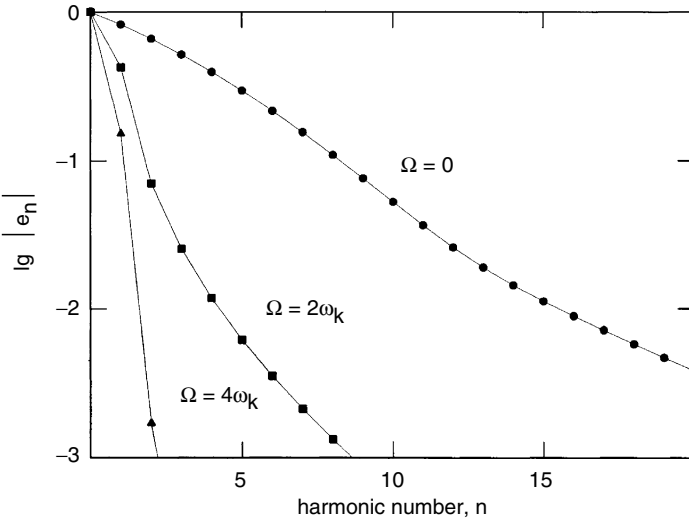

FIGURE 5.11. Dependence of the absolute value of the amplitude of spatial harmonic $|e_n|$ on the number n for different values of the frequency detuning [68].

nearby $2\omega_K$. Increase and decrease of the detuning has to be accompanied by jumps of $|E_K(t)|$ and hysteresis.

Spatial inhomogeneity of the pump intensity and external field leads to nonuniform broadening of the resonances and blurring of fine spectral features. Fluctuations of the positions of the light fringes owing to uncontrollable air draughts give a similar result.

Let us summarize the experimental observations made in the noncoupling geometry with a $Bi_{12}SiO_{20}$ sample [67, 68]. The presence of the zero peak (in addition to the distorted fundamental peak) is clearly seen from Fig. 5.12. With decreasing contrast, this peak disappears. The positive nonlinear frequency shift for the fundamental peak has been detected as well. The second and third harmonics can only be observed in a narrow detuning range near zero. No effects of bistability and hysteresis were observed. Similar results on the zero and fundamental peaks were also obtained in a coupling geometry with the use of a thin (3 mm) $Bi_{12}SiO_{20}$ crystal [69]. The positive shift of fundamental-maximum position was as large as $\approx 50\%$. Thus, there is a reasonable qualitative agreement between theory and experiment with respect to the rough distinctive features of the spectral dependences.

5.5.2 *Rectification Effect*

With the phase modulation technique, employing the intensity modulation $\delta I/I_0 = m\cos(z - \theta\cos\Omega t)$ (see Section 5.3.1), it is possible to detect and describe new SCW effects for $m,\ \theta \ll 1$ [79, 80]. The most interesting of them

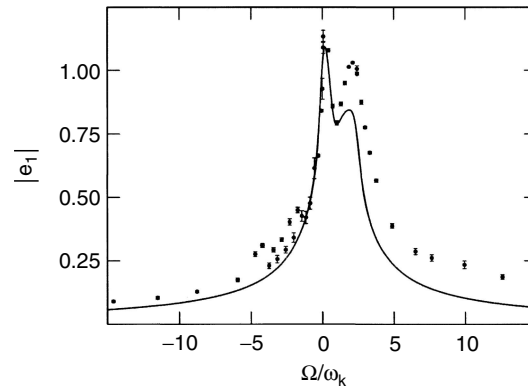

FIGURE 5.12. Measured dependence $|e_1|(\Omega)$ for $m = 0.9$, $E_0 = 4.5$ kV/cm, and $\Lambda = 20$ μm. The solid line is fit the theory to the experiment, see [68].

is perhaps the rectification effect: excitation of additional spatially and/or temporally constant electric fields and currents. Consider briefly this issue.

Among the quadratic nonlinear terms in the basic equations, there is the spatially uniform one that is proportional to $m^2\theta \exp(\pm i\Omega t)/(\Omega - \omega_K + i\gamma_K)$ for $\Omega \approx \omega_K$. It gives a correction to the uniform field (and to the direct current passing through the sample), which is oscillating as $\exp(i\Omega t)$. The resonant frequency dependence of the field correction can be measured electro-optically. The corresponding result for a $Bi_{12}GeO_{20}$ crystal is shown in Fig. 5.13. The presence of the effect and its expected resonant behavior is evident. An oscillation structure of the left wing can be attributed to the low-frequency peculiarities of PR response.

The nonlinear terms proportional to $m^2\theta^2$ are relevant to the correction to the applied field which is spatially-uniform and time-independent; it is referred to as the overall rectification. The experimental measurements of this effect show a reasonable qualitative agreement with the theory [80].

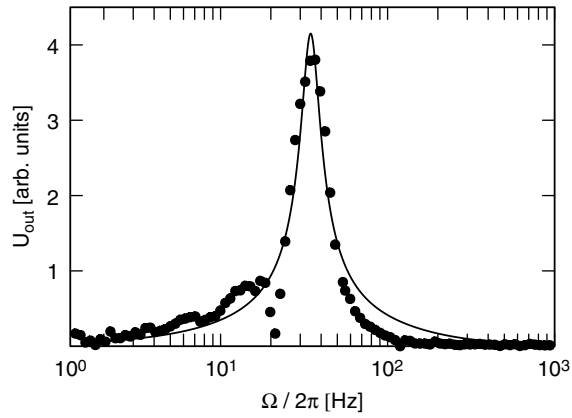

FIGURE 5.13. Dependence of the spatial rectification degree U_{out} on the detuning frequency Ω for a $Bi_{12}GeO_{20}$ crystal, $\Lambda = 50\,\mu$m, $I_0 = 60\,\text{mW/cm}^2$, $E_0 = 7.5\,\text{kV/cm}$, $m = 0.23$, and $\theta = 0.5$. The solid line is theoretical fit. After [79].

5.5.3 Singularity of Photorefractive Response in AC-Case

We suppose that the AC field has a square-wave shape, $\mathbf{E}_{ex}(t) = p\mathbf{E}_0$, and the period of $p(t) = \pm 1$ is much shorter than γ_K^{-1}. We neglect the diffusion contribution to the current density, which is valid for $E_0 \gg (k_B T N_E/\epsilon\epsilon_0)^{1/2}$ and well justified for AC experiments with the sillenites. Then it is possible to additionally simplify the nonlinear Eq. (5.30) using the method of averaging over fast temporal oscillations. Initially, this method was used within the low-contrast approximation [8, 9].

Prior to proceeding particular results, we mention that the AC technique is useful not only for beam coupling applications but also for nonlinear beam propagation. In this connection, the relation $I = I_0 + \delta I$ for the light intensity will be used for two purposes: First, it will be applied for an analysis of grating recording; in this case, I_0 is the total pump intensity and $\delta I = mI_0 \cos(Kz)$. Second, it will be used in an analysis of the field profile, which is induced by a single light beam. Here I_0 and $\delta I = \delta I(z)$ are the background and beam intensities and δI is typically much larger than I_0.

To perform the time-averaging, we set $E_{sc} = E_0(e + \tilde{e})$, where e and $\tilde{e}$ are slow and fast normalized components of space-charge field, such that $\langle e \rangle = e$, $\langle \tilde{e} \rangle = 0$, and $|\tilde{e}| \ll |e|$. By taking the average of Eq. (5.30), recalling that $E_{sc} = -\varphi_z$, and using the fact $N_E \simeq N_A \ll N_0$ in the sillenites, we obtain in the leading approximation:

$$\langle p\tilde{e}_{zt} \rangle = \frac{q s_i N_D I}{\epsilon\epsilon_0 E_0} e. \tag{5.41}$$

Multiplying (5.30) by $p(t)$ and repeating the averaging, we arrive at another algebraic relation between e and $\langle p\tilde{e}_{zt} \rangle$. Combining it with (5.41), we obtain in steady state [73]:

$$\left[\frac{I(1-e^2)}{1 + l_s e_z}\right]_z + \frac{eI}{l_0} = 0; \tag{5.42}$$

as earlier, $l_0 = \mu\tau E_0$ and $l_s = \epsilon\epsilon_0 E_0/qN_E$ are the drift and saturation lengths.

Thus, we have an ordinary second-order differential equation for the field profile. Nonlinearity of this equation comes from the terms e^2 and $l_s e_z$ in the numerator and denominator. In the linear-contrast approximation we return to relation (5.27) for the fundamental grating amplitude. As follows from (5.42), an even intensity distribution $I(z)$ gives an odd field profile $e(z)$. This means that the PR response remains nonlocal in the whole contrast range.

An important observation is that $l_s/l_0 = 1/4Q_{max}^2 \ll 1$, i.e., l_s is the smallest characteristic length parameter in our problem. With $N_E = 10^{16}\,\mathrm{cm}^{-3}$, $\mu\tau = 4 \times 10^{-7}\,\mathrm{cm}^2/\mathrm{V}$, $\epsilon = 56$, and $E_0 = 25\,\mathrm{kV/cm}$ we have $l_s \simeq 0.4\,\mu\mathrm{m}$, $l_0 \simeq 60\,\mu\mathrm{m}$, and $l_s/l_0 \simeq 7 \times 10^{-3}$.

If the characteristic scale of the intensity profile is much larger than l_s, it would be natural to expect the same from the light-induced field profile. If so,

the term $l_s e_z$ in (5.42) is negligible. However, with this term removed, Eq. (5.42) becomes the first-order equation. Its solution cannot meet two always existing physical constrains: $e(z) \to 0$ for $z \to \pm\infty$ in the case of localized beam and $\langle e \rangle = 0$ and $e(z) = e(z + \Lambda)$ for grating recording. Hence the term $l_s e_z$ must be kept. This means that the field profile possesses discontinuities, where the derivative e_z is very high.

Fig. 5.14a shows the distribution $e(z)$ induced by a Gaussian beam, $\delta I/I_0 = f_0 \exp(-4z^2/d^2)$, of the width $d = 0.6 l_0$ for several values of the amplitude f_0. For $f_0 \geq 0.5$, the field profile is characterized by a very pronounced discontinuity at $z = 0$. Outside the narrow discontinuity region, the term $l_0 e_z$ in is negligible. The broad maximum of $e(z)$ occurs far from the discontinuity; an increase of f_0 shifts the position of the maximum to the right and the maximum field saturates approaching 1. The low-contrast approximation is invalid for the main body of the field distribution. The field discontinuity corresponds, indeed, to the singularity of the space-charge distribution; the width of this singularity is about l_s. The case of grating recording is illustrated by Fig. 5.14b. The field profile has the same discontinuity up to very low values of m. For $d \gtrsim 8 l_0$ (or $\Lambda \gtrsim 8 l_0$), the discontinuity disappears; nonlinear SCW effects are weak in this range.

Using (5.42), one can find the amplitudes $e_n(m)$ relevant to grating recording in the whole contrast range [105]. These Fourier components are imaginary quantities; it is sufficient to know their absolute values. Representative results for $n = 1, 2, 3$ are displayed in Fig. 5.15. The normalized fundamental amplitude e_1 grows linearly with m up to $m \approx 0.02$ (the low-contrast range); for larger values of the contrast, the growth of $e_1(m)$ is strongly slowed down. The data of Fig. 5.15 correspond to $Q_K \simeq 6.2$. It is remarkable that fairly wide changes of the parameters N_E, $\mu\tau$, and $\Lambda = 2\pi/K$ do not strongly affect the dependence $|e_1|(m)$, provided that the corresponding values of the quality factor lie in the range (5–7); this range is of prime importance for experiment. Thus, the solid curve in Fig. 5.15a can be considered as a characteristic one.

The data on $e_1(m)$ comply well with the early results of direct numerical calculations and also with an empirical relation for the fundamental grating

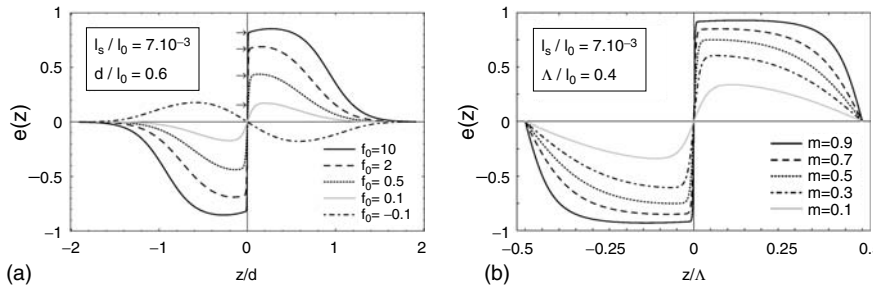

FIGURE 5.14. Normalized space-charge field $e(z)$ induced by a Gaussian light beam of the width $d = 0.6 l_0$ (a) and periodic light pattern of the period $\Lambda = 0.4 l_0$ (b) [73].

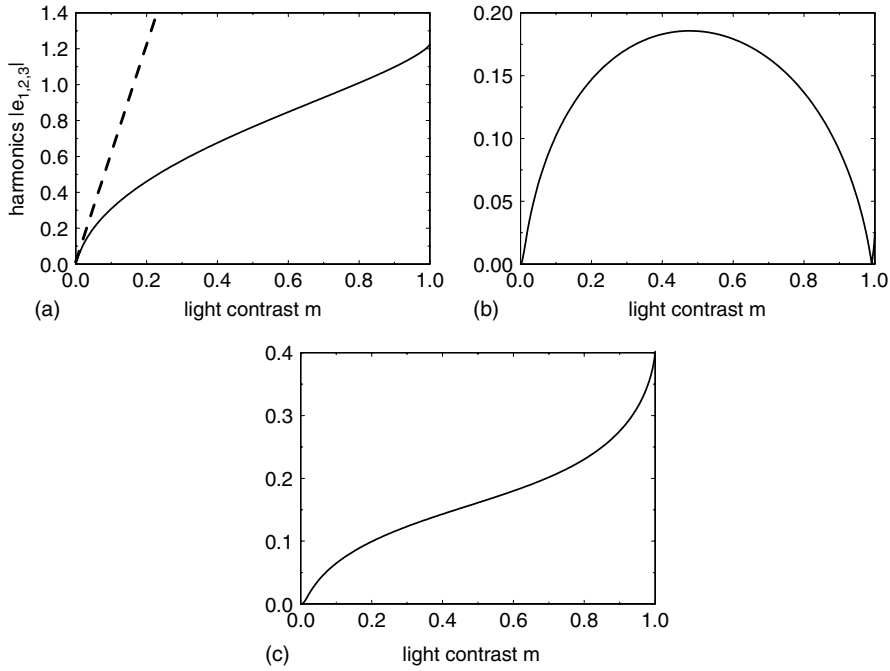

FIGURE 5.15. Dependences $|e_{1,2,3}|(m)$ calculated for $E_0 = 13\,\mathrm{kV/cm}$ and $\Lambda = 13\,\mu\mathrm{m}$; the dashed line in the case (a) shows the result of the linear-contrast approximation [105].

amplitude [106]. They have also serious experimental confirmation obtained in precise 2W-coupling experiments with $Bi_{12}TiO_{20}$ crystals [107]. As follows from Fig. 5.15a, the region of very small contrasts is optimum for spatial amplification of weak signals; enhancement of the fundamental grating results here in extremely high available gain factors. The region of large contrast is best suited for the applications based on distortionless grating recording.

Turn now to the dependences $|e_{2,3}|(m)$ shown in Figs. 5.15b,c. The first function peaks at $m \simeq 0.5$ and approaches zero for $m = 1$. Its maximum value, $|e_2|(0.5)$, is about 0.2. The function $|e_3|(m)$ looks differently. It tends first to saturate at $m \simeq 0.2$ but grows then up to ≈ 0.4 with m approaching 1. The described dependences can be considered as the fingerprints of the AC response. It seems to be, they were never measured in experiment.

5.6 Joint Action of Material and Optical Nonlinearities

Joint action of the material and optical nonlinearities may lead not only to a quantitative complication of the situation but also to qualitatively new optical effects. Below we present two examples of such effects.

5.6.1 Critical Enhancement of Photorefractive Beam Coupling

Consider the arrangement depicted in Fig. 5.16a. Two pump beams, 1 and 2, frequency detuned by Ω, propagate symmetrically near the x-axis of a DC biased crystal appropriate for subharmonic generation. Additionally, a weak signal beam 0, detuned by $\Omega/2$, propagates along the x-axis. Under these conditions, the pump forms a running grating with the grating vector $\mathbf{K}$ while the light pairs 1, 0 and 0,2 contribute to a $\mathbf{K}/2$-grating running with the same velocity. By saying so, we imply that the x-components of the light wavevectors are the same, see Fig. 5.16b. A small deficit (mismatch) Δ of the wavevector k_0 can be treated within the envelope approximation.

Let now the detuning meet the parametric resonance condition $\Omega = 2\omega_{K/2} = 4\omega_K$. It corresponds to the excitation of the subharmonic $K/2$. Furthermore, we assume that the contrast of the pump interference pattern m does not exceed the threshold value $m_{th} = 3/Q_{K/2}$, i.e., the fundamental grating is stable against parametric generation of SCWs.

Prior to writing down the material equation for the subharmonic grating, we present the space-charge field in the form

$$E_{sc} = \frac{E_0}{2}\left[e_1 e^{i(Kz-\Omega t)} + e_{1/2}e^{i(Kz-\Omega t)/2} + c.c.\right], \tag{5.43}$$

where e_1 and $e_{1/2}$ are the normalized amplitudes of the K and $K/2$ gratings. The complex amplitudes of the light waves 0, 1, and 2 we denote as a_0, a_1, and a_2, respectively. They are normalized in such a way that the total intensity $|a_0|^2 + |a_1|^2 + |a_2|^2 \simeq |a_1|^2 + |a_2|^2 \simeq 1$. Correspondingly, the contrast of the pump interference pattern $m = 2|a_1 a_2^*|$. Then, taking into account the results of Sections 5.3 and 5.4, we have for $e_{1/2}$:

$$\left(\frac{\partial}{\partial t} + \gamma_{\mathbf{K}/2}\right)e_{1/2} = i|\omega_{K/2}|\left(\frac{2}{3}a_1 a_2^* e_{1/2}^* - a_0 a_2^* - a_1 a_0^*\right). \tag{5.44}$$

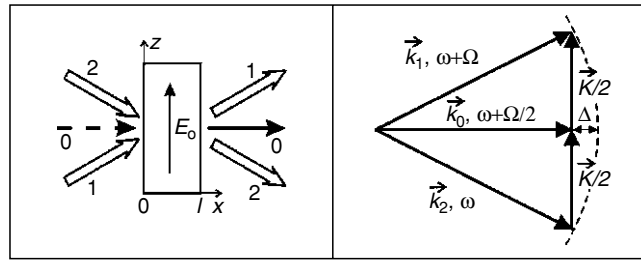

FIGURE 5.16. Schematic of an experiment (a) and wavevector diagram (b) relevant to the critical enhancement; Δ is Bragg mismatch for the central beam.

This equation combines the known constituents. The last two terms of the right-hand side correspond to the linear resonant excitation of the $K/2$ grating by the light pairs 0,2 and 1,0, whereas the first term is relevant to the parametric excitation. This term was missed in the early attempts to explain the subharmonic generation by the optical nonlinearity [18, 19].

Resolving (5.44) in steady state, we get:

$$e_{1/2} = -\frac{iQ}{1-\xi^2}\left[a_0 a_2^*\left(1-\frac{2i}{3}Q|a_1|^2\right)+a_0^* a_1\left(1-\frac{2i}{3}Q|a_2|^2\right)\right], \tag{5.45}$$

where $Q = Q_{K/2}$ and $\xi = m/m_{th} < 1$. One sees that the subharmonic amplitude increases drastically when the contrast m approaches from below the threshold value m_{th}. This feature is robust; it reflects the fact that the subharmonic grating is very liable to the driving force near the threshold.

The amplitude of the central beam a_0 changes with the propagation coordinate x owing to diffraction of the pump beams 1 and 2 on the subharmonic grating, (see Fig. 5.16). The corresponding governing equation has the form

$$\left(\frac{d}{dx}-i\Delta\right)a_0 = -i\kappa(a_1 e_{K/2}^* + a_2 e_{K/2}), \tag{5.46}$$

where $\kappa = \pi n_0^3 r E_0/\lambda, n_0$ is the refractive index, r is the effective electro-optic coefficient, and λ is the light wavelength. The term $i\Delta$ accounts for the Bragg mismatch of the central beam.

Relation (5.45) for $e_{K/2}$ yields a coupling between a_0 and a_0^*. This parametric optical coupling expresses the possibility for beam 1 (or 2) to diffract on the grating that is recorded with the participation of beam 2 (or 1). Such a coupling scheme is typical of PR four-wave processes [108].

By setting $a_0, a_0^* \propto \exp(\Gamma x)$ in (5.45), (5.46), we obtain for two possible values of the gain factor (spatial increment) Γ [76]:

$$\frac{\Gamma_\pm}{\kappa Q} = \frac{W}{1-\xi^2} \pm \sqrt{\left(\frac{W\xi}{1-\xi^2}\right)^2 - \frac{\Delta}{\kappa Q}\left(\frac{6}{Q}\frac{\xi^2}{1-\xi^2}+\frac{\Delta}{\kappa Q}\right)}, \tag{5.47}$$

where $W = |a_1|^2 - |a_2|^2$ is the normalized difference of the pump intensities. The signs $\pm$ correspond to different choices of the phase of the complex input amplitude $a_0(0)$. The positive sign of the product κW favors strongly the spatial amplification. This sign is controlled by the pump ratio and polarization. Below, we focus our attention on this case.

The most important feature of (5.47) is that the upper branch of $\Gamma(m)$ grows infinitely while m is approaching m_{th}. In the close vicinity of the threshold the mismatch Δ is not important and

$$\Gamma \simeq \frac{|\kappa| Q m_{th}\sqrt{1-m_{th}^2}}{m_{th}-m}. \tag{5.48}$$

It is remarkable that the effect of mismatch Δ is negative for $\kappa > 0$, $W > 0$ and positive for $\kappa < 0$, $W < 0$, and $\Delta(1 - \xi^2) < 6|\kappa|\xi^2$. The physical meaning of this feature is simple: Depending on the sign of k, the pump produces a positive or negative correction δk_0 to the wavevector k_0; if this correction is positive, it can be compensated by the mismatch. Optimization of the mismatch effect can be achieved using the dependence of the sign of r on the pump polarization in cubic crystals.

Fig. 5.17 illustrates the contrast dependence of $\Gamma'_{\pm} = \mathrm{Re}(\Gamma_{\pm})$ the sillenites. The chosen parameters are: $\lambda = 514\,\mathrm{nm}$, $E_0 = 7\,\mathrm{kV/cm}$, $n_0 = 2.6$, $|r| = 4.6\,\mathrm{pm/V}$, $Q_{K/2} = 6$, and $\Lambda = 8\,\mu\mathrm{m}$. The solid curves 1,2 and 3,4 are plotted for the cases $\kappa, W < 0$ and $\kappa, W > 0$, respectively. The dashed curve shows the dependence $\Gamma'(m)$ without the effect of material nonlinearity. The curves 1, 2, 3, and 4 coincide for sufficiently small m, when the square root in (5.47) is imaginary. With increasing contrast, the function $\Gamma'(m)$ experiences a bifurcation; the bifurcation point is closer to zero for $\kappa, W < 0$. After the bifurcation, the upper branch goes up rapidly and tends to infinity.

Indeed, the gain factor Γ cannot be infinitely large. The corresponding restriction is, however, rather weak, $\Gamma \lesssim \Lambda^{-1}$. It gives saturation of Γ on the level of $\sim 10^3\,\mathrm{cm}^{-1}$. To avoid the pump depletion, the input intensity of the central beam and the crystal thickness have to be sufficiently small.

To distinguish the critical enhancement from the usual 2W-amplification, it is sufficient to block the weakest pump beam. A strong drop in the gain will prove unambiguously an anomalous strength of the initial effect and the prime role of coupling between the *K* and *K/2* gratings.

Among the factors that are beyond the above model are the effects of vectorial beam coupling and spatial inhomogeneity. They influence quantitatively the

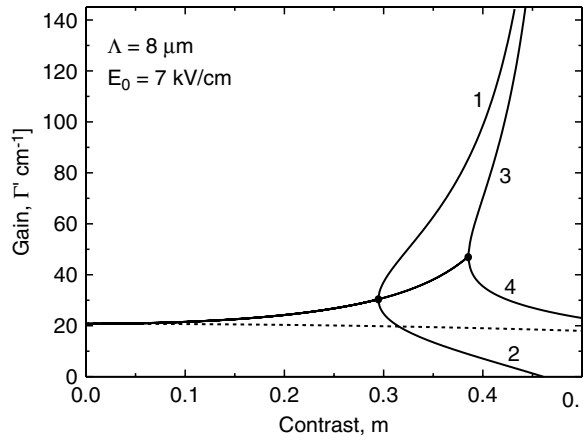

FIGURE 5.17. Dependence of the gain factor $\Gamma'_{\pm}$ on the pump contrast m. The curves 1, 2 and 3, 4 correspond to the cases $\kappa < 0, W < 0$ and $\kappa < 0, W < 0$, respectively. The dashed curve is plotted by setting $\xi = 0$ [76].

output characteristics of interacting light beams but do not suppress the major effect. Particular recommendations for experiment, given on the basis of numerical modeling, include the use of thin (≈ 1 mm) crystals and also the choice of optical configurations and light polarizations [77, 78]. No substantial efforts have been made yet to detect the critical enhancement.

Possibly, the effect in question has manifested itself in early experiments with $Bi_{12}SiO_{20}$ crystals [109]. Using an optical arrangement similar to that shown in Fig. 5.16 and extremely weak input central beams, the authors obtained surprisingly high (up to 10^4) amplification factor despite the strong negative effect of spatial inhomogeneity reducing the net interaction length.

5.6.2 Soliton-Like Beam Propagation in AC-Biased Crystals

We know from Section 5.5 that a localized light beam creates in the AC case a narrow discontinuity of the space-charge field (and refractive index) at the intensity maximum. This discontinuity separates the regions of strong self-focusing/defocusing. Two opposing tendencies occur here. On the one hand, the material nonlinearity works to support the discontinuity. On the other hand, diffraction by the abrupt index profile tends to wash it out. What kind of nonlinear beam propagation is expected in this situation? Is it beam broadening accompanied by disappearance of the charge singularity, or soliton propagation coupled with the field discontinuity, or something else? This question is of interest for both theory and experiment.

To illuminate the background of the problem, we mention that the soliton propagation is not possible in the case of nonlocal gradient response driven by diffusion transport [110, 111]. The known cases of soliton propagation in PR materials are associated with the local response [112].

To describe the nonlinear beam propagation, Eq. (5.42) for $e(z)$ was solved numerically together with the nonlinear 2D Srödinger equation for the beam envelope Ψ,

$$2ikn_0\Psi_x + \Psi_{zz} = k^2 n_0^4 r E_0 e \Psi, \tag{5.49}$$

where $k = 2\pi/\lambda$, $|\Psi|^2 = I$, and x is the propagation coordinate.

The simulation results for the distributions of light intensity $I(x, z)$ and index change $\delta n(x, z)$ are presented in Fig. 5.18 [75]. The propagation distance $x_0 = 6$ mm exceeds considerably the characteristic nonlinear length of the intensity changes $(kn_0^3 r E_0)^{-1} \simeq 0.5$ mm. Thus, the depicted spatial evolution is strongly nonlinear.

The solid lines in Fig. 5.19 are the snapshots of the transverse intensity profile for several values of the propagation distance. As seen from Fig. 5.19b, already at $x = 1$ mm the beam experiences remarkable changes. It splits into the main central component (core) and two side filaments. These changes are mainly due to diffraction at the discontinuity and focusing/defocusing on

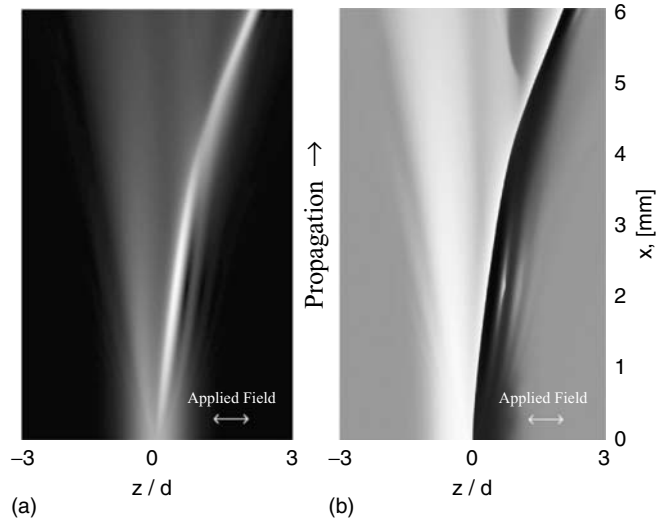

FIGURE 5.18. Spatial evolution of the light intensity (a) and the light-induced index (b) for an input Gaussian beam. The bright areas correspond to the high values of the variables. The model parameters correspond to Fig. 5.14, the normalized beam amplitude $f_0 = 10$, and the input beam width $d = 36\,\mu$m.

the negative/positive regions of the input ($x = 0$) index profile. The subsequent evolution involves strong changes of the index profile. The core of the light beam remains of the same width after the initial compression (see Fig. 5.19c–f). Its amplitude pulsates modestly with x. The index discontinuity persists; it runs toward the right with a roughly quadratic displacement in x, Fig. 5.18. The main beam is attached to the discontinuity, it shows a permanent bending. In the gradient case, the beam disperses quickly because of diffraction.

The described behavior resembles the soliton propagation [112, 113]. Trapping of the beam core certainly takes place. However, identification of the trapped component with a soliton would not be fully correct. Energy leakage from the core permanently takes place so that the beam would be dispersed for sufficiently long propagation distances. For moderate distances, which are of practical interest, the energy losses can be disregarded. The robustness of the trapped component is due to the specific properties of the AC response.

The only experiment relevant to the subject was performed with a $Bi_{12}SiO_{20}$ crystal [114]. The observed filamentation of a Gaussian beam is in line with the model results. However, optical activity affected strongly the nonlinear propagation. To avoid this harmful effect, the use of $Bi_{12}TiO_{20}$ crystals is needed. The above scalar model is applicable to this material.

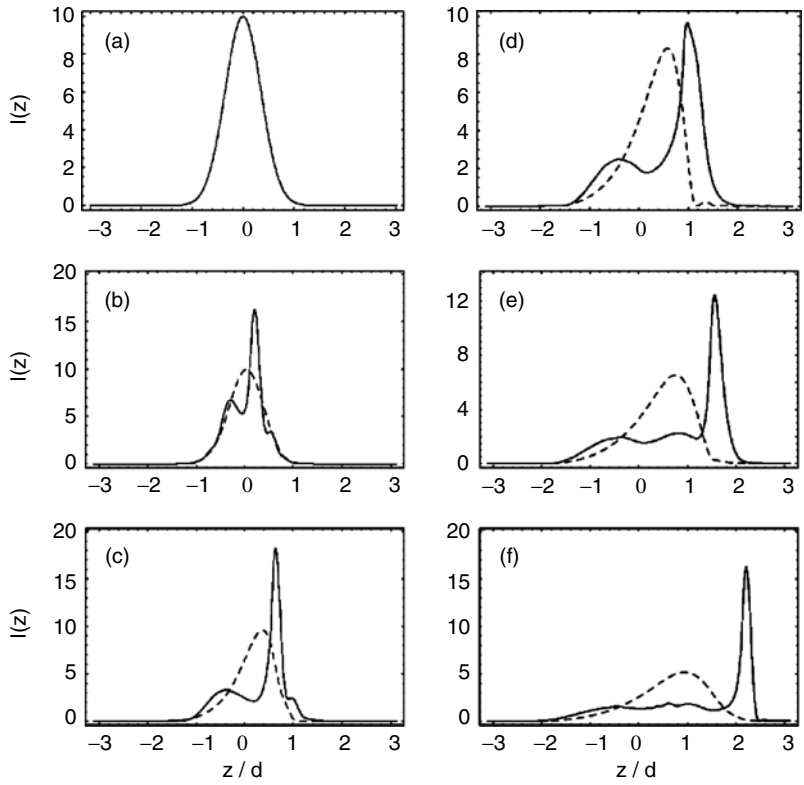

FIGURE 5.19. Normalized beam profiles (a)–(f) corresponding to the propagation distance $x = 0, 1, 3, 4, 5$, and 6 mm, respectively. The dotted lines refer to the case of the gradient response of the same strength [75].

5.7 Conclusions

We have considered above a broad spectrum of the effects relevant to the excitation of weakly damped eigen-modes in fast and slow PR materials. These SCW effects are fully due to large values of the quality factor, $Q_{\mathbf{k}} \gg 1$. They include a great deal of the fundamental physical content owing to generality of the concept of resonance. Instability of the light-induced gratings—one of the pillars of the photorefractive science—is a good example of importance of the subject matter. The SCW effects are typically very pronounced because of an interplay between the space-charge and light waves. Many of them are important (or potentially important) for applications.

Involvement of the material nonlinearity is a remarkable feature of the SCW effects. This involvement becomes already pronounced at low levels of the light contrast. It makes illusive the hopes to describe universally the medium

response in the whole contrast range on the basis of low-contrast approximations. Variety of charge transport properties in photorefractive materials leads to a wealth of expected resonant phenomena combining the optical and material nonlinearities.

A number of SCW effects are already well established. Among them are the DC and AC enhancement of the space-charge field, generation of spatial subharmonics, high-contrast peculiarities of the photorefractive response in the sillenites, the effect of rectification. At the same time, vast and promising areas of the studies remain almost unexplored. Among them are semiconductive PR crystals like GaAs and CdTe, ferroelectrics like $LiNbO_3$ and SBN, the effects occurring above the threshold of instability of the fundamental grating, the effects combining strong material and optical nonlinearities.

The terms and methods of wave interactions provide the natural language for understanding and description of the effects involving weakly damped space-charge waves. They give a link with the other known and important wave phenomena. The ratio $\gamma_{\mathbf{k}}/|\omega_{\mathbf{k}}| \equiv Q_{\mathbf{k}}^{-1}$ serves as the small parameter in analyzing the characteristics of SCW effects.

Acknowledgements: I am grateful to P.M. Johansen and S.G. Odoulov for discussions and to M.V. Gorkounov and O.S. Filippov for technical support.

References

1. R.F. Kazarinov, R.A. Suris, B.I. Fuks: Sov. Phys. Semicond. **6**, 500 (1972); *ibid* **7**, 102 (1973).
2. N.G. Zhdanova, M.S. Kagan, R.A. Suris, B.I. Fuks: Sov. Phys. JETP **47**, 189 (1978).
3. J.-P. Huignard, A. Marrakchi: Opt. Commun. **38**, 249 (1981).
4. S.I. Stepanov, K. Kulikov, M. Petrov: Opt. Commun. **44**, 19 (1982).
5. P. Refregier, L. Solymar, H. Rajbenbach, J.-P. Huignard: J. Appl. Phys. **58**, 45 (1985).
6. G. Hamel de Montchenault, B. Loiseaux, J.P. Huignard, Electron. Lett. **22**, 1030 (1986).
7. L. Solymar, D.J. Webb A Grunnet-Jepsen: *The Physics and Applications of Photorefractive Materials*, Oxford, Clarendon Press (1996).
8. S.I. Stepanov, M.P. Petrov: Opt. Commun. **53**, 292 (1985).
9. M.P. Petrov, S.I. Stepanov, A.V. Khomenko: *Photorefractive Crystals in Coherent Optical Systems*, Springer-Verlag, Berlin (1991).
10. S. Mallick, B. Imbert, H. Ducollet et al: J. Appl. Phys. **63**, 5660 (1988).
11. D.J. Webb, L. Solymar: Opt. Commun. **74**, 386 (1990).
12. D.J. Webb, L.B. Au, D.C. Jones, L. Solymar: Appl. Phys. Lett. **57**, 1602 (1990).
13. D.C. Jones, S.F. Lyuksyutov, L. Solymar: Appl. Phys. B **52**, 173 (1991).
14. J. Takacs, M. Schaub, L. Solymar: Opt. Commun. **91**, 252 (1992).
15. J. Takacs, L. Solymar: Opt. Lett. **17**, 247 (1992).
16. C.H. Kwak, M. Shamonin, J. Takach, L. Solymar: Appl. Phys. Lett. **62**, 328 (1993).
17. A. Grunnet-Jepsen, S.J. Elston, I. Richter et al: Opt. Lett. **18**, 2147 (1993).
18. K.H. Ringhofer, L. Solymar: Appl. Phys. Lett. **53**, 1039 (1988).

19. K.H. Ringhofer, L. Solymar: Appl. Phys. B **48**, 395 (1989).
20. L.B. Au, L. Solymar: Opt. Lett. **13**, 660 (1990); J. Opt. Soc. Am. A **7**, 1554 (1990).
21. L.B. Au, L. Solymar, K.H. Ringhofer: Tech. Digest of Topical Meeting on "Photorefractive Materials, Effects and Devices II," Aussois, France, p. 87 (1989).
22. A. Bledowski, B.I. Sturman, J. Otten, K.H. Ringhofer: Proc. Topical Conf. on "Photorefractive Materials, Effects and Devices," Beverly, USA, (1991).
23. O.P. Nestiorkin: Opt. Commun. **81**, 315, (1991).
24. B.I. Sturman, M. Mann, J. Otten et al: Appl. Phys. A **55**, 55 (1992).
25. B.I. Sturman, A. Bledowski, J. Otten, K.H. Ringhofer: J. Opt. Soc. Am. B **9**, 672 (1992).
26. A. Bledowski, J. Otten, K.H. Ringhofer, B.I. Sturman: Sov. Phys. JETP **75**, 215 (1992).
27. B.I. Sturman, M. Mann, K.H. Ringhofer: Opt. Lett. **17**, 1620, (1992).
28. B.I. Sturman, M. Mann, K.H. Ringhofer: Appl. Phys. A **55**, 235 (1992).
29. O.P. Nestiorkin, Y.P. Shershakov: J. Opt. Soc. Am. B **10**, 1909, (1993).
30. Y.P. Shershakov, O.P. Nestiorkin: Opt. Commun. **96**, 271, (1993).
31. B.I. Sturman, M. Mann, J. Otten, K.H. Ringhofer: J. Opt. Soc. Am. B **10**, 1919 (1993).
32. V.N. Alimpiev, R. Gural'nik: Sov. Phys. Semicond. **20**, 512 (1986).
33. T.E. McClelland, D.J. Webb, B.I. Sturman, K.H. Ringhofer: Phys. Rev. Lett. **73**, 3082 (1994).
34. B.I. Sturman, T.E. McClelland, D.J. Webb et al: J. Opt. Soc. Am. B **12**, 1621 (1995).
35. H.C. Pedersen, P.M. Johansen, D.J. Webb: J. Opt. Soc. Am. B **11**, 1528 (1998).
36. H.C. Pedersen, D.J. Webb, P.M. Johansen: J. Opt. Soc. Am. B **11**, 2439 (1998).
37. V.S. Liberman, B. Ya. Zel'dovich: Optical and Quantum Electronics **25**, 231 (1993).
38. M. Shamonin: Appl. Phys. A **57**, 153 (1993).
39. C.H. Kwak, J. Takach, L. Solymar: Opt. Commun. **96**, 278 (1993).
40. A. Grunnet-Jepsen, I. Richter, M. Shamonin, L. Solymar: J. Opt. Soc. Am. B **11**, 132 (1994).
41. H. Pedersen, P.M. Johansen: Opt. Lett. **19**, 1418 (1994).
42. E. Serrano, M. Carrascosa, F. Agullo-Lopez, L. Solymar: Appl. Phys. Lett. **64**, 658 (1994).
43. I. Richter, A. Grunnet-Jepsen, J. Takacs, L. Solymar: IEEE J. Quantum Electron. **QE-30**, 1645 (1994).
44. H.C. Pedersen, P.M. Johansen: J. Opt. Soc. Am. B **12**, 1065 (1995).
45. P.M. Johansen, R.S. Hansen, T. Olsen: Opt. Commun. **115**, 308 (1995).
46. P. Buchhave, S. Lyuksyutov, M. Vasnetsov: Opt. Lett. **20**, 2363 (1995).
47. R.V. Litvinov, S.N. Pinchenko, A.V. Reshet'ko: Sov. Tech. Phys. Lett. **21**, 134 (1995).
48. H.C. Pedersen, P.M. Johansen: Phys. Rev. Lett. **77**, 3106 (1996).
49. P. Buchhave, S. Lyuksyutov, M. Vasnetsov, C. Heyde: J. Opt. Soc. Am. B **13**, 2595 (1996).
50. H.C. Pedersen, P.M. Johansen: J. Opt. Soc. Am. B **13**, 590 (1996).
51. B.I. Sturman, M. Aguilar, F. Agullo-Lopez, K.H. Ringhofer: Phys. Rev. E **55**, 6072 (1997).
52. R.V. Litvinov, S.M. Shandarov, D.V. Yakimov et al: Sov. Tech. Phys. **42**, 1400 (1997).
53. Yu.M. Miklyaev, V.I. Safonov: J. Nonlinear Optical Physics and Materials **6**, 103 (1997).
54. H.C. Pedersen, P.M. Johansen: J. Opt. Soc. Am. B **14**, 1418 (1997).

55. B.I. Sturman, E. Shamonina, K.H. Ringhofer: Proceedings of the Topical Meeting on Photorefractive Materials, Effects, and Devices, PRM'97, 145, Chiba, Japan (1997).
56. E.V. Podivilov, H.C. Pedersen, P.M. Johansen et al: Phys. Rev. E **57**, 6112, (1998).
57. B.I. Sturman, A.I. Chernykh, E.A. Shamonina: J. Experimental and Theoretical Physics **87**, 563 (1998).
58. H.C. Pedersen, P.M. Johansen, E.V. Podivilov, B.I. Sturman: Phys. Rev. A **58**, 1601, (1998).
59. B. Sturman, A. I. Chernykh, E. Shamonina et al: J. Opt. Soc. Am. B **16**, N 7 (1999).
60. P.M. Johansen, H.C. Pedersen, E.V. Podivilov, B.I. Sturman: J. Opt. Soc. Am. B **16**, 103, (1999).
61. K. Shcherbin: Appl. Phys. B **70, 1** (2000).
62. B.I. Sturman, E. Shamonina, M. Mann, K.H. Ringhofer: J. Opt. Soc. Am. B **12**, 1642 (1995).
63. M. Luennemann K. Buse, B. Sturman: J. Appl. Phys. **94**, N 10 (2003).
64. B. Sturman, M. Aguilar, F. Agullo-Lopez: Phys. Rev. B **54**, 13737 (1996).
65. N.A. Kornev, J.J. Sanchez Modragon, S.I. Stepanov: Opt. Commun. **133**, 109 (1997).
66. B.I. Sturman, M. Mann, K.H. Ringhofer: Opt. Lett. **18**, 702 (1993).
67. T.E. McClelland, D.J. Webb, B.I. Sturman, M. Mann, K.H. Ringhofer: Opt. Commun. **113**, 371 (1995).
68. T.E. McClelland, D.J. Webb, B.I. Sturman et al: Opt. Commun. **131**, 315 (1996).
69. M. Vasnetsov, P. Buchhave, S. Lyuksyutov: Opt. Commun. **137**, 181 (1997).
70. H.C. Pedersen, P.M. Johansen, E. Podivilov, D.J. Webb: Opt. Commun. **154**, 93 (1998).
71. B.I. Sturman, E. Podivilov, A.I. Chernykh et al: J. Opt. Soc. Am. B **16**, 556 (1999).
72. S.M. Shandarov, N.I. Nazhestkina, O.V. Kobosev, A.A. Kamshilin: Appl. Phys. B **68**, 1007 (1999).
73. G.F. Calvo, B. Sturman, F. Agullo-Lopez, M. Carrascosa: Phys. Rev. Lett. **84**, 3839 (2000).
74. G.F. Calvo, B. Sturman, F. Agullo-Lopez, M. Carrascosa: Opt. Materials, **18**, 175 (2001).
75. G.F. Calvo, B. Sturman, F. Agullo-Lopez, M. Carrascosa: Phys. Rev. Lett. **89**, 033902 (2002).
76. E. Podivilov, B.I. Sturman, H.C. Pedersen, P.M. Johansen: Phys. Rev. Lett. **85**, 1867 (2000).
77. E.V. Podivilov, B.I. Sturman, K.H. Ringhofer et al: Phys. Rev. E **65** 046623 (2002).
78. M.V. Gorkunov, E.V. Podivilov, B.I. Sturman: J. Experimental and Theoretical Physics **94**, 470 (2002).
79. M.P. Petrov, A.P. Paugurt, V.V. Bryksin et al: Phys. Rev. Lett. **84**, 5114 (2000).
80. M.P. Petrov, V.V. Bryksin, H. Vogt et al: Phys. Rev. B **66**, 085107 (2002).
81. H.C. Pedersen, D.J. Webb, P.M. Johansen: J. Opt. Soc. Am. B **15**, 2573 (1998).
82. M.P. Petrov, V.V. Bryksin, V.M. Petrov et al: Phys. Rev. A **60**, 2413 (1998).
83. P. Günter and J.-P. Huignard, eds., *Photorefractive Materials* and Their Applications, *I, Vol. 61 of Topics in Applied Physics, Springer-Verlag, Berlin* (1988).
84. A.M. Glass, D. von der Linde, T.J. Negran: Appl. Phys. Lett. **25**, 233 (1974).
85. B.I. Sturman, V.M. Fridkin: *Photovoltaic and Photorefractive Effects in Noncentrocymmetric Materials*, Gordon & Breach, Philadelphia (1992).
86. K. Buse: Appl. Phys. B **64**, 391 (1997).
87. A.S. Furman: Sov. Phys. Solid State **29**, 617 (1987).
88. A.S. Furman: Ferroelectrics **83**, 41 (1988).
89. M. Luennemann, U. Hartwig, K. Buse: J. Opt. Soc. Am. B **20**, 1643 (2003).

90. I. Aubrecht, H.C. Ellin, A. Grunnet-Jepsen, L. Solymar: J. Opt. Soc. Am. B **12**, 1918 (1995).
91. G. Martin and S. Makram-Ebeid: In *Deep Centers in Semiconductors, a State of the Art Approach*, edited by S. T. Pantelides Chap. 6, p. 399, Gordon and Breach, New York (1985).
92. P. Silverberg, P. Omling, L. Samuelson: Appl. Phys. Lett. **52**, 1689 (1988).
93. M.B. Klein, S.W. McCahon, T.F. Boggers, G.C. Valley: J. Opt. Soc. Am. B **5**, 2467 (1988).
94. G.C. Valley, H. Rajbenbach, H.J. Bardeleben: Appl. Phys. Lett. **56**, 364 (1990).
95. B. Imbert, H. Rajbenbach, S. Mallick et al: Opt. Lett. **13**, 327 (1988).
96. V. Ya. Prinz, S.N. Rechkunov: Phys. Stat. Sol. B **118**, 159 (1983).
97. K. Walsh, A.K. Powell, C. Stace, T.J. Hall: J. Opt. Soc. Am. B **7**, 288 (1990).
98. E. Raita, A. Kamshilin, V. Prokofiev, T. Jaaskelainen: Appl. Phys. Lett. **70**, 1641 (1997); H. Tuovinen, A. Kamshilin, T. Jaaskelainen: J. Opt. Soc. Am. B **14**, 3383 (1997).
99. A. Yariv, P. Yeh: *Optical Waves in Crystals*, Ch. 12 Wiley & Sons (1984).
100. J. Takacs, L. Solymar: unpublished (1991).
101. B.I. Sturman, E.V. Podivilov, E. Shamonina et al: Phys. Rev. E **60**, 3332 (1999).
102. B.I. Sturman, D.J. Webb, R. Kowarschik et al: J. Opt. Soc. Am. B **11**, 1813 (1994).
103. S.L. Lyuksyutov, P. Buchhave, M. Vasnetsov: Phys. Rev. Lett. **79**, 67 (1997).
104. B.I. Sturman, E. Podivilov, H.C. Pedersen, P.M. Johansen: Opt. Lett. **24**, 1163 (1999).
105. O. Filippov, K.H. Ringhofer, B.I. Sturman: Eur. Phys. J. D **23**, 285 (2003).
106. G.A. Brost: J. Opt. Soc. Am. B **9**, 1454 (1992).
107. J.E. Millerd, E.M. Garmine, M.B. Klein et al: J. Opt. Soc. Am. B **9**, 1449 (1992).
108. B.I. Sturman, S.G. Odoulov, M. Yu. Goul'kov: Phys. Reports **275**, 197 (1996).
109. D.C. Jones, L. Solymar: Electron. Lett. **25**, 844 (1989).
110. D.N. Christodoulides, M.I. Carvalho: Opt. Lett. **19**, 1714 (1994).
111. D.N. Christodoulides, T.H. Coskun: Opt. Lett. **21**, 1460 (1996).
112. G.I. Stegeman, M. Segev: Science **286**, 1518 (1999); M. Segev, G.C. Valley, B. Crosignany et al: Phys. Rev. Lett. **73**, 3211 (1994).
113. G.L. Lamb Jr. *Elements of Soliton Theory*, (Willey, New York, 1980).
114. C.A. Fuentes-Hernandez, A.V. Khomenko: Phys. Rev. Lett. **83**, 1143 (1999).

6

Feedback-Controlled Photorefractive Beam Coupling

B.I. Sturman[1] E.V. Podivilov[1], M.V. Gorkunov[2], and S.G. Odoulov[3]

[1] International Institute for Nonlinear Studies, Institute of Automation and Electrometry, 630090 Novosibirsk, Russia
sturman@iae.nsk.su
[2] University of Osnabrück, D-49069 Osnabrück, Germany
mgorkoun@uni-osnabrueck.de
[3] Institute of Physics, National Academy of Science, 252650 Kiev, Ukraine
odoulov@iop.kiev.ua

Implementation of certain electronic feedbacks between the optical output and input is able not only to stabilize the photorefractive setups against phase fluctuations, but also to shape the characteristics of grating recording and beam coupling. In particular, the feedback can make the index gratings fully diffractive and transparent. We summarize the results of experimental and theoretical studies of the feedback-controlled beam coupling. This includes the feedback loop specification, an analysis of the operation modes of the whole nonlinear system, a description of the observable characteristics, and comparison with experiment. We consider both the transmission and reflection coupling geometries and touch upon the major applications.

It is important that the feedback-controlled beam coupling represents a fundamentally new nonlinear system, which has no close analogs among the known optical phenomena. This is concerned with several aspects: Formulation of the feedback conditions for the light amplitudes requires a refined notion of the diffractive properties of dynamic index gratings—it cannot be accomplished in the terms of spatially-uniform gratings. Inertia of the feedback loop ensures the permanent operation of the whole system. The conventional set of dynamic equations for the light and grating amplitudes, being supplemented by the feedback conditions, ceases often to admit both the traditional means for analytical analysis and the familiar steady-state solutions. Instead of a steady state, the system arrives at a periodic state that is characterized by a strong phase modulation.

6.1 Introduction

The photorefractive (PR) nonlinearity implies charge separation under light and refractive index changes via the linear electro-optic effect [1–3]. It is often saturated in the mW-intensity range and manifests itself in numerous optical effects already in fairly thin ($\sim$ 1 mm) samples. These effects include recording of diffraction gratings, spatial amplification of weak signals, phase conjuga-

tion, optical oscillations, formation of spatial solitons, and others. Among the relevant PR materials are ferroelectric crystals ($LiNbO_3$, $BaTiO_3$, SBN...), crystals of the sillenite family (BSO, BTO, and BGO), semiconductors GaAs, CdTe, InP..., and numerous polymers. The strength and availability of the photorefractive effects make them attractive for many applications [4].

An inherent feature of the PR nonlinearity is its slowness. The characteristic response (build-up) time is usually inversely proportional to the light intensity and ranges (depending on the material) from 10^{-2} to 10^2 s in continuous-wave experiments [1, 2]. This time is attributed to the processes of drift and/or diffusion of photo-excited electrons (holes). The buildup time of the index changes increases by several orders of magnitude in the case of thermal fixing, which makes the light-induced gratings permanent and implies migration of low-mobile ions [5, 6]. The condition of stability of the light-interference pattern during such long times, which is necessary for employment of the PR effects, is often inaccessible because of various mechanical fluctuations and air draughts.

The idea of an active stabilization of the photorefractive setups by means of introduction of electronic feedbacks goes back to the late 1960s, see [7–9]. It makes use of the property of slowness of the PR nonlinearity. A number of feedback schemes were aimed first at compensation of the input phase differences, i.e., at prevention of movement of the light-interference pattern at the input, by using linear optic elements. Such schemes do not lead to new nonlinear optical effects.

The photorefractive schemes that we shall deal with are distinguished by the fact that the feedback condition couples the *input* and *output* values of the light amplitudes. The nonlinear behavior of the amplitudes inside the medium is expected to obey the conventional dynamic equations for the PR beam coupling. The relevant feedback condition incorporates thus the coupling effects in the bulk; it is essentially nonlinear and cannot be reduced to stabilization of the input light pattern. At the same time, it compensates for the phase fluctuations, i.e., is noise-free.

The electronic feedback loop in question, governing the input phase φ_s, (see Fig. 6.1), was implemented first in 1986 in two-wave coupling experiments with $Bi_{12}TiO_{20}$ crystals [10]. In this and the subsequent feedback experiments conducted in the transmission geometry, it was found that the feedback produces remarkable changes in the dynamics of two-beam coupling and in the diffractive properties of the recorded index grating [11–16]. In particular, the grating could be made almost fully diffractive or transparent whereas mechanical instabilities and light-induced scattering, inherent in many PR experiments, could be strongly suppressed [12, 13, 15]. The same feedback was successfully used for stabilization of the thermal fixing procedure [17]. Recently, it was also applied to stabilize two-wave coupling in SPS crystals [18] that are distinguished by strong charge competition and nontrivial grating dynamics [19].

Interpretation of the experimental data given in the above papers was based on the assumption of a spatially-uniform grating whose amplitude is constant across the sample and whose fringes are not bent. Unfortunately, this

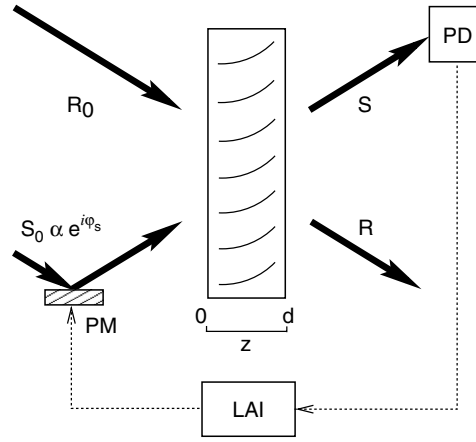

FIGURE 6.1. Schematic of a feedback-controlled two-wave coupling experiment; PD is a photo-diode, LAI is a lock-in amplifier and integrator, and PM is a piezo-mirror. The bent lines show schematically the grating fringes.

assumption is not compatible with the conventional basic relations for the PR beam coupling. At the same time, this interpretation included the distinct idea of $\pm\pi/2$ phase shift between the diffracted and transmitted components of the signal wave (S-wave in Fig. 6.1). This idea was found to be fruitful in the subsequent studies.

The first consistent formulation of the feedback problem for the transmission geometry was proposed in 1997 [21]. It admitted arbitrary distortions of the grating fringes, included the known dynamic equations for the light and grating amplitudes, and included new boundary conditions properly expressing the idea of the $\pm\pi/2$ phase shift Φ_s between the diffracted and transmitted components of the signal beam. Despite its apparent simplicity, the formulated physical problem turned out to be essentially new; it had no analogs among the known nonlinear wave phenomena. This new quality is deeply rooted in the peculiarity of the whole situation—the temporal development of a nonlinear distributed system is constrained by a nonlinear feedback condition $\Phi_s = \pm\pi/2$ that couples the wave amplitudes on the opposite faces of the sample.

The progress ensuing the first formulation was greatly based on numerical simulations. The main findings for the case of local PR response, typical of $LiNbO_3$ crystals, can be summarized as follows [21]:

- The feedback conditions $\Phi_s = \pm\pi/2$ are not always compatible with the presence of steady-state solutions of the coupled-wave equations.
- Steady states, if they exist, can be achieved (after a transient stage) only within a restricted (below-threshold) area of the input parameters—the coupling strength and the intensity ratio.
- By adjusting the phase difference Φ_s to $\pm\pi/2$, the feedback introduces generally a frequency shift Ω between the S- and R-beams in steady state, i.e., makes the index grating moving.
- For sufficiently large values of the coupling strength and small differences in the input intensities, the feedback leads the system to a state with $\eta = 1$ or 0

(η is the diffraction efficiency of the grating); the corresponding transient time is comparable with the PR response time. The feedback signal, however, inevitably turns to zero at this ultimate state so that the model remains correct only within a restricted time interval. The permanent evolution of the system, which is the case of experiment, cannot be governed by the feedback conditions $\Phi_s = \pm\pi/2$, which will be referred to as the ideal ones.

The next step in modelling of the feedback-controlled beam coupling was made in 2001 [23, 24]. It was found that weak inertia of the feedback loop is responsible for the permanent operation of the whole system. With this factor taken into account, the feedback conditions become dynamic—they include the time derivatives and the feedback-loop response time t_f. The inertial feedback conditions possess an important general property: If the diffraction efficiency η is not very close to the ultimate values 1 or 0 and the time t_f is small as compared to the PR response time t_r, they are not significantly different from the ideal $\pm\pi/2$ feedback conditions.

The inertial feedback conditions, as it was proven in numerical experiments, ensure the permanent operation. At the initial stage, when η is far from its ultimate values, they keep the phase difference Φ_s between the diffracted and transmitted components of the signal wave very close to the ideal $\pm\pi/2$ values. As the efficiency η approaches 1 or 0, the deviations of Φ_s from $\pm\pi/2$ become more and more pronounced and the inertia becomes more and more important.

Finally the system arrives at a periodic state (attractor) that is controlled by the feedback inertia. At this state, the diffraction efficiency η experiences small periodic oscillations nearby the ultimate values 1 or 0; the phase difference Φ_s experiences strong anharmonic oscillations, whereas the input phase φ_s shows strong quasi-harmonic oscillations superimposed on a linear trend. The last feature means the introduction (by the feedback) of a permanent frequency detuning Ω between the interacting light beams. The oscillation period T decreases with decreasing t_f. The predicted behavior differs dramatically from the behavior typical of the feedback-free beam coupling.

It is significant that the periodic state is not unique. Different attractors are distinguished from each other by such observable features as the period, frequency detuning, and shape of the phase modulation. Which periodic state has to be realized depends on the thickness of the sample, on the intensity ratio of the incident beams, on the type of the PR response, and, sometimes, on the recording history.

The input phase behavior remained almost unexplored during the initial stage of experimental studies so that the presence of the predicted periodic states required an experimental check. Special feedback experiments, carried out with $LiNbO_3$ crystals possessing the local PR response, gave solid evidences of the presence of different periodic states and showed a good qualitative agreement with the expected behavior [23, 24].

Considerable efforts have been undertaken in the subsequent studies to understand various aspects of the feedback operation in the transmission geometry:

- An analogy between the emergence of periodic states and the second-order phase transitions has been established [25].
- The conditions for the achievement and specific features of the periodic states have been analyzed for the nonlocal (diffusion) and the resonant (inherent in fast PR materials) nonlinear response [26].
- A number of prominent features of the periodic states were interpreted in the terms of theory of fast phase modulation [27].
- It was found that the light pattern distribution inside the sample, which is relevant to the periodic states, consists of domains moving with the opposite velocities [28].
- Special analytical methods for the description of the periodic states were developed [29, 30].
- The influence of noise-factors on the operation of the feedback device was analyzed [31].
- The effect of the feedbacks $\Phi_s = 0,\ \pi$, which can easily be realized experimentally, has been studied [32].

In 2003, the studies of the feedback-controlled beam coupling took a new direction that is relevant to the reflection coupling geometry. This geometry is interesting and important in three respects. First, stabilization of the light fringes is especially important here in view of ultimately small grating periods ($\lesssim 0.1\,\mu$m); it is crucial for long-term experiments. Second, we enter a new physical domain. The combination of the small grating periods with the possibility to apply extremely high electric fields (up to 650 kV/cm, see [33]) meets the condition for the resonant excitation of low-frequency eigen-modes (space-charge waves) in slow PR materials like $LiNbO_3$ and $LiTaO_3$ [34, 35]. Third, the diffraction efficiency cannot achieve here the ultimate value $\eta = 1$ owing to counter-propagation of the interacting light waves. This should strongly affect the feedback operation.

Experimental and theoretical studies of the feedback-controlled beam coupling and grating recording in $LiNbO_3$ crystals have led to the following main results for the reflection case [36, 37]: The $\pm\pi/2$ feedback ensures maximization of the diffraction efficiency of the dynamic index grating. The feedback brings the system to a steady state (not to a periodic state); this state is characterized by a frequency shift between the light beams (moving grating). The feedback-introduced detuning frequency is resonant to the eigen-mode frequency—the resonant excitation of weakly-damped space-charge waves takes place. By introducing the frequency detuning, the feedback inhibits the energy exchange between the light beams.

Our description of the feedback-controlled wave coupling possesses an important general feature. It is based on the decomposition of the wave amplitudes into the diffracted and transmitted components without making use of particular properties of the photorefractive response and the grating structure. This new issue, having important implications for the description of various readout processes, is considered in detail in the theoretical part of this chapter.

6.2 Operation Principle of the Feedback Setup

6.2.1 Feedback Setup and Feedback Equation

It is assumed that two coherent light beams, referred to as signal and reference ones, are coupled in a transparent sample of the thickness d via Bragg diffraction from a volume refractive-index grating (see Fig. 6.1). This grating can be either dynamic (relevant to the photorefractive effect) or permanent. The slowly varying complex amplitudes of the signal and reference beams we denote as S and R, respectively; they are generally functions of the propagation coordinate z and time t. For the input $[S(0,t),\ R(0,t)]$ and output $[S(d,t),\ R(d,t)]$ wave amplitudes, we shall use the symbols S_0, R_0 and S_d, R_d.

We suppose that the input intensities $|S_0|^2$ and $|R_0|^2$ are constant, whereas the input phases φ_s and φ_r can be functions of time. The input phase changes are one reason for the temporal variations of the light amplitudes inside the sample. Another reason is the dynamic processes of grating buildup. Of course, only the phase difference $\varphi_s - \varphi_r$ affects the observable characteristics of two-wave coupling. It is convenient to prescribe the temporal fluctuations of this difference to the input phase φ_r and treat the feedback-controlled phase φ_s as fluctuation free. The last preliminary is the choice of normalization of the light amplitudes. Since the total intensity of the S- and R-beams remains constant during propagation, it is convenient to normalize the amplitudes in such a way that $|S|^2 + |R|^2 = 1$. With this choice, the quantity $m_0 = 2|R_0 S_0|$ is the input light contrast.

The function of the feedback loop is to adjust the input phase $\varphi_s = \arg(S_0)$ depending on the output intensity $|S_d|^2$. The phase adjustment is accomplished with the help of a modulation technique. An auxiliary oscillating component $\delta\varphi_s = \psi_d \sin\omega t$, whose amplitude ψ_d and period $2\pi/\omega$ are much smaller than 1 and the PR response time t_r, respectively, is introduced into φ_s. This component cannot affect the grating; it serves for initiation of the electronic feedback loop.

The output amplitude S_d consists obviously of the diffracted and transmitted components. The first one is due to the diffraction of the incident R-beam from the grating; it is proportional to R_0. The second contribution is due to transmission of the incident S-beam; it is proportional to $S_0 \exp(i\psi_d \sin\omega t)$. Thus, we have in the general case:

$$S_d = f_D\ R_0 + f_T\ S_0\ e^{i\psi_d \sin\omega t}, \tag{6.1}$$

where f_D and f_T are certain complex coefficients characterizing the diffraction and transmission properties of the index grating. Actually, this relation expresses the superposition principle inherent in the linear diffraction problem. The value $\eta = |f_D|^2$ is nothing else than the grating diffraction efficiency. One can guess (see also Section 6.3.2), that $|f_T|^2 = 1 - \eta$.

According to Eq. (6.1), the output intensity $|S_d|^2$ acquires high-frequency components oscillating as $\sin\omega t$ and $\cos 2\omega t$. Their amplitudes are

$$I_\omega = m_0\sqrt{\eta(1-\eta)}\;\psi_d \sin\Phi_s, \quad I_{2\omega} = 0.25 m_0\sqrt{\eta(1-\eta)}\;\psi_d^2 \cos\Phi_s, \tag{6.2}$$

where $\Phi_s = \arg(f_D R_0/f_T S_0)$ is just the phase difference between the diffracted and transmitted components of the signal beam. The amplitudes I_ω and $I_{2\omega}$ are generally functions of time; they are expected to vary slowly as compared to $\sin\omega t$ and $\cos 2\omega t$.

Further steps of the feedback operation can be commented with the help of Fig. 6.1. The photo-detector (PD) transforms linearly the output intensity $|S_d|^2(t)$ into an electric-voltage signal. This signal is filtered using the heterodyne principle and the components $I_\omega(t)$ and $I_{2\omega}(t)$ are extracted. Lastly, they arrive at a lock-in amplifier and integrator (LAI). One of the amplified and integrated signals drives a piezo-mirror (PM). Details of the electronics can be found in [12, 17].

Since the PM displacement is proportional to the driving voltage, the time derivative of the input phase $\dot{\varphi}_s$ is proportional to I_ω or $I_{2\omega}$. Supposing for definiteness that the integrated $I_{2\omega}$ signal is chosen to govern the input phase, we arrive at the feedback equation:

$$\dot{\varphi}_s = \mp\frac{m_0}{t_f}\sqrt{\eta(1-\eta)}\cos\Phi_s, \tag{6.3}$$

where t_f is a new time constant determined by the LAI and PM specifications. It will be referred to as the feedback loop response time. The feedback inertia is weak when $t_f \ll t_r$; this case is indeed of our prime interest. Note the possibility of choice between the signs + and − in the feedback equation. As we shall see, the operation modes for the signs + and − are strongly different. The feedback equation relevant to the use of I_ω signal can be obtained by the replacement of $\cos\Phi_s$ by $\sin\Phi_s$ in Eq. (6.3).

6.2.2 The Case of Spatially-Uniform Index Grating

To illustrate the simplest applications of the feedback equation, we consider the case of permanent refractive index grating. Let the index change be given by $\Delta n = n_K \cos Kx$ with the amplitude n_K being a positive constant. Then the complex light amplitudes are given by the Kogelnik relations [38]

$$R = R_0\cos gz + iS_0\sin gz, \quad S = S_0\cos gz + iR_0\sin gz, \tag{6.4}$$

where $g = \pi n_K/\lambda\cos\theta, \lambda$ is the wavelength, and θ is the half-angle between the S- and R-beams in the medium. Correspondingly, we have $f_D = i\sin gd$, $f_T = \cos gd$, $\eta = \sin^2 gd$, $\cos\Phi_s = (\sin 2gd/|\sin 2gd|)\;\sin(\varphi_s - \varphi_r)$, and the feedback Eq. (6.3) acquires the form

$$\dot{\varphi}_s = \mp\frac{m_0\sin 2gd}{2t_f}\sin(\varphi_s - \varphi_r). \tag{6.5}$$

With this simple differential equation, one can make the following observations: If fluctuations of φ_r are slow on the scale of the feedback response time t_f, the input phase difference $\varphi_s - \varphi_r$ relaxes quickly to 0 for $\mp\sin 2gd < 0$ and to π for $\mp\sin 2gd > 0$. The input light pattern is fully stabilized; it is in phase or in counter-phase with the refractive index profile. The phase difference Φ_s between the diffracted and transmitted components relaxes to $+\pi/2$ for the upper sign in Eq. (6.5) and to $-\pi/2$ for the lower sign; the signal $I_{2\omega}$ relaxes to 0 in both cases. This is why the feedback conditions given by Eqs. (6.3) and (6.5) are replaced often by the ideal conditions, $\Phi_s = \pm\pi/2$, and $I_{2\omega}$ is called the error signal. It is evident also from Eq. (6.5) that the relaxation rate tends to zero when $\eta(1-\eta) \to 0$.

The use of I_ω as an error signal forces the phase difference Φ_s to relax quickly to 0 or π($I_\omega \propto \sin\Phi_s \to 0$) unless $\eta(1-\eta) \simeq 0$. The spatial phase shift between the input intensity profile and the refractive index distribution relaxes here to $\pm\pi/2$.

The above described feedback scheme for stabilization of the light fringes, which is based on the use of permanent gratings, is known since 1977 [9]. Its inconvenience is in the spatial separation of the master sample (permanent hologram) from the actual object.

6.2.3 General Remarks on the Impact of Dynamic Effects

Employment of the electronic feedback loop in photorefractive schemes leads generally to qualitatively new phenomena. A dynamic grating, which is being recorded under the feedback control, serves as a reference for the feedback signal. In addition to the stabilization function, the feedback changes dramatically the apparent characteristics of grating recording and beam coupling. The thicker the sample, the stronger are the changes.

Fig. 6.2 illustrates the feedback-controlled grating recording in a 1.78 mm-thick $LiNbO_3$. The $\pm I_{2\omega}$ signal is used to drive the piezo-mirror while the I_ω signal is monitored. During the first stage of recording (segment 1), the error signal is $+I_{2\omega}$. The I_ω signal grows initially, passes a maximum, reaches zero, and then holds this value. Switching the error signal from $+I_{2\omega}$ to $-I_{2\omega}$ results (see segment 2) in a negative oscillation of I_ω that ends up on a zero level. Switching to the $+I_{2\omega}$ error signal leads again to the positive oscillation of I_ω, etc. The zero values of $I_\omega(t)$ can be kept indefinitely long. The described behavior is observed in a wide range of the input beam ratio $r_0 = |R_0|^2/|S_0|^2$ [12, 13].

Interpretation of the data given in [12, 13] was based on the Kogelnik relations (see Section 6.2.2). Since the value of $\sin^2\Phi_s$ is expected to be unity here, it was concluded that the diffraction efficiency η grows from 0 to 1 during the first stage. This growth was associated with the constructive interference of the R- and S-beams. The negative oscillations of I_ω were interpreted as erasure of the recorded grating (decrease of η from 1 to 0) owing to the destructive interference caused by the π-change of the phase shift between the light and index fringes. Furthermore, the conclusion about achievement of the ultimate values of the diffraction efficiency was confirmed by direct measurements of η.

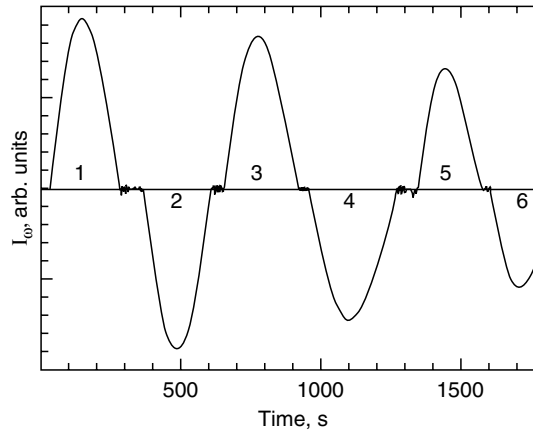

FIGURE 6.2. Measured signal I_ω during feedback-controlled grating recording in a $LiNbO_3$:Fe sample at $r_0 \simeq 2$. The odd and even cycles correspond to the use of $+I_{2\omega}$ and $-I_{2\omega}$ as the error signal. Diffraction efficiency η measured at the end of the cycles is ≈ 1 and ≈ 0, respectively. After [13]

It was also found that the feedback considerably modifies the intensity coupling between the R- and S-beams and significantly suppresses the harmful effect of light-induced scattering [12, 13, 15]. Generation of a frequency detuning between the R- and S-beam in feedback experiments with sillenite crystals ($Bi_{12}RO_{20}$, R = Si, Ti, Ge) has been detected as well [16, 20]. This detuning corresponds to the linear phase changes, $\varphi_s \propto t$.

While the conclusion about the impact of the feedback on the recording and wave-coupling characteristics is beyond dispute, the understanding of the relevant dynamic effects is not satisfactory:

- First, the gratings recorded during PR coupling are generally bent, tilted, and spatially nonuniform in the amplitude [1, 2]. This is especially true for nonlinearly thick samples that provide strong coupling effects and large values of the diffraction efficiency. The beam-coupling effects make invalid the particular expressions for the diffracted and transmitted parts of the amplitude S_d, used in Section 6.2.2.
- Second, the behavior of the system in the vicinity of $\eta = 1$ or 0 requires a careful consideration. The feedback signal is very weak here; it cannot govern the evolution of the input-phase φ_s. Correspondingly, the notion of a fixed phase difference Φ_s breaks down in this region. It is unclear, in particular, whether the states with $\eta \simeq 1$ or 0 can be treated as steady states.

The absence of theory of the feedback-controlled beam coupling makes uncertain the status of this phenomenon and the prospects for its practical use. Below we provide the reader with the basic knowledge of this new subject.

6.3 Basic Relations for Feedback-Controlled Beam Coupling

6.3.1 Coupled-Wave and Material Equations

In the case of dynamic diffraction, the refractive index change is due to formation of the space-charge field under light and the linear electro-optic effect. In accordance with Fig. 6.1, we present the space-charge field as $E_{sc} = (1/2)E_K \exp(iKx) + c.c.$, where $E_K = E_K(z, t)$ is the complex slowly-varying grating amplitude. The index change is given by $\Delta n = -rn^3 E_{sc}/2$, where r is the relevant electro-optic coefficient and n is the background refractive index.

The coupled-wave equations for the light amplitudes S and R, which describe Bragg diffraction from the grating, follow from Maxwell equations. For the transmission geometry, they can be presented as [1, 2]

$$\frac{\partial R}{\partial z} = i\kappa\, E_K\, S, \quad \frac{\partial S}{\partial z} = i\kappa E_K^* R, \tag{6.6}$$

where $\kappa = \pi n^3 r/\lambda$ is the known real coefficient and the asterisk means complex conjugation. It is essential that Eqs. (6.6) are linear in R and S and they do not include the time derivatives. The last feature means that light follows slow index changes. The total intensity $|R|^2 + |S|^2$ is a conserving quantity within Eqs. (6.6); it equals 1 for the chosen normalization of R and S.

The grating amplitude E_K obeys a material equation that accounts for the processes of charge separation under light. In what follows, we restrict ourselves to the following fairly general model equation:

$$\left(t_r \frac{\partial}{\partial t} + 1\right) E_K = F \frac{2RS^*}{|R|^2 + |S|^2}, \tag{6.7}$$

where t_r is, as earlier, the nonlinear response time and F is a complex coefficient characterizing the PR nonlinearity. The absolute value of the fraction in the right-hand side is nothing else than the light contrast m.

In steady state, with R and S being time independent (standing light pattern), we have $E_K = F \cdot 2RS^*/(|R|^2 + |S|^2)$. The absolute value $|F|$ is here the coefficient of proportionality between $|E_K|$ and m while $\Psi = \arg F$ is the spatial phase shift between the standing grating and light fringes.

Material Eq. (6.7) is valid for any coupling geometry. In the actual case of transmission geometry, where the total light intensity is conserving, we have $|R|^2 + |S|^2 = 1$ for the chosen normalization of R and S.

The limiting cases of real and imaginary F ($\Psi = 0, \pi$ and $\pm\pi/2$) correspond to the so-called local and nonlocal PR response, respectively [1]. The local response is usually due to the drift of photo-excited charge carriers and/or the bulk photovoltaic effect [39, 40]. The nonlocal response is often due to diffusion of the charge carriers.

The rate coefficient t_r^{-1} is usually proportional to the total light intensity [1–3]. In certain special cases, it possesses a relatively large imaginary part which means the presence of weakly-damped space-charge waves [34, 35, 41]; Eq. (6.7) can be restricted there to the values of light contrast $m \ll 1$. Unless such cases are indicated, we will treat t_r as a real relaxation constant and use Eq. (6.7) in the whole contrast range, $0 < m \leq 1$.

In the literature, one can find numerous model relations expressing F and t_r through the applied field E_0, the grating vector K, and material parameters [2]. For many PR ferroelectrics ($LiNbO_3$, $LiTaO_3$, $BaTiO_3$, $KNbO_3$, etc) and the transmission case, it will be sufficient to suppose that $F \simeq E_{pv} - E_0 \mp iE_D$ and $t_r = t_{di}$, where E_{pv} is the photovoltaic field, $E_D = Kk_bT_0/e$ is the diffusion field, k_b is the Boltzmann constant, T_0 is the absolute temperature, e is the elementary charge, and t_{di} is the dielectric relaxation (Maxwell) time. The upper and lower signs correspond to the photo-excitation of electrons and holes, respectively. For many fast PR materials (including the sillenites) and the transmission case, it will be sufficient to set $F = -E_0 - iE_D$ and $t_r^{-1} = \gamma_K - i\omega_K$, and accept that $|\omega_K| \gg \gamma_K$ within a certain range of E_0 and K. This range is relevant to the presence of weakly damped space-charge waves [35, 41] and to the resonant enhancement of the PR response [2, 42]. The necessary relations for the reflection geometry can be found in Section 6.5.3.

Quite a lot of characteristics of beam coupling and grating recording can be described with the help of the set (6.6), (6.7). These includes the output intensities and phases of the S- and R-beams in steady state (with R, S, E_K being time constants or in the presence of a frequency shift Ω when $RS^*, E_K \propto \exp(i\Omega t)$)) and the diffraction efficiency of the recorded dynamic grating [1, 2, 43, 44]. The Kogelnik relations (6.4) are applicable only in the limit of weak coupling when $|\kappa F|d \ll 1$ and $\eta \ll 1$.

The feedback equation has to be presented in the form of a boundary condition for Eqs. (6.6) that couples the light amplitudes on the input ($z = 0$) and output ($z = d$) faces of the sample. The form of Eq. (6.3) does not meet this requirement because the phase difference Φ_s between the diffracted and transmitted components of the S-beam is not expressed yet by S_0, S_d, R_0, R_d. Below we obtain the necessary general relation for Φ_s.

6.3.2. Fundamental Amplitudes

Since the problem of Bragg diffraction is linear, we can represent the amplitudes S and R as linear combinations of the transmitted (first) and diffracted (second) components [21, 45],

$$S = S_0 f_T^s + R_0 f_D^s, \quad R = R_0 f_T^r + S_0 f_D^r. \tag{6.8}$$

The fundamental amplitudes $f_T^r(z,t)$ and $f_D^s(z,t)$ correspond to testing of the grating by a unit R-beam, see Fig. 6.3a. They meet the same coupled-wave equations as R and S, respectively; the boundary conditions for them are

$f_T^r(0,t)=1$, $f_D^s(0,t)=0$. The fundamental amplitudes $f_D^r(z,t)$ and $f_T^s(z,t)$ correspond to testing of the same grating by a unit S-beam, see Fig. 6.3b. Their input values are 0 and 1, respectively. The amplitudes $f_{T,D}^r$ and $f_{T,D}^s$ fully describe the transmission and diffraction properties of the dynamic grating in the absolute reference frame.

At first sight, Eqs. (6.8) are useless because we cannot express four fundamental amplitudes by S and R. However, by making the complex conjugation of the coupled-wave equations for f_T^r and f_D^s, one can see easily that

$$f_T^s=(f_T^r)^*, \quad f_D^s=-(f_D^r)^*. \tag{6.9}$$

In other words, only two fundamental amplitudes (let them be f_T^s and f_D^s) are independent owing to the symmetry properties of the coupled-wave equations. Using Eqs. (6.8) and (6.9), we express f_T^s and f_D^s through the recording amplitudes,

$$f_T^s=S_0^*S+R_0R^*, \quad f_D^s=R_0^*S-S_0R^*. \tag{6.10}$$

Some other properties of the fundamental amplitudes are useful as well. In accordance with our definitions (see also Fig. 6.3) and Eqs. (6.9), we have $\eta=|f_D^s(d)|^2=|f_D^r(d)|^2$. These relations prove that the result of measurements of η does not depend on which of the recording beams (R of S) is blocked. They allow us to express η explicitly through the recording amplitudes [44]. Furthermore, we have $|f_T^s(d)|^2=|f_T^r(d)|^2=1-\eta$. Note an obvious consequence of these equalities: The output intensities of the recording waves coincide with the input ones ($|S_d|^2=|S_0|^2$, $|R_d|^2=|R_0|^2$) in the case $\eta=0$ and interchange with each other ($|S_d|^2=|R_0|^2$, $|R_d|^2=|S_0|^2$) when $\eta=1$.

Using Eqs. (6.8) and (6.9), we calculate now the phase difference Φ_s between the diffracted and transmitted components of the S-beam,

$$\Phi_s=\varphi_r-\varphi_s+\arg[(S_0S_d^*+R_0^*R_d)(R_0^*S_d-S_0R_d^*)]. \tag{6.11}$$

This expression represents the difference of the feedback-controlled input phase φ_s and the terms which vary slowly on the scale of t_f. This is why the adjustment of Φ_s to $\pm\pi/2, 0$, or π is not much different from that considered above for the permanent grating.

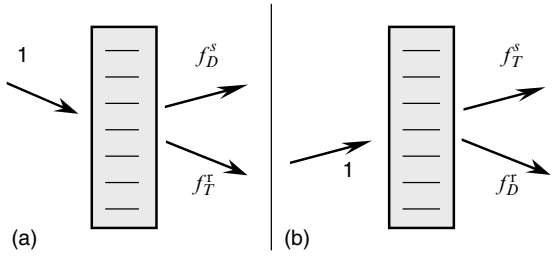

FIGURE 6.3. Geometrical schemes relevant to the definition of the fundamental amplitudes in the transmission geometry.

The ideal feedback conditions $\Phi_s = \pm\pi/2$ and the feedback conditions given by Eq. (6.3) acquire now the form of explicit relations that couple the recording amplitudes at the input and output. They serve as nonlocal and nonlinear boundary conditions to the set (6.6), (6.7).

It is worth noting that the role of the fundamental amplitudes goes beyond the purposes of our feedback studies. Broadly speaking, the method used allows to express any readout characteristic of the dynamic grating through the input and output recording amplitudes regardless of the type of PR response. Particular applications of this method can be found in [44].

6.3.3 Steady-State Solutions

In the general case, a frequency detuning Ω exists between R- and S-beams in steady state so that the light and index fringes are moving with a constant velocity Ω/K. We attribute this detuning to the linear change of the input phase $\varphi_s(t)$. It is sufficient to set $S \propto \exp(-i\Omega t)$ and $E_K \propto \exp(i\Omega t)$ to take it into account. Eqs. (6.6), (6.7) then give the known relations for the wave amplitudes [1, 2, 43],

$$R = R_0 \exp(\Gamma z/2)/D, \quad S^* = S_0^* \exp(-\Gamma z/2)/D, \tag{6.12}$$

where the denominator $D = D(z)$ is given by

$$D = [|R_0|^2 \exp(\Gamma' z) + |S_0|^2 \exp(-\Gamma' z)]^{\Gamma/2\Gamma'} \tag{6.13}$$

and $\Gamma = \Gamma' + i\Gamma''$ is the complex rate constant,

$$\Gamma = i\Gamma_0/(1 + i\Omega t_r) \quad \text{with} \quad \Gamma_0 = 2\kappa F\cdot \tag{6.14}$$

Its real part Γ' is referred to as the amplitude gain factor; the imaginary part Γ'' characterizes the phase coupling.

Using Eqs. (6.10), (6.12), and (6.13), one can find the following explicit relations for the fundamental amplitudes:

$$f_T^s = [|R_0|^2 \exp(\Gamma^* z/2) + |S_0|^2 \exp(-\Gamma^* z/2)]/D^* \tag{6.15}$$

$$f_D^s = -R_0^* S_0\, [\exp(\Gamma^* z/2) - \exp(-\Gamma^* z/2)]/D^*. \tag{6.16}$$

Since $\eta = |f_D^s(d)|^2$, we obtain for the steady-state diffraction efficiency:

$$\eta = \frac{m_0^2}{2} \frac{\cosh(\Gamma' d) - \cos(\Gamma'' d)}{\cosh(\Gamma' d) + W_0 \sinh(\Gamma' d)}, \tag{6.17}$$

where $W_0 = |R_0|^2 - |S_0|^2 = (r_0 - 1)/(r_0 + 1)$ is the normalized input intensity difference. This relation incorporates the coupling effects; it is equivalent to the expression known since 1979 [43].

Let us maximize and minimize η with respect to the coupling parameters $\Gamma' d$ and $\Gamma'' d$. The maximum value of the efficiency $\eta_{max} = 1$. The maximizing value

of $\Gamma'' d$ meets the condition $\cos(\Gamma'' d) = -1$, i.e., $\Gamma'' d = \pm\pi,\ \pm 3\pi,\ \ldots$ The maximizing value of $\Gamma' d$ is unique; it is given by $\tanh(\Gamma' d/2) = -W_0$. The minimum value $\eta_{\min} = 0$ is achieved when $\Gamma' = 0$ and $\Gamma'' d = \pm 2\pi,\ \pm 4\pi, \ldots$ Two different conditions have to be satisfied thus to turn η to 1 (or to 0). The reason is simple: The value $\eta = 1$ (or 0) is achieved when both real and imaginary parts of $f_T^s(d)$ (or $f_D^s(d)$) are zeros.

The derived conditions play an important role in analysis of the feedback-controlled behavior. The condition $\eta = 1$ (or $\eta = 0$) gives us a sequence of branches for $|\Gamma_0| d$ as a function of r_0, i.e., a sequence of curves on the $|\Gamma_0| d, r_0$-plane. These curves, as we will see, separate the regions with essentially different feedback behavior. They will be referred to as the *separatrices* or *threshold curves*. Each point of a separatrix corresponds to a unique value of the frequency detuning, i.e., $\Omega = \Omega(r_0)$.

Let us go further. Using Eqs. (6.15) and (6.16), we easily calculate the steady-state phase difference Φ_s,

$$\Phi_s = \arg[W_0 \cos(\Gamma'' d) + i \sin(\Gamma'' d) - \sinh(\Gamma' d) - W_0 \cosh(\Gamma' d)]. \qquad (6.18)$$

It is well-defined unless $\eta(1 - \eta) = 0$.

The feedback is able to adjust Φ_s by varying the detuning Ω. Consider the main possibilities:

- $\Phi_s = \pm\pi/2$. In this case, the following two conditions are fulfilled:

$$\sinh(\Gamma' d) + W_0 \cosh(\Gamma' d) = W_0 \cos(\Gamma'' d), \quad \sin(\Gamma'' d) \gtrless 0. \qquad (6.19)$$

- $\Phi_s = 0,\ \pi$. In this case, we have instead of Eq. (6.19):

$$\Gamma'' d = j\pi, \quad \sinh(\Gamma' d) + W_0 \cosh(\Gamma' d) \lessgtr W_0(-1)^j, \qquad (6.20)$$

where $j = 0,\ \pm 1, \ldots$

If we replace the sign $\gtrless$ by the sign $=$ in Eqs. (6.19) and (6.20), we obtain new curves on the $r_0,\ |\Gamma_0| d$–plane that separate the regions where steady states with $\Phi_s = \pi/2$ and $-\pi/2$ and $\Phi_s = 0$ and π can take place. Different separatrices and regions look fairly simple when we restrict ourselves to not very large values of the coupling strength $|\Gamma_0| d$. Below, we consider a number of important particular cases.

Particular Cases

The local PR response: Here we set first, see Eq. (6.14), $\Gamma_0 = |\Gamma_0|$ to obtain

$$\Gamma' = \frac{|\Gamma_0| \Omega t_r}{1 + \Omega^2 t_r^2}, \quad \Gamma'' = \frac{|\Gamma_0|}{1 + \Omega^2 t_r^2}. \qquad (6.21)$$

With $\Omega = 0$ the rate coefficient Γ is pure imaginary.

The condition $\eta = 1$ is fulfilled when

$$|\Gamma_0|d = j\pi + \frac{1}{j\pi}\ln^2 r_0, \tag{6.22}$$

where $j = 1, 3, \ldots$ Separatrix 1 in Fig. 6.4a shows the coupling strength $|\Gamma_0|d$ versus the input intensity ratio $r_0 = |R_0|^2/|S_0|^2$ for j = 1 (the branches with $j = 3, 5, \ldots$ correspond to higher values of $|\Gamma_0|d$). This dependence is symmetric to the replacement r_0 by r_0^{-1}. The minimum value of the coupling strength, $(|\Gamma_0|d)_{\min} = \pi$, takes place at $r_0 = 1$. The detuning relevant to the condition $\eta = 1$ is given by $\Omega t_r = -\ln r_0/\pi$; it changes sign when r_0 is replaced by r_0^{-1}. The condition $\eta = 0$ is fulfilled when $\Omega = 0$ and $|\Gamma_0|d = 2\pi, 4\pi, \ldots$ (see line 3 in Fig. 6.4a).

Turn now to the feedback-controlled steady states [32]. Two additional lines, 2 and 4, are necessary to specify the regions of different behavior for $|\Gamma_0|d < 3\pi$ (see Fig. 6.4a). Below line 2, i.e., for $|\Gamma_0|d < \pi$, the only possible steady state corresponds to $\Phi_s = \pi/2$. This state is stable, it is achievable via a feedback-controlled transient stage. The value of steady-state diffraction efficiency ranges here from 0 to 1. The use of "forbidden" feedbacks $-\pi/2, 0,$ and π leads (for $|\Gamma_0|d < \pi$) to very large values of Ω and a strong erasure effect.

Two additional states with $\Phi_s = 0$ (or with $\Phi_s = \pi$) can formally be found within the region restricted by the curves 1, 2, and 4. Only one of these new states is stable and can, in addition to the old one, be realized in practice. The number of instable steady states increases dramatically with increasing $|\Gamma_0|d$, see, e.g., the regions restricted by curves 1 and 4; such states are of little interest.

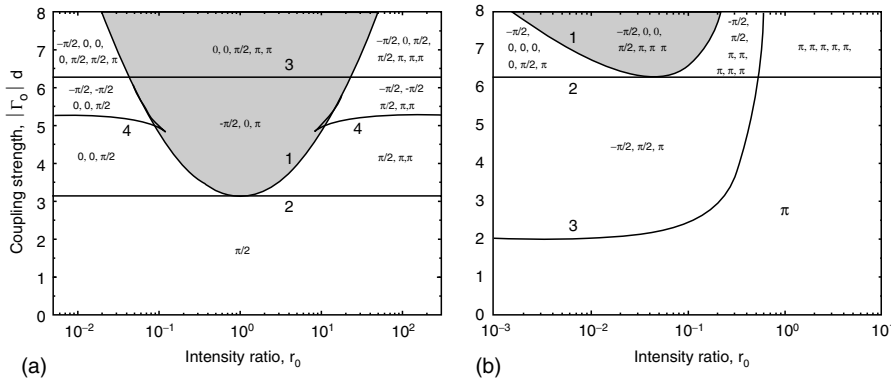

FIGURE 6.4. Lines separating different regions on the r_0, $|\Gamma_0|d$– plane for the local (a) and nonlocal (b) responses. Separatrix 1 corresponds to the condition $\eta = 1$; above it (within the gray regions), the periodic states take place. The signs 0, $\pi/2, \ldots$ mean that steady state solutions with $\Phi_s = 0,\ \pi/2, \ldots$ can be found formally within the indicated regions. Repetition of the same sign means the frequency degeneration—two, three, ... steady states with the same value of Φ_s but different values of Ω correspond to the same r_0 and $|\Gamma_0|d$.

Consider finally the gray region restricted from below by separatrix 1. All steady states that can formally be found are not stable in this region. The use of the $\pi/2$ feedback leads to periodic states with $\eta \simeq 1$, see the Section 6.4.

It should be emphasized that the feedback influence on stable steady states is reduced to the introduction of a proper frequency shift Ω. The same state can be achieved when the feedback is switched off and the necessary shift is introduced at the input.

To clarify for the reader the meaning of the term "unstable steady state," we describe the results of two numerical experiments [21]. Initially, the feedback is switched off and the frequency detuning Ω is chosen in such a way that the temporal evolution brings the system very near to the steady state with $\Phi_s = \pi/2$ (see curve 1 in Fig. 6.5). Then the $\pi/2$ feedback is switched on. One sees that within a time interval comparable with the response time t_r, the system departs far away from the steady state (with $\eta \simeq 0.2$) and reaches a state with $\eta \simeq 1$. Within a similar simulation, the input detuning was chosen in such a way to bring the system very near to the steady state with $\Phi_s = -\pi/2$. The corresponding steady-state efficiency is close to 1 (see curve 2). Switching the feedback $\Phi_s = -\pi/2$ on results in a quick drop η to zero. The above numerical results are in line with experiment (see Fig. 6.2). They show that steady states of the system governed by the $\pm\pi/2$ feedback are unstable for sufficiently thick samples. What happens if the sign of the local response is inverted, $\Gamma_0 = -|\Gamma_0|$? The answer is simple: Within all above regions, the feedback sign (and the sign of Ω) has to be inverted to ensure the same behavior of the system. The form of separatrix 1 remains unchanged.

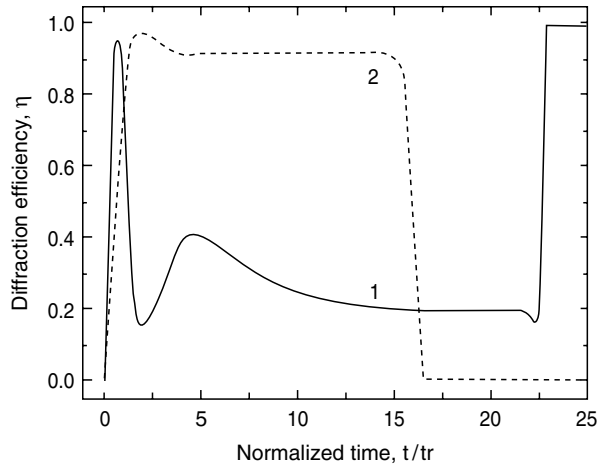

FIGURE 6.5. Up to the point $t/t_r = 20$, curve 1 corresponds to the input phase $\varphi_s = \Omega t$, $W_0 = -0.5$, and $|\Gamma_0|d = 7.3$; the value $\Phi_s(20t_r) \simeq 1.01(\pi/2)$. Then the feedback $\Phi_s = \pi/2$ is on. For curve 2, the feedback $\Phi_s = -\pi/2$ is switched on at $t \simeq 13t_r$. The relevant figures are $|\Gamma_0|d = 7.3$, $W_0 = 0.5$, and $\Phi_s(13t_r) \simeq -1.01(\pi/2)$.

The nonlocal response: Here we set first $\Gamma_0 - i|\Gamma_0|$, which gives the relations

$$\Gamma' = \frac{|\Gamma_0|}{1+\Omega^2 t_r^2}, \quad \Gamma'' = -\frac{|\Gamma_0|\Omega t_r}{1+\Omega^2 t_r^2}. \tag{6.23}$$

The rate coefficient Γ is real for $\Omega = 0$ and $S \to R$ energy transfer occurs.

The condition $\eta = 1$ is fulfilled when [26]

$$|\Gamma_0|d = -(\ln r_0 + \pi^2/\ln r_0). \tag{6.24}$$

This relation describes the lowest branch of the dependence of $|\Gamma_0|d$ on r_0 (see separatrix 1 in Fig. 6.4b). The allowed values of r_0 are smaller than 1 so that the contrast m is increasing during beam propagation. The absolute minimum of the coupling strength, $(|\Gamma_0|d)_{min} = 2\pi$, is two times higher than that for the local response; it occurs at $r_0 = \exp(-\pi) \simeq 0.043$. The relevant dependence $\Omega(r_0)$ is given by $\Omega t_r = \pi/\ln r_0$; the optimizing value of Ωt_r is -1.

Apart from separatrix 1, lines 2 and 3 shown in Fig. 6.4b are important to describe possible steady states. For sufficiently small values of the coupling strength, the only possible state corresponds to the condition $\Phi_s = \pi$. This state is stable and achievable via a feedback-controlled temporal evolution. Diffraction efficiency η is small at this state. The use of "forbidden" 0 and $\pm\pi/2$ feedback conditions leads to very large values of Ω and a strong erasure effect. Two additional steady states with $\Phi_s = \pm\pi/2$, which can be found formally within the region restricted by the lines 2 and 3, are not stable. The only stable state corresponds here to $\Phi_s = \pi$. Within the gray region, the only stable steady state meets the condition $\Phi_s = \pi$. The feedbacks $\pm\pi/2$ and 0 lead to periodic states.

What happens if the response sign is inverted, $\Gamma_0 = +i|\Gamma_0|$, i.e., the energy transfer is $R \to S$? Separatrix 1 in Fig. 6.4b is replaced by the mirror-reflected one, i.e., the allowed values of r_0 are larger than 1. The sign of Ω has also to be inverted.

The resonant response: This case is relevant to the sillenite crystals [2, 35]. The actual values of the applied field E_0 are much higher here than E_D (typically $E_0 = 6 - 10\,\mathrm{kV/cm}$ and $E_D \lesssim 1\,\mathrm{kV/cm}$) and $t_r^{-1} = \gamma_K - i\omega_K$ (see Section 6.3.1). The rate coefficient Γ can be presented as

$$\Gamma = \frac{i\Gamma_0\omega_K}{\Omega - \omega_K - i\gamma_K}, \tag{6.25}$$

with $\Gamma_0 = \kappa E_0$ The dependence $\Gamma(\Omega)$ exhibits a resonant behavior [35, 42]. When $\Omega\kappa \equiv \omega_K$, the rate coefficient Γ becomes real and its value is enhanced by a factor of $Q = |\omega_K|/\gamma_K \gg 1$ as compared to the value relevant to the static case ($\Omega = 0$). The resonant enhancement is restricted to small values of the light contrast, $m \lesssim Q^{-1} \approx (0.15 - 0.3)$.

Achievement of $\eta = 1$ is not the prime aim for the resonant case. A more important task is to ensure the maximum resonant value of the rate of spatial amplification, $Q|\kappa E_0|$, in steady state. This can be done with the use of the

feedback condition $\Phi_s = 0$ or π (depending on the sign of κE_0). The feedback loop automatically adjusts the frequency detuning to the resonance, $\Omega \simeq \omega_K$. Such an adjustment has been demonstrated in experiments with $Bi_{12}TiO_{20}$ crystals [16, 20]. The steady states with $\Phi_s = \pm\pi/2$ are not possible for modestly thin samples.

It is worthy of mentioning that the scalar wave coupling can be achieved only in special cases in the sillenite crystals. In the general case, because of optical isotropy and optical activity, the changes of light amplitudes and phases cannot be separated from polarization changes (see [46, 47] and references therein). This circumstance has to be taken into account on analysis of experimental data.

6.4. Periodic states

6.4.1. Results of Numerical Simulations

Ideal Feedback

First numerical simulations of the feedback-controlled beam coupling [21] dealt with the case of an almost local response, $\Gamma_0 \simeq |\Gamma_0|$, and were based on the use of the ideal feedback conditions $\Phi_s = \pm\pi/2$. These simulations were relevant to experiments with $LiNbO_3$ crystals [12, 13]. A small seed value of the grating amplitude E_K was used as the initial condition.

The essence of the results obtained for the feedback $\Phi_s = \pi/2$ is presented in Fig. 6.6. Line 4 corresponds to a coupling strength of 2.2 and $r_0 = 19$, i.e., to the under-threshold region in Fig. 6.4a. The efficiency $\eta(t)$ grows monotonously and approaches the value $\simeq 0.33$ relevant to the feedback-controlled steady state. The light and grating fringes are moving with a constant velocity. Curves 1, 2, and 3 are plotted for $r_0 = 1$, 9, and 19, respectively; the coupling strength is 6.6. In other words, we are inside the above-threshold region and recede step by step from separatrix 1. The behavior of $\eta(t)$ is different here. The efficiency reaches unity within a finite time. The smaller $\ln r_0$ and larger $|\Gamma_0|d$, the shorter is the transient time.

In fact, when η reaches a certain value that is very close to 1 (the grade of proximity depends on the calculation accuracy), the ideal feedback ceases to govern the temporal evolution. This is due to the fact that the transmitted component $f_T^s(d)$ becomes very small and an accurate calculation of its phase becomes impossible. Artificial means for regularization of the numerical procedure were used in the close vicinity of 1. For example, the input phase φ_s was kept equal to the last controllable value; this resulted in decreasing η and made it possible to switch the feedback on again. Each new switching on returns η quickly to a unit value (see the inset in Fig. 6.6). The described regularization procedure has indeed nothing to do with the real operation of the feedback loop; it shows, however, how robust the feedback effect is.

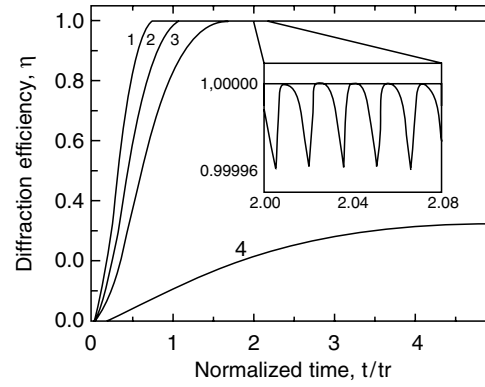

FIGURE 6.6. Dependence $\eta(t)$ for the ideal feedback condition $\Phi_s = \pi/2$. Curves 1, 2, 3 are plotted for $r_0 = 1$, 9, and 19 and $|\Gamma_0|d = 6.6$; curve 4 corresponds to $|\Gamma_0|d = 2.2$ and $r_0 = 19$. The insert shows in detail the region with $\eta \simeq 1$ for curve 2.

The situation with the ideal feedback $\Phi_s = -\pi/2$ is as follows: Any switching on of this feedback makes the grating transparent ($\eta \simeq 0$) within a finite time irrespective of the initial state and the values of $|\Gamma_0|d$ and r_0, see, e.g., Fig. 6.5. In the close vicinity of zero, the ideal feedback cannot govern the input phase φ_s and some regularization means are needed again for numerical calculations.

In the case of local response $\Gamma_0 = -|\Gamma_0|$, the feedback sign has to be inverted to ensure the same effect on the diffraction efficiency.

Inertial Feedback

Inertial feedback Eq. (6.3), supplemented by the exact relation (6.11) for the phase difference Φ_s, allow the system to operate permanently in all cases where the ideal feedback fails. The feedback-controlled system here exhibits a great variety of periodic states (attractors) instead of familiar steady states [24, 23]. Basically, such states are inherent in complicated dynamic systems [48, 49]

Consider first the case of local response $\Gamma_0 = |\Gamma_0|$ and accept the upper sign in Eq. (6.3); the latter means that inertia of the $+\pi/2$ feedback is taken into account. By turning to the operation modes, we set $|\Gamma_0|d = 6.6$ and start with an intermediate beam ratio r_0 (between 1 and the value $r_0^{max}/-\simeq 27$ belonging the separatrix 1 (see Fig. 6.4a).

Fig. 6.7 shows the time dependences of φ_s, η, and $\cos\Phi_s$ for $t_f/t_r = 10^{-3}$, and $r_0 = 4$. After a relatively short initial stage, $0 < t \lesssim t_r$, the phase φ_s shows a quite regular but not periodic behavior. It is characterized by almost periodic steps upward, each of them as large as $\simeq 340^\circ$. The time distance between them is $\simeq 0.35t_r$. The steps produce a considerable positive average slope of the dependence $\varphi_s(t)$, i.e., a considerable average detuning frequency, $\Omega_s t_r \gg 1$. The phase steps are accompanied by apparently periodic oscillations of the diffraction efficiency in the vicinity of 1. The period of these oscillations ($\simeq 0.35t_r$) is the same as the distance between the phase steps. The phase Φ_s, responsible for the error signal, remains close to $\pi/2$ only during the initial stage; further time development is characterized by strong quasi-periodic

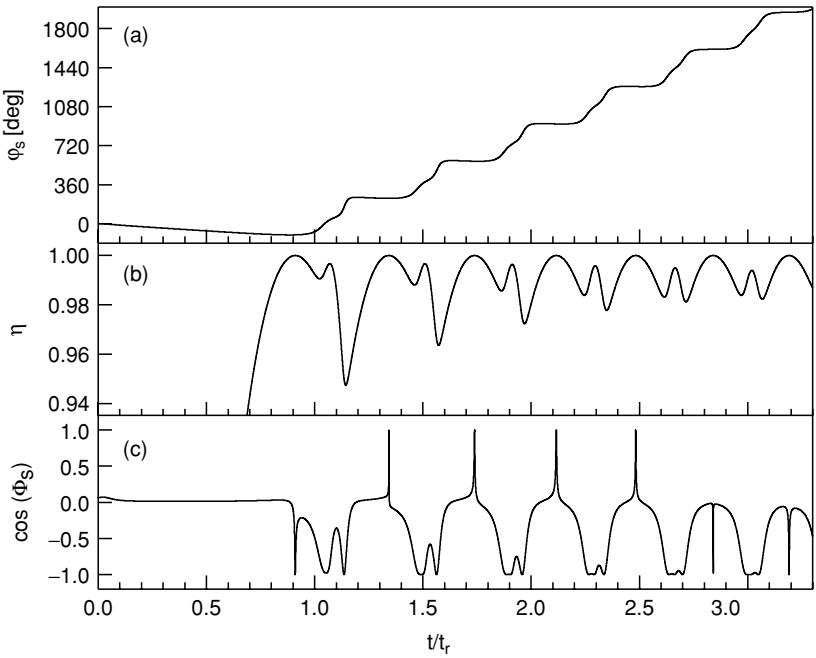

FIGURE 6.7. Dependences $\varphi_s(t)$, $\eta(t)$, and $\Phi_s(t)$ for the initial stage of feedback-controlled behavior at $|\Gamma_0|d = 6.6$ and $r_0 = 4$. The feedback response time $t_f = 10^{-3}t_r$.

oscillations of $\cos\Phi_s$. The subsequent evolution makes the phase steps of φ_s and the oscillations of η and $\cos\Phi_s$ perfectly periodic.

In addition to the time dependences of φ_s, η, and Φ_s, it is useful to characterize the system by the trajectory $f_T^s(d,t)$ on the complex plane. In particular, the distance to the origin $|f_T^s(d,t)| = \sqrt{1-\eta(t)}$. The solid closed line in Fig. 6.8a exhibits this trajectory for $6t_r \le t \le 8t_r$; about 7 revolutions occur during that time. This shows clearly that the point $\mathrm{Re}f_T^s(d,t), \mathrm{Im}f_T^s(d,t)$ moves along a limit cycle (an attractor). This motion is clockwise and strictly periodic; its period, $T \simeq 0.354t_r$, corresponds to the period of $\eta(t)$ and $\cos\Phi_s(t)$ and to the the duration of one step of $\varphi_s(t)$. While $f_T^s(d,t)$ moves along the attractor, the point $f_D^s(d,t)$ (characterizing the diffracted component) moves with small and constant angular velocity Ω along the unit circle, $|f_D^s(d,t)| \simeq 1$. The latter motion is superimposed by fast periodic oscillations of the same period T.

At this point the reader may ask, how it is possible to combine the periodic behavior of $f_T^s(d)$ and $\cos\Phi_s$ with the nonperiodic behavior of $f_D^s(d)$ and φ_s? To clarify this important point, we represent φ_s and the argument of $f_D^s(d)$ as

$$\varphi_s = \varphi_s^p + \Omega_s t, \quad \arg[f_D^s(d)] = \arg[f_D^s(d)]^p + \Omega t, \tag{6.26}$$

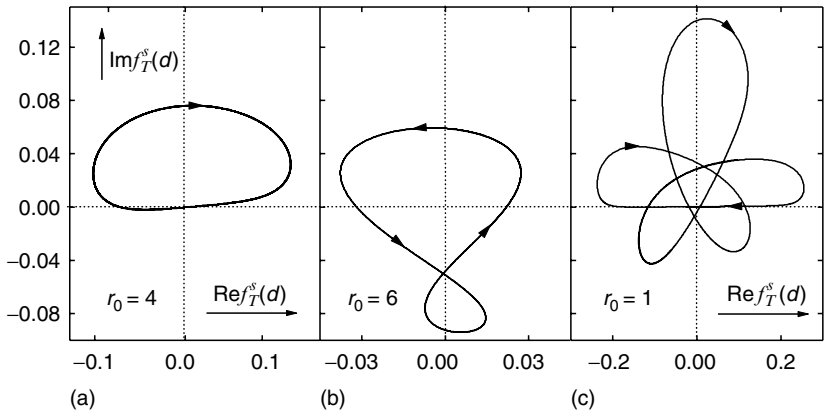

FIGURE 6.8. Periodic trajectories for $|\Gamma_0|d = 6.6$, and three different values of the input intensity ratio r_0. Weak asymmetry of the orbits is due to a small admixture of the nonlocal response.

where $\varphi_s^p(t)$ and $\arg[f_D^s(d,t)]^p$ are T-periodic time functions with zero average value, Ω_s is the apparent frequency detuning for the signal beam, and Ω is the average angular velocity for the amplitude $f_D^s(d,t)$. Then, keeping in mind that $\Phi_s = \arg[R_0 f_D^s(d)/S_0 f_T^s(d)]$, one can see that the only possibility to meet the feedback Eq. (6.3) is to demand that

$$\Omega_s = \Omega + 2\pi N/T, \tag{6.27}$$

with $N = 0, \pm 1, \pm 2, \ldots$. The number N determines the shape of the limit circle; it can be considered as a global characteristic of the periodic states. For the attractor presented in Fig. 6.8a, we have $N = 1$. The replacement $r_0 = 4$ by $r_0 = 1/4$ changes the sign of N (and the sign of Ω_s).

An interesting feature of the described behavior is the relatively long period of the oscillations, $T \simeq 0.354 t_r$. It is not much shorter than the PR response time t_r and much longer than the feedback response time, $t_f = 10^{-3} t_r$. The following numerical experiment was performed to investigate the dependence $T(t_f)$ [24]: Starting from $t = 12 t_r$ (when the periodic state with $r_0 = 4$ is practically achieved), the time t_f decreased from $10^{-3} t_r$ to $4 \cdot 10^{-5} t_r$ with a very small rate causing very slow (adiabatic) changes of the periodic state characteristics. During this procedure, the attractor decreased in size, preserving the bagel-like form. The period T also decreased with decreasing t_f. Another interesting question that has been answered within this adiabatic procedure is how the average $\langle 1 - \eta(t) \rangle_T$ depends on the feedback response time. With good accuracy, the found dependences of T and $\langle 1 - \eta(t) \rangle_T$ on t_f meet the scaling relations

$$T = C_T (t_f/m_0)^{1/2}, \quad \langle 1 - \eta \rangle_T = C_\eta t_f/m_0 \tag{6.28}$$

with $C_T \simeq 14$ and $C_\eta \simeq 6.6$. The same scaling relations (but with different values of C_T and C_η) hold true for other periodic states. Fast oscillations of the input phase φ_s remain strong even when $t_f \to 0$.

Now we turn to the case $r_0 = 6$, keeping the other parameters the same. The corresponding attractor (with $N = 0$) is shown in Fig. 6.8b. It consists of two loops and the trajectory moves around zero in an anti-clockwise direction. The size of this attractor is considerably smaller than that of the previous one. Only one revolution around the origin occurs during the period $T \simeq 0.33 t_r$. Fig. 6.9a shows the corresponding dependence $\varphi_s(t)$. The average slope is now negative; it corresponds to $\Omega_s t_r \simeq -0.924$, which is much smaller than earlier. This feature is favorable for experiment because it requires fewer resets of the piezo-driver.

Lastly we consider the case of equal input intensities, $r_0 = 1$. Here the temporal development of $f_T^s(d)$ ends up by attraction to the limit cycle shown in Fig. 6.8c. Its geometry is new again and the number $N = 3$. The full period corresponds here to three revolutions around zero. This leads to a period tripling of $\varphi_s(t)$, $\eta(t)$, and other variables. The size of the attractor is noticeably larger than earlier; this gives larger periodic oscillations of $\eta(t)$ in the vicinity of 1. The time dependence of φ_s is shown in Fig. 6.9b. Here the period $T \simeq 0.97\, t_r$; it is approximately three times larger than before. The average slope of $\varphi_s(t)$ is positive and pretty large, $\Omega_s t_r \simeq 19.3$.

The questions arise about what happens if we choose other values of the beam ratio and what kind of transitions take place between different periodic states with changing r_0. The answer to the first question is simple: No new types

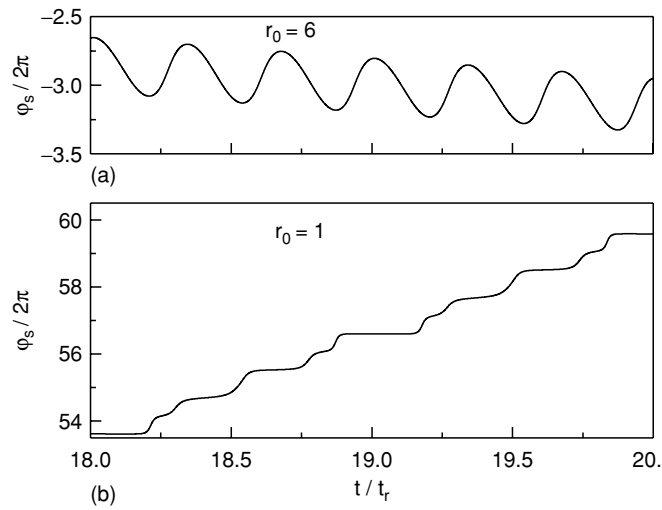

FIGURE 6.9. Time dependence of the input phase $\varphi_s(t)$ for the intensity ratio $r_0 = 6$ (a) and $r_0 = 1$ (b); the coupling strength $|\Gamma_0|d = 6.6$.

of attractors occur in the whole above-threshold range of the pump ratio for $|\Gamma_0|d = 6.6$. The answer to the second question is more complicated.

Imagine first that we gradually increase r_0 starting from 1. Then a gradual convergence of different loops of the attractor shown in Fig. 6.8c takes place. At $r_0 \simeq 2$, the three-loop structure has already transformed into one-loop trajectory similar to that shown in Fig. 6.8a. Correspondingly, the period tripling disappears. This behavior is similar to the second-order phase transition [50, 51]. It is not accompanied by dramatic changes of $\Omega_s(r_0)$, but the value of N transforms sharply from 3 to 1.

Increase of r_0 from 2 to ≈ 6 results in gradual changes of the form of the bagel presented in Fig. 6.8a. With r_0 approaching $\simeq 6.8$, these changes accelerate and within the interval $6.8 \lesssim r_0 \lesssim 7.3$, the trajectory $f_T^s(d, t)$ becomes apparently irregular. Then, for $r_0 \simeq 7.4$, a new two-loop attractor corresponding to $N = 0$ is formed. This transition is similar to the first-order phase transitions because it cannot be performed continuously [51]. In particular, it is very pronounced for the time dependence of φ_s. The change of $\Omega_s(r_0)$ and of the shape (but not the period) of the oscillations is very sharp.

With r_0 increasing from 7.4 to the threshold value $\simeq 27$, the attractor with $N = 0$ experiences only quantitative changes. The amplitudes of the temporal oscillations tend to zero and a gradual transition to the steady state (where $\eta < 1$) takes place.

The described behavior is robust. It is not subjected to considerable changes when the PR response is not purely local (i.e., Γ_0 is not purely real). Introduction of a weak noise source into the dynamic equations does not produce any strong effect on the periodic states; it can, however, make the transient stage shorter [31]. The use of different initial conditions for the grating amplitude E_K does not change the final result of the feedback-controlled evolution; that is, the establishment of a certain periodic state.

Some efforts have been undertaken to simulate the feedback operation for the nonlocal and resonant PR responses [26]. Within the below-threshold region of $|\Gamma_0|d$ and r_0, the feedback leads the system to a steady state, if such a state exists (see Section 6.3.3). Otherwise we have a state with $\eta \simeq 0$. Above threshold, i.e., for $|\Gamma_0|d > 2\pi$, the system is able to reach a periodic state with $\eta \simeq 1$. No such states are realized yet in experiment.

Some analytical methods were developed during the last years to describe the periodic states [29, 30]. It was found that the number of different attractors (with different values of N) increases rapidly with increasing coupling strength. Near the threshold, however, the only possible periodic state corresponds to $N = 0$, i.e., to a small value of Ω_s. Similarities between the periodic states relevant to $\eta = 1$ and 0 were established. It was also shown that the degree of inhomogeneity of the grating, being small at $r_0 = 1$, increases noticeably with increasing $|\ln r_0|$ for the case of local response. Quantitatively, this feature is described by the curves presented in Fig. 6.10. One sees that both the amplitude and phase distortions are important in the case of nonequal input intensities; these distortions grow with increasing coupling strength.

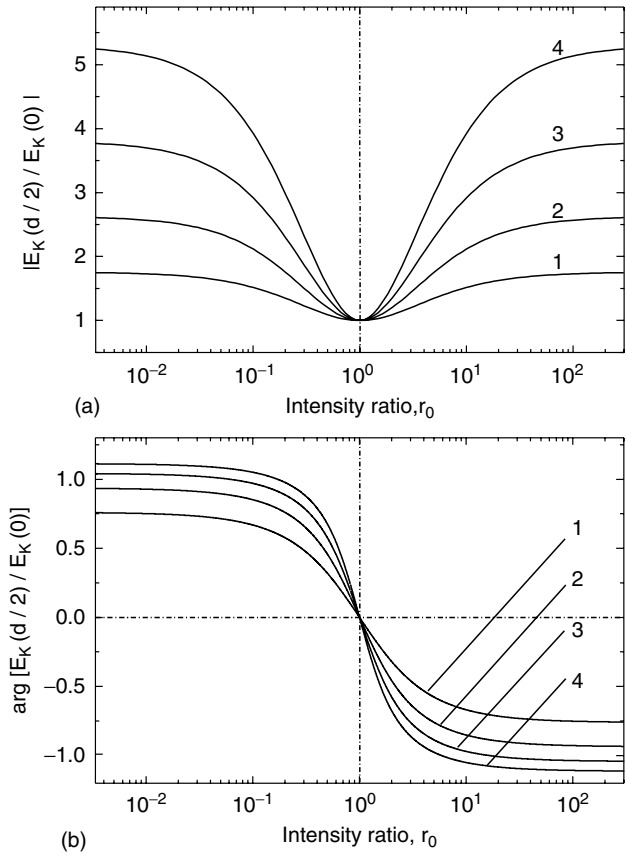

FIGURE 6.10. Dependences of the parameters $|E_K(d/2)|/|E_K(0)|$ and arg $[E_K(d/2)/E_K(0)]$, characterizing the degree of the amplitude and phase distortions of the grating, on the input intensity ratio for the local response and $\pi/2$ feedback. Curves 1, 2, 3, and 4 are plotted for $|\Gamma_0|d = 4,\ 6,\ 8$, and 10, respectively.

6.4.2 Experimental Results

The time dependence of the input phase φ_s was not reported in the first feedback experiments. Special measurements were therefore needed to check the main elements of the concept of the periodic states. The relevant experiments have been performed with a 0.35 mm thick sample of $LiNbO_3$:Fe [24, 23]. Its $4 \times 5\,mm^2$ input/output faces are parallel to the polar axis. The crystal has a congruent composition and contains 0.1 wt. % of Fe_2O_3. The dominating charge-transport mechanism is the photovoltaic effect. The main elements of the feedback setup are similar to that described in Section 6.2.1.

The feedback operation has been studied at two wavelengths for extraordinarily polarized laser beams. Two light sources were used: A 100 mW frequency-

doubled YAG: Nd^{3+} laser ($\lambda = 532\,\text{nm}$) and a 50 mW He-Ne laser ($\lambda = 633\,\text{nm}$). At 532 nm, the response time t_r was about 60 s for the total intensity $I_0 = 130\,\text{mW/cm}^2$, whereas the characteristic photovoltaic field $E_{pv} \approx 100\,\text{kV/cm}$ and the coupling strength $|\Gamma_0|d \approx 8$. At 633 nm, the time t_r was about 240 s and the coupling strength is about 3.5. The angle between the incident light beams was $\simeq 12^\circ$. At 532 nm, this corresponds to the grating period $2\pi/K \simeq 2.2\,\mu\text{m}$ and to a diffusion field of $E_D \simeq 0.65\,\text{kV/cm}$. At 633 nm, the corresponding numbers are $\simeq 3\,\mu\text{m}$ and $\simeq 0.54\,\text{kV/cm}$. In both cases, $E_D \ll E_{pv}$ so that the PR response is almost local.

To verify the fact that the feedback loop meets the feedback condition (6.3), the transmission factor of the integrator, K_ω, was measured as a function of the frequency ω of an input harmonic signal. It was found that $K_\omega \propto \omega^{-1}$ within a wide frequency range $\omega \leq 10^2\,s^{-1} \approx 10^4\,t_r^{-1}$. Therefore, the Fourier component of the mirror displacement $x_\omega \propto \omega^{-1}$ and the Fourier component of the mirror velocity, $-i\omega x_\omega$, do not depend on the modulation frequency. This proves the validity of the linear relation (6.3) between $\dot{\varphi}_s$ and the error signal with a great safety margin. The value of the response time of the feedback loop was estimated as $t_f \approx 10^{-3} t_r$.

Turn now to the experimental results for the $+\pi/2$ feedback. No auto-oscillations were observed at 532 nm for sufficiently large and small beam ratios, $r_0 \lesssim 0.03$ and $r_0 \gtrsim 50$. The diffraction efficiency η remains here smaller than 1 and the feedback effect is reduced to the introduction of a frequency detuning $\Omega = \dot{\varphi}_s$ (see Fig. 6.11). The sign of Ω is determined by the sign of $\ln r_0$ and the absolute value $|\Omega|$ (the value of the tilt of the line $\varphi_s(t)$) is increasing with growing $|\ln r_0|$. This is in full agreement with the properties of steady states considered in Section 6.3.3.

Within the interval $0.03 \lesssim r_0 \lesssim 50$, the situation was different. Fig. 6.12 gives an example of the experimental dependences of $\eta(t)$ and $\varphi_s(t)$ for $r_0 \approx 1/9$ and $t_r \approx 200\,\text{s}$. In agreement with theory, the efficiency monotonously approaches 1 during the initial state, whereas the input phase φ_s shows a quasi-linear growth.

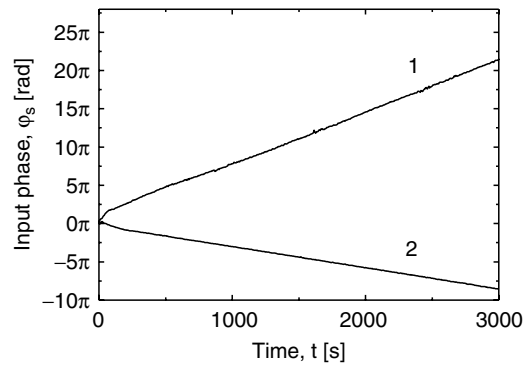

FIGURE 6.11. Experimental time dependences of the input phase φ_s in steady state for the sample of $LiNbO_3$. Curves 1 and 2 correspond to $r_0 = 120$ and 0.013, respectively; the wavelength $\lambda = 532\,\text{nm}$.

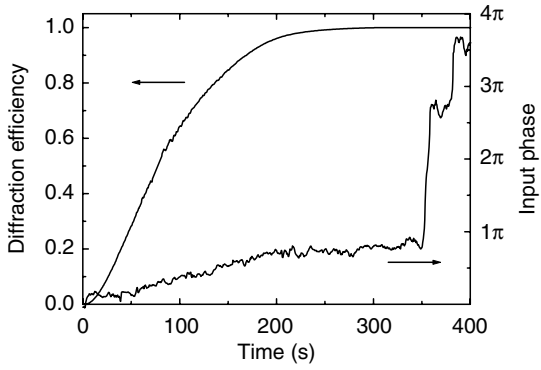

FIGURE 6.12. Experimental dependences $\eta(t)$ and $\varphi_s(t)$ for the $\pi/2$ feedback and $^1/_9$.

The initial stage ends up at $t \approx 350$ s when the phase first experiences a jump; the value of η is practically saturated at this stage. Note that the dependence $\varphi_s(t)$ looks noisy as compared to $\eta(t)$. This reflects the stabilizing effect of the feedback loop.

Fig. 6.13 shows the saturated value of η versus r_0 for $\lambda = 633$ and 532 nm, which corresponds to two different values of the coupling strength. It is clearly seen that the ultimate value $\eta \simeq 1$ is achieved within a certain interval of the input beam ratio. The larger is the coupling strength, the wider this interval. This feature is also in full agreement with the expected one.

A number of recognizable periodic states (with permanently operating feedback and the diffraction efficiency $\eta \simeq 1$) have been observed within the interval $r_0 = 0.03 - 50$ for $\lambda = 532$ nm. It seems that all the states described in Section 6.4.1 were observed. Figure 6.14a shows a typical fragment of the feedback-controlled dependence $\varphi_s(t)$ for $r_0 = 10$. A large average slope and quasi-periodic phase steps are clearly seen in this plot. These elements are similar to those presented in Fig. 6.7. The time distance between the subsequent steps can be estimated as $\simeq 0.2t_r$. The next Fig. 6.14b corresponds to $r_0 = 6.6$.

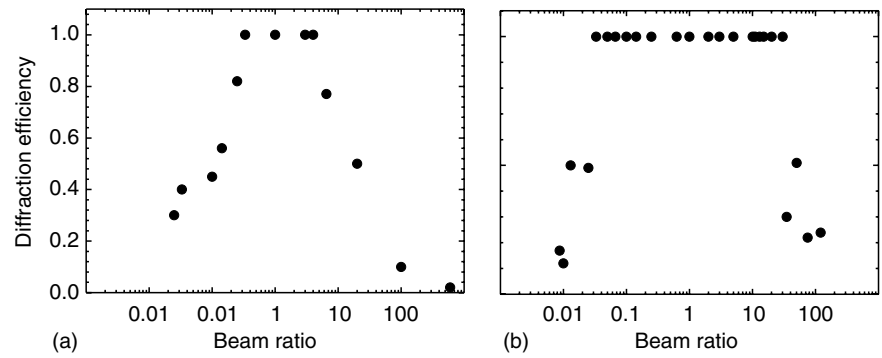

FIGURE 6.13. The saturated value of η versus r_0 at $\lambda = 633$ nm (a) and 532 nm (b).

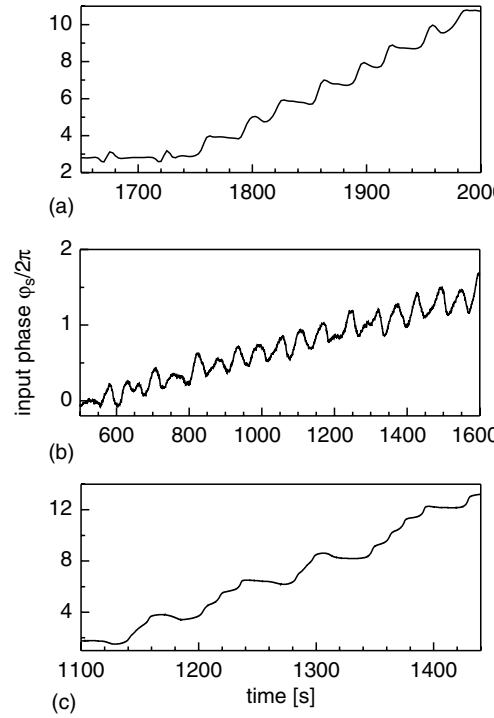

FIGURE 6.14. Fragments of experimentally obtained feedback-controlled phase dependences $\varphi_s(t)$ at $\lambda = 532\,\text{nm}$. The subfigures (a), (b), and (c) correspond to the input intensity ratio $r_0 = 10$, 6.6, and 1, respectively. Note the different vertical scales for the cases a), b), and c).

It shows a considerably smaller slope and clearly pronounced quasi-periodic phase oscillations. The period of the oscillations is estimated here as $\simeq 0.3\,t_r$. These features are similar to those presented in Fig. 6.9a. Lastly, Fig. 6.14c shows a representative dependence $\varphi_s(t)$ for $r_0 = 1$; it corresponds to the period tripling, compare with Fig. 6.9b. The full period, $\approx 0.82 t_r$, is approximately 3 times larger than it is in the previous case.

It would be unreal indeed to expect an exact coincidence between the experiment and numerical simulations because of mechanical perturbations, air draughts, and other factors affecting the experimental results and also because of some uncertainty in the values of material parameters. Nevertheless, a good semi-quantitative agreement is evident.

6.4.3 A Simple View on the Periodic States

As we already know, the periodic states with $\eta \simeq 1$ or 0 are due to the presence of a proper frequency detuning Ω_s and a proper periodic oscillation $\varphi_p(t)$ in the input S-beam. Furthermore, we know that the modulation period T is considerably shorter than t_r for sufficiently small feedback time t_f. These general features allow us to gain a simple view of the feedback operation.

Fast modulation of the input phase φ_s produces an erasure effect on the grating. The same effect comes from the large frequency detuning, $\Omega_s t_r \gg 1$.

Both of these factors work to compensate the overshot that takes place when the coupling strength $|\Gamma_0|d$ exceeds the value given by the threshold equation $\eta(|\Gamma_0|d,\ r_0) = 1$ (see Fig. 6.4). Adjustment of Ω_s cannot compensate the overshot because two conditions, $\mathrm{Re}[f_T^s(d,\ \Omega_s)] = 0$ and $\mathrm{Im}[f_T^s(d,\ \Omega_s)] = 0$, cannot be fulfilled with only one variable parameter in hand. From this general viewpoint, the appearance of the periodic component $\varphi_p(t)$ looks natural.

To extract the net effect of periodic phase modulation, it is helpful to recall that $\varphi_s = \varphi_p + \Omega_s t$ and $\Omega_s = 2\pi NT^{-1} + \Omega$, where $\Omega \ll t_r^{-1}$. The input phase φ_s enters all physical relations via the exponent $\exp(i\varphi_s) \equiv \exp(i\varphi_p + 2\pi iNt/T)\cdot \exp(i\Omega t)$. The first factor in the right-hand side is a T-periodic function of time; it is the genuine mediator of the fast-modulation influence. The reduced detuning Ω characterizes the slow degrees of freedom.

In fact, the major effect of the periodic modulation on the grating recording and beam coupling is determined by only one real characteristic parameter [27]

$$\varepsilon = \left|\langle \exp(i\varphi_p + 2\pi iN\ t/T)\rangle_T\right|, \tag{6.29}$$

where the brackets mean averaging over the period. This assertion stems from a simple idea: The inertial process of grating formation is sensitive not to fine features of the fast external changes, but to their average properties. Parameter ε ranges from 1 to 0; these limit values correspond to zero and ultimately large phase modulation, respectively.

Leaving aside technical issues, one can say that the observable characteristics of the periodic states, such as $\eta, |S_d|^2, |R_d|^2$, are algebraically expressed by ε and Ω in the leading approximation in T/t_r. This approximation leaves aside small and fast oscillations of the grating amplitude; the latter can be taken into account in the next approximation. By setting $\eta(\varepsilon,\ \Omega;|\Gamma_0|d,\ r_0) = 1$ or 0, it is possible to find the values of ε and Ω as functions of $|\Gamma_0|d$ and r_0 within the above-threshold region of the experimental parameters.

Fig. 6.15 shows ε^2 and Ω versus r_0 for the states with $\eta \simeq 1$ and the local response. These results are in agreement with those obtained by the averaging of the numerical data of section 6.4.1. The value of ε decreases rapidly with increasing coupling strength for $|\Gamma_0|d > \pi$, i.e., the strength of the fast modulation is increasing. The detuning is an odd function of the beam ratio; its absolute values are fairly small.

The above results allow us to understand the rough features of the periodic states. They say nothing, however, about the shape of the phase oscillations and other fine characteristics of the periodic states. This information becomes available within the next approximation in t_f/t_r [29].

6.4.4. *Light Domains*

In this subsection, we focus on the spatial structure of the light and grating fringes that are relevant to the periodic states. This structure possesses distinguishing features that cannot be realized in steady states. For definiteness, we

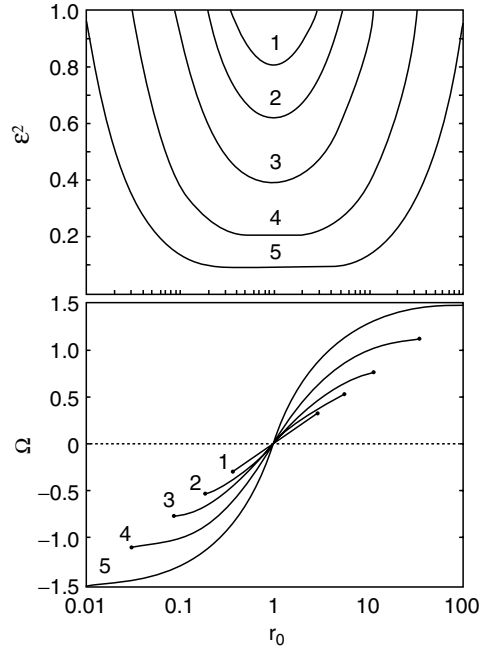

FIGURE 6.15. Dependences $\varepsilon^2(r_0)$ and $\Omega(r_0)$ for the periodic states with $\eta \simeq 1$ in the case of local PR response $\Gamma_0 = i|\Gamma_0|$. The curves 1, 2, 3, 4, and 5 are plotted for $|\Gamma_0|d =$ 3.5, 4, 5, 7, and 10, respectively. The dots in the second graph mark the end points of the permitted interval of r_0.

consider the case of local response $\Gamma_0 = |\Gamma_0|$, the feedback $\pi/2$, and the coupling strength $|\Gamma_0|d = 6.6$. The characteristics in question are the spatial distributions of the intensity modulation $\Delta I(x, z) = (1/2)\ S(z)R^*(z)\exp(iKx) + c.c.$ and of the light-induced space-charge field $E_{sc}(x, z) = (1/2)E_K(z)\exp(iKx) + c.c.$ The latter is proportional to the index changes.

Fig. 6.16 exhibits a spatial distribution $E_{sc}(x, z)$ for $r_0 = 1$ obtained by the direct numerical simulations. The grating fringes experience only very weak T-periodic oscillations around average positions. Moreover, they are practically straight, which is in line with the discussion in the end of section 6.4.1. The relevant time dependence $\varphi_s(t)$ is presented in Fig. 6.9.

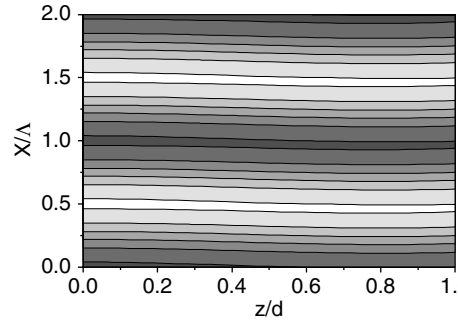

FIGURE 6.16. Dependence of E_{sc} on the propagation coordinate z and fringe coordinate x for $|\Gamma_0|d = 6.6$ and $r_0 = 1$. The darkest areas correspond to the biggest values of the space-charge field.

Fig. 6.17 shows four representative distributions $\Delta I(x, z)$; they are plotted for four sequential time moments. In contrast to Fig. 6.16, the light-interference pattern experiences remarkable changes. It consists actually of two domains moving in the opposite $\pm x$ directions. The boundary between these domains, where fringe breaking periodically takes place, is situated at $z = d/2$. The fringe switching occurs six times a period, the total change of $\varphi_s(t)$ is $\simeq 6\pi$. During the time intervals where $\varphi_s(t)$ remains almost constant (see Fig. 6.9b), the light pattern looks uniform.

The described behavior of the index and light fringes changes only in details for the periodic state with $r_0 = 6$. The main distinctions from the case $r_0 = 1$ are as follows: The grating is noticeably nonuniform, its fringes are bent, and its amplitude is considerably larger at the center ($z = d/2$) as compared to that nearby the input and output crystal faces. The grating is moving (in average) with a small velocity Ω/K.

The presented physical picture contrasts strongly with the conventional one, known for recording of dynamic index gratings in the absence of the feedback. Within the conventional concept, the light and index fringes are strongly coupled with each other in steady state; they are moving (for $\Omega \neq 0$) with the

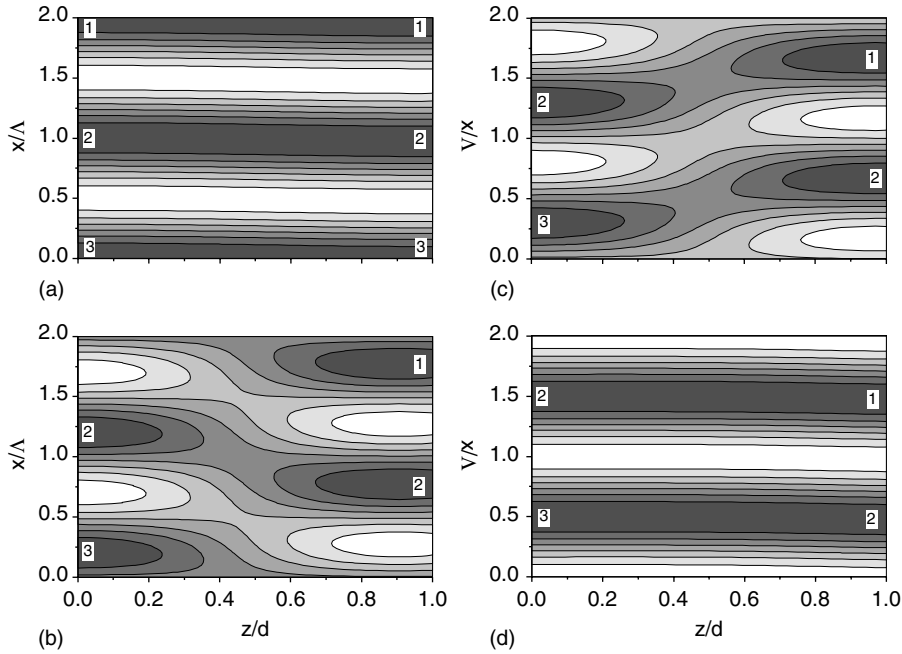

FIGURE 6.17. Light intensity distributions at four time moments within one period $T \simeq 0.97 t_r$; the numbers 1, 2, and 3 mark the domain fringes at the input and output faces. The pictures (b) and (c) show in detail the switching process.

same velocity and experience no breaking. Below we explain the apparently peculiar behavior of the light fringes in the periodic states.

Let us revisit the case $r_0 = 1$. The input phase of the S-beam is here $\varphi_s = \Omega_s t + \varphi_p$, where $\varphi_p(t)$ is a T-periodic function and the detuning $\Omega_s \simeq 6\pi/T$. Obviously, the corresponding light-interference pattern is moving with an average velocity Ω_s/K at the input face ($z = 0$). Diffraction of such a phase modulated S-wave and a nonmodulated R-wave from a fully diffractive ($\eta = 1$) static index grating results in an interchange of the amplitudes R and S at the crystal output ($z = d$). The light-interference pattern is traveling here in the opposite direction. Moreover, the Kogelnik theory gives the following simple relation for the spatio-temporal dependence of the light intensity in the case of spatially-uniform static grating with $\eta = 1$:

$$\Delta I = \cos^2(\pi z/2d)\cos(Kx - \varphi_s) + \sin^2(\pi z/2d)\cos(Kx + \varphi_s). \tag{6.30}$$

It describes all of the above described features of the light fringes. It is clear, in particular, from this relation that the fringe switching occurs for $z = d/2$ at the time moments when $\cos\varphi_s = 0$, which corresponds to the numerical data.

The remaining question is: *How can the moving two-domain light pattern be consistent with the static index grating?*

To answer this question, we recall first that the factor $\exp(i\varphi_s)$ entering the input amplitude S_0 is a periodic quickly oscillating function of time. It possesses not only a zero Fourier harmonic but also higher harmonics with the temporal frequencies $2\pi/T, 4\pi/T, \ldots$ The amplitudes of the latter are not small. The same assertion is applicable indeed to the input intensity pattern. The higher intensity harmonics are inefficient for grating recording because of its inertia. This does not mean, however, that the higher harmonics of $S_0(t)$ can be neglected. The point is that diffraction from a static (or quasi-static) grating transforms instantaneously the fast component of the S-beam into the R-beam. Interference of fast S- and R-components contributes then to the slow component of the light intensity. Therefore, the higher Fourier harmonics of $\exp(i\varphi_s)$ affect the grating formation in thick crystals. The recorded grating is static for $r_0 = 1$ because the reduced detuning $\Omega = 0$. The higher intensity harmonics result in small oscillations of the fringe positions. Quantitative side of the grating formation in the case of strong phase modulation and beam coupling can be found in [27, 28].

In the case $r_0 \neq 1$, the reduced frequency detuning Ω is not zero so that the index fringes are moving. The assumption of a spatially-uniform index grating works badly for nonequal input intensities and the light pattern inside the sample cannot be satisfactorily described by the Kogelnik theory.

It should be emphasized that the unusual behavior of the light fringes in the feedback presence comes from a fine balance between the effects of periodic phase oscillations (φ_p) and the linear growth ($\Omega_s t$). Distortions of the form of the phase steps and/or the average slope of the dependence $\varphi_s(t)$ produce qualitative changes in the fringe behavior.

6.5. Feedback Operation in Reflection Geometry

6.5.1. General Features of the Reflection Case

The key feature of the reflection geometry is counter-propagation of the interacting waves (see Fig. 6.18). It causes a number of important distinctions from the transmission case considered in sections 6.2–6.4.

The light and grating fringes are parallel now to the input/output faces. The fact that the R-wave is traveling in the negative direction results in modification of the coupled-wave equations. They read now:

$$\frac{\partial R}{\partial z} = -i\kappa E_K\ S, \quad \frac{\partial S}{\partial z} = +i\kappa E_K^*\ R, \tag{6.31}$$

Compare to Eqs. (6.6). Not the sum but the difference of the light intensities is conserving in the reflection case, $|R(z)|^2 - |S(z)|^2 = const$. The input light amplitudes are now S_0 and R_d, while the output amplitudes are S_d and R_0. The structure of the material Eq. (6.7) for the grating amplitude E_K remains unchanged.

An inherent feature of the reflection configuration is the fact that the diffraction efficiency η cannot reach the value of 1. It is evident already within the Kogelnik theory relevant to the case of spatially-uniform grating, $E_K(z) = const$; within this theory, $\eta = \tanh^2(\kappa|E_K|d) < 1$. One can expect that the feedback does not lead to periodic states with $\eta \simeq 1$.

The grating period is ultimately small for the reflection geometry. As the propagation angles inside the sample are small, it can be estimated as $\Lambda \simeq \lambda/2n$, which is $\approx 100\,\text{nm}$ for typical experimental conditions. Charge saturation effects are often strong in this range. This means, in particular, that the PR response time t_r has to be treated as a complex quantity.

The requirement of mechanical stability is especially tough for the reflection geometry owing to the smallness of Λ. One can say that reproducible long-term experiments with such materials as lithium niobate, and also the use of thermal fixing technique [5, 6], are inconceivable without an active stabilization. Since

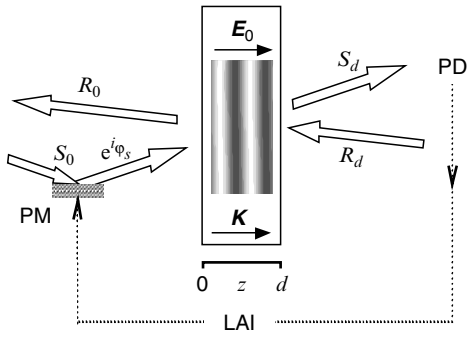

FIGURE 6.18. Schematic of a feedback experiment in the reflection geometry; the grating vector **K** and the applied field $\mathbf{E}_0$ are parallel to the propagation axis z and the light beams are incident onto the opposite crystal faces, $z = 0$ and d.

the feedback stabilization is a strongly nonlinear phenomenon, sensitive to the PR response of the medium, it is important to know what can be expected in the actual cases.

Feedback experiments in the reflection geometry have become available only recently [33]. They deal with $LiNbO_3$ crystals subjected to very large electric fields (up to 650 kV/cm). Application of such high fields would be extremely difficult in the transmission case. The combination of ultimately small spatial periods with very large applied fields brings about a new wealth of photorefractive phenomena.

The reader can find below a number of general issues relevant to the feedback use, as well as particular applications to the case of $LiNbO_3$ crystals.

6.5.2. Feedback Conditions

Separation of the recording amplitudes R and S into the diffracted (D) and transmitted (T) components is again the key point for understanding the feedback operation. It is given by:

$$S = S_0 f_T^s + R_d f_D^s, \quad R = R_d f_T^r + S_0 f_D^r, \tag{6.32}$$

Compare with Eqs. (6.8). The first and second contributions correspond to the T- and D-components, respectively. The fundamental amplitudes $f_{T,D}^s(z,t)$ and $f_{T,D}^r(z,t)$ correspond to testing of the reflection grating by single beams of a unit amplitude (see Fig. 6.19). The diffraction efficiency is given by the expressions $\eta = |f_D^s(d)|^2 = |f_D^r(0)|^2$; its value does not depend on which of the input beams (S or R) is blocked.

The fundamental amplitudes are expressed by the recording amplitudes as follows [44]:

$$f_T^s = (S_d^* S - R_d R^*)/I_1, \quad f_D^s = (S_0 R^* - R_0^* S)/I_1 \tag{6.33}$$

$$f_T^r = (S_0 S^* - R_0^* R)/I_1, \quad f_D^r = (S_d^* R - R_d S^*)/I_1, \tag{6.34}$$

where $I_1 = S_0 S_d^* - R_0^* R_d$ is a complex constant. As follows from here, the pairs f_T^s, f_T^r and f_D^s, f_D^r are coupled with each other by the symmetry relations

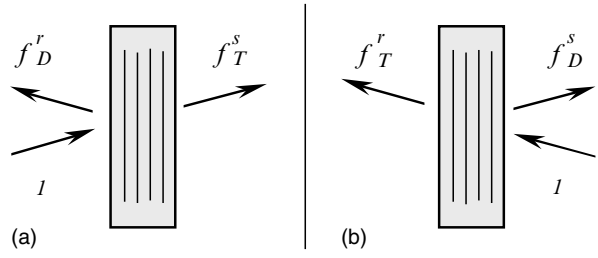

FIGURE 6.19. Geometrical schemes relevant to the definition of the fundamental amplitudes in the reflection geometry.

$f_T^s = f_T^{r*}(0 \leftrightarrow d)$, $f_D^s = f_D^{r*}(0 \leftrightarrow d)$ that generalize Eqs. (6.9) for the transmission case. The sign $\leftrightarrow$ means interchanging of the subscripts 0 and d. Using Eqs. (6.33) and (6.34) one can, in particular, express η by the input and output values of the recording amplitudes.

If $\varphi_s = \arg S_0$ is the feedback-controlled phase of the input S-beam and $\varphi_r = \arg R_d$ is the phase of the incident R-beam, then $\Phi_s = \varphi_r - \varphi_s + \arg [f_D^s(d)/f_T^s(d)]$ is the phase difference between the D- and T-components of the signal wave.

Apart from the differences in expressing Φ_s through the recording amplitudes, implementation of the feedback in the reflection case is not much different from that in the transmission geometry (see Section 6.2.1). As far as $\eta(1-\eta) \neq 0$, the use of $I_{2\omega}$ as an error signal leads to adjustment of Φ_s to $\pm\pi/2$ during the time $\approx t_f$. The use of I_ω ensures the adjustment of Φ_s to π or 0. The feedback equation (6.3) is applicable to the reflection geometry if we accept that the input contrast is $m_0 = 2|S_0 R_d|/(|S_0|^2 + |R_d|^2)$.

6.5.3. *Application to* $LiNbO_3$*: Fe crystals*

Photorefractive Response

The PR response of $LiNbO_3$:Fe crystals can be satisfactorily described within the one-species model where the ions of Fe^{2+} and Fe^{3+} serve as donors and acceptors and the photo-excited charge carriers are electrons [3]. This model gives the following expressions for the parameters t_r and F in Eq. (6.7):

$$\frac{1}{t_r} \simeq \frac{|S|^2 + |R|^2}{t_{di}} \frac{E_q + E_D + i(E_{pv} - E_0)}{E_q}, \tag{6.35}$$

$$F \simeq \frac{E_q(E_{pv} - E_0 - iE_D)}{E_q + E_D + i(E_{pv} - E_0)}. \tag{6.36}$$

Here t_{di} is the dielectric relaxation time calculated for the total input intensity, E_{pv} is the photovoltaic field, E_D is the diffusion field, and $E_q = eN_t/\epsilon\epsilon_0 K$ is the saturation field with $N_t = N_{Fe}^{2+} N_{Fe}^{3+}/(N_{Fe}^{2+} + N_{Fe}^{3+}) \approx N_{Fe}^{2+}$ being the effective trap concentration. The light amplitudes are normalized now in such a way that $|S_0|^2 + |R_d|^2 = 1$. The material parameters entering Eqs. (6.35) and (6.36) are known in experiments with $LiNbO_3$: Fe crystals.

In the transmission geometry, where the grating period $\Lambda \gtrsim \lambda$, the saturation field E_q exceeds the other characteristic fields for typical concentration $N_t \approx N_{Fe}^{2+} \sim 10^{18}\,\mathrm{cm}^{-3}$ and $E_D \ll E_{pv} \sim 10^5\,\mathrm{V/cm}$. In this case, $t_r \approx t_{di}$ and $F \approx E_{pv} - E_0$, i.e., the PR response is almost local.

In the reflection geometry, the situation is different because the saturation field E_q is relatively small. To clarify this difference, we make numerical estimates relevant to experiment. By setting $\lambda = 488\,\mathrm{nm}$, $\Lambda = 100\,\mathrm{nm}$ and $N_t = 10^{18}\,\mathrm{cm}^{-3}$, we obtain $E_q \simeq 100\,\mathrm{kV/cm}$. The photovoltaic field does not depend on N_t when the fraction of donors is small; it can be estimated as

$E_{pv} \approx 100\,\mathrm{kV/cm}$. The diffusion field is considerably smaller, $E_D \simeq 16\,\mathrm{kV/cm}$. If the maximum value of E_0 is about 650 kV/cm, we have a range of applied fields where $|E_0 - E_{pv}| \gg E_q, E_D$. Within this range, the relaxation rate t_r^{-1} is almost imaginary, $\mathrm{Re}(t_r^{-1}) \ll \mathrm{Im}(t_r^{-1})$. Physically, this means that the grating is running during relaxation (under a uniform illumination) with the velocity of $\mathrm{Im}(t_r^{-1})/K$ and decays relatively slowly. In other words, we have an eigen-mode—weakly damped space-charge wave [34].

The main outcome of the presence of the eigen-mode for the grating recording is as follows: If the frequency detuning Ω between the light beams is zero (static fringes), the grating amplitude in steady state is $E_K \approx -2iE_qS^*R/(|S|^2 + |R|^2)$. In other words, the grating is $\pi/2$ shifted against the light interference pattern and an energy exchange occurs between the light beams. If the detuning $\Omega = \mathrm{Im}(t_r^{-1})$, i.e., the resonant excitation of the eigen-mode takes place, then $E_K \approx (E_{pv} - E_0)2S^*R/(|S|^2 + |R|^2)$. The PR response is local (the energy exchange is suppressed) and the grating amplitude is enhanced by a factor of $|E_{pv} - E_0|/E_q \gg 1$.

The question is now whether the $\pm\pi/2$ feedback leads to the enhanced local response by introducing the necessary frequency detuning into the S-beam. Both analytical and numerical calculations give a positive answer to this question [36, 37]. Thus the feedback is expected to lead to the resonant excitation of weakly damped space-charge waves. The dependence of the feedback-introduced detuning Ω on E_0 should follow the field dependence of the eigen-frequency, $\omega_K = \mathrm{Im}(t_r^{-1}) \propto E_0 - E_{pv}$.

Experimental Results

A congruently melted $LiNbO_3$:Fe crystal with an iron concentration $N_{Fe} \simeq 18 \times 10^{18}\,\mathrm{cm^{-3}}$ and a thickness $d = 0.22\,\mathrm{mm}$ was used in the feedback experiments [36, 37]. The polar axis was perpendicular to the input faces. The concentration of Fe^{2+} ions was varied by annealing treatments between ≈ 0.7 to $\approx 2.3 \times 10^{18}\,\mathrm{cm^{-3}}$. The field E_0 ranged from 0 to 650 kV/cm and was parallel to the spontaneous polarization vector. Application of larger fields leads to electric breakdown. Equally strong fields of the opposite direction would reverse the spontaneous polarization.

Two pump beams of equal intensity ($\approx 0.1\,\mathrm{W/cm^2}$ each) at 488 nm were incident at small angles onto the opposite crystal faces. The corresponding grating period was $\Lambda \simeq 105\,\mathrm{nm}$. The temporal evolution of the output intensities, the diffraction efficiency η, and the feedback signal driving the input phase φ_s were measured.

It has been mentioned first that the sign of the error signal $\pm I_{2\omega}$ has to be different in the regions $E_0 - E_{pv} < 0$ and $E_0 - E_{pv} > 0$ to ensure maximization of the diffraction efficiency. This observation is in full agreement with the theoretical expectations.

It was found then that the piezo-signal governing the input phase φ_s is generally linear in steady state; no periodic (or quasi-periodic) oscillations of

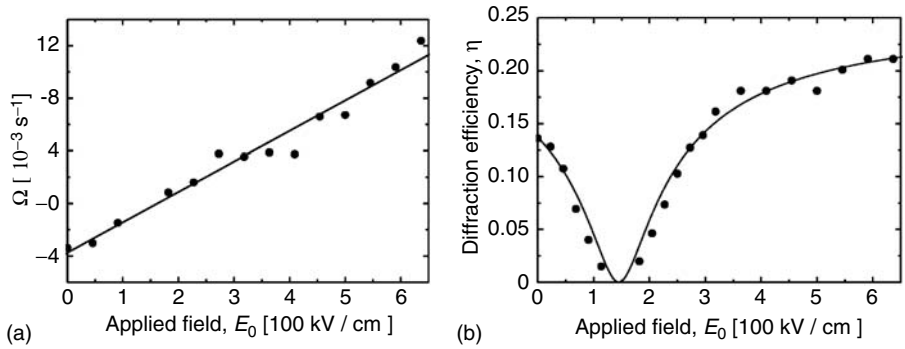

FIGURE 6.20. Field dependences the frequency detuning Ω and the diffraction efficiency η measured in feedback experiments with $LiNbO_3$: Fe.

this signal were observed. The detuning $\Omega = \dot{\varphi}_s$ was negative for $E_0 \lesssim 100\,\mathrm{kV/cm}$ and positive for $E_0 \gtrsim 100\,\mathrm{kV/cm}$. Within the range $100 \lesssim E_0 \lesssim 200\,\mathrm{kV/cm}$ operation of the feedback loop was not stable enough to ensure reproducible measurements of the frequency detuning.

The experimental data on the field dependence of Ω are presented in Fig. 6.20a. The dots are well fitted by a linear function. Furthermore, it was estimated that the maximum value of Ω exceeds the reciprocal dielectric relaxation time t_{di}^{-1} by a factor of ≈ 4.3. The main source of a spread of experimental dots are fluctuations of the input phase difference, which are compensated by the feedback loop. Extreme precautions are necessary to diminish these fluctuations.

The dots in Fig. 6.20b show the data on the field dependence of η; the solid line is a theoretical fit. Agreement between experiment and theory is pretty good. The dip in $\eta(E_0)$ occurs at $E_0 \approx E_{pv} \simeq 130\,\mathrm{kV/cm}$; it is caused by the compensation of the drift and photovoltaic contributions to the PR response.

It was found lastly that the energy exchange between the R- and S-beams is fairly weak, which is due to the presence of the frequency detuning.

The presented experimental data show that the expected space-charge waves do exist in iron-doped lithium niobate crystals in the range of high spatial frequencies, that the $\pm\pi/2$ feedback generates a grating moving with a constant velocity, and that the feedback-introduced detuning is resonant to the frequency of space-charge waves, i.e., the resonant excitation of these eigenmodes and the expected modification of the PR response take place.

6.6 Summary

We have given above an extended introduction into a new field of photorefractive studies—the feedback-controlled wave coupling. It includes a historical sketch, theoretical and experimental aspects of the feedback operation and implementation, as well as a review of feedback effects and applications.

The electronic feedback loop not only ensures an active long-term stabilization of the fringe positions in noisy environments. It is able to carry additional useful functions—to modify the type of nonlinear response, to maximize and minimize the diffraction efficiency of dynamic gratings, to keep this efficiency near the ultimate values 1 or 0.

For sufficiently small values of the coupling strength, the feedback brings the system to a steady state unless the presence of this state is incompatible with the chosen feedback condition. A frequency detuning Ω between the interacting beams exists generally in the steady state; it serves as an adjustable parameter to meet the feedback condition. The value and sign of Ω depend on the type of PR response and the feedback condition in question.

There are many situations when the imposed feedback is incompatible with the presence of steady states. A typical scenario of the feedback operation in such cases is erasure of dynamic gratings and achievement of zero diffraction efficiency.

New possibilities appear in the range of large coupling strength $|\Gamma_0|d$ for the transmission geometry. This range is bounded by the threshold curve (separatrix) on the plane of coupling strength–input beam ratio; this curve is given by the steady-state relation $\eta(|\Gamma_0|d,\ r_0) = 1$. The form and position of the separatrix depends on the type of PR response.

Within the above-threshold region, the $\pm\pi/2$ feedback leads the system to a variety of periodic states. A periodic state is characterized by periodic oscillations of $\eta(t)$ in the close vicinity of 1 or 0, by the presence of a frequency detuning between pump beams, and by strong periodic oscillations of the feedback-controlled input phase φ_s. Different periodic states are distinguished by the values and shapes of the above observable quantities.

Reflection geometry occupies a special place in the feedback studies. It allows us to study the photorefractive processes (including charge-separation effects) in the range of ultimately small grating periods ($\approx 10^{-1}\,\mu$m). Stabilization effect of the feedback loop is highly important for long-term experiments with slow ferroelectrics (like $LiNbO_3$, $LiTaO_3$, SBN) and also for the purposes of thermal fixing of dynamic gratings. The use of the feedback technique has allowed us to detect the presence of weakly damped space-charge waves and modification of the PR response in $LiNbO_3$: Fe crystals.

A correct description of the feedback-controlled wave coupling is not possible within the Kogelnik theory, which deals with spatially-uniform index gratings. This description requires a refined knowledge of the diffraction and transmission properties of dynamic gratings. Inertia of the feedback loop is crucial for the periodic states with $\eta \simeq 1$ and 0. The notion of the ideal feedback conditions (with a fixed value of the phase difference between the diffracted and transmitted components of the signal wave) is applicable only to the feedback-controlled steady states.

The potential and specific features of the feedback-controlled devises are not fully recognized yet. This is applicable not only to photorefractive crystals but to all materials possessing relatively slow nonlinear response [52], liquid crystals, orientational polymers, structural glasses, and so on.

Acknowledgements: We thank K.V. Shcherbin for discussions and technical support. Financial support from Russian Foundation for Fundamental Studies (Grant 03-02-16083) is gratefully acknowledged.

References

1. P. Günter and J.-P. Huignard, eds., *Photorefractive Materials and Their Applications, I, Vol. 61 of Topics in Applied Physics*, Springer-Verlag, Berlin (1988).
2. L. Solymar, D.J. Webb, and A. Grunnet-Jepsen, *The Physics and Applications of Photorefractive Materials*, Clarendon Press, Oxford (1996).
3. K. Buse: Appl. Phys. B **64**, 391 (1997).
4. S. Stepanov: Rep. Prog. Phys. **57**, 396 (1994).
5. A. Yariv, S.S. Orlov, G.A. Rakuljic: J. Opt. Soc. Am. B **13**, 2513 (1996).
6. K. Buse, S. Breer, K. Peithmann, S. Kapphan, M. Gao, E. Krätzig: Phys. Rev. B **56**, 1225 (1997).
7. D.B. Neumann, H.W. Rose: Appl. Opt. **6**, 1097 (1967).
8. R.C. Weyrick, *Fundamentals of Automatic Control*, Chap. 6, McGraw-Hill, N.Y. (1975).
9. D.R. MacQuigg: Appl. Opt. **16**, 291 (1977).
10. A.A. Kamshilin, J. Frejlich, L. Cescato: Appl. Opt. **25**, 2375 (1986).
11. J. Frejlich, L. Cescato, and G.F. Mendes: Appl. Opt. **27**, 1967 (1988).
12. A. Freschi, J. Frejlich: J. Opt. Soc. Am. B **11**, 1837 (1994).
13. P.M. Garcia, K. Buse, D. Kip, J. Frejlich: Opt. Commun. **117**, 35 (1995).
14. A.A. Freschi, J. Frejlich: Opt. Lett. **20**, 635 (1995).
15. P.M. Garcia, A.A. Freschi, J. Frejlich, E. Krätzig: Appl. Phys. B **63**, 207 (1996).
16. A. Freschi, P.M. Garsia, J. Frejlich: Opt. Commun. **143**, 257 (1997).
17. S. Breer, K. Buse, K. Peithmann, H. Vogt, E. Krätzig: Review of Scientific Instruments, **69**, 1591 (1998).
18. A. Shumelyuk, S. Pavlyuk, D. Barilov, G. Brost: Trends in Optics and Photonics Series, **62**, 601 (2001).
19. S.G. Odoulov, A.N. Shumelyuk, G.A. Brost: J. Opt. Soc. Am. B **15**, 2125 (1998).
20. M.C. Barbosa, I. de Oliveira, J. Frejlich: Opt. Commun. **201**, 293 (2002).
21. V.P. Kamenov, K.H. Ringhofer, B.I. Sturman, J. Frejlich: Phys. Rev. A **56**, R2541 (1997).
22. J. Frejlich, P.M. Garsia, K.H. Ringhofer, E. Shamonina: J. Opt. Soc. Am. B **14**, 1741 (1997).
23. E.V. Podivilov, B.I. Sturman, S.G. Odoulov, S.L. Pavlyuk, K.V. Shcherbin, V.Ya. Gayvoronsky, K.H. Ringhofer, V.P. Kamenov: Opt. Commun. **192**, 399 (2001).
24. E.V. Podivilov, B.I. Sturman, S.G. Odoulov, S.L. Pavlyuk, K.V. Shcherbin, V.Ya. Gayvoronsky, K.H. Ringhofer, V.P. Kamenov: Phys. Rev. A **63**, 053805 (2001).
25. K. Shcherbin, S. Pavlyuk, S. Odoulov, K. Ringhofer, V. Kamenov, E. Podivilov, B. Sturman: Trends in Optics and Photonics Series, **62**, 616 (2001).
26. B.I. Sturman, V. Kamenov, M.V. Gorkounov, K.H. Ringhofer: Opt. Commun. **216**, 225 (2003).
27. K.H. Ringhofer, V.P. Kamenov B.I. Sturman, A.I. Chernykh: Phys. Rev. E **61**, 2029 (2000).
28. B.I. Sturman, A.S. Gorkounova, K.H. Ringhofer: Eur. Phys. J. **23**, 291 (2003).

29. E.V. Podivilov, B.I. Sturman, and M.V. Gorkunov: J. Experimental and Theoretical Physics, 98, 896 (2004).
30. E.V. Podivilov, B.I. Sturman, and M. Gorkunov: Ukr. J. Phys. **49**, 418 (2004).
31. A. Gorkounova, B. Sturman: (to be published).
32. B. Sturman, E. Podivilov, and M. Gorkunov: Phys. Rev. E **71**, 016231 (2005).
33. M. Luennemann, U. Hartwig, K. Buse: J. Opt. Soc. Am. B **20**, 1643 (2003).
34. B.I. Sturman, E. Shamonina, M. Mann, K.H. Ringhofer: J. Opt. Soc. Am. B **12**, 1642 (1995).
35. B.I. Sturman: in *Photorefractive Materials and Applications*, Vol. 2, Springer-Verlag (2004).
36. M. Gorkunov, B. Sturman, M. Luennemann, K. Buse: Appl. Phys. B **77**, 43 (2003).
37. M. Luennemann, K. Buse, B. Sturman: J. Appl. Phys. **94**, 6274 (2003).
38. H. Kogelnik: Bell Syst. Tech. J. **48**, 2909 (1969).
39. A.M. Glass, D. von der Linde, T.J. Negran: Appl. Phys. Lett. **25**, 233 (1974).
40. B.I. Sturman, V.M. Fridkin, *The Photovoltaic and Photorefractive Effects in Non-centrosymmetric Materials*, Gordon and Breach, Philadelphia (1992).
41. B.I. Sturman, M. Mann, J. Otten, K.H. Ringhofer: J. Opt. Soc. Am. B **10**, 1919 (1993).
42. P. Refregier, L. Solymar, H. Rajbenbach, J.-P. Huignard: J. Appl. Phys. **58**, 45 (1985).
43. N.V. Kukhtarev, V.B. Markov, S.G. Odulov, M.S. Soskin, V.L. Vinetskii: Ferroelectrics **22**, 949 (1979).
44. B.I. Sturman, D.M. Giel: Phys. Rev. E **69**, 066603 (2004).
45. J. Frejlich, P.M. Garcia, K.H. Ringhofer, E. Shamonina: J. Opt. Soc. Am. B **140**, 1741 (1997).
46. A. Marrakchi, R.V. Johnson, J.A.R. Tanguay: J. Opt. Soc. Am. B **3**, 321 (1986).
47. B.I. Sturman, E.V. Podivilov, E. Shamonina, V.P. Kamenov, E. Nippolainen, V.V. Prokofiev, A.A. Kamshilin: Phys. Rev. E **60**, 3332 (1999).
48. L. D. Landau, E. M. Lifshitz, *Fluid Mechanics*, Chapt. 3, Pergamon-Press, Oxford (1987).
49. E. Ott, *Chaos in Dynamical Systems*, Cambridge University Press (1997).
50. H. Haken, *Advanced Synergetics*, Springer-Verlag, Berlin (1983).
51. L. D. Landau, E. M. Lifshitz, *Statistical Physics*, Pergamon-Press, Oxford (1980).
52. R.W. Boyd, *Nonlinear Optics*, Academic Press, NewYork (1992).

7

Band-to-Band Photorefraction

Germano Montemezzani[1,2], Philipp Dittrich[1], and Peter Günter[1]

[1] Nonlinear Optics Laboratory, Swiss Federal Institute of Technology, Zürich (Switzerland)
[2] Present address: Laboratoire Matériaux Optiques, Photoniques et Systèmes, University of Metz and Supélec, Metz (France)
germano.montemezzani@metz.supelec.fr

7.1. Introduction

In conventional photorefraction, which is the matter of most of the chapters in this book series, the photoexcitation at the origin of the charge transport process occurs from mid-gap defect levels introduced by intentional or unintentional doping of the material being used. The doping level is usually moderate as compared to the intrinsic density of potentially available charges, which in the example of crystalline materials is of the order of the density of states at the top of the valence band or at the bottom of the conduction band. In the case of conventional photorefractive effects, the moderate doping level leads to a rather inefficient photoexcitation process and therefore to a rather slow photorefractive response. As discussed in detail in Chapter 3 of the second volume of this book series, the Maxwell dielectric time τ_{die} and the excitation time τ_{ex} are both inversely proportional to the photoexcitation rate and limit the response speed in different regimes. Therefore, for a given material, a significant enhancement of the response speed can only be achieved by improving in some way the efficiency of the photoexcitation process.

An effective way to increase the photoexcitation rate is to forget the dopants altogether and concentrate on phototransitions between the intrinsic levels across the band-gap of the material. These transitions are allowed if light of sufficient photon energy is used. Since every electron promoted to the upper mobile state will leave behind a hole in the lower mobile state, a photorefractive space-charge field will be created only if the motion of the electrons differs from the one of the holes, which is usually the case. This *interband photorefractive effect* presents characteristic features differing from those of the conventional effect, which involve specially the photoconductive properties and the dependence of the effect on light intensity. Besides the highly improved response speed, its other main advantage is the robustness of the involved gratings. The latter refers to the fact that a grating recorded by the interband photorefractive effect can be simultaneously read out by a very intensive light wave possessing a sub-band-gap photon energy without significantly erasing it. Speed and robustness open interesting perspectives of such interband photorefractive gratings for

parallel optical processing and optical wave manipulation tasks, such as dynamic splitters, switchers or filters.

This chapter will present the basics underlying interband photorefractive effects under cw illumination and highlight the main differences with respect to the conventional case. The considerations will be limited here to one-photon processes in bulk materials. It should be noted, however, that interband phototransitions may be induced also by two-photon processes at wavelengths significantly longer than the material band-edge. In semiconductors, such an approach can lead, for instance, to valuable information about two-photon, free-carrier, and deep-level cross sections [1]. Also, in semiconductors, a strong resonant electro-optic response can be obtained by illuminating the sample at wavelengths near the material band-edge and making use of the Franz-Keldysh effect [2, 3, 4] or, in structured materials, of the quantum-confined Stark effect [5, 6]. In contrast to the optical nonlinearity discussed in this chapter, these resonant effects are strong only in a limited wavelength range around the band-edge of the bulk semiconductor or of the multiple quantum-well structure. A vast literature exists on these subjects in semiconductor materials and the reader is referred to several excellent reviews [7, 8] and particularly to two chapters appearing in the second volume of this book series. The two-photon processes mentioned above have to be distinguished from two-photon excitation out of impurity levels which does not directly involve band-to-band transitions. With the help of short-pulse excitation, the latter approach was already used in the early stages of the photorefractive field to create stable holograms that could be read out nondestructively using a weaker intensity at the same wavelength, which is unable to create a significant amount of two-photon transitions [9, 10]. This is closely related to more recent investigations involving two-photons and two-colors hologram recording, performed with the aim to obtain quasi-fixed holograms for storage applications. The interested reader is referred to the next chapter in this volume.

The present chapter is structured in the following way. Section 7.2 will present the theoretical background with the help of a highly simplified model of the charge redistribution under interband photoexcitation conditions. The consequences for the photoconductivity, the space-charge fields, the grating dynamics, and the grating thickness will be discussed. Section 7.3 shortly discusses observed results in different materialsm, specifically $KNbO_3$, $LiTaO_3$ and $Sn_2P_2S_6$ while Section 7.4 describes some demonstrated potential applications for dynamic light-induced waveguides, switches and filters, and for parallel processing with the examples of incoherent-to-coherent conversion and optical correlation.

7.2 Interband Photorefraction with cw Recording Waves

This section describes very shortly the simplest theory and summarizes the main features of interband photorefractive effects recorded under cw illumination. The most important differences with respect to conventional photorefraction are pointed out.

7.2.1 Basic Equations

For interband photorefractive effects, the photoexciting light wavelength is in the high absorption spectral region for electronic resonances. Therefore the primary charge transfer mechanism is the phototransition of electrons between the valence and conduction band. In the simplest approximation, one may completely neglect all transitions involving mid-gap levels and write the material equations valid for an ideal trap-free material. This leads to a significant simplification in the mathematics. Here we will limit ourselves to the description of this limiting case. More complete models that consider the influence of recombination into mid-gap traps and photoexcitation out of them were given in [11]. It can be shown that for a sufficiently high cw illumination intensity, the solutions obtained with such models converge to the solutions of the *trap-free model* described here, which is based on following equations [11]

$$\frac{\partial n(\boldsymbol{r})}{\partial t} = gI(\boldsymbol{r}) - \gamma_{dir} n(\boldsymbol{r}) p(\boldsymbol{r}) + \frac{1}{e}\nabla \cdot \boldsymbol{J}_e(\boldsymbol{r}), \tag{7.1a}$$

$$\frac{\partial p(\boldsymbol{r})}{\partial t} = gI(\boldsymbol{r}) - \gamma_{dir} n(\boldsymbol{r}) p(\boldsymbol{r}) - \frac{1}{e}\nabla \cdot \boldsymbol{J}_p(\boldsymbol{r}), \tag{7.1b}$$

$$\boldsymbol{J}_e(\boldsymbol{r}) = en(\boldsymbol{r})\mu_{\mathrm{e}}\boldsymbol{E}(\boldsymbol{r}) + k_B T\mu_{\mathrm{e}} \cdot \nabla n(\boldsymbol{r}), \tag{7.1c}$$

$$\boldsymbol{J}_p(\boldsymbol{r}) = ep(\boldsymbol{r})\mu_{\mathrm{p}}\boldsymbol{E}(\boldsymbol{r}) - k_B T\mu_{\mathrm{p}} \cdot \nabla p(\boldsymbol{r}), \tag{7.1d}$$

$$\nabla \cdot \boldsymbol{E}(\boldsymbol{r}) = \frac{e}{\epsilon_{eff}\epsilon_0}(p(\boldsymbol{r}) - n(\boldsymbol{r})), \tag{7.1e}$$

where $\boldsymbol{r}$ is the position vector and all space-dependent variables are also time-dependent. Here $\boldsymbol{E}$ is the total internal electric field, ϵ_0 is the permittivity of vacuum, ϵ_{eff} is the (scalar) effective dielectric constant for the given photorefractive configuration (see Chapter 4 of this volume), e is the absolute value of the elementary charge, k_B is the Boltzmann-constant, and T is the absolute temperature. Further, n and p are the electron density in the conduction band and the hole density in the valence band, respectively, $\boldsymbol{J}_e$, $\boldsymbol{J}_p$, μ_{e} and μ_{p} are the electron and hole current densities and mobility tensors, respectively, γ_{dir} is the direct recombination constant between the two bands. Here the direct band-to-band photoexcitation process is expressed by the term $gI(\boldsymbol{r})$, where g is a photoexcitation constant given by $g = \alpha_{dir}/(\hbar k_0 c) = \alpha_{dir}/h\nu$, α_{dir} being the (intensity) absorption constant for the band-to-band transition, $k_0 = 2\pi/\lambda$ being the free space light wavevector, and $h\nu$ being the photon energy. By writing the photoexcitation term in this form, we have implicitly assumed that the photoexcitation process is isotropic with respect to the polarization of the interacting waves. If this is not the case, the light intensity I has to be replaced by a term containing a dissipated energy density, in a way similar as described in Chapter 4 for the case of conventional photorefraction.

The set of Eqs. (7.1a)–(7.1e) can be solved by taking the same kind of approach used for the equations describing the conventional photorefractive effect and discussed in other chapters of this book [12]. By assuming a sinusoidal light illumination, the space- and time-dependent variables are developed in a Fourier series that is being broken after the first harmonic term in space, a procedure that is well justified for small light modulation amplitudes.

7.2.2 Photoconductivity

Given a certain light intensity, the terms up to zero-order in the Fourier series give information about the average density of free electrons and free holes in the conduction and valence band, respectively.

Since Eqs. (7.1a)–(7.1e) neglect any charge recombination into trap levels and are symmetric with respect to electrons and holes, they predict an equally large free electron (n_0) and free hole (p_0) concentration; that is,

$$n_0 = p_0 = \sqrt{\frac{gI_0}{\gamma_{dir}}}. \tag{7.2}$$

The inclusion of recombination channels involving deep traps breaks this symmetry at low intensities (see [11]). However, it can be easily shown that for a sufficiently high light intensity, the limit above is always retrieved. Therefore, the free carrier concentration, and thus also the photoconductivity $\sigma_{ph} \equiv e(\mu_e n_0 + \mu_h p_0)$, are expected to increase with the square root of light intensity, as opposed to the linear increase expected for the simplest model of conventional photorefraction.

The deviation from the the relationship (7.2) at low intensities is shown in the example of Fig. 7.1, which shows measured photocurrent in pure $KNbO_3$ illuminated at the wavelength $\lambda = 364\,\text{nm}$. In this case, a nearly linear increase of the photocurrent is observed at intensities below $1\,\text{mW/cm}^2$, while above this limit, the behaviour expected from (7.2) is well reproduced.

7.2.3 Space-Charge Fields

Under a sinusoidal light intensity distribution of the type

$$I(\boldsymbol{r}) = I_0 \text{Re}[1 + m\exp(i\boldsymbol{K}\cdot\boldsymbol{r})], \tag{7.3}$$

the Eqs. (7.1a–7.1e) can be solved in a similar way as in the case of the single carrier band transport model. For the steady-state scalar space-charge field amplitude E_1 one obtains [11]

$$\boldsymbol{E}_1 = \hat{\boldsymbol{K}}\left\{-im\frac{[E_D(E_{Rh}-E_{Re}) - iE_0(E_{Re}+E_{Rh})]E_{qf}}{[(2E_{qf}+E_D)(E_D+E_{Re}+E_{Rh})+E_0^2] + iE_0[E_{Re}-E_{Rh}]}\right\}, \tag{7.4}$$

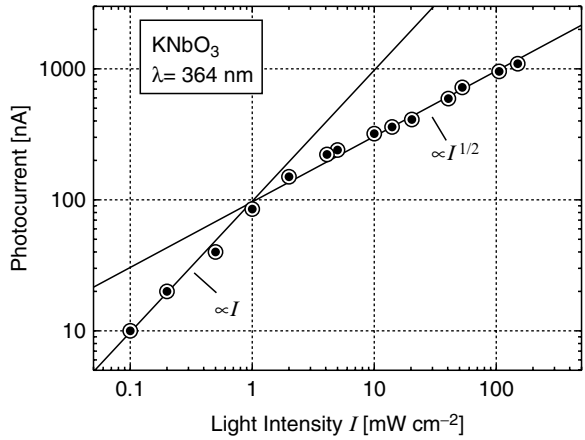

FIGURE 7.1. Photocurrent as a function of light intensity under interband illumination of $KNbO_3$. In the low intensity regime, the photocurrent increases linearly and charge recombination in deep traps plays a major role. In the high intensity regime, the photocurrent increases with the square root of light intensity and interband transitions dominate the process. (After [13])

where $\hat{\boldsymbol{K}}$ is the unit vector in direction of the grating vector $\boldsymbol{K}, E_0$ is the projection of an externally applied electric field in direction $\hat{\boldsymbol{K}}$, and $E_D \equiv |\boldsymbol{K}| k_B T/e$ is the diffusion field. The fields E_{qf}, E_{Re} and E_{Rh} are less familiar,

$$E_{qf} \equiv \frac{e}{\epsilon_0 \epsilon_{eff} |\boldsymbol{K}|} n_0 \tag{7.5}$$

is the free charge limiting field and stays in full analogy with space-charge limiting field E_q found in conventional photorefraction, while

$$E_{Re} \equiv \frac{1}{|\boldsymbol{K}| \mu_e} \gamma_{dir} p_0 \tag{7.6}$$

and

$$E_{Rh} \equiv \frac{1}{|\boldsymbol{K}| \mu_p} \gamma_{dir} n_0 \tag{7.7}$$

are the electron and hole recombination fields, respectively. Their magnitude can be interpreted as the average internal electric fields in which electrons (or holes) drift for an average distance $(K)^{-1} = \Lambda/2\pi$ before a recombination to the other band takes place. The scalar mobilities μ_e and μ_p in (7.6) and (7.7) correspond to the projection of the electron and hole mobility tensors along the direction $\hat{\boldsymbol{K}}$, as described in Chapter 4 of this volume.

Fig. 7.2 shows the typical dependence of the space-charge field amplitude on grating spacing for the interband case. At long grating spacings, one finds a saturation value in presence of an applied field of $E_1 = mE_0/2$, which is half as big with respect to the case of conventional photorefractive effects. The reason for this is the quadratic recombination process leading to relationship (7.2) for the free charge density; as a consequence, the modulation amplitude of the photoexcited charges is only half as big as the one of the light intensity. Another big difference with the conventional photorefraction is the behavior at small grating spacings Λ. While in the conventional case the space-charge field rises proportional to Λ, in interband photorefraction the initial rise is proportional to Λ^3. This is due to the fact that not only the free-carrier limiting field E_{qf} is giving a limitation to the space-charge field amplitude, but also the recombination fields E_{Re} and E_{Rh}. The overlinear increase of $\mathrm{Im}(E_1)$ with grating spacing was confirmed experimentally in pure $KNbO_3$ by means of interband two-

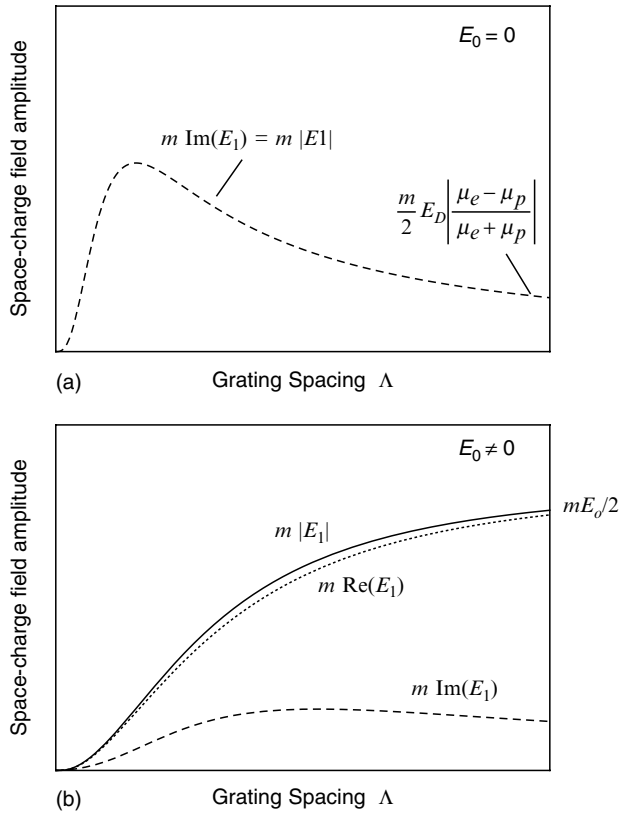

FIGURE 7.2. Dependence of space-charge field amplitude on grating spacing for interband photorefractive effects in absence of deep traps (4). a) No applied field; b) With externally applied field.

wave mixing investigations [11, 14]. Figure 7.2 (a) also shows that in absence of an external field the space-charge field is bound by the function $(m/2)E_D|(\mu_e - \mu_p)/(\mu_e + \mu_p)|$, therefore, as expected, no space-charge field can build up in this regime if the electron and hole mobilities are the same.

The role of the pseudo-fields E_{qf}, E_{Re} and E_{Rh} merits some additional discussion. A significant space-charge field amplitude can be reached only if E_{qf} and at least one among the recombination fields E_{Re} and E_{Rh} are large enough, say, of the order of 1 kV/cm. Looking at Eq. (7.5) one recognizes that the requirement of a large field E_{qf} means nothing else than the charge density n_0 should be large enough to sustain the modulated space-charge field. The second condition implies that at least one of the carrier mobilities should be small enough so that, before recombination, the carrier is prevented from drifting too far as compared to the fringe distance. If the drift or diffusion distances are too long, the carrier looses coherence with the illuminating light distribution and the resulting space-charge field modulation amplitude decreases. In pure $KNbO_3$, the limitations due to E_{qf}, E_{Re} and E_{Rh} normally become important only at grating spacings below $\sim 0.5\,\mu$m. In general, significant space-charge field amplitudes at submicron grating spacing can be easily achieved already for an illuminating intensity of the order of few tens of mW/cm^2($\lambda = 364$ nm). For experiments where the typical distances are larger ($5 - 10\,\mu$m), such as the dynamic waveguides described in Section 7.4.3, the constraints on E_{qf}, E_{Re} and E_{Rh}, and thus on the illumination intensity, are even less stringent.

7.2.4. Grating Dynamics

The dynamic behavior of interband photorefractive effects is more complex than the one for the conventional case. In the latter situation, the carriers are photoexcited from mid-gap levels and the equilibrium average carrier density in the conduction (or valence) band is reached in a time, which is short as compared to the build-up time of the space-charge field. This is no longer true for interband gratings. The large free carrier density has to build up first and the time required for this process may be comparable or even longer than the characteristic time constants for the charge redistribution process, such as the dielectric time $\tau_{die} \equiv e\mu n_0/(\varepsilon_0 \varepsilon_{eff})$ or the diffusion time $\tau_D \equiv e/(K^2 k_B T \mu)$ for electrons or holes. As discussed in more depth in [11], it is clear that the space-charge field cannot reach a steady-state before the average charge density $n_0(t)$ also does so. Upon switching on the illumination at time $t = 0$, in absence of deep traps, the latter grows approximately as

$$n_0(t) = n_0(t = \infty)\ \tanh\ (\Gamma_{dir} t), \tag{7.8}$$

where $n_0(t = \infty)$ is the steady-state value given by (7.2) and

$$\Gamma_{dir} \equiv \gamma_{dir} n_0(t = \infty) = \sqrt{g I_0 \gamma_{dir}} \tag{7.9}$$

is the recombination rate that governs the charge density build-up. Correspondingly, upon switching off the illumination, the free charge density initially decays in the dark as

$$n_0(t) \equiv n_0(t=0)\frac{1}{1+\Gamma_{dir}t}. \tag{7.10}$$

In pure $KNbO_3$ at wavelengths around 350 nm, the time rate Γ_{dir} is typically of the order of $(10\,\mu s)^{-1}$ for illumination intensities of the order of $100\,mW/cm^2$. As will be shown later, the photorefractive response time in the interband regime is also in the $10-100\,\mu s$ range, which is faster by at least two orders of magnitude with respect to the typical speed of the same material in the conventional photorefractive regime.

Eqs. (7.8) and (7.10) describe the build-up and decay of the average charge density and therefore do not consider any charge transport issues that are important to describe the formation of the space-charge field. An exact analytical solution of the dynamic Eqs. (7.1a)–(7.1e) is made difficult by the above time dependence of n_0. Therefore we rely here on a simpler approach that assumes that the build up of the modulated space-charge field starts from a state in which the average free carrier density is already established. In other words, at time $t=0$, only the modulation m in (7.3) is being switched on. Following [15], the dynamic solution of the set (7.1a)–(7.1e) takes the form

$$\boldsymbol{E}_1(t) = \boldsymbol{E}_{1,sat}\{1-\frac{1}{2}[(1-B/C)e^{-\Gamma_1 t}+(1+B/C)e^{-\Gamma_2 t}]\}, \tag{7.11}$$

where $\boldsymbol{E}_{1,sat}$ corresponds to the steady-state solution (7.4) and

$$B \equiv (E_D+E_{qf})(E_{Re}+E_{Rh})+iE_0(E_{Re}-E_{Rh})+2E_{Re}E_{Rh}, \tag{7.12}$$

$$C \equiv \{[(E_D+E_{qf})(E_{Re}-E_{Rh})-iE_0(E_{Re}+E_{Rh})]^2+4E_{Re}E_{Rh}(E_{qf}-E_{Re})(E_{qf}-E_{Rh})\}^{1/2}. \tag{7.13}$$

The exponential time rates $\Gamma_{1,2}$ are given by

$$\Gamma_{1,2} = \frac{\Gamma_{dir}}{2E_{Re}E_{Rh}}(B \mp C). \tag{7.14}$$

Fig. 7.3 shows the dependence of the time rates Γ_{dir}, Γ_1 and Γ_2 on light intensity. Note that in general, depending on material parameters, the time rates Γ_1 and Γ_2 may be either larger (as in the case represented here) or smaller than the direct recombination rate Γ_{dir}. Note also that despite of this, in the former case, if the experiment starts from an unilluminated crystal, the grating build-up time is still limited by the time needed to build up the average charge distribution and therefore, cannot be faster than $1/\Gamma_{dir}$.

Fig. 7.3 contains also experimental data from [16] which confirm the expected square-root dependence of time rate on intensity. It has to be noticed

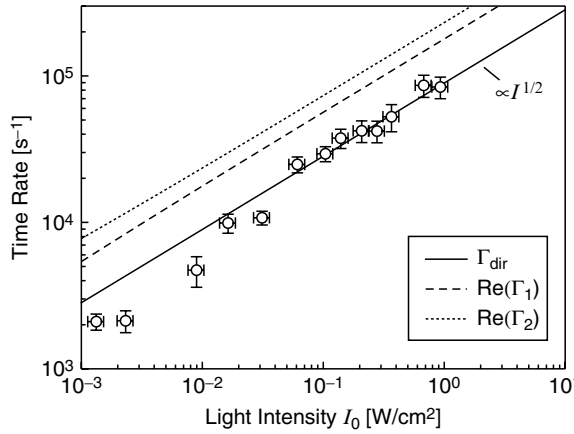

FIGURE 7.3. Intensity dependence of the direct recombination rate Γ_{dir} and of the photorefractive time rates Γ_1 and Γ_2 according to Eqs. (7.9) and (7.14). The parameters used for the plots are $g = 10^{24}\ \mathrm{J^{-1}m^{-1}}$, $\gamma_{dir} = 8 \cdot 10^{-19}\,\mathrm{m^3/s}$, $\mu_e = 10^{-9}\,\mathrm{m^2/(Vs)}$, $\mu_h = 3 \cdot 10^{-9}\,\mathrm{m^2/(Vs)}$, $\Lambda = 4.7\,\mu\mathrm{m}$ and $E_0 = 2.2\,\mathrm{kV/cm}$. The points show corresponding measured time rates in pure $KNbO_3$ under illumination at the wavelength $\lambda = 351\,\mathrm{nm}$ [16], which are found to follow well the expected square root dependence on intensity.

that the value of the recombination constant γ_{dir} has been adjusted in such a way as to normalize the value of Γ_{dir} to the experimentally measured data.

It is worth noting that in some limits, the time rates Γ_1 and Γ_2 may be expressed in a simpler form. First, for small grating spacings ($\Lambda \to 0$), the rates Γ_1 and Γ_2 converge toward the diffusion rates for holes and electrons $\Gamma_{Dh} \equiv k_B T K^2 \mu_p / e$ and $\Gamma_{De} \equiv k_B T K^2 \mu_e / e$, respectively. In the opposite limit, for large grating spacings Λ, one has ($E_D \ll E_{qf}$) and for the case where the free charge limiting field is the dominating quantity ($E_{qf} \gg E_{Re}, E_{Rh}$) the expression (7.11) takes the simpler form

$$\boldsymbol{E}_1(t) = -im\hat{\boldsymbol{K}}\frac{E_D}{2}\frac{\mu_p - \mu_e}{\mu_p + \mu_e}\{1 - \exp[-(\Gamma_{die} + \Gamma_{dih})t]\}, \tag{7.15}$$

where $\Gamma_{die} \equiv (e\mu_e n_0/\epsilon_0\epsilon_{eff}) = (\tau_{die})^{-1}$ is the dielectric rate for electrons and Γ_{dih} is the corresponding dielectric rate for holes. Eq. (7.15) is valid for $E_0 = 0$. Therefore, multiple measurements of the time dynamics in the latter regime allow the determination of the ratio of the effective bipolar mobility μ_p/μ_e along the different crystallographic directions, as performed in [13].

7.2.5. Grating Thickness

For conventional photorefractive effects, the thickness of the recorded grating usually correspond to the thickness of the nonlinear sample being used. Since the incident recording light is being strongly absorbed, this is no longer true for

interband photorefraction. For the ideal "trap-free" case (7.2) and (7.4) predict that the space-charge field should depend on the square root of the light intensity and thus should decay exponentially inside the sample. This behaviour can be effectively observed near the surface where the light intensity is large and interband processes dominate over processes involving the residual deep traps. For specific situations, such as in the case where the sample is flooded by an intense sub-bandgap light [11], the exponential decay can extend over longer distances. However, in the general case, the grating strength departs from the exponential decay at depths where the recording intensity is so low that the carrier recombination into deep traps is dominating. The total extension of the grating reaches the depth where the remaining nonabsorbed photons are still able to create a photoconductivity larger or equal to the material dark conductivity. This depth can largely exceed the $1/\alpha$ level of the typical decay depth of the light intensity. For instance, in $KNbO_3$ at typical intensities of $100\,mW/cm^2$($\lambda = 364\,nm$, *c*-polarized light), the grating is found to extend until about $200\,\mu m$ below the surface. Since the corresponding intensity absorption constant is $\alpha_c \approx 550\,cm^{-1}$, this depth corresponds to about 10 times the $1/\alpha$ level.

As will be seen also later, experimental evidence show that in general, the crystal contains two distinct regions, one close to the surface where the grating is dominated by free charges, and a deeper one where trapped charges dominate. The position of the transition region between the two regions depends on intrinsic and extrinsic properties of the sample (purity, doping level, ...), on wavelength and polarization, and, of course, on light intensity. Detailed investigations on the influence of light intensity on grating shape was performed in [15].

7.3. Materials

It has to be expected that any electro-optic photoconducting crystal should exhibit interband photorefractive effects when illuminated with light whose photons have an energy exceeding the band-gap. For oxide type crystals typically used in conventional photorefraction, such as lithium niobate ($LiNbO_3$), potassium niobate ($KNbO_3$), and lithium tantalate ($LiTaO_3$), for example, the high absorption spectral region lies in the ultraviolet. But materials exhibiting interband photorefraction also in the visible spectral range are also available, e.g., tin hypothiodiphosphate ($Sn_2P_2S_6$, SPS).

In this section, we will shortly summarize the main characteristics of band-to-band photorefractive gratings recorded in the crystals $KNbO_3$, $LiTaO_3$, and $Sn_2P_2S_6$. Before starting, let us shortly recall that holographic investigations of the interband photorefractive effect are typically performed in two kinds of geometries: The longitudinal geometry, where the planes of incidence of the recording waves and of the read-out wave is the same, and the transverse geometry, where the two planes of incidence are perpendicular to each other. In the latter case, the read-out wave propagates parallel to the input surface of the recording beams and can be used to probe the grating at a well defined depth.

7.3.1. Potassium Niobate ($KNbO_3$)

Potassium niobate has a room temperature band-gap energy of 3.3 eV, therefore near ultraviolet light in the region of 350 nm to 365 nm leads to direct transitions between the valence band (related to the $2p$ orbitals of the oxygen ions) and the conduction band (related to the $4d$ orbitals of the Nb ions). The interband photorefractive properties of nominally pure $KNbO_3$ under illumination in the above mentioned spectral range were studied in Refs. [11, 13, 15–19]. Here we mention solely the most relevant features observed under cw illumination at the wavelengths 364 and 351 nm.

- The photoconductivity deviates from a linear dependence on light intensity for intensities of the order of $1\,\mathrm{mW/cm^2}$. Above this level, one reaches a regime with square root dependence (compare Fig. 7.1), an indication of interband effects.
- The interband gratings are composed of two principal components. The modulated charges giving rise to the first one are energetically located in the two bands and in shallow trap levels with fast thermal exchange with the bands. This component dominates for local light intensities above $50\,\mathrm{mW/cm^2}$ ($\lambda = 364\,\mathrm{nm}$) and is referred to as the *band grating*. The second component is composed of a carrier modulation in deep trap levels and is hence referred to as the *trap grating*. It dominates for local light intensities below $0.1\,\mathrm{mW/cm^2}$ and therefore it is the dominant component far enough from the entrance surface illuminated by the UV light. The average amplitude of the first grating component is about 5 to 10 times stronger than the one of the second one. In undoped crystals and in absence of externally applied electric fields, the two components are mutually phase shifted by π, which is supported by several pieces of evidence.

    (a) Direct depth resolved Bragg diffraction investigations in transverse geometry [11] show a minimum of diffraction efficiency at an intermediate depth for which band and trap grating have a comparable amplitude but cancel each other;
    (b) Off-Bragg angle Bragg diffraction investigations in longitudinal geometry [15] evidence the interesting and expected feature that at steady-state the maximum of diffraction efficiency is not observed at the Bragg angle, but at a nearby angle for which the destructive interference between the waves diffracted off the band and the trap grating turns to a constructive interference. This is illustrated in Fig. 7.4, which shows the angular dependence of the diffraction efficiency η (rocking curve) for various recording intensities in a $47\,\mu\mathrm{m}$ thick sample. Thus the grating evolution leads to very interesting time dynamics of the rocking curve measured in longitudinal geometry, as discussed in detail in [15]. As a result, the curve $\eta(t)$ shows a complex behavior that strongly depends on the

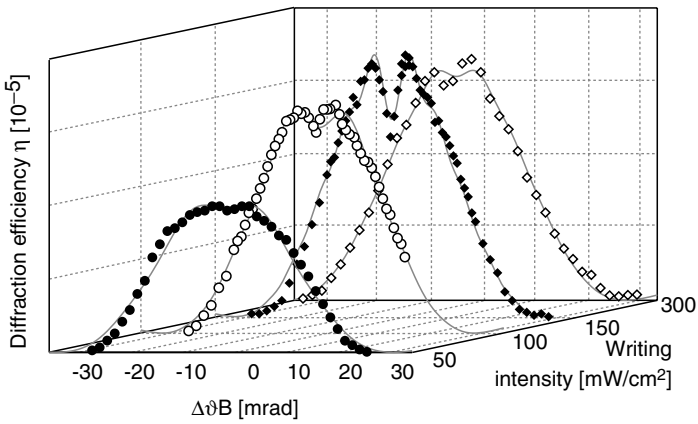

FIGURE 7.4. Measured internal angular selectivity of the diffraction efficiency for isotropic Bragg diffraction obtained in a 47 μm thin sample of $KNbO_3$ for different ultraviolet writing intensities ($\lambda = 364$ nm, grating spacing $\Lambda = 0.5\,\mu$m, grating vector along the c axis). The modulation depth is $m = 0.2$ and all the light beams are p-polarised. The solid lines are calculated from a simple model involving two grating components. See [15] for details.

light intensity (see Fig. 7.5) and on the angular deviation with respect to the Bragg angle. Despite the apparent complexity of the behavior, the dynamics can be satisfactorily modeled by considering solely the evolution of the two grating components discussed above, being displaced in space and in phase [15]. Note also in this respect, that if the intensity is large enough so that the band grating component dominates the diffraction, the slow evolution of the trap grating component loses importance and the dynamics measured in longitudinal geometry becomes simpler.

(c) The effective UV two-wave mixing gain coefficient has opposite signs for low and high wave intensities [15] as seen in Fig. 7.6. The fitted curves show that the trap-free model of Section 7.2.1 describes well the behaviour of the photorefractive gain at large light intensities, where the band grating dominates. However, this model cannot predict the observed zero crossing at low intensities. Inclusion of the charges trapped in deep levels is necessary. A highly simplified model of this kind was shown to correctly predict the observed transition with increasing light intensity [18].

- The average refractive index change modulation Δn obtained by the interband photorefractive effect is few times 10^{-5} and is of the same order of magnitude to what can be reached by conventional photorefractive effects in the same material.
- While the grating component stored in deep traps is affected by below bandgap visible illumination, the free carrier grating component is not. There-

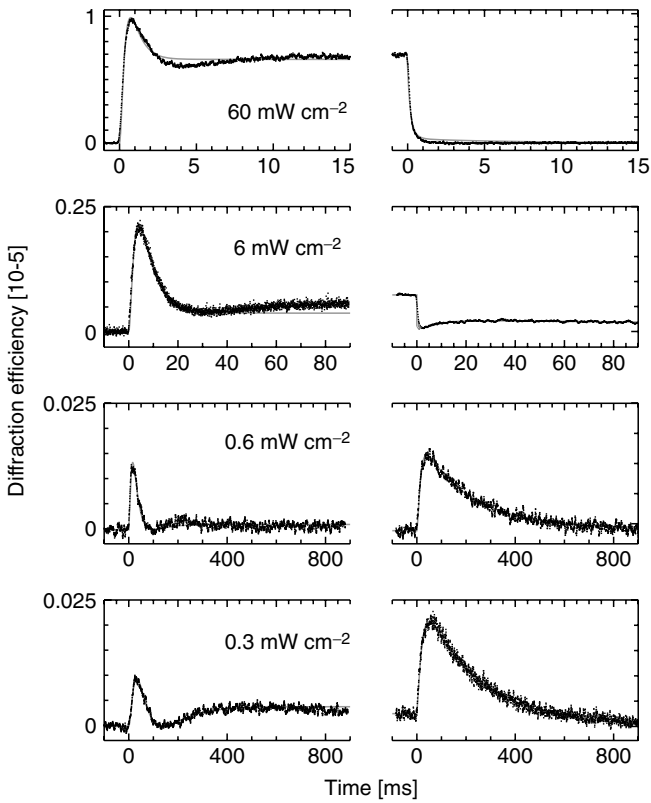

FIGURE 7.5. Intensity dependence of the dynamics of the diffraction efficiency measured in longitudinal geometry during the build-up (left) and the dark decay (right) obtained in a 47 μm thin sample of $KNbO_3$ for a fixed angle of incidence very close to the exact Bragg angle ($\Delta\vartheta < 2$ mrad). The oscillating dynamics is due to the interference between a fast band grating close to the front surface and a slower trap grating deeper inside the sample. The gray lines are calculated according to a simple model involving the evolution of these two gratings, as discussed in detail in [15].

fore, the near surface grating is extremely robust against optical erasure at wavelengths longer than those used for recording. In $KNbO_3$, it has been shown that incoherent visible light more than five orders of magnitude more intense than the ultraviolet recording beams does not significantly affect the free carrier component of the grating.

- At the intensity of 1 W/cm^2, the fast grating component shows a build-up and decay time of about 10 μs for $\lambda = 351$ nm and *b*-polarized light, where the intensity absorption constant is $\approx 5500\,\mathrm{cm}^{-1}$. This response time is increased by less than a factor of 4 for $\lambda = 364$ nm and *c*-polarized light, which are associated with a 10 times lower intensity absorption constant of $540 \pm 50\,\mathrm{cm}^{-1}$. As predicted by theory, the response time depends inversely

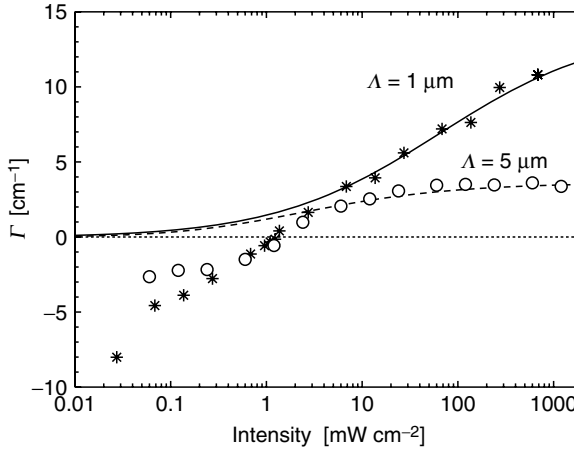

FIGURE 7.6. Intensity dependence of two-wave mixing gain for interband photorefraction in $KNbO_3$. The curves show the behavior predicted by "trap-free" model of the interband photorefractive effect (Eq. (7.4)). The zero-crossing point at the intensity of about 1 mW/cm^2 is not predicted by Eq. (7.4) and is due to the fact that at low intensity, a deep trap grating being out of phase by 180 degrees with respect to the free charge grating becomes the dominant component. Electrons are the dominant charge carriers at low intensities (electron-type conductivity dominates) while at large intensities, the conductivity is dominated by hole motion. $\lambda = 364$ nm, grating vector $||c$-axis, wave polarization in the bc-plane, modulation index $m = 0.11$. After [15].

proportional to the square root of light intensity (see Fig. 7.3). Note that the response times for conventional photorefraction in $KNbO_3$ range typically between ≈ 1 ms and few seconds depending on doping and chemical treatment. These are about two to six order of magnitude slower than the interband photorefractive gratings.

- For most samples, at typical intensities of 100 mW/cm^2($\lambda = 364$ nm, c-polarization), the grating is found to extend until about 200 μm below the illuminated surface, that is about 10 times the $1/2\alpha$ level. The maximum depth can be characterized by the point where the remaining nonabsorbed photons are still able to create a photoconductivity larger than the material dark conductivity. Therefore, as expected, the grating depth depends on light intensity, polarization, and wavelength. The position of the border between the two regions mutually dominated by the free carrier grating components and by the trapped grating component also depends on these quantities as well as on intrinsic and extrinsic properties of the sample (purity, doping level, ...) [15]. For conditions under which the trapped grating is not being significantly erased, the point at which the two gratings components have the same amplitude (but opposite sign) can extend up to about 100 μm below the surface.
- In the framework of the simple model presented in Section 7.2, all measurements in pure samples are consistent with an effective mobility for the

slowest carrier (electrons) slightly smaller than $10^{-5}\,\mathrm{cm}^2/(\mathrm{Vs})$. This small value is given by a trap limiting effect due to carriers falling into shallow trap levels (mainly oxygen vacancies) in thermal equilibrium with the band. The effect of shallow traps is not explicitly included in the model of Section 7.2 and the band grating is in reality a grating induced by carriers sitting in the pseudo-band formed by the true band and the nearby shallow levels [11, 14].

- In principle, due to the strong absorption of the UV light, thermal effects such as direct thermooptic gratings [20], thermoelectric gratings [21], or gratings induced by pyroelectric space-charge fields [22, 23] could also give a contribution to the observations in diffraction experiments. However, direct experimental verification in several different geometries as well as theoretical estimations of the size of the effects based on the known material parameters show that none of these effects give a significant contribution at the cw intensities up to $\approx 1\,\mathrm{W/cm}^2$ relevant for our investigations. Attempts performed with the aim to detect a possible presence of surface gratings using a reflection type geometry showed that also this effect is negligible.

7.3.2 *Lithium Tantalate* ($LiTaO_3$)

Due to its wide band-gap, lithium tantalate ($LiTaO_3$) is a promising material for short-wavelength holographic data storage and dynamic holography. The renewed interest in this materials is driven mostly by the successful growth of near-stoichiometric crystals, i.e. crystals with a composition very close to stoichiometry [24, 25, 26]. Compared to congruently grown $LiTaO_3$, near-stoichiometric $LiTaO_3$ shows a significant reduction of optical damage in the visible and an enhancement of the photosensitivity and of the diffusion-type photorefractive effect in the near ultraviolet [27, 28, 29]. Further, the absorption edge is shifted from about 275 nm for congruent $LiTaO_3$ toward about 260 nm [30]. It has been shown that for near stoichiometric $LiTaO_3$, the two-wave mixing gain coefficient is doubled compared to congruent $LiTaO_3$ at the UV wavelength $\lambda = 364\,\mathrm{nm}$. At the same time, the typical photorefractive build-up and decay time constants are decreased by a factor of five [28]. Further, a distinct reduction of the saturated space-charge field is observed, which is due to a larger increase in the photoconductivity relative to the photogalvanic effect [27, 29].

Reviews about the conventional photorefractive properties of congruent and stoichiometric $LiTaO_3$ can be found in two chapters in the second volume of this book series. In the following, we will summarize the main properties of near stoichiometric pure and Mg doped $LiTaO_3$ regarding interband photorefraction [31, 32]. Investigations were performed at the deep UV wavelength $\lambda = 257\,\mathrm{nm}$, a wavelength lying lower than the absorption edge of $LiTaO_3$.

- As for $KNbO_3$, the photoconductivity of near stoichiometric $LiTaO_3$ deviates from a linear dependence on light intensity for intensities of the order of $10\,\mathrm{mW/cm}^2$.

- In analogy to $KNbO_3$, the presence of a band grating and of a trap grating could be identified and are also found here to be mutually out-of-phase. The first component reaches approximately from the surface until the depth d_b at which therecording UV intensity equals approximately the characteristic intensity I_c separating the linear and square root intensity regimes of the photoconductivity. Because of the exponential decrease of the UV light inside the crystal, this transition depth is given by $d_b \cong \alpha_{UV}^{-1} \ln(I_0/I_c)$. The second component extends approximately from the depth d_b until the depth at which the light intensity equals the dark intensity I_d. The latter is defined as the intensity where the induced photoconductivity equals the dark conductivity. The thickness of this second component is given approximately by $d_t \cong \alpha_{UV}^{-1} \ln(I_c/I_d)$. A direct, depth resolved observation of these two grating components by diffraction measurements in transverse geometry is shown in Fig. 7.7.
- The partial compensation between band and trap grating components can be undone by optically erasing the trap grating component using an intense nonresonant illumination unable to induce interband phototransitions. A significant increase of diffraction efficiency in longitudinal geometry is observed under such illumination conditions.
- Typical time constants for the interband effects for pure near-stoichiometric $LiTaO_3$ are in the order of a few tens of milliseconds for UV light intensities of about $100\,mW/cm^2$, three orders of magnitude faster than the time constants reported previously for lithium tantalate [28].
- It is well known that Mg ions act as compensators for intrinsic defects related to the deviation from stoichiometry in crystals of $LiNbO_3$ and $LiTaO_3$ [33, 34, 35, 36]. This compensation results in an increased photoconductivity and

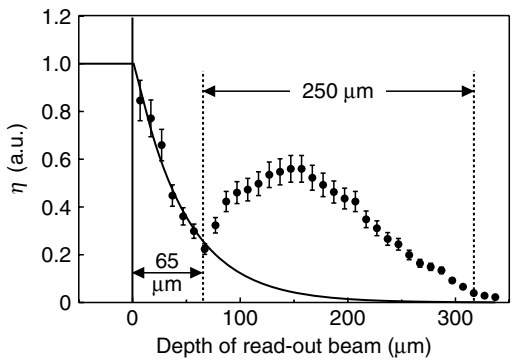

FIGURE 7.7. Bragg diffraction efficiency η as a function of the depth of the read-out beam d beneath the illuminated crystal surface, which is indicated by the solid vertical line at $d = 0\,\mu m$. The region $0 \leq d \leq 65\,\mu m$ is characterized by a dominant band grating. Its strength follows the exponential decrease ($\alpha = 450\,cm^{-1}$) of the UV intensity inside the crystal, indicated by the solid curve. The trap grating is dominant at larger depths, as recognized by the structure with its maximum at approximately $150\,\mu m$. The UV intensity at the crystal surface was $I_{UV} = 140\,mW/cm^2$.

a significantly reduced optical damage in Mg-doped samples as compared to congruently grown undoped samples. In the same way, in near-stoichiometric crystals, inclusions of a small amount of Mg helps compensating the remaining smaller amount of intrinsic defects. Recently it has been demonstrated that Mg doping (1 mol %) of near-stoichiometric $LiTaO_3$ increases the response rate of interband photorefractive gratings by a factor of 20 compared with the one in undoped crystals [32]. For UV light intensities larger than $500\,mW/cm^2$, the response time is faster than one millisecond. Note that in the near UV ($\lambda = 351\,nm$), a sensitivity enhancement by doping with Mg has been also demonstrated recently for lithium niobate crystals [37] in the conventional photorefractive regime.

The high spatial resolution of UV holography and the present response speed of less than one millisecond in Mg-doped near stoichiometric $LiTaO_3$ are such that applications of this type of crystals for the realization of high resolution real-time optical processing elements appear promising. Integrated optical functions that can be dynamically modified can also potentially be realized in this technologically very important crystal by means of interband photorefraction.

7.3.3. *Tin Hypothiodiphosphate,* $Sn_2P_2S_6$

Tin hypothiodiphosphate ($Sn_2P_2S_6$, SPS) is a ferroelectric crystal with large electro-optic coefficients [38] and a moderate band-gap energy of 2.3 eV. In the conventional sense, this material exhibits very good photorefractive properties in the red and near infrared spectral range [39, 40, 41, 42, 43, 44]. More detailed information about this material and its properties in connection with conventional photorefractive effects can be found in Chapter 9 of the second volume of this book series.

Since blue and green light are being strongly absorbed, SPS is suitable for hologram recording via interband photorefraction using visible light. Here we summarize some of the observations in this regime [45, 46, 47].

- For the wavelengths 514 and 488 nm, which are well within the interband absorption regime, the photoconductivity σ_{ph} follows well the square-root dependence on light intensity predicted from (7.2) for incident intensities larger than few mW/cm^2. The same is true for the wavelength $\lambda = 532\,nm$, which is at the edge of the absorption band, but only at elevated temperatures of about 50°C [47]. At this temperature and wavelength, the absorption constant exceeds $100\,cm^{-1}$ (X-polarization) and is increased by more than a factor of 4 with respect to room temperature, where the photoconductivity behavior evidences a mixed regime. For incident intensities I well below $1\,mW/cm^2$, two kinds of behaviors have been observed depending on crystal sample. Either a linear regime where σ_{ph} depends linearly on I (as for $KNbO_3$ and $LiTaO_3$), or a regime where the photoconductivity tends to approach a nearly constant plateau with a very weak dependence on intensity [48]. The latter behavior is expected if one of the conducting bands is being charged

with carriers as a result of a highly asymmetrical level of carrier exchange between the two bands and deep impurities [11].

- The refractive index change induced associated with interband photorefractive gratings in $Sn_2P_2S_6$ can reach few times 10^{-4} at $\lambda = 514\,\text{nm}$ and intensities exceeding $500\,\text{mW/cm}^2$, as confirmed by Bragg diffraction angular dependent measurements in longitudinal geometry and recent beam coupling investigations in thin samples [48].
- The contribution of possible mechanisms other than the photorefractive effect, such as absorption gratings, space-charge gratings induced by the pyroelectric effect, thermo-optic gratings, or surface deformation gratings are found to be negligible as compared to the observed effects [47, 49].
- The build-up of the space-charge grating, as measured in the cw regime in longitudinal geometry, can be described satisfactorily by a double exponential behavior. The associated fast and slow time constants for the recording wavelength $\lambda = 488\,\text{nm}$ are of the order of $10\,\mu\text{s}$ and $100\,\mu\text{s}$, respectively (Y-polarization, $I \approx 0.7\,\text{W/cm}^2$ [47]). At $\lambda = 514\,\text{nm}$, these times become slightly longer.
- The response can be made even faster if the energy deposition is made more rapidly, such as in the case of pulsed excitation. For instance, using 50 ns pulses at 532 nm and a fluence of $100\,\mu\text{J/cm}^2$ (corresponding to the energy deposited in the cw regime during $100\,\mu\text{s}$ at the intensity of $1\,\text{W/cm}^2$), one observes the rise of the diffraction efficiency to its maximum within about $1\,\mu\text{s}$ with a consequent decay (see Fig. 7.8, [45]). Note that if a high pulse repetition rate is necessary, such as in the case described later in Section 7.4.2, it is also important, after the signal peak, to have a quick return of the diffraction efficiency to zero, which is the case here.

To conclude, interband photorefraction in SPS is characterized by fast response times and large nonlinearity as a result of the high electro-optic

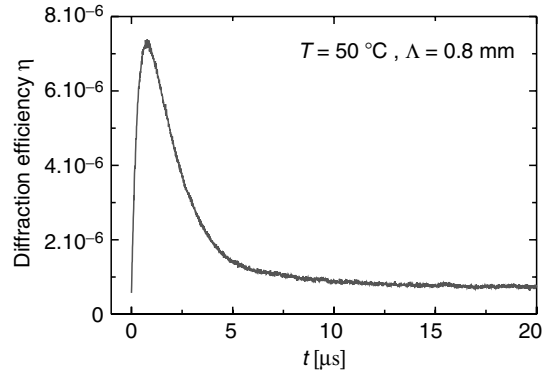

FIGURE 7.8. Dynamics of the diffraction efficiency in $Sn_2P_2S_6$ under pulsed grating recording at 532 nm. Pulse length = 50 ns; Fluence = $100\,\mu\text{J/cm}^2$. (After [45])

coefficients. This is combined with the advantage that the effect can be induced using visible wavelengths, a spectral range where cheaper light sources and compact sources offering a high pulse repetition rate for processing applications are readily available.

7.4 Applications

Owing to the large absorption constant, interband photorefractive effects are not useful for applications in which the recording light needs to be used further, such as two-wave mixing light amplification and related applications, self-pumped or four-wave mixing phase conjugation, and so on. In contrast, due to the faster dynamics with respect to conventional photorefraction, interband effects are very interesting for applications requiring a large parallel processing speed or a relatively quick switching time.

Four examples are demonstrated here: An optically addressed spatial light modulator (incoherent-to-coherent converter) based on interband photorefraction in $KNbO_3$, a high speed optical correlator based on interband photorefraction in SPS, and again in $KNbO_3$, reconfigurable light induced 1D waveguides with switching times in the 100 μs region, as well as a tunable Bragg filter operating at telecommuncation wavelengths near 1.55 μm.

7.4.1 High-Speed Optical Processing in $KNbO_3$ *with High Resolution: PICOC*

The fast response time of band-to-band photorefraction, combined with the high resolution proper to short-wavelength light, leads to an extremely high effective parallel processing rate. This may be demonstrated by a photorefractive incoherent to coherent optical converter (PICOC) operated in the interband regime. A PICOC is basically an optically addressed spatial light modulator (SLM) based on the photorefractive effect by which an incoherent wave is transferred onto a coherent beam as illustrated in Fig. 7.9. The information transfer between incoherent and coherent light occurs through diffraction at a modulated holographic phase grating. The latter is the key element that determines the time response and influences the optical resolution. Several implementations making use of conventional photorefraction were demonstrated [50, 51, 52, 53, 54].

An experimental demonstration of a PICOC based on interband photorefractive effects has been performed using a 47 μm thick sample of nominally pure, single domain $KNbO_3$ crystal and the approach schematically depicted in Fig. 7.9 [55]. A very important figure of merit for a incoherent-to-coherent converter is its resolution. In the experimental implementation, an excellent resolution of 124 line pairs/mm (lp/mm) was obtained, which is close to the resolution of 148 lp/mm allowed by the optical system for the incoherent

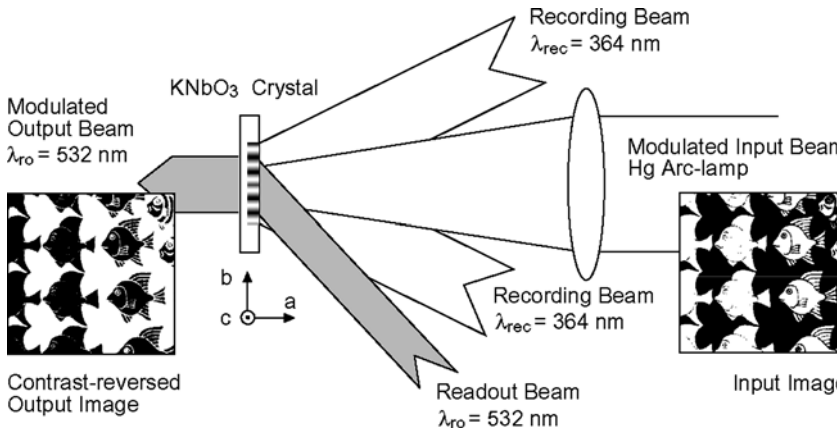

FIGURE 7.9. Principle of a photorefractive incoherent-to-coherent optical converter (PICOC): A projected input image, caried by incoherent light, modulates a superimposed photorefractive Bragg grating that is produced by two interfering recording waves. The (anisotropically) Bragg diffracted read-out laser beam carries the contrast reversed image.

illumination, and to the limiting resolution of 160 lp/mm set by the Bragg diffraction process. The latter depends on the grating thickness and the wavelength used [56, 52].

PICOCs based on interband photorefraction are interesting not only because of the achievable resolution, but obviously, also because of the short build-up and reconfiguration time. For the experimental parameters giving the maximum resolution (recording intensity $= 85\,\mathrm{mW/cm^2}$, average incoherent erasure intensity $= 70\,\mathrm{mW/cm^2}$, read-out intensity $= 5\,\mathrm{W/cm^2}$), a response time of $35\,\mu$s with an overall contrast better than 10:1 was measured. The diffraction efficiency for the read-out wave was $\eta = 0.4\%$.

The intensities mentioned above elucidate another important feature of the interband photorefractive effect. The fact that the gratings are robust against illumination with light of sub band-gap photon energy allows to use very intense read-out waves without affecting the PICOC operation.

The demonstrated write-read-erase cycle was $\tau_c = 70\,\mu$s and represents the achievable frame time. It is possible to combine this with the corresponding resolution and define an incoherent-to-coherent conversion rate by the expression $\Gamma \equiv (2R)^2/\tau_c$, which corresponds to a number of switchable pixels per unit time and unit area. For the PICOC described here, one has $\Gamma = 88\,\mathrm{Gbit}/(s\,cm^2)$, a number rivaled only by optically addressed spatial light modulators based on multiple quantum wells devices [55, 57].

The key performance characteristics mentioned above can be easily extrapolated to other optical processing devices at low intensities such as, for instance, optical correlators. In the next section, we describe a further example where one

makes use of the favorable properties of interband photorefraction for the demonstration of a high repetition rate optical correlator.

7.4.2 Joint Fourier Transform Correlation

In the past, the speed of optical correlators was often limited by the input electronic interface device, such as the input spatial light modulator (SLM) used in one or both arms of the joint Fourier transform (JFT) scheme first proposed by Weaver and Goodman [58]. Today, the advent of faster display devices such as ferroelectric liquid crystals SLMs has shifted the limiting factor back to the nonlinear device element [59]. It is therefore important to provide a material where the optical processing operation can be performed at a rate at least equal to the input data rate. Among the low-power nonlinear optical effects coming into consideration, the interband photorefractive effect discussed in this chapter is particularly attractive because of the high sensitivity and speed, and because the relatively small thickness of the recorded gratings leads to higher spatial resolution and an increased shift invariance of the correlator.

If an optical correlator has to compete with the steadily improving purely electronic alternatives, its operation frame rate has to be high enough. For electronic correlators, the processing time T required for calculating the correlation between two images of pixel size $N_{\mathrm{px}} \times N_{\mathrm{px}}$ is $T \propto N_{\mathrm{px}}^2 \log_2 N_{\mathrm{px}}$. A JFT optical correlator with 10 kHz frame rate is therefore faster than a 2 GHz clock rate state of the art dedicated digital processor as long as the number of pixels exceeds $N_{\mathrm{px}} \approx 50$.

A system was built to perform fast JFT correlations using $Sn_2P_2S_6$ as nonlinear optical processing element and an angularly multiplexed holographic storage memory [46]. Fig. 7.10 shows the conceptual idea, while a scheme of the setup can be found in the original reference [46]. The system was operated in the pulsed regime using a high repetition rate frequency doubled Nd:YAG laser at the wavelength of 532 nm. The use of the holographic memory permits us to overcome the available speed limitation of the electronic/optic interface device and to operate the JFT correlator at a rate of 10 kHz. As discussed earlier in this chapter, if the holograms performing the correlation operation are being recorded in SPS, the operation can be performed in less than the pulse distance of 100 μs.

The library images were recorded in an angularly multiplexed holographic memory implemented using a thick $LiNbO_3$ crystal. High speed image sequences were produced by reading out 10 phase modulated images of the kind shown on top in Fig. 7.11 at a rate of 10'000 frames/s from the holographic memory. Each image was then compared with an image presently displayed through a ferroelectric liquid crystal spatial light modulator (SLM). The comparison was performed by means of the thin dynamic hologram recorded in real-time in the SPS crystal by the interband photorefractive effect. Two typical correlation traces are shown in Fig. 7.11. The 10 mutual correlation peaks can be clearly identified.

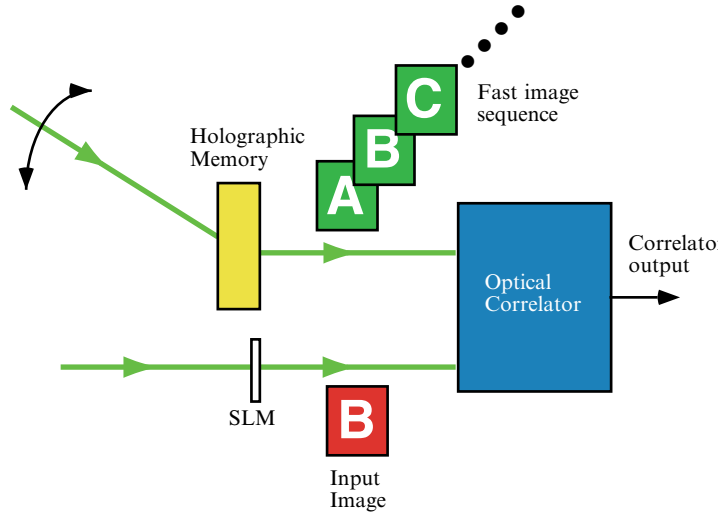

FIGURE 7.10. Principle of operation of a high-rate JFT correlator with an image library stored in a holographic memory.

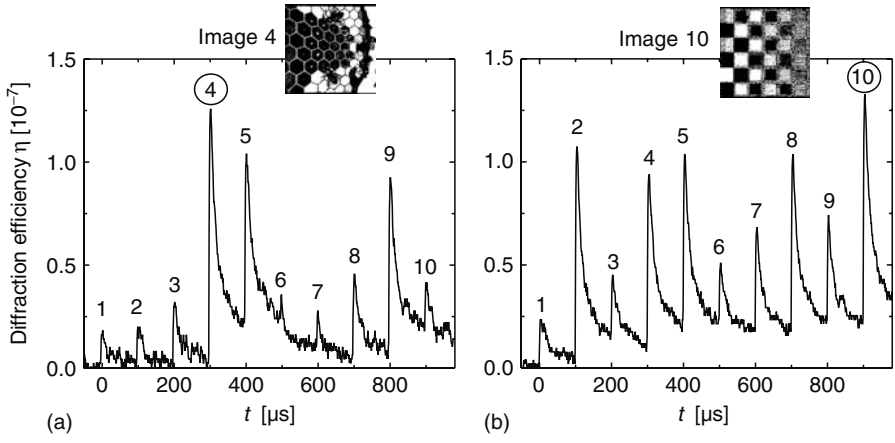

FIGURE 7.11. Intensity of the correlation peaks produced by comparing image 4 (a) and image 10 (b) with an image sequence extracted from the holographic memory at the rate of 10 kHz.

Peak 4 in (a) and peak 10 in (b) are the highest and correspond to the correctly identified displayed images on the SLM.

It can be concluded that, by a combination of a holographic memory with fast dynamic holography, realization of a joint Fourier transform optical correlator working at a frame rate of at least 10 kHz is possible, thus competing

favorably with current electronics. Typical applications of such correlators are pattern and position recognition (fingerprints, faces, industrial tools, objects, ...), tracking of unknown objects or search in large databases of page coded information.

7.4.3 Light Induced Waveguides

The creation of waveguides that can be dynamically reconfigured at will is a very desirable feature, for instance for applications for optical switching or dynamic optical interconnection. The photorefractive effect, by its own nature, offers the possibility for such reconfigurability. While photorefractive waveguides may be created by several means [60, 61, 62, 63, 64], only the interband photorefractive effect offer the possibility of reconfiguration in the microsecond time range.

The technique discussed here makes use of a controlling beam illuminating the top surface of an electro-optic crystals (pure $KNbO_3$) and imposing the desired waveguide shape [65]. By using interband absorbed light, the latter can be reconfigured in a time of few tens of microseconds with moderate light intensities of the order of $1\,mW/cm^2$. The mechanism underlying waveguide formation is the local screening of an externally applied electric field E, as shown in Fig. 7.12. This is analogous with the mechanisms acting in the case light induced waveguides are produced by beam self-focusing [61] or light induced domain switching [66]. If the light polarization and field direction are chosen properly, the refractive index decreases homogeneously across the sample apart for the regions that are externally illuminated. There the field is screened by bipolar charge transport. Because the desired structure can be

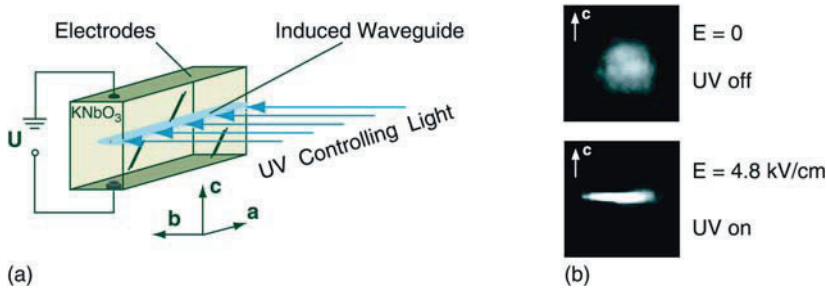

FIGURE 7.12. a. Schematic view of the setup to produce light induced waveguides. An electric field is applied along the c-axis. The controlling UV light, which induces the waveguide, has a photon energy larger than the 3.3 eV bandgap of $KNbO_3$. Due to the strong absorption of UV light in pure $KNbO_3$ (intensity absorption coefficient $\alpha_c = 540 \pm 50\,cm^{-1}$) [11], the UV stripe can induce field screening only for about $150\,\mu m$ below the surface. b. CCD images of the intensity distribution of a HeNe probe beam at the exit face of the crystal (picture size is $240 \times 240\,\mu m$) show the diffracted beam without applied E field and without UV illumination (top), as well as the guided beam for applied E field and with UV illumination (bottom).

imaged onto the surface by a deflector or a photolithographic like process, various waveguide configurations can be easily produced in this way.

With this technique, straight waveguides, Y-branches, and 1×4 and 1×8 connectors have been demonstrated [67] for guiding red probe light as well as light at the telecommunication wavelengths of 1.3 and 1.55 μm. Obviously, due to the larger natural diffraction, larger fields are required to achieve the same waveguide width in this case. The guided beam full-width-at-half maximum scales roughly as $\lambda/E^{1/2}$. Note that the guiding properties are found to be unchanged as the intensity of a HeNe probe beam is increased from 0.004 to 200 $\mathrm{W/cm^2}$, confirming therefore the robustness of refractive-index changes induced by band-to-band photorefraction. The total losses in the induced waveguide correspond to an intensity loss coefficient $\alpha < 0.02\,\mathrm{cm^{-1}}$, i.e., less than 0.1 dB/cm.

On the base of the method described above, attractive all-optical devices may be created, such as switches, real time beam deflectors, tunable Y-branches, or reconfigurable optical interconnects compatible with telecommunication wavelengths. Alternatively such low loss light induced waveguides might be used also in connection with nonlinear optical frequency conversion.

7.4.4 Tunable Bragg Filters

In wavelength division multiplexing (WDM) and dense WDM (DWDM) systems, tunable optical filters are needed to manipulate or select a desired wavelength from the band of available channels and a suitable tunable optical filter needs both a large tuning range and a narrow bandwidth. Among the various possible approaches [68, 69], tunable filters based on volume holograms offer the important advantage of a very high wavelength selectivity of the filter [70, 71].

Interband photorefraction in pure $KNbO_3$ were used in [71] to implement dynamic narrow-bandwidth thick holographic reflection gratings for telecommunication wavelengths near 1550 nm. The tuning can be done in microseconds and is achieved by using an acousto-optic deflector to control the direction of the recording beams and hence the spacing of the photorefractive gratings, as shown in Fig. 7.13. A bandwidth of 0.13 nm and fast tuning between channels spaced by 50 GHz frequency were demonstrated.

Any crystal that exhibits interband photorefractive effect could be used for such a task instead of $KNbO_3$: In particular materials like $Sn_2P_2S_6$ where interband photorefraction at visible recording wavelengths is possible, as discussed in Section 7.3.3.

7.5 Conclusions

In this chapter, we have given a short introduction to interband photorefractive effects and described them by a simple model for the limiting case of neglecting any mid-band-gap states. The principal advantages of interband photorefraction are the much faster response speeds than achievable through conventional

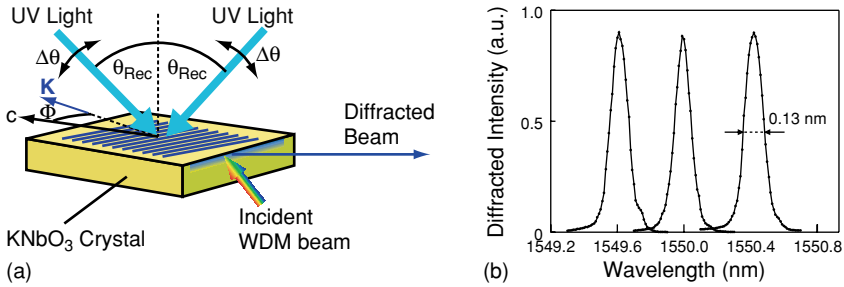

FIGURE 7.13. (a) Principle of a tunable optical filter by volume holography. The Bragg wavelength of the filter is tuned by changing the mutual angle $2\theta_{Rec}$ between the interfering writing beams symmetrically. This induces a change of the grating constant but no change in the direction of the grating vector K. From the multiple wavelengths of an incident WDM beam only the one corresponding to the Bragg wavelength of the grating is diffracted if the filter's bandwidth is smaller than the WDM channel spacing. (b) Wavelength selectivity scan for three different grating vectors separated by 0.4 nm (50 GHz). The three peaks are obtained by using three different grating constants. (After [71])

photorefraction, and the great robustness of the induced refractive index variations against erasure with light at longer wavelengths.

On the other hand, the drawbacks of interband photorefractive effects are related with the large absorption constant. Any application where the recording light has to be reused or detected after the nonlinear material is better performed using conventional photorefractive effects. Examples of such applications can be found in the fields of holographic storage, adaptive interferometry, coherent image amplification, laser beam cleanup, and phase conjugation. Many of these examples are discussed in this book series. If, in contrast, the recording light can be fully sacrificed in the nonlinear sample, one is better off by using the interband processes.

Three electro-optic materials, $KNbO_3$, $LiTaO_3$, and $Sn_2P_2S_6$ have been discussed in more detail. In the first material, the band-to-band processes occur at near ultraviolet wavelengths; in the second one, at deep ultraviolet wavelengths; in the third one, they occur already in the blue-green spectral region. For $KNbO_3$ and $Sn_2P_2S_6$, response times of a few μs can be achieved at conventional cw intensity levels, while response times for $LiTaO_3$ are in the few ms region for near-stoichiometric crystals and slightly faster than 1 ms for Mg doped near stoichiometric $LiTaO_3$. Due to the speed of response, the interband photorefractive effect is interesting for applications in fast parallel optical processing. Examples of an optically addressed spatial light modulator and of a Joint Fourier transform optical correlator were given. Other examples were given in connection with the manipulation and guiding of an optical beam by means of a controlling light pattern, and with the recording of dynamically reconfigurable narrow-bandwidth holographic reflection gratings for wavelength filtering.

The existence of interband photorefractive effects is not expected to be limited to the materials discussed here; depending on the required wavelength of operation, other electro-optic compounds may be selected and investigated in this context.

References

1. G.C. Valley, T.F. Boggess, J. Dubard, A.L. Smirl, J. Appl. Phys. **66**, 2407 (1989).
2. A. Partovi, A. Kost, E. Garmire, G.C. Valley, M.B. Klein, Appl. Phys. Lett. **56**, 1089 (1990).
3. V.W. Franz, Z. Naturforschg. **13a**, 484 (1958).
4. L.V. Keldysh, Soviet Phys. JETP **34**, 788 (1958).
5. D.D. Nolte, D.H. Olson, G.E. Doran, W.H. Knox, and A.M. Glass, J. Opt. Soc. Am. B **7**, 2217 (1990).
6. D.A. Miller, D.S. Chemla, T.C. Damen, A.C. Goddard, W. Wiegmann, T.H. Wood, and C.A. Burrus, Phys. Rev. Lett. **53**, 2173 (1984).
7. D.D. Nolte and R.M. Melloch, in *Photorefractive Effects and Materials, Electronic Materials: Science and Technology*. pp. 373–451 edited by D. D. Nolte, Kluwer Academic Publishers, Boston (1995).
8. E. Garmire, IEEE J. Sel. Topics QE **6**, 1094 (2000).
9. D. Von der Linde, A.M. Glass, and K.F. Rodgers, Appl. Phys. Lett. **25**, 155 (1974).
10. D. Von der Linde, A.M. Glass, and K.F. Rodgers, Appl. Phys. Lett. **26**, 22 (1975).
11. G. Montemezzani, P. Rogin, M. Zgonik, and P. Günter, Phys. Rev. B **49**, 2484 (1994).
12. N.V. Kukhtarev, V.B. Markov, S.G. Odulov, M.S. Soskin, and V.L. Vinetskii, Ferroelectrics **22**, 949 (1979).
13. P. Bernasconi, G. Montemezzani, I. Biaggio, and P. Günter, Phys. Rev. B **56**, 12196 (1997).
14. P. Bernasconi, Dissertation, Diss. ETH No. 12761, Swiss Federal Institute of Technology, Zürich (1998).
15. P. Bernasconi, G. Montemezzani, and P. Günter, Appl. Phys. B **68**, 833 (1999).
16. G. Montemezzani, P. Rogin, M. Zgonik, and P. Günter, Opt. Lett. **18**, 1144 (1993).
17. M. Ewart, M. Zgonik, and P. Günter, Opt. Commun. **141**, 99 (1997).
18. M. Carrascosa, F. Agullo-Lopez, G. Montemezzani, and P. Günter, Appl. Phys. B **72**, 697 (2001).
19. G. Montemezzani, P. Bernasconi, Ph. Dittrich, R. Ryf, and P. Günter, Proc. SPIE **4358**, 1 (2001).
20. H.J. Eichler, P. Günter, and D.W. Pohl, *Laser-induced dynamic gratings*, Springer Verlag, Berlin (1986).
21. N. Kukhtarev, T. Kukhtareva, and P. P. Banerjee, Proc. IEEE **87**, 1857 (1999).
22. S. Ducharme, Opt. Lett. **16**, 1791 (1991).
23. K. Buse, J. Opt. Soc. Am. B **10**, 1266 (1993).
24. F. Jermann, M. Simon, and E. Krätzig, J. Opt. Soc. Am. B **12**, 2066 (1995).
25. L. Kovács, G. Ruschhaupt, K. Polgár, G. Corradi, and M. Wöhlecke, Appl. Phys. Lett. **70**, 2801 (1997).
26. Y. Furukawa, K. Kitamura, E. Suzuki, and K. Niwa, J. Crystal Growth **197**, 889 (1999).

27. P. Bernasconi, G. Montemezzani, P. Günter, Y. Furukawa, and K. Kitamura, Ferroelectrics **223**, 373 (1999).
28. Y. Furukawa, K. Kitamura, K. Niwa, H. Hatano, P. Bernasconi, G. Montemezzani, and P. Günter, Jpn. J. Appl. Phys. **38**, 1816 (1999).
29. M. Jazbinšek, M. Zgonik, S. Takekawa, M. Nakamura, K. Kitamura, and H. Hatano, Appl. Phys. B **75**, 891 (2002).
30. Ch. Bäumer, C. David, A. Tunyagi, K. Betzler, H. Hesse, E. Krätzig, and M. Wöhlecke, J. Appl. Phys. **93**, 3102 (2003).
31. Ph. Dittrich, B Koziarska-Glinka, G. Montemezzani, P. Günter, S. Takekawa, K. Kitamura, and Y. Furukawa, J. Opt. Soc. Am. B **21**, 632 (2004).
32. Ph. Dittrich, G. Montemezzani, M. Habu, M. Matsukura, S. Takekawa, K. Kitamura, and P. Günter, Opt. Commun. **234**, 131 (2004).
33. F. Nitanda, Y. Furukawa, S. Maiko, M. Sato, and K. Ito, Jpn. J. Appl. Phys. I **34**, 1546 (1995).
34. M. Nakamura, S. Takekawa, K. Terabe, K. Kitamura, T. Usami, K. Nakamura, H. Ito, and Y. Furukawa, Ferroelectrics **273**, 199 (2002).
35. Y. Furukawa, K. Kitamura, S. Takekawa, K. Niwa, and H. Hatano, Opt. Lett. **23**, 1892 (1998).
36. G.Q. Zhang, G.Y. Zhang, S.M. Liu, J.J. Xu, Q. Sun, and X.Z. Zhang, J. Appl. Phys. **83**, 4392 (1998).
37. J. Xu, G. Zhang, F. Li, X. Zhang, Q. Sun, S. Liu, F. Song, Y. Kong, X. Chen, H. Qiao, J. Yao, and Z. Lijuan, Opt. Lett. **25**, 129 (2000).
38. D. Haertle, G. Caimi, A. Haldi, G. Montemezzani, P. Günter, A. A. Grabar, I.M. Stoika, and Yu. M. Vysochanskii, Opt. Commun. **215**, 333 (2003).
39. A.A. Grabar, Ferrolelectrics **170**, 133 (1995).
40. S.G. Odoulov, A.N. Shumelyuk, U. Hellwig, R.A. Rupp, and A.A. Grabar, Opt. Lett. **21**, 752 (1996).
41. S.G. Odoulov, A.N. Shumelyuk, U. Hellwig, R.A. Rupp, A.A. Grabar, and I.M. Stoyka, J. Opt. Soc. Am. B **13**, 2352 (1996).
42. A.A. Grabar, I.V. Kedyk, M.I. Gurzan, I.M. Stoika, A.A. Molnar, and Y.M. Vysochanskii, Opt. Commun. **188**, 187 (2001).
43. A. Shumelyuk, S. Odoulov, D. Kip, and E. Krätzig, Appl. Phys. B **72**, 707 (2001).
44. M. Jazbinsek, G. Montemezzani, P. Günter, A.A. Grabar, I.M. Stoika, and Yu. M. Vysochanskii, J. Opt. Soc. Am. B **20**, 1241 (2003).
45. R. Ryf, G. Montemezzani, P. Günter, A.A. Grabar, I.M. Stoika, and Y.M. Vysochanskii, Trends Opt. Photon. **62**, 11 (2001).
46. R. Ryf, G. Montemezzani, P. Günter, A.A. Grabar, I.M. Stoika, and Yu. M. Vysochanskii, Opt. Lett. **26**, 1666 (2001).
47. G. Montemezzani, R. Ryf, D. Haertle, P. Günter, A.A. Grabar, I.M. Stoika, and Yu, M. Vysochanskii, Ukr. J. Phys. **49**, 333 (2004).
48. R. Mosímann and D. Haertle, Private Communication.
49. R. Ryf, Dissertation, Diss. ETH No. 13546, Swiss Federal Institute of Technology, Zürich (2000).
50. A.A. Kamshilin and M.P. Petrov, Sov. Tech. Phys. Lett. **6**, 144 (1980).
51. Y. Shi, D. Psaltis, A. Marrakchi, and A.R. Tanguay, Appl. Opt. **22**, 3665 (1983).
52. P. Amrhein and P. Günter, J. Opt. Soc. Am. B **12**, 2387 (1990).
53. J.S. Zhang, H.T. Wang, S. Yoshikado, and T. Aruga, Opt. Lett. **22**, 1612 (1997).
54. J.S. Zhang, H.T. Wang, S. Yoshikado, and T. Aruga, Appl. Opt. **38**, 995 (1999).

55. P. Bernasconi, G. Montemezzani, M. Wintermantel, I. Biaggio, and P. Günter, Opt. Lett. **24**, 199 (1999).
56. A. Marrakchi, A.R. Tanguay, J. Yu, and D. Psaltis, Opt. Eng. **24**, 124 (1985).
57. S.R. Bowman, W.S. Rabinovich, G. Beadie, S.M. Kirkpatrick, D.S. Katzer, K. Ikossi-Anastasiou, and C.L. Adler, J. Opt. Soc. Am. B **15**, 640 (1998).
58. C.S. Weaver and J.W. Goodman, Appl. Opt. **5**, 1248 (1966).
59. J. Colin, N. Landru, V. Laude, S. Breugnot, H. Rajbenbach, and J.P. Huignard, J. Opt. A: Pure Appl. Opt. **1**, 283 (1999).
60. K. Itoh, O. Matoba, and Y. Ichioka, Opt. Lett. **19**, 652 (1994).
61. M.F. Shih, Z.G. Chen, M. Mitchell, M. Segev, H. Lee, R.S. Feigelson, and J.P. Wilde, J. Opt. Soc. Am. B **14**, 3091 (1997).
62. O. Matoba, T. Inujima, T. Shimura, and K. Kuroda, J. Opt. Soc. Am. B **15**, 2006 (1998).
63. D. Kip, Appl. Phys. B **67**, 131 (1998).
64. O. Matoba, K. Itoh, and K. Kuroda, Proc. IEEE **87**, 2030 (1999).
65. Ph. Dittrich, G. Montemezzani, P. Bernasconi, and P. Günter, Opt. Lett. **24**, 1508 (1999).
66. A. Bekker, A. Peda'el, N.K. Berger, M. Horowitz, and B. Fischer, Appl. Phys. Lett. **72**, 3121 (1998).
67. Ph. Dittrich, Dissertation, Diss. ETH No. 15414, Swiss Federal Institute of Technology, Zürich (2004).
68. H. Kobrinski and K.-W. Cheung, IEEE Commun. Mag. **27**, 53 (1989).
69. D. Sadot and E. Boimovich, IEEE Commun. Mag. **36**, 50 (1998).
70. V.M. Petrov, C. Denz, A.V. Shamray, M.P. Petrov, and T. Tschudi, Opt. Mater. **18**, 191 (2001).
71. Ph. Dittrich, G. Montemezzani, and P. Günter, Opt. Commun. 214, 363 (2002).

8

Two-Step Recording in Photorefractive Crystals

Eckhard Krätzig[1] *and Karsten Buse*[2]

[1] Department of Physics, University of Osnabrück, Barbarastr. 7, D–49069 Onabrück, Germany
[2] Institute of Physics, University of Bonn, Wegelerstr. 8, D–53115 Bonn, Germany

Two-step excitation processes have been used for hologram storage in photorefractive crystals. By this means the interference pattern can be formed with red or near-infrared (near–IR) light and nondestructive readout of information is possible. Often shallow levels are involved in the holographic recording process in photorefractive crystals. The shallow levels can be populated by illumination with visible or UV pulses forming states with relatively long lifetimes, thus sensitizing the crystals for holographic recording with IR pulses. In $LiNbO_3$ and $LiTaO_3$, the most important shallow levels have been identified. They result from Nb_{Li}^{5+} and Ta_{Li}^{5+} antisite defects (Nb^{5+} or Ta^{5+} on Li^+ site). The crystals can also be preilluminated with visible light of a cw argon ion laser or of a Xenon lamp and holograms can be recorded with red light of a laser diode. The sensitization process is possible for other photorefractive crystals, too. A further approach is based on the pyroelectric effect. In all cases, the holograms can be read nondestructively with infrared (IR) light and can be erased with green light. The hologram lifetime is limited by electron tunneling or by an ionic conductivity. Lifetimes up to years can be achieved. Recording of components for telecommunication applications with IR light allows us to create reconfigurable, and thus more versatile devices.

8.1 Introduction

Storage of volume phase holograms in electrooptic crystals like $LiNbO_3$ offers fascinating possibilities for many applications, as can be seen from the scope of this book. The involved photorefractive effect is based on the transposition of a light pattern into a refractive index pattern. Under nonuniform illumination, charge carriers—electrons or holes—are excited and trapped at new sites. By this means electrical space-charge fields build up that give rise to an electro-optic modulation of the refractive index. The trapped charge can be released and the field pattern erased by uniform illumination or by heating.

But there are two main drawbacks: First, the crystals are insensitive in the interesting near-IR region. Second, retrieval of stored information requires homogeneous illumination and thus necessarily leads to erasure effects.

To overcome these drawbacks, the use of two-photon excitations has been proposed for hologram recording by von der Linde *et al.* [1]. Then the holograms can be recorded with near-IR pulses. Furthermore, read-out without erasure is possible using pulses of reduced light intensity. The Bragg condition is fulfilled because the light wavelength remains unchanged, but the energy of one photon is not sufficient to excite an electron to the conduction band and thus redistribution of electrons does not occur. On the other hand, optical erasure may be performed with the help of two-photon processes.

A serious disadvantage of two-photon recording using virtual intermediate states is the necessity of extremely high peak intensities of the light pulses. If impurity ions exhibiting real intermediate states with long lifetimes can be utilized, a considerable reduction of the peak intensity required for two-photon recording is possible, though the intensity has to be still much larger than in the case of usual one-step recording.

Since about 1990 it became clear that shallow levels are often involved in the holographic recording process in photorefractive crystals. The shallow levels can be populated by illumination with visible or UV light forming states with relatively long lifetimes, thus sensitizing the crystals for holographic recording with IR light.

A further approach for two-step IR recording is based on the pyroelectric effect. A thermal grating is created by interfering IR beams leading to a pyroelectric field via absorption processes. By excitation of electrons with visible light, this pyroelectric field is converted into a stable space charge field.

In the present contribution, two-step processes for holographic recording in different photorefractive crystals are investigated. We discuss the use of near-IR light and nondestructive read-out. Models for the underlying physical processes are presented. Recent data about hologram lifetimes will be shown and general considerations for the application of two-step methods with the fabrication of telecommunication components will be discussed.

8.2 Early Experiments

First two-step excitation measurements in photorefractive crystals have already been performed in 1974 [1]. Frequency-doubled light pulses of a mode-locked Nd:YAG laser (wavelength 0.53 μm, pulse duration 10 ps) induced a phase retardation in doped $LiNbO_3$ crystals. It was found that the measured refractive index changes depend quadratically on the exposure energy. The influence of additional IR pulses (1.06 μm) was demonstrated, too. Furthermore, $LiNbO_3$:Cr and $LiTaO_3$:Cr crystals have been investigated [2] to utilize the long living $^4T_2$ excited state of Cr^{3+} (lifetime 500 ns). In this case, the peak intensity is reduced and pulse lasers with higher repetition rates can be used.

We have demonstrated nondestructive read-out in $LiTaO_3$:Fe [3]. Holograms were recorded by simultaneous illumination with 30 ps pulses of a mode-locked Nd:YAG laser at 1.06 μm, forming the interference pattern, and with spatially homogeneous frequency-doubled pulses of the same laser at 0.53 μm. Results are shown in Fig. 8.1. The holograms can be read nondestructively at 1.06 μm. From the experimental accuracy it was concluded that more than 10 000 read-out processes are possible. Similar results were obtained for $LiNbO_3$:Cr using 40 ns pulses of a Q-switched ruby laser at 0.694 μm [4].

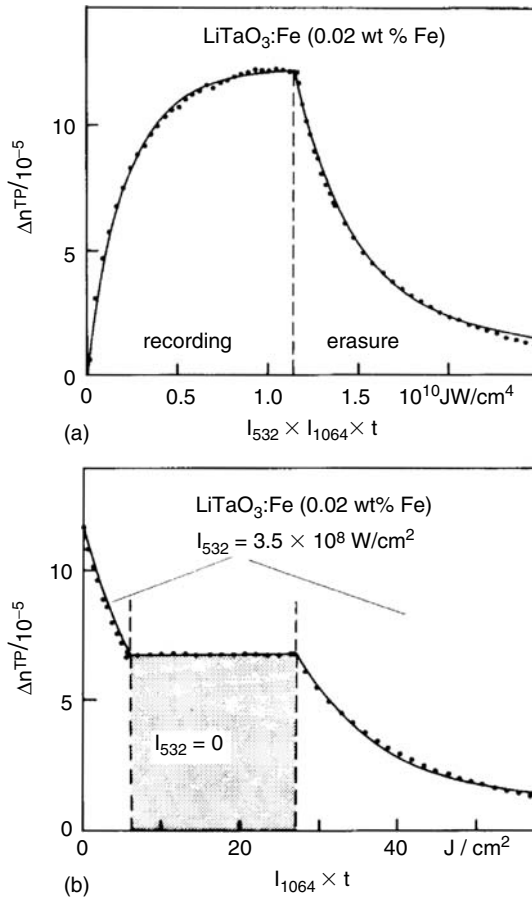

FIGURE 8.1 a) Two-photon recording-erasure cycle. The refractive index amplitude Δn^{TP} is plotted versus the product $I_{532} \times I_{1064} \times t$ of green and IR intensities and time. b) Experiment as in a), but now Δn^{TP} is plotted only versus the product $I_{1064} \times t$ of IR intensity and time. Without green light ($I_{532} = 0$, hatched region), no erasure is observed.

8.3 Shallow Levels, Two-Level Models

Since about 1990 it became clear that—at least at high light intensities—shallow levels are nearly always involved in the holographic recording process in photorefractive crystals. Two-level models—the two-center and the three-valence model—were developed and successfully applied for the description of the light-induced charge transport in many photorefractive crystals.

A very important step for the understanding of photorefractive properties of ferroelectric perovskites was the discovery of light-induced absorption in $BaTiO_3$ by Motes and Kim [5]. This increase of absorption under illumination was interpreted in terms of two kinds of centers involved [6], each of them occurring in two different states. Holtmann successfully applied this two-center model to describe the transport properties of $BaTiO_3$ [7].

Because the photoconductivity of ferroelectric perovskites is mostly dominated by holes in the valence band [7, 8], in the following discussion of the two-center model only hole transport is assumed. For electron transport, an analogous argumentation holds. With the help of Fig. 8.2, the transport of charge may be described as follows: We consider two different photorefractive centers C_1 and C_2. For each species, $i = 1, 2$, there are hole sources and traps. We denote the concentration of sources C_i^+ by N_i^+ and the concentration of traps C_i^0 by N_i^0. The total concentration of centers of type i is

$$N_i = N_i^+ + N_i^0. \tag{8.1}$$

Charge conservation requires

$$N_1^+ + N_2^+ + N_h = N_c, \tag{8.2}$$

where N_h is the concentration of holes in the valence band and N_c a constant concentration. The first center has to be a deep-level impurity, e.g., iron, and

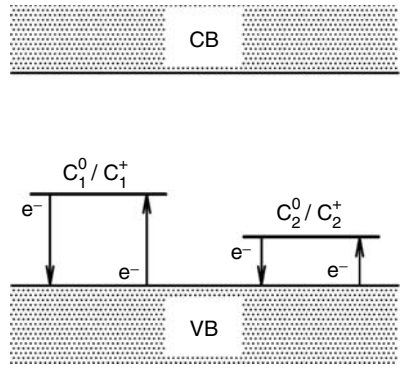

FIGURE 8.2. Band diagram of the two-center charge-transport model (CB: conduction band, VB: valence band, C_1: center 1, C_2: center 2).

the second one should be a more shallow trap with respect to the valence-band edge. The center C_2 has a relatively low thermal activation energy, such that $N_2^0 \gg N_2^+$ holds in the dark. Upon illumination, holes are generated by excitation of electrons from the valence band into C_1^+ centers. The holes migrate in the valence band and are trapped either by C_1^0 or by C_2^0 centers. Trapping at the latter creates C_2^+ centers. With increasing light intensity, more and more holes are generated and N_2^+ grows, too. By this means absorption processes become possible, which result from optical excitations of valence band electrons to C_2^+ centers. This leads to light-induced absorption changes, if C_1^+ and C_2^+ have different photon absorption cross sections. The rate equations read:

$$\frac{\mathrm{d}N_i^+}{\mathrm{d}t} = -(q_i S_i I + \beta_i)N_i^+ + r_i(N_i - N_i^+)N_\mathrm{h}, \quad i = 1, 2. \tag{8.3}$$

Here q_i denote the quantum efficiencies for generating a hole upon absorption of a photon, S_i the absorption cross sections, β_i the thermal generation rates, and r_i the recombination coefficients.

Many experimental results can be understood on the basis of this two-center model, among them the nonlinearity of the photoconductivity in the light intensity; details are described, e.g., in Ref. [9].

But there exists a further possibility to explain the charge transport properties of perovskites. As we pointed out [10], the assumption of one impurity center occurring in three different valence states—the so-called three-valence model—leads to similar conclusions as the two-center model.

The situation is illustrated in Fig. 8.3. The three valence states of the center C are denoted by 0, + and 2+. The arrows indicate the considered excitation and recombination processes of electrons. At low intensities, only C^0 and C^+ states are present, because thermally excited valence band electrons fill C^{2+}. Illumination excites electrons from the valence band into C^+ and generates holes that

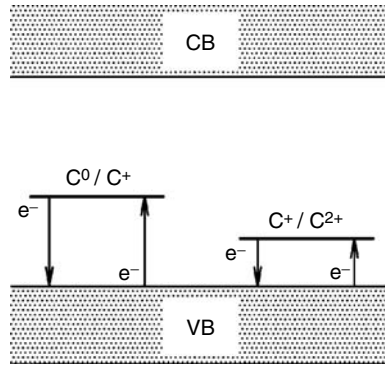

FIGURE 8.3. Band diagram of the three-valence model (CB: conduction band, VB: valence band; the valence states of the center C are indicated by 0, + and 2+).

are annihilated by electrons from C^0. For sufficiently high light intensities, the hole concentration becomes large enough that an appreciable number of electrons from C^+ can recombine with holes and generate C^{2+} contributing to absorption. Thus light-induced absorption changes appear.

Furthermore, participation of C^{2+} in the charge transport may provide a photoconductivity increasing nonlinearly with light intensity.

Rate equations, charge conservation, and constant trap density may be written as:

$$\frac{dN^+}{dt} = +r^0 N^0 N_h - (\beta^+ + q^+ S^+ I)N^+ - r^+ N^+ N_h + (\beta^{2+} + q^{2+} S^{2+} I)N^{2+}, \tag{8.4}$$

$$\frac{dN^{2+}}{dt} = +r^+ N^+ N_h - (\beta^{2+} + q^{2+} S^{2+} I)N^{2+}, \tag{8.5}$$

$$2N^{2+} + N^+ + N_h = N_c, \tag{8.6}$$

$$N^0 + N^+ + N^{2+} = N. \tag{8.7}$$

Here again N^0, N^+, and N^{2+} are the concentrations of C^0, C^+ and C^{2+}, N is the entire impurity concentration, N_h is the concentration of holes in the valence band, β^+ and β^{2+} are the thermal generation rates, q^+ and q^{2+} are the quantum efficiencies for hole generation upon absorption of a photon, S^+ and S^{2+} are the photon absorption cross-sections, r^0 and r^+ are the recombination coefficients, and N_c is a constant concentration. It should be emphasized that the above equations of the three-valence model cannot be derived from those of the two-center model by introducing a special relation between the concentrations of deep and shallow traps. But both models lead to similar conclusions.

Though it is often difficult to decide between the two-center and the three-valence model [10], in both cases shallow levels are involved, which may be utilized for two-step excitations.

These models that were developed originally for perovskite-type crystals can be applied to other materials as well. One special case of the two-center model is the situation of two deep centers, i.e., the thermal generation rates β_i are both negligible. Such a system is, e.g., $LiNbO_3$ doped with Mn and Fe where $Mn^{2+/3+}$ is a deeper impurity than $Fe^{2+/3+}$. The material can be used for persistent optical data storage [11]. Homogeneous UV light excites electrons from Mn^{3+} into the conduction band. These electrons are partially trapped by Fe^{3+} forming Fe^{2+} centers. From these Fe^{2+} centers, electrons can be excited by red or by green light. By this means the material is sensitized for red or green recording. The hologram is partially stored in the Mn and in the Fe centers. Reconstruction of the hologram with the reading light erases only the hologram in the Fe centers since the photon energy is not large enough to excite electrons

from Mn^{2+}. Thus, part of the hologram is resistant against reading. This method works with continuous-wave light since there are no competing thermal processes. But it is not useful for near-IR recording since two deep centers are involved.

8.4 Two-Step Excitations via Shallow Levels

Population of shallow levels with nanosecond pulses of visible light (frequency-doubled Nd:YAG laser, $\lambda = 0.53\,\mu$m) and hologram recording with nanosecond IR pulses (Nd:YAG laser, $\lambda = 1.06\,\mu$m) have been demonstrated in the ferroelectric perovskite $BaTiO_3$ [12]. Similar experiments have also been performed in the tungsten-bronze-type crystal $Sr_{1-x}Ba_xNb_2O_6$: Ce ($0.25 \leq x \leq 0.75$) [13], in the nonferroelectric sillenites $Bi_{12}SiO_{20}$ (BSO) [14] and $Bi_{12}TiO_{20}$ (BTO) [15], in $Sn_2P_2S_6$ (SPS) [16], and in the semiconductors CdZnTe:V [17] and CdTe:Ge [18].

But also the early experiments in $LiNbO_3$ and $LiTaO_3$ [1, 3, 4, 19] have to be discussed with respect to the new knowledge about the light-induced charge transport. In these materials shallow levels have been identified [20, 21]. They result from Nb_{Li}^{5+} and Ta_{Li}^{5+} antisite defects (Nb^{5+} or Ta^{5+} on Li^+ site) that are present in great quantities in congruent crystals. The highly charged Nb^{5+} or Ta^{5+} ions trap mobile electrons and form small polarons.

There are two possibilities for two-step excitations in these crystals, via excited states of the deep traps and via shallow traps. These possibilities are explained in Fig. 8.4 for $LiNbO_3$: Fe.

To decide between the two possibilities, measurements with time-delayed pulses have been performed [22, 23]. Results are summarized in Fig. 8.5 for $LiNbO_3$: Fe. The crystal is illuminated with a homogeneous green (0.53 μm) pulse and two intersecting IR (1.06 μm) pulses of about 20 ns duration. In order to sensitize the crystal for IR holographic recording, previous or simultaneous

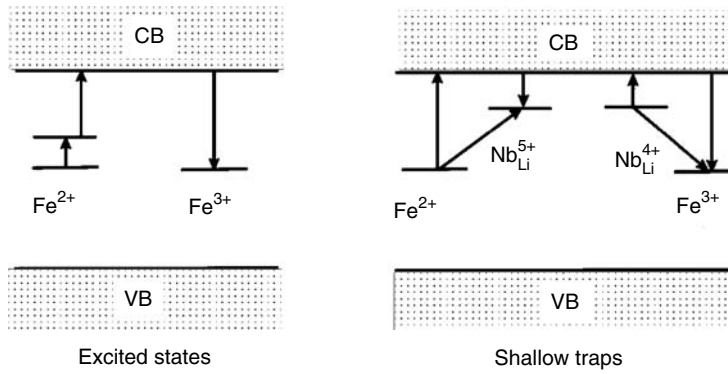

FIGURE 8.4. Two possible two-step excitations in $LiNbO_3$: Fe, via excited states of Fe^{2+} (left) and via Nb_{Li}^{5+} shallow traps (right).

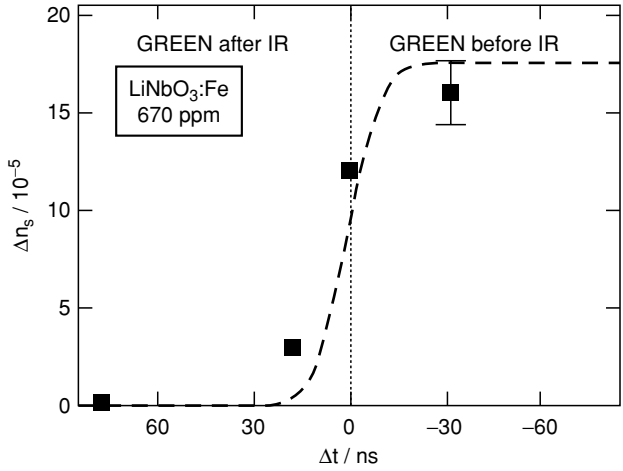

FIGURE 8.5. Saturation value of refractive index change Δn_s versus delay time $t_{532} - t_{1064}$ between IR and green pulses in $LiNbO_3$: Fe. The squares represent measured values and the solid line is a guide to the eye.

illumination with the green light is necessary. If the green pulse impinges after the IR pulses, no refractive index change is obtained. These results clearly indicate that indeed shallow traps are involved in the two-step excitation process; the photon energy of the IR light is not sufficient to populate shallow traps. Analogous results have been obtained for $LiNbO_3$: Cu [23] and $LiTaO_3$: Fe [24].

Furthermore, we have investigated the dependences of the inverse time constant τ^{-1} and of the saturation value Δn_s of the refractive index changes. The inverse time constant τ^{-1} is proportional to the photoconductivity σ_{ph},

$$\tau^{-1} = \sigma_{ph}/(\varepsilon\varepsilon_0), \tag{8.8}$$

where ε is the static dielectric constant and ε_0 the vacuum permittivity. The quantities τ^{-1} and Δn_s depend on the concentrations of the impurity ions involved and on the intensities of the IR and the visible light. Experimental results are shown in the Figs. 8.6 and 8.7.

From these results, the following relations have been deduced, which are valid for $LiNbO_3$: Cu [22], $LiNbO_3$: Fe [23] and $LiTaO_3$: Fe [24]:

$$\sigma_{ph} \propto (c_D^f/c_D^e)I^{VIS}, \tag{8.9}$$

$$\Delta n_s \propto c_D^e I^{IR}, \tag{8.10}$$

where c_D^f denotes the concentration of filled deep traps (Fe^{2+}, Cu^+), c_D^e the concentration of empty deep traps (Fe^{3+}, Cu^{2+}), I^{VIS} the intensity of the

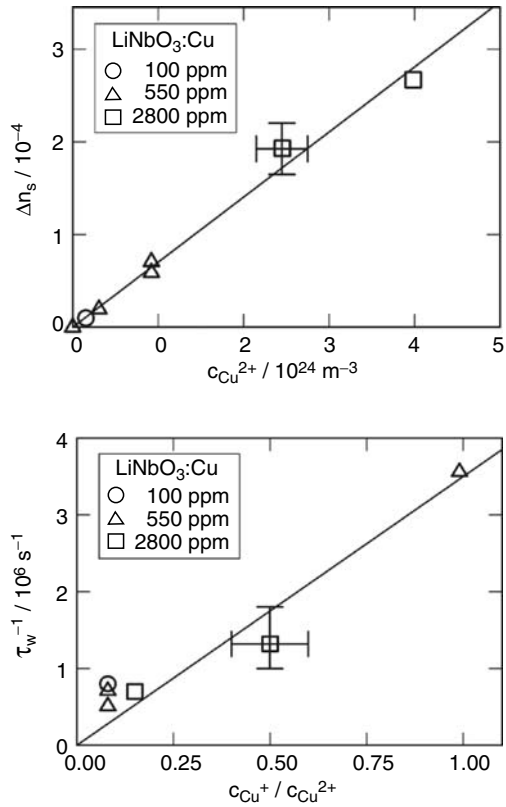

FIGURE 8.6. Saturation value of refractive index change Δn_s versus Cu^{2+} concentration $c_{Cu^{2+}}$ (upper part) and inverse writing time constant τ_w^{-1} (proportional to the photoconductivity σ_{ph}) versus ratio $c_{Cu^+}/c_{Cu^{2+}}$ of the Cu^+ and Cu^{2+} concentration (lower part) for $LiNbO_3$: Cu.

visible light, I^{IR} the intensity of the IR light, and Δn_s the saturation value of the refractive index amplitude.

These relations can be derived from the above model assuming the participation of shallow levels [24] (Fig. 8.4, right-hand side). The light-induced charge transport in doped $LiNbO_3$ and $LiTaO_3$ is mainly determined by the bulk photovoltaic effect [25]. The photovoltaic current density j_{pv} contains the modulated intensity I^{IR} of the IR light:

$$j_{pv} = \kappa_{Sh}^{IR} I^{IR} c_{Sh}^{f}, \tag{8.11}$$

where κ_{Sh}^{IR} is the photovoltaic constant and c_{Sh}^{f} the concentration of filled shallow traps (Nb_{Li}^{4+}, Ta_{Li}^{4+}). The photoconductivity $\sigma_{ph} = e\mu_e c_e = e\mu_e g_e \tau_e$ (μ_e mobility, c_e concentration, g_e generation rate, τ_e lifetime of excited carriers)

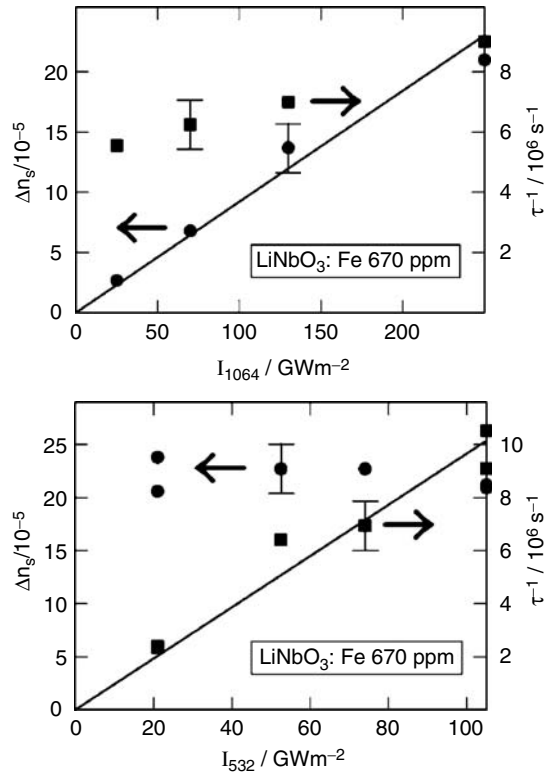

FIGURE 8.7. Saturation value of refractive index change Δn_s and inverse writing time constant τ^{-1} versus intensity I_{1064} of the IR light (upper part) and versus intensity I_{532} of the green light (lower part), respectively, for $LiNbO_3$: Fe.

may result from excitations from filled deep traps (Fe^{2+}, Cu^{+}) and filled shallow traps (Nb_{Li}^{4+}, Ta_{Li}^{4+}):

$$\sigma_{ph} = e\mu_e(S_D^{VIS} q_D^{VIS} I^{VIS} c_D^f + S_{Sh}^{VIS} q_{Sh}^{VIS} I^{VIS} c_{Sh}^f + S_{Sh}^{IR} q_{Sh}^{IR} I^{IR} c_{Sh}^f) \times (r_D c_D^e + r_{Sh} c_{Sh}^e)^{-1}, \tag{8.12}$$

where S denotes the cross-sections (for filled deep and shallow traps), q the quantum efficiencies (for filled deep and shallow traps), and r the recombination coefficients (for empty deep and shallow traps).

The description of the experimental results requires the following assumptions:

$$\begin{aligned} \sigma_{ph} &= e\mu_e(S_D^{VIS} q_D^{VIS} I^{VIS} c_D^f)(r_D c_D^e)^{-1} \propto (c_D^f / c_D^e) I^{VIS}, \\ j_{pv} &= \kappa_{Sh}^{IR} I^{IR} c_{Sh}^f \propto I^{IR} I^{VIS} c_D^f. \end{aligned} \tag{8.13}$$

Then we obtain

$$\Delta n_s \propto j_{pv}/\sigma_{ph} \propto c_D^e I^{IR}. \tag{8.14}$$

The Eqs. (8.13) and (8.14) are in perfect agreement with the experimental results, Eqs. (8.9) and (8.10). The photoconductivity is mainly determined by excitations of filled deep traps (Fe^{2+}, Cu^{+}) with VIS (or UV) light (homogeneous intensity), the photovoltaic effect by excitations on filled shallow traps (Nb_{Li}^{4+}, Ta_{Li}^{4+}) with IR light (modulated intensity). The shallow centers are populated by direct excitation of electrons from filled deep centers by VIS (or UV) light ($c_{Sh}^f \propto I^{VIS} c_D^f$).

Excitations via shallow levels have been established for many crystals. Samples may be sensitized with visible light of a cw laser or a Xenon lamp and hologram recording is even possible with a laser diode [26, 27, 28]. Two-photon excitations via intermediate states cannot be excluded in some cases, but have not yet been demonstrated unambiguously.

Holographic experiments have also been performed with laser pulses in the 100–fs range [29, 30]. Then undoped $BaTiO_3$ crystals are sensitive even in the $1.5-\mu$m wavelength regime [29], but it is again difficult to decide whether excitations via intermediate states or via shallow traps are involved.

8.5 Hologram Recording Utilizing Pyroelectric Fields

Of special interest is holographic recording at telecommunication wavelengths around $1.5\,\mu$m. However, the relatively large optical activation energy of small polarons is a serious difficulty. For this reason, a further method has been suggested based on the pyroelectric effect [31]. As demonstrated earlier [32], this effect also provides a charge driving force which may be utilized for two-step processes. A thermal grating is recorded by two interfering IR beams. The corresponding pyroelectric field is compensated by electrons excited by visible light. To obtain sufficiently large pyroelectric fields, a considerable absorption at the IR recording wavelength is required. The method has been demonstrated with stoichiometric $LiTaO_3$: Fe crystals that contain only very few Nb_{Li}^{4+} polarons [31]. IR pulses of a Nd:YAG laser (duration 7 ns, $\lambda = 1.06\,\mu$m) generate the pyroelectric field and a homogeneous green pulse (second harmonic generation, $\lambda = 0.53\,\mu$m) excites electrons. Using only IR pulses, no holographic recording is possible. If the green pulse impinges on the crystal before the IR pulses, the refractive index changes are very small, one order of magnitude smaller than in congruently melting crystals indicating that indeed very few Nb_{Li}^{4+} polarons are present. However, if the IR pulses impinge upon the crystal before the green pulse or simultaneously, considerable index changes are observed (Fig. 8.8).

The saturation value of the refractive index changes increases linearly with the intensity of the IR recording light (Fig. 8.9) and does not depend on the

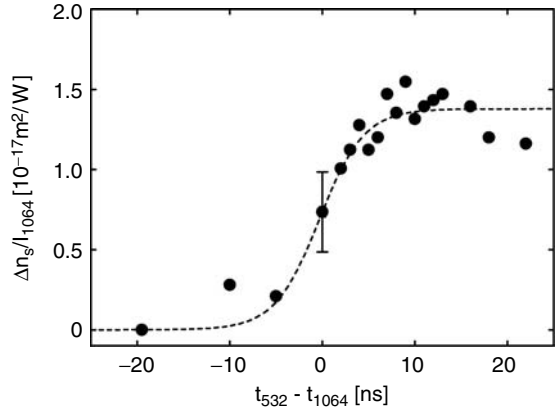

FIGURE 8.8. Saturation values Δn_s of the refractive index changes as a function of delay time $t_{532} - t_{1064}$ between the infrared and the green pulse for a $LiTaO_3$: Fe crystal. The refractive index change is normalized to the infrared intensity I_{1064}. At positive delay times, the green pulse reaches the crystal after the infrared pulse. The dotted line is a guide to the eye.

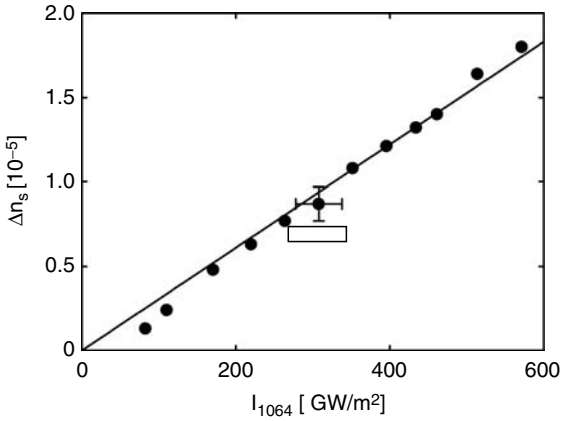

FIGURE 8.9. Saturation value Δn_s of refractive index change as a function of infrared recording light intensity I_{1064}. The solid line is a linear fit to the measured data.

intensity of the green light in the intensity range investigated ($< 600\,\mathrm{GW/m^2}$). Furthermore, the saturation value increases linearly with the absorption at $1.06\,\mu$m that is proportional to the concentration of Fe^{2+} ions (Fig. 8.10). The build up of holograms follows a monoexponential law with a time constant τ. The photoconductivity $\sigma_{ph} = \epsilon\epsilon_0/\tau$ (ϵ_0 is the permittivity of the vacuum and ϵ the permittivity of the material) does not depend on the intensity of the IR light and increases linearly with the intensity of the green light. These

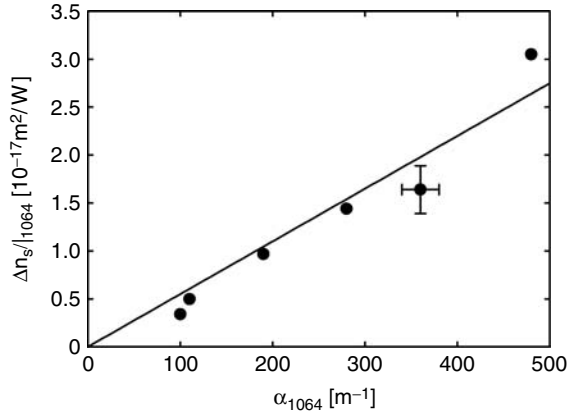

FIGURE 8.10. Saturation value Δn_s of refractive index change versus absorption coefficient α_{1064} at $\lambda = 1.064\,\mu$m. The solid line is a linear fit to the measured data.

experimental results cannot be explained by excitations via shallow traps, but are in perfect agreement with recording via pyroelectric fields [33]. We assume that the IR recording pulses impinge on the crystal before the green pulse and generate a thermal grating with the maximum amplitude [31]

$$\Delta T^{\max} = \frac{m t_p \alpha I_0}{\rho c_p}. \tag{8.15}$$

Here m denotes the modulation of the light pattern, t_p the duration of the recording pulses, α the absorption at $1.06\,\mu$m, I_0 the total intensity of the recording pulses, ρ the density, and c_p the specific heat capacity of the material. The pyroelectric effect yields the field with the amplitude [33]

$$E_{\text{pyro}}^{\max} = -\frac{1}{\epsilon\epsilon_0}\frac{\partial P_s}{\partial T}\Delta T^{\max}, \tag{8.16}$$

where $\partial P_s/\partial T$ is the pyroelectric coefficient. There is no bulk photovoltaic field, the crystal is short-circuited to rule out external fields, and diffusion can be neglected. Thus only the pyroelectric field is responsible for the build up of the space-charge field with the saturation value [33]

$$E_{sc}(t \to \infty) = m\frac{1}{\epsilon\epsilon_0}\frac{\partial P_s}{\partial T}\frac{t_p \alpha I_0}{\rho c_p}. \tag{8.17}$$

The electro-optic effect yields the refractive index change for extraordinarily polarized light

$$\Delta n_s = -\frac{1}{2} n_e^3 r_{333} m \frac{1}{\epsilon\epsilon_0}\frac{\partial P_s}{\partial T}\frac{t_p \alpha I_0}{\rho c_p}, \tag{8.18}$$

with the refractive index n_e for extraordinarily polarized probe light and the corresponding electro-optic tensor element r_{333}. Eq. (8.18) describes the observed dependences very well. The relations $\Delta n_s \propto I_0 = I_{1064}$ and $\Delta n_s \propto \alpha = \alpha_{1064}$ are in perfect agreement with the results shown in the Figs. 8.9 and 8.10. Furthermore, the value $\Delta n_s = 4.9 \times 10^{-5}$ calculated from Eq. (8.18), which has to be compared with the measured value $\Delta n_s = 1.8 \times 10^{-5}$, yields the right order of magnitude. The results clearly reveal the possibility to record holograms in $LiTaO_3$: Fe via the pyroelectric effect. This two-step process offers the opportunity to store nonvolatile holograms with light of any wavelength at which a large absorption can be achieved. In the $LiTaO_3$: Fe crystals, the absorption at 1.06 μm is caused by Fe^{2+} ions, the same dopant from which the electrons are excited to form space-charge fields. Other compositions are possible, especially for holographic recording at telecommunication wavelengths. Then a doubly-doped pyroelectric and photoconductive crystal is needed. One dopant may be, e.g., a rare earth element with high absorption at the desired recording wavelength and the other one a filled electron trap sensitive for the light generating free charge carriers by homogeneous illumination. The magnitude of the achieved refractive index change then depends on the concentration of the rare earth dopant and the recording light intensity used, whereas the time constant for recording and erasure depends on the concentration ratio of filled and empty traps.

8.6 Lifetime of the Holograms

For practical applications in, e.g., telecommunications, the lifetime of the components is a critical issue. Wavelength filters that are based on holographic gratings in photorefractive $LiNbO_3$ crystals [34, 35, 36, 37] utilize so far the method of "thermal fixing" [38]. Holograms are recorded at a higher temperature (typically 180°C) where ions are mobile. These ions migrate and compensate for the electronic space-charge field. Spatially modulated concentrations of filled and empty electron traps as well as a spatially modulated concentration of the compensating ions build up. After cooling to room temperature, the ions are practically immobile. Homogeneous illumination now generates spatially modulated currents because of the modulated densities of filled and empty electron traps. Space-charge fields and electro-optic refractive index changes arise (see [39] and references therein). After reaching a steady-state, further net charge redistribution is not possible since the ionic grating is fixed.

From accelerated aging experiments assisted by a theoretical description of the processes, it can be shown that the lifetime of thermally fixed holograms in $LiNbO_3$ can reach hundreds of years at room temperature [40]. Usually protons (H^+) form the ionic grating [39, 41]. The key to get good lifetimes is a dehydration of the $LiNbO_3$ crystals [40, 42]. Then the compensating ions are—most probably—lithium ions instead of hydrogen [42]. Since the mobility of Li^+ in $LiNbO_3$ is less than that of H^+, the lifetime of the thermally fixed gratings is

improved. By this means the telecommunication lifetime standards (Bellcore, Telecordia) can be easily fulfilled.

However, thermal fixing has two drawbacks: (1) Optical erasure and rewriting of components is not possible. For many applications, an all-optical control of the diffractive components is desirable. Just to name one example: Guiding one light beam into one of many fibers can be done by recording of a proper hologram that provides this coupling. For switching the channel into another fiber, a new hologram is required. Optical erasure of the old hologram and recording of a new hologram can provide such a reconfigurable switch. Thermally fixed holograms do not provide this flexibility. (2) Photorefractive crystals show, in general, an anisotropic thermal expansion. Thus after recording and cooling to room temperature, the Bragg condition is typically not fulfilled anymore. This can be compensated by, e.g., a change of the angle of incidence or of the wavelength of the reading light. However, this is limited to gratings only. For other waves, Bragg matching cannot be achieved by a simple modification of the reading light. Waves with so-called "wavevector spectra" might be one solution [43], but this limits the quality of the component, i.e., the focal spot of nominally spherical waves would be enlarged and the cross-talk for wavelength-division-multiplexing components would be increased. Another solution to this problem is the "low-high-low" fixing schedule where the hologram is recorded at room temperature and heated afterwards. However, for this method the obtainable refractive index changes, i.e., the diffraction efficiencies, are smaller. To summarize this point: Thermal fixing works well for applications where elementary gratings are involved but fails for more sophisticated components.

By two-step excitation processes, these problems can be overcome. Such components are optically erasable and rewritable; the recording light always fulfills the Bragg condition. However, there is one drawback: The lifetime is not as good as that of thermally fixed holograms. Recent studies reveal the mechanisms that are responsible for the erasure of unfixed holograms in $LiNbO_3$ [44, 45]. Because of the two-step recording process, reading with IR light does not erase the holograms. However, there is always a dark conductivity σ_d present that limits the hologram lifetime given by

$$\tau_{life} = (\epsilon\epsilon_0)/\sigma_d. \tag{8.19}$$

The lifetime in the dark is the same for holograms recorded by one-step or by two-step processes.

Two situations need to be distinguished: For $LiNbO_3$ crystals containing a high amount of iron or copper (typically in excess of 0.05 wt. % Fe_2O_3 or CuO), the dark conductivity is dominated by tunneling of electrons between these deep impurities [44]. Fig. 8.11a shows the dark conductivity of a $LiNbO_3$: Fe crystal where the Fe^{2+}/Fe^{3+} concentration ratio was changed by thermal annealing. As it can be seen, the dark conductivity is proportional to the effective trap density N_{eff} that is defined as $N_{eff} = (1/c_{Fe^{2+}} + 1/c_{Fe^{3+}})^{-1}$. For small Fe^{2+} concentrations $c_{Fe^{2+}}$ the number of electrons that can tunnel is given

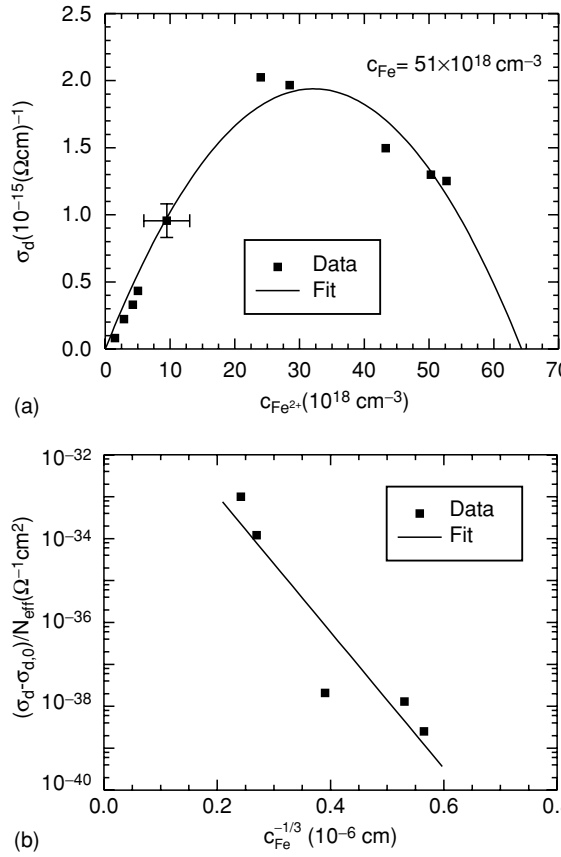

FIGURE 8.11. a) Dark conductivity σ_d versus Fe^{2+} concentration $c_{Fe^{2+}}$ of a $LiNbO_3$ sample doped with 51×10^{18} cm^{-3}Fe. The solid line shows a fit of $\sigma_d \propto N_{eff}$ to the experimental data, where N_{eff} is the effective trap density (see text) and c_{Fe} is the fit parameter. The result of the fit, $c_{Fe} \approx 65 \times 10^{18}$ cm^{-3}, agrees pretty well with the known iron concentration. b) Normalized dark conductivity σ_d versus the cubic root of the iron concentration c_{Fe} for crystals with various iron concentrations. Here $\sigma_{d,0}$ is an iron-independent background dark conductivity and N_{eff} is again the effective trap density. The solid line is a fit of conductivity $(\sigma_d - \sigma_{d,0})/N_{eff} \propto \exp(-ac_{Fe}^{-1/3})$, where a is a fit parameter.

by $c_{Fe^{2+}}$ itself while for high Fe^{2+} concentrations a lack of empty Fe sites, i.e., of Fe^{3+}, limits the tunneling and hence the dark conductivity is proportional to the density of $c_{Fe^{3+}}$. This explains the dependence $\sigma_d \propto N_{eff}$ and at the same time, shows that electron tunneling is indeed responsible for the dark conductivity. Since the tunneling probability depends exponentially on the distance between the ions, the overall iron concentration also plays an important role. As Fig. 8.11b shows, the dark conductivity (normalized to N_{eff}) indeed increases exponentially according to $\exp(-ac_{Fe}^{-1/3})$, where $c_{Fe}^{-1/3}$ is the averaged spacing

between the iron centers and a is a fit parameter. Based on this curve—for the case of iron-dominated conductivity—the dark storage time of the holograms can be deduced.

The second situation is that of a relatively low doping level. In this case, the ionic conductivity at room temperature dominates the charge transport [44, 45]. This conductivity can be reduced by dehydration of the crystal. Thus the best lifetimes are obtained in weakly doped crystals with a small H^+ content. However, weak doping implies small refractive index changes as it can be inferred, e.g., from Fig. 8.6. For realistic conditions and after optimization, hologram lifetimes at room temperature of the order of months to years can be achieved. At higher temperatures, e.g., at 50°C, lifetimes of only days or weeks are expected. This is not satisfactory for telecommunication applications. The consequence is that such components need either to be temperature stabilized or they must contain an apparatus that can rewrite or refresh the components on demand. For dynamic components, this is not necessarily a drawback since they may contain in any case a recording laser.

8.7 Advantages of Infrared Recording

For single-step volatile recording in photorefractive crystals usually ultraviolet or visible light is required. Only in a few cases is single-step recording with near-IR light possible [46]: Crystals of the sillenite type are sensitive to near-IR light, and two-step recording processes have been demonstrated in this material as well [15], but the dark storage time is not satisfactory for most applications. Semiconductor crystals like CdTe and GaAs are sensitive in the telecommunication wavelength region (1.3 to 1.6 μm), but the refractive index changes are too small since the electro-optic coefficients are tiny. Only photorefractive multiple quantum wells provide large refractive index changes for recording in the telecommunication wavelength region, but the operational wavelength range is small. In very few cases, e.g., for highly-doped $KNbO_3$ waveguides, a photorefractive response in the telecommunication region has been reported [47]. Thus two-step recording has—besides the resistance against reading with IR light—still one more substantial advantage: Devices can be fabricated with light of the wavelength where they are finally used. This is different compared to the current approach where gratings are recorded by, e.g., green light and finally read by IR light [34, 35, 36, 37]. Since volume effects are used, this approach is limited to gratings only. For other elements, Bragg matching in the IR spectral range would be impossible.

Fig. 8.12 shows that recording with IR light that has exactly the wavelength of the light used in the final device can be very helpful. A four-channel wavelength-demultiplexer (DEMUX) is depicted. In the input fiber, many wavelengths, e.g., 128 or 256, might be multiplexed. A gradient-index (GRIN) lens forms a parallel beam that passes the photorefractive material and is coupled by another GRIN lens into the throughput fiber. However, inside the photorefractive material, there are four holograms that are Bragg-

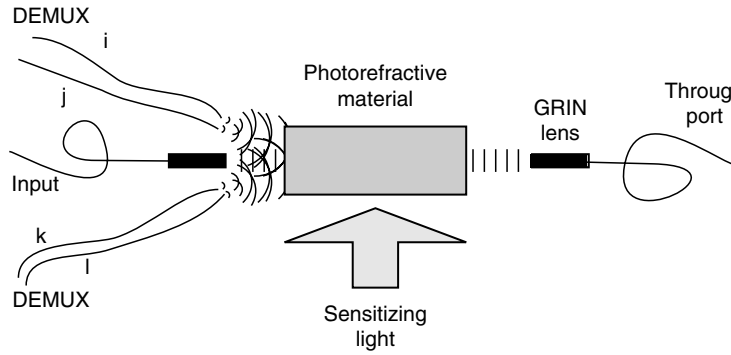

FIGURE 8.12. Filter for demultiplexing (DEMUX) of four channels ($\lambda_i, \lambda_j, \lambda_k, \lambda_l$) in a wavelength-division-multiplexing network. Only the input and the through port require gradient-index (GRIN) lenses to collimate the beam. Holograms can be multiplexed in such a way that the diffracted light is coupled into the four separate fibers without any additional optics. The required holograms can be recorded in the device itself by a two-step process if sensitizing light is present. The sensitizing light is not required for operation of the device.

matched to four of the channel wavelengths $\lambda_i, \lambda_j, \lambda_k$, and λ_l. The diffracted waves should have a spherical shape. At the focal point, a fiber end is positioned that collects the dropped light. Since the four waves are diffracted from different holograms, the focal spots can be separated and the light is coupled into four independent fibers. Compared to other devices, this approach has the advantage that no additional optics in front of these four fibers are required. This makes such a device more compact, simpler, and cheaper.

For fabrication of devices like that shown in Fig. 8.12, one problem typically appears that can be also solved by IR recording: It is the alignment issue. The hologram must not only be properly recorded, the photorefractive material and all the fibers must also be precisely positioned in order to keep the insertion loss and the drop losses small. For IR recording, this can be achieved easily: The device can be built first and after fixing the fibers, e.g., with glue, recording can be performed. Two-step writing requires the presence of sensitizing light. The IR recording light is then provided through the fibers, which ensures for the final operation perfect alignment of the hologram and of the fibers. Although this method has not been experimentally demonstrated so far, it seems to be likely that next-generation components may use this technology.

8.8 Conclusions

Many photorefractive crystals that are insensitive in the IR spectral region may be sensitized for IR recording by two-step processes. Nondestructive readout of the holograms recorded by two-step processes is possible. In contrast to other

methods for hologram stabilization, e.g., thermal fixing, the versatility of desired optical erasure is maintained. Utilization of the pyroelectric effect even promises to shift the recording wavelength to the region of the telecommunication wavelengths around 1.5 μm. The lifetime of the holograms can approach years in materials like $LiNbO_3$ if the doping level is optimized and if the crystals are dehydrated. Direct IR recording with light of the operational wavelength has two practical advantages: (1) Not only gratings, but also more sophisticated components can be fabricated. A wavelength filter that focuses the diffracted light into a fiber is one example. (2) The holograms can be recorded in the final device. This simplifies assembling and adjustment of the components.

Acknowledgements: the authors are indebted to H. Eggert, A. Gerwens, H. Hesse, L. Holtmann, J. Imbrock, F. Jermann, D. Kip, M. Müller, I. Nee, M. Simon, H. Vormann, S. Wevering, and M. Ye for valuable help and discussions. Financial support of the Deutsche Forschungsgemeinschaft and of the Volkswagen-Stiftung is gratefully acknowledged.

References

1 D. von der Linde, A.M. Glass, and K.F. Rodgers, "Multiphoton Photorefractive Processes for Optical Storage in $LiNbO_3$," Appl. Phys. Lett. **25**, 155 (1974).
2 D. von der Linde, A.M. Glass, and K.F. Rodgers, "High–Sensitivity Optical Recording in KTN by Two–Photon Absorption," Appl. Phys. Lett. **26**, 22 (1975).
3 H. Vormann and E. Krätzig, "Two Step Excitation in $LiTaO_3$:Fe for Optical Data Storage," Solid State Commun. **49**, 843 (1984).
4 Y. Ming, E. Krätzig, and R. Orlowski, "Photorefractive Effects in $LiNbO_3$:Cr Induced by Two–Step Excitation," phys. stat. sol. (a) **92**, 221 (1985).
5 A. Motes and J. J. Kim, "Intensity–Dependent Absorption Coefficient in Photorefractive $BaTiO_3$ crystals," J. Opt. Soc. Am. B **4**, 1379 (1987).
6 G.A. Brost, R.A. Motes, and J.R. Rotgé, "Intensity–Dependent Absorption and Photorefractive Effects in Barium Titanate," J. Opt. Soc. Am. B **5**, 1879 (1988).
7 L. Holtmann, "A Model for the Nonlinear Photoconductivity of $BaTiO_3$," phys. stat. sol. (a) **113**, K89 (1989).
8 L. Holtmann, K. Buse, G. Kuper, A. Groll, H. Hesse, and E. Krätzig, "Photoconductivity and Light–Induced Absorption in $KNbO_3$:Fe," Appl. Phys. A **53**, 81 (1991).
9 K. Buse and E. Krätzig, "Light–Induced Charge Transport in Photorefractive Crystals" in Photorefractive Optics: Materials, Properties and Applications, ed. by F. Yu and S. Yin. Academic Press, 2000.
10 K. Buse and E. Krätzig, "Three-Valence Charge-Transport Model for Explanation of the Photorefractive Effect," Appl. Phys. B **61**, 27 (1995).
11 K. Buse, A. Adibi, and D. Psaltis, "Non-Volatile Holographic Storage in Doubly Doped Lithium Niobate Crystals," Nature **393**, 665 (1998).
12 K. Buse, L. Holtmann, and E. Krätzig, "Activation of $BaTiO_3$ for Infrared Holographic Recording," Opt. Commun. **85**, 183 (1991).

13 A. Gerwens, M. Simon, K. Buse, and E. Krätzig, "Activation of Cerium-Doped Strontium-Barium Niobate for Infrared Holographic Recording," Opt. Commun. **135**, 347 (1997).
14 A. Kamshilin and M.P. Petrov, "Infrared Quenching of the Photoconductivity and Holographic Data Storage in $Bi_{12}SiO_{20}$," Sov. Solid State Physics **23**, 3110 (1981).
15 S.G. Odoulov, K.V. Shcherbin, and A.N. Shumeljuk, "Photorefractive Recording in BTO in the Near Infrared," J. Opt. Soc. Am. B **11**, 1780 (1994).
16 S.G. Odoulov, A.N. Shumelyuk, U. Hellwig, R.A. Rupp, A.A. Grabar, and I.M. Stoyka, "Photorefraction in Tin Hypothiodiphosphate in the Near Infrared," J. Opt. Soc. Am. B **13**, 2352 (1996).
17 P. Pogany, H.J. Eichler, and M. Hage Ali, "Two-Wave Mixing Gain Enhancement in Photorefractive CdZnTe:V by Optically Stimulated Electron-Hole Resonance," J. Opt. Soc. Am. B **15**, 2716 (1998).
18 K. Shcherbin, F. Ramaz, B. Farid, B. Briat, and H.-J. von Bardesleben, "Photoinduced Charge Transfer Processes in Photorefractive CdTe:Ge," OSA TOPS **27**, 54 (1999).
19 D. von der Linde and A.M. Glass, "Photorefractive Effects for Reversible Holographic Storage of Information," Appl. Phys. **8**, 85 (1975).
20 F. Jermann and J. Otten, "The Light-Induced Charge Transport in $LiNbO_3$: Fe at High Light Intensities," J. Opt. Soc. Am. B **10**, 2085 (1993).
21 M. Simon, F. Jermann, and E. Krätzig, "Intrinsic Photorefractive Centers in $LiNbO_3$: Fe," Appl. Phys. B **61**, 89 (1995).
22 K. Buse, F. Jermann, and E. Krätzig, "Infrared Holographic Recording in $LiNbO_3$: Cu," Appl. Phys. A **58**, 191 (1994).
23 K. Buse, F. Jermann, and E. Krätzig, "Infrared Holographic Recording in $LiNbO_3$: Fe and $LiNbO_3$: Cu," Opt. Mat. **4**, 237 (1995).
24 J. Imbrock, S. Wevering, K. Buse, and E. Krätzig, "Nonvolatile Holographic Storage in Photorefractive Lithium Tantalate Crystals with Laser Pulses," J. Opt. Soc. Am. B **16**, 1302 (1999).
25 A.M. Glass, D. von der Linde, and T.J. Negran, "High-Voltage Bulk Photovoltaic Effect and the Photorefractive Process in $LiNbO_3$," Appl. Phys. Lett. **25**, 233 (1974).
26 Y.S. Bai and R. Kachru, "Nonvolatile Holographic Storage with Two-Step Recording in Lithium Niobate Using cw Lasers," Phys. Rev. Lett. **78**, 2944 (1997).
27 H. Guenther, G. Wittmann, R.M. Macfarlane, and R.R. Neurgaonkar, "Intensity Dependence and White-Light Gating of Two-Color Photorefractive Gratings in $LiNbO_3$," Opt. Lett. **22**, 1305 (1997).
28 J. Imbrock, D. Kip, and E. Krätzig, "Nonvolatile Holographic Storage in Iron-doped Lithium Tantalate with Continuous-Wave Laser Light," Opt. Lett. **24**, 1302 (1999).
29 M. Horowitz, B. Fischer, Y. Barad, and Y. Silberberg, "Photorefractive Effect in a $BaTiO_3$ Crystal at the 1.5 μm Wavelength Regime by Two-Photon Absorption," Opt. Lett. **21**, 1120 (1996).
30 K. Oba, P.-C. Sun, and Y. Fainman, "Nonvolatile Photorefractive Spectral Holography," Opt. Lett. **23**, 915 (1998).
31 H.A. Eggert, J. Imbrock, C. Bäumer, H. Hesse, and E. Krätzig, "Infrared Holographic Recording in Lithium Tantalate Crystals via the Pyroelectric Effect," Opt. Lett. **28**, 1975 (2003).
32 K. Buse, "Thermal Gratings and Pyroelectically Produced Charge Redistribution in $BaTiO_3$ and $KNbO_3$," J. Opt. Soc. Am. B **10**, 1266 (1993).

33 K. Buse and K.H. Ringhofer, "Pyroelectric Drive for Light-Induced Charge Transport in the Photorefractive Process," Appl. Phys. A **57**, 161 (1993).
34 V. Leyva, G.A. Rakuljic, and B. O'Conner, "Narrow Bandwidth Volume Holographic Optical Filter Operating at the Kr Transition at 1547.82 nm," Appl. Phys. Lett. **65**, 1079 (1994).
35 R. Müller, M.T. Santos, L. Arizmendi, and J.M. Cabrera, "A Narrow-Band Interference Filter with Photorefractive $LiNbO_3$," J. Phys. D: Appl. Phys. **27**, 241 (1994).
36 S. Breer and K. Buse, "Wavelength Demultiplexing with Volume Phase Holograms in Photorefractive Lithium Niobate," Appl. Phys. B **66**, 339 (1998).
37 S. Breer, H. Vogt, I. Nee, and K. Buse, "Low-Crosstalk WDM by Bragg Diffraction from Thermally Fixed Reflection Holograms in Lithium Niobate," Electronics Letters **34**, 2419 (1999).
38 J. J. Amodei and D.L. Staebler, "Holographic Pattern Fixing in Electro–Optic Crystals," Appl. Phys. Lett. **18**, 540 (1971).
39 K. Buse, S. Breer, K. Peithmann, S. Kapphan, M. Gao, and E. Krätzig, "Origin of Thermal Fixing in Photorefractive Lithium Niobate Crystals," Phys. Rev. B **56**, 1225 (1997).
40 L. Arizmendi, E.M. Miguel-Sanz, and M. Carrascosa, "Lifetimes of Thermally Fixed Holograms in $LiNbO_3$: Fe Crystals," Opt. Lett. **23**, 960 (1998).
41 H. Vormann, G. Weber, S. Kapphan, and E. Krätzig, "Hydrogen as Origin of Thermal Fixing in $LiNbO_3$: Fe," Solid State Commun. **40**, 543 (1981).
42 I. Nee, K. Buse, F. Havermeyer, R.A. Rupp, M. Fally, and R.P. May, "Neutron Diffraction from Thermally Fixed Gratings in Photorefractive Lithium Niobate Crystals," Phys. Rev. B **60**, R9896 (1999).
43 H.C. Külich, "A New Approach to Read Volume Holograms at Different Wavelengths," Opt. Commun. **64**, 407 (1987).
44 I. Nee, M. Müller, K. Buse, and E. Krätzig, "Role of Iron in Lithium-Niobate Crystals for the Dark Storage Time of Holograms," J. Appl. Phys. **88**, 4282 (2000).
45 Y.P. Yang, I. Nee, K. Buse, and D. Psaltis, "Ionic and Electronic Dark Decay of Holograms in $LiNbO_3$ Crystals," Appl. Phys. Lett. **78**, 4076 (2001).
46 K. Buse, "Light-Induced Charge Transport Processes in Photorefractive Crystals II: Materials," Appl. Phys. B **64**, 391 (1997).
47 S. Brülisauer, D. Fluck, P. Günter, L. Beckers, and C. Buchal, "Photorefractive Effect in Proton-Implanted Fe-doped $KNbO_3$ Waveguides at Telecommunication Wavelengths," J. Opt. Soc. Am. B **11**, 2544 (1996).

9

Spatio-Temporal Instabilities and Self-Organization

Cornelia Denz and Philip Jander

Institut für Angewandte Physik, Westfälische Wilhelms-Universität,
Corrensstrasse 2, D-48149 Münster, Germany
http://www.uni-muenster.de/ Physik/AP/Denz
denz@uni-muenster.de

Spontaneous generation of patterns, pattern formation and complex spatio-temporal structures in nonequilibrium systems [1] are one of the most intriguing current topics in science. Spanning as diverse disciplines as biology, chemistry, sociology, economics, hydrodynamics, solid-state physics, and optics, the phenomena identified as effects of self-organization [2–5] have been actively researched for several decades. Spirals formed by chemical reactions, ripples in the sand, convection cells in a heated fluid layer are all examples of extended nonlinear systems under nonequilibrium conditions. Pattern formation can be observed in these systems if a transverse coupling correlates spatial regions and dissipation allows for the existence of attracting fixed points.

Although the microscopic nature of each of these experimental situations is completely different, the resulting effects are strikingly similar (Fig. 9.1). A homogenous state (e.g., a steady fluid layer, drying layer of paint, plane light wave) spontaneously bifurcates into an ordered state. The transverse scale of the pattern evolving is generally independent of initial and lateral boundary conditions and intrinsic microscopic scales. Instead, the properties of the spatial coupling (i.e., gradient terms and external feedback) determine the instabilities. General features such as nonlocality of the coupling can lead to long-distance correlations, resulting in preferred symmetries. An example is the prevalent hexagonal or honeycomb structure observed not only in nonlinear optics but in many other systems, e.g., Rayleigh-Bénard convection.

The aim of this contribution is to provide an introduction to transverse instabilities and pattern formation in photorefractive media. The authors would also like to present in detail the large number of different experimental configurations using photorefractive materials. As a concession to the limited space, we combine an overview of effects observed in experimental situations using photorefractive nonlinearities with an exemplary in-depth presentation of a single specific system. Finally, we introduce the current topics of pattern control, selection, and stabilization.

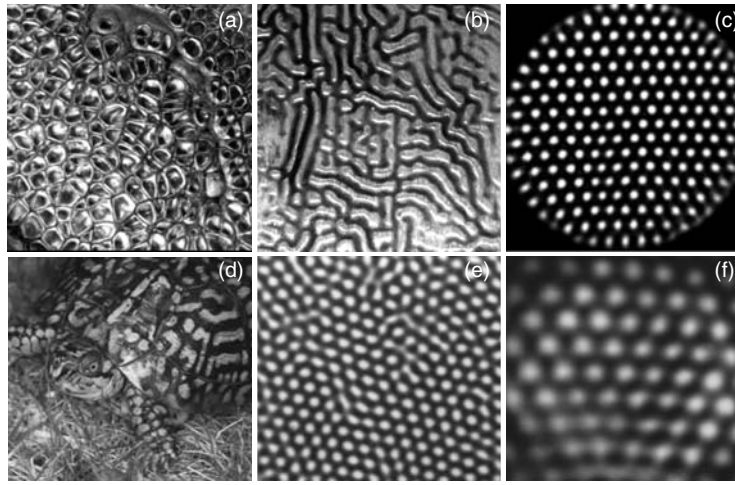

FIGURE 9.1. Examples of transverse pattern formation: (a) Bénard convenction cells [6], (b) wrinkles in dried paint [6], (c) typical hexagonal near field in an optical system (LCLV) [7], (d) patterned tortoise shell [6], (e) patterns in a chemical reactor [8], (f) hexagonal pattern in photorefractive two-wave mixing. Images courtesy of S. Camazine (a,b,d), O. Jakoby (c). H.L. Swinney (e),

9.1 Pattern Formation in Nonlinear Optics

During the last two decades, nonlinear optical materials have been proven to be excellent media for the investigation of spontaneous pattern formation [9–13]. Optical experiments allow for direct observation of amplitude and phase in the lateral plane. Furthermore, analysis of spatial frequencies contained in any pattern is easily performed using a single lens to obtain an optical Fourier transform. Controlling self-organizing phenomena is a straightforward task in optics. Light can be influenced in amplitude and phase by spatial light modulators (SLMs). Spatial frequency filtering is as convenient as local filtering, a feature distinguishing optics from every other field where self-organization is observed. Time scales of self-organizing phenomena in optics using photorefractive materials are typically in the range of tens of milliseconds up to several seconds, permitting real-time measurements of dynamics with commonly used laboratory equiment.

Since the beginning of laser physics, nonlinear optics had been largely confined to the temporal and longitudinal domain. Applications of lasers and fiber optics naturally prefer TEM_{00} modes. Additionally, many scenarios allow for neglection of the transverse derivative in the wave equation, thus working under a plane wave approximation. Therefore, transverse effects observed in the past were often considered unwanted and summed under *transverse*

perturbations. While this is still true in many applications, the success of self-organization in hydrodynamics, chemistry, and discrete systems, as well as the rising potential for applications in nonlinear optics as e.g. reconfigurable optical waveguides, has finally raised interest in similar phenomena in nonlinear optics.

In the late 1980s, transverse nonlinear optics began to grow as a discernible field of optics. Starting from the investigation of nontransverse laser dynamics, transverse effects in cavities were increasingly considered. Primary attention was given to lasers as the prototype of pattern forming system in optics [9, 10, 11]. Currently semiconductor lasers in general and vertical cavity surface emitting lasers (VCSELs) in particular are preferred systems due to their inherent large apertures, high Fresnel numbers, and their technological relevance. While the observation of pattern dynamics in lasers usually touches the limits of available image capturing equipment, an equivalence of oscillators with photorefractive gain to class A lasers can be used to provide a photorefractive model system for laser dynamics (see section 9.2.3).

Due to strong inherent instabilities, counterpropagating beams in passive nonlinear media are current prominent systems exhibiting pattern formation. Experiments are realized employing a number of different nonlinearities, such as liquid crystals [14, 15], atomic vapor [16, 17], optically addressable spatial light modulators (OASLMs or LCLVs) [7], organic films [18], and photorefractive materials [19].

9.1.1. Mechanism of a pattern forming instability

Let us adopt as an introductory example what is probably the conceptually most simple pattern forming system: A thin slab of Kerr medium with a feedback mirror and a single incident plane wave (in one transverse dimension, (Fig. 9.2). The feedback mirror creates a second counterpropagating wave.

Optical systems with counterpropagating beams can be modeled by two coupled paraxial propagation equations using the slowly varying envelope amplitude approximation (SVEA).

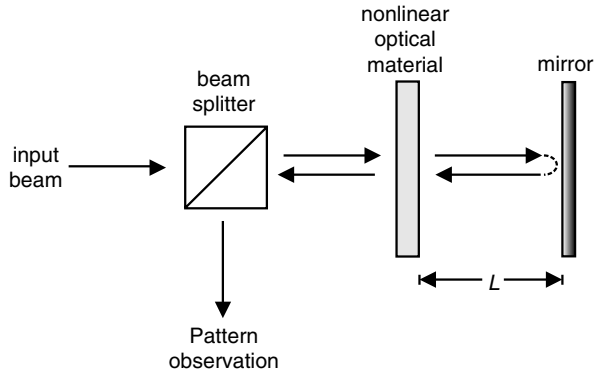

FIGURE 9.2. Schematic illustration of a thin Kerr slice with single mirror feedback.

$$\partial_z A_1 - i f \Delta_\perp A_1 = \gamma \mathcal{N}_1(A_{1,2}) \tag{9.1}$$

$$-\partial_z A_2 - i f \Delta_\perp A_2 = \gamma \mathcal{N}_2(A_{1,2}) \tag{9.2}$$

where A_i are the envelope amplitudes of the light field, e.g.,

$$E_1(\boldsymbol{r},\ t) = A_1(\boldsymbol{r},\ t) \exp(\mathrm{i}\boldsymbol{k}_1 \boldsymbol{r}) \exp(-\mathrm{i}\omega t) + \text{c.c.} \tag{9.3}$$

$\mathcal{N}$ is a nonlinear function of the fields. It is scaled by the control parameter γ. In the Kerr case considered here, $\mathcal{N}$ depends on the total intensity.

Additionally, the boundary conditions for A_1 and A_2 have to be considered. Open boundary conditions are feasible [20]; however, single mirror feedback has become a common experimental setup [21]. This is largely due to the fact that it allows — combined with a thin slice of nonlinear material—for simplification of (9.1)–(9.2). Within the thin nonlinear material, the diffraction term $\Delta_\perp A_i$ can be neglected, while for the round-trip propagation to the mirror, the nonlinearity is absent ($\mathcal{N} = 0$). Hence, the analytical and numerical treatment of the model equations is tremendously simplified. With photorefractive media, the large longitudinal extension of the nonlinear medium with respect to the diffraction length forbids this reduction, but leads to the generation of a rich variety of patterns (see section 9.3).

The initial condition for our exemplary system, before the onset of modulational instability, is completely symmetric with respect to any lateral translation. For its two-dimensional (2d) counterpart, the same would be true for rotations, as well. Any random variation in local intensity or phase will diffract and diminish during the round-trip propagation to the mirror. In Fourier space we would observe corresponding modes,

$$A(x,\ z,\ t) = a_0(z,\ t) + \sum_{k_x} a_{k_x}(z,t) \exp(ik_x x) \exp(\lambda_{k_x} t), \tag{9.4}$$

to be damped in time ($\lambda_{k_x} < 0$ for all k_x). If the nonlinearity is increased, a threshold is found where one Fourier mode becomes undamped ($\lambda_{k_x} = 0$ for a single k_c). The plane wave is now unstable with respect to a modulation corresponding to this mode. Beyond the threshold, this active mode will grow exponentially in time, from the slightest initial perturbation. Oversimplified, a local increase in intensity leads (via the Kerr effect) to the formation of a local focussing region. Hence, the beam is focused into areas where its intensity is already increased and defocused in darker regions. Diffraction leads to a coupling of neighboring areas with a preferred lateral distance corresponding to the active mode: For a given mirror distance **L**, there are several wave numbers, for which the phase modulation acquired by propagation through the Kerr slab is transformed into an in-phase intensity modulation by the linear propagation to the mirror and back (Talbot effect, [22]). Hence, the mirror distance governs the transverse wave number of the modulation growing in this scenario [23].

Continuous translational symmetry is lost as a modulation appears: only translations corresponding to the unstable mode map the light field to itself.

Therefore, the transition from a homogeneous to a modulated state is a symmetry breaking bifurcation. For one-dimensional systems, the bifurcation is usually transcritical, comparable to the bifurcation of a laser at threshold. In the language of self-organization, the nonlinearity is the control parameter of the bifurcation while the amplitude of the modulation (a_{k_x}) is an order parameter.

Passing the bifurcation point and slightly beyond, the degrees of freedom of our system are immensely reduced. We can now describe its evolution by just determining the active modes, their respective growth rates, and interactions. A linear stability analysis can be employed to find the initially unstable wave number and the range of wave numbers that are undamped at and slightly above the threshold (Fig. 9.3a). In two dimensions, this corresponds to a ring of unstable or active modes (Fig. 9.3b). If all of these modes were independent, arbitrary 2d patterns could be observed. However, unequal growth rates, nonlinear interaction of modes, and symmetries imposed by the mirror feedback limit the number of 2d patterns that can actually grow. Thus, the rotational symmetry is broken by nonlinear interaction of modes. A nonlinear stability analysis can be employed to determine the growth rates of twodimensional modes. Very often, one finds a resonant excitation of three wave vectors with equal modulus at angles of $2\pi/3$, a hexagon, to be the strongest growing 2d mode. That is also the case for many experiments using a photorefractive nonlinearity.

9.2 Overview of Pattern Formation in Photorefractive Media

In contrast to Kerr media, pattern formation in photorefractive media is based on wave mixing. Energy can be exchanged between beams, mediated by

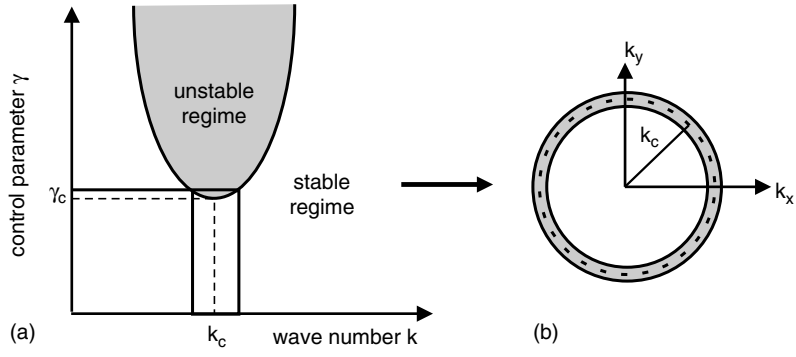

FIGURE 9.3. (a) Sketched diagram of marginal linear stability for a system displaying modulational instability. The curve of marginal stability (zero growth rate) separates the stable and unstable regime. It indicates the minimum control parameter γ_c required for any mode with wave number k to become active. The mode with minimum γ_c is the first mode (k_c) to grow exponentially when the control parameter is slowly increased. (b) Ring of active modes for the indicated value of γ slightly above the critical threshold γ_c.

refractive index gratings. The latter results from intensity modulations by interference between mixing beams.

Longitudinal boundary conditions are essential for determining the possible effects of self-organization found in a system. One observes increasing complexity with the addition of feedback boundary conditions.

In *single beam propagation*, wave propagation in time and in longitudinal direction is analogous. Beam filamentation and related optical spatial solitons, generated through nonlinear self-focusing of beams, can be observed. Since solitary beam propagation is an important part of nonlinear transverse optics, especially where photorefractive media are used, an entire chapter of this volume (Chapter 11) is devoted to that subject. For pattern formation, single beam propagation is less interesting, as no symmetric patterns are observed. Additionally, any transverse modulation can only grow exponentially in propagation direction, but not locally in time. As real media are limited in extension, the development of instabilities requires a finite seeding. Therefore, we restrict ourselves to a brief introduction to beam filamentation and present current developments in this area.

Systems with counterpropagating beams show distinct effects of self-organization and are prominent experimental scenarios for demonstration of pattern formation. Two beams are initially coupled via photorefractive two-wave mixing. The second beam can be an external pump beam or it can be obtained by means of a mirror. In both cases, feedback allows for the growth of absolute instabilities. Note that it is not necessary for the light to stay inside a cavity to enable absolute instabilities. The modulation actually grows in time in the spatial correlation of the nonlinear response (i.e., refractive index change). The light field only couples the spatial regions and drives the nonlinearity. Most of the systems considered in this contribution are of this type.

Systems with two mirror boundaries, i.e., cavities, display rich transverse nonlinear phenomena, leading from competition of few cavity modes up to complex spatio-temporal chaos. In contrast to the single counterpropagating scenario, cavities do not allow fields consisting of arbitrary plane waves. Instead, any system state is a superposition of linear cavity modes. The nonlinear interaction of these modes then becomes the basic mechanism for pattern formation.

9.2.1 Filamentation of a Single Beam

Already a single beam propagating through a photorefractive crystal can show modulational instability [24]. Thin, near one-dimensional stripe beams, as well as broad two-dimensional beams, locally self focus into equidistant spots of comparable size. As the filaments arising out of local self-focusing are of the same size as solitons, beam filamentation is generally seen as a precursor to soliton formation. Due to the anisotropic electrooptic coefficients of photorefractive media, a broad 2d beam first breaks into an array of stripe beams. However, since the stripes are also unstable with respect to filamentation, they again break up into individual spots after short propagation (Fig. 9.4).

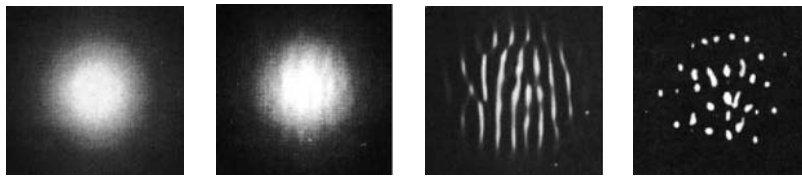

FIGURE 9.4. Numerical evolution of a radially symmetric Gaussian beam in a photorefractive SBN crystal biased with an external field. (a) At propagation length z=0, (b, c, d) z=5,15,25. The initial break-up into stripes and subsequently into small filaments due to anisotropy is clearly visible. After [24], reproduced with kind permission of Mark Saffman.

The modulation developing in the beams arises from initial noise, given a sufficiently long propagating distance. The further evolution of the filaments is dynamic and does not reach a symmetric state, as patterns in systems with feedback do.

Recently, the filamentation of incoherent beams in nonlinear media has attracted increased interest, following the observation of partially incoherent solitons in photorefractive materials. Soljacic et al. predicted a threshold for the onset of modulational instability in noninstantaneous saturable media [25]. Increasing transverse incoherence, as well as saturation, were seen to eventually take the system below that threshold. Subsequent experiments using SBN as a focusing nonlinear medium confirmed filamenting beam propagation of incoherent beams as predicted [26, 27, 28].

9.2.2 Spatial Instabilities with Two Coupled Beams

Coupling of two beams in longitudinally extended media increases the potentional complexity of modulational instability beyond filamentation. Inherent feedback appears as a result of longitudinally extended coupling between the counterpropagating beams. Therefore, the growth of instabilities is no longer limited to the longitudinal propagation of light. Instead, modulations can grow in time from practically smooth initial conditions: an absolute instability. Feedback and diffraction provide transverse coupling leading to preferred symmetries. Due to bidirectional feedback, the system needs not to reach a final steady state. Instead, dynamical behavior is possible on time scales governed by the photorefractive effect. This is in contrast to unidirectional beam propagation, where a steady state in any transverse plane (the "first" plane is the input boundary condition) ensures a steady state in "later" planes, after transient dynamics.

In this subsection, we introduce different experimental scenarios with counterpropagating beams leading to transverse modulational instabilities. Single-mirror feedback setups are the most important class of systems. Here, we give a short introduction to the history of experiments using these setup and will

return to them in more detail in Section 9.3. A couple of variations that have been investigated will be presented in the remaining part of this subsection.

Photorefractive Single Feedback Systems

The first experimental observation of pattern formation in photorefractives was reported by Honda in 1993 [19], using a nominally undoped $KNbO_3$ crystal. A second pump beam was obtained by a $BaTiO_3$ self-pumped phase conjugate mirror (Fig. 9.5a) as well as by reflection at the exit face of the crystal. In the far field, Honda reported six sidebands at an angle of about one degree around the central beam. However, the sidebands were azimuthally unstable, i.e., rotating about the pump beam such that the hexagonal structure was only observable in short time exposures. Tilting of the beams led to excitation of a stable roll (stripe) pattern instead of the hexagonal one.

Honda observed the patterns' disappearance in case of mutually incoherent pumps and hence identified two-wave mixing through photorefractive gratings as the underlying mechanism. In standard two-wave mixing, the coupling for reflection and transmission gratings was compared in $BaTiO_3$ [30], which exhibits similar phenomena. The difference of about a factor of 20 was a strong indication that pattern formation is mainly supported by reflection gratings.

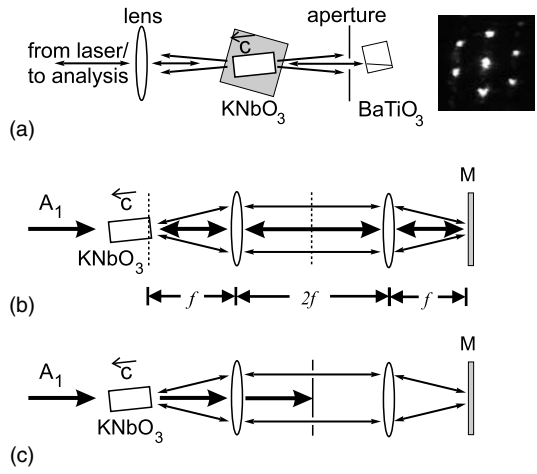

FIGURE 9.5. (a) Schematic illustration of Honda's original experiment [19] using a phase conjugate mirror and a $KNbO_3$ cyrstal in immersion oil. To the right, a typical far field hexagon is shown, as obtained from two counterpropagating waves in $KNbO_3$. (b) Standard single-mirror feedback setup as used in many experiments. The mirror is projected into a virtual mirror, in this case, located at the end of the crystal. A Fourier plane is accessible in the center of the 4f setup. (c) Setup for single-mirror feedback system without second pump beam [29]. The central beam is blocked by an annular aperture transmitting only a small band of wave vectors. (The arrows along the crystals' c-axes represent the direction of energy transfer.)

Due to the dominantly diffusive redistrubution of charge carriers in $KNbO_3$, the photorefractive nonlinearity is nonlocal in this configuration; i.e., a phase shift of $\pi/2$ between intensity modulation and resulting refractive index grating leads to pure energy coupling. The reflected beam is amplified and the original pump beam is depleted. In this context, it is interesting to note that a minimum reflection off the back surface of the crystal is sufficient to seed the backward propagating beam. Amplification by energy coupling will ensure that the beam power is sufficient to attain the same order of magnitude as the primary pump.

Following the initial reports, the dynamical behavior of the patterns became a topic of systematic investigation [31]. An additional beam was used to partially destroy the pump grating, stabilizing the orientation of the hexagonal patterns. Banerjee et al. [32, 33] reported the observed rotation of the far field to depend on the crystal tilt. For very small misalignments, a locking behaviour of the steady state is observed and the rotation ceases. Beyond that limit, the near field begins to flow in the direction corresponding to the misalignment [34, 35]. The far field starts a periodic "rock-and-roll" motion: Rotations of the hexagon are followed by rapid reorientations back to the original position.

When using a crystal face as mirror, the phase retardation $\varphi(k_x)$ for each transverse mode k_x due to linear diffraction is fixed. In the introductory example, we already noted that change of the mirror distance from the nonlinear medium is an important experimental parameter, leading to a variable phase retardation. Therefore, external mirrors are widely used in photorefractive systems, too. It has become customary to image a mirror to the desired location using a 4f assembly (Fig. 9.5b). Thereby, the projected ("virtual") mirror can be positioned within the photorefractive medium. This formally results in phase retardations corresponding to negative mirror positions, allowing for the experimental investigation of new nonhexagonal patterns and pattern multistability (Section 9.3). Also, access to a Fourier plane allows spatial frequency filtering of the feedback signal. This is exploited by Fourier control techniques (Section 9.4).

Modulational instability in two-wave mixing using a nonlocal nonlinearity was investigated theoretically by Saffman et al. [36]. A threshold condition was obtained by means of a linear stability analysis. However, a disagreement with the experimental observations was already seen by the original authors. In a subsequent analysis by Honda and Banerjee, a slightly modified approach led to improved agreement with experiments [37]. In the same letter, the authors experimentally confirmed a dependence of the transverse wave numbers on the mirror distance. For positive feedback mirror distances (i.e., well outside the crystal), a constant relation

$$2\Delta kL = \pi \tag{9.5}$$

can be found, indicating again reflection gratings [30] and relevance of the Talbot effect [22, 23] (compare Section 9.1) for pattern formation in photorefractives: this distance corresponds to an inversion of the intensity modulation for the observed wave numbers during free-space propagation.

In more recent experiments with larger photorefractive coupling, non-hexagonal patterns were observed using an external feedback mirror [35, 38 – 40]. We will focus on current results of single mirror feedback systems with $KNbO_3$ and the theoretical description in more detail in the remaining sections of this contribution. But first, we will present a number of systems related to but distinct from the type presented before.

Variations to the Theme

Two Pump Beam Coupling Without Mirror

Feedback through an external mirror is not a necessary prerequisite for pattern formation in photorefractives. Through the inherent feedback provided already by the counterpropagation of light waves, two external pump beams are sufficient to observe modulational instability. Mamaev and Saffman demonstrated this by counterpropagating two *incoherent* pump beams (derived from two separate lasers) in slightly Cerium-doped SBN:60 [41]. Obviously, reflection gratings cannot form in this scenario. Instead, the instability is now mediated by transmission gratings formed by pump beams and copropagating sidebands. The photorefractive effect is also somewhat different in this setup. Instead of diffusion dominated gratings induced by interference, an externally applied field is screened by the photorefractive space charge field. The resulting nonlinearity can be described as an anisotropic saturable Kerr nonlinearity, identical to that used for the generation in optical spatial solitons and also by Soljacic et al. for spatially incoherent single beam propagation (Section 9. 2.1). Due to anisotropy, roll patterns are stable above threshold, with their orientation fixed by the anisotropy. However, upon increasing the nonlinearity, hexagons are stabilized and no remaining sign of anisotropy in the generated pattern is observed.

In experiments with dominant reflection gratings, pattern formation is also observable without external feedback. Schwab et al. showed theoretically and experimentally the existence of transverse patterns in $KNbO_3$ for two coherent pump beams without a mirror [42]. However, one of the pump beams had to be frequency detuned with respect to the other one. Although this is not a general requirement, frequency detuning lowers the threshold for modulational instability. Microscopically, frequency detuning corresponds to a longitudinally moving reflection grating in the crystal sample and also leads to a frequency shift in the sidebands. A linear stability analysis (see Section 9.3.2) covering the case of external pump beams with frequency detuning is published in [43, 44].

Sideband Feedback Without Second Pump Beam

All counterpropagating pattern formation schemes rely on interaction of two counterpropagating pump waves. However, this is also not a strict requirement, as Lushnikov and Mamaev showed using again a single feedback system with $KNbO_3$ [29] (Fig. 9.5c). A circular band-pass aperture can be inserted in the Fourier plane in the 4f feedback setup. Thereby it is possible to block the pump beam but allow feedback of sidebands with a selectable range of wave numbers.

When the aperture permits a large range of sidebands, the resulting near and far field show speckled scattered light with complex spatio-temporal dynamics. By reducing the band pass to about the size of 3–4 far field speckles, the near field starts to develop hexagonal symmetry and the far field shows the familiar six symmetric sidebands in a steady state. In this case, the forward scattered field serves as a seed wave for the growth of a hexagonal mode. However, this mode only remains stable if most other wave numbers are forcibly suppressed by means of the aperture stop.

Materials with Local Response

Most scenarios leading to pattern formation with photorefractive materials are based on two-beam coupling via reflection gratings with a nonlocal nonlinearity; i.e., materials with dominant diffusive charge transport and hence refractive index gratings with a phase shift of about $\pi/2$ with respect to the intensity modulation are used. For the case of a local nonlinearity, a mechanism called 'mirrorless coherent oscillation' was previously known to support an absolute instability leading to spontaneous emission of two sidebands [45]. A similar mechanism was proposed to result in transverse modulational instability and hexagon formation for local photorefractive nonlinearities [46]. A threshold condition was obtained but yielded too high quantitative values and indicated the locality of the nonlinearity as a requirement for the oscillation.

Using a modified model, the same group later proposed a revised linear stability analysis for the case of local response through dominant photovoltaic fields [47]. Odoulov et al. experimentally demonstrated the generation of hexagonal patterns in $LiNbO_3$:Fe [48] with a strong photovoltaic effect. Also, the temporal development of pattern formation was considered. However, a detailed experimental analysis of the threshold was never performed for this material, probably in a large part due to the extremely long time constants. As the photorefractive coupling was decreased toward the threshold, the authors report rise times for the patterns up to one hour.

Coherent Oscillation in Materials with Nonlocal Response

With the modified analysis published in [47], the mechanism called coherent oscillation became feasible for the case of nonlocal photorefractive nonlinearites as well [49]. In fact, the semantically different approaches called transverse modulational instability in two-wave mixing [37] and mirrorless coherent oscillation as a four-wave mixing effect [47, 49] are seen to be equivalent approaches to identical effects. Hence, it is not surprising that the respective threshold conditions obtained by linear stability analyses in both approaches were found to be in good agreement.

We will revisit the linear stability analysis for the single-mirror feedback system in Section 9.3.2. For the remainder of the present section, we shall briefly look at systems where the photorefractive medium is enclosed by two mirrors: cavities.

9.2.3 *Pattern Formation in Cavities*

Using a cavity, a laser beam can be repeatedly fed back into a nonlinear medium, creating an actively oscillating system. Such a cavity with a photorefractive gain offers increased complexity of nonlinear effects [50]. Within a photorefractive oscillator, the competition between linear cavity losses and nonlinear gain coupled with diffraction provides a basic mechanism for self-organization.

The control parameter of this nonlinear system is the photorefractive gain. A threshold is found below which existing modes are only finitely amplified as cavity losses limit the growth rates. Above threshold, active modes can arise from noise. Depending on the number of modes allowed by the cavity, mode competition can lead to arbitrarily complex patterns.

Naturally, the modes in cavities are not plane waves with continuous spectra of transverse wave numbers. Rather, a discrete set of Laguerre-Gaussian and Hermite-Gaussian modes represent the basis for self-organization. The number of allowed modes depends on the Fresnel number of the cavity, which is defined as the smallest aperture in the cavity divided by resonator length and wavelength (Fig. 9.6). For low Fresnel numbers, the system dynamics are limited to a few competing modes [53]. Higher Fresnel numbers allow for complex spatio-temporal states [51, 54]. In the latter case, the system can be described based on phenomenological amplitude equations in analogy to hydrodynamical system. [1])

It can be shown that in a limit, the photorefractive oscillator is formally equivalent to class A laser systems [55]. However, the temporal dynamics of photorefractive systems are considerably slower than that of their laser counterparts. Therefore, operating with a low Fresnel number and a low number of modes, the dynamics of lasers can be modeled by photorefractive oscillators. Not surprisingly, in the investigation of these systems, some emphasis has been placed on nonlinear coupling of a few fundamental modes [56, 57, 58].

Beyond this application, resonators with photorefractive gain offer distinct characteristics, making them interesting experimental systems in themselves. Exemplarily, owing to the extremely narrow wavelength selectivity of photorefractive gratings, the gain line of photorefractive media is orders of magnitude

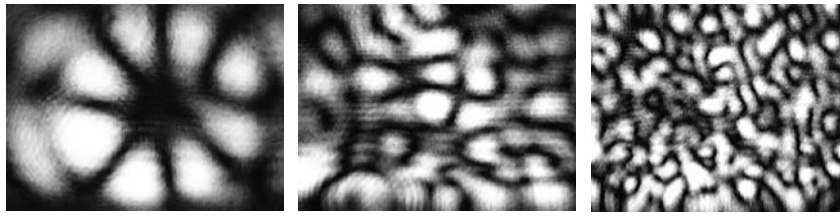

FIGURE 9.6. Transverse patterns in cavities with different Fresnel number. (a) Low fresnel number ($F \approx 3$), (b) medium Fresnel number ($F \approx 10$), (c) high Fresnel number ($F \approx 1000$) [51, 52].

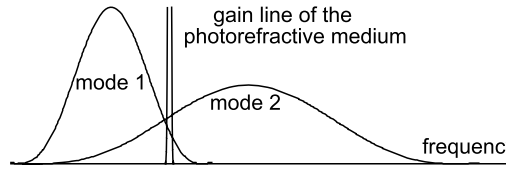

FIGURE 9.7. Illustration of mode competition and the possibility to "scan" the cavity modes with the very narrow photorefractive gain line. While the cavity modes have bandwidths in the MHz range, the gain line has less than 1 Hz. In the situation depicted here, competition between the two modes and mode beating would be observed [52].

narrower than of conventional laser gain media. As a consequence, the mode spectrum of a resonator can be accurately investigated by tuning the frequency of the pump beam (Fig. 9.7). A discussion of self-organization in a photorefractive unidirectional ring resonator can be found in a recent publication by one of us (C. Denz, [52]).

9.3 Spotlight: $KNbO_3$: Fe Single Feedback System

In this section, we will present a specific photorefractive (PR) pattern forming system in detail. We consider the single mirror feedback setup with potassium niobate ($KNbO_3$: Fe) as the photorefractive nonlinearity (Section 9.2.2). Being close to Honda's initial experiment, this configuration has received wide attention in the past. Today, it is one of the few PR systems where analytical and numerical results have been compared with detailed experimental data. Experimentally, a rich variety of stationary and nonstationary patterns is observed, including coexistence and competition of patterns with nonhexagonal symmetries.

Starting with the experimental and analytical models, the outlines and results of a linear stability analysis (LSA) are discussed in this section. In addition, a recently developed experimental verification for LSA predictions is presented. Nonlinear stability analyses are briefly outlined, discussing the implications for stability of nonhexagonal patterns. We continue with presenting selected experimental observations. A brief introduction to the numerical treatment of the model equation closes this section.

9.3.1 Experimental and Theoretical Model

A typical setup is shown in Fig. 9.8. A focused laser-beam illuminates the crystal (A_1) and interferes with its reflection (A_2) from the feedback mirror. The PR crystal is oriented to provide maximum amplification of the reflected beam via photorefractive two-wave mixing (c-axis nearly parallel propagation direction, a-axis along light polarization).

In early experiments, the feedback mirror was located directly behind the crystal (initially, Honda used a $BaTiO_3$ self pumped phase conjugate mirror

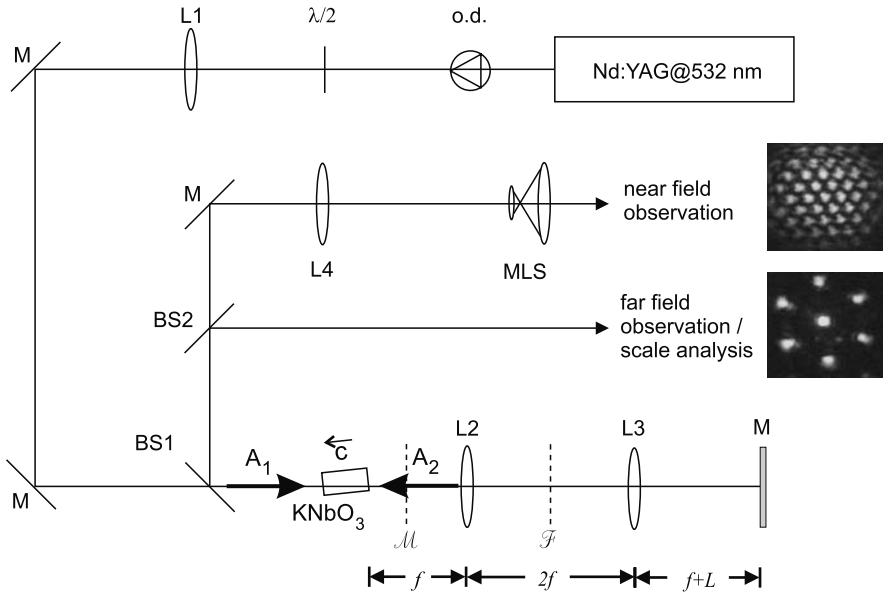

FIGURE 9.8. Experimental setup for pattern formation in counterpropagating two-wave mixing using $KNbO_3$. The crystal is oriented to provide amplification of beam A_2 and tilted by a few degrees to avoid on-axis reflections at the faces. The 4f feedback arm projects a virtual mirror ($\mathcal{M}$) at a distance L off the crystal exit face. Additionally, the Fourier plane is accessible in the feedback arm ($\mathcal{F}$). o.d.:optical diode; M: mirrors; BS: beam splitters; MLS: mircoscope lens system.

[19]). However, it is convenient to use a feedback assembly that contains a 4f projection setup. Effectively, a virtual mirror can be created in any desired location, including within the photorefractive crystal. This configuration gives access to the Fourier plane of the feedback system. This can be exploited to control pattern formation using the method of Fourier filtering (Section 9.4). Virtual mirror positions inside the crystal are required for investigation of nonhexagonal patterns (Section 9.3.4). The virtual mirror's distance L from the crystal's exit face is normalized to the length l of the crystal:

$$d = \frac{n_0 L}{l} \tag{9.6}$$

where $n_0 \approx 2.33$ is the linear refractive index for $KNbO_3$: Fe. When the virtual mirror is located at the back face of the crystal, the normalized diffraction length (or normalized feedback distance) d is equal to 0, and $d = -1$ when the virtual mirror is located at the front face of the crystal.

The strength of the nonlinearity, the photorefractive coupling γl, can be selected experimentally by rotating the polarization angle α of the pump beam using a half-wave plate ($\lambda/2$). Effectively, the b-polarization component

induces a second grating. However, the influence to both polarization components is small: coupling to the b-component is weaker by nearly an order of magnitude, due to the different electro-optic coefficients of $KNbO_3$ ($r_{113} = 10^{-11} pm/V$, $r_{223} = 0.2 r_{113}$ for light polarized along the crystal's a- and b-axis respectively [59], compare (9.14)). For the a-component, the Bragg condition is not met due to the anisotropic linear refractive index. Thus, changing the polarization influences the amplitude of the induced refractive index modulation and the photorefractive coupling:

$$\gamma l = \gamma_0 l \left(\cos^2(\alpha) + \frac{r_{223}}{r_{113}} \sin^2(\alpha) \right) \tag{9.7}$$

where $\gamma_0 l$ is the maximum possible coupling for the crystal sample.

Typical experimental conditions are a frequency doubled Nd:YAG cw laser focussed into a beam of several hundred microns waist diameter at the back face of the crystal. Incident powers on the crystal are in the range of a few to 30 mW. Crystals vary in iron dopant level and medium length. Exemplary values are 2000–5000 ppm Fe in the mold and 5–8 mm crystal length along the c-axis.

Model Equations

Consider two counterpropagating plane waves interfering in a photorefractive medium. Ignoring the vectorial nature of the electromagnetic field and assuming the same polarizations, the interference of the waves

$$E_1(\boldsymbol{r},\ t) = A_1(\boldsymbol{r},\ t) \exp(\mathrm{i}\boldsymbol{k}_1 \boldsymbol{r}) \exp(-\mathrm{i}\omega t) + \text{c.c.} \tag{9.8}$$

$$E_2(\boldsymbol{r},\ t) = A_2(\boldsymbol{r},\ t) \exp(\mathrm{i}\boldsymbol{k}_2 \boldsymbol{r}) \exp(-\mathrm{i}\omega t) + \text{c.c.} \tag{9.9}$$

results in an interference pattern

$$I(\boldsymbol{r},\ t) = |E_1 + E_2|^2 = |A_1|^2 + |A_2|^2 + A_1 A_2^* \exp(\mathrm{i}\Delta\boldsymbol{k} \cdot \boldsymbol{r}) + \text{c.c.} \tag{9.10}$$

The intensity modulation is characterized by its grating vector $\boldsymbol{K} = \Delta\boldsymbol{k} = \boldsymbol{k}_2 - \boldsymbol{k}_1$, the mean intensity $I_0 = |A_1|^2 + |A_2|^2$, and the fringe visibility $m = A_1 A_2^* / I_0 + \text{c.c.}$

In our case of frequency degenerate waves counterpropagating along the z-direction, we can rewrite (9.10) as

$$I(z,\ t) = I_0[1 + m\cos(2kz)] \tag{9.11}$$

Using the Kukhtarev model (see Chapter 3), the intensity modulation resuts in a modulation of the space charge field. Assuming a linear medium response, we can recover a space charge field, which follows the intensity modulation with a phase lag of $\pi/2$ due to the predominant diffusion in $KNbO_3$: Fe.

$$\hat{E}_{sc} = E_{sc} \sin(2kz) \tag{9.12}$$

The approximation of a linear response requires that the modulation m is small compared to 1 [60]. Due to the mirror boundary condition in our case, however, $m \approx 1$ throughout the interaction region. Nevertheless, it was shown that a constant correction factor can accomodate this mismatch [61].

Via the linear electroopic effect, the static space charge field induces a change in the refractive index:

$$\Delta n = -\frac{1}{2} n_0^3 < \mathbf{p}|\mathrm{r} \cdot \mathbf{E}_{sc}|\mathbf{p} > \tag{9.13}$$

[59] where $\mathbf{p}$ is the unit vector of light polarization and r is the electro-optic tensor of rank 3. As $\mathbf{E}_{sc}$ is parallel to the propagation direction, which is also the c-axis of the PR crystal, (9.13) reduces to

$$\Delta n = -\frac{1}{2} n_0^3 [r_{113} \cos^2 \alpha + r_{223} \sin^2 \alpha] E_{sc} \tag{9.14}$$

where α is the angle between the polarization and the crystallographic a-axis[1].

The nonlinear refractive index and the ansatz of two coupled waves are inserted into the paraxial wave equation. The final model [61, 62] consists of two coupled partial differential equations describing the propagation in the nonlinear medium

$$\partial_z A_1 - \mathrm{i} f \Delta_\perp A_1 = -Q A_2 \tag{9.15}$$

$$-\partial_z A_2 - \mathrm{i} f \Delta_\perp A_2 = Q^* A_1 \tag{9.16}$$

and the time evolution of the refractive index grating Q:

$$\tau \partial_t Q + Q = \frac{1}{2} \gamma \frac{A_1 A_2^*}{I_0 + I_d} \tag{9.17}$$

where $\gamma = k_0 L / n_0 \, \hat{\Delta} n$ is proportional to the largest attainable refractive index change, I_d is the dark intensity (typically several orders of magnitude smaller than the laser intensity), and $f = L/2k_0 w_0^2$ collects the scaling of spatial coordinates (L: crystal length, k_0: wave number of the pump waves, w_0: transverse beam waist). Note that the material response does not depend on total intensities but only on the ratio of the pump beams. However, the dynamics can still be influenced by the total intensity, as the photorefractive time constant τ decreases with increasing intensity.

For characterization and analysis of the patterns generated, the wave numbers and symmetries of a modulation developing in the pump beams are primary observables. The former can be compared with wave numbers of unstable modes obtained by linear stability analysis.

---

[1] Strictly speaking, for $KNbO_3$, one should distinguish the refractive indices along the a- and b-axes. However, their difference is minute and hence usually neglected at this point.

9.3.2 Linear Stability Analysis and Experimental Verification

A linear stability analysis yields the threshold of marginal stability of the plane wave solution against growth of transverse modulations. For simplicity we consider the model (9.15–9.17) in one transverse dimension:

$$\mathrm{i}f\Delta_{\perp}A_i \rightarrow \mathrm{i}f\partial_x^2 A_i \tag{9.18}$$

A plane wave ansatz (Fig. 9.9) with a weak single mode transverse perturbation is assumed:

$$A_n = A_{n,p}[1 + a_{n+}(x)\exp(\mathrm{i}k_x x + \Lambda t) + a_{n-}(x)\exp(-\mathrm{i}k_x x + \Lambda t)], \tag{9.19}$$

with $n = 1,\ 2$, dropping terms quadratical in $a_{n\pm}$. Here, $A_{1,2}$ are the counterpropagating envelope amplitudes; k_x is the wave number of the transverse modulation, and x is the transverse direction. The corresponding boundary conditions are open at the input face of the crystal ($z = 0$) and a mirror in a distance d (9.6) from the $z = l$ face.

$$a_{1\pm}(x,\ z = 0,\ t) = 0 \tag{9.20}$$

$$a_{2\pm}(x,\ z = l,\ t) = -\sqrt{R}\mathcal{F}^{\mathrm{I}}\{\exp[i\varphi_d]\mathcal{F}\{a_{1\pm}(x,\ z = l,\ t)\}\} \tag{9.21}$$

$\mathcal{F}$ and $\mathcal{F}^{\mathrm{I}}$ are forward and backward Fourier transforms and R is the mirror reflectivity. ϕ_d is the phase lag introduced by the round trip to the mirror and back

$$\phi_d = k_d l d;\ k_d = \frac{k_x^2}{2k_0 n_0} \tag{9.22}$$

and can be easily derived by integrating the free space propagation equation. Here, k_d is a normalized transverse wave number (but with a square relation to k_x), n_0 is again the refractive index of the medium ($n_0 \approx 2.33$ for $KNbO_3$: Fe), Λ in (9.19) is the complex growth rate of the considered transverse mode,

$$\Lambda = \lambda + \mathrm{i}\delta. \tag{9.23}$$

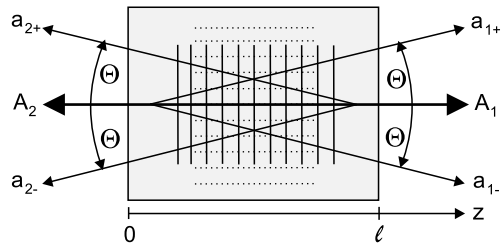

FIGURE 9.9. Schematic interaction geometry for linear stability analysis. Counterpropagation of two plane waves ($A_{1,p},\ A_{2,p}$) and 4 weak sidebands at angles Θ. A sideband emitted at angle Θ corresponds to a modulation with transverse wave number $k_x \approx \Theta k_0$, where k_0 is the wave number of the pump beam.

In the following, we restrict ourselves to nonoscillating modes ($\delta = 0$)[2]. The real part of the growth rate λ determines whether the unperturbed plane wave solution is stable:

for $\lambda < 0$, the unperturbed solution is stable

for $\lambda > 0$, the unperturbed solution is unstable

for $\lambda = 0$, we find neutral or marginal stability.

As we are interested in determining the threshold of instability, we set $\Lambda = 0$. After some calculation, we can obtain [37, 44, 61, 63] a threshold condition connecting the control parameter γl, feedback distance d and modulation wave number $k_d l$:

$$\cos \chi l \cos k_d l + \frac{k_d l}{\chi l} \sin \chi l \sin k_d l + \frac{\gamma l}{2\chi l} \{ \sin \chi l \cos (k_d l(1 + 2d)) \} = 0 \quad (9.24)$$

with $\chi l = \sqrt{(k_d l)^2 - \frac{(\gamma l)^2}{4}}$.

Discussion of linear stability analysis Results

The condition for marginal stability (9.24) is evaluated numerically. Fig. 9.10a displays a curve of marginal stability typical for this system. In contrast to experiments using thin media, we do not necessarily observe separate balloons of unstable regions. Instead, given a sufficiently high control parameter, broad bands (in the case shown a single band) of unstable modes are found.

Generally, results of linear stability analyses should only be considered close to the first threshold (denoted "I" in Fig. 9.10a). However, experiments show

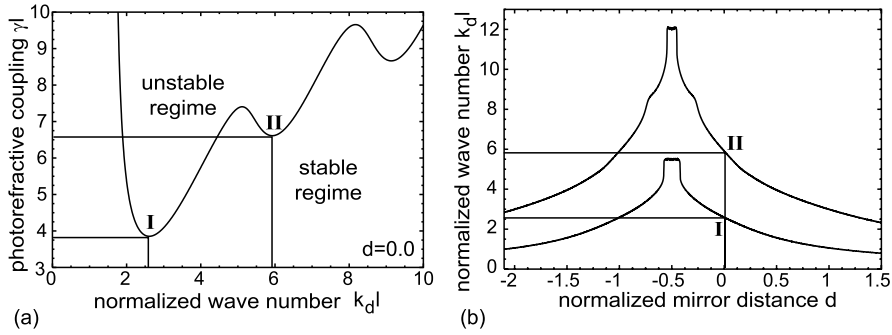

FIGURE 9.10. Numerical evaluation of the threshold condition (24): (a) Marginal stability curve for feedback distance $d = 0$. For each mode $k_d l$, the minimum control parameter value γl is determined, where the plane wave becomes unstable with respect to this mode. (b) Evolution of the modes with minimum γl for different mirror positions d. The first (I) and second (II) minimum from (a) are marked in both plots. A comparable plot (not shown) can be created tracking the control parameter values of the minima.

[2] Nonoscillating modes were considered in the initial linear stability analyses for this system [36, 37]. A recent expansion includes oscillating modes that are important for the analysis of open boundary conditions [43, 44, 63].

that even when driving the system far above threshold, the principal modes' wave numbers do not change appreciably. Hence, the evolution of the minima (I, II) is of special interest. Fig. 9.10b plots the change of the wave numbers of the first two minimas, as the feedback mirror is moved. Note that according to (9.6), feedback distances $-1 < d < 0$ correspond to virtual mirror positions within the photorefractive crystal.

The wave numbers can be converted into an angular sideband separation. As this corresponds directly to the lateral size of the far-field pattern, experimental data concerning this quantity had been published earlier [30, 38, 40]. A good agreement for virtual mirror locations outside of the crystal has been confirmed. For mirror positions around $d = -0.5$, a disagreement between observed pattern size and LSA prediction had been reported [38].

Experimental Stability Analysis

A recently developed technique [64] for directly measuring the curves of marginal stability in nonlinear optical systems in general was employed by us to investigate this disagreement: A mask permitting only transmission of pump beams and a single sideband pair is inserted in the feedback assembly's Fourier plane. Subsequently, the photorefractive coupling is increased slowly until onset of modulational instability is observed. Scanning all available wave numbers and all available mirror feedback distances, the complete threshold curves are determined. Being very close to the analytical version, this procedure is an experimental stability analysis.

Figure 9.11a gives exemplary results of this procedure O. Kamps, Ph. Jander, C. Denz, ''Instability threshold of a photorefractive pattern-forming system'', Phys. Rev. E 72 (2005) 016215. Qualitatively, the shape of the curves of marginal stability was confirmed. However, a significant disagreement in the values of photorefractive coupling was observed. Given the maximum PR coupling available from the PR crystal, many of the modes detected should not have been accessible. Wave numbers of modes corresponding to minima of the threshold and their dependence on the mirror position are shown in Fig. 9.11b. For mirror positions within the nonlinear medium, a significant deviation is observed, in complete agreement with earlier reports based on the transverse size of rolls and hexagons in the free-running system [38].

The discrepancies found are presently unclear and therefore are topics of ongoing research. They are actually further investigated with respect to their consequences for the observation of non-hexagonal patterns in this system.

Beyond the initial wave numbers, the evolution of the full 2d pattern is still a challenge to theory and numerics. As we will see in Section 9.3.4, the single feedback system with $KNbO_3$: Fe supports a rich variety of basic and composite patterns. At the time of writing, numerical treatment of this problem (Section 9.3.5) is still not able to yield sufficient 1d data for investigating the experimental data reported in this section. Two-dimensional simulations are computationally expensive and suffer the same convergence problems as 1d numerics.

Therefore, the only theoretical access to 2d pattern formation is the nonlinear analysis of the bifurcation.

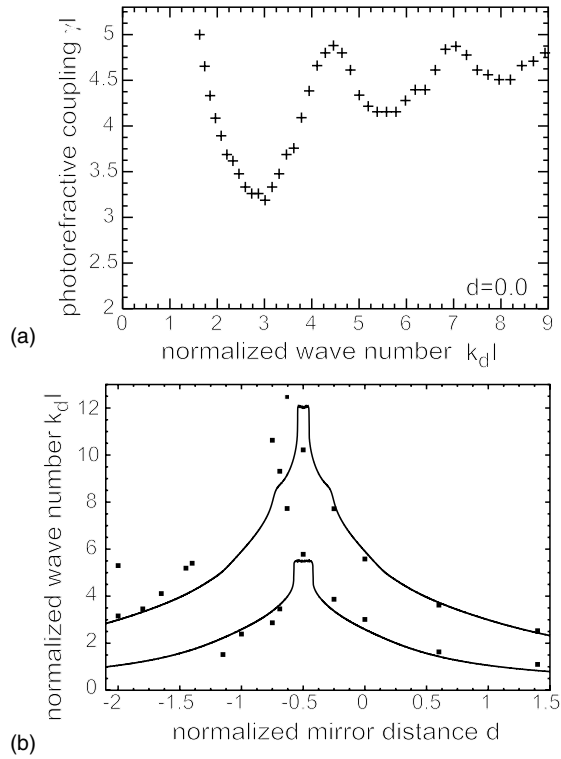

FIGURE 9.11. (a) Experimental stability analysis for $d = 0$. Qualitative agreement of the shape of the LSA curves (Fig. 9.10a) and the minimas' wave numbers is visible. The control parameter values disagree significantly. (b) Wave numbers of threshold minima vs. mirror distance. For virtual mirror positions within the PR crystal, a significant disagreement is observed. Figures courtesy of O. Kamps.

9.3.3 *Nonlinear Stability Analysis*

Performing a nonlinear analysis, it is possible to attain more insight to the evolution of the two-dimensional patterns beyond the initial threshold. A nonlinear analysis takes into account interactions between the weak sidebands neglected in the linear stability analysis, which determine the final two-dimensional pattern. For analyzing the evolution of two-dimension modes, one first needs to select the relevant wave vectors, whose interaction is to be examined. Unfortunately, selection of these basic modes is a manual task and essentially guesswork. An initial nonlinear analysis by Lushnikov [65] concentrated on three primary modes with intermode azimuthal angles of $2 \cdot \pi/3$ and degenerate wave numbers. As for each wave vector $\boldsymbol{k}_\perp$, a conjugate wave $-\boldsymbol{k}_\perp$ exists, the stability of hexagons vs. roll patterns and the unperturbed solution can be

analyzed using this approach. One obtains a set of three order parameter equations of the Ginzburg-Landau type

$$\partial_t A_i = \nu_0 A_i + \mu A_j^* A_k^* - [g_0|A_i|^2 + 2g_{\pi/3}(|A_j|^2 + |A_k|^2)]A_i \tag{9.25}$$

where $i, j, k = 1, 2, 3$. The first term describes the linear instability of the mode A_i. It is proportional to the distance $\gamma - \gamma_{th}$ from the threshold. The second term corresponds to a geometrical interaction of the modes and supports an explosive resonant excitation of hexagonal patterns that is saturated by the generation of higher harmonics by four-wave mixing (third term). This kind of order parameter or amplitude equation is common to many systems developing hexagonal patterns [1]. Essentially, all specifics of a given system are contained in the coefficients for the individual terms.

The resonant excitation and generation of higher harmonics is sketched in Fig. 9.12. Higher harmonics can be generated by wave mixing of the basic modes (corresponding to geometric addition of their wave vectors in the Fourier plane), e.g., $2\boldsymbol{k}_1$ (with modulus $2k_0$), $\boldsymbol{k}_1 - \boldsymbol{k}_2$ (with modulus $\sqrt{3}k_0$), etc. A special case is $\boldsymbol{k}_i + \boldsymbol{k}_j$, which results in $-\boldsymbol{k}_k$. Here the mixing of two modes is in resonance with the third mode, leading to the characteristic explosive instability of hexagon solutions.

Eqs. (9.25) have four pure classes of stationary solutions: The homogenous state ($A_i = A_j = A_k = 0$), roll or stripe solutions ($A_i \neq 0,\ A_j = A_k = 0$), and positive and negative hexagonal solutions, depending on the relative phases of the three modes. From the resonant second-order term, one can already infer the stability of hexagonal solutions over rolls above the threshold. In fact, for other systems described by (9.25), a potential minimum for hexagonal solutions can be shown (e.g., Bénard instability, [2]).

Lushnikov determined the coefficients for the photorefractive $KNbO_3$ nonlinearity with external feedback mirror in [65]; the corresponding bifurcation diagram is shown in Fig. 9.13. Negative hexagons bifurcate subcritically and

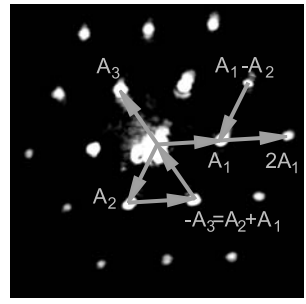

FIGURE 9.12. Two-dimensional hexagon composed of three basic wave vectors with degenerate modulus ($A_1,\ A_2,\ A_3$). Two examples of higher harmonics are highlighted: 2^*A_1 and $A_1 - A_2$. Note the condition for mutual resonant excitation of all three wave vectors is only available in hexagonal arrangement: $A_1 + A_2 + A_3 = 0$.

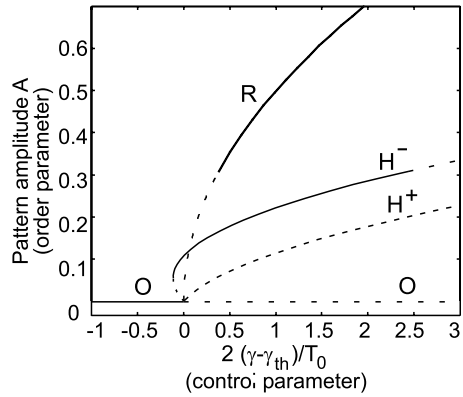

FIGURE 9.13. Bifurcation diagram for three mode patterns. After an initial subcritical bifurcation, negative hexagons are stable. Around the bifurcation, single roll patterns are relatively unstable but can coexist and finally become the only stable solution for higher control parameter values.

are stable above threshold. Only for very high order parameter values, they lose stability to roll patterns. Coexistence of stable roll and hexagon solutions is known to be connected with penta-hepta defects in hexagonal structures [66], which are readily observable in experiment. Subcritical bifurcation of hexagons has been experimentally verified and interpreted as a first-order optical phase transition [67].

Taking into account only three transverse modes at fixed angles, the initial nonlinear analysis was unable to make predictions about the stability of experimentally observed squares and dodecagonal patterns (see Section 9.3.4). Sandfuchs et al. generalized the analysis to include 6 fundamental modes, thus supporting all named classes of patterns [68]. The subcritical bifurcation of hexagons was reproduced. Squares and dodecagons were shown to be stable far above threshold for a mirror distance of $d = 0$, but this has not yet been confirmed experimentally. The required nonlinearity is still too high for currently available crystal samples. In the parameter ranges where squares and dodecagons were observed in experiment, no nonlinear stability analysis has been executed to our knowledge.

9.3.4 Experimental Observations: Multiple Pattern Region

The typical pattern in the single-mirror feedback system with $KNbO_3$ as photorefractive nonlinearity is the hexagonal pattern (Fig. 9.14). The corresponding far field shows six primary sidebands and several higher harmonics. Many experimental observations for this system have already been described in Section 9.2.2 of this contribution. Here we would like to concentrate on the observation of nonhexagonal patterns for a small parameter range of the virtual mirror

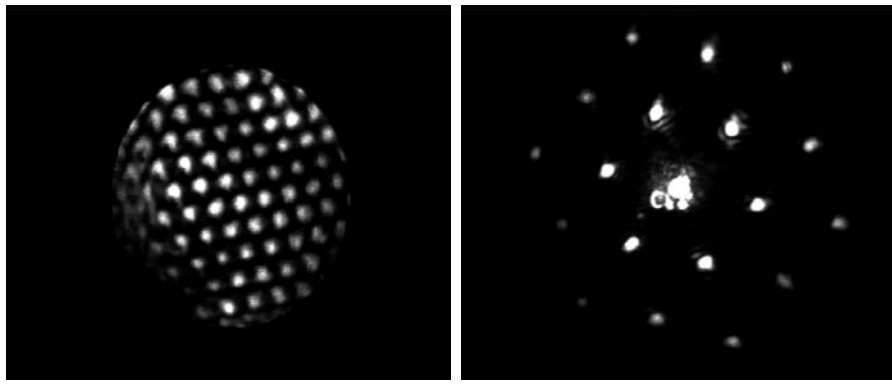

FIGURE 9.14. (a) Typical hexagonal honeycomb structure in the near field. The beam leaving the crystal is imaged in the input face plane. Beam diameter approx. 350 μm. (b) Far field, Fourier transform of (a). The far field pattern is primarily observed as it shows the wave vectors contrubuting to the pattern. Angle between central beam and primary sidebands here approx. 0.8 degree.

position, as the available variety of nonhexagons is a unique characteristic of single-mirror feedback systems with a photorefractive nonlinearity.

Patterns with hexagonal symmetry are observed for normalized feedback mirror distances $d < -0.8$ and $d > -0.3$ for any photorefractive coupling above the threshold, i.e., for all virtual mirror positions far enough away from the crystal center. With the range $-0.8 < d < -0.3$, multiple types of non-hexagonal patterns are observed.

"Squeezed hexagonal" patterns (Fig. 9.15b), which consist of three modes with two distinct wave numbers, are dominantly observed. In contrast to experiments with noncollinear pump beams (Section 9.2.2, [34]), this pattern can be observed with different azimuthal orientation. Hence, symmetry breaking by misalignment can be ruled out. It is interesting to note that the two wave numbers present in this pattern lie on different branches of wave number development (see. Fig. 9.11b). Observed at about $d = -0.7$, the two inner spots correspond to the lower left-hand branch, increasing toward the crystal center while the four outer spots have wave numbers on the lower right hand branch, which features increasing wave numbers through the crystal center. Indeed, changing the mirror position d leads to wave number changes in the squeezed hexagon corresponding closely to these branches' evolution.

Less commonly, one can observe patterns with 12-fold symmetry (Fig. 9.15d, upper row). This class is only observed immediately after the onset of modulational instability. There are two kinds of this "dodecagonal" pattern that can be distinguished by observing the near field. The common type has a near field consisting of two hexagonal domains rotated by 30 degrees and separated by a line of penta-hepta defects. The second, rarer type shows a quasicrystalline near

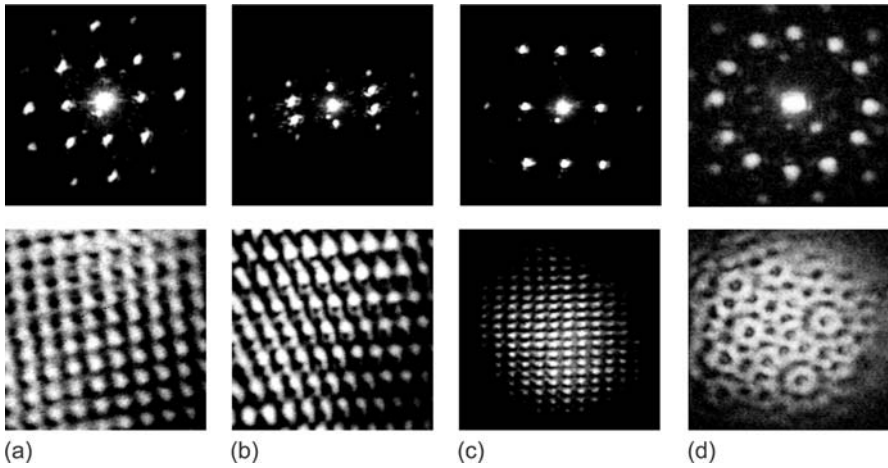

FIGURE 9.15. Pure patterns observed in the *multiple pattern region*. (a) Square pattern, (b) squeezed patern, (c) rectangular pattern, (d) dodecagonal pattern. Upper row: Far field; lower row: Typical near field pattern.

field (Fig. 9.15d, lower row). The latter kind of patterns are well known as quasipatterns in experiments with sodium vapor [69].

The second prominent pattern class are "square" patterns (which are in fact sometimes closer to parallelograms, Fig. 9.15a,c). They exist for mirror positions $-0.7 < d < -0.3$ and can coexist and compete with simultaneously excited hexagons (Fig. 9.16h) and squeezed hexagons. When competing, two patterns will usually share a single roll component.

Other combinations of competing and coexisting patterns are shown in Fig. 9.16(a–g). Some can obviously be composed into basic patterns, however, in many cases, the underlying patterns no longer can be recognized.

Due to the rich variety of patterns observable in a small parameter range, this region of normalized feedback distances $-0.8 < d < -0.3$ has been called *multiple pattern region* [40]. For most virtual mirror positions within this region, more than one pattern type is accessible in experiment. The probability for each pattern to be generated after an experiment is switched on shows a strong dependence of the mirror position d, with overlapping nonzero probabilities for different patterns. If two patterns have about equal probability, very often, switching between one type and the other can be observed on a long time scale (tens of seconds to minutes vs. 1–5 seconds for initial pattern build-up) [44]. In between periods of coexistence can be in the range of 30 seconds.

As the existence of nonhexagonal patterns has only been hinted at by theory, but no stability analyses comparable to experimental scenarios are available at present, a numerical investigation of the model (15–17) could lead to further insight.

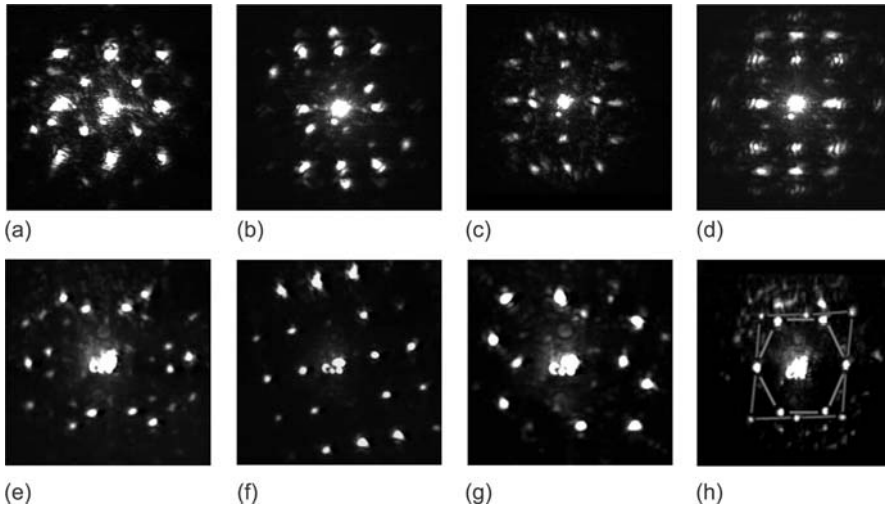

FIGURE 9.16. Complex patterns observed in the *multiple pattern region*. (a) Two square patterns rotated by 45 degrees such that higher harmonics of the interior pattern conincide with the exterior's fundamental wave numbers, (b) two rectangular patterns rotated such that they can share one component wave vector, (c) two rectangular patterns rotated by 90 degree, (d) square and rectangular patterns, (e) complex coexistence of several rolls without obvious decomposition into basic patterns, (f) square pattern missing two fundamental spots while their wave vector is still present in the total pattern, (g) complicated pattern, consisting of an elongated hexagon with 2 extra rolls, (h) competing hexagonal and square pattern. While both patterns share a common wave vector, state (h) falls into one of its component state after about 10 seconds. Note that this is considerably longer than the average build-up time of a pattern.

9.3.5 *Numerical Treatment*

In contrast to many other optical nonlinear pattern formation setups, the photorefractive medium is not a thin slice, but a bulk medium. Thereby, the numerical treatment is considerably complicated. Recall (9.1):

$$\partial_z A_1 - \mathrm{i} f \Delta_\perp A_1 = \gamma \mathcal{N}_1(A_{1,2}). \tag{9.26}$$

For the thin Kerr medium considered in Section 9.1, diffraction could be neglected within the medium while no nonlinearity was present outside of the medium. Therefore, Eq. (9.1) could be separated into a nonlinear part and a linear part, which can both be readily solved, even with a full 3d model (in which the nonlinearity is essentially only a 2d plane). This separation is impossible with photorefractive media. The medium length required for any appreciable reflection grating is such that the diffraction during propagation cannot be neglected.

As the propagation part is solved in Fourier space, while the nonlinear term is only treatable in real space, every propagation step requires two Fourier transforms. For each step, the propagation part is solved independently and a nonlinear correction is applied. This procedure is known as split step beam propagation method [68]. Concurrent beam propagation in a fixed material is iterated within a relaxation procedure until convergence. This is again contained in a loop for the temporal evolution of the material (9.17). Especially for full (2+1+time)d treatment of the problem, this procedure [61] is computationally highly expensive.

Fig. 9.17 shows the A_2 (back-propagating) component. The temporal development starts with an unperturbed plane wave solution. The increase in power due to energy exchange with the incident pump A_1 is clearly visible. A transverse modulation develops within a time corresponding to 4 seconds. The transverse modulation of the second pump (not shown) has a phase shift of π.

Using the numerical procedure described here, Sandfuchs [61] investigated the threshold and the transverse wave numbers of modulational instability for different mirror distances with one-dimensional numerics (Fig. 9.18). The resulting wave numbers are in agreement with both the linear stability analysis and experimental data. For the multiple pattern region, where a strong disagreement between experiment and theory was found, the model was not solved numerically due to strong divergences. The comparison of numerical with linear stability analysis and experimental data in this highly interesting parameter region still remains an open task. Further theoretical understanding is crucial, especially for the employment of this system as a model for the investigation of control techniques in extended nonlinear systems.

9.4 Controlling Pattern Formation

The key to any application of pattern formation is its control. External control of self-organization enables the experimenter to choose any state out of multiple existing solutions. Accessing data storage or processing capabilities of nonlinear systems requires the ability to address and stabilize any desired

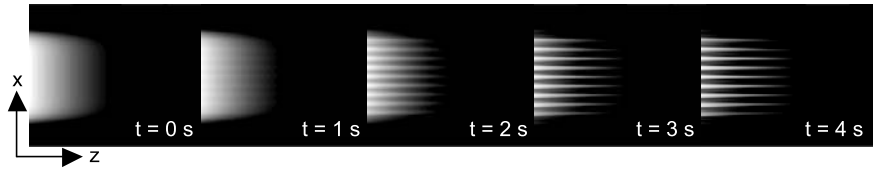

FIGURE 9.17. Numerical simulation of the model equations 15–17 (A_2 component is depicted). The mirror is to the right of each time frame, such that the beam propagates to the left.

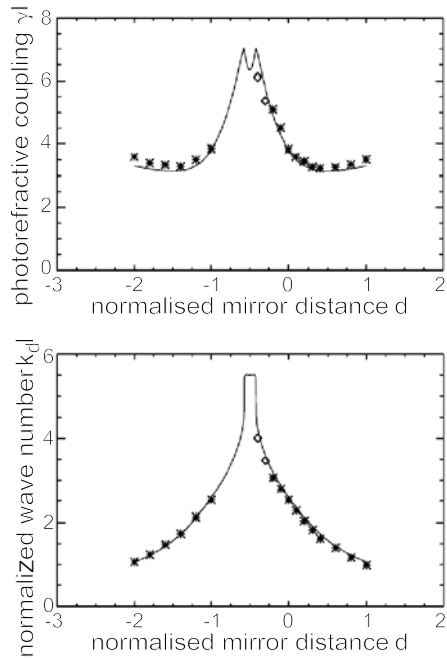

FIGURE 9.18. Threshold value and wave number derived from numerical solution of 1d model equations (15–17). Crosses represent stationary, open marks oscillating thresholds. Due to divergences, no data could be obtained for the multiple pattern region. Reproduced from [61] with kind permission of Oliver Sandfuchs.

solution, preferably without changing the physical system and its spectrum of solutions (noninvasive control).

The aim of controlling pattern formation is to select and stabilize solutions of the system that are relatively unstable with respect to another solution. This could mean stabilizing the homogeneous solution, thus suppressing undesired modulational instability. However, specific pattern states could also be exploited as basic units of self-organizing data storage or processing devices. Pattern formation in photorefractives offers unique properties for the investigation of control schemes in transversely extended optical systems.

Control of nonlinear systems started with the pioneering work by Ott, Grebogi, and Yorke, who proposed stabilization of unstable orbits in chaotic systems by application of small well-chosen perturbations [70]. As choosing the control signal requires knowledge of the systems' phase space, its direct application to many optical systems is difficult. Pyragas proposed continous driving with small perturbations derived from a measurable system quantity [71], where prior analytical knowledge of the system is unnecessary (delayed feedback method). Following the technologically highly relevant suppression of spatio-temporal dynamics in lasers [72], spatial control of patterns has now been

established as a essential branch of transverse nonlinear optics, including the systems presented in this contribution [73].

With the ability to manipulate a system in real time in the Fourier plane without any computational effort, Fourier control is a prominent control method in optical systems [73 – 79].

In the single-mirror feedback system using $KNbO_3$ as nonlinearity, several control schemes have been implemented and analyzed. Besides few experiments considering control in local space [80], control was primarily performed using masks in the Fourier plane of the feedback arm [76, 81]. A binary mask changes the system by strongly inhibiting the feedback-blocked modes. Forcing a desired solution changes the underlying system appreciably, therefore noninvasive control methods are desirable [82, 83]. A minimally invasive Fourier control mechanism was investigated in [84]. In this scheme (Fig. 9.19), the feedback arm is replaced by a Michelson interferometer, which offers two Fourier planes. A part of the intensity is reflected into the second arm, where it passes an arbitrary mask in the Fourier plane. The central pump beam is blocked in the "control arm," to avoid interferences with the main pattern arm. By adjusting the relative phase of the two Michelson arms, both positive and negative feedback can be generated. In the latter case, a minimally invasive Fourier control scheme has been realized.

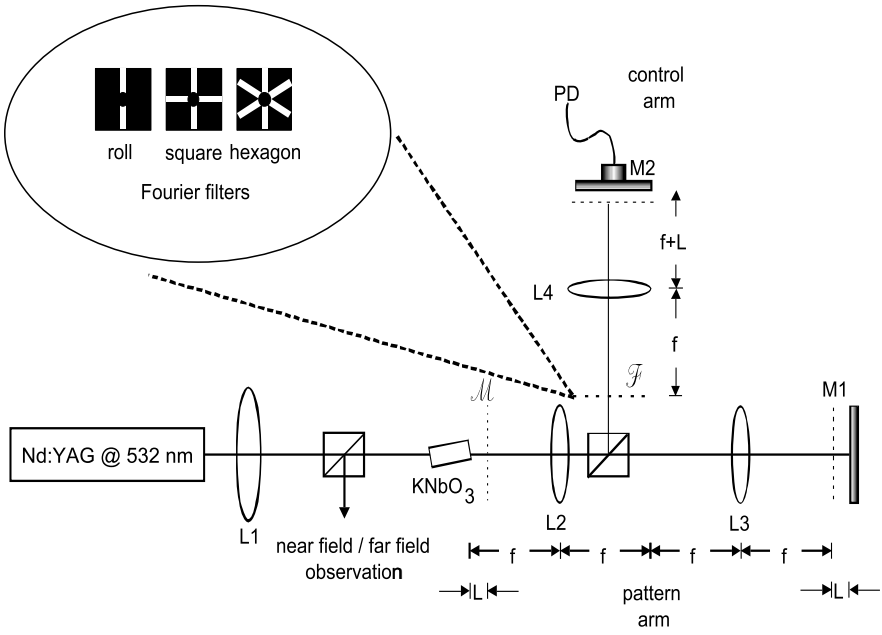

FIGURE 9.19. Experimental setup for Fourier control. M mirrors, L Feedback distance, $\mathcal{M}$ virtual mirror plane, $\mathcal{F}$ Fourier plane for filters. Inset: Different Fourier filters permitting roll square and hexagonal modes without central pump beam.

Positive feedback leads to preference of modes passing through the Fourier mask. Thereby, it is possible to stabilize patterns with a preferred orientation and symmetry (Fig. 9.20a). While the control signal does not vanish upon reaching the desired state, still a significant improvement over invasive control schemes is reached. For the experiments reported in [84], the intensity in the additional control arm was only 5% of that in the total pattern arm. Therefore, the basic pattern forming system can be considered essentially unaltered.

Negative control is obtained by adjusting the relative phase between the two Michelson arms to obtain destructive interference between the sideband signals. Hence, any modes passing through the mask are damped. This scheme has been used to control the orientation of hexagons by inhibition of undesired states (Fig. 9.20b). In the case of negative feedback, minimally invasive control is achieved. The control signal (corresponding directly to the undesired system state), vanishes as the hexagon assumes the target orientation. However, noise inherent in this system always causes a small control signal.

To test the efficiency, negative Michelson Fourier control has been modeled using a slow cubic nonlinearity. In a configuration comparable to this experimental scenario, the remaining control signal was seen to be below 0.4% of the total power in the feedback arm [84].

Fourier control is a simple yet effective method for manipulating, selecting, and stabilizing patterns in nonlinear optical systems. By using the minimally invasive scheme with Michelson geometery outlined in this section, unstable solutions can be targeted and stabilized without changing the system and its spectrum of solutions. By tracking relatively unstable states, Fourier control has been used to investigate the spectrum of solutions and their respective growth rates (Section 9.3.2). The possibility for control of pattern formation in the Fourier plane practically is an exclusive realm of optics. Hence, systems using a photorefractive nonlinearity are excellent objects of study to investigate general aspects of pattern control with implications far beyond optics.

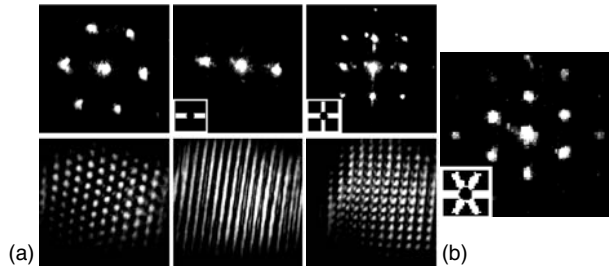

FIGURE 9.20. Patterns observed under Fourier control (Michelson scheme). (a) Positive feedback, left: Hexagonal far and near field without control; center: Reduction to roll pattern by using a slit mask; right: Stabilization of square pattern. (b) Selection of azimuthal orientation by negative feedback. Original hexagon was rotated by 30 degrees and destabilized by out-of-phase feedback. [84]

9.5 Summary and Outlook

In this contribution, we discussed the concept of modulational instability and self-organization for beam propagation in photorefractive media. Nonlinear optics and photorefractive systems in particular offer several distinct advantages for investigating general pattern forming behaviour. An essential feature is the easy observation and manipulation of the system state in the transverse Fourier plane. We combined a brief overview of instability with a more detailed presentation of a specific system.

Filamentation is the basic form of an instabiliy and closely related to the topic of spatial optical solitons (see Chapter 11). By introducing coupling between two counterpropagating beams, the possibility for an absolute instabiliy and the observation of self-organized patterns arises. In most experimental scenarios used today, the second pump beam is obtained by means of a mirror, providing external feedback and lowering the threshold for the onset of pattern formation. Prominent patterns using a photorefractive nonlinearity are of hexagonal symmetry, comparable with many other optical and nonoptical pattern forming systems. Generally, the basic mechanism is photorefractive two-wave mixing, mediated by reflection gratings formed by the counterpropagating beams. Symmetry and transverse size of the patterns depend on the distance of the mirror from the crystal face.

Considering a single-mirror feedback system with an iron-doped potassium niobate crystal, the derivation of model equations was outlined. At the threshold, a linear stability analysis of the model equations has been carried out to determine the wave number of the initial modulation. Experimental results generally agree with the predictions, however, a significant deviation is found in a parameter region highly of interest to experiment. In the multiple pattern region, several nonhexagonal patterns are observed—pure, coexisting and competing. This parameter range corresponds to positions of the projected, virtual mirror inside the crystal.

The existence of multistability marks this system as a model for the investigation of control in pattern formation. We briefly presented a specific control scheme, a Michelson-type feedback assembly. Results of positive, in-phase feedback were demonstrated, showing the stabilization of roll and square patterns over hexagons. Using negative, out-of-phase feedback, a minimally invasive control method for selecting the orientation of patterns was described.

While most applications for pattern formation consist of inhibiting undesired modulational instability, a few positive applications have been envisaged. These include usage of self-organized configurable hexagonal spot arrays for multiplexing of information flow or self-organized system states as basic units of information processing devices. Some are presented in volume three of this edition. Many ideas for applications are currently in very early stages. In any case, a thorough knowledge of the system, its mechanisms, spectra of solutions and accessibility for control is required. While quite a bit of experimental data

and theoretical understanding has been accumulated on the different systems, there remain many open questions, from the theoretical and numerical modeling of basic mechanisms to experimental realization of control schemes. Maybe the most promising application is the actual usage of optical pattern forming systems for investigating fundamental mechanisms of self-organization and synergetic phenomena.

Acknowledgments: We acknowledge cooperation with Michael Schwab and Oliver Sandfuchs and their kind permission to use parts of their material published in [44, 61]. The results shown in this contribution have been partially supported by the Deutsche Forschungsgemeinschaft, under contract De 486/10 and within the Graduiertenkolleg (graduate school) "Nichtlineare kontinuierliche Systeme".

References

1 M.C. Cross and P.C. Hohenberg. Pattern formation outside of equilibrium. *Rev. Mod. Phys*., 65:851 (1993).
2 H. Haken, editor. *Synergetics. An Introduction*. Springer Verlag, ISBN 3-540-08866-0 (1978).
3 H. Haken, editor. *Advanced Synergetics*. Springer Verlag, ISBN 3-540-12162-5 (1983).
4 D. Walgraef. *Spatio-temporal pattern formation—With Examples from Physics, Chemistry, and Materials Science (Partially Ordered Systems)*. Springer Verlag, ISBN 0-387-94857-0 (1995).
5 M.A. Vorontsov and W.B. Miller. *Self-organization in optical systems and applications in information technology*. Springer Verlag, ISBN 3-540-64125-4 (1995).
6 S. Camazine, N.R. Franks, and J.-L. Deneubourg. *Self-Organization in Biological Systems (Princeton Studies in Complexity)*. Princeton University Press, ISBN 0691012113 (2001).
7 R. Neubecker, G.L. Oppo, B. Thüring, and T. Tschudi. Pattern formation in a liquid crystal light-valve with feedback, including polarization, saturation, and internal threshold effects. *Phys. Rev. A 52*, page 791 (1995).
8 Q. Ouyang and H.L. Swinney. Transition from a uniform state to hexagonal and striped turing patterns. *Nature*, 352:610 (1991).
9 F.T. Arecchi, S. Boccaletti, and P. Ramazza. Pattern formation and competition in nonlinear optics. *Phys. Rep*., 318:1 (1999).
10 L.A. Lugiato. Spatio-temporal structures part I. *Phys. Rep*., 219:293–310 (1992).
11 C.O. Weiss. Spatio-temporal structures part II. *Phys. Rep*., 219:311–338 (1992).
12 L.A. Lugiato. Transverse nonlinear optics: introduction and review. *Chaos Solitons and Fractals*, 4:1251–1258 (1994).
13 L.A. Lugiato (ed.). Nonlinear optical structures, patterns, chaos. *Chaos, Solitons and Fractals*, 4 (1994).
14 R. Macdonald and H.J. Eichler. Spontaneous optical pattern formation in a nematic liquid crystal with feedback mirror. *Opt. Commun*., 89:289–295 (1992).
15 M. Tamburrini, M. Bonavita, S. Wabnitz, and E. Santamato. Hexagonally patterned beam filamentation in a thin liquid-crystal film with a single feedback mirror. *Opt. Lett*., 18:855 (1993).

16 G. Grynberg, A. Maitre, and A. Petrossian. Flowerlike patterns generated by a laser beam transmitted through a rubidium cell with single feedback mirror. *Phys. Rev. Lett*., 72:2379–2382 (1994).
17 T. Ackemann and W. Lange. Non- and nearly hexagonal patterns in sodium vapor generated by single-mirror feedback. *Phys. Rev. A*, 50:R4468 (1994).
18 J. Glückstad and M. Saffman. Spontaneous pattern formation in a thin film of bacteriorhodopsin with mixed absorptive-dispersive nonlinearity. *Opt. Lett*., 20:551 (1995).
19 T. Honda. Hexagonal pattern formation due to counterpropagation in $KNbO_3$. *Opt. Lett*., 18:598 (1993).
20 W.J. Firth, A. Fitzgerald, and C. Pare. Transverse instabilities due to counterpropagation in Kerr media. *J. Opt. Soc. Am. B*, 7:1087 (1990).
21 G. D' Alessandro and W.J. Firth. Hexagonal spatial patterns for a Kerr slice with a feedback mirror. *Phys. Rev. A*, 46:537 (1992).
22 W.H.F. Talbot. Facts relating to optical sciences IV. *Philos. Mag*. **9** *(Third series)*, page 401 (1836).
23 E. Ciaramella, M. Tamburrini, and E. Santamato. Talbot assisted hexagonal beam patterning in a thin liquid crystal film with a single feedback mirror at negative distance. *Appl. Phys. Lett*., 63:1604 (1993).
24 A.V. Mamaev, M. Saffman, D.Z. Anderson, and A.A. Zozulya. Propagation of light beams in anisotropic nonlinear media: From symmetry breaking to spatial turbulence. *Phys. Rev. A*, 54:870 (1996).
25 M. Soljacic, M. Segev, T. Coskun, D.N. Christodoulides, and A. Vishwanath. Modulation instability of incoherent beams in noninstantaneous nonlinear media. *Phys. Rev. Lett*., 84:467 (2000).
26 D. Kip, M. Soljacic, M. Segev, E. Eugenieva, and D.N. Christodoulides. Modulation instability and pattern formation in spatially incoherent light beams. *Science*, 290:495 (2000).
27 D. Kip, M. Soljacic, M. Segev, S.M. Sears, and D.N. Christodoulides. (1+1)-dimensional modulation instability of spatially incoherent light. *J. Opt. Soc. Am. B*, 19:502 (2002).
28 Z. Chen, J. Klinger, and D.N. Christodoulides. Induced modulation instability of partially spatially incoherent light with varying perturbation periods. *Phys. Rev. E*, 66:066601 (2002).
29 P.M. Lushnikov and A.V. Mamaev. Spontaneous hexagon formation in photorefractive crystal with a single pump wave. *Opt. Lett*., 24:1511 (1999).
30 T. Honda and H. Matsumoto. Buildup of spontaneous hexagonal patterns in photorefractive $BaTiO_3$ with a feedback mirror. *Opt. Lett*., 20:1755 (1995).
31 T. Honda. Flow and controlled rotation of the spontaneous optical hexagon in $KNbO_3$. *Opt. Lett*., 20:851–853 (1995).
32 P.P. Banerjee, H.-L. Yu, D.A. Gregory, N. Kukhtarev, and H.J. Caulfield. Self-organization of scattering in photorefractive $KNbO_3$ into a reconfigurable hexagonal spot array. *Opt. Lett*., 20:10 (1995).
33 N.V. Kukhtarev, T. Kukhtareva, H.J. Caulfield, P.P. Banerjee, H.-L. Yu, and L. Hesselink. Broadband dynamic, holographically selfrecorded, and static hexagonal scattering patterns in photorefractive $KNbO_3$: Fe. *Opt. Eng*., 34:2261 (1995).
34 A.V. Mamaev and M. Saffman. Modulational instability and pattern formation in the field of noncollinear pump beams. *Opt. Lett*., 22:283 (1997).
35 M. Schwab, M. Sedlatschek, B. Thüring, C. Denz, and T. Tschudi. Origin and control of dynamics of hexagonal patterns in a photorefractive feedback system. *Chaos, Solitons and Fractals*, 10:701 (1999).

36 M. Saffman, A.A. Zozulya, and D.Z. Anderson. Transverse instability of energy-exchanging counterpropagating waves in photorefractive media. *J. Opt. Soc. Am. B*, 11:1409 (1994).
37 T. Honda and P. Banerjee. Threshold for spontaneous pattern formation in reflection-grating-dominated photorefractive media with mirror feedback. *Opt. Lett. 21*, pages 779–781 (1996).
38 T. Honda, H. Matsumoto, M. Sedlatschek, C. Denz, and T. Tschudi. Spontaneous formation of hexagons, squares and squeezed hexagons in a photorefractive phase conjugator with virtually internal feedback mirror. *Opt. Commun.*, 133:293 (1997).
39 C. Denz, M. Schwab, M. Sedlatschek, T. Tschudi, and T. Honda. Pattern dynamics and competition in a photorefractive feedback system. *J. Opt. Soc. Am. B*, 15:2057 (1998).
40 M. Schwab, C. Denz, and M. Saffman. Multiple-pattern stability in a photorefractive feedback system. *Appl. Phys. B*, 69:429 (1999).
41 A.V. Mamaev and M. Saffman. Hexagonal optical patterns in anisotropic nonlinear media. *Europhys. Lett.*, 34:669 (1996).
42 M. Schwab, C. Denz, and M. Saffman. Transverse modulational instability in counterpropagating two-wave mixing with frequency-detuned pump beams. *J. Opt. Soc. Am. B*, 18:628 (2001).
43 M. Schwab, C. Denz, A.V. Mamaev, and M. Saffman. Manipulation of optical patterns by frequency detuning of the pump beams. *J. Opt. B*, 3:318 (2001).
44 M. Schwab. *Manipulation and Control of Self-organized Transverse Optical Patterns*. Shaker Verlag Aachen, ISBN 3-8265-9239-5 (2001).
45 B.I. Sturman, S.G. Odoulov, U. van Olfen, G. Jakel, R.K. Schulz, and E. Krätzig. Physical origin of mirrorless parametric oscillation in $BaTiO_3$. *J. Opt. Soc. Am. B*, 11:1700 (1994).
46 B. Sturman and A. Chernykh. Mechanism of transverse instability of counter-propagation in photorefractive media. *J. Opt. Soc. Am. B*, 12:1384 (1995).
47 A.I. Chernykh, B.I. Sturman, M. Aguilar, and F. Agullo-Lopez. Threshold for pattern formation in a medium with a local photorefractive response. *J. Opt. Soc. Am. B*, 14:1754 (1997).
48 S. Odoulov, B. Sturman, and E. Krätzig. Seeded and spontaneous light hexagons in $LiNbO_3$: Fe. *Appl. Phys. B*, 70:645 (2000).
49 Y. Uesu, A. Ueno, M. Kobayashi, and S. Odoulov. Hexagon formation in photorefractive crystals as mirrorless coherent oscillation. *J. Opt. Soc. Am. B*, 15:2065 (1998).
50 F.T. Arecchi, G. Giacomelli, P.L. Ramazza, and S. Residori. Experimental evidence of chaotic itinerancy and spatiotemporal chaos in optics. *Phys. Rev. Lett.*, 65:2531 (1990).
51 G. Balzer, C. Denz, O. Knaup, and T. Tschudi. Circling vortices and pattern dynamics in a unidirectional photorefractive ring oscillator. *Chaos, Solitons and Fractals*, 10:725 (1999).
52 C. Denz, M. Schwab, and C. Weilnau, editors. *Transverse-Pattern Formation in Photorefractive Optics*. Springer Tracts in Modern Physics, Springer Verlag, ISBN 3-540-02109-4 (2003).
53 S. Juul Jensen, R. Nicolaus, and C. Denz. Spatial mode dynamics in a photorefractive ring oscillator with induced astigmatism. *J. Opt. Soc. Am. B*, 18:966 (2001).
54 Z. Chen, D. McGee, and N.B. Abraham. Pattern dynamics in photorefractive bidirectional ring-resonator experiments. *J. Opt. Soc. Am. B*, 13:1482 (1996).

55 K. Staliunas, M.F.H. Tarroja, G. Slekys, C.O. Weiss, and L. Dambly. Analogy between photorefractive oscillators and class-A lasers. *Phys. Rev. A*, 51:4140 (1995).
56 M. Vaupel and C.O. Weiss. Circling optical vortices. *Phys. Rev. A*, 51:4078 (1995).
57 J. Malos, M. Vaupel, K. Staliunas, and C.O. Weiss. Dynamical structures of a photorefractive oscillator. *Phys. Rev. A*, 53:3559 (1996).
58 A.V. Mamaev and M. Saffman. Optical vortex patterns in a unidirectional ring oscillator. *Phys. Script. T*, 67:21 (1996).
59 P. Yeh, editor. *Introduction to photorefractive nonlinear optics*. J. Wiley and sons, Wiley series in pure and applied optics, ISBN 0-471-58692-7 (1993).
60 N.V. Kukhtarev, V.B. Markov, S.G. Odulov, M.S. Soskin, and V.L. Vinetskii. Holographic storage in electro-optic crystals. Beam coupling and light amplification. *Ferroelectrics*, 22:961–964 (1979).
61 O. Sandfuchs. *Self-Organization, Amplitude Equations and Fourier Control in a Nonlinear Optical Feedback System*. Shaker Verlag Aachen, ISBN 3-8265-9959-4 (2001).
62 W. Krolikowski, M.R. Belic, M. Cronin-Golomb, and A. Bledowski. Chaos in photorefractive four-wave mixing with a single grating and a single interaction region. *J. Opt. Soc. Am. B*, 7:1204 (1990).
63 M. Schwab, C. Denz, and M. Saffman. Manipulation of optical patterns by frequency detuning of the pump beams. *OSA TOPS*, 62:621 (2001).
64 M. Pesch, E. Grosse Westhoff, T. Ackemann, and W. Lange. Direct measurement of multiple instability regions via a Fourier filtering method in an optical pattern forming system. *Phys. Rev. E*, 68:016209 (2003).
65 P.M. Lushnikov. Hexagonal optical structures in photorefractive crystals with a feedback mirror. *Journ. Exp. Theo. Phys.*, 86:614 (1998).
66 S. Ciliberto, P. Coullet, J. Lega, E. Pampaloni, and C. Perez-Garcia. Defects in roll-hexagon competition. *Phys. Rev. Lett.*, 65:2370 (1990).
67 S.G. Odoulov, M.Y. Goulkov, and O.A. Shinkarenko. Threshold behavior in formation of optical hexagons and first order optical phase transition. *Phys. Rev. Lett.*, 83:3637 (1999).
68 O. Sandfuchs, F. Kaiser, and M.R. Belic. Self-organization and Fourier selection of optical patterns in a nonlinear photorefractive feedback system. *Phys. Rev. A*, 64:063809 (2001).
69 A. Aumann, T. Ackemann, E. Grosse Westhoff, and W. Lange. Eightfold quasi-patterns in an optical pattern-forming system. *Phys. Rev. E*, 66:046220 (2002).
70 E. Ott, C. Grebogi, and J.A. Yorke. Controlling chaos. *Phys. Rev. Lett.*, 64:1196 (1990).
71 K. Pyragas. Continuous control of chaos by self-controlling feedback. *Phys. Lett. A*, 170:421 (1992).
72 M.E. Bleich, D. Hochheiser, J.V. Moloney, and J.E.S. Socolar. Controlling extended systems with spatially filtered, time-delayed feedback. *Phys. Rev. E*, 55:2119 (1997).
73 J.V. Moloney. Spontaneous generation of patterns and their control in nonlinear optics. *J. Opt. B Quant. Semiclass. Op*, 1:183 (1999).
74 E.V. Degtiarev and M.A. Vorontsov. Spatial filtering in nonlinear two-dimensional feedback systems: phase-distortion suppression. *J. Opt. Soc. Am. B*, 12:1238 (1995).
75 R. Martin, A.J. Scroggie, G.-L. Oppo, and W.J. Firth. Stabilization, selection, and tracking of unstable patterns by Fourier space techniques. *Phys. Rev. Lett.*, 77:4007 (1996).
76 A.V. Mamaev and M. Saffman. Selection of unstable patterns and control of optical turbulence by Fourier plane filtering. *Phys. Rev. Lett.*, 80:3499 (1998).

77 T. Ackemann, B. Giese, B. Schäpers, and W. Lange. Investigations of pattern forming mechanisms by Fourier filtering: properties of hexagons and the transition to stripes in an anisotropic system. *J. Opt. B: Quantum Semiclass. Opt*., 1:70–76 (1999).
78 G.K. Harkness, G.L. Oppo, E. Benkler, M. Kreuzer, R. Neubecker, and T. Tschudi. Fourier space control in an LCLV feedback system. *J. Opt. B: Quantum Semiclass. Opt*., 1:177–182 (1999).
79 E. Benkler, M. Kreuzer, R. Neubecker, and T. Tschudi. Experimental control of unstable patterns and elimination of spatiotemporal disorder in nonlinear optics. *Phys. Rev. Lett*., 84:879–882 (2000).
80 P.-J. Wang and M. Saffman. Selecting optical patterns with spatial phase modulation. *Opt. Lett*., 24:1118 (1999).
81 S. Juul Jensen, M. Schwab, and C. Denz. Manipulation, stabilization, and control of pattern formation using Fourier space filtering. *Phys. Rev. Lett*., 81:1614 (1998).
82 R. Martin, G.-L. Oppo, G.K. Harkness, A.J. Scroggie, and W.J. Firth. Controlling pattern formation and spatio-temporal disorder in nonlinear optics. *Opt. Expr*., 1:39 (1997).
83 G.K. Harkness, G.-L. Oppo, R. Martin, A.J. Scroggie, and W.J. Firth. Elimination of spatiotemporal disorder by Fourier space techniques. *Phys. Rev. A*, 58:2577 (1998).
84 M. Schwab, M. Saffman, C. Denz, and T. Tschudi. Fourier control of pattern formation in an interferometric feedback configuration. *Opt. Commun*., 170:129 (1999).

10

Photorefractive Waveguides

Detlef Kip[1] and Monika Wesner[2]

[1] Institute of Physics and Physical Technologies, Clausthal University of Technology, 38678 Clausthal-Zellerfeld, Germany
detlef.kip@tu-clausthal.de
[2] Physics Department, University of Osnabrück, 49069 Osnabrück, Germany
monika.wesner@uos.de

10.1 Introduction

In photorefractive crystals, the materials' refractive index can be altered by light illumination with spatially inhomogeneous intensity. This allows for a wide spectrum of applications, e.g., optical data storage, pattern recognition, adaptive optics, or dynamic holography [1, 2]. In this chapter, we will focus on a special geometry of photorefractive materials: Optical waveguides. On the one hand, due the high light intensities that are inherent in waveguide geometries, photorefractive effects in optical waveguides [3, 4] are feared as optical damage, as they can degrade the performance of integrated optical devices. On the other hand, both dynamic wave mixing and permanent holographic gratings in waveguides are of considerable interest for the development of new components for integrated optics.

In this contribution, we will focus on photorefractive waveguides in oxide crystals, and have to redirect the interested reader to other chapters of this book for materials like semiconductors or photorefractive polymers. After some basics on optical waveguide properties, a review of recent results and techniques for waveguide formation is given. Here investigations in materials with illmenite structure ($LiNbO_3$, $LiTaO_3$), perovscites ($BaTiO_3$, $KNbO_3$), crystals with tungsten-bronze structure (SBN, KNSBN), and sillenites (BSO, BTO, BGO) are discussed. As an outlook, the suitability of photorefractive waveguides for applications is demonstrated in some examples.

10.2 Fundamentals of Photorefractive Waveguides

In this section, we will briefly discuss the fundamentals of photorefractive optical waveguides as well as the experimental techniques for, e.g., the determination of refractive index profiles, electrooptic properties, and light-induced refractive index changes in waveguide samples.

10.2.1 Optical Waveguides

Optical waveguides are the key components for the development of integrated optical devices. In integrated optics, several optical components, like lasers, beam splitters, or modulators, are integrated on a suitable substrate material [5]. Here optical waveguides provide the connections between these components.

An optical waveguide consists of a dielectric material that is surrounded by another dielectric material of lower refractive index. Guidance of light is based on total internal reflection of electromagnetic waves at the boundaries of the inner medium so that radiation into the surrounding medium is forbidden. One can distinguish between planar waveguides, where the light is confined along one transverse direction while diffracting along the other transverse coordinate, and two-dimensional waveguides, where the light is guided in both transverse directions (Fig. 10.1). In the latter case, typical geometries are either channel or strip waveguides, respectively, and optical fibers with radial symmetry.

To discuss some fundamental properties of dielectric waveguides, we consider a planar structure as in Fig. 10.1a. In a ray-optics picture of waveguiding, light is guided by multiple reflections from two parallel infinite plane boundaries that act as lossless mirrors. For an electromagnetic analysis of this structure, each ray is described by a plane wave, where the total electromagnetic field consists of the sum of these plane waves. Here the self-consistency condition requires that, as a wave is reflected twice at the upper and lower boundary, its phase has to undergo a phase shift of multiples of 2π, i.e., the wave has to reproduce itself. In this way, discrete solutions for the electromagnetic field are obtained that are called the modes of the waveguide. These modes have a certain transverse electromagnetic field that is maintained during propagation along the waveguide. Depending on the light polarization, one can distinguish between TE (transverse electric) modes, where the transverse electric field points perpendicular to the waveguide normal and the propagation direction, and TM (transverse magnetic) waves, where the magnetic field is along this direction. Each mode is fully described by its transverse mode profile, its polarization, and the propagation constant $\beta = k_0 n_{\text{eff}}$, where k_0 is the wave number and n_{eff} is the effective refractive index of the mode.

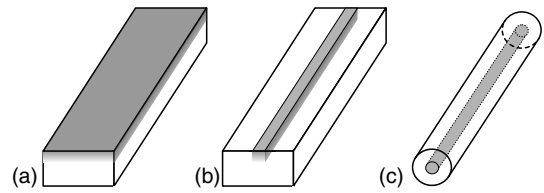

FIGURE 10.1. Different types of optical waveguides. a) Planar waveguide; b) channel waveguide, and c) optical fiber.

The most simple case of a planar waveguide is that with a step-like refractive index jump at the boundary ($x = d$) of substrate and waveguiding layer, and another jump at the boundary of the waveguide and the top cladding ($x = 0$), which is usually air (see left part of Fig. 10.2a). In analogy to the eigenfunctions of a step-like potential well, the waveguide modes are harmonic functions, where the field amplitude exponentially decays in the cladding and substrate layers, respectively. For these modes, the effective refractive index n_{eff} is larger then the two indices of the surrounding layers. If n_{eff} is close to but slightly lower than the index of the substrate material, leaky or substrate modes of the waveguide can be excited that continuously loose energy to the substrate.

A more general profile is that of a graded-index waveguide, where the refractive index of the waveguiding layer continuously decreases from a higher surface value to the substrate refractive index. Typical examples for this type are in-diffused waveguides where the refractive index profile is determined by the diffusion profile of some in-diffused species. As a main difference to step-like profiles, different modes of a graded-index waveguide propagate in different effective depths d_{eff} of the waveguiding layer. Examples of the electric field distribution E_m of the first modes $m = 0$, 1, and 2 of a step-like and a graded-index waveguide are given in Fig. 10.2.

A universal method for coupling light into and out of a planar waveguide is the use of prism coupler. Prism coupler allow a direct measurement of the coupling efficiency as well as a mode selective excitation of the waveguide, which may be preferred for the investigation of multimode waveguides where depth dependent measurements of waveguide properties become possible in this way. Grating couplers may be used as well, but fabrication is difficult and coupling efficiencies are often low. Direct endface coupling is of particular interest for waveguides in $BaTiO_3$, $KNbO_3$, or SBN, because sample dimensions are usually small, and mechanical stress that is inherent in the prism-waveguide coupler may not be applied to these materials.

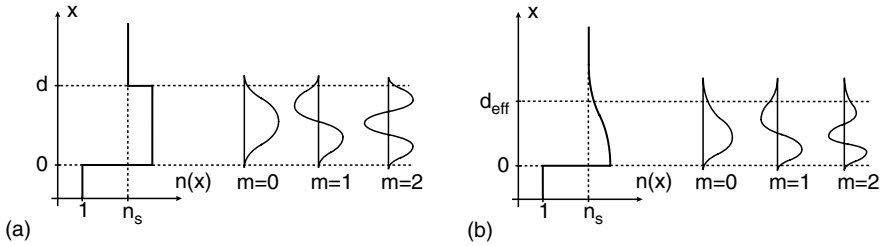

FIGURE 10.2. Typical refractive index profiles and electric field distribution E_m of the lowest guided modes for a) step-like and b) graded-index planar waveguide.

10.2.2 Photorefractive Effects in Waveguide Samples

Photorefractive effects in planar waveguides can be studied by two principal holographic methods: A two-beam interferometric setup, or by monitoring the output intensity and the beam shape of a single guided beam. Here, similar as for bulk samples, a wide range of different holographic measurement techniques exists, which allow for the determination of photorefractive parameters like saturated refractive index changes, dark and photoconductivity, photovoltaic constants, or holographic sensitivity. For the investigation of channel waveguides often pump-probe techniques are utilized, where a low-power beam of larger wavelength is used to probe the refractive index change that are induced by a stronger pump beam.

An overview of different geometries for recording of elementary refractive index gratings in waveguide samples is given in Fig. 10.3. In a standard setup gratings are written by two guided beams of the same polarization and mode number intersecting inside the waveguide (Fig. 10.3a and 10.3b). For light coupling into and out of the sample, either prism couplers or direct endface coupling can be used. Alternatively, the two beams may differ in polarization or mode number. Furthermore, gratings may be written in planar (Fig. 10.3c) or channel waveguides (Fig. 10.3d) by external beams that impinge upon the surface of the waveguiding layer. To record grating coupler for in- and out-coupling of light from the waveguide the interaction of substrate and guided modes can be used, too (Fig. 10.3e).

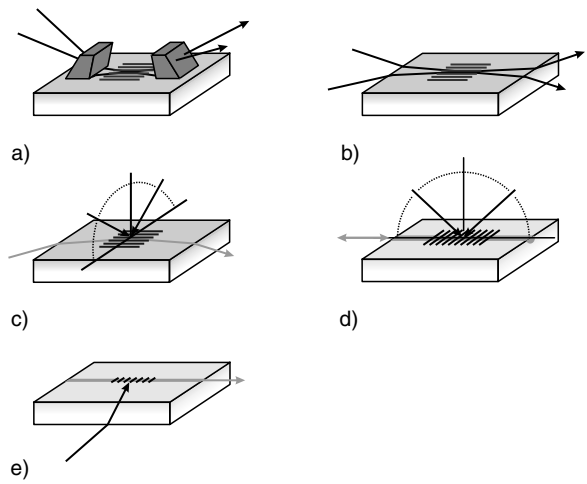

FIGURE 10.3. Geometries for recording of holographic gratings in waveguides using either guided waves or external writing beams. a) Two-beam interference of guided beams using prism couplers or b) endface coupling, c) grating recording with external beams, d) reflection holograms in channel waveguides, and e) recording of grating couplers.

The light-induced charge transport in photorefractive oxide crystals is treated in detail in other chapters of this book. In general, the obtained models and equations for one and more photorefractive centers and for different mechanisms of charge redistribution can be transferred to waveguide samples, too. However, in most investigations of photorefractive waveguides, averaged quantities have been used to describe both, the light distribution inside the sample and the photorefractive properties. Examples are effective widths and propagation depths of the excited modes, averaged light intensities, or refractive index changes and photovoltaic constants where the values are averaged over the depth of the waveguiding layer [6]. For these averaged quantities, the Kogelnik theory of the interaction of plane waves can be used to interpret the results. As an example, the averaged refractive index change of mode m of a y-cut planar waveguide is described by

$$(<\Delta n>)_m = \frac{\int |E_m(y)|^2 \Delta n(y)\, dy}{\int |E_m(y)|^2 dy}, \tag{10.1}$$

where the diffraction efficiency η of a grating of length d that is read out with a wavelength λ is described by a modified Kogelnik equation

$$\eta = \sin^2\left(\frac{\pi(<\Delta n>)_m d}{\lambda}\right). \tag{10.2}$$

However, in some cases, the simplified treatment of the interacting beams as plane waves has failed to describe the experimental observations. In this case, the exact two-dimensional intensity distribution has to be taken into account. For example, the two-wave interaction of Gaussian beams in a multimode planar waveguiding layer can be interpreted in terms of a two-dimensionally varying time constant for the grating build-up time. This time constant is smallest in the beam center and shows an additional variation with depth [7], thus the resulting time dependence of the wave mixing, i.e., the build-up of a refractive index grating, may show significant deviations from a mono-exponential behavior.

When only a single beam is coupled into a planar photorefractive waveguide, both, light-induced phase changes in the beam path and holographic scattering reduce the transmitted power in the beam direction [8, 9]. In this case photoconductivity, refractive index changes, and holographic sensitivity can be quantitatively determined by variation of the input power and time dependent measurements of the resulting changes in the shape of the outcoupled intensity spectrum [10].

10.2.3 Experimental Methods

Different methods can be used for the fabrication of waveguides in photorefractive crystals. Typical examples are diffusion, ion exchange, implantation of ions, or the deposition of thin epitaxial layers. As the different techniques are

predominantly specific for one class of oxide crystals, a detailed description of the waveguide fabrication method is given in the respective material subsections of the next section. Here we will give a short overview on different techniques for the reconstruction of refractive index profiles and the measurement of electro-optic coefficients, as well as on the holographic investigation methods that can be used for the determination of photorefractive properties.

Refractive index profiles with typical dimensions of only a few micrometers can hardly be determined by direct measurement. Very often the reconstruction of planar waveguide profiles is based on a set of measured effective refractive indices $n_{\mathrm{eff},\mathrm{i}}$, which can be determined by dark-line or mode spectroscopy [11]. Here two different strategies have been established. At first, one may assume a family of plausible profiles that are characterized by a set of fit parameters. With this method, good results have been obtained for ion-implanted waveguides [12, 13], where the profiles can be well predicted by using simulations of the implantation process. A second procedure commonly used for profile reconstruction of multimode waveguides is the inverse WKB method [14]. For channel waveguides, different numerical approximations are used to calculate the effective refractive indices of the modes of an assumed or given refractive index profile, e.g., the methods of finite differences or finite elements.

Although the electro-optic properties of substrate materials for waveguide fabrication are well known in most cases, these values may differ for waveguides because of material changes that are due to the waveguide fabrication itself. Therefore techniques have been developed to measure electro-optic coefficients in both planar and channel waveguides. In planar waveguides, attenuated total reflection (ATR) spectroscopy may be used, a method that is well known from the investigation of electro-optic polymer layers [15, 16]. Alternatively, interferometric methods can be applied [17, 18]. In channel waveguides, the electro-optically induced phase changes in integrated Mach-Zehnder [19] or Fabry-Perot interferometers [20] have been used to measure electro-optic coefficients in $LiNbO_3$ and $LiTaO_3$ samples.

10.3 Materials with Illmenite Structure

Among all ferroelectric materials, photorefractive effects have been studied most extensively in lithium niobate ($LiNbO_3$) [1]. Crystals with diameters up to six inches and of superior optical quality can be grown, which makes this material the preferred candidate for applications in integrated optics. $LiNbO_3$ has large electro-optic and SHG coefficients of $r_{33} \approx 30\,\mathrm{pm/V}$ and $d_{33} \approx 32\,\mathrm{pm/V}$, respectively. Typical devices realized in $LiNbO_3$ waveguides are integrated lasers [21], electrooptic modulators with low half-wave voltages, quasi-phase matched structures for frequency conversion, or integrated Sagnac interferometers for high-precision rotation sensing.

Lithium tantalate ($LiTaO_3$) possesses electro-optic, nonlinear optical, and photorefractive properties similar to $LiNbO_3$. On the one hand, in some aspects

$LiTaO_3$ is even more attractive for applications in integrated optics than $LiNbO_3$. It is less sensitive to optical damage, it has a larger transparency in the UV down to 270 nm, and it has a smaller birefringence. However, high temperature waveguide fabrication that exceeds the Curie temperature of about 620°C (for the congruently melting composition) requires additional repoling, and crystal growth is more difficult because of the high melting point of $LiTaO_3$ of about 1650°C. Nevertheless, waveguide devices for electro-optic modulation and frequency doubling in the visible spectral region are now commercially available.

Advantages of $LiNbO_3$ and also $LiTaO_3$ are the possibility to form low-loss waveguides, the chemical and mechanical resistance, a wide range of nonlinear optical interactions, and finally the availability of large crystals at a reasonable cost. Because of the relatively empty illmenite lattice structure, many metal ions can be indiffused into $LiNbO_3$ and $LiTaO_3$ to form low-loss waveguiding layers or channels. Titanium diffusion into $LiNbO_3$ is by far the most common technique for waveguide fabrication. On the other hand, diffusion is also an easy method to increase the photorefractive sensitivity by surface doping of the waveguide substrates. As an alternative method for waveguide formation the proton exchange technique in $LiNbO_3$ and $LiTaO_3$ has proved to result in low-loss waveguides, which are particularly well suited for applications where high intensities occur, e.g., for second harmonic generation of blue and green light.

Besides the two methods mentioned above a wide range of different epitaxial techniques has been developed in the past. A large number of oxide crystals have been fabricated in thin film form by, e.g., sputtering of a suitable target material, including the materials $LiNbO_3$ and $LiTaO_3$. These techniques include diode, reactive, ion beam, magnetron, bias sputtering, or pulsed laser deposition (PLD), as well as liquid phase epitaxy (LPE) [22] and molecular beam epitaxy (MBE) [23]. Here PLD and MBE allows fabrication of films with high optical quality and nonlinear properties that are similar to the bulk material [24, 25].

10.3.1 Titanium Diffusion

The diffusion of thin films of titanium evaporated or sputtered onto the substrate surface is a widely used method for waveguide formation in $LiNbO_3$ and in part also in $LiTaO_3$ crystals, and most of the integrated optical devices available today are based on titanium-diffused $LiNbO_3$ waveguides. In $LiNbO_3$ the extraordinary refractive index increases linearly with titanium concentration, whereas the ordinary index shows a slightly sublinear behavior [26]. Larger changes are obtained for extraordinarily polarized light. No significant reduction of the electro-optic or nonlinear optical coefficients have been reported. Diffusion of titanium has been used to produce waveguides in $LiTaO_3$ [27], too. The low diffusion coefficient requires temperatures of above 1300°C, thus exceeding the material's Curie temperature, which requires additional poling of the samples.

The diffusion process has been investigated in detail in $LiNbO_3$ and consists of several complex steps [28, 29]. Here annealing is usually performed at temperatures around 1000°C. At about 500°C, titanium is oxidized to TiO_2, and above 600°C $LiNb_3O_8$ epitaxial crystallites are formed at the surface, connected with a loss of lithium. For temperatures larger than 950°C, a $(Ti_{0.65}Nb_{0.35})O_2$ mixed oxide appears, which acts as the diffusion source for titanium indiffusion. With increasing annealing time, titanium diffuses deeper into the crystal, and the titanium-niobium oxide layer decomposes. For temperatures above 600°C, a loss of Li or Li_2O at the crystal surface is observed. Because this mechanism increases the extraordinary refractive index Li, outdiffusion has to be prevented in particular for channel waveguide formation. This is often realized by annealing of the samples in water vapor or a Li-rich atmosphere.

Besides titanium a large number of other metals can be diffused into $LiNbO_3$ to form waveguiding layers, e.g., iron, copper, vanadium, nickel, niobium, cobalt, silver, or gold [30]. Here zinc is of special interest as the diffusion of zinc into $LiNbO_3$ has been found to produce low-loss waveguides with higher resistance to optical damage [31, 32] when compared to titanium.

Planar and channel $LiTaO_3$ waveguides have been fabricated by diffusion of, e.g., titanium [27], niobium [33], or zinc [20]. For this high-temperature process, repoling of the samples is necessary to recover the electro-optic properties of $LiTaO_3$.

For application of the photorefractive effect, waveguides fabricated by combined titanium and iron or copper diffusion, respectively, have shown considerably improved holographic sensitivity [34, 35].

10.3.2 Proton Exchange

Proton exchange (PE) is a low temperature process ($T < 250$°C) that has been successfully used for waveguide fabrication in $LiNbO_3$ [36, 37] and $LiTaO_3$ [38, 39]. Basically, hydrogen that is provided by an appropriate acid is partially exchanged for lithium ions of the crystal. In the case of $LiNbO_3$, the chemical composition $Li_{1-x}H_xNbO_3$ is formed where x, $0 \leq x \leq 1$, is the exchange degree.

A widely used technique for the formation of proton-exchanged waveguides is the immersion of the substrate in a bath of molten benzoic acid [37]. This liquid-phase treatment produces a mixture of crystalline β-phases on the sample surface with an exchange degree in the range of $0.5 < x < 0.85$ [40], and a nearly step-like refractive index profile. The maximum index change depends on the used acid. Typical values for benzoic acid are $\delta n_e = 0.12$, $\delta n_o = -0.05$ ($LiNbO_3$, [36]) and $\delta n_e = 0.02$, $\delta n_o \approx 0$ ($LiTaO_3$, [39, 41]), and higher changes up to $\delta n_e = 0.145$ [42] for $LiNbO_3$ are obtained using phosphoric acid. When using benzoic acid, the acidity of the melt can be diluted by the addition of some mol percent of lithium benzoate [36]. In this way, $LiNbO_3$ channel waveguides fabricated with pure benzoic acid show typical propagation losses

between 0.5 and 1 cm^{-1} for extraordinarily polarized light, while lower values of about 0.2 cm^{-1} have been reported for the use of phosphoric acid [42].

A significant degradation of electro-optic and nonlinear optical properties of proton-exchanged $LiNbO_3$ waveguides was found very early [43], which is caused by the lattice disorder and mixture of β-phases in strongly exchanged layers [44, 45]. A partial solution to this problem is the use of an additional post-annealing treatment at temperatures above 350°C [19]. These so-called annealed proton-exchanged (APE) waveguides have a graded refractive index profile. The waveguiding layer is completely converted to the α-phase [44] with $x < 0.12$ and an index change of $\delta n_e < 0.03$ [16]. Furthermore, for APE waveguides, very small loss coefficients of about 0.03 cm^{-1} have been measured [46]. Alternatively, waveguides with well defined phases can be obtained by carefully controlling the exchange degree. In this case, large electrooptic coefficients for PE layers up to $r_{33} = 22$ pm/V for $LiNbO_3$ can be obtained without additional annealing treatment [47]. In most work on proton-exchanged $LiTaO_3$ waveguides, electro-optic coefficients have been found to be strongly decreased after the exchange [48], and the values were at least partially restored after additional annealing treatment [17, 18, 49].

Very recently a new method, vapor-phase proton exchange (VPE) has been reported for $LiNbO_3$ [50] and $LiTaO_3$ [51], which results in high damage resistance, low optical losses ($\alpha < 0.1\ cm^{-1}$), and fully preserved electro-optic and nonlinear properties. For this method, samples are treated in an evacuated ampoule with benzoic acid powder at the bottom while the substrate is held in the top of the ampoule. Typical annealing temperatures are about 300°C and exchange times vary from several hours to a few days. As for the PE process, the resulting VPE waveguides have a nearly step-like index profile, and for not-too-long exchange times, a high-quality κ_2 phase structure can be obtained that is well suited for nonlinear optical applications [52].

By using proton exchange in $LiNbO_3$ and $LiTaO_3$, waveguides with strongly enhanced photorefractive sensitivity can be fabricated when the exchange of protons is combined with a successive copper exchange from melts containing Cu^+ or Cu^{2+} ions [16, 53]. As this technique of copper doping is a low-temperature process well below the Curie temperature of, e.g., $LiTaO_3$, it is of particular interest for the fabrication of photorefractive waveguides in this material.

10.3.3 Lithium Niobate Waveguides

Light-induced refractive index changes in optical materials can be considered from two points of view. On the one hand, these photorefractive effects are of considerable interest for applications in information storage and optical communication technology. On the other hand, the same mechanism is feared as optical damage; e.g., in waveguide devices, light-induced phase shifts may degrade the optical performance. The latter is particularly important for nonlinear applications of $LiNbO_3$ waveguides, where the performance of integrated

modulators and switches, lasers, or optical parametric oscillators may suffer from optical damage effects.

Optical Damage in Planar Waveguides

The optical damage resistance of planar $LiNbO_3$ waveguides fabricated by proton exchange, annealed proton exchange, vapor-phase proton exchange, metal diffusion, and epitaxy has been investigated in many works. However, a detailed comparison of the different methods still remains difficult. Although most of the used substrates are nominally undoped, they may differ a lot in the remaining impurity concentration. What is even more difficult is the influence of different light intensities and wavelengths when probing optical damage. In general, steady-state refractive index changes, holographic sensitivity, and photoconductivity depend on light intensity [54, 55]. For certain fabrication methods, both dark and photoconductivity of the waveguiding layer are considerably enlarged, and particularly at higher light intensities more than one photorefractive center can be involved in the charge transport [56], thus making the above quantities intensity dependent. Therefore, we restrict ourselves to some general remarks regarding photorefractive effects in differently prepared waveguides. A qualitative overview of some properties of $LiNbO_3$ waveguides is given in Table 10.1. For a more detailed comparison of photorefractive $LiNbO_3$ waveguide properties, see Ref. [4].

For titanium-diffused waveguides, high holographic sensitivity and large light-induced refractive index changes have been found [10]. It has been recognized that Fe^{2+} centers are stabilized by Ti^{4+} ions against oxidation [6], thus increasing the sensitivity to optical damage. On the other hand, a higher photorefractive damage resistance has been obtained for waveguides prepared by the diffusion of zinc into $LiNbO_3$ and for moderate light intensities of the order of $10^5 W/cm^2$ [31]. This may be attributed to a reduction of anti-site defects, where zinc ions are build-in on empty lithium sites instead of niobium.

Proton exchange leads to lower values of holographic sensitivity both for annealed (APE), non-annealed (PE), and vapor-phase (VPE) treated samples

TABLE 10.1. Overview of general photorefractive properties (optical damage or saturated refractive index change, photoconductivity, holographic sensitivity, and temporal stability of refractive index profiles) of $LiNbO_3$ waveguides fabricated by different methods: PE, proton exchange; APE, annealed proton exchange; VPE, vapor-phase proton exchange. These properties are only a general tendency of the different processes.

Fabrication	Opt. damage	Photoconduct.	Hol. sensitivity	Temporal stab.
Ti-Diffusion	High	Low	High	High
PE	Moderate	High	Low	Low
APE	Moderate	Moderate	Moderate	Moderate
VPE	Moderate/Low	Moderate	Low	Moderate/High

[10, 50, 57] when compared with titanium diffusion. In strongly exchanged waveguides, no light-induced refractive index changes are found [58], and this effect has been attributed to both a large increase of dark and photoconductivity [54], and a strong degradation of the electro-optic properties [43]. Here a conversion of Fe^{2+} to Fe^{3+} has been found for the proton exchange process [59], which can explain the observed decrease in holographic sensitivity, too.

In thermal fixing of holographic gratings in $LiNbO_3$ and $LiTaO_3$ at elevated temperatures, protons are believed to compensate for the electronic space charge field [55, 60]. In proton-exchanged waveguides, a similar mechanism is observed at room temperature, when light-induced electronic charge gratings are compensated for by light-insensitive, positively charged ions [61, 62], which may be explained by a considerably enlarged protonic conductivity of the PE layers.

Annealing treatment of PE layers with a higher exchange ratio leads to a recovery of the electro-optic coefficients [19, 47], while at the same time photoconductivity only slightly decreases [54]. Although the holographic sensitivity of APE samples is thus increased with annealing time, it is still two orders of magnitude lower than for titanium in-diffused samples. Excellent results have been obtained for vapor-phase proton-exchanged layers, where the photorefractive damage threshold has been reduced by one to two orders of magnitude when compared to APE samples [50]. On the other hand, the use of MgO-doped $LiNbO_3$ substrates for proton exchange has resulted in only slightly enlarged photorefractive damage resistance [57].

Planar waveguides fabricated by LPE [22] have shown higher holographic sensitivity than PE samples, but the values are still lower than for titanium diffusion [10, 24]. Other methods of thin film deposition have recently been used to grow epitaxial $LiNbO_3$ layers, e.g., sputtering [63], the sol-gel process [64], and PLD [25], but no photorefractive properties have been reported.

Wave-Mixing and Scattering

Quite a few optical wave mixing experiments have been performed in planar $LiNbO_3$ waveguides, and most of the used samples were treated to enhance photorefractive effects, e.g., by iron or copper in-diffusion, or combined proton and copper exchange. The published work may be subdivided into isotropic wave mixing, where the interacting light beams have the same polarization, and anisotropic wave mixing, where orthogonally polarized modes interact.

In contrast to wave mixing in the bulk where elementary refractive index gratings are usually recorded utilizing plane waves, in waveguides the inhomogeneity of the interacting fields and the presence of different modes have to be taken into account [34, 65, 66]. As a result, several photorefractive processes have been identified in waveguides that have no true analogs in volume crystals, e.g., polarization conversion of copropagating TE and TM modes [67, 68], or the recording of gratings where the photovoltaic current flows perpendicular to the grating vector [69].

In multimode planar waveguides, light can be scattered under discrete angles from an excited mode into other modes with different mode indices, but with the same polarization. In this interaction, the pump and the scattered waves have to fulfill a corresponding phase matching condition, thus stray light can be amplified by parametric interaction. Because light waves that belong to different modes of the waveguide are involved in this type of wave mixing, the interaction is called parametric inter-mode scattering [34, 70, 71].

In $LiNbO_3$ as well as in $LiTaO_3$ waveguides, orthogonally polarized modes can write holographic gratings via photovoltaic currents, enabling strong anisotropic wave mixing [67] and the generation of phase-conjugate [72] waves. This interaction, also known as polarization conversion, was observed first in y- and z-cut channel waveguides [73] and later also in planar y-cut waveguides [72, 74, 75]. The interaction can be understood by redistribution of photoexcited charge carriers by the photovoltaic effect, where the generated space-charge field is proportional to the polarization dependent photovoltaic current density [76]

$$j_k = \sum_{l,m} (\beta^s_{klm} + i\beta^a_{klm}) E^*_l E_m. \tag{10.3}$$

Here $\beta^{s,a}$ are the real linear and circular components of the photovoltaic tensor, and $E_{l,m}$ are the interacting light fields. Anisotropic interaction in $LiNbO_3$ and $LiTaO_3$ is enabled through the nondiagonal elements $\beta_{15} = \beta_{24}$ of the photovoltaic tensor. The corresponding current is modulated with the grating period $\Lambda = \lambda/(n_o - n_e)$, where λ is the light wavelength in vacuum (see Fig. 10.4).

The perturbation $\Delta\epsilon$ of the dielectric tensor has a local contribution according to β^s and a nonlocal part according to β^a [77]. As is well known, the shifted (nonlocal) grating leads to an energy exchange between the two interacting beams, where the direction of energy exchange depends on the sign of β^a. For iron-doped $LiNbO_3$, ordinarily polarized light is converted to extraordinary polarization, and for $LiTaO_3$: Fe, an opposite coupling direction is observed.

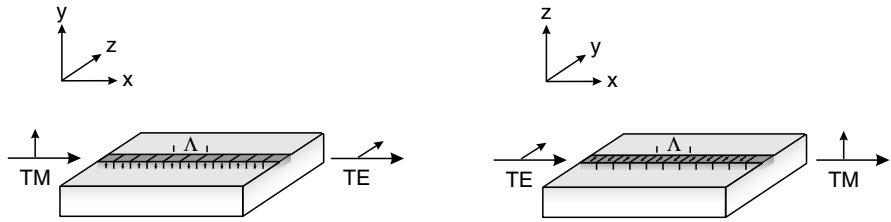

FIGURE 10.4. Illustration of the photovoltaic current responsible for polarization conversion in $LiNbO_3$ and $LiTaO_3$ channel waveguides. a) y-cut substrate, and b) z-cut substrate. Here the c-axis is parallel to the z-axis of the sample.

Optical Damage in Channel Waveguides

Different kinds of channel waveguides in nominally pure and MgO-doped $LiNbO_3$ have been formed by titanium indiffusion, PE, APE, VPE, and ion implantation, and the corresponding photorefractive properties and damage thresholds of these waveguides have been investigated. Fujiwara et al. have compared the photorefractive properties of titanium-diffused, PE, and APE samples using an integrated Mach-Zehnder interferometer [78, 79]. For low intensities of some W/cm^2, saturated refractive index changes of titanium-diffused samples are about three orders of magnitude larger than in PE, and two orders of magnitude larger than in APE waveguides. This may be attributed to the large increase of conductivity for the PE and APE samples [79], and partly reduced electro-optic coefficients of the PE waveguides. Furthermore, holographic sensitivity is increased by a factor of four for APE waveguides [78] when compared with PE waveguides, mainly because of the restored electro-optic properties, and probably because of a further enlarged conductivity in the APE samples, too.

The use of $LiNbO_3$ doped with MgO has reduced the refractive index changes in APE channel waveguides by nearly two orders of magnitude at intensities of some kW/cm^2 [80], and photoconductivity has been decreased at the same time, too. Here it has been concluded that strongly reduced photovoltaic currents in $LiNbO_3$: MgO waveguides are responsible for this effect.

Implantation of H^+ into $LiNbO_3$ with subsequent annealing treatment has resulted in waveguides with strong light-induced refractive index changes [81] that are larger than for APE waveguides and almost comparable with titanium-diffused samples. Simultaneously, both dark and photoconductivity are at least as high as for APE waveguides. On the other hand, strongly reduced optical damage has been found for a combination of proton exchange and ion implantation, when APE waveguides are additionally implanted with 1 MeV H^+ through the existing waveguide channels [82].

In a more recent work, light-induced shifts in the phase matching curve of second harmonic generation in both single domain and domain-inverted $LiNbO_3$ channel waveguides have been investigated by using a pump-probe technique [83]. A high photorefractive sensitivity connected with a two-step two-photon excitation has been found for single-domain samples, whereas optical damage was strongly reduced for domain-inverted samples.

10.3.4 Lithium Tantalate Waveguides

A general problem of $LiTaO_3$ waveguides is believed to be the observed instability of optical damage or light-induced refractive index changes in waveguides fabricated by diffusion or proton-exchange [84, 85]. A possible explanation for this effect might be the obtained mixture of different phases in proton-exchanged layers and a migration of protons at room temperature as well as the high number of defect sites (tantalum on lithium site) and high strain values that are inherent to crystals with non-stoichiometric composition.

Optical damage effects in zinc-diffused $LiTaO_3$ channel waveguides have been investigated in [86], and refractive index changes of $\Delta n_e \approx 5 \cdot 10^{-5}$ at a wavelength of 488 nm and an intensity of $1\,kW/cm^2$ have been measured. Proton-exchanged planar $LiTaO_3$ waveguides have shown similar refractive index changes of about $4 \cdot 10^{-5}$ [87], but at a larger wavelength of 632.8 nm.

Anisotropic two- and four-wave mixing has been used to determine the photorefractive properties of titanium-diffused $LiTaO_3$: Ti: Fe waveguides [88]. In a more recent work [53], photorefractive $LiTaO_3$ waveguides were fabricated by combined proton and copper exchange at low temperatures, which avoids repoling of the samples. Here a post-annealing treatment resulted in a full recovery of the preferred α-phase of $LiTaO_3$ [53, 89].

Thin epitaxial $LiTaO_3$ films have been grown by different methods, and research has been stimulated again recently by the large interest in $LiTaO_3$ waveguides with domain-inverted structures for second harmonic generation. An overview of recent work can be found in [90].

10.4 Materials with Perovscite Structure

10.4.1 Ion Implantation

Because of the low-temperature phase transitions, large chemical inertness, and the densely packed perovscite lattice, waveguide formation techniques like ion diffusion or exchange are more difficult in crystals with perovscite structure like $BaTiO_3$ and $KNbO_3$. For these reasons, the method of ion implantation is especially well suited for perovscites [91, 92] as well as for crystals of the tungsten-bronze family, in particular SBN [93]. The implantation of light ions like H^+ and He^+ with energies of some MeV has successfully been used for waveguide formation in a wide range of optical materials, including photorefractive ferroelectrics and sillenites. Apart from epitaxial techniques like PLD, ion implantation today is the only method that reliably results in low-loss single crystalline waveguides for $BaTiO_3$, $KNbO_3$, or SBN.

Impinging upon the crystal, the implanted ions slow down because of energy loss from interactions with the electrons of the target. At the end of their path, the ions' energy is in the range of some keV. Here, nuclear collision sets in, producing a well-defined damaged barrier layer with reduced refractive index. Light is guided above the barrier layer in the region of electron excitation. A typical magnitude of the refractive index decrease is about 5% of the substrate value; deeper barriers up to 10% have been obtained for $KNbO_3$ [13].

The ion-dose dependence of the refractive index decrease generally shows a saturation behavior, whereas the initial growth rate and the saturation level depend on ion energy [12]. Because of the well-defined penetration depth of the ions, nearly step-like refractive index profiles are obtained by ion implantation. Optical tunneling through the barrier, however, can lead to an increase of propagation losses for large mode numbers. Besides this mechanism, the loss

mechanism in ion-implanted waveguides is rather complex. It consists of contributions by material and implantation-induced absorption as well as surface scattering. A detailed overview on optical effects of ion implantation can be found in [94].

To a large extent, the electro-optic and photorefractive properties of the bulk crystal are maintained in the waveguiding layer. Frequently observed is a chemical reduction of the waveguiding layer as a result of the implantation process [95, 96]. Moreover, the electro-optic coefficients may be reduced due to depolarization effects [97, 98]. For a low dose of the implanted ions in the range of some 10^{13} to $10^{15}\,\mathrm{cm}^{-2}$, a slight increase of the extraordinary refractive index has been observed for several ferroelectric crystals [99]. This effect has been used to fabricate nonleaky waveguides [100], where light is confined without the possibility of barrier tunneling. Higher doses of $10^{16}\,\mathrm{cm}^{-2}$ and more have resulted in a decrease of both refractive indices. Furthermore, the implantation through an appropriate mask on the substrate surface has enabled the fabrication of both single and multimode channel waveguides in various materials [99, 101].

10.4.2 Barium Titanate

Photorefractive barium titanate ($BaTiO_3$) crystals are currently used for a wide range of nonlinear optical applications [1, 102, 103]. One of the most interesting features of $BaTiO_3$ is its electro-optic coefficient $r_{51} \approx 1600\,\mathrm{pm/V}$, which is one of the largest values known for any crystal. However, the practical use of $BaTiO_3$ crystals is at least partially limited by the relatively long response time of grating formation. Obviously, a significant decrease in response time can be achieved by using planar $BaTiO_3$ waveguides, i.e., by making use of the high intensities inherent in waveguide geometries. Another drawback of $BaTiO_3$ is a phase transition that occurs around 6 °C that is connected with mechanical stress to the samples and therefore may result in cracking of the crystal. Here $BaTiO_3$ may be replaced by barium-calcium titanate (BCT) crystals, a material with very similar electro-optic and photorefractive properties where this problematic phase transition is missing.

Planar optical waveguides in $BaTiO_3$ were first fabricated by Moretti et al. [91] in 1990 by implantation of 2 MeV He^+ at a dose of $10^{16}\,\mathrm{cm}^{-2}$. Both the ordinary and the extraordinary refractive index were decreased in the region of the implanted barrier [104]. Two-wave mixing in a 1.5 MeV H^+-implanted $BaTiO_3$ waveguide was reported by Youden et al. [105] in 1992. In Fig. 10.5, a decrease of response time of about two orders of magnitude when compared to the response time at same input power in the substrate has been observed. Frequently, the beam coupling direction is reversed to that of the substrate. This can probably be attributed to a change in the dominant charge carrier species from holes to electrons because of electrochemical reduction of impurities by the ion beam. Two-wave mixing even at 854 nm with a maximum gain of $24\,\mathrm{cm}^{-1}$ has been achieved in a Rh-doped $BaTiO_3$ crystal [106]. Both

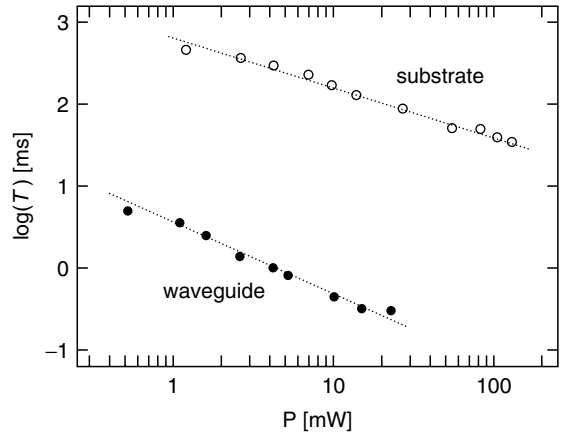

FIGURE 10.5. Time constant of two-beam coupling measured in a $BaTiO_3$ planar waveguide (•) and in the substrate (○) for the wavelength 488 nm as a function of light power P [105].

self-pumped phase conjugation [107] and mutually pumped phase conjugation [108] in the same sample have been obtained, too.

Epitaxial and very smooth films have been fabricated by PLD combined with *in situ* annealing of the growing film [109, 110]. Planar waveguides with propagation losses of 2 to 3 dB/cm at 633 nm with an electro-optic coefficient of $r_{51} = 86\,\mathrm{pm/V}$ have been obtained for c-axis films [98]. For a-axis films, an electro-optic coefficient $r_{\mathrm{eff}} = 536\,\mathrm{pm/V}$ has been found for low applied electric fields. A variety of other deposition techniques has successfully been used for the formation of $BaTiO_3$ thin films on adequate substrates, e.g., by MBE, the sol-gel process, or MOCVD. With MOCVD, channel waveguides have been fabricated using an additional etching in HF solution. These waveguides have shown moderate optical loss of 1 to $2\,\mathrm{cm}^{-1}$ at $1.55\,\mu\mathrm{m}$ [111] and effective electro-optic coefficients of about 50 pm/V [112].

10.4.3 Potassium Niobate

Potassium niobate ($KNbO_3$) belongs to the most promising ferroelectric oxides with excellent optical properties [113]. Large nonlinear and electro-optic coefficients in the spectral range of visible and infrared diode lasers and a high photorefractive sensitivity make the crystal a particularly attractive candidate for applications in integrated optics.

Methods of waveguide formation that have been successfully applied to other materials like diffusion or ion exchange have been found to be not applicable to $KNbO_3$, probably because of the densely packed lattice of the perovscite structure. The first permanent waveguides in $KNbO_3$ were realized by implantation of He^+ in 1988 by Bremer et al. [102]. Low-loss planar waveguides with damping coefficients of about $1\,\mathrm{cm}^{-1}$ (wavelength 632.8 nm) can be formed by He^+

implantation at low doses of some $10^{14}\,cm^{-2}$ [114]. Even lower propagation loss of only $0.2\,cm^{-1}$ has been found for a slightly higher dose of $1.5 \cdot 10^{15}\,cm^{-2}$ [115]. For H^+ implantation, doses of $10^{16}\,cm^{-2}$ and higher are used to produce good optical waveguides; here damping coefficients of 1 to $3\,cm^{-1}$ for visible light have been reported [116, 117]. Channel waveguides in $KNbO_3$ with damping coefficients as low as $0.3\,cm^{-1}$ for red light have been realized by Fluck et al. [101] by repeated He^+ implantation as well as by ultra-low dose implantation that leads to an increase of the refractive index of the implanted area [100].

Two-wave mixing experiments have been performed to characterize the photorefractive properties of iron-implanted planar waveguides in $KNbO_3$. Both H^+ and He^+ implantation have been used in nominally pure and iron-doped substrate crystals. In all published work, the beam coupling direction in the implanted waveguides in $KNbO_3$ was reversed to that of the substrate [118], and high logarithmic gain coefficients up to $40\,cm^{-1}$ have been obtained [116]. Smaller beam coupling coefficients of $2.2\,cm^{-1}$ and a response time of only 60 ms have been measured for a wavelength of $1.3\,\mu m$ in a H^+-implanted $KNbO_3$: Fe waveguide [117].

To fabricate thin films of $KNbO_3$, different deposition techniques like LPE, MOCVD, PLD, ion beam, or rf-sputtering have been used to fabricate single-crystal layers of $KNbO_3$ for applications in nonlinear optics. For the last method, a SHG coefficient of 5 pm/V, which is one third of the bulk value, has been reported [119], and higher coefficients of almost the bulk value have been measured in samples prepared by MOCVD [120].

10.4.4 Other Materials

In several other photorefractive perovscite crystals, waveguiding layers have been fabricated. These crystals include potassium-tantalate niobate (KTN), $KTa_{1-x}Nb_xO_3$, and barium-strontium titanate (BST), $Ba_{1-x}Sr_xTi_2O_6$. In the KTN crystallographic system, the largest electro-optic coefficients among all photorefractive oxide crystals are found: The value of r_{51} can approach 10^4. Waveguides in this material have been formed by ion-implantation [121]. By PLD thin films of usually polycrystalline BST have been deposited on different substrates like MgO(001) and sapphire, and a large quadratic electro-optic coefficient of $1 \times 10^{15}\,m^2/V^2$ has been measured [122].

10.5 Materials with Tungsten-Bronze Structure

10.5.1 Strontium-Barium Niobate (SBN)

Strontium-barium niobate crystals ($Sr_xBa_{1-x}Nb_2O_6$, $0.25 \leq x \leq 0.75$, SBN) are characterized by particularly large pyro- and piezoelectric, electro- and thermo-optic coefficients, robustness, and an excellent optical quality. The electro-optic coefficients are about ten (SBN61) to forty times (SBN75) larger

than those in $LiNbO_3$. The most widely investigated composition is the congruently melting one, $x = 0.61$ (SBN61). Another interesting composition is the strontium-enriched $x = 0.75$ (SBN75) with a lowered phase transition temperature. The open tungsten bronze structure allows doping with a variety of rare-earth and transition metal materials to improve the photorefractive sensitivity. SBN permits many applications in optical data storage and processing [123, 124], and a lot of fundamental research has been done demonstrating the excellent photorefractive properties of this material [125, 126]. Since the discovery of the photorefractive soliton in 1992/1993 [127, 128], SBN has become the most widely used material in this outstanding research field.

Planar waveguide formation in SBN by He^+ implantation was first mentioned by Youden et al. [105] in 1992, and later was investigated in more detail in [103]. Low-loss waveguides ($0.35\,cm^{-1}$ at the wavelength 632.8 nm) are obtained for low-dose He^+ implantation or intermediate doses using H^+. The photorefractive properties of SBN61 and SBN75 waveguides formed by H^+ or He^+ implantation are investigated in Refs. [95, 129]. When compared to data for the bulk material at the same intensity, the response time for two-wave mixing in SBN waveguides is decreased by one or two orders of magnitude both for H^+ [95] and low-dose He^+ [129] implantation. In the latter work, with an increasing dose of implanted He^+, a strong degradation of the photorefractive properties was observed. High logarithmic gain coefficients of up to $45\,cm^{-1}$ with time constants of the order of milliseconds have been obtained for extraordinarily polarized blue light, adequate cerium doping, and optimized implantation parameters [129].

Polycrystalline SBN thin films of various compositions have been obtained by LPE, rf-sputtering, MOCVD [120], and the sol-gel process. Epitaxial SBN61 [130] and SBN75 [131] films on MgO substrates with high electrooptic coefficients r_{33} of 380 pm/V and 844 pm/V, respectively, have been fabricated by PLD, but only little is known about the optical properties of such films [132].

Planar and channel waveguide formation in SBN substrate crystals has been also performed using sulphur [133] and zinc [134] indiffusion, but the achieved waveguides exhibit high losses greater than $2.5\,cm^{-1}$. Recently, channel waveguides in SBN have been fabricated by a refractive index increase because of the static strain-optic effect [135] and fast electro-optic modulation in the GHz range has been demonstrated [136].

10.5.2 Other Materials

Apart from SBN, waveguides in other tungsten bronze crystals have recently received considerable attention, too. Well known examples are potassium-sodium strontium-barium niobate $(K_yNa_{1-y})_{2A-2}(Sr_xBa_{1-x})_{2-A}Nb_2O_6$ (KNSBN) and barium-strontium titanate-niobate $Ba_{1-x}Sr_xTi_yNb_{2-y}O_6$ (BSTN). Planar waveguides have been fabricated by ion implantation in KNSBN, and two-wave mixing experiments have been performed [137, 138]. Low-loss, strain-induced waveguides have been also formed in BSTN [139].

10.6 Sillenites

Sillenite crystals of the type $Bi_{12}MO_{20}$ with M = Si (BSO), Ge (BGO), and Ti (BTO) possess a large photoconductivity and holographic sensitivity for visible and near-infrared light, which makes these materials attractive candidates for applications of dynamic holography and optical phase conjugation. For the fabrication of waveguides in sillenites, LPE, i.e., the thermally-controlled overgrowth of single-crystal films from the melt on a single-crystalline substrate may be used. When compared to MBE, the uniformity and surface morphology of LPE films are poor, but deposition rates are high. Together with PLD and in part also ion implantation, LPE is the preferred method to form waveguides in the sillenites BGO, BTO, and BSO.

The fabrication of optical waveguides in sillenites has been reported in quite a few papers, however, only little is known about the photorefractive properties of these samples. Waveguiding has been observed in epitaxial BTO films fabricated by LPE on BGO substrates [140], as well as BGO and BSO layers formed by PLD on single-crystalline zirconia and sapphire [141, 142]. For the latter, electrooptic and nonlinear optical properties have been proved [143]. Two-wave mixing in planar BTO waveguides grown on BGO and BSO substrates by LPE has been observed in [144, 145]. To improve the photorefractive properties of these BTO waveguides, the melts have been doped with d-(Cu, Cr, Fe, Co, Ni), p-(Ga) and s-(Ca) elements of the periodic table. The measured electro-optic coefficients as well as the beam coupling gain have been found to be lower than for the bulk material, but high two-beam coupling coefficients up to $8\,cm^{-1}$ have been found for copper doping of BTO layers. An increase of the gain value has been also obtained by applying an external electric AC field along the grating direction [146].

10.7 Applications

Since the first fabrication of optical waveguides in $LiNbO_3$ in 1974, a large number of different optical components based on photorefractive waveguides has been proposed, and devices like spectrometers, optical amplifiers, phase conjugators, reconfigurable optical interconnections, or narrow-bandwidth filters have been experimentally demonstrated. Corresponding to the various applications, quite different requirements of waveguide and photorefractive parameters have to be fulfilled. In the following section, some of the applications of photorefractive waveguides will be presented.

10.7.1 Optical Interconnections

Different types of optical switches and interconnections using photorefractive waveguides have been experimentally investigated. Holographic interconnections in a planar $LiNbO_3$ waveguide have been proposed in [147] and further

developed and experimentally confirmed about ten years later in [148]. In [149] an array of intersecting parallel channel waveguides in $LiNbO_3$, where coupling is obtained via holographic gratings in the overlap regions, has been used. Another method uses an array of reconfigurable photorefractive waveguides for optical interconnections, where either a bulk $LiNbO_3$ crystal is illuminated by an interference fringe pattern [150] or by three dimensional scanning of a focused laser [151, 152]. A recent review of these works can be found in [153]. Very recently reconfigurable optical interconnections have been also realized in the crystal $KNbO_3$. Here optical channel waveguides are formed by illuminating a crystal surface with a focused UV beam using the inter-band photorefractive effect in $KNbO_3$. An even more promising alternative for dynamic interconnections is the use of spatial solitons, which is explained in short in the next subsection.

10.7.2 Spatial Solitons

Since their discovery in 1992/1993, photorefractive spatial solitons have attracted considerable interest [127, 128]. Only low power levels of the order of microwatts are necessary to form these non-diffracting beams. Solitons possess unique properties, for instance in their interaction, which make them attractive for all-optical switches and routers. Chapter 11 of this book extensively treats the interesting properties of photorefractive solitons, so we will here concentrate on special features of photorefractive solitons in waveguides.

In planar waveguides, spatial solitons are formed in a true (1+1)-dimensional medium, thus getting rid of the transverse instability that is inherent to soliton formation in bulk crystals. Moreover, for applications in switching and routing, the planar waveguide's geometry is easily compatible with fiber optics. Photorefractive bright spatial solitons have been formed in $Sr_{0.61}Ba_{0.310}Nb_2O_6$ (SBN) waveguides produced by He^+-implantation [154]. Here, photorefractive solitons can be formed over a wide wavelength range, from visible to telecommunication wavelengths up to 1.5 μm [97]. The suitability for beam steering and forming as well as for switching and routing by interaction of solitons and applications such as *y*-junctions has been demonstrated [155, 156]. Dark photovoltaic solitons have been studied in $LiNbO_3$ planar waveguides fabricated by indiffusion of titanium, iron, and copper [157].

10.7.3 Reflection Filters

In the last few years, fiber Bragg gratings (FBG) have achieved considerable interest for applications as optical sensors for the measurement of, e.g., temperature, vibrations, or mechanical stress, for uses as fiber laser resonators, or for dense wavelength division multiplexing (DWDM). All of these devices make use of the narrow spectral bandwidth of the recorded reflection gratings in photosensitive glass fibers. In some of these devices, the peak reflection

wavelength is adjusted by external mechanical stress on the fiber using piezo drivers.

A promising alternative to FBGs in glass are holographically recorded refractive index gratings in channel waveguides in $LiNbO_3$ [158]. Such single mode waveguides for infrared light around 1.55 μm can be formed by titanium in-diffusion. To increase their holographic sensitivity and light-induced refractive index changes, the samples can additionally be diffusion-doped with either iron or copper. In combination with a thermal fixing technique of the refractive index patterns [21, 159], which makes the gratings insensitive against the erasure with visible light, this allows to design a variety of devices that operate in the infrared wavelength region.

A scheme of the holographic recording geometry is given in Fig. 10.6. Light of the photosensitive blue or green spectral region is used to record a grating for the infrared in a standard two-beam setup using external writing beams. The grating is directed along the c-axis, and for proper choice of the waveguide fabrication parameters the filter works polarization independent. In this way, peak reflectivities exceeding 99.9% and bandwidths of 0.1 nm (FWHM) for a 15 mm-long grating have been obtained. Such gratings are of large interest for application as electrically switchable add-drop-filters in DWDM [158] or for use as mirrors for integrated lasers [21].

10.7.4 Integrated Sagnac-Interferometers

A practical example of integrated optics in $LiNbO_3$ that suffers from photorefractive effects are laser gyros or Sagnac interferometer, respectively, which are used for the precise measurement of small angular velocities with application in car navigation, aviation, or rocket stabilization [160]. In such a device, the light of a coherent polarized light source with frequency ω_0 is split in two parts, then passes a polarization maintaining fiber coil in two opposite directions, and finally the two counterpropagating waves interfere on a photodiode.

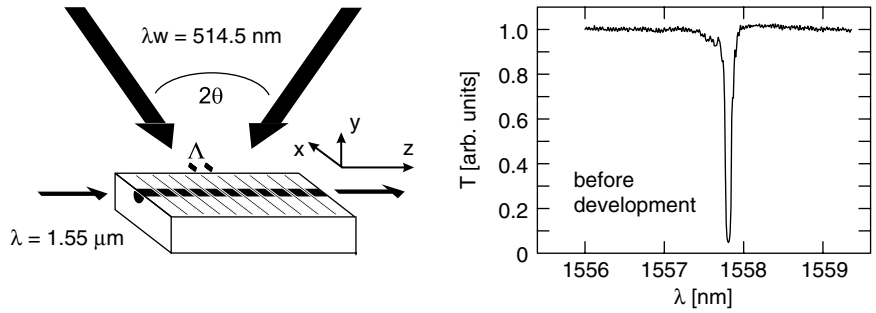

FIGURE 10.6. Holographically recorded reflection filters in $LiNbO_3$: Ti: Cu channel waveguides. a) Geometry for recording and read-out of the grating, and b) typical transmission spectrum $T(\lambda)$ of a 15 mm-long filter.

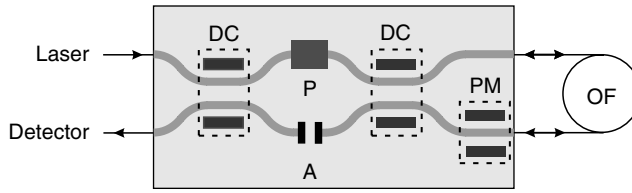

FIGURE 10.7. Example of an integrated Sagnac interferometer for rotation sensing. DC, electrically adjustable directional couplers; P, polarizer; A, light absorbers; PM, phase modulator; OF, optical fiber coil.

When the fiber coil of diameter D and length L rotates with an angular velocity Ω, a phase difference

$$\Delta_\gamma = \frac{LD\omega_0\Omega}{c^2} \tag{10.4}$$

is measured in the output interference signal, where c is the speed of light in vacuum. In a standard configuration, a phase modulator in one arm of the interferometer leads to an additional difference phase modulation of the output signal, which can be used for a closed-loop operation of the Sagnac interferometer.

Because of the high requirements on stability and exact reciprocity of the device and the need for phase modulation of the optical signals, a realization of a compact, integrated optical Sagnac interferometer in $LiNbO_3$ is favorable. Such a component where all optical components are integrated on a single chip is shown in Fig. 10.7. Today, these devices are in use, e.g., in civil and military aviation. However, although much work has been spent on the optimization of design and production techniques, the fabrication yield is still heavily limited and may be as low as about ten percent in some cases, which can be at least in part attributed to undesired photorefractive effects in the $LiNbO_3$ chip [161].

10.8 Conclusions and Outlook

In this chapter, recent results on formation and investigation of photorefractive waveguides have been summarized, and some interesting applications of these samples have been outlined. Further improvement and simplification of the necessary fabrication technologies, e.g., by low-cost thin film deposition, as well as tailored photorefractive properties and geometries of the waveguides, will stimulate future developments in this active research area.

References

1. P. Günter, J.-P. Huignard (Eds.): *Photorefractive Materials and Their Applications I+II*, Topics Appl. Phys., Vol. 61 and 62, Springer-Verlag, Berlin (1998).

2. M.P. Petrov, S.I. Stepanov, A. Khomenko (Eds.): *Photorefractive Crystals in Coherent Optical Systems*, Springer-Verlag, Berlin (1991).
3. An older but excellent review of this topic can be found in V.E. Wood, P.J. Cressman, R.L. Holman, C.M. Verber: in *Photorefractive Materials and Their Applications II*, P. Günter, J.-P. Huignard (Eds.), Topics Appl. Phys., Vol. 62, Springer-Verlag, Berlin (1988).
4. D. Kip: Appl. Phys. B **67**, 131 (1988).
5. A.M. Prokhorov, Y.S. Kuzminov: *Ferroelectric Thin-Film Waveguides in Integrated Optics*, Cambridge International Science, Cambridge (1996).
6. V. Gericke, P. Hertel, E. Krätzig, J.P. Nisius, R. Sommerfeld: Appl. Phys. B **44**, 155 (1987).
7. D. Fluck, J.A. Weiss, S. Brülisauer, P. Günter: Opt. Lett. **19**, 2080 (1994).
8. L. Wan, Y. Yuan, G. Assanto: Opt. Commun. **73**, 439 (1989).
9. L. Wan, Y. Yuan, G. Assanto: Opt. Commun. **74**, 361 (1990).
10. A. Yamada, H. Tamada, M. Saitoh: J. Appl. Phys. **76**, 1776 (1994).
11. P.K. Tien, R. Ulrich: J. Opt. Soc. Am. **60**, 1325 (1970).
12. L. Zhang, P.J. Chandler, P.D. Townsend: Nucl. Instr. and Meth. B **59/60**, 1147 (1991).
13. D. Fluck, D.H. Jundt, P. Günter, M. Fleuster, C. Buchal: J. Appl. Phys. **74**, 6023 (1993).
14. P. Hertel, H.P. Menzler: Appl. Phys. B **44**, 75 (1987).
15. S. Herminghaus, B.A. Smith, J.D. Swalen: J. Opt. Soc. Am. B **8**, 2311 (1991).
16. F. Rickermann, D. Kip, B. Gather, E. Krätzig: phys. stat. sol. (a) **150**, 763 (1995).
17. I. Savatinova, S. Tochev, R. Todorov, M.N. Armenise, V.M.N. Passaro, C.C. Ziling: J. Lightwave Technol. **14**, 403 (1996).
18. T. Yuhara, K. Tada, Y.-S. Li: J. Appl. Phys. **71**, 3966 (1992).
19. P.G. Suchoski, T.K. Findakly, F.J. Leonberger: Opt. Lett. **13**, 1050 (1988).
20. T. Suzuki, O. Eknoyan, H.F. Taylor: J. Lightwave Technol. **11**, 285 (1993).
21. B.K. Das, R. Ricken, W. Sohler: Appl. Phys. Lett. **82**, 1515 (2003).
22. A. Yamada, H. Tamada, M. Saitoh: J. Cryst. Growth **132**, 48 (1993).
23. F. Gitmans, Z. Sitar, P. Günter: Vacuum **46**, 939 (1995).
24. Y. Kondo, T. Kouyama, K. Ohno, M. Tsuji, M. Nakamura, Y. Fujii: Jpn. J. Appl. Phys. **33**, L338 (1994).
25. W.S. Hu, Z.G. Liu, Y.-Q. Lu, S.N. Zhu, D. Feng: Opt. Lett. **21**, 946 (1996).
26. S. Fries, P. Hertel, H.P. Menzler: phys. stat. sol. (a) **108**, 449 (1988).
27. V.V. Atuchin, K.K. Ziling, D.P. Shipilova: Sov. J. Quant. Electron. **14**, 671 (1984).
28. R.J. Holmes, D.M. Smyth: J. Appl. Phys. **55**, 3531 (1984).
29. M. De Sario, M.N. Armenise, C. Canali, A. Carnera, P. Mazzoldi, G. Celotti: J. Appl. Phys. **57**, 1482 (1985).
30. R.V. Schmidt, I.P. Kaminow: Appl. Phys. Lett. **25**, 458 (1974).
31. W.M. Young, R.S. Feigelson, M.M. Fejer, M.F.J. Digonnet, H.J. Shaw: Opt. Lett. **16**, 995 (1991).
32. Y. Shigematsu, M. Fujimura, T. Suhara: Jap. J. Appl. Phys. **41**, 4825 (2002).
33. J.M. Hammer, W. Phillips: Appl. Phys. Lett. **24**, 545 (1974).
34. A.D. Novikov, S.G. Odoulov, V.M. Shandarov, S.M. Shandarov: Sov. Phys. Tech. Phys. **33**, 969 (1988).
35. D. Kip, B. Gather, H. Bendig, E. Krätzig: phys. stat. sol. (a) **139**, 241 (1993).
36. J.L. Jackel, C.E. Rice, J.J. Veselka: Ferroelectrics **50**, 165 (1983).

37. J.M. Cabrera, J. Olivares, M. Carrascosa, J. Rams, R. Müller, E. Dieguez: Adv. Phys. **45**, 349 (1996).
38. V.A. Ganshin, Y.N. Korkishko, T.V. Morozova, V.V. Saraikin: phys. stat. sol. (a) **114**, 457 (1989).
39. V.V. Atuchin, T.I. Zakharyash: Sov. Phys. Tech. Phys. **29**, 584 (1984).
40. W.Y. Hsu, C.S. Willand, V. Gopalan, M. Gupta: Appl. Phys. Lett. **61**, 2263 (1992).
41. K. Tada, T. Murai, T. Nakabayashi, T. Iwashima, T. Ishikawa: Jpn. J. Appl. Phys. **26**, 503 (1987).
42. K. Yamamoto, T. Taniuchi: J. Appl. Phys. **70**, 6663 (1991).
43. R.A. Becker: Appl. Phys. Lett. **43**, 131 (1986).
44. Y.N. Korkishko, V.A. Fedorov: J. Appl. Phys. **82**, 99 (1997).
45. M. Minakata, K. Kumagi, S. Kawakami: Appl. Phys. Lett. **49**, 992 (1986).
46. N. Goto, G.L. Yip: Appl. Opt. **28**, 60 (1989).
47. A. Mendez, G. De la Paliza, A. Garcia-Cabanes, J.M. Cabrera: Appl. Phys. B **73**, 485 (2001).
48. H. Ahlfeldt, F. Laurell, G. Arvidsson: Electron. Lett. **29**, 819 (1993).
49. Y.N. Korkishko, V.A. Federov, A.N. Alkaev, F. Laurell: Appl. Phys. B **73**, 519 (2001).
50. J. Rams, J.M. Cabrera: J. Opt. Soc. Am. B **16**, 401 (1999).
51. R. Osellame, R. Ramponi, M. Marangoni, V. Russo: Electron. Lett. **36**, 431 (2000).
52. D.H. Tsou, M.H. Chou, P. Santhanaraghavan, Y.H. Chen, Y.C. Huang: Mat. Chem. Phys. **78**, 474 (2002).
53. S.M. Kostritskii, D. Kip, E. Krätzig: Appl. Phys. B **65**, 517 (1997).
54. R. Göring, Z. Yuan-Ling, S. Steinberg: Appl. Phys. A **55**, 97 (1992).
55. K. Buse: Appl. Phys. B **64**, 273 (1997).
56. F. Jermann, J. Otten: J. Opt. Soc. Am. B **10**, 2085 (1993).
57. Y. Kondo, S. Miyaguchi, A. Onoe, Y. Fujii: Appl. Opt. **33**, 3348 (1994).
58. J. Jackel, A.M. Glass, G.E. Petersen, C.E. Rice, D.H. Olsen, J.J. Veleska: J. Appl. Phys. **55**, 269 (1984).
59. J. Olivares, E. Dieguez, F.J. Lopez, J.M. Cabrera: Appl. Phys. Lett. **61**, 624 (1992).
60. J.J. Amodei, D.L. Staebler: Appl. Phys. Lett. **18**, 540 (1971).
61. A. Mendez, A. Garcia-Cabanes, M. Carrascosa, J.M. Cabrera: Opt. Mat. **18**, 111 (2001).
62. A. Mendez, A. Garcia-Cabanes, M. Carrascosa, J.M. Cabrera: J. Opt. Soc. Am. B **17**, 1412 (2000).
63. S. Tan, T. Gilbert, C.-Y. Hung, T.E. Schlesinger, M. Migliuolo: J. Appl. Phys. **79**, 3548 (1996).
64. K. Nashimoto, M.J. Cima: Mater. Lett. **10**, 348 (1991).
65. M. Aguilar, M. Carrascosa, F. Agullo-Lopez, L.F. Magana: J. Appl. Phys. **78**, 4840 (1995).
66. I.I. Itkin, S.M. Shandarov: Sov. Phys. Tech. Phys. **35**, 1317 (1990).
67. P.G. Kazansky: IEEE J. Quant. Electron. **QE-25**, 736 (1989).
68. D. Kip, R. Fink, T. Bartholomäus, E. Krätzig: Opt. Commun. **95**, 33 (1993).
69. D. Kip, F. Rickermann, E. Krätzig: Opt. Lett. **20**, 1139 (1995).
70. A.D. Novikov, S.G. Odoulov, V.M. Shandarov, E.S. Shandarov, S.M. Shandarov: J. Opt. Soc. Am. B **8**, 1298 (1991).
71. V.L. Popov, E.S. Shandarov, S.M. Shandarov: J. Opt. Soc. Am. B **9**, 1661 (1992).
72. D. Kip, E. Krätzig: Opt. Lett. **17**, 1563 (1992).

73. E.M. Zolotov, P.G. Kazansky, V.A. Chernykh: Sov. Tech. Phys. Lett. **7**, 397 (1981).
74. I.I. Itkin, S.M. Shandarov: Sov. Tech. Phys. Lett. **16**, 357 (1990).
75. Y. Solomonov, S.M. Shandarov, V.M. Shandarov: Ferroelectrics **201**, 195 (1997).
76. V.I. Belinicher, B.I. Sturman: Sov. Phys: Uspheki **23**, 199 (1980).
77. S.G. Odoulov: Sov. Phys. JETP Lett. **35**, 10 (1982).
78. T. Fujiwara, X. Cao, R. Srivastava, R.V. Ramaswamy: Appl. Phys. Lett. **61**, 743 (1992).
79. T. Fujiwara, R. Srivastava, X. Cao, R.V. Ramaswamy: Opt. Lett. **18**, 346 (1993).
80. S. Steinberg, R. Göring, T. Hennig, A. Rasch: Opt. Lett. **20**, 683 (1995).
81. M. Rottschalk, T. Bachmann, S. Steinberg, J.-P. Ruske: Opt. Commun. **106**, 187 (1994).
82. E.E. Robertson, R.W. Eason, Y. Yokoo, P.J. Chandler: Appl. Phys. Lett. **70**, 2094 (1997).
83. D. Eger, M.A. Arbore, M.M. Fejer, M.L. Bortz: J. Appl. Phys. **82**, 1998 (1997).
84. P.J. Matthews, A.R. Mickelson: J. Appl. Phys. **71**, 5310 (1992).
85. D.B. Maring, R.F. Tavlykaev, R.V. Ramaswamy, S.M. Kostritskii: J. Opt. Soc. Am. B **19**, 1575 (2002).
86. O. Eknoyan, H.F. Taylor, W. Matous, T. Ottinger, R.R. Neurgaonkar: Appl. Phys. Lett. **71**, 3051 (1997).
87. Y. Kondo, Y. Fujii: Jpn. J. Appl. Phys. **34**, L365 (1995).
88. D. Kip, T. Bartholomäus, P.M. Garcia, E. Krätzig: J. Opt. Soc. Am. B **11**, 1737 (1994).
89. S. Kostritskii, D. Kip: phys. stat. sol. (a) **169**, 171 (1998).
90. H. Xie, W.-H. Hsu, R. Raj: J. Appl. Phys. **77**, 3420 (1995).
91. P. Moretti, P. Thevenard, G. Godefroy, R. Sommerfeld, P. Hertel, E. Krätzig: phys. stat. sol. (a) **117**, K85 (1990).
92. T. Bremer, W. Heiland, B. Hellermann, P. Hertel, E. Krätzig, D. Kollewe: Ferroelectrics Lett. **9**, 11 (1988).
93. D. Kip, S. Aulkemeyer, P. Moretti: Opt. Lett. **20**, 1256 (1995).
94. P. Townsend, P.J. Chandler, L. Zhang: *Optical Effects of Ion Implantation*, Cambridge University, Cambridge, UK (1994).
95. E.E. Robertson, R.W. Eason, M. Kaczmarek, P.J. Chandler, X. Huang: Opt. Lett. **21**, 641 (1996).
96. S. Brülisauer, D. Fluck, P. Günter, L. Beckers, C. Buchal: Opt. Commun. **153**, 375 (1998).
97. M. Wesner, C. Herden, D. Kip, E. Krätzig, P. Moretti: Opt. Commun. **188**, 69 (2001).
98. A. Petraru, J. Schubert, M. Schmid, Ch. Buchal: Appl. Phys. Lett. **81**, 1375 (2002).
99. P.D. Townsend: Nucl. Instr. and Meth. B **46**, 18 (1990).
100. F.P. Strohkendl, D. Fluck, P. Günter, R. Irmscher, C. Buchal: Appl. Phys. Lett. **59**, 3354 (1991).
101. D. Fluck, P. Günter, M. Fleuster, C. Buchal: J. Appl. Phys. **72**, 1671 (1992).
102. T. Tschudi, A. Herden, J. Goltz, H. Klumb, F. Laeri, J. Albers: IEEE J. Quant. Electron. **QE-22**, 1493 (1986).
103. Z. Zhang, Y. Zhang, C. Yang, J. Kang, S. Zheng, Y. Zhu, Y. Chen, X. Wu, P. Fu: J. Opt. Soc. Am. B **11**, 1991 (1994).
104. P. Moretti, P. Thevenard, R. Sommerfeld, G. Godefroy: Nucl. Instr. and Meth. B **59/60**, 1228 (1991).

105. K.E. Youden, S.W. James, R.W. Eason, P.J. Chandler, L. Zhang, P.D. Townsend: Opt. Lett. **17**, 1509 (1992).
106. P. Mathey, A. Dazzi, P. Jullien, D. Rytz, P. Moretti: J. Opt. Soc. Am. B **18**, 344 (2001).
107. S.W. James, K.E. Youden, P.M. Jeffrey, R.W. Eason, P.J. Chandler, L. Zhang, P.D. Townsend: Opt. Lett. **18**, 1138 (1993).
108. S.W. James, K.E. Youden, P.M. Jeffrey, R.W. Eason, P.J. Chandler, L. Zhang, P.D. Townsend: Appl. Opt. **32**, 5299 (1993).
109. A. Ito, A. Machida, M. Obara: Jpn. J. Appl. Phys. **36**, L805 (1997).
110. L. Beckers, J. Schubert, W. Zander, J. Ziesmann, A. Eckau, P. Leinenbach, C. Buchal: J. Appl. Phys. **83**, 3305 (1998).
111. D.M. Gill, B.A. Block, C.W. Conrad, B.W. Wessels, S.T. Ho: Appl. Phys. Lett. **69**, 2968 (1996).
112. D.M. Gill, C.W. Conrad, G. Ford, B.W. Wessels, S.T. Ho: Appl. Phys. Lett. **71**, 1783 (1997).
113. P. Günter: Phys. Rep. **93**, 199 (1982).
114. F.P. Strohkendl, P. Günter, C. Buchal, R. Irmscher: J. Appl. Phys. **69**, 84 (1991).
115. T. Pliska, D. Fluck, P. Günter, L. Beckers, C. Buchal: J. Opt. Soc. Am. B **15**, 628 (1998).
116. S. Brülisauer, D. Fluck, P. Günter: Electron. Lett. **31**, 312 (1995).
117. S. Brülisauer, D. Fluck, P. Günter, L. Beckers, C. Buchal: J. Opt. Soc. Am. B **13**, 2544 (1996).
118. M. Zha, D. Fluck, P. Günter, M. Fleuster, C. Buchal: Opt. Lett. **18**, 577 (1993).
119. S. Schwyn, H.W. Lehmann, P. Günter: Appl. Phys. Lett. **61**, 373 (1992).
120. M.J. Nystrom, B.W. Wessels, W.P. Lin, G.K. Wong, D.A. Neumayer, T.J. Marks: Appl. Phys. Lett. **66**, 1726 (1995).
121. D. Fluck, R. Gutmann, P. Günter, R. Irmscher: J. Appl. Phys. **70**, 5147 (1991).
122. D.Y. Kim, S.E. Moon, E.K. Kim, S.J. Lee, J.J. Choi, H.E. Kim, S.I. Kwun: J. Korean Phys. Soc. **42**, S1347 (2003).
123. M.D. Ewbank, R.R. Neurgaonkar, W.K.Cory, J. Feinberg: J. Appl. Phys. **62**, 374 (1987).
124. J. Ma, T. Chang, J. Hong, R.R. Neurgaonkar, G. Barbastathis, D. Psaltis: Opt. Lett. **22**, 1116 (1997).
125. G.L. Wood, W.W. Clark III, M.J. Miller, E.J. Sharp, G.J. Salamo, R.R. Neurgaonkar: IEEE J. Quant. Electron. **QE-23**, 2126 (1987).
126. R.A. Vazquez, M.D. Ewbank, R.R. Neurgaonkar: Opt. Commun. **80**, 253 (1991).
127. M. Segev, B. Crosignani, A. Yariv, B. Fischer: Phys. Rev. Lett. **68**, 923 (1992).
128. G. Duree, J.L. Schultz, G. Salamo, M. Segev, A. Yariv, B. Crosignani, P. DiPorto, E. Sharp, R.R. Neurgaonkar: Phys. Rev. Lett. **71**, 533 (1993).
129. D. Kip, B. Kemper, I. Nee, R. Pankrath, P. Moretti: Appl. Phys. B **65**, 511 (1997).
130. Y.Y. Zhu, R.F. Xiao, G.K.L. Wong: J. Appl. Phys. **82**, 4908 (1997).
131. P. Tayebati, D. Trivedi, M. Tabat: Appl. Phys. Lett. **69**, 1023 (1996).
132. X.L. Guo, Z.G. Liu, S.N. Zhu, T. Yu, S.B. Xiong, W.S. Hu: J. Cryst. Growth **165**, 187 (1996).
133. O. Eknoyan, C.H. Bulmer, H.F. Taylor, W.K. Burns, A.S. Greenblatt, L.A. Beech, R.R. Neurgaonkar: Appl. Phys. Lett. **48**, 13 (1986).
134. O. Eknoyan, V.P. Svenson, J.D. Quinn, R.R. Neurgaonkar: Appl. Phys. Lett. **59**, 28 (1991).

135. J.M. Marx, Z. Tang, O. Eknoyan, H.F. Taylor, R.R. Neurgaonkar: Appl. Phys. Lett. **66**, 274 (1995).
136. J.M. Marx, O. Eknoyan, H.F. Taylor, R.R. Neurgaonkar: IEEE Phot. Technol. Lett. **8**, 1024 (1996).
137. F. Lu, M. Q. Meng, K. M. Wang, W. Li, L. Z. Chai, Y. R. Wang, H. C. Chen, D.Y. Shen: Opt. Commun. **140**, 204 (1997).
138. F. Lu, M.Y. Meng, K.M. Wang, X.D. Liu, H.C. Chen, D.Y. Shen: Opt. Lett. **22**, 163 (1997).
139. J.M. Marx, O. Eknoyan, H.F. Taylor, Z. Tang, R.R. Neurgaonkar: Appl. Phys. Lett. **67**, 1381 (1995).
140. E.I. Leonov, S.E. Khabarov, M.S. Vershinin, V.A. Gusev, V.M. Orlov, L.G. Khokha: Sov. Phys. Tech. Phys. **30**, 1307 (1985).
141. K.E. Youden, R.W. Eason, M.C. Gower, N.A. Vainos: Appl. Phys. Lett. **59**, 1929 (1991).
142. T. Okada, F. Yahiro, H. Uetsuhara, Y. Nakata, M. Maeda, S. Higuchi, K. Ueda: Appl. Phys. A **69**, 723 (1999).
143. V. Chevrier, A. Inam, S. Etemad, D. Harris, J.C. Launay: Technical Digest of the Topical Meeting on "Photorefractive Materials, Effects, and Devices 1993," (PRM '93), Kiev, Ukraine, 220 (1993).
144. Y.F. Kargin, I.V. Tsiar, Y.R. Salikaev, S.M. Shandarov: Tech. Phys. Lett. **20**, 1997 (1994).
145. M.N. Frolova, M.V. Borodin, S.M. Shandarov, V.M. Shandarov, Y.F. Kargin, A. Egorysheva, and D. Kip: Europhysics Conference Abstracts Vol. 27E, CF3-6-TUE (2003).
146. Y. Salikaev, S.M. Shandarov, Y. Kargin: Proc. SPIE **2795**, 203 (1996).
147. T. Jannson: J. Opt. Soc. Am. **71**, 342 (1981).
148. D.J. Brady, D. Psaltis: Appl. Opt. **30**, 2324 (1991).
149. L.B. Aronson, L. Hesselink: Opt. Lett. **15**, 30 (1990).
150. O. Matoba, K. Itoh, Y. Ichioka: Opt. Lett. **21**, 122 (1996).
151. K. Itoh, O. Matoba, Y. Ichioka: Opt. Lett. **19**, 652 (1994).
152. O. Matoba, K. Itoh, Y. Ichioka: Opt. Eng. **35**, 2175 (1996).
153. O. Matoba, K. Itoh, K. Kuroda: Proc. IEEE **87**, 2030 (1999).
154. D. Kip, M. Wesner, V.M. Shandarov, P. Moretti: Opt. Lett. **23**, 921 (1998).
155. D. Kip, M. Wesner, C. Herden, V. Shandarov: Appl. Phys. B **68**, 971 (1999).
156. D. Kip, C. Herden, M. Wesner: Ferroelectrics **274**, 135 (2002).
157. V. Shandarov, D. Kip, M. Wesner, J. Hukriede: J. Optics A **2**, 500 (2000).
158. J. Hukriede, D. Runde, D. Kip: J. Phys. D: Appl. Phys. **36**, R1 (2003).
159. J. Hukriede, I. Nee, D. Kip, E. Krätzig: Opt. Lett. **23**, 1405 (1998).
160. K.T.V. Grattan, B.T. Meggit: *Optical Fiber Sensor Technology. Volume 2: Devices and Technology*, Chapman & Hall, London (1998).
161. I.A. Andronova, G.B. Malykin: Phys. Uspekhi **45**, 793 (2002).

11

Photorefractive Solitons

E. DelRe[1], M. Segev[2], D. Christodoulides[3], B. Crosignani[4], and G. Salamo[5]

[1] Dipartimento di Ingegneria Elettrica e dell'Informazione, Università dell'Aquila, 67040 Monteluco di Roio (L'Aquila), Italy
edelre@ing.univaq.it
[2] Physics Department, Technion, Haifa, Israel
msegev@tx.technion.ac.il
[3] School of Optics-CREOL, University of Central Florida, Orlando, FL 32816-2700, USA
demetri@creol.ucf.edu
[4] Dipartimento di Fisica, Universit*à* dell'Aquila, 67010 L'Aquila, Italy and Istituto Nazionale Fisica della Materia - UdR Roma "La Sapienza", 00185 Roma, Italy
bruno.crosignani@aquila.infn.it
[5] Physics Department, University of Arkansas, Fayetteville, AR 72703, USA
salamo@uark.edu

This chapter is dedicated to Galit and Ofer Staier, who have lost their son Assaf (11) and four other family members in the terror attack at the Maxim Restaurant in Haifa on October 4, 2003.

11.1 Introduction

Solitons are universal phenomena that appear in a wealth of systems in nature. The past few decades have witnessed their identification and observation in diverse physical systems: shallow and deep water waves, charge density waves in plasma, sound waves in liquid helium, matter waves in Bose-Einstein condensates, excitations on DNA chains, "branes" at the end of open strings in superstring theory, domain walls in supergravity, and many more. Solitons can even appear for electromagnetic waves in *vacuum*, where they are supported by QED nonlinearities. And, of course, in optics, where solitons were originally discovered as temporal solitons in optical fibers [1, 2]. In the spatial optical domain, solitons manifest themselves in a large variety of settings (for reviews of optical spatial solitons, see Refs. [3, 4, 5, 6]). In all these diverse systems, which vary in every aspect from size to dimensionality, from underlying forces to physical mechanisms, propagation leads to a family of nonlinear waves—solitons—that have the same, universal, features: They are all self-trapped entities possessing particle-like behavior.

In this chapter, we outline the mechanisms through which photorefraction can support optical spatial solitons (for a specific review, see pages 61–125 in [6]), give an account of the development of the main underlying ideas, and describe the associated phenomenology. Since the discovery of photorefractive solitons in 1992 [7], they have become one of the most important experimental

means to study universal soliton features. The rich diversity of photorefractive effects has allowed experimental investigations into a large variety of soliton phenomena, many of which have been the *first* observation in any soliton-supporting system in nature. For example, it was with photorefractive solitons that specific interaction effects, such as 3D soliton spiraling, fission, and annihilation, were first demonstrated. Likewise, random-phase (or incoherent) solitons were first observed in photorefractives, and also multimode solitons, both in 1D and in 2D. And, more recently, solitons in two-dimensional nonlinear photonic lattices were first demonstrated in photorefractives, the lattice itself being optically induced in real-time. The intrinsic complexity of photorefractive effects, being driven by several charge transport mechanisms, utilizing linear and quadratic electro-optic effects, and having a polarization-dependent tensorial behavior, contributes in giving rise to the rich phenomenology underlying photorefractive solitons. Much is understood now about the formation processes of the various types of photorefractive solitons, and many of the parameters can be controlled individually: At the same time, numerous questions are still open. Research on solitons in photorefractives has also introduced a number of new ingredients to photorefractive studies at large. For example, understanding the propagation of beams in photorefractives, including the formation of self-oscillators (e.g., the so-called "double phase conjugator") has considerably benefited from the understanding gained in photorefractive soliton research. Likewise, exploring spatially-localized effects that emerge and find their full realization directly *within* the sample, such as instabilities and spontaneous pattern formation, with and without a cavity, are now understood through the explicit connection between solitons and modulation instability [6]. In this chapter, we provide an updated overview on the fascinating phenomenon of photorefractive solitons.

11.2 The Discovery of Solitons in Photorefractives

In the wake of renewed interest in soliton propagation, triggered by studies of temporal solitons, the early 1990s saw an intense effort aimed at finding accessible physical systems in which to experimentally investigate spatial solitons. "Conventional" schemes relying on the Optical Kerr effect presented crippling limitations connected to the extremely high optical intensities involved, and suffering from the fundamental constraints associated with the instabilities and catastrophic collapse of Kerr solitons in bulk media (a process which can be arrested in some systems [8]). Motivated by the strong nonlinear response of photorefractive crystals, at low optical intensities, M. Segev, B. Crosignani, and A. Yariv, proposed in 1992 the first photorefraction-based self-trapping mechanism. This embryonic idea sets the beginning of the field, and, indeed, of our description [7].

A spatial soliton is a beam that, by virtue of a robust balance between diffraction and nonlinearity, does not change its shape during propagation. A

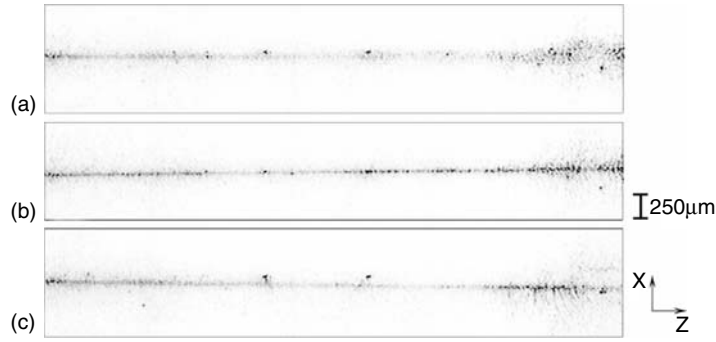

FIGURE 11.1. Top view of spurious scattered light produced by transient photorefractive solitons in a biased sample of potassium-lithium-tantalate-niobate (KLTN). (a) Linear diffraction from an input Full-Width-Half-Maximum (FWHM) of 6 μm to 150 μm. (b-c) Solitons formed with opposite values of external field. Taken from [14].

direct observation of a spatial soliton in photorefractives is shown in Fig. 11.1. Before the discovery of photorefractive solitons, nonlinear optics in photorefractives was centered on diffusion-driven wave-mixing schemes, typically resulting in exchanges between the interacting waves, a mechanism at the heart of photorefractive self-oscillation and "passive" phase conjugators. At that time, other settings, which exhibited strong phase-coupling (and much lower energy-exchange), attracted much less interest. Furthermore, diffusion-driven photorefractive wave-mixing is typically accompanied by massive amplification of scattered noise (the so-called "beam fanning"). During the fanning process, energy is transferred from the incident beam(s) into modes not present in the launch, resulting in a highly delocalized state: the exact *opposite* of self-localization effects that are at the heart of solitary waves. Segev et al. [7] argued that since wave-mixing was intrinsically accompanied by a mutual phase-modulation, one could find a condition in which the plane-wave components of a diffracting beam could mix so as to lead to a trapping self-phase modulation: Their mutual exchange could compensate for the linear dephasing between the plane-wave components of a beam, and thus counteract diffraction altogether. They observed that, in contrast to schemes where the main mixing agent is diffusion, leading to the highly asymmetric fanning process, a symmetric mutual phase-modulation could be achieved through the application of an *external bias field*. They concluded that, when the diffusion space-charge field could be neglected with respect to the external bias field, a symmetric self-focusing occurs and self-trapping effects should emerge, whereas fanning would have a minute effect [9].

It is essential to achieve phase-coupling that is symmetric with respect to the propagation axis. In one simple scheme to do that, the beam should be launched in a zero-cut uniaxial sample along the ordinary axis a, with the external biasing field E_0 applied along the poling optical axis c, through two electrodes brought to a relative potential V. An optimal arrangement was identified in Stontium-Barium-Niobate (SBN) doped with rhodium impurities.

Characterized by an $r_{33} \simeq 220\,pm/V$, for an extraordinary c polarized beam launch, index modulations of the order of $|\Delta n| \simeq (1/2)n^3 r_{33} E_0 \sim 2 - 5 \cdot 10^{-4}$ for achievable fields of the order of $E_0 \sim 1 - 3\,\mathrm{kV/cm}$ could be reached, a nonlinearity sufficient to support the formation of a $10\,\mu m$ wide soliton.

The first pioneering experiments, reported in [10] were carried out with the setup shown in Fig. 11.2. In relating the first results, we more often delve upon details of transient—as opposed to steady-state—effects, and miss the main and revolutionary point: Where no previous phenomenology even hinted at self-focusing, these first experiments indicated, unmistakably, that a visible continuous-wave beam propagating in a biased sample would actually self-trap, the ensuing spatial soliton being readily accessible to direct observation (see Fig. 11.1). These pioneering results established that very narrow beams launched in a properly-biased photorefractive crystal would self-trap, and propagate in a robust fashion, undistorted by fanning and other noise sources in the crystal or even fairly large deviations from optimal launch conditions [11]. For example, it was established that a $15\,\mu m$ sized continuous-wave 457 nm μW beam would not suffer fanning and self-trap for external fields from 400–500 V/cm. This observation led to a rapid series of predictions and experiments, which now form the phenomenological basis of photorefractive spatial solitons [11, 12, 13].

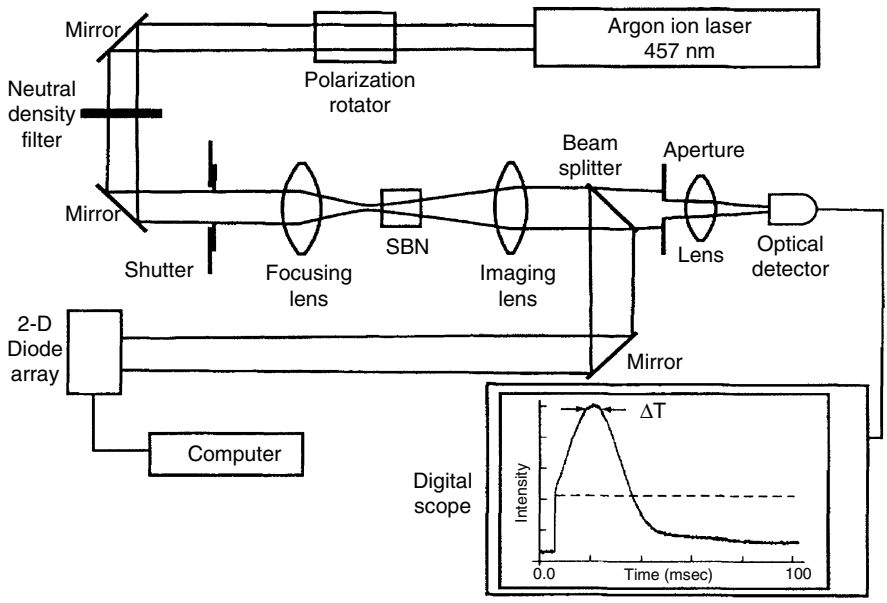

FIGURE 11.2. The original soliton observation scheme, as reported in [10]. The extraordinarily-polarized launch beam is focused at the input facet. Transient dynamics were detected recording the output intensity transmitted through an appropriate aperture positioned before the output detector.

As often occurs when scientific progress is in action, those first experiments posed more questions that answers. First, the results indicated a *transient* self-trapping process (see insert in Fig. 11.2), during a time window of several hundreds of milliseconds, *not* characterized by stringent existence conditions (as would have been expected for normal self-trapping, where diffraction is exactly balanced by a specific value of nonlinearity). On the contrary, the beam intensity and the applied bias field, two parameters determining the strength of the nonlinear index change, could be considerably varied without significant changes in self-trapping. But even more astonishingly, the tentative launch of two-dimensional (circular) beam led to its stable self-trapping. This at once indicated that the underlying nonlinear mechanism was not Kerr-like, since the catastrophic collapse associated with self-focusing in Kerr media did not occur. For some reason, the intrinsic anisotropy of the light-induced space-charge-field, resulting both from the application of an external bias along one transverse direction only, and the directionally resolved electro-optic response, allowed for a two-dimensional soliton [10, 11, 12]. This observation of a two-dimensional soliton in a bulk medium has attracted much interest yet also much debate. At the same time, the transient nature was generally looked upon as an undesired and limiting effect. It cast a shadow both as to the nature of the interaction, but more importantly, as to its stability. Transient effects of the sort had a history in photorefraction, and they were attributed to charge accumulation in dark regions of the sample of the photoexcited charge, depleting illuminated portions and possibly screening external bias.

This triggered the idea that the transient nature of the self-trapping was an effect of charge accumulation screening E_0: Free-charges would be photoexcited across the beam profile, and, drifting in the external field, would reach the bordering dark regions, and get trapped there. These trapped charges would give rise to an internal (space-charge) field with a polarity opposite to E_0. In SBN, this lowering (screening) of the applied field at the illuminated regions would locally lead to electro-optic lensing. The decay of this (induced) lens with time would then be a consequence of the fact that charge would continue to separate until E_0 was totally screened, thereby saturating and flattening the induced "lens". In this, investigators found the solution: They would foresee a compensating mechanism through which accumulated charge could be eliminated by homogeneously illuminating the sample, which amounts to increasing the dark sample conductivity (see Fig. 11.3). On the basis of the relative intensity of the beam to the background, there would exist a dynamic equilibrium leading to a steady-state lensing effect [15, 16, 17, 18]. Photorefractive solitons have since been observed in SBN, BSO, BGO, BTO, $BaTiO_3$, $LiNbO_3$, InP, CdZnTe, KLTN, $KNbO_3$, polymers and organic glass.

As the model was reformulated on this new, and to some extent simpler, screening idea, foreseeing the artificial enhancement of crystal dark conductivity, David Iturbe-Castillo et al. [19] reported steady-state self-focusing, using a homogeneous illumination to free accumulated charge. Finally, Shih et al. [20, 21] and Kos et al. [22] were able to observe this nontransient (steady-state)

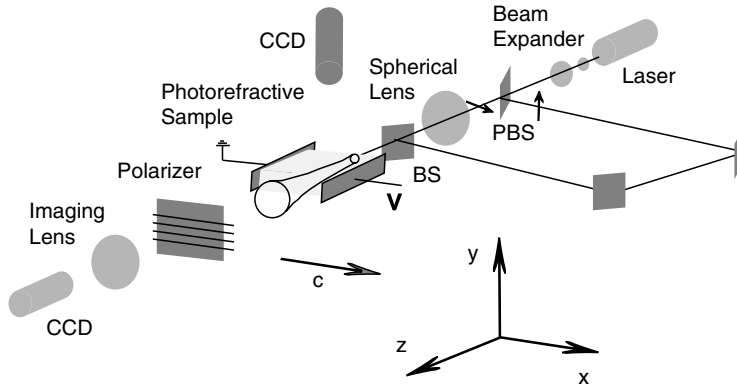

FIGURE 11.3. A scheme to generate screening solitons [20]. The extraordinarily-polarized soliton-forming beam is copropagating with an ordinarily-polarized beam of uniform intensity.

soliton phenomenology and relate it to the new model. This type of self-trapping is since termed a *screening soliton*, and constitutes the most commonly studied type of photorefractive soliton. Its explanation cannot rely on the linearized equations commonly-used to describe the interaction between plane waves in photorefractives.

11.3 A Saturable Nonlinearity

The formulation of a descriptive and predictive theory for photorefractive solitons involves aspects and theoretical tools that differ from those employed in traditional wave-mixing theories. First, no periodic structure is present, and second, in most configurations, all the physical variables vary across the beam profile by a large fraction (e.g., from peak to zero intensity) such that the modulation cannot be treated as a small perturbation. However, steady-state photorefractive solitons have two intrinsic symmetries that reduce the problem: They are evidently time-independent, and their intensity I is independent of the propagation coordinate z. Yet the heart of complexity is nonlinearity, and even for a z-invariant photoionizing intensity I, there is still a wide range of parameters, of which only a small subset can support solitons.

In order to formulate a semi-analytic theory, a one-dimensional reduction can be implemented: The beam should be such that no y-dynamics emerge, the soliton intensity being solely x-dependent [$I(x)$]. Experimentally, this was achieved by launching a beam focused down through a cylindrical lens, and quite similarly, this has led to quasi-steady-state self-trapping in the absence of background [12], and to steady-state screening solitons for appropriate values of E_0 (see Fig. 11.4) [22].

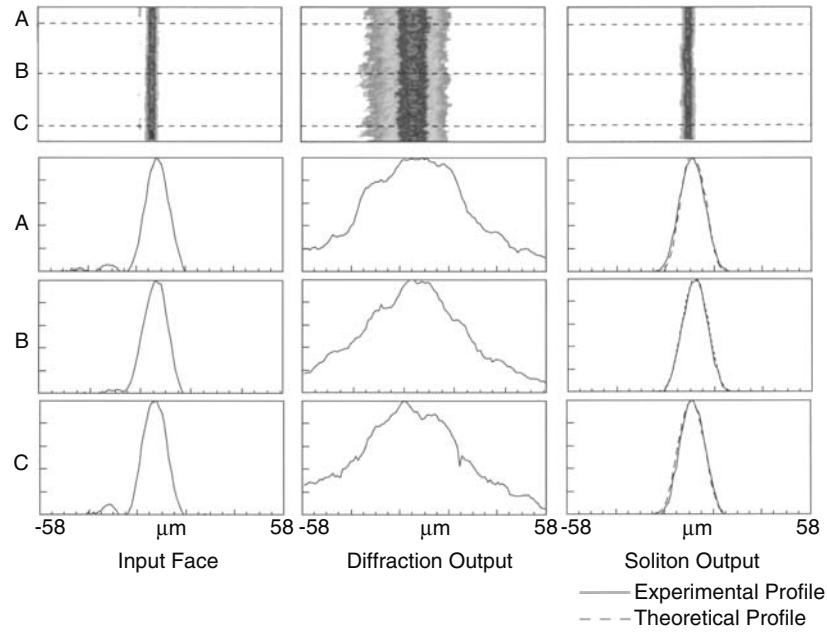

FIGURE 11.4. A one dimensional soliton observed in biased SBN. Top: Input intensity distribution, output linear diffraction (no bias), and output self-trapped beam. Center and bottom: Profiles. As reported in [22].

In fact, in many aspects, these one-dimensional (stripe) waves, generally termed one-plus-one dimensional screening solitons [(1+1D)], share a similar behavior to that of their needle-like counterparts, which are therefore called two-plus-one-dimensional screening solitons [(2+1D)]. Although (2+1)D self-trapping in photorefractive media is still not fully theoretically understood (see Section 11.4), the theory of (1+1)D photorefractive solitons [15, 16, 17, 18] constitutes the basic confirmation that photorefraction supports self-trapping.

In most conditions of interest, the optical intensity distribution $I(x)$ is such that, for an electron-dominated photorefraction, the resulting concentration of photoexcited electrons N, the concentration of acceptor impurities N_a, and the concentration of donor impurities N_d follow the scaling $N << N_a << N_d$. Under these generally valid assumptions, the space-charge field E is related to the optical intensity I through the nonlinear differential equation [23]

$$\boldsymbol{E}(I_b + I)\frac{1}{1 + \dfrac{\epsilon}{N_a q}\dfrac{d\boldsymbol{E}}{dx}} + \frac{k_b T}{q}\frac{d}{dx}\left((I_b + I)\frac{1}{1 + \dfrac{\epsilon}{N_a q}\dfrac{d\boldsymbol{E}}{dx}}\right) = g. \qquad (11.1)$$

Here, ϵ is the sample dielectric constant, q is the electron charge, k_b is the Boltzmann constant, T is the temperature, and g is a constant related to the boundary conditions, i.e., to the voltage V applied on the x-facets L_x apart. I_b is the effective background illumination, the homogeneous optical intensity that controls the conductivity of the crystal. We emphasize that none of the small-modulation methods can be used to linearize Eq. (11.1) and solve for solitons.

11.3.1 Nonlinearity

The structure of Eq. (11.1) and the presence of the term $(1 + \frac{\epsilon}{N_a q}\frac{dE}{dx})$ indicate a natural normalization procedure to enact an approximate approach: $Y = E/E_0$, $Q = (I_b + I)/I_b$, and $\xi = x/x_q = x/[\epsilon E_0/(N_a q)]$. We might note that, using the conventional scaling implemented for wave-mixing, x_q can be identified with a saturation scale, i.e., that spatial scale under which the maximum attainable charge (when the concentration of ionized donors $N_d^+ \approx N_a$) cannot screen E_0 (which becomes comparable with the saturation field E_q). From Eq. (11.1) Y and Q are now related through

$$\frac{YQ}{1+Y'} + a\left[\frac{Q'}{1+Y'} - \frac{Q}{(1+Y')^2}\,Y''\right] = G, \tag{11.2}$$

with $a = N_a k_b T/\epsilon E_0^2$ and $G = gE_0/I_b$. The prime stands for $(d/d\xi)$. Eq. (11.2) can be rewritten

$$Y = -a\frac{Q'}{Q} + \frac{G}{Q} + \frac{GY'}{Q} + a\frac{Y''}{1+Y'}. \tag{11.3}$$

We can now identify the various terms with precise physical processes, as we shall see. Eq. (11.3) is rendered tractable by the fact that the greater part of spatial soliton studies involve the trapping of beams with an intensity Full-Width-Half-Maximum (FWHM) $\Delta x \sim 10\,\mu m$. For most configurations, $x_q \sim 0.1\,\mu m$, and $\eta = x_q/\Delta x \sim 0.01$ represents a smallness parameter. A dimensional evaluation of the various terms for the appropriate high-modulation regime indicates that

$$Y^{(0)} = \frac{G}{Q} + o(\eta), \tag{11.4}$$

since $a \sim 2.5$, and $G \simeq -1$ [18]. A first correction is obtained by iterating this solution into Eq. (11.3), and the resulting expression for Y is

$$Y^{(1)} = \frac{G}{Q} - a\frac{Q'}{Q} - \frac{Q'}{Q}\left(\frac{G}{Q}\right)^2 + o(\eta^2). \tag{11.5}$$

The first dominant term is generally referred as the screening term. It represents, in our discussion, the main agent leading to solitons. It is local, in that it does not involve spatial integration, has the same symmetry of the

optical intensity Q, and represents a decrease in E with respect to E_0 on consequence of charge rearrangement ($G \simeq -1$). So perhaps the most astonishing fact of our discussion is that for a large variety of conditions, this form of self-focusing (including self-defocusing) *is* the dominant effect, as the plentiful family of reported observations that have followed the 1992–1993 discovery imply. The second term, of first order in η, is simply the high-modulation version of what is generally called the diffusion field (E_d). The third, again of first order in η, is the coupling of the diffusion field with the screening field, a component sometimes referred to as deriving from charge-displacement [25]. Both these two last terms involve a spatial derivative, and thus provide an antisymmetric contribution to the space charge field (Y) for a symmetric beam $I(x) = I(-x)$. That is, these last two terms lead to a beam self-action with symmetry opposite to that required to support solitons. For "conventional" photorefractive wave mixing, these antisymmetric terms play the central role, leading to energy exchange etc. But for highly localized beams, under the appropriate applied field and intensity conditions, such terms merely lead to beam self-bending, which for most configurations amounts to a slight parabolic distortion of the preferentially z-oriented trajectory. The subject has attracted interest over the years and has helped build an understanding into the limits of the local saturable nonlinearity model [13, 21, 25, 26, 27, 28, 29, 30, 31, 32, 33].

In order to identify the nonlinearity, we must now translate the space-charge field E into an index modulation. The standard configuration for generating screening solitons is such that a zero-cut uniaxial crystal is positioned so that the x-axis is the direction along which E_0 is applied, the soliton beam of intensity I is extraordinarily-polarized and is propagating along z, while I_b is obtained through a copropagating ordinarily-polarized plane-wave [20]. For a noncentrosymmetric photorefractive crystal, like SBN, $\Delta n = -\frac{1}{2}n^3 r_{33} E$, n being the unperturbed crystal index of refraction, and r_{ij} the linear electro-optic tensor of the sample. Consistent with our iterative scheme of Eq. (11.4), we obtain the nonlinearity

$$\Delta n(I) = -\frac{1}{2}n^3 r_{33}\frac{V}{L_x}\frac{1}{1+I/I_b} = -\Delta n_0 \frac{1}{1+I/I_b}, \tag{11.6}$$

which constitutes a saturable nonlinearity, identical (within a constant term) to the nonlinear index change in a homogeneously-broadened two-level-system.

11.3.2 The Soliton-Supporting Nonlinear Equation

A soliton is loosely defined as a wave that preserves its shape and velocity throughout propagation, while, very importantly, displaying a particle-like behavior when made to interact ("collide") with other solitons. As such, solitons possess a number of conserved quantities, such as power, momentum, Hamiltonian, etc. [6]. Optical spatial solitons, in their scalar manifestation, are governed by the nonlinear equation for a monochromatic paraxial beam

$$\left[\frac{\partial}{\partial z} - \frac{i}{2k}\frac{\partial^2}{\partial x^2}\right] A(x,\ z) = -\frac{ik}{n}\Delta n A(x,\ z) \tag{11.7}$$

where $k = 2\pi n/\lambda$ is the wave-vector, A is the extraordinary component of the slowly varying optical field, i.e., $E_{opt}(x,\ z,\ t) = A(x, z)\exp(ikz - i\omega t)$, $\omega = 2\pi c/n\lambda$, and $I = |A(x,\ z)|^2$. We seek stationary (non-diffracting) solutions of the form $A(x,\ z) = u(x)e^{i\Gamma z}\sqrt{I_b}$, normalize the transverse spatial scale to the so-called nonlinear length scale $d = (\pm 2kb)^{-1/2}$, i.e., $\xi = x/d$, which for photorefractive solitons is obtained from the expression $b = (1/2)kn^2 r_{33}(V/L_x)$, and obtain [15, 18]

$$\frac{d^2u(\xi)}{d\xi^2} = \pm\left(\frac{\Gamma}{b} - \frac{1}{1+u(\xi)^2}\right)u(\xi). \tag{11.8}$$

The plus sign is for $b > 0$, the minus for $b < 0$. The sign of b corresponds to the sign of Δn_0, and implies a self-focusing, for $b > 0$, or a self-defocusing, for $b < 0$, nonlinearity, having established that E decreases across the beam profile. Applying the external bias in a particular direction with respect to the crystalline axes uniquely establishes the sign of the nonlinearity through the sign of r_{33}. For example, in SBN, applying E_0 in the direction of the crystalline (ferroelectric) c axis implies $b > 0$, and we observe a self-focusing nonlinearity. It is possible to apply E_0 in a direction opposite to ferroelectric axis, thus effectively changing the sign of b, and then E_0 must be smaller than the coercive field; otherwise, it may render the ferroelectric crystalline structure unstable and de-pole the crystal. Both defocusing and focusing nonlinearities support solitons. A self-focusing nonlinearity traps a conventional bell-shaped beam into a bright soliton. A self-defocusing nonlinearity can support a dark soliton: a notch in a uniform beam generated by a π phase jump.

Eq. (11.8) can be integrated (by quadrature) once [15, 18] giving the relationship $\Gamma/b = \log(1 + u_0^2)/\ u_0^2$ for bright beams, and $\Gamma/b = 1/(1 + u_\infty^2)$ for dark, where $u_\infty = u(\infty) = -u(-\infty)$, and $u_0 = u(0)(u_0^2 = I(0)/I_b$ being referred to as the intensity ratio).

11.3.3 Soliton Waveforms and Existence Curve

As can be imagined, the self-trapped waves u, solutions of Eq. (11.8), form an isolated subset of all possible solutions of Eq. (11.7). The imposition of z-invariance implies not only a specific relationship between beam parameters, but fixes the actual waveform u in all its details (see Fig. 11.5). For solitons, we have two countering effects, diffraction and self-focusing, which are coupled by nonlinearity to form a feedback mechanism. The result is that most soliton solutions are stable to perturbations, and represent an attractor to system dynamics [6]. This, in turn, contains the beauty and physical appeal of soliton physics: That a propagating beam, interacting in a nontrivial way with a host

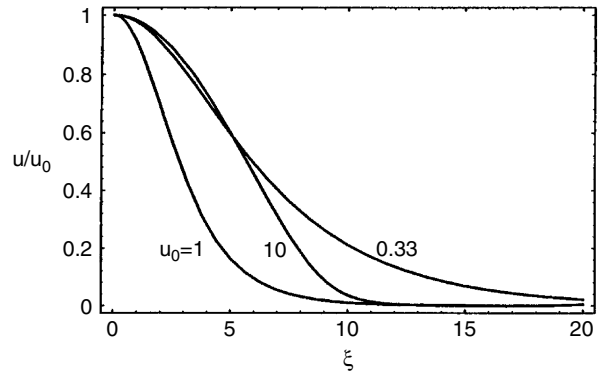

FIGURE 11.5. Soliton waveforms for bright solitons, as reported in [18].

medium, should preferably be attracted to a robust, propagation-invariant, and very specific wave-form.

Returning to our system, what are the soliton wave-forms, and, more importantly, what are the beam parameters, $\Delta\xi$ (associated to Δx) and intensity ratio u_0^2, that characterize the subset of soliton solutions? The issue is of particular importance, because launch experiments are designed to deterministically lead to a soliton, a scheme that requires the launch to be close enough to a self-trapped wave in parameter space (intensity u_0^2 and normalized width $\Delta\xi$) [22]. For the family of integrable nonlinear equations, such as the Sine-Gordon, the Nonlinear Schroedinger, and the Korteweg and de-Vries equations, an explicit solution can be found, for which the relationship between beam $\Delta\xi$ and u_0^2 is unique. However, for the saturable nonlinearity described by Eqs. (11.6) and (11.8) the $\Delta\xi$ versus u_0^2 relation is not explicit and single-valued, but instead yields a continuous curve commonly termed the soliton existence curve [18] (see Fig. 11.6).

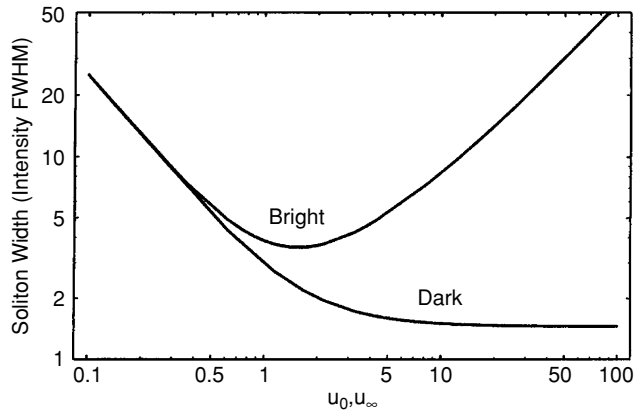

FIGURE 11.6. Soliton bright and dark existence curve, as reported in [18].

The wave functions of bright photorefractive screening solitons are bell-shaped functions that are neither a Gaussian nor a hyperbolic secant [34]. Experimentally, such solitons are generated by launching a focused-down one-dimensional Gaussian beam with a Δx and peak intensity I_0 such that, for the given configuration of crystal parameters n, r_{33}, and I_b, for the given bias E_0, the resulting values of $\Delta\xi$ and u_0 lie on the existence curve or close enough to it. For dark solitons, in turn, the same procedure can be implemented for the relevant (u_∞, $\Delta\xi$) parameter space.

11.3.4 Experiments and Theory

The main advantage of having formulated the theory highlighting the saturable nature of the nonlinearity is that, within the limits in which the underlying approximations are valid, it allows the prediction of solitons as a specific feature independent of the particular experimental configuration. Thus, a physically *identical* soliton will emerge for two self-trapped beams of, say 10 and 20 μm, as long as the applied voltage V, material response, beam intensity, and background illumination are such as to project the two conditions on the very same point on the (u_0, $\Delta\xi$) parameter space. Note that this powerful tool breaks down as soon as we consider the $o(\eta)$ terms, or even simple corrections in the actual nonlinearity, such as those deriving from dielectric nonlinearity [35].

The comparison between experimental results and theory are shown in Fig. 11.7 for bright solitons [22, 36, 37], and in Fig. 11.8 for dark [24]. The qualitative agreement is full, but quantitative agreement is weaker. At present

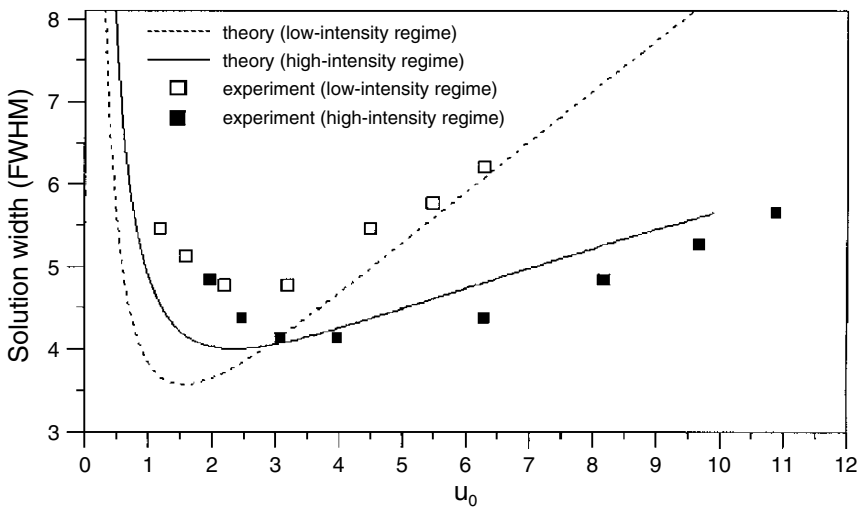

FIGURE 11.7. Comparison between experiments and theory for (1 + 1)D bright screening solitons, from [36]. Here the low-intensity regime is what we specifically term screening solitons.

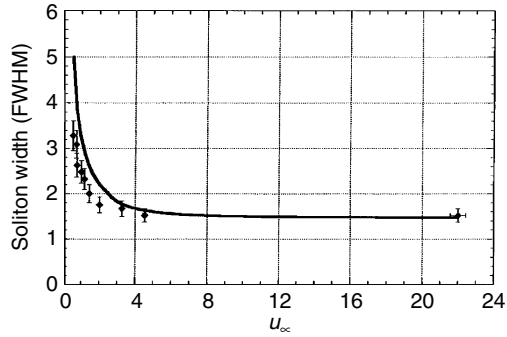

FIGURE 11.8. Comparison between experiments and theory for (1 + 1)D dark screening solitons, from [24].

it is believed that the discrepancy is due more to the presence of extraneous effects than to a deficiency in the model. For example, it has been observed that some of the background illumination, which is made to be ordinarily polarized in order to not undergo substantial evolution (and stay uniform in space), is actually guided (through the non-zero r_{13} coefficient) by the index change induced by the soliton. Thus, the intensity ratio is not a constant, but is actually slightly varying across the beam profile. Another source of uncertainty is connected to the difficulty in establishing the precise value of r_{ij} for the given sample: This can depend on the level of overall crystal poling, on the presence of considerable clamping, and on temperature.

Concerning more fundamental aspects of the model, we note that although the results shown in Fig. 11.7 support the approximation contained in Eq. (11.4), the actual beam evolution shows a clear and reproducible self-bending effect that is explained by the full expression of Eq. (11.5). It appears that, even though these correction terms produce a parabolic trajectory, they do not greatly influence the existence curve. From a different perspective, we note that self-bending becomes an important issue when experiments are carried in highly solitonic regimes, characterized by a large ratio between self-trapped propagation distance and linear diffraction length L_z/L_d.

11.4 Two-Dimensional Solitons

The (1 + 1)D screening solitons represent the firm experimental and theoretical footing on which a large part of research rests, especially because of the appealing nature of the saturable nonlinearity that gives rise to numerous soliton interactions not present with Kerr-type solitons. However, the most important achievement from the physical point of view is the self-trapping of (2+1)D solitons. As their lower-dimensional counterparts, such self-trapped needles form both in the transient regime—as quasi-steady-state self-trapping [10]—and in temporal steady state

as (2+1)D screening solitons [20, 21]. Such needle-like solitons were originally observed in SBN, and have been reproduced in most soliton-supporting photorefractive media, such as other ferroelectrics [38], semiconductors [39], paraelectrics [40], sillenites [41], and indeed for most types of self-trapping, including photovoltaic solitons [42], multimode solitons [43–45], and incoherent solitons [46, 47], to name a few. Furthermore, even (2+1)D dark solitons were observed in photorefractives, in quasi-steady-state [48] and in steady-state [49] under a bias field, as well as photovoltaic [50] and incoherent [51] dark "vortex" solitons. An example of a dark vortex screening soliton is shown in Fig. 11.12.

Two-plus-one dimensional solitons form when a circularly symmetric beam is focused down onto the input face of the sample, and the initially diffracting beam collapses into a nonspreading 2D beam having an almost ideally circularly-symmetric shape (see Fig. 11.9). These studies, which constitute one of the rare possibilities of observing (2+1)D solitons, have greatly contributed to the understanding of the physics associated with higher-than-one-dimensional

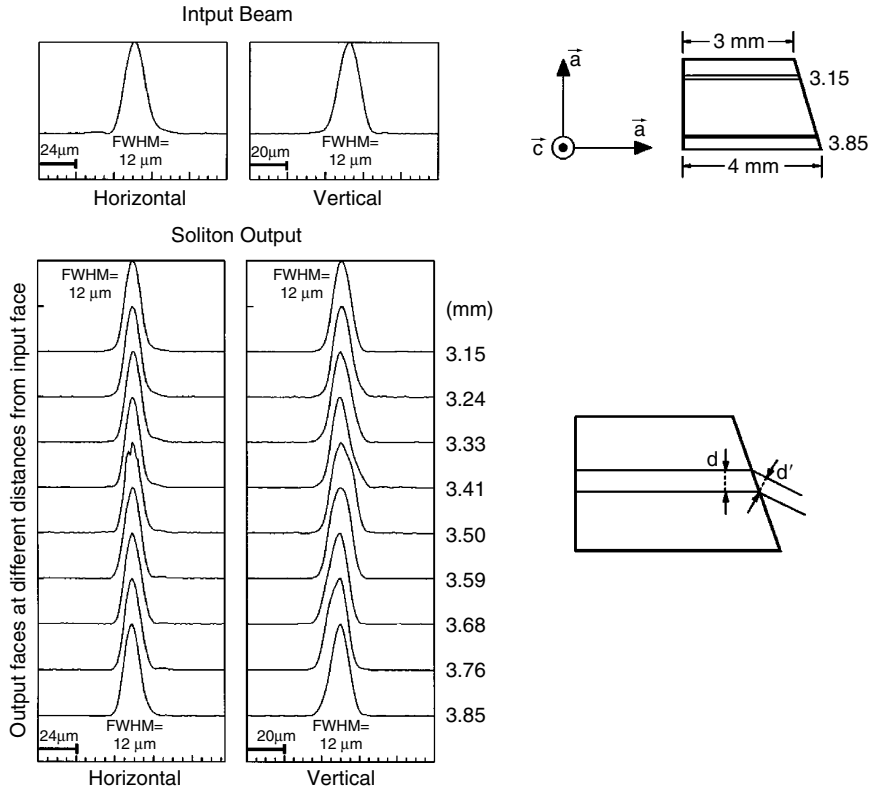

FIGURE 11.9. The direct and detailed observation of a circularly-symmetric 12 μm needle phenomenology in a nonzero-cut sample of SBN, from [21].

nonlinear waves. The observation of soliton spiraling in full 3D [52], as well as fusion, fission, birth, and annihilation of (2+1)D solitons [53, 54, 55], have extended the very *concept* of soliton-particle behavior.

The description and understanding of the mechanisms that support (2+1)D solitons is still incomplete. This is because the propagation involves a nontrivial three-dimensional, anisotropic, and spatially nonlocal nonlinear problem [56, 57, 58, 59, 60, 61]. The fact that photorefractives can support self-trapped needles of (almost ideally) circularly-symmetric shape seems very surprising right from the outset. More specifically, the external field is applied between two parallel planar electrodes, and thus breaks the circular symmetry of the problem. The explanation relates to the fact that the (space charge) field lines bend in the regions of higher illumination, and, for some range of parameters seem to yield a quasi-radial distribution of the field component giving rise to a nonlinear index change. For example, in SBN this means that the *c*-component of the space charge field has roughly a circular symmetry. The very fact that such (2+1)D solitons propagate in a stable fashion, not undergoing catastrophic collapse (as such solitons in Kerr media would), is a direct indication that the photorefractive nonlinearity is saturable also in two (transverse) dimensions. However, during the temporal transients, and for various values of applied field, self-trapping manifests considerable beam ellipticity [56], indicating that a circularly-symmetric 2D saturable model is not really applicable. Nevertheless, the large amount of experimental evidence on 2D solitons in almost every photorefractive material in which solitons have been identified implies that a modified model, possibly anisotropic and slightly nonlocal, should exist [59]. What clears the picture are the studies on (2+1)D soliton interaction-collisions. On the one hand, spiraling and large angle collisions show that whatever anisotropic components emerge, they do remain localized around the beam [52, 62], whereas lower angle collisions unmistakably indicate the presence of a saturable yet anisotropic nonlinear behavior, as evidenced by the observation of repulsion between (2+1)D screening solitons undergoing an incoherent collision [63]. Such collisions are always attractive when the nonlinearity is isotropic and local. However, in [63], the interacting solitons, launched at a particular separation between them, are observed to repel, as a consequence of the transverse anisotropy of the photorefractive screening nonlinearity.

From a theoretical perspective, the system has two fundamental anisotropies: The boundary conditions associated with the application of the external bias along the *x*-direction, and the electro-optic response, which implies a complex tensorial index modulation depending on the beam polarization, direction of the local electric field **E**, and the relative orientation with respect to the crystal lattice. The result is that the nonlinear response has a nonlocal component that is superimposed on the saturable component [58]. In order for a quasi-circular optical symmetry to appear, the underlying space-charge field **E** must be anisotropic, manifesting two characteristic lateral lobes (see Fig. 11.10) [64]. The appearance of these features, which have an increased complexity with respect to the ionizing intensity $I(x, y)$, are the basic manifestation of a nonlocal mechanism.

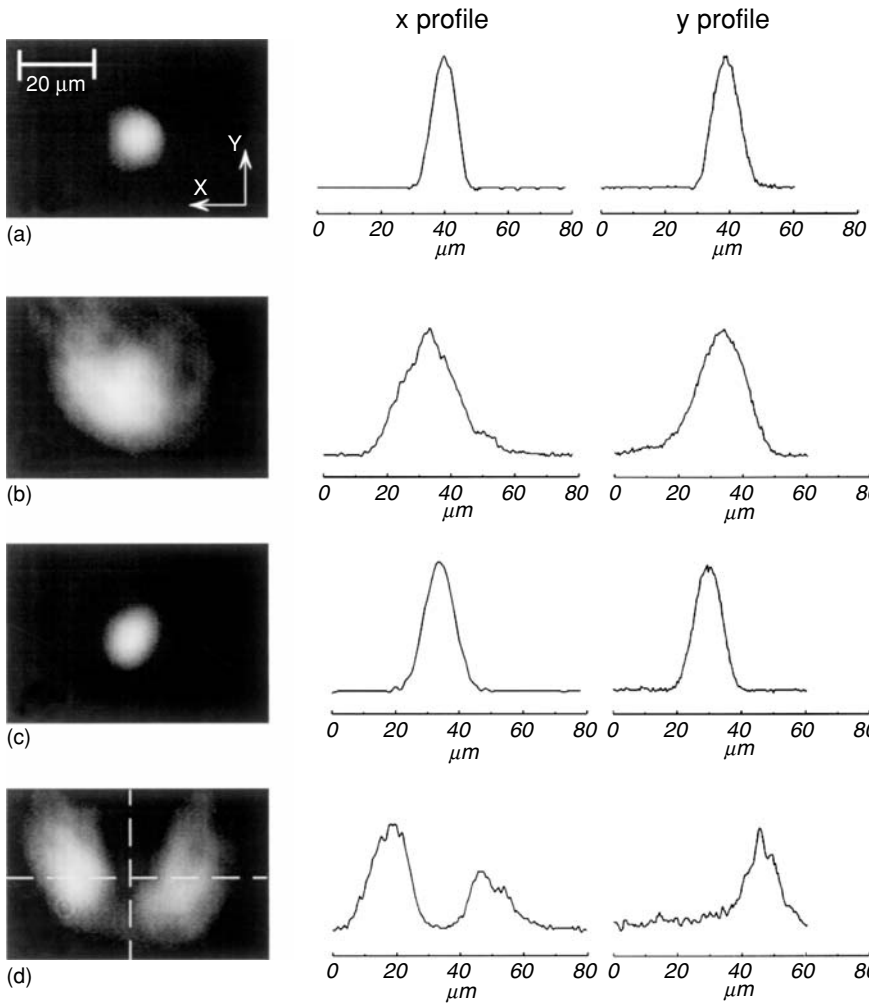

FIGURE 11.10. Needle electroholography from [64]. (a) input beam, (b) diffracted output beam at zero voltage, (c) output soliton beam, (d) the two "anisotropic lobes" on either side of the soliton visualized via electro-holography.

In the 2+1D case, we start from the basic relation, valid to zero order in η,

$$\nabla \cdot (\boldsymbol{Y}Q) = 0 \tag{11.9}$$

and the irrotational condition

$$\nabla \times \boldsymbol{Y} = 0. \tag{11.10}$$

From these, the lobular structure illustrated in Fig. 11.11 emerges.

The fact that 2+1D solitons are supported by this more complex nonlinearity does not substantially modify our soliton picture. One consequence, however, is that we do not have a means to formulate in a straightforward manner an

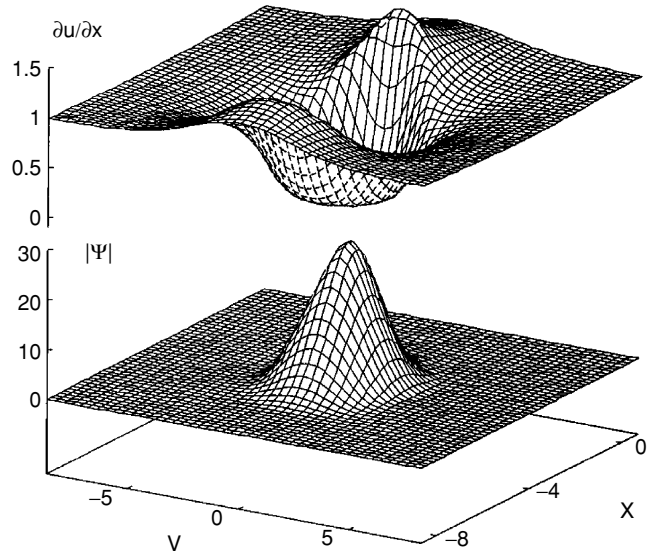

FIGURE 11.11. Numerically evaluated x-component of E (top) ($\partial u/\partial x \propto Y_x$) for the soliton beam profile (bottom) ($|\psi| \propto I^{1/2}$), from [59].

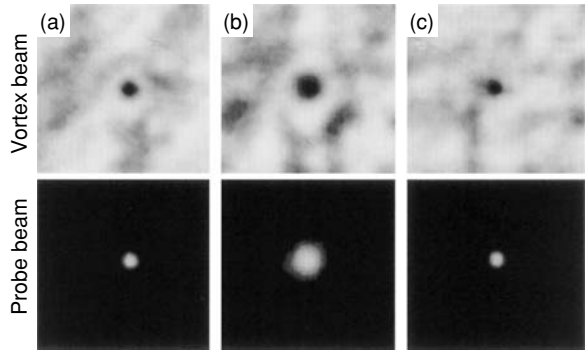

FIGURE 11.12. A vortex screening soliton from [49]. (a) Input intensity distribution of the vortex; (b) Diffracting vortex after linear propagation to the output of the sample; (c) Self-trapped output intensity distribution in a biased sample. (bottom) Probe beam guided propagation.

existence curve for (2+1)D solitons. Nevertheless, if we phenomenologically build the set of points in which it is possible to observe circular-symmetric self-trapping [21, 40], we find a single valued continuous curve that behaves and looks just like the existence curve of (1+1)D solitons (albeit at somewhat higher values of $\Delta\xi$).

Evidence on both the existence of circularly-symmetric solitons and of their intrinsic difference from (1+1)D solitons in photorefractives is highlighted by the

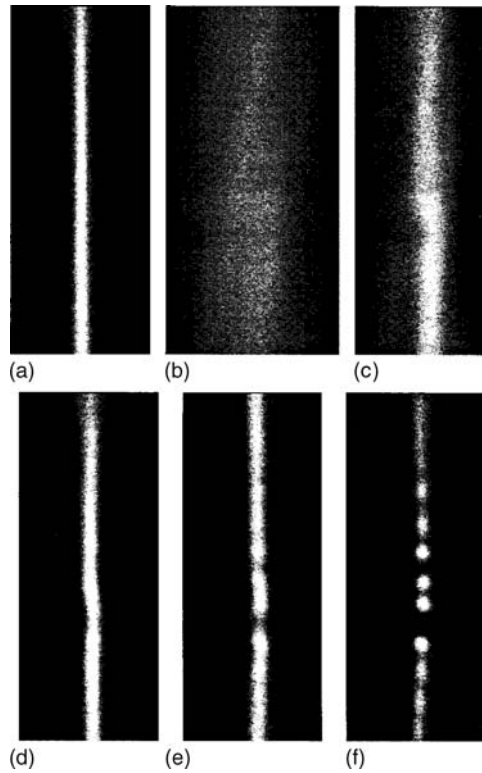

FIGURE 11.13. Transition from (1+1)D to (2+1)D self-trapping, from [65].

experimental studies on transverse instability of (1+1)D solitons in bulk media. In those experiments, increasing the nonlinearity leads to a (1+1)D soliton, at the proper value of nonlinearity vs. intensity ratio, as determined by the existence curve. Then, a further increase in the nonlinearity results in beam break-up into an array of *circularly-symmetric* solitons, as shown in Fig. 11.13 [65].

11.5 Temporal Effects and Quasi-Steady-State Dynamics

One of the main characteristics of photorefraction is that it is a process that builds up in time. This is the origin of its high nonlinear response even at low optical intensities. Evolution is dominated by a charge redistribution process that leads to a time constant $\propto 1/I$. If I is almost constant (i.e., the beam is almost uniform in space), then a single time constant can be identified. Otherwise, different regions in the nonlinear medium evolve at different time scales: Faster in illuminated regions, and slower in darker regions. In this respect, a spatial soliton has strongly varying

intensity both in the transverse plane, and, during the formation process, also along the propagation axis. The result is an evolution that presents a number of surprising phenomena that are complicated and difficult to describe (an example that goes beyond soliton studies can be found in [66]).

Possibly the most important effect is observed when launching a diffracting beam in a biased sample, without any appreciable background illumination. As reported in the very first experiments on solitons by Duree et al. [10], the beam is observed to form, after a time interval of the order of 10ms, a spatial soliton, remain almost stationary for an interval of 20ms, and then decay into a once again diffracting beam. This peculiar sequence, which involves a time plateau, is referred to as a quasi-steady state soliton.

The time dependent version of Eq. (11.2) truncated at zero order in η reads

$$\frac{\partial Y}{\partial \tau} + QY = G, \tag{11.11}$$

where $\tau = t/\tau_d$, $\tau_d = \epsilon_0 \epsilon_r \gamma N_a/(q\mu s(N_d - N_a)I_b)$ is the characteristic dielectric time constant, γ is the recombination rate, μ the electron mobility, s the donor impurity photoionization efficiency. As occurs for most configurations of interest to soliton dynamics, the charge recombination time $\tau_r = 1/\gamma N_a$ is much shorter than charge transport time, and no time dependence in the boundary conditions is considered ($G = -1$). For small modulation, Eq. (11.11) gives the characteristic exponential dynamics with a characteristic time constant τ_d/Q, but as soon as Q is spatially dependent and evolving, a continuum of different time constants contribute. Seen in a different perspective, soliton time evolution is highly time-nonlocal, as the formally equivalent integral version of Eq. (11.11)

$$Y = Ge^{-\int_0^\tau Q d\tau'} \left(1 + \int_0^\tau d\tau' e^{\int_0^{\tau'} Q d\tau''}\right), \tag{11.12}$$

indicates [58]. The full complexity of this behavior emerges during transients, i.e., when I changes in an appreciable manner with time. This occurs most evidently during the very first collapsing stage, for times $\tau \leq 1/(1 + u_0^2)$, and leads to a stretched exponential evolution [67]. A characteristic of multiscale processes, this behavior is common to the entire family of soliton supporting cumulative nonlinearities, which also include thermal and liquid crystal nonlinearities [67]. A numerical approach to Eq. (11.12) coupled to the parabolic wave equation confirms experimental findings, but to date there is no clear understanding why the soliton should pass through a plateau, and, more importantly, how to evaluate the so-called threshold nonlinearity for which self-trapping is achieved, the duration of the plateau, and the nonlinear equation, such as Eq. (11.8), for which the waves are eigen-functions. Furthermore, we do not have a means to predict the actual trapping Δx at the plateau for a given nonlinearity.

In very special cases in which the beam does not undergo time evolution, we can considerably simplify the prediction for the build of the space-charge field [68]. In this case, Eq. (11.12) is simplified to give

$$Y = e^{-\tau Q}(1 + \frac{1}{Q}(e^{\tau Q} - 1)). \tag{11.13}$$

This approach can be meaningful and useful for conditions in which a soliton (i.e., the beam I) is steady, such as for steady-state incoherent solitons that we will describe below. It has been speculated that Eq. (11.13) could be valid when a negligible amount of diffraction is involved [69, 70, 71, 72, 73].

While delaying the discussion of incoherent self-trapping, a (consequence of a non-instantaneous time response), to Section 11.10, we mention here the wide range of transient effects that occur for higher-dimensional needles [74], and those associated to a time-dependent external bias E_0 [14, 75, 76, 77]. Lastly, we should mention the study of *single* pulse propagation and space-charge build-up [78, 79].

11.6 Various Photorefractive Mechanisms Supporting Self-Trapping

Several mechanisms can support solitons in photorefractives. Apart from the solitons described in the previous section, which rely on an externally-applied bias field, self-trapping in photorefractives can also arise from photovoltaic effects [80], from diffusion-driven effects [81], or from effects caused by the excitation of both electrons and holes [82]. In several cases, combinations of two of these effects can also lead to solitons [e.g., solitons supported by the photovoltaic and the screening nonlinearities simultaneously]. Furthermore, in some cases, self-trapping can arise from semipermanent changes in the crystalline structure, either though clustering of ferroelectric domains [83], or through repoling of macroscopic regions [84, 85], both being driven by the local space charge field. Such permanent changes are in fact ''fixed'' (soliton-induced) waveguides, acting as microstructure optical interconnects ''impressed'' into the volume of the bulk nonlinear crystal. To this date, this is one of the very few techniques to create intricate 3D optical circuitry. In this section, we briefly review these additional mechanisms supporting self-trapping of optical beams in photorefractive media.

11.6.1 Photovoltaic Solitons

Soliton-supporting mechanisms appear in photorefractives also in the absence of electric fields, the major example being photovoltaic solitons [80, 86]. Here, in open-circuit conditions and for the $(1 + 1)$D geometry, the nonuniform optical excitation translates into a nonuniform photoinduced current. This, at

steady state, must be countered by the drift of photoexcited charge (electrons) in response to E. Under conditions analogous to those leading to Eq. (11.4), for a beam with features Δx of the order of several microns, we arrive again at a saturable nonlinearity

$$\Delta n(I) = -\frac{1}{2} n^3 r_{33} E_p \frac{I}{I_d + I} = -\Delta n_{0,p} \frac{I}{I_d + I}, \tag{11.14}$$

where $E_p = \beta_{ph} N_a \gamma / (q\mu s)$, I_d the equivalent dark illumination, the constitutive relation for the current along x being $J = q\mu NE + \beta_{ph}(N_d - N_d^+)$. Much in the same fashion of Eq. (11.8), this nonlinearity leads to a nonlinear wave equation that supports bright and dark solitons on the basis of the sign of $\Delta n_{0,p}$, i.e., on the sign of β_{ph} [80, 86].

Most of the experiments with photovoltaic solitons have been carried out in $LiNbO_3$, for which β_{ph} is negative for an extraordinarily-polarized beam propagating along the principal axis a. This has led to the observation of one-dimensional dark photovoltaic solitons (see the experimental apparatus described in Fig. 11.14) and results in Fig. 11.15 [87].

As occurs for the screening type nonlinearity, photovoltaic solitons can also form in the higher-dimensional case. For $LiNbO_3$, these form as dark vortex solitons that are supported by a "spiraling" transverse phase modulation [50] (see Fig. 11.16)). In KNSBN, photovoltaic self-action is self-focusing, and even bright (2+1)D photovoltaic solitons have been detected [42]. Moreover, it has been predicted and demonstrated that the use of a background illumination, not a strict requirement in photovoltaics, allows the transitions from the defocusing to a focusing nonlinearity in $LiNbO_3$ [88].

11.6.2 Resonantly-Enhanced Self-Trapping in Semiconductors

One of the nicest features of photorefractive solitons is the very low power level at which they can form, allowing soliton experiments with microwatt (and lower) power levels. As will be discussed in the section on applications, photorefractive

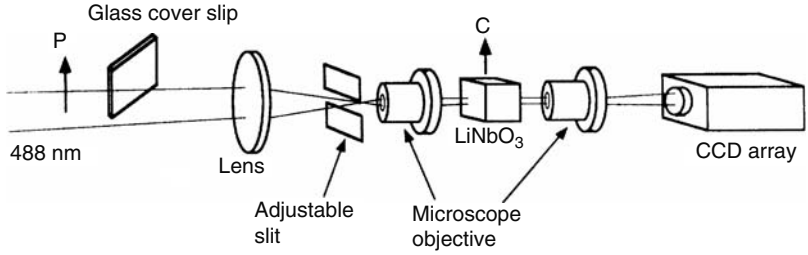

FIGURE 11.14. Photovoltaic dark soliton setup, from [87]. Note the use of a resolved transverse phase-structure obtained by having part of the launch beam pass through an appropriate piece of glass.

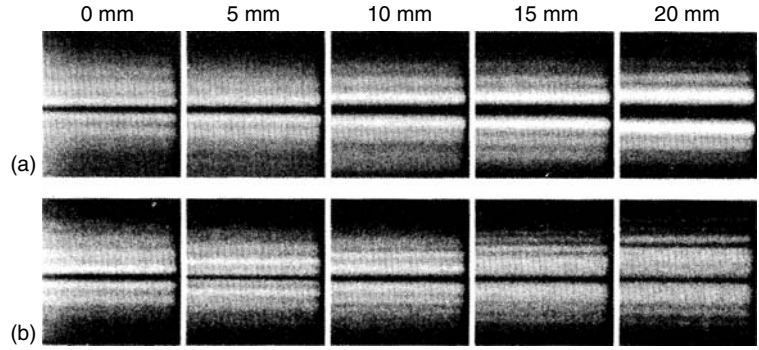

FIGURE 11.15. Observations of dark photovoltaic solitons, from [87]. (a) Linearly diffracting intensity distribution of a dark notch; (b) self-trapped intensity distribution, for various propagation distances in the sample.

solitons, and the waveguides they induce, combine properties that suggest interesting applications ranging from reconfigurable directional couplers, beam splitters, waveguide switching devices, tunable waveguides for second harmonic generation, and for highly efficient optical parametric oscillators. In general, however, the formation time of solitons in most photorefractive materials is rather long, compared to Kerr or quadratic solitons [6], except when very high intensities are used [36]. This is because the photorefractive nonlinearity relies on charge separation, as discussed in Section 11.5, for which the response time is the dielectric relaxation time, i.e., inversely proportional to

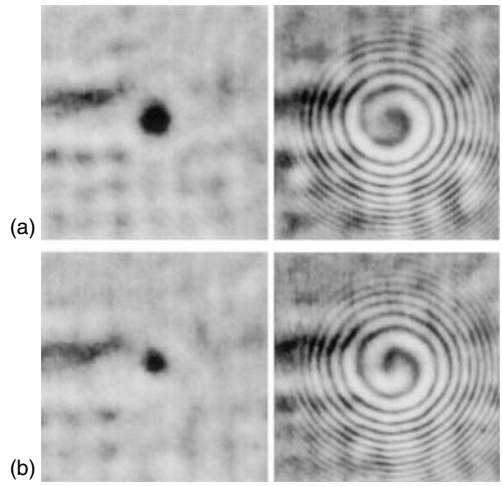

FIGURE 11.16. Self-trapping of a photovoltaic vortex, from [50]. (a) Output intensity distribution before self- focusing begins, and phase pattern; (b) output intensity distribution trapped by the photovoltaic field, and phase pattern.

the product of the mobility and the optical intensity, and the mobility in photorefractive oxides is low. In principle photorefractive semiconductors, (e.g., InP, CdZnTe), have a high mobility and could offer formation times a thousand-fold faster than in the other photorefractives. However, the electro-optic effects in these semiconductors are tiny, which implies that solitons that are as narrow as 20 optical wavelengths necessitate very large applied fields, making solitons in them almost impossible to observe. But, in some of these materials (InP and CdZnTe) that have both holes and electrons as charge carriers, a unique resonance mechanism can greatly enhance the space charge field by as much as 10 times (and more) over the applied electric field. This enhancement yields large enough self-focusing effects that can support narrow spatial solitons. The resonant enhancement of the space charge field has led to the observation of solitons in photorefractive InP [39, 82] and CdZnTe [89].

As mentioned, the resonant enhancement of the space charge field occurs in materials with both types of charge carriers, both being excited from a common trap level: One excited optically and the other excited by temperature (or by a second optical beam of a longer wavelength). These two excitations work in opposing fashions: One fills (populates) the mid-gap traps whereas the other empties them. At steady state, when a focused beam illuminates a biased crystal of this kind, and the beam intensity is such that the photo-excitation rate of one type of carrier is comparable to the thermal excitation rate of the other type of carrier, the concentration of both free carriers at the illuminated region decrease drastically. The intuitive explanation is as follows [90]. Under proper conditions, the ratio between the concentrations of electrons and holes is equal to their ratio in the absence of light, and thus has a constant (coordinate-independent) value. The net excitation rate of the traps is the difference between the thermal (holes) and optical (electrons) excitation rates. At resonance, the net excitation rate goes to zero. At the same time, at steady state the excitation rate must be equal to the recombination rate, which, in turn, is proportional to the free charge concentration. Hence, at resonance (when the excitation rates of holes and electrons are comparable), the free charge concentration becomes extremely small. Consequently, the local electric field is highly enhanced because the current at steady state must remain constant throughout the crystal. For a given temperature, this enhancement occurs at a specific intensity (the resonance intensity), for which the thermal and optical excitation rates are comparable. It is a resonant enhancement, although it is an intensity-resonance and not an atomic resonance. The enhanced electric field compensates for the smallness of the electro-optic coefficient and enables a sufficiently large change in the refractive index to support narrow solitons (see Fig. 11.17).

The observation of solitons in photorefractive semiconductors [39, 82, 89] is especially important for several reasons. First, the solitons are generated at optical telecommunications wavelengths. Second, they allow microsecond soliton formation times even at very low (microwatt) optical power. These features suggest that optical spatial solitons could form from light beams emerging from ordinary optical fibers (conventional data-transmission lines)

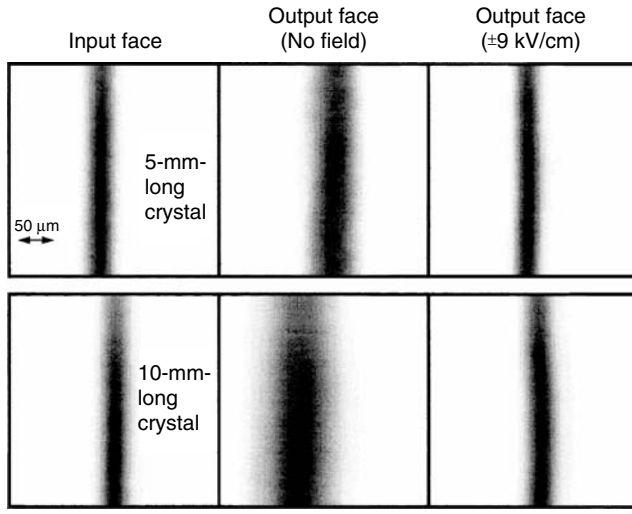

FIGURE 11.17. Observed transverse intensity distribution for (1+1)D self-trapping in InP, from [82].

on nanoseconds time scales, and could be all-optically switched on-off by employing the intensity resonance in photorefractive semiconductors.

11.6.3 Diffusion-Driven Self-Action

In a conventional noncentrosymmetric crystalline phase, such as that characterizing SBN or $BaTiO_3$ at room temperature, charge diffusion leads to an asymmetric index profile, which translates into a transverse phase chirp that produces self-bending. As discussed in Section 11.3.1 in conjunction with Eq. (11.5), the diffusion field is typically just a small correction to the expression for the space charge field supporting screening solitons.

Consider now a situation where no external field is applied. On the basis of Eq. (11.1) with $g = 0$ (null current), $E = -\frac{k_b T}{q}\frac{1}{I+I_b}\frac{dI}{dx}$. Higher order corrections due to saturation in this case are even less important, such that for a $10\,\mu$m beam, they represent a relative contribution of the order of $\epsilon_r \cdot 10^{-6}$, where ϵ_r is the relative dielectric constant. For a sample heated above the ferroelectric-paraelectric phase-transition, manifesting a *quadratic* electro-optic response, the resulting nonlinearity leads to a *symmetric* lensing effect, of the type $\Delta n(I) \propto (\frac{1}{I+I_d}\frac{dI}{dx})^2$. Although in most conditions, such self-action is negligible, in the very proximity of the phase-transition, where ϵ_r attains values of the order of 10^4, self-focusing, the precursor of soliton formation, has been observed [81, 91]. The resulting nonlinear equation, which can be extended also to the full (2+1)D case, represents the singular situation in which a nonlocal nonlinearity (involving a spatial derivative) allows for the explicit analytical prediction of the observed nonlinear diffraction. In particular, we recall

ellipticity recovery (see Fig. 11.18) that consists in a beam with an elliptical transverse profile that, spreading, conserves the ratio between the two transverse widths $\Lambda = \Delta y/\Delta x$.

11.6.4 Fixing the Photorefractive Soliton: Self-Trapping by Altering the Crystalline Structure

Solitons in photorefractives are typically supported by the linear response of the dc crystalline polarization to the local (dc) space-charge field, $\boldsymbol{P} = \epsilon \boldsymbol{E}$. However, optical beams can also self-trap in photorefractive media by altering the crystalline structure of the nonlinear medium in which the beam propagates. This happens when the local space charge field E becomes comparable with the coercive field E_c, and is directed in a direction different from the poling direction. For low-modulation index gratings, such conditions rarely occur. But photorefractive solitons, being entities with an inherently high index contrast, are always associated with locally high electric fields that can readily depolarize a sample. Consider a screening soliton, which exists as a consequence of an external bias E_0 directed along the poling axis x. Once the soliton has formed, charge has redistributed so as to partially screen the field. This means that across the beam profile, the charge distribution results in a field that is approximately opposite the bias field. Removing the illumination (and the background) and switching the external bias off exposes this field. The result is that $E_{V=0} \simeq -E_0$ in the region that before gave rise to the soliton. In SBN Klotz et al., have shown how this field can not only depolarize the sample, but also permanently fix the waveguiding structure that accompanies the soliton, an achievement that can have considerable impact in soliton based devices [84, 85].

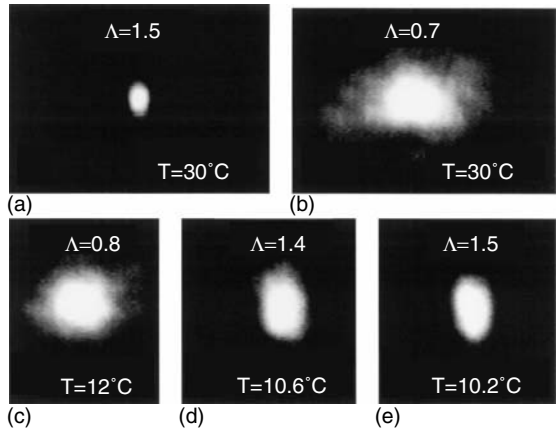

FIGURE 11.18. Diffusion-driven ellipticity recovery. The input ellipticity (a) Λ is recovered at the output (b–e) as the crystal temperature T is brought closer to the Curie temperature, enhancing diffusion- driven effects, from [91].

Ferroelectric clusters, i.e., micrometer-sized regions in which spontaneous polarization has a common orientation, can also play a more dynamic role in spatial self-trapping, when they interplay with light-generated space-charge during soliton formation. This has been observed in a metastable paraelectric material, for temperatures near the transition temperature, where diffusion fields become comparable to E_c [83]. The result is a complicated optical-domain interaction which also leads, in appropriate conditions, to a form of spatial self-action known as spontaneous self-trapping (see Fig. 11.19). The description of these processes, which requires the modeling of domain formation, and their light-matter interaction throughout propagation, is beyond the linear polarization approach. Such a theory has yet to be formulated.

11.7 Alternative Photorefractive Materials

Research into nonlinear beam propagation has also been carried out in sillenites, such as BTO, BSO, and BGO, paraelectrics, such as KLTN, and photorefractive polymers [92, 93] and organic gels [94].

In nonferroelectric sillenites, photorefractive self-trapping was obtained in a configuration similar to that used for ferroelectric samples [19, 95, 96, 97].

The main difference between the physical processes is that sillenites present a fairly strong natural optical activity, which leads to polarization rotation (during propagation) of both the self-focused and the background beams. This causes the effective nonlinearity to change in the direction of propagation [98, 99, 100]. Strictly speaking, solitons cannot exist in such optically-active materials, at least not in the typical scheme of screening solitons. However, using very short samples (a typical value of optical activity is $\rho_0 \simeq 6^\circ/mm$), and employing precompensation (in which the beams are not extraordinarily- and ordinarily-polarized, but evolve to these halfway through the sample), does allow the observation of non-diffracting beams for some propagation distance. Another difficulty in using sillenite crystals is in the weak effective electro-optic coefficient $r_{eff} \simeq 5pm/V$ (for BTO), as compared to ferro-electrics. Altogether,

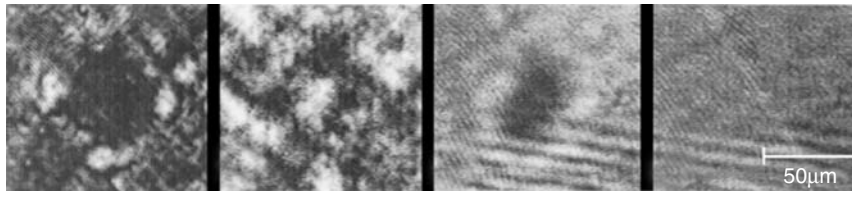

FIGURE 11.19. Domain and cluster structure induced by a spontaneous self-trapped process in metastable KLTN, from [83], (a–b) Underlying domain structure as seen with the two principal polarizations; (c–d) melting away of domains into clusters, clusters into a homogeneous structure, as temperature is increased from the Curie point.

the sillenite crystals have served an important role in the first explorations of steady-state self-focusing [19], but have been rarely used for solitons experiments since then, simply because other materials offer more favorable conditions for soliton generation.

Part of screening soliton studies are carried out in paraelectrics, where the quadratic electro-optic effect supports a screening nonlinearity in all similar to the noncentrosymmetric counterpart of the form $\Delta n \propto (E_0)^2/(1 + I/I_b)^2$ [101]. In these, almost all the conventional photorefractive soliton phenomenology can be observed, from (1 + 1)D [37] to (2 + 1)D solitons [40]. Dark solitons have yet to find an appropriate material (with an accessibly low temperature paraelectric phase), because in such crystals, the nature of the index change cannot be reversed upon reversal of the applied field, as is the case for noncentrosymmetric crystals with the linear electrooptic effect. Given the generally weak electro-optic response in the high-symmetry phase, most studies are carried out in proximity of the ferroelectric-paraelectric transition: The crystals must be thermalized to stabilize their dielectric response.

11.8 Soliton Interaction-Collisions

Nonlinearity generally allows the coupling and energy exchange among beams and modes. For solitons, nonlinearity not only supports their propagation-invariant nature, but leads to a unique coupling dynamic in which the individual solitons behave as quasi-rigid particles when they are made to interact with one another. In fact, this particle-like behavior is the reason for the term "soliton" [102]. Interactions between solitons are commonly referred to as *soliton collisions*, and constitute the most fascinating features of soliton phenomena. Soliton interactions can be generally classified into coherent and incoherent interactions. *Coherent interactions of solitons* occur when the nonlinear medium can respond to interference effects that take place when the beams overlap. The material responds to the interference introducing a mutual attraction or repulsion, depending on the relative phase between the beams. *Incoherent interactions*, on the other hand, occur when the relative phase between the (soliton) beams varies much faster than the response time of the medium. In this case, the resultant force between such bright solitons is always attractive. Altogether, soliton interaction-collisions are universal, exhibiting the same basic features in spite of the widely diverse physical origins for the self-trapping. For a detailed review on soliton interaction forces, see [5].

Photorefractive solitons played an especially important role in the study of soliton interactions, and in doing that have greatly contributed to soliton research at large. This role is a consequence of a series of factors: The relative ease in soliton generation, which lowers the complexity of multiple soliton-supporting schemes; the saturable nature of the nonlinearity, which offers many features that are simply nonexistent with ideal Kerr-type solitons; the existence of both (1 + 1)D and (2 + 1)D solitons, in a 3D bulk medium; and the

relatively slow response of photorefractive materials which facilitates the possibility of studying both coherent and incoherent collisions in the same material system. Consequently, many soliton collision features have been demonstrated first with photorefractive solitons, and only later on experiments in other nonlinear media followed up.

The physical intuition behind soliton collisions relies on the universal idea that a soliton is a bound state of its own induced potential, or in optics a guided mode of its own induced waveguide . Having this in mind, one can understand soliton collisions by comparing the collision angle to the (complementary) critical angle for guidance in the single soliton-induced waveguides (the angle with the propagation axis below which total internal reflection occurs). Whether or not energy is coupled from one soliton into the waveguide induced by the other soliton, depends on the relation between the collision angle and that critical angle. In terms of "potential well," capture depends on whether the kinetic energy of the colliding wave-packets results in a velocity that is smaller than the escape velocity. If the collision occurs at an angle larger than the critical angle, the solitons simply go through each other unaffected—very similar to the behavior of Kerr solitons (the beams refract twice while going through each other's induced waveguide but cannot couple light into it). If the collision occurs at "shallow" angles, the beams can couple light into each other's induced waveguide. Now if the waveguide can guide only a single-mode (a single bound state), the collision outcome will be elastic, essentially very similar to that of a similar collision in Kerr media (with the exception that now some very small fraction of the energy is lost to free radiation). However, if the waveguide can guide more than one mode, and if the collision is attractive, higher modes are excited in each waveguide and, in some cases, the waveguides merge and the solitons fuse to form one single soliton beam. Such a fusion process is always followed by a small energy loss to radiation waves, much like inelastic collisions between real particles. This naive picture of soliton interactions gives qualitative understanding of the complex behavior of soliton collisions, yet it is incomplete. In reality, the interacting solitons affect each other's induced waveguide, and the true collision process is much more complicated.

The first experimental papers on collisions between photorefractive solitons were also the first papers reporting fusion of solitons in any medium (see Fig. 11.22) [53, 103] (in parallel to a similar observation with solitons in atomic vapor, for which the nonlinearity is also saturable). These experiments reported on incoherent collisions, between $(2+1)$D [53] and between $(1+1)$D solitons [103], during which at large collision angles the solitons passed through one another unaffected, whereas at shallow collision angles, they fused to one another (see Fig. 11.20). Following these experiments, a team headed by W. Krolikowski studied coherent collisions and demonstrated fission of solitons ("birth" and annihilation of solitons [54, 55], which also constitutes the first observation of such effects in any solitonic system. Other groups have followed and mapped out coherent interactions between $(1+1)$D and $(2+1)$D solitons [105, 106]. All of these were collisions between solitons launched with trajec-

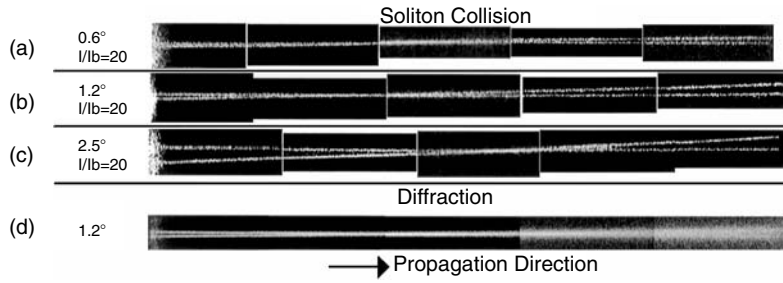

FIGURE 11.20. Collisions, from [53]. Top view of colliding incoherent diffracting beams and solitons for different relative angles.

tories in the same plane. However, because the photorefractive nonlinearity is saturable, one can also look at collisions of $(2 + 1)$D solitons with trajectories that also do *not* lie in the same plane: Full 3D interactions. When nonparallel solitons with trajectories that do not lie in the same plane are launched simultaneously, they interact (attract or repel each other) via the nonlinearity and their trajectories bend. A description of soliton trajectories suggests an intuitive analogy to mechanics. Inertia is represented by the tendency of the beam to evolve in a direction orthogonal to the constant-phase planes, velocity by the component of the wavevector orthogonal to the propagation axis, and interaction forces those mechanisms that modify the direction of the constant phase planes. These, modifying the direction of propagation, change the velocity and therefore induce the equivalent of an acceleration. In this intuitive analogy to mechanics, the soliton system can be thought of possessing initial angular momentum: If the soliton attraction exactly balances the "centrifugal force" due to rotation, the solitons can capture each other into orbit and spiral about, like two celestial objects or two moving charged particles. This idea was suggested in the context of coherent collisions [107]. However, because coherent interactions are critically sensitive to phase, in this case solitons can never attain stable orbits, and spiral about each other. Instead, they always either fuse to form a single beam, or escape away from each other. On the other hand, the purely attractive nature of an incoherent collision between solitons and its independence of the relative phase between these interacting solitons makes such a scheme ideal for the orbiting observation. Under proper initial conditions of separation and beam trajectories, solitons capture each other into an elliptic orbit (see Fig. 11.23) [52]. If the initial distance between the solitons is increased, their trajectories slightly bend toward each other, but their velocity is larger than the equivalent escape velocity, and they do not form a "bound pair." On the other hand, if their separation is too small, they spiral on a "converging orbit" and eventually fuse. In reality, the 3D spiraling-interaction mechanism is much richer and more complicated than initially thought. It turns out that the two spiraling-interacting solitons exchange energy by coupling light into each other's induced waveguide. This is because the nonlinearity is

saturable and the trajectories are at shallow angles. But because the two interacting solitons have equal power, the energy exchange is symmetric. The coupled light is, of course, coherent with its "source" but incoherent with the soliton into which it was coupled. Thus, even though the solitons are initially incoherent with each other, the energy exchange induces partial coherence and thus contributes to the forces involved, which are the result of beam overlap and interference. The end result is that the two solitons orbit periodically about each other and at the same time exchange energy periodically, with the two periods (the spiraling period and the energy exchange period) being only indirectly related [108]. This complicated motion is stable over a wide range of parameters [108]. To some extent, whether or not the spiraling can go on indefinitely is yet an open question, because it is possible that, after long enough propagation distances (far beyond the present experimental reach), the solitons eventually merge [109]. Another interesting feature of spiraling-interacting solitons is the fact that if one adds a tiny seed of light in one of the input solitons that is coherent with the other soliton, the relative phase between these coherent components (the seed and the other soliton) controls the outcome of the collision process, and can turn a spiraling motion into fusion or repulsion [108]. Altogether, the observation of spiraling-interacting solitons has introduced new concepts to soliton physics: Not only energy (power) and momentum are conserved, but also the conservation of angular momentum, which is the fundamental symmetry that enables spiraling.

It is interesting to compare soliton and plane-wave interactions in a photorefractive. The crossing of two plane waves, even at low angles of the order of fractions of a degree, leads to energy transfer. Two solitons, on the other hand, behave in a diametrically opposite manner: They cross each other without appreciable energy transfer even when they are mutually coherent. This difference has a straightforward geometrical explanation: Even though no soliton mechanism forbids the formation of a coupling grating in the region where the two beams overlap, this overlap is spatially limited by the mutual angle θ in their propagation direction and their very narrow width Δx, which is typically no more than 20 wavelengths wide. Thus, in two-wave-mixing terminology, even though the coupling coefficient γ can be reasonably high, the equivalent energy transfer $e^{\gamma L}$, where L is the effective interaction distance in the sample, is negligible. Altogether, soliton interactions, even in photorefractives (which could give rise to energy transfer driven by the diffusion field) is well described by means of soliton interaction forces based on wave-overlap integrals, and the intrinsic energy coupling mechanism that acts in two-wave-mixing is absent.

Photorefraction also allows the investigation of soliton collisions between two solitons of different dimensionality (see Fig. 11.21) [110]. The possibility of carrying out these studies arises from the saturable nature of the nonlinearity, which facilitates stable (2+1)D solitons, as well as the quasi-stable propagation of (1+1)D solitons in 3D bulk media.

A more recent series of studies targeted collisions of solitons propagating in opposite directions [111, 112, 113, 114]. The concept actually applies to any

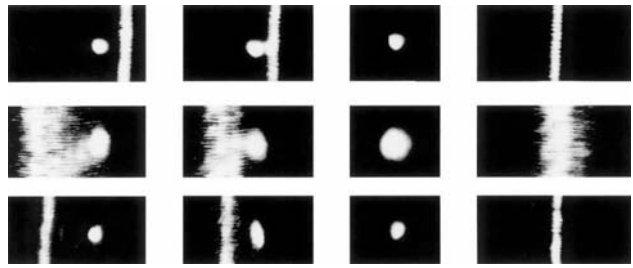

FIGURE 11.21. Hybrid-soliton collisions, from [110]. (a) Input launch of a two-dimensional and a one-dimensional diffracting beam, output intensity distribution with no applied field, output intensity distribution with applied self-trapping field; (b) same as (a) but for a smaller collision angle; (c–d) single beam self-trapping in the same experimental conditions.

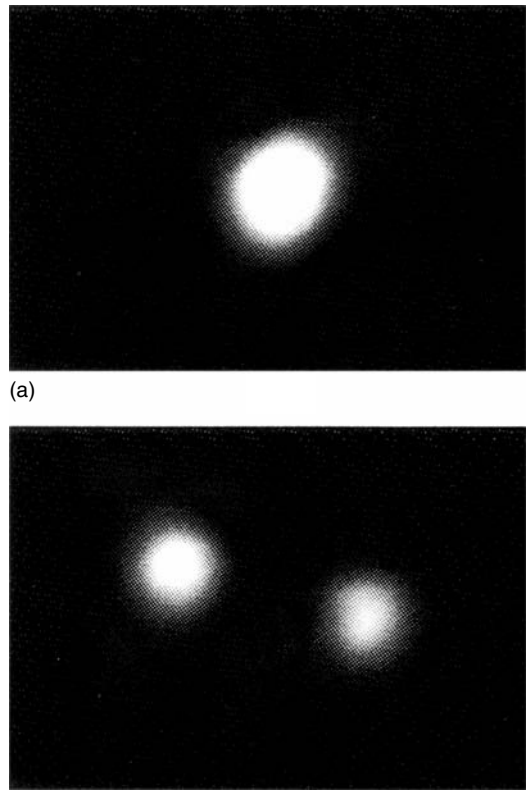

FIGURE 11.22. Soliton fusion, from [54]. Two identical solitons fuse at the output of the sample when they are in-phase (a), whereas they repel when they are out-of-phase (b).

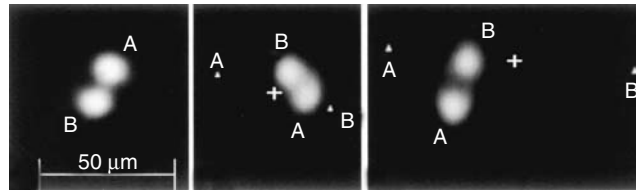

FIGURE 11.23. Soliton spiralling, from [52]. (a) Beams A and B at the input face of the crystal, (b) the spiraling soliton pair after 6.5 mm of propagation, and (c) after 13 mm of propagation. The centers of diffracting A and B are marked by white triangles. The white cross indicates the center of mass of the diffracting beams A and B in (b) and (c).

soliton-supporting system and introduces a different scenario for interacting solitons [115]. Experimentally, thus far only incoherent collisions between such solitons have been studied [112, 114], whereas the more interesting case of coherent collisions [115, 113] is still unexplored, apart for the very specific case of a vector soliton formed between counter-propagating components [116]. In photorefractives, the interaction between the solitons occurs along a spatially extended region (both through mutual phase-modulation and the interference grating), hence spatially nonlocal effects, such as self-bending driven by diffusion fields, have an important impact on the collision dynamics. The experiments of [112, 114] show that the soliton collision dramatically modifies the self-bending of both solitons, in a way that can be directly utilized for all-optical beam deflection, steering, and control.

11.9 Vector and Composite Solitons

In their most basic form, solitons are described by a single optical field. The simplest (so-called scalar) soliton occurs when the soliton constitutes of a single field, which excites (“populates”) the lowest mode of its own induced-waveguide. A more complex soliton, a vector soliton, occurs when more than one field populates the lowest mode of the potential induced jointly by the overall intensity of the soliton. The first vector soliton was suggested by Manakov in Kerr media, when self- and cross-phase modulation are equal [117]. Vector solitons, however, can be also composite: They can be composed of fields that populate *different* modes of their jointly induced potential (waveguide). In one realization, composite solitons are made of a bell-shaped (bright) component populating the lowest mode and a dark component being the second mode. A more interesting situation occurs when the field constituents of the composite soliton populate different bound modes of their jointly-induced potential. These composite, multimode solitons can have two or more intensity humps, and can appear in (1+1)D and in (2+1)D in a variety of intriguing combinations, including (2+1)D composite solitons carrying angular momentum within their field constituents. As will be explained below, almost all the

experiments with vector solitons, and practically all the experiments with multimode solitons, were carried out in photorefractives.

A key issue regarding a vector soliton is that interference terms between the soliton constituents should not contribute to the nonlinear index change (otherwise the induced potential would vary periodically during propagation). Thus, the field constituents making up a vector soliton could originate from orthogonal polarizations states, or from fields at widely-spaced frequencies. In the polarization-based technique, there are no interference terms, whereas in the widely spaced frequencies method, the interference terms are not synchronized with either of the soliton constituents. Photorefractives, however, have offered a much more appealing technique to generate vector solitons: making up a vector soliton from field constituents that are incoherent with one another; that is, their relative phases are randomly fluctuating. When the relative phase between the fields making up the soliton fluctuates much faster than the response time of the nonlinearity, the contribution of interference terms to the nonlinear index change averages out to zero. This method, suggested by Christodoulides et al. [118], has revolutionized the field of vector solitons. With this mutual incoherence method, first a degenerate (Manakov-like) soliton was observed [119], the same year that the first Manakov-type solitons were observed in Kerr media [120]. This was followed by an observation of a vector soliton made up of a bright and a dark component [121]. Shortly thereafter, the first multimode/multihump solitons were observed (see Fig. 11.24) [122]. In this multimode soliton experiment, the two input field distributions resembled the first and/or second and third modes of a slab waveguide. Interestingly, the experiment has also shown that it is possible to observe multimode solitons made up of solely higher modes (the second plus the third modes, trapped in their jointly-induced potential [122]). That is, the experiment has indicated that multimode solitons can exist and propagate in a stable fashion for distances much larger than the diffraction length, in spite of the fact they are made up of only higher-order modes. Several years later, (2+1)D dipole-type composite solitons were also demonstrated experimentally [43, 44]. These vector solitons consist of a bell-shaped component jointly trapped with a 2D dipole mode. The ability to generate (2+1)D composite solitons opens up a whole new range of possibilities that has no counterpart in a lower dimensionality. One fascinating example is the observed rotating ''propeller'' soliton [45]. This is a composite soliton made of a rotating dipole component jointly trapped with a bell-shaped component. It carries and conserves angular momentum, although its constituents exchange angular momentum as they propagate. This soliton is so robust even during inelastic collisions with other composite solitons, the collision products are predicted to be also composite rotating propeller solitons [123].

The relative ease with which vector and composite solitons are generated in photorefractives, by employing the mutual incoherence technique, has also led to a series of experimental efforts demonstrating interaction-collisions between

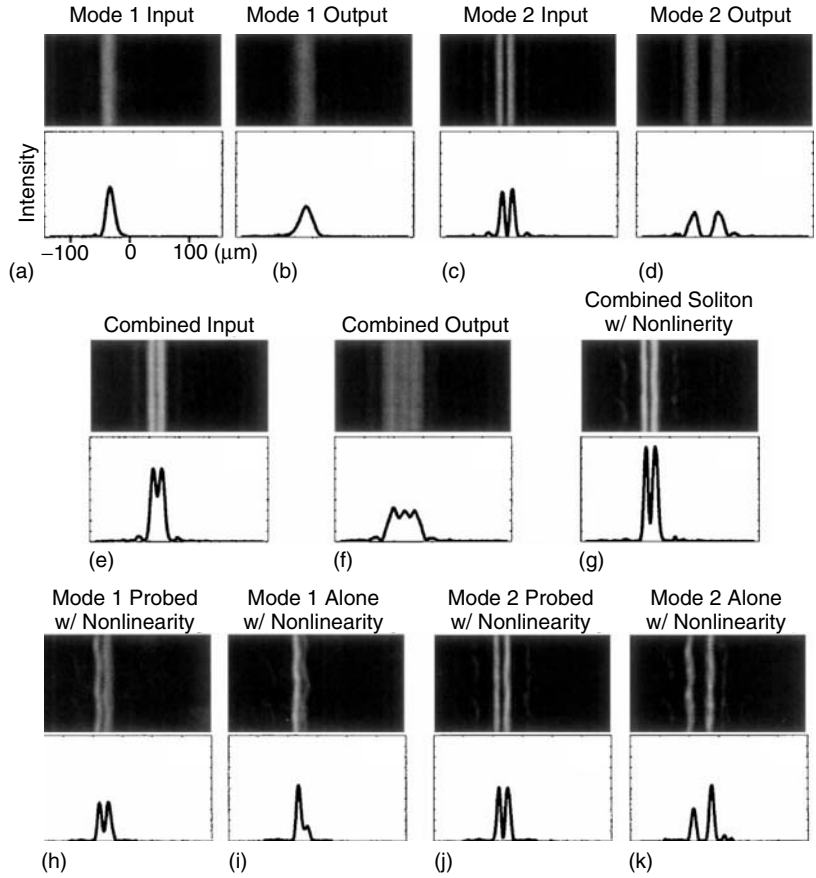

FIGURE 11.24. The observation of a multimode soliton, from [122], with mode 2/mode 1 = 1.0 (a),(b) input (18 μm FWHM) and linear diffraction (27 μm) of mode 1; (c),(d) input (28 μm) and linear diffraction (62 μm) of mode 2; (e),(f) combined input (26 μm) and combined linear diffraction (58 μm); (g) composite soliton formed (26 μm) with application of 800 V/4 mm; (h) first mode obtained after quickly blocking second mode; (i) steady state of first mode alone with nonlinearity on; (j) second mode obtained after quickly blocking first mode; and (k) steady state of second mode alone with nonlinearity on.

vector solitons. It turns out that temporal optical vector solitons, and nonoptical vector solitons are very difficult to generate. For example, it has been predicted, more than two decades ago, that collisions between Manakov-like vector solitons give rise to a symmetric exchange of energy between the soliton constituents [117]. This phenomenon was observed only recently, with photorefractive vector (Manakov-like) solitons [124, 125]. The energy-exchanges

between the soliton components (which have nothing to do with photorefractive two-wave mixing) have direct implications in a new form of reversible computing, in which a "state" is coded as the ratio between the soliton components [126]. In this scheme, computation is performed through the energy-exchange interactions (in which the "states" change) during collisions between vector solitons. The experiments have shown that, not only do such symmetric energy exchanges occur, but also information can be transferred through a series of cascaded collisions between vector solitons [124, 125].

Finally, photorefractives were also the means for experimental studies of interaction-collisions between multimode solitons, in which shape transformations were observed [127]. These were the first ever experiments with collisions of multimode solitons.

The general ideas behind multicomponent vector solitons proved invaluable for later developments and in particular to the area of incoherent solitons discussed in the next section.

11.10 Incoherent Solitons: Self-trapping of Weakly-Correlated Wavepackets

Until 1996, the commonly held belief was that all soliton structures should be inherently coherent entities. In that year, however, Mitchell et al. demonstrated that self-trapping of a partially spatially-incoherent light beam [46] is possible if the nonlinearity has a noninstantaneous temporal response. In that experiment, the optical beam was quasi-monochromatic, but partially spatially-incoherent and the nonlinear medium was photorefractive, with a response much slower than the characteristic time of the phase fluctuations in the incoherent beam. The resultant self-trapped beam is now commonly referred to as an "incoherent soliton" or a "random-phase soliton." One year later, Mitchell and Segev observed a similar self-trapping effect with white light from an incandescent light bulb emitting in the 380–720 nm band. This was the first observation of a self-trapped beam made of light both temporally and spatially incoherent: A white light soliton [47]. In yet another experiment, self-trapping of dark incoherent "beams", i.e., 1D or 2D "voids" nested in a spatially incoherent beam, was also demonstrated [51].

For self-trapping of an incoherent beam (an incoherent soliton) to occur in a local nonlinearity, several conditions must be satisfied. First, the nonlinearity must be noninstantaneous with a response time that is much longer than the phase fluctuation time across the optical beam. Such a nonlinearity responds to the time-averaged envelope and not to the instantaneous "speckles" that constitute the incoherent field. Second, the multimode (speckled) beam should be able to induce, via the nonlinearity, a multimode waveguide. Otherwise, if the induced waveguide is able to support only a single guided mode, the incoherent beam will simply undergo spatial filtering, thus radiating all of its

power but the small fraction that coincides with that guided mode. Third, as with all solitons, self-trapping requires self-consistency: The multimode beam must be able to guide itself in its own induced waveguide (pages 86–125 in Ref.[6]).

The experiments demonstrating incoherent solitons have taken the solitons community by surprise, because typically, in most of soliton research (also beyond optics), all experiments were preceded by a theory predicting the main effects. The experiments demonstrated beyond doubt that incoherent solitons indeed exist. Yet, at the time, something quite important was still missing: A theory! Unlike the case of coherent solitons, where the evolution equation can be straightforwardly derived by adding the nonlinearity to the paraxial equation of diffraction, the description of incoherent solitons was far from being clear. The experiments were of course based on insight and intuition, but then again, they gave only few clues, if any, as to how one could develop a theory. Only one thing was certain The theory of incoherent solitons had to be derived from first principles. Within a year, two different theories were developed to describe incoherent solitons: The coherent density theory [128] and the modal theory [129]. The coherent density theory is, by its very nature, a dynamic approach that is better suited to study the evolution dynamics of incoherent waves, their interactions, instabilities, and so on, as they occur in experimental setups. In this formalism, the incoherent field is described by means of an auxiliary nonobservable function from where one can deduce the optical intensity as well as the associated correlation statistics. The modal theory, on the other hand, by virtue of its inherent simplicity, allows the identification of incoherent solitons, their range of existence, and correlation properties. One year later, yet another theory was proposed: The theory describing the propagation of the mutual coherence [130]. Interestingly enough, even though at first sight these three theoretical approaches seem to be dissimilar, they are in fact formally equivalent to one another, and therefore ultimately provide identical answers [131]. All describe quasi-monochromatic yet partially spatially incoherent solitons: They explain the behavior of such entities, provide their statistical properties, and predict their behavior as they interact with one another. As such, they became a very powerful analytical and numerical tool. More recently, these theories were expanded to describe white light solitons: Solitons that are made of temporally and spatially incoherent light [132, 133].

The pioneering experiments of Refs. [46, 47, 51] that were the first to show the unexpected fact that random-phase solitons can exist with both spatial and temporal incoherence, opened the way for several other important results. These include for example, anti-dark incoherent states [134], elliptic incoherent solitons [135, 136], coherence control using interactions of incoherent solitons [137, 138], and more. Especially noteworthy are the fundamental studies on modulation instability of incoherent waves and spontaneous pattern formation in weakly-correlated systems (systems of partial coherence). It has been found, theoretically and experimentally, that such systems indeed

exhibit modulation instability: A uniform (homogeneous) partially incoherent wavefront breaks up into an array of soliton-like filaments. However, for this to occur, the nonlinearity needs to exceed a threshold value determined by the coherence properties of the waves [139, 140, 141, 142, 143, 144]. This fact stands in a sharp contradistinction with coherent systems, for which there is no such threshold for modulation instability (in a coherent self-focusing system, a uniform wave always breaks up into an array of soliton-like structures). Once this threshold is exceeded, the partially incoherent uniform wave breaks up into an array of localized structures, each behaving as an incoherent soliton. These solitonic "breakup products" interact with one another in an incoherent fashion, exerting long-range attraction on each other. After sufficiently large propagation distance, they aggregate and form clusters of fine-scale structures, leaving large voids between adjacent soliton clusters (aggregates of solitons) [145, 146]. More recent work along these lines is the prediction of modulation instability of white light [147], along with its very recent experimental observation [148], and the work on incoherent pattern formation in cavities [149, 150, 151, 152].

Studies on incoherent solitons and incoherent pattern formation have established that these are not some kind of esoteric processes, specific to photorefractives, but are a new class of solitons, whose existence is relevant to many other diverse fields beyond nonlinear optics. For example, we envision that incoherent modulation instability effects, soliton clustering, and incoherent pattern formation relate to many systems in nature: From clustering in a cooled atomic gas to self-supported "stripes" of electrons in semiconductors, as well as to gravitational-like effects. In fact, the underlying physics relates to any weakly-correlated wave-system having a noninstantaneous nonlinearity. Altogether, it is fair to say that incoherent solitons are most probably the single most important discovery made with self-trapping effects in photorefractive systems. It has introduced a new concept into soliton research, and has implications beyond optics, into other areas where random-phase waves and nonlinearities are involved.

11.11 Applications

11.11.1 Passive Devices

Photorefractive solitons have a series of useful attributes. A photorefractive soliton can passively guide a second beam of longer wavelength, a consequence of the fact that the nonlinear index change is only weakly wavelength dependent, and will act on an infrared beam in much the same manner that it acts on the soliton [153, 154, 155, 156, 157, 158, 159]. This property can be used to make a waveguide in a bulk medium, and hence integrate, into the volume of the material, a fiber or waveguide device without the development of a crystal-specific technique to grow or tailor a waveguide.

Passive waveguiding enables differentiating between a nonlinear and a linear behavior. Consider, for example, a dark soliton, which consists of a nondiffracting intensity notch generated by a π phase jump. In the very same conditions that lead to its formation, the waveguide structure induced by the (dark) soliton can passively guide a bright beam of a longer wavelength, even though such a bright beam (at the shorter wavelength) could *never* self-trap in the same conditions.

More complicated passive devices can be demonstrated, such as reconfigurable directional couplers based on two bright solitons formed in close proximity, Y-junctions, along with more complex multisoliton structures and hybrid soliton-fabricated-waveguides systems [160, 161, 162, 163, 164, 165, 166]. Moreover, in conditions in which the guided beam excites charges, a considerable advantage can be obtained by implementing the ferroelectric fixing technique of the soliton-induced routing device [167].

11.11.2 Active Devices

A second functionality is based on the fact that photorefractives offer all-optical functionality even at low intensities, without any electrical input, even though this is burdened by slow time response [168, 169, 170, 171, 172, 173]. For example, logic operations can be carried out simply by having two solitons interact, or by modulating two different components of a single vector soliton [124, 125]. Another alternative is to use the all-optical operation (via soliton interactions) to steer signals borne on beams guided by solitons.

A second form of active device is that for which soliton dynamics are controlled externally by means of a modulation in the supporting physical parameters, for example, electrically. Thus, for example, the output direction of propagation can be changed by varying the bias voltage, as a consequence of self-bending [25]. Once again, whereas the signal can be delivered in a fast capacity-limited regime (the time constant for charging the equivalent capacitor formed by the sample), the optical response will be dominated by the photorefractive time constants.

11.11.3 Electro-Optic Manipulation

Passive electro-optic effects have been investigated for soliton-deposited space-charge in paraelectric samples [174]. This allows the fast capacity-limited manipulation of optical circuitry through the electro-optic effect, much in the same manner as electroholographic technology [175].

In order to grasp the phenomenon, note that in a linear electro-optic response, once a soliton has been formed through a self-trapping Δn_s, the application of an arbitrary control external bias E_{con} in combination with E_0 leads to a $\Delta n(E_{con}) \propto (E + E_{con})$, which simply changes the constant pedestal on which the soliton guiding pattern induced by the space-charge field E is embedded. This means, for example, that passive guiding can be achieved also for a zero applied external field. For a paraelectric, which is characterized by a quadratic response,

$\Delta n(E_{con}) \propto (E + E_{con})^2 = E^2 + 2EE_{con} + E_{con}^2$. The second mixed term allows for an electro-optic *distortion* of the pattern without any charge redistribution, through a purely spatially resolved electro-response. This has allowed the demonstration of a series of beam manipulation devices, culminating in a two-needle switching device [176] (see Fig. 11.25).

11.11.4 Nonlinear Frequency Conversion in Waveguides Induced by Photorefractive Solitons

The most promising application of waveguides induced by photorefractive solitons is nonlinear frequency conversion [177–180]. The conversion efficiency in χ^2 processes is proportional to the intensity of the pump beam, so it is desirable to work with very narrow beams. One easy way to achieve that is to use a focused pump beam. However, in a bulk crystal, the more tightly focused a beam is, the faster it diffracts, and diffraction limits the frequency conversion efficiency because as the interacting beams diffract, (1) their intensities decrease, and (2) the phase-matching condition cannot be satisfied across their entire cross-section. Using waveguides for frequency conversion overcomes these problems and can greatly improve the conversion efficiency. But thus far it has been difficult to fabricate waveguides from most materials that allow for phase matching, and two-dimensional waveguides are especially difficult to make. At the same time, (2+1)D photorefractive solitons induce 2D waveguides, and almost all photorefractives are highly efficient in χ^2 frequency conversion. Hence, waveguides induced by photorefractive solitons seem promising for nonlinear frequency conversion purposes. This said, the frequency conversion processes must be phase-matched. In waveguides, phase-matching should take place among the propagation constants of the guided modes, and is typically obtained through birefringence or periodic poling. In a fabricated waveguide, however, the structure is fixed, so tuning techniques rely on varying the temperature, or on lateral

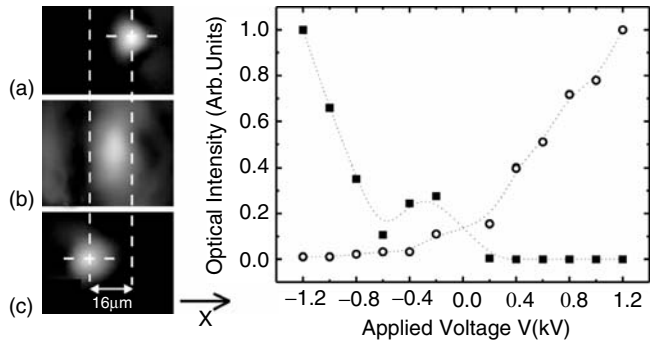

FIGURE 11.25. Electro-optic switching, from [176]. Output intensity distribution with a positive applied field (a); a zero applied field (b); and a negative applied field (c). The beam is routed onto two modes that are 16 μm apart, with a corresponding peak intensity (squares and circles) taken at the two points indicated in (a) and (c).

translation in structures with several periods of poling parallel to one other. But waveguides induced by photorefractive solitons offer much flexibility also with respect to phase-matching, because their waveguide structure and propagation axis (with respect to the crystalline axes) can be modified at will and in real time. Working with photorefractive solitons, one can achieve wavelength tunability while avoiding diffraction by simply rotating the crystal and launching a soliton in the new direction. One can also fine-tune the frequency conversion process by changing the propagation constants of the guided modes through varying the intensity ratio and external voltage, allowing tuning with no mechanical movements.

The first step in the direction of nonlinear frequency conversion in waveguides induced by photorefractive solitons was the demonstration of efficient second-harmonic generation (see Fig. 11.26 and Fig. 11.27) [177, 178]. The experiments have shown that the conversion efficiency can be considerably increased [177], and high tunability can be obtained by rotating the crystal [178]. However, a much more important scenario occurs in a soliton-based optical parametric oscillator (OPO). In an OPO, the threshold pump power is dependent on the signal gain per pass through the crystal. To lower the threshold, one has to increase the signal gain per pass. A waveguide that confines the pump beam as well as the signal and idler in a small area is one very effective way to achieve this. Consider a Gaussian beam at the pump frequency launched into a nonlinear crystal and assume that phase matching is satisfied at the waist, located at the input surface. The threshold pump power is proportional to $[z_0 \arctan^2(L/z_0) + \ln^2(1+ L^2/z_0^2)/4]^{-1}$, where z_0 is the Rayleigh (diffraction) length of the beam and L is the crystal length. For a given L, there exists an optimum beam size for minimum threshold pump power, when $z_0 = L/2.84$. However, if a waveguide is used to keep all beams at the same widths throughout propagation in the crystal, the threshold is simply proportional to z_0/L^2, which continues to decrease as we focus the beam more. The minimum threshold is determined by the smallest size of the waveguide that can

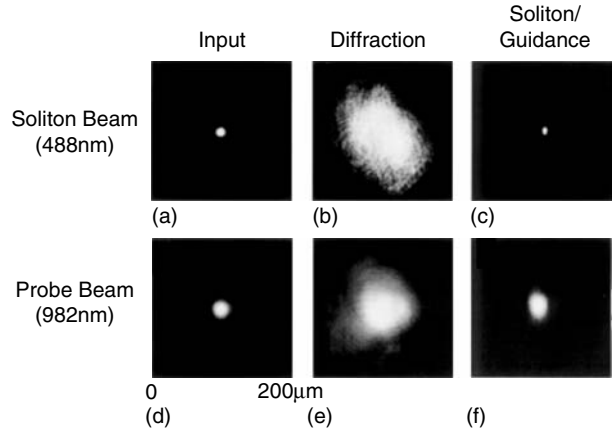

FIGURE 11.26. Second harmonic generation in photorefractive solitons, from [177].

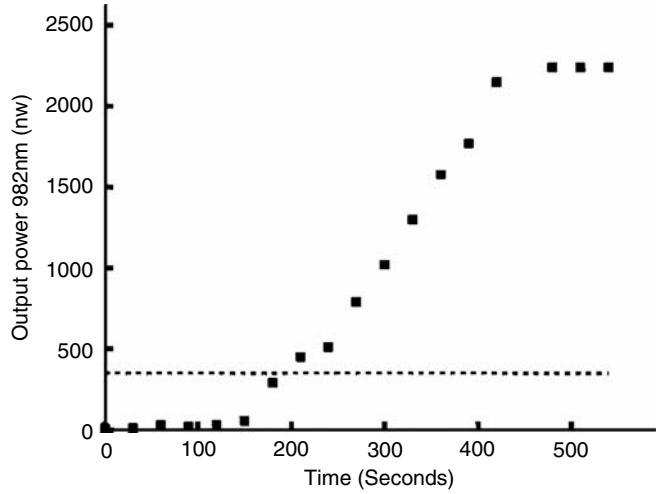

FIGURE 11.27. Second harmonic conversion efficiency increase mediated by spatial solitons, from [177]

be made. To estimate the improvement, consider a focused Gaussian beam with a minimum beam waist of 21 mm and a 15 mm long crystal. An OPO constructed in a waveguide has a threshold pump power 60 percent lower than that of an OPO with the same beam waist in bulk. Therefore, in a waveguide OPO, the signal gain per pass can be considerably improved, and the threshold pump power can be substantially lowered for the same cavity loss. This general idea was recently demonstrated with a doubly-resonant optical parametric oscillator in a waveguide induced by a photorefractive soliton [180]. The OPO threshold was considerably lowered by constructing it within a soliton-induced waveguide. This technique should work even better with singly resonant OPOs and it can substantially reduce the threshold pump power when very narrow solitons are employed. For example, using a soliton beam with a beam waist of 8 mm and a 15 mm long crystal, the OPO threshold pump could be reduced to only 3.5 percent of that for an OPO in the same nonlinear medium, using the same mirrors but without the soliton.

11.12 New Ideas and Concluding Remarks

As we hope transpires from the brief review, there is still much to be understood as to the mechanisms underlying spatial photorefractive self-trapping, from the formation of 2+1D solitons to quasi-steady-state solitons, from dark incoherent solitons to spontaneous self-trapping. The field, however, is in constant expansion, and we cannot refrain from just mentioning the important achievements in the field of lattice solitons (“discrete solitons”) which were recently demonstrated in photorefractive SBN [181, 182, 183, 184], 2D arrays of solitons [185–187] and in the trapping of more exotic excitations such as rings [188].

Although we have attempted to give a detailed account of all aspects of photorefractive self-trapping, the field has undergone such a rapid and extensive evolution that we can hardly guarantee that all contributions have been cited and described. Perhaps this is yet another accomplishment of photorefraction; that is, having given to the soliton science community a powerful and accessible tool with which to further its research and develop new and possibly useful scientific and practical tools.

11.13 Acknowledgements

The authors express their deep gratitude to the numerous funding agencies that have supported their work over the years. These include the US Army Research Office, the US National Science Foundation, the Israeli Science Foundation, the German-Israeli DIP program, the US-Israel Bi-national Science Foundation, and the Italian National Institute for Condensed Matter Physics. We convey our special thanks to Dr. Mikael Ciftan of US Army Research Office, who has supported and closely followed our research from its earliest days. Moti Segev, Greg Salamo and Demeti Christodoulides deeply value his friendship and more than a decade of ongoing support.

References

1. Hasegawa A. and Tappert F., Transmission of stationary nonlinear optical pulses in dispersive dielectric fibers. I. Anomalous dispersion, Appl. Phys. Lett. 23, 142–145 (1973).
2. Mollenauer L.F., Stolen R.H., and Gordon J.P., Experimental observation of picosecond pulse narrowing and solitons in optical fibers, Phys. Rev. Lett. 45–48, 1095 (1980).
3. Segev M., Stegeman G. Self-trapping of optical beams: Spatial solitons, Phys. Today 51, 42–48 (1998).
4. Segev M., Optical spatial solitons, Opt. Quant. Electron. 30, 503–533 (1998).
5. Stegeman G.I., Segev M., Optical spatial solitons and their interactions: Universality and diversity, Science 286, 1518–1523 (1999).
6. Trillo S., and Torruellas W. (Eds.), Spatial Solitons, Springer-Verlag, Berlin Heidelberg (2001).
7. Segev M., Crosignani B., Yariv A, et al., Spatial solitons in photorefractive media, Phys. Rev., Lett. 68, 923–926 (1992).
8. Barthelemy A., Maneuf S., and Froehly C., Propagation soliton et auto-confinement de faisceaux laser par non linearité optique de kerr, Opt. Comm. 55, 201 (1985).
9. Crosignani B., Segev M., Engin D., et al. Self-trapping of optical beams in photorefractive media, J. Opt. Soc. Am B 10, 446–453 (1993).
10. Duree G.C., Shultz J.L., Salamo G.J., et al. Observation of self-trapping of an optical beam due to the photorefractive effect, Phys. Rev. Lett 71, 533–536 (1993).

11. Segev M., Crosignani B., Diporto P., et al. Stability of photorefractive spatial solitons, Opt. Lett. 19, 1296–1298 (1994).
12. Duree G., Salamo G., Segev M., et al. Dimensionality and size of photorefractive spatial solitons, Opt. Lett. 19, 1195–1197 (1994).
13. Christodoulides D.N., Carvalho M.I., Compression, self-bending, and collapse of Gaussian beams in photorefractive crystals, Opt. Lett. 19, 1714–1716 (1994).
14. Tosi-Beleffi G.M., Presi M., DelRe E., et al. Stable oscillating nonlinear beams in square-wave-biased photorefractives, Opt. Lett. 25, 1538–1540 (2000).
15. Segev M., Valley G.C., Crosignani B., et al. Steady-state spatial screening solitons in photorefractive materials with external applied-field, Phys. Rev. Lett. 73, 3211–3214 (1994).
16. Singh S.R., Christodoulides D.N., Evolution of spatial optical solitons in biased photorefractive media under steady-state conditions, Opt. Commun. 118, 569–576 (1995).
17. Christodoulides D.N., Carvalho M.I., Bright, dark, and gray spatial soliton states in photorefractive media, J. Opt. Soc. Am. B 12, 1628–1633 (1995).
18. Segev M., Shih M.F., Valley G.C., Photorefractive screening solitons of high and low intensity, J. Opt. Soc. Am. B 13, 706–718 (1996).
19. Castillo M.D.I., Aguilar P.A.M., Sanchezmondragon J.J., et al. Spatial solitons in photorefractive Bi12Tio20 with drift mechanism of nonlinearity, Appl. Phys. Lett. 64, 408–410 (1994).
20. Shih M.F., Segev M., Valley G.C., et al. Observation of 2-dimensional steady-state photorefractive screening solitons, Electron. Lett. 31, 826–827 (1995).
21. Shih M.F., Leach P., Segev M., et al. Two-dimensional steady-state photorefractive screening solitons, Opt. Lett. 21, 324–326 (1996).
22. Kos K., Meng H.X., Salamo G., et al. One-dimensional steady-state photorefractive screening solitons, Phys. Rev. E 53, R4330–R4333 (1996).
23. DelRe E., Ciattoni A., Crosignani B., et al. Approach to space-charge field description in photorefractive crystals, J. Opt. Soc. Am. B 15, 1469–1475 (1998).
24. Chen Z.G., Mitchell M., Shih M.F., et al. Steady-state dark photorefractive screening solitons, Opt. Lett. 21, 629–631 (1996).
25. Carvalho M.I., Singh S.R., Christodoulides D.N., Self-deflection of steady-state bright spatial solitons in biased photorefractive crystals, Opt. Commun. 120, 311–315 (1995).
26. Sheng Z.M., Cui Y.P., Cheng N., et al. Photorefractive self-trapping and deflection of optical beams, J. Opt. Soc. Am. B 13, 584–589 (1996).
27. Carvalho M.I., Singh S.R., Christodoulides D.N., Self-deflection of steady-state bright spatial solitons in biased photorefractive crystals, Opt. Commun. 124, 642–642 (1996).
28. Singh S.R., Carvalho M.I., Christodoulides D.N., Higher-order space charge field effects on the evolution of spatial solitons in biased photorefractive crystals, Opt. Commun. 130, 288–294 (1996).
29. Krolikowski W., Akhmediev N., LutherDavies B., et al. Self-bending photorefractive solitons, Phys. Rev. E 54, 5761–5765 (1996).
30. Liu J.S., Lu K.Q., Screening-photovoltaic spatial solitons in biased photovoltaic-photorefractive crystals and their self-deflection, J. Opt. Soc. Am. B 16, 550–555 (1999).
31. Petter J., Weilnau C., Denz C., et al. Self-bending of photorefractive solitons, Opt. Commun. 170, 291–297 (1999).

32. Aleshkevich V., Kartashov Y., Vysloukh V., Self-bending of the coupled spatial soliton pairs in a photorefractive medium with drift and diffusion nonlinearity, Phys. Rev. E 63, 016603 (2001).
33. Liu J.S., Hao Z.H., Higher-order space-charge field effects on the self-deflection of bright screening photovoltaic spatial solitons, J. Opt. Soc. Am. B 19, 513–521 (2002).
34. Montemezzani G., Gunter P., Profile of photorefractive one-dimensional bright spatial solitons, Opt. Lett. 22, 451–453 (1997).
35. DelRe E., Agranat A.J., Dielectric nonlinearity in photorefractive spatial soliton formation, Phys. Rev. A 65, 053814 (2002).
36. Kos K., Salamo G., Segev M., High-intensity nanosecond photorefractive spatial solitons, Opt. Lett. 23, 1001–1003 (1998).
37. DelRe E., Crosignani B., Tamburrini M., et al. One-dimensional steady-state photorefractive spatial solitons in centrosymmetric paraelectric potassium lithium tantalate niobate, Opt. Lett. 23, 421–423 (1998).
38. Lan S., Shih M.F., Segev M., Self-trapping of one-dimensional and two-dimensional optical beams and induced waveguides in photorefractive KNbO3, Opt. Lett. 22, 1467–1469 (1997).
39. Chauvet M., Hawkins S.A., Salamo G.J., et al. Self-trapping of two-dimensional optical beams and light-induced waveguiding in photorefractive InP at telecommunication wavelengths, Appl. Phys. Lett. 70, 2499–2501 (1997).
40. DelRe E., Tamburrini M., Segev M., et al. Two-dimensional photorefractive spatial solitons in centrosymmetric paraelectric potassium-lithium-tantalate-niobate, Appl Phys. Lett. 73, 16–18 (1998).
41. Fazio E., Ramadan W., Belardini A., et al. (2+1)-dimensional soliton formation in photorefractive Bi12SiO20 crystals, Phys. Rev. E 67, 026611 (2003).
42. She W.L., Lee K.K., Lee W.K., Observation of two-dimensional bright photovoltaic spatial solitons, Phys. Rev. Lett. 83, 3182–3185 (1999).
43. Carmon T., Anastassiou C., Lan S., et al. Observation of two-dimensional multimode solitons, Opt. Lett. 25, 1113–1115 (2000).
44. Krolikowski W., Ostrovskaya E.A., Weilnau C., et al. Observation of dipole-mode vector solitons, Phys. Rev. Lett. 85, 1424–1427 (2000).
45. Carmon T., Uzdin R., Pigier C., et al. Rotating propeller solitons, Phys. Rev. Lett. 87, 143901 (2001).
46. Mitchell M., Chen Z.G., Shih M.F., et al. Self-trapping of partially spatially incoherent light, Phys. Rev. Lett. 77, 490–493 (1996).
47. Mitchell M., Segev M., Self-trapping of incoherent white light, Nature 387, 880–883 (1997).
48. Duree G., Morin M., Salamo G., et al. Dark photorefractive spatial solitons and photorefractive vortex solitons, Phys. Rev. Lett. 74, 1978–1981 (1995).
49. Chen Z.G., Shih M.F., Segev M., et al. Steady-state vortex-screening solitons formed in biased photorefractive media, Opt. Lett. 22, 1751–1753 (1997).
50. Chen Z.G., Segev M., Wilson D.W., et al. Self-trapping of an optical vortex by use of the bulk photovoltaic effect, Phys. Rev. Lett. 78, 2948–2951 (1997).
51. Chen Z.G., Mitchell M., Segev M., et al. Self-trapping of dark incoherent light beams, Science 280, 889–892 (1998).
52. Shih M.F., Segev M., Salamo G., Three-dimensional spiraling of interacting spatial solitons, Phys. Rev. Lett. 78, 2551–2554 (1997).
53. Shih M.F., Segev M., Incoherent collisions between two-dimensional bright steady-state photorefractive spatial screening solitons, Opt. Lett. 21, 1538–1540 (1996).

54. Krolikowski W., Holmstrom S.A., Fusion and birth of spatial solitons upon collision, Opt. Lett. 22, 369–371 (1997).
55. Krolikowski W., Luther-Davies B., Denz C., et al. Annihilation of photorefractive solitons, Opt. Lett. 23, 97–99 (1998).
56. Zozulya A.A., Anderson D.Z., Mamaev A.V., et al. Self-focusing and soliton formation in media with anisotropic nonlocal material response, Europhys. Lett. 36, 419–424 (1996).
57. Gatz S., Herrmann J., Propagation of optical beams and the properties of two-dimensional spatial solitons in media with a local saturable nonlinear refractive index, J. Opt. Soc. Am. B 14, 1795–1806 (1997).
58. Crosignani B., DiPorto P., Degasperis A., et al. Three-dimensional optical beam propagation and solitons in photorefractive crystals, J. Opt. Soc. Am. B 14, 3078–3090 (1997).
59. Gatz S., Herrmann J., Anisotropy, nonlocality, and space-charge field displacement in (2+1)-dimensional self-trapping in biased photorefractive crystals, Opt. Lett. 23, 1176–1178 (1998).
60. Belic M.R., Vujic D., Stepken A., et al. Isotropic versus anisotropic modeling of photorefractive solitons, Phys. Rev. E 65, 066610 (2002).
61. Calvo G.F., Agullo-Lopez F., Carrascosa M., et al. Two-dimensional soliton-induced refractive index change in photorefractive crystals, Opt. Commun. 227, 193–202 (2003).
62. Meng H.X., Salamo G., Segev M., Primarily isotropic nature of photorefractive screening solitons and the interactions between them, Opt. Lett. 23, 897–899 (1998).
63. Krolikowski W., Saffman M., Luther-Davies B., et al. Anomalous interaction of spatial solitons in photorefractive media, Phys. Rev. Lett. 80, 3240–3243 (1998).
64. DelRe E., Ciattoni A., Agranat A.J., Anisotropic charge displacement supporting isolated photorefractive optical needles, Opt. Lett. 26, 908–910 (2001).
65. Mamaev A.V., Saffman M., Anderson D.Z., et al. Propagation of light beams in anisotropic nonlinear media: From symmetry breaking to spatial turbulence, Phys. Rev. A 54, 870–879 (1996).
66. Shih M.F., Jeng C.C., Sheu F.W., et al. Spatiotemporal optical modulation instability of coherent light in noninstantaneous nonlinear media, Phys. Rev. Lett. 88, 133902 (2002).
67. C. Dari-Salisburgo, E. DelRe, and E. Palange Molding and stretched evolution of optical solitons in cumulative nonlinearities, Phys. Rev. Lett. 91, 263903 (2003).
68. Fressengeas N., Maufoy J., Kugel G., Temporal behavior of bidimensional photorefractive bright spatial solitons, Phys. Rev. E 54, 6866–6875 (1996).
69. Fressengeas N., Maufoy J., Wolfersberger D., et al. Experimental transient self-focusing in Bi12TiO20 crystal Ferroelectrics 202, 193–202 (1997).
70. Fressengeas N., Wolfersberger D., Maufoy J., et al. Build up mechanisms of (1+1)-dimensional photorefractive bright spatial quasi-steady-state and screening solitons, Opt. Commun 145, 393–400 (1998).
71. Fressengeas N., Wolfersberger D., Maufoy J., et al. Experimental study of the self-focusing process temporal behavior in photorefractive Bi12TiO20, J. Appl, Phys 85, 2062–2067 (1999).
72. Wolfersberger D., Fressengeas N., Maufoy J., et al. Experimental study of the behaviour of narrow nanosecond laser pulses in biased photorefractive Bi12TiO20 Ferroelectrics, 223, 381–388 (1999).

73. Maufoy J., Fressengeas N., Wolfersberger D., et al. Simulation of the temporal behavior of soliton propagation in photorefractive media, Phys. Rev. E 59, 6116–6121 (1999).
74. Denz C., Krolikowski W., Petter J., et al. Dynamics of formation and interaction of photorefractive screening solitons, Phys. Rev. E. 60, 6222–6225 (1999).
75. Tosi-Beleffi G.M., Curti F., Boschi D., et al. Soliton-based Y-branch in photorefractive crystals induced through dispersion-shifted optical fiber, Opt. Lett. 28, 1561–1563 (2003).
76. Fuentes-Hernandez C.A., Khomenko A.V., Beam collapse and polarization self-modulation in an optically active photorefractive crystal in an alternating electric field, Phys. Rev. Lett. 83, 1143–1146 (1999).
77. Frolova M.N., Shandarov S.M., Borodin M.V. Self-action of a light beam in a photorefractive crystal in an alternating electric field upon synchronous intensity modulation, Quantum. Electron. 32, 45–48 (2002).
78. Wolfersberger D., Fressengeas N., Maufoy J., et al. Self-focusing of a single laser pulse in a photorefractive medium, Phys. Rev. E 62, 8700–8704 (2000).
79. Wolfersberger D., Lhomme F., Fressengeas N., et al. Simulation of the temporal behavior of one single laser pulse in a photorefractive medium, Opt. Commun. 222, 383–391 (2003).
80. Valley G.C., Segev M., Crosignani B., Yariv A., Fejer M.M., and Bashaw M., Dark and bright photovoltaic spatial solitons, Phys. Rev. A **50**, R4457–R4460 (1994).
81. Crosignani B., DelRe E., Di Porto P., et al. Self-focusing and self-trapping in unbiased centrosymmetric photorefractive media, Opt. Lett. 23, 912–914 (1998).
82. Chauvet M., Hawkins S.A., Salamo G.J., et al. Self-trapping of planar optical beams by use of the photorefractive effect in InP:Fe, Opt. Lett. 21, 1333–1335 (1996).
83. DelRe E., Tamburrini M., Segev M., et al. Spontaneous self-trapping of optical beams in metastable paraelectric crystals, Phys. Rev. Lett. 83, 1954–1957 (1999).
84. Klotz M., Meng H.X., Salamo G.J., et al. Fixing the photorefractive soliton, Opt. Lett. 24, 77–79 (1999).
85. Klotz M., Crosser M., Guo A., et al. Fixing solitonic y junctions in photorefractive strontium-barium-niobate, Appl. Phys. Lett. 79, 1423–1425 (2001).
86. Segev M., Valley G.C., Bashaw M.C., et al. Photovoltaic spatial solitons, J. Opt. Soc. Am. B 14, 1772–1781 (1997).
87. Taya M., Bashaw M.C., Fejer M.M., Segev M. and Valley G.C., Observation of dark photovoltaic spatial solitons, Phys. Rev. A **52**, 3095–3100 (1995).
88. Anastassiou C., Shih M.F., Mitchell M., et al. Optically induced photovoltaic self-defocusing-to-self-focusing transition, Opt. Lett. 23, 924–926 (1998).
89. Schwartz T., Ganor Y., Carmon T., et al. Photorefractive solitons and light-induced resonance control in semiconductor CdZnTe, Opt. Lett. 27, 1229–1231 (2002).
90. Uzdin R., Segev M., Salamo G.J., Theory of self-focusing in photorefractive InP, Opt. Lett. 26, 1547–1549 (2001).
91. Crosignani B., Degasperis A., DelRe E., et al. Nonlinear optical diffraction effects and solitons due to anisotropic charge-diffusion-based self-interaction, Phys. Rev. Lett. 82, 1664–1667 (1999).
92. Shih M.F., Sheu F.W., Photorefractive polymeric optical spatial solitons, Opt. Lett. 24, 1853–1855 (1999).
93. Sheu F.W., Shih M.F., Photorefractive polymeric solitons supported by orientationally enhanced birefringent and electro-optic effects, J. Opt. Soc. Am. B 18, 785–793 (2001).

94. Chen Z.G., Asaro M., Ostroverkhova O., et al. Self-trapping of light in an organic photorefractive glass, Opt. Lett. 28, 2509–2511 (2003).
95. Castillo M.D., Sanchez-Mondragon J.J., Stepanov S.I., et al. Probe Beam Wave-Guiding Induced By Spatial Dark Solitons In Photorefractive Bi12TiO2 Crystal, Rev. Mex. Fis 41, 1–10 (1995).
96. Castillo M.D., Sanchez-Mondragon J.J., Stepanov S.I., et al. (1+1)-Dimension Dark Spatial Solitons In Photorefractive Bi12TiO2 Crystal, Opt. Commun. 118, 515–519 (1995).
97. Sarabia C.M.G., Aguilar P.A.M., Mondragon J.J.S., et al. Dynamics of photo-induced lens formation in a photorefractive Bi12TiO2 crystal under an external dc electric field, J. Opt. Soc. Am. B 13, 2767–2774 (1996).
98. Singh S.R., Christodoulides D.N., Effects of optical activity on photorefractive spatial solitons in a biased Bi12TiO2 crystal, J. Opt. Soc. Am. B 13, 719–724 (1996).
99. Krolikowski W., Akhmediev N., Andersen D.R., et al. Effect of natural optical activity on the propagation of photorefractive solitons, Opt. Commun. 132, 179–189 (1996).
100. Fazio E., Babin V., Bertolotti M., et al. Solitonlike propagation in photorefractive crystals with large optical activity and absorption, Phys. Rev. E 66, 016605 (2002).
101. Segev M., Agranat A.J., Spatial solitons in centrosymmetric photorefractive media, Opt. Lett. 22, 1299–1301 (1997).
102. Zabusky N.J. and Kruskal M.D., Interaction of "solitons" in a collisionless plasma and the recurrence of initial states, Phys. Rev. Lett. 15, 240–243 (1965).
103. Shih M.F., Chen Z.G., Segev M., et al. Incoherent collisions between one-dimensional steady-state photorefractive screening solitons, Appl. Phys. Lett. 69, 4151–4153 (1996).
104. Askar'yan G. A., Sov. Phys. JETP 15, 1088 (1962).
105. Meng H.X., Salamo G., Shih M.F., et al. Coherent collisions of photorefractive solitons, Opt. Lett. 22, 448–450 (1997).
106. Mamaev A.V., Saffman M., Zozulya A.A., Phase-dependent collisions of (2+1)-dimensional spatial solitons, J. Opt. Soc. Am. B 15, 2079–2082 (1998).
107. Mitchell D.J., Synder A.W., and Poladian L., Spiraling spatial solitons, Opt. Comm. 85, 59–62 (1991).
108. Buryak A.V., Kivshar Y.S., Shih M.F., et al. Induced coherence and stable soliton spiraling, Phys. Rev. Lett. 82, 81–84 (1999).
109. Belic M.R., Stepken A., Kaiser F., et al., Spiraling behavior of photorefractive screening solitons, Phys. Rev. Lett. 82, 544–547 (1999); Stepken A., Belic M.R., Kaiser F. et al., Three dimensional trajectories of interacting incoherent photorefractive solitons, Phys. Rev. Lett. 82, 540–543 (1999).
110. DelRe E., Trillo S., Agranat A.J., Collisions and inhomogeneous forces between solitons of different dimensionality, Opt. Lett. 25, 560–562 (2000).
111. DelRe E., Ciattoni A., Crosignani B., et al. Nonlinear optical propagation phenomena in near-transition centrosymmetric photorefractive crystals J. Nonlinear, Opt., Phys. 8, 1–20 (1999).
112. Kip D., Herden C., Wesner M., All-optical signal routing using interaction of mutually incoherent spatial solitons Ferroelectrics, 274, 135–142 (2002).
113. Belic M., Jander P., Strinic A., et al. Self-trapped bidirectional waveguides in a saturable photorefractive medium, Phys.Rev.E 68, 025601 (2003).

114. Rotschild C., Cohen O., Manela O., Carmon T., and Segev M., Interactions between spatial screening solitons propagating in opposite directions, J. Opt. Soc. Am. B 21, 1354, 2004.
115. Cohen O., Uzdin R., Carmon T., Fleischer J.W., Segev M., and Odoulov S., Collisions between Optical Spatial Solitons Propagating in Opposite Directions, Phys. Rev. Lett. 89, 133901 (2002).
116. Cohen O., Lan S., Carmon T., Giordmaine J. A., and Segev M., Spatial vector solitons consisting of counter-propagating fields, Opt.Lett. 27, 2013 (2002).
117. Manakov S.V., Sov., Phys. JETP 38, 248 (1974).
118. Christodoulides D.N., Singh S.R., Carvalho M.I., et al. Incoherently coupled soliton pairs in biased photorefractive crystals, Appl. Phys. Lett. 68, 1763–1765 (1996).
119. Chen Z.G., Segev M., Coskun T.H., et al. Observation of incoherently coupled photorefractive spatial soliton pairs, Opt. Lett. 21, 1436–1438 (1996).
120. Kang J.U., Stegeman G.I., Aitchison J.S., and Akhmediev N., Observation of Manakov spatial solitons in AlGaAs planar waveguides, Phys. Rev. Lett. 76, 3699–3702 (1996).
121. Chen Z., Segev M., Coskun T., Christodoulides D., Kivshar Y., and Afanasjev V., Observation of incoherently coupled dark-bright photorefractive spatial soliton pairs, Opt. Lett. 21, 1821 (1996).
122. Mitchell M., Segev M. and Christodoulides D. N., Observation of multi-hump multi-mode solitons, Phys. Rev. Lett. 80, 4657–4660 (1998).
123. Pigier C., Uzdin R., Carmon T., Segev M., Nepomnyashchy A. and Musslimani Z. H., Collisions between (2+1)D rotating propeller solitons, Opt. Lett. 26, 1577 (2001).
124. Anastassiou C., Segev M., Steiglitz K., et al. Energy-exchange interactions between colliding vector solitons, Phys. Rev. Lett. 83, 2332–2335 (1999).
125. Anastassiou C., Fleischer J. W., Carmon T., Segev M., and Steiglitz K., Information transfer through cascaded collisions of vector solitons, Opt. Lett. 26, 1498 (2001).
126. Jakubowski M. H., Steiglitz K. and Squier R., Phys. Rev. E 58, 6752 (1998).
127. Krolikowski W., Akhmediev N., Luther-Davies B., Collision-induced shape transformations of partially coherent solitons, Phys. Rev. E 59, 4654–4658 (1999).
128. Christodoulides D.N., Coskun T.H., Mitchell M., et al. Theory of incoherent self-focusing in biased photorefractive media, Phys. Rev. Lett. 78, 646–649 (1997).
129. Mitchell M., Segev M., Coskun T.H., et al. Theory of self-trapped spatially incoherent light beams, Phys. Rev. Lett. 79, 4990–4993 (1997).
130. Shkunov V.V. and Anderson D.Z., Radiation Transfer Model of Self-Trapping Spatially Incoherent Radiation by Nonlinear Media, Phys. Rev. Lett. 81, 2683–2686 (1998).
131. Christodoulides D.N., Eugenieva E.D., Coskun T.H., et al. Equivalence of three approaches describing partially incoherent wave propagation in inertial nonlinear media, Phys. Rev. E 63, 035601 (2001).
132. Buljan H., Segev M., Soljacic M., Efremidis N.K., and Christodoulides D.N., White light solitons, Opt. Lett. 28, 1239–1241 (2003).
133. Buljan H., Siber A., Soljacic M., Schwartz T., Segev M., and Christodoulides D.N., White light solitons in logarithmically saturable nonlinear media, Phys. Rev. E 68, 036607 (2003).
134. Coskun T.H., Christodoulides D.N., Kim Y.R., et al. Bright spatial solitons on a partially incoherent background, Phys. Rev. Lett. 84, 2374–2377 (2000).

135. Eugenieva E.D., Christodoulides D.N., Segev M., Elliptic incoherent solitons in saturable nonlinear media, Opt. Lett. 25, 972–974 (2000).
136. Katz O., Carmon T., Schwartz T., Segev M. and Christodoulides D.N., Observation of elliptic incoherent spatial solitons, Opt. Lett. 29, 1248–1250 (2004).
137. Coskun T.H., Grandpierre A.G., Christodoulides D.N., et al. Coherence enhancement of spatially incoherent light beams through soliton interactions, Opt. Lett. 25, 826–828 (2000).
138. Coskun T.H., Christodoulides D.N., Mitchell M., et al. Dynamics of incoherent bright and dark self-trapped beams and their coherence properties in photorefractive crystals, Opt. Lett. 23, 418–420 (1998).
139. Soljacic M., Segev M., Coskun T., et al. Modulation instability of incoherent beams in noninstantaneous nonlinear media, Phys. Rev. Lett. 84, 467–470 (2000).
140. Kip D., Soljacic M., Segev M., Eugenieva E., and Christodoulides D.N., Modulation instability and pattern formation in spatially incoherent light beams, Science 290, 495 (2000); Kip D., Soljacic M., Segev M., et al. (1+1)- Dimensional modulation instability of spatially incoherent light, J. Opt. Soc. Am. B 19, 502–512 (2002).
141. Anastassiou C., Soljacic M., Segev M., Kip D., Eugenieva E., Christodoulides D.N. and Musslimani Z.H., Eliminating the transverse instabilities of Kerr solitons, Phys. Rev. Lett. 85, 4888–4891 (2000).
142. Torres J.P., Anastassiou C., Segev M., Soljacic M. and Christodoulides D.N., Transverse instability of incoherent solitons in Kerr media, Phys. Rev. E 65, 15601 (2001).
143. Jeng C.C., Shih M., Motzek K., Kivshar Y., Partially incoherent optical vortices in self-focusing nonlinear media, Phys. Rev. Lett. 92, 043904 (2004).
144. Anderson D., Helczynski-Wolf L., Lisak M., et al., Features of modulational instability of partially coherent light: importance of the incoherence spectrum, Phys. Rev. E. **69**, 025601–025604 (2004).
145. Chen Z., Sears S.M., Martin H., Christodoulides D.N. and Segev M., Clustering of solitons in weakly correlated systems, Proceedings of the US National Academy of Science (PNAS) 99, 5223 (2002).
146. Sears S.M., Soljacic M., Christodoulides D.N. and Segev M., Pattern formation via symmetry breaking in nonlinear weakly correlated systems, Phys. Rev. E 65, 36620 (2002).
147. Buljan H., Siber A., Soljacic M., and Segev M., Propagation of incoherent "white" light and modulation instability in non-instantaneous nonlinear media, Phys. Rev. E 66, R35601 (2002).
148. Schwartz T., Buljan H., and Segev M., Modulation instability and pattern formation with white incoherent light, Phys. Rev. Lett. 93, 223901–223904 (2004).
149. Carmon T., Soljacic M., and Segev M., Pattern formation in a cavity longer than the coherence length of the light in it, Phys. Rev. Lett. 89, 183902 (2002).
150. Schwartz T., Fleischer J.W., Carmon T., Cohen O., Buljan H., and Segev M., Pattern formation in a ring cavity with a temporally-incoherent feedback, J. Opt. Soc. Am. B 21, 2197–2205 (2004).
151. Buljan H., Soljacic M., Carmon T., and Segev M., Cavity pattern formation with incoherent light, Phys. Rev. E 68, 016616 (2003).
152. Carmon T., Buljan H., and Segev M., Spontaneous pattern formation in a cavity with incoherent light, Opt. Exp. 12, 3481–3487 (2004).
153. Morin M., Duree G., Salamo G., et al. Wave-guides formed by quasi-steady-state photorefractive spatial solitons, Opt. Lett. 20, 2066–2068 (1995).

154. Torres-Cisneros G., Sanchez-Mondragon J., Iturbe-Castillo M., et al. Optical wave-guides generated by spatial solitons, Rev. Mex. Fis 41, 662–694 (1995).
155. Shih M.F., Segev M., Salamo G., Circular waveguides induced by two-dimensional bright steady-state photorefractive spatial screening solitons, Opt. Lett. 21, 931–933 (1996).
156. Liu S.M., Zhang G.Q., Sun Q., et al. Waveguides written and stored by photovoltaic dark spatial solitons in $LiNbO_3$:Fe crystals, Chin., Phys. Lett. 13, 737–740 (1996).
157. Shih M.F., Chen Z.G., Mitchell M., et al. Waveguides induced by photorefractive screening solitons, J. Opt. Soc. Am. B 14, 3091–3101 (1997).
158. Petter J., Denz C., Stepken A., et al. Anisotropic waveguides induced by photoreftactive (2+1)D solitons, J. Opt. Soc. Am. B 19, 1145–1149 (2002).
159. Kip D., Anastassiou C., Eugenieva E., et al. Transmission of images through highly nonlinear media by gradient-index lenses formed by incoherent solitons, Opt. Lett. 26, 524–526 (2001).
160. Lan S., DelRe E., Chen Z.G., et al. Directional coupler with soliton-induced waveguides, Opt. Lett. 24, 475–477 (1999).
161. Chen Z.G., Mitchell M., Segev M., Steady-state photorefractive soliton-induced Y-junction waveguides and high-order dark spatial solitons, Opt. Lett. 21 (10): 716–718 MAY 15 (1996).
162. Taya M., Bashaw M.C., Fejer M.M., et al. Y junctions arising from dark-soliton propagation in photovoltaic media, Opt. Lett. 21, 716–718 (1996).
163. Chen Z.G., Segev M., Singh S.R., et al. Sequential formation of multiple dark photorefractive spatial solitons: Experiments and theory, J. Opt. Soc. Am. B 14, 1407–1417 (1997).
164. Kip D., Wesner M., Shandarov V., et al. Observation of bright spatial photorefractive solitons in a planar strontium barium niobate waveguide, Opt. Lett. 23, 921–923 (1998).
165. Wesner M., Herden C., Kip D., et al. Photorefractive steady state solitons up to telecommunication wavelengths in planar SBN waveguides, Opt. Commun. 188, 69–76 (2001).
166. Chauvet M., Chauvin S., Maillotte H., Transient dark photovoltaic spatial solitons and induced guiding in slab $LiNbO_3$ waveguides, Opt. Lett. 26, 1344–1346 (2001).
167. Guo A., Henry M., Salamo G.J., et al. Fixing multiple waveguides induced by photorefractive solitons: directional couplers and beam splitters, Opt. Lett. 26, 1274–1276 (2001).
168. Eugenieva E.D., Roussev R.V., Dinev S.G., Soliton-controlled switching in photorefractive media, J. Mod. Optic. 44, 1127–1140 (1997).
169. Andrade-Lucio J. A., Mendez-Otero M.M., Gomez-Sarabia C.M., et al. Controllable optical Y-junctions based on dark spatial solitons generated by holographic masks, Opt. Commun. 165, 77–82 (1999).
170. Malomed B. A., Multichannel switchable system for spatial solitons, J. Opt. Soc. Am. B 16, 1197–1203 (1999).
171. Dittrich P., Montemezzani G., Bernasconi P., et al. Fast, reconfigurable light-induced waveguides, Opt. Lett. 24, 1508–1510 (1999).
172. Andrade-Lucio J. A., Alvarado-Mendez B., Rojas-Laguna R., et al. Optical switching by coherent collision of spatial solitons Electron, Lett. 36, 1403–1405 (2000).
173. Petter J., Denz C., Guiding and dividing waves with photorefractive solitons, Opt. Commun. 188, 55–61 (2001).

174. DelRe E., Tamburrini M., Agranat A. J., Soliton electro-optic effects in paraelectrics, Opt. Lett. 25, 963–965 (2000).
175. Balberg M., Razvag M., Vidrio S., Refaeli E., Agranat A. J., Opt. Lett. 21, 1544–1546 (1996).
176. DelRe E., Crosignani B., Di Porto P., et al. Electro-optic beam manipulation through photorefractive needles, Opt.Lett. 27, 2188–2190 (2002).
177. Lan S., Shih M.F., Mizell G., et al. Second-harmonic generation in waveguides induced by photorefractive spatial solitons, Opt. Lett. 24, 1145–1147 (1999).
178. Lan S., Anastassiou C., Segev M., et al. Tuning of second-harmonic generation in waveguides induced by photorefractive spatial solitons, Appl. Phys. Lett 77, 2101–2103 (2000).
179. Boardman A.D., Ilecki W., Liu Y., Spatial solitons in a photorefractive medium sustaining second-harmonic generation J. Opt. Soc. Am. B 19, 832–838 (2002).
180. Lan S., Giordmaine J.A., Segev M., et al. Optical parametric oscillation in soliton-induced waveguides, Opt. Lett. 27, 737–739 (2002).
181. Efremidis N.K., Sears S., Christodoulides D.N., et al. Discrete solitons in photorefractive optically induced photonic lattices, Phys. Rev. E 66, 046602 (2002).
182. Fleischer J.W., Carmon T., Segev M., et al. Observation of discrete solitons in optically induced real time waveguide arrays, Phys. Rev. Lett. 90, 023902 (2003).
183. Fleischer J.W., Segev M., Efremidis N. K., and Christodoulides D. N., Observation of two-dimensional discrete solitons in optically-induced nonlinear photonic lattices, Nature 422, 147 (2003).
184. Neshev D., Ostrovskaya E., Kivshar Y., et al. Spatial solitons in optically induced gratings, Opt. Lett. 28, 710–712 (2003).
185. Chen Z., and MacCarthy K., Spatial soliton pixels from partially coherent light, Opt. Lett. 27, 2019–2021 (2002).
186. Petter J., Schroder J., Trager D., et al. Optical control of arrays of photorefractive screening solitons, Opt. Lett. 28, 438–440 (2003).
187. Petrovic M., Trager D., Strinic A., et al. Solitonic lattices in photorefractive crystals, Phys. Rev. E 68, 055601 (2003).
188. Anastassiou C., Pigier C., Segev M., et al. Self-trapping of bright rings, Opt. Lett. 26, 911–913 (2001).

12

Thermal Fixing of Photoinduced Gratings

M. Carrascosa, L. Arizmendi, and J.M. Cabrera

Dpto. Física de Materiales C-IV, Universidad Autónoma de Madrid Cantoblanco, Madrid E-28049, Spain
m.carrascosa@uam.es

In this Chapter, the present knowledge on thermal fixing of photorefractive bulk and waveguide holograms is reviewed. First, the basic technique together with the phenomenological model for thermal fixing, mostly developed for $LiNbO_3$, are described. Then, a coherent and clear picture of thermal fixing is provided through a recent mathematical formulation of the model. The capabilities and reliability of this general framework to explain and/or predict most experimental results via the development of approximate models is illustrated with applications to relevant situations such as the design of long lifetime photorefractive devices. Within the experimental aspects of thermal fixing, details are given on experimental methods and techniques together with comments on their advantages and drawbacks. Relevant experimental data on bulk and waveguides geometries are provided and discussed within the mentioned theoretical approach. In addition, thermal fixing applications of $LiNbO_3$ to practical devices in both geometries are presented and discussed. Situations out of the standard model as well as thermal fixing in other materials different from $LiNbO_3$ are briefly considered.

12.1 Introduction

The discovery of the photorefractive effect in $LiNbO_3$ by Ashkin and coworkers [1] in 1966 opened the door to a large variety of experiments and applications [2, 3, 4, 5], many of them related to the memory effect of the photorefractive phenomenon. However, photorefraction is a reversible effect by which the reading-beam used to retrieve the recorded pattern continuously modifies it. This is a major drawback in those applications requiring long lifetime of the pattern such as information storage, beam modulators and deflectors, narrow-band interference filters, and so on. Because of that, already early workers investigated possible routes for increasing the lifetime of the recorded patterns, and since then a considerable effort has been devoted to the subject.

Several methods have been developed for increasing the duration of recorded patterns in $LiNbO_3$, as well as in other materials that present a photorefractive effect similar to that of $LiNbO_3$. Some methods are based on using a reading

wavelength with very low photorefractive efficiency, so optical erasing is negligible (nondestructive read-out). This can be achieved by reading at a wavelength (for example, infrared) different from the recording one (for example, green) and is usually called *two-wavelength technique*. An alternative procedure is the so-called *two-photon recording*. This method consists of shining the crystal with an additional light source that is not present during reading. The additional light acts as activator during recording and its absence during reading prevents pattern degradation. These subjects are considered in other chapters in this book.

The methods named by *fixing* are based on the generation of a light-insensitive replica of the electronic pattern via some structural property of the crystal as the spontaneous polarization in ferroelectric crystals (*electrical fixing*), or some mobile ionic charges as protons in $LiNbO_3$ and other similar oxides (*thermal fixing*). The latter method was first reported by Amodei and Staebler for $LiNbO_3$ in 1972 [6, 7] and has become a key technique for the fabrication of diffractive devices either in bulk or in waveguide configuration. Since the Amodei and Staebler work, many papers have been published on the subject, discussing the origin of thermal fixing, trying to establish sound physical basis for theoretical treatments, as well as to increase the pattern duration in applications. In fact, thermal fixing has produced the first marketed photorefractive device consisting of a very narrow bandwidth interference filter [8, 9]. Experiments and modeling have been even extended to photorefractive waveguides because of their potential interest in optical communication devices. The present chapter focuses on the physical basis of thermal fixing (including important experiments and theoretical developments), major recent advances to increase the storage lifetime, and relevant applications.

12.2 The Thermal Fixing Technique

The basic procedure for the thermal fixing technique, first reported by Amodei and Staebler for $LiNbO_3$ [6, 7], continues almost unchanged. In brief, the method consists of recording a pattern at room temperature, heating the sample at high temperature (over 100°C) and, after cooling down to room temperature, shining the sample with homogeneous light. Amodei and Staebler's explanation assumed the generation of a replica of the trapped charge pattern (light-erasable), as that sketched in Fig. 12.1, into a fixed matching ionic pattern (light-insensitive). It is now generally accepted that in $LiNbO_3$ [10, 11, 12, 13, 14] thermal fixing is produced by migration of protons that are present in common as-grown crystals. In bulk $LiNbO_3$, protons become mobile at temperatures above ~ 70°C, whilst trapped electrons are thermally excited at a much smaller rate between this temperature and ~ 180°C in nonreduced $LiNbO_3$. (In reduced samples, shallow electron traps are present with a detrapping temperature much lower [15]). Between these two temperatures, typically ~ 150°C, protons can migrate driven by the space charge field created by trapped electrons, the process being much faster than electron detrapping.

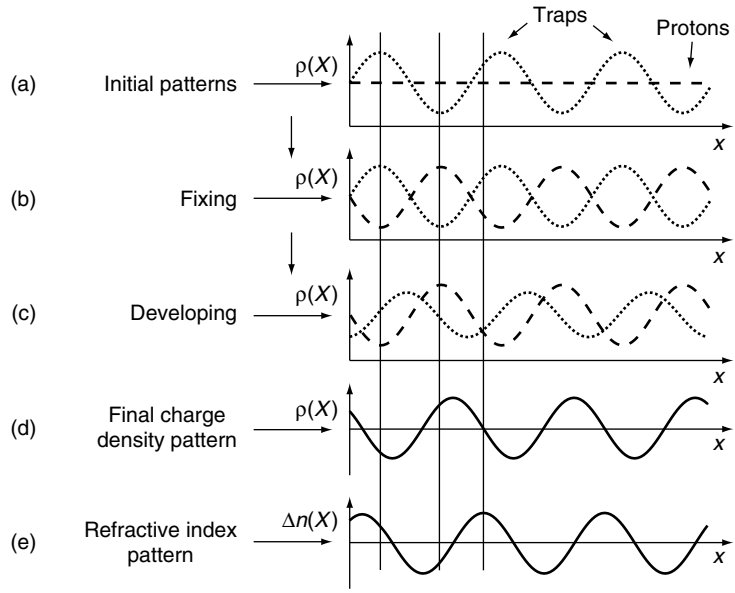

FIGURE 12.1. Stages of photorefractive fixing. a) Initial trap pattern recorded at room temperature, together with an homogeneous proton distribution. b) During thermal fixing (100°CT180°C), ions migrate in the space charge field until charge compensation is reached (electrons remain trapped). c) During developing with homogeneous illumination, migration of photoelectrons produces an amplitude decrease and a phase shift of the trap pattern. d) Charge density pattern resulting from the proton and trap patterns, and e) induced refractive index pattern. Vertical lines are references for phase comparison.

Photorefractive thermal fixing has been also observed in a number of other materials such as $BaTiO_3$, $Bi_{12}SiO_{20}$, and so on. Their properties will be listed in Section 12.4.4. Anyhow, in these materials, the performance of fixed holograms is substantially lower than in $LiNbO_3$, greatly limiting their practical use for permanent storage.

A fixed grating has inevitably a finite lifetime, although it is much longer than the nonfixed hologram. Even in the dark, there always exists a slow decay of the diffraction efficiency with a corresponding lifetime ranging between weeks to years, depending on materials and dopants. On the other hand, the developed pattern can be purposely erased by heating the sample above 200 °C. This treatment gives rise to a completely fresh sample without any memory of previously stored information.

12.2.1 Physical Model for Thermal Fixing

The following two basic stages take place during the fixing process. In the first stage, at temperatures ranging within $\sim 100°C - \sim 180°C$, proton migration proceeds till the trapped-electron space-charge field is compensated. On a

subsequent cooling down to room temperature, ionic migration is frozen and the pattern of ionic charge, matching the initial trapped electron pattern, is said to be *fixed*. This first stage of the fixing process has been illustrated in Fig. 12.1(a,b). Recording can also be performed at high temperature (between $\sim 100°C$ and $\sim 180°C$) instead of at room temperature. In that case, the amplitudes of both trapped electron and proton patterns keep increasing, because they electrically compensate each other along the process, until a final saturating field is reached [16, 17]. This results in much higher final amplitudes for both patterns, i. e., higher fixing efficiency, although electrical breakdown can happen under certain circumstances [13].

The proton pattern is *developed* at room temperature by homogeneous illumination, which gives rise to some redistribution of trapped electrons. Electron redistribution involves both amplitude decrease and phase shift of the electronic grating with respect to the protonic one. The phase shift is due to the photovoltaic effect and becomes particularly important in $LiNbO_3$ [18, 19, 20]. The result is a stable index grating originated by the partially uncompensated protonic grating (see a microphotometric investigation in reference [21, 20] and a macroscopic confirmation in [13]). Fig. 12.1 c, d, and e schematically illustrates the process. Further homogeneous illuminations during later readings act as additional developings and will not at all erase the fixed-developed pattern. When recording is performed at room temperature, the method is called a *three-step method* in reference to the number of stages of the procedure. Correspondingly, when recording is carried out at high temperature, simultaneously to proton migration, the method is called a *two-step method*. An alternative terminology that appears in some works uses *low-high-low* or *high-low*, respectively in reference to the temperature of each step. The developing can be also performed with a sinusoidal light pattern with an appropriate phase shift [22]. In that case, the process is faster and a much greater transient developed diffraction efficiency is obtained.

As $LiNbO_3$ remains the most promising crystal for storage applications, particularly via thermal fixing, and a large majority of work has been done on this material, the discussion in this chapter will mainly refer to $LiNbO_3$.

12.3 Mathematical Formulation of the Model

12.3.1 General Equations

A number of authors have investigated the mathematical formulation of the physical model described above for thermal fixing. Early formulations [23, 24] explained some aspects of the fixing kinetics. The main limitations of those models were that they did not adequately deal with the photovoltaic transport mechanism and dealt only qualitatively with the developing process, apart from ignoring electron detrapping. Later models are more complete. In [25], the developing process is studied in detail in a nonphotovoltaic material such as

SBN. In [17, 26, 27], the photovoltaic effect (which plays a relevant role in the photorefractive effect in $LiNbO_3$) is taken into account, whereas electron detrapping is considered in [16, 17]. In particular, dark electronic conductivity has been shown to be of key importance to account for photorefractive phenomena in the high temperature range ($\sim 200°C$) [28]. The more recent model developed by Carrascosa and Agulló-López [16, 18] and Sturman et al [17] has provided a plausible explanation of most fixing features.

For the one-dimensional situation, under a photon flux I, the model involves the rate and transport equations for free carriers, donors, acceptors, and protons, apart from the Poisson and continuity equations, i.e.,:

$$\frac{\partial n}{\partial t} = (S_T + S_{ph}I)(N - N^+) - S_r n N^+ - \frac{1}{e}\frac{\partial j_e}{\partial x} \tag{12.1}$$

$$-\frac{\partial (N - N^+)}{\partial t} = \frac{\partial N^+}{\partial t} = (S_T + S_{ph}I)(N - N^+) - S_r n N^+ \tag{12.2}$$

$$\frac{\partial E}{\partial x} = \frac{\rho}{\epsilon} \tag{12.3}$$

$$\frac{\partial_{jH}}{\partial x} = -e\frac{\partial H}{\partial t} \tag{12.4}$$

$$j_e = e\mu_e n E + eD_e\frac{\partial n}{\partial x} + eS_{ph}L_{pv}(N - N^+)I \tag{12.5}$$

$$j_H = e\mu_H H E - eD_H\frac{\partial H}{\partial x}. \tag{12.6}$$

In these equations, both thermal and optical electron excitation are included. The meanings of the used symbols are as follows:

n, electronic carrier concentration;
$S_T = S_{T0}\exp[-\epsilon_e^T/(k_B T)]$, thermal ionization probability of donors per unit time;
S_{ph}, photoionization cross section;
S_r, trapping coefficient for acceptors;
N, total impurity concentration;
N^+, ionized donor (electron acceptor) concentration;
$(N - N^+)$, electron donor concentration;
$N_A = < N^+ >$, average acceptor concentration;
$n_0 = (S_T + S_{ph}I_0)N_D/(S_r N_A)$, average electron concentration;
j_e, j_H, electron and proton current density respectively;
E, field induced by charge distribution;
ρ, photoinduced charge density;
H_0, H, average and spatially varying proton concentrations;
μ_e, μ_H, electron and proton mobilities respectively;
$D_e = D_{e0}\exp[-\epsilon_e^D/(k_B T)]$, diffusion constant for electrons;

L_{pv}, photovoltaic transport length;
$D_H = D_{H0} \exp[-\epsilon_H/(k_B T)]$, effective diffusion constant for protons.

Note that we have just assumed Arrhenius expressions for thermal electron excitation and for diffusion of electrons and protons with activation energies ϵ_e^T, ϵ_e^D, ϵ_H, respectively. μ_H, μ_e are related with D_H, D_e through the Einstein relation ($D = \mu k_B T/e$). Finally, e is the absolute value of the electronic charge, ϵ the dielectric constant, and k_B the Boltzmann's constant. When using light beams of medium and low power, the free electron contribution to the charge density can be neglected and it can be written

$$\rho = [H - H_0 + N^+ - N_A]e. \tag{12.7}$$

12.3.2 Coupled First Order Equations: Relaxation Modes

For the practical simple case of a sinusoidal one-dimensional light pattern ($I = I_0(1 + me^{iKx})$, $\Lambda = 2\pi/K$), a useful common approximation is to disregard for all variables harmonics higher than the first one in the Fourier series decomposition. For example, the space charge field will be written $E(x) = E_K e^{iKx}$ and analogous sinusoidal expressions will apply to other variables. This is the linear approximation in the contrast m of the light-fringe pattern, which is strictly valid for $m << 1$. Then, Eqs. (12.1–6) can be cast, after some manipulations, in the form [17]:

$$\frac{dN_K^+}{dt} + \bar{\gamma}_e(1 + \xi_e)N_K^+ + \bar{\gamma}_e H_K = F_K \tag{12.8}$$

$$\frac{dH_K}{dt} + \gamma_H N_K^+ + \gamma_H(1 + \xi_H)H_K = 0 \tag{12.9}$$

where $\bar{\gamma}_e = \gamma_e(1 + K^2 D_e/(S_r N_A))$ (it is very close to γ_e as the last term is very small) and the electronic γ_e and protonic γ_H relaxation rates are given by

$$\gamma_e = \gamma_e^{ph} + \gamma_e^T = \frac{e\mu_e n_0}{\epsilon}, \quad \gamma_H = \frac{e\mu_H H_0}{\epsilon}. \tag{12.10}$$

Here, γ_e^{ph} and γ_e^T are the photon and thermal contributions to γ_e. In addition, the parameters

$$\xi_e = \frac{E_D}{E_q} - i\frac{E_{pv}}{E_q}\frac{N_A}{N}\frac{\gamma_e^{ph}}{\gamma_e}, \quad \xi_H = \frac{E_D}{E_q}\frac{N_t}{H_0} \tag{12.11}$$

have been also introduced for normalization; in most common cases they are much smaller than one, i.e., ξ_e, $\xi_H << 1$. Here, $N_t = N_A(N - N_A)/N$ is the effective trap concentration and

$$E_D = \frac{Kk_B T}{e}, \quad E_q = \frac{eN_t}{\epsilon K}, \quad E_{pv} = \frac{L_{pv} S_r N_A}{\mu_e} \tag{12.12}$$

are the so-called diffusion, saturation, and photovoltaic fields. The right-hand of Eq. (12.8) is the effective driving force

$$F_K = -i\frac{m}{2} N_t \gamma_e^{ph} \frac{E_{pv} + iE_D}{E_q}. \tag{12.13}$$

The space charge field E_K (which is a key measurable value through the diffraction efficiency) is obtained straightforwardly from Eq. (12.3) in terms of N_K^+ and H_K:

$$E_K = \frac{-iE_q(N_K^+ + H_K)}{N_t} \tag{12.14}$$

In order to solve the set of equations, they must be completed with the experimental initial conditions. In principle, they permit to deal with any design of fixing experiments, including measurements on the developing process and the lifetime of the fixed hologram. In this latter case, the set of equations becomes much simpler, since developing is performed at room temperature where either proton migration or thermal electron detrapping can be disregarded. The structure of Eqs. (12.8) and (12.9) indicate that, when $F_K = 0$, the time evolution of the amplitudes N_K and H_K, as well as, E_K given by (12.14), is characterized by two exponential solutions or *relaxation modes*, proportional to $e^{-\Gamma_{f,s}t}$ with time constants Γ_f (called fast) and Γ_s (slow). The values of these time constants depend, apart from the particular experimental conditions, on the stage of the process, i.e., recording, fixing, developing, or long-term storage.

In most common cases, in particular for bulk $LiNbO_3$ which can be considered the reference material for thermal fixing, the parameters ξ_e and ξ_H are much smaller than one. Under this condition, the expressions for Γ_f and Γ_s are considerably simplified and reduce to:

$$\Gamma_f = \gamma_e + \gamma_H, \qquad \Gamma_s = \frac{\gamma_e \gamma_H}{\gamma_e + \gamma_H}(\xi_e + \xi_H). \tag{12.15}$$

Eqs. (12.15) also indicate that the fast relaxation constant Γ_f is essentially controlled by the greatest of γ_e^{ph}, γ_e^T and γ_H, whereas the slow relaxation constant Γ_s is basically controlled by the smallest of them.

The approximation $\xi_e << 1$, $\xi_H << 1$ will be assumed henceforth. However, it is not fully valid for some special cases such as for heavily Fe-doped $LiNbO_3$ samples in a highly oxidized state, where $\xi_e \lesssim 1$.

12.3.3 Recording at High Temperature

Let us consider the recording of a photorefractive grating at high temperature as the first step for getting a fixed hologram. Solving Eqs. (12.8) and (12.9) and taking into account Eq. (12.14), the amplitude of the space charge electric field

E_K, can be written in terms of experimental boundary conditions and the time constants Γ_f and Γ_s as follows

$$E_K(t) = E_f(1 - e^{-\Gamma_f t}) + E_s(1 - e^{-\Gamma_s t}) \tag{12.16}$$

where E_f and E_s are the components of the stationary amplitude $E_K(\infty)$ related to the fast and slow processes. E_f is the quasistationary amplitude of $E_K(t)$, because it is the value reached at the end of the fast stage, which varies very slowly afterward.

These fast and slow components can be also calculated [17] and written as

$$E_f = \frac{m}{2} E_{eff} \frac{\gamma_e^{ph}}{\gamma} \tag{12.17}$$

$$E_s = E_{eff} \frac{\gamma_H \xi_H - \gamma_e \xi_e}{\gamma_e(\xi_H + \xi_e)} \tag{12.18}$$

where $E_{eff} = E_{pv} + iE_D$ is the effective driving field and $\gamma = \gamma_e + \gamma_h$. Then, the final electric field amplitude

$$E_K(\infty) = E_f + E_s = \frac{m}{2} E_{eff} \frac{\gamma_e^{ph}}{\gamma} \frac{1}{1 + \dfrac{\xi_e}{\xi_H}}. \tag{12.19}$$

The quasistationary amplitude E_f is controlled by the balance between the diffusion and photovoltaic electronic currents on one hand (which are the origin of charge separation), and the electronic and protonic currents driven by the space charge field on the other side. During the slow process, both the protonic and the electronic gratings grow simultaneously keeping a quasi-compensation of charge. So, they could reach rather high values if the recording is long enough, although the total space charge field E_K remains small. (Fig. 12.2 illustrates this situation). The corresponding slow component of the space charge field E_s associated to the little unbalance between the trapped electronic and the protonic gratings deserves some attention. It can change its sign as a function of temperature. When E_s has the same sign as E_f, i.e., $\gamma_H \xi_H > \gamma_e \xi_e$ according to (12.18), it follows from Eq. (12.16) that the electric field amplitude $E_K(t)$ grows monotonically. This kind of behaviour is exhibited by E_K in the example plotted in Fig. 12.2. Conversely, if $\gamma_H \xi_H < \gamma_e \xi_e$, the fast E_f and slow E_s components have opposite signs and consequently $E_K(t)$ has a maximum at $t = \Gamma_f^{-1}$, and then decreases until it reaches the value $E_K(\infty)$ [29]. A typical case of this second behavior is presented by high temperature recording in proton exchange $LiNbO_3$ waveguides and it will be illustrated in Fig. 12.6 (see Section 12.5).

The critical point (if there exists) at which the type of kinetics changes is defined by the condition $E_s = 0$ that is fulfilled when $\gamma_H \xi_H = \gamma_e \xi_e$. It is possible to demonstrate (see reference [17]) that the corresponding critical temperature verifies

$$T_c = \frac{\epsilon_e^T - \epsilon_H}{k_B \ln\left(\frac{\mu_e^0}{\mu_H^0}\right)}. \tag{12.20}$$

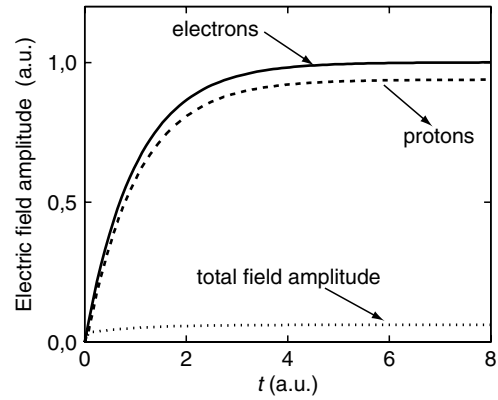

FIGURE 12.2. Time evolution of the amplitude of the space charge field associated to the trapped electronic grating (continuous line), the protonic grating (dashed line), and the total charge grating (dotted line) during recording at high temperature.

12.3.4 *Light and Dark Relaxation: Developing and Hologram Lifetimes*

When the light pattern is removed (i.e., $m = 0$), E_K will write

$$E_K(t) = E_f e^{-\Gamma_f t} + E_s e^{-\Gamma_s t} \tag{12.21}$$

which is applicable to either homogeneous light or dark relaxation with appropriate parameters. In the case of light relaxation, i.e., under uniform illumination ($I = I_0,\ m = 0$), the fast stage at room temperature corresponds to the *developing* process that complete the fixing procedure. Hence, in order to know the developing efficiency, we have to find out the amplitude of the grating at the end of this fast stage. This amplitude can be very easily obtained taking into account that at room temperature, protons are nearly immobile and so $\frac{dH_K}{dt} = 0$. Then, using Eq. (12.8) with $m = 0$ (i.e., $F_K = 0$) and Eq. (12.14), one obtains:

$$E_K = \frac{e}{\epsilon} H_K \frac{\xi_e}{1 + \xi_e}. \tag{12.22}$$

Therefore the fraction D_r of the protonic field, $E_K^H = \frac{e}{\epsilon} H_K$, which is developed, is given by

$$D_r = \frac{\xi_e}{1 + \xi_e}. \tag{12.23}$$

Note that ξ_e is a complex number whose imaginary part is controlled by the photovoltaic effect. This imaginary part indicates the existence of a phase shift between the protonic and the electronic gratings and this is the dominant effect

in the developing process for highly doped $LiNbO_3$ crystals. This aspect is well discussed in the next section and was reported in references [18, 19, 20].

In turn, the slow stage of the relaxation represents the long term behavior of the photorefractive hologram. Therefore, $1/\Gamma_s$ determines the *hologram lifetime*, which is a very relevant parameter for applications. In general, its value is different under light illumination than in dark because in the former case, there is a contribution of photoelectrons that does not exist without light. However, both values can be equal when $\gamma_e^{ph} << \gamma_e^T,\ \gamma_H$.

Let us consider in detail the particular but very relevant case of bulk $LiNbO_3$. Under illumination, a simplified expression for the light hologram lifetime Γ_s is obtained from Eq. (12.15), taking into account that at room temperature γ_e^T, $\gamma_H << \gamma_e^{ph}$:

$$\frac{1}{\tau} = \Gamma_s = D_H K^2 \left(\frac{H_0}{N_t} + 1 \right). \tag{12.24}$$

The above expression indicates that the lifetime is proportional to the square of the grating spacing, $\Lambda^2 = 4\pi^2/K^2$ and decreases on increasing the ratio H_0/N_t. In addition, τ is inversely proportional to the proton diffusion constant D_H, so it is controlled by the thermal activation of proton migration. This key expression has been discussed in detail in references [14, 30].

On the other hand, under dark conditions, the developed hologram is compensated by proton and thermal electron migration during the fast process controlled by Γ_f according to Eqs. (12.15). Thus, the corresponding time constant is independent of K and often proportional to $1/H_0$. This fading of the diffraction efficiency does not indicate that the fixed grating has disappeared; only a small fraction of it has been destroyed (approximately that not compensated by trapped electrons). The diffraction efficiency can be recovered by further optical developing (see references [17, 31] for more details). A complete hologram erasure without any possible retrieval occurs for longer times i.e., during the slow dark relaxation process.

12.3.5 Fixing After Recording at Room Temperature

It is worthwhile to also devote a few paragraphs to the three-step method of thermal fixing in which the grating is recorded at room temperature and afterward, the sample is heated. In this case, protons move to compensate the previously written holographic grating $N_{K0}^+ \exp(iKr)$. Then, during the process at high T, the protonic grating grows up, but the electronic grating also decays. In general, the amplitude reached by the protonic grating is much lower than in the two-step fixing method. The theoretical description of the process is based in Eqs. (12.8) and (12.9) with homogeneous illumination ($m = 0$). The solution is again a double exponential but with different initial conditions: $N_K^+(0) = N_{K0}^+ \exp(iKr)$, $H_K(0) = 0$. More details can be found in the work by Carrascosa et al [16].

A particular and simple solution is obtained assuming that electron detrapping is negligible during proton compensation (as occurs in $LiNbO_3$ crystals for relatively low fixing temperature around 100°C). In that case, the maximum amplitude reached by the protonic grating is obtained from Eq. (12.9) assuming constant N_K^+:

$$H_K = -\frac{N_{K0}^+}{1+\xi_H}. \tag{12.25}$$

For the subsequent developing process and for hologram lifetimes, nothing changes with regard to the two-step fixing method and the same expressions as well as the same discussion of previous section are valid.

12.3.6 Situations Out of the Standard Model

There are some experimental situations that are not considered by the above standard model. Let us briefly comment on them.

a) When the pattern modulation m is close to one, linearization is not possible. A recent numerical study [32] has concluded that the solution for the first harmonic obtained in the model is representative of the general behavior in most cases. This result is similar to that of a previous work for unfixed gratings [33]. It should also be remarked that the latter result does not take into account the situation of very long fixings at high temperature, where the modulations of either trap or ion concentrations may reach saturation (no more traps or ions are available for charge compensation).

b) Depending on material conditions, more than one type of electron trap or proton location may be present in the crystal. For example, reduced $LiNbO_3$ presents some electronic contribution to the room temperature dark conductivity [15] involving Nb_{Li}^{4+} defects as electron donors [34]. These traps are not considered in the ordinary Fe^{2+}-Fe^{3+} scheme used by the model. Under low intensity illumination, typically they are not relevant compared with the Fe^{2+} donors that dominate the photoconductivity [35]. However, at higher intensities, the second center appears to strongly contribute to the photovoltaic effect and plays a relevant role [36, 37]. In particular, it is likely the origin of a greater developing efficiency at high intensities reported by Breer et al [38].

c) When the proton concentration is purposely decreased down to $\sim 10^{23}\,m^{-3}$ (dehydrated samples), thermal fixing has been attributed to a different ionic species [13] (likely a residual defect like lithium self-interstitial [39]). In this case, the ionic conductivity seems to have a higher activation energy (1.4 eV) [40, 41]. On the other hand, two or more different proton sites are also inferred from the various peaks of the OH^- infrared absorption band [12, 42]. Up to the present, there has been neither experimental report on

the possible effects of these sites on the transport properties of protons, nor theoretical analysis of this type of situation. In addition, it has been suggested that, apart from the standard electro-optic contribution of the space charge field to the index grating, protons themselves could contribute up to 10^{-4} to the index grating, much in the same way as they strongly modify the substrate index in proton exchanged waveguides [43].

d) Finally, a new mechanism for thermal fixing that does not require light developing has been recently reported for Cu-doped $LiNbO_3$ crystals and waveguides [44]. Obviously, this process, which will be briefly discussed in the next section, cannot be described by the standard model.

12.4 Experimental Aspects of Thermal Fixing

12.4.1 Experimental Procedures for Thermal Fixing

As previously mentioned, two different procedures (three-step) and (two-step) can be used to obtain thermal fixed holograms that differ essentially in the recording temperature. Let us revisit these two methods, paying attention to the experimental aspects.

a) Three-Step Method: Fixing After Recording

The usual holographic recording at room temperature produces the growth of the spatial charge grating up to the saturation level, which in iron doped lithium niobate, could lead to a refractive index change of about 10^{-3}. A maximum diffraction effciency of 1 can then be observed in a sample of less than 1 mm thickness. For thermal fixing, the crystal is heated after recording to a temperature in the range 100–180°C. Then, the ionic charges move by drift in the field of the electronic spatial charge distribution. After some minutes, depending on the selected temperature, the electronic charge field has been compensated almost completely by the ionic field. An idea about the speed of this process is given by the fact that almost complete compensation is achieved in less than ten minutes at 150°C. The compensation is not strictly complete because of the diffusion driving force of the protons at the fixing temperature, which tends to redistribute them uniformly (see Eq. (12.25)). In fact, this small miscompensation between gratings produces a residual diffraction efficiency that has been used to obtain the absolute hydrogen concentration in the crystal [45]. Cooling down to room temperature highly reduces the mobility of protons. Then the hologram must be developed. This is usually done by uniform illumination with white light. The light affects the electronic charge grating, producing its amplitude decrease (by diffusion) as well as its phase shift by photovoltaic effect [18, 19]. Both effects contribute to the resulting uncompensated charge grating. Of course, the uniform light cannot fully remove the electronic grating.

b) Two-Step Method: High Temperature Recording and Fixing

In this case, the sample is kept at a temperature of about 180°C during recording. This situation has been theoretically discussed in Section 12.3.3. At this temperature, protons present a relatively large mobility and screen almost instantaneously the recording space electric field. Because of this, the electronic charge grating, as well as the compensating ionic grating, can grow continuously to a rather high value. The essential difference with the three-step fixing method is that this one usually leads to much deeper compensated gratings. After recording, the sample must be cooled down to room temperature and developed with uniform light for grating unbalance. The main experimental difficulty of this fixing procedure is to keep stable the light pattern during the recording time, which can last more than one hour. As the sample is heated at a temperature higher than the surroundings, air convections are produced close to the sample holder. These air currents perturb the beam optical paths, and hence give rise to light pattern vibrations. A solution used against this effect is to enclose the sample holder and heater inside a vacuum chamber provided of big optical windows [28].

Another solution is the use of an *active stabilization* system similar to that developed and generally used for recording at RT by J. Frejlich [46]. Light pattern stabilization is achieved acting on the beam paths by moving a mirror by means of a piezoelectric element to which it is attached. Breer et al [47] have proposed two alternative ways of pattern stabilization differing in the nature of the signal used. The first one uses a light interference pattern as a signal to induce the required mirror movement. This is the interference produced by superposition of one transmitted recording beam and a part of the other recording beam that is reflected on a lateral face of the sample. The second method uses as signal the intensity of one of the transmitted recording light beams behind the sample as proposed in [46]. The intensity of this beam changes depending on the instantaneous coupling condition, i.e., the instantaneous position of the light pattern with respect to the recorded refractive index grating. A mirror movement modulated at frequency Ω provides the control signal. The second harmonic component (of frequency 2Ω) of that light beam intensity should be zero at any time during stable recording. Departure from this value means a different light pattern position that could be restored to its correct place by operating on the piezo-mirror mean position. This second method of dynamic control is preferred because of several reasons: Both transmitted and diffracted beams which give rise to the coupled wave travel exactly through the same optical path behind the sample; further adjustment is not required after a recording angle change for multiplexing, and the first harmonic can be used to know the recorded grating amplitude [47]. The real disadvantage of this method consists in the very small signal which can be detected because of the almost instantaneous compensation of the recording grating. This compensation is faster as the recording temperature is higher, reducing the control signal appreciably.

A local thermal fixing process by use of a CO_2 pulsed laser has been also reported [48]. This could be of interest for applications requiring gratings stored in a small part of the sample.

The *developing process* is the last step of the thermal fixing technique in both methods in order to produce an unbalance between the electronic and ionic gratings. A uniform illumination of the hologram with light of a sensitive wavelength range is commonly used for this purpose. In fact, it is preferable to use incoherent light, which avoids the formation of interference gratings in the sample. A practical important question is to know how large the developed space charge field will be with respect to the initially recorded one. This is evaluated by the final developed ratio D_r, which is given by Eq. (12.23) and has been studied experimentally as well as theoretically by de Miguel et al. [19]. Assuming enough proton concentration, as it happens in almost all practical cases, this ratio depends on the oxidation state of the crystal ($[Fe^{3+}]/[Fe]$) through ξ_e and on the spatial frequency of the hologram. This can be observed in Fig. 12.3 [19]. It can be also noticed that for oxidized samples and gratings of relatively large spatial frequency (small spacing), this ratio could reach values close to 0.8. This means that for initial diffraction efficiency close to 100%, the fixed hologram could have about 65% diffraction efficiency. In order to obtain higher fixed diffraction efficiency, the initial hologram could be recorded up to a space electric field in excess of that needed for one hundred percent of unfixed efficiency at room temperature [49]. On the other hand, the dependence of the developed field with the grating spatial frequency is relatively moderate to produce appreciable loss of quality in the information stored in a hologram. The previous theoretical study on the developing process (see Section 12.3.4) shows that the light effect is to simultaneously produce a decrease of the

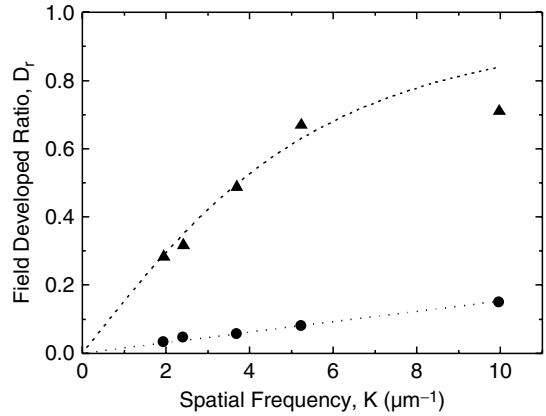

FIGURE 12.3. Developed spatial field ratio D_r versus the hologram spatial frequency, after [18, 19]. Full triangles for an oxidized sample, $[Fe^{2+}]/[Fe] = 0.001$, and full circles for a less oxidized sample, $[Fe^{2+}]/[Fe] = 0.1$.

amplitude and a phase shift of the electronic grating [18, 19]. It has been determined that the photovoltaic effect is of capital importance in the developed diffraction efficiency value. Higher diffraction efficiency can be expected for iron doped $LiNbO_3$ samples than for samples with other transition metal dopants as copper because of its lower photovoltaic coefficient values [13]. When developed holograms are stored in the dark or used with infrared light, they tend to lose diffraction efficiency. This is due to compensation of the spatial field by thermally excited electronic charges. This effect is more important the more conductive is the crystal used and is well described by the standard model as the fast relaxation process in dark (see Section 12.3.4). In practice, this leads to the need of redeveloping the hologram after some time periods to restore the initial diffraction efficiency.

Development without light. Nee et al. [50] studied the effect of electric fields on the diffraction efficiency of fixed holograms. These authors found that for holograms recorded and fixed simultaneously at 180°C, after recording during 90 minutes, the modulation of donors could reach a value of about 0.5. The application of an electric field to the samples with these fixed holograms resulted in an increase of the diffraction efficiency without light development that was quadratic in the field value. An electric field of 5 kV/cm produced even 50% diffraction efficiency. This could be explained as an effect of spatially modulated electric currents due to the modulation of Fe^{2+} donors in the presence of the uniform external electric field. The research was done with highly iron doped crystals that presented relatively large dark conductivity. This dark developing could be interesting in the design of devices for infrared light applications. In this case, it is not necessary to illuminate the crystals with visible light from time to time.

Efficient diffraction without developing. It has been observed in Cu in-diffused samples that fixed holograms produced by recording at high temperature presented high diffraction efficiency without developing [44]. In fact, just after recording/fixing the gratings presented a constant Bragg back reflection of more than 90 percent of the light. This was observed in samples for which the copper was in-diffused at high temperature in a reducing atmosphere. It is clear that, since protons are mobile at the recording temperature of 180°C, no spatial electric field could be present in the sample before developing. Then, the refractive index grating must have a nonelectro-optic origin. An absorption grating was discarded as origin of this high efficiency. To explain these gratings, there are two possibilities. First, the deep modulation of Cu^{+} and Cu^{2+} can already lead to local material changes that cause a refractive index modulation in the crystal. Second, the Cu distribution itself could be changed during fixing at 180°C. One has to take into account that the grating periods in that experiment were as small as 350 nm, and that the diffusion constant of Cu at high temperature is more than 500 times higher than for Fe under the same conditions. Anyhow, the origin of these gratings is not yet clear. These gratings, not being produced by space charge fields, do not present compensation effects; they exhibit stable diffraction efficiency, and do not need to be periodically

redeveloped. This could be a valuable advantage for application in inaccessible devices.

12.4.2 Lifetime of Fixed Holograms

A very important aspect to be taken into account with fixed holograms is their useful lifetime. The commonly used word "fixed" for these holograms does not mean their everlasting existence. In fact, even at room temperature, the ions responsible of this fixing effect can move to redistribute along the material. This movement, although very slow, could be not negligible in a time scale of years of device operation. Experiments of hologram lifetime have been performed at temperatures that allow the measurement of diffraction efficiency decays. Two kinds of measurements have been done. Diffraction efficiency time decays of fixed holograms under continuous developing light [14], and holographic decays in the dark during the fixing process itself at a constant fixing temperature [51, 52]. Let us briefly comment these measurements:

Fixed hologram diffraction efficiency light decays versus temperature. The experiment reported by de Miguel et al. [14] consisted of the measurement of the diffraction efficiency decay of a fixed hologram at constant temperatures. Several of these decays were observed for different temperatures in the range 50–110°C. During the process, the sample was illuminated with uniform developing light. This was done in order to avoid a possible screening in the dark by thermally excited electrons. The conditions of the experiment guaranteed that the decays corresponded to the movement of the hydrogen ions. In all cases, good single exponential decays were obtained, proving that they are due to a single process. These decays were measured for three different samples differing only in the concentration of hydrogen and in the oxidation state of iron. Arrhenius-like plots of the decay time constants versus inverse absolute temperature resulted in a straight line ordering of points for each sample, as correspond to a thermally activated process. As it can be seen in Fig. 12.4, the same activation energy was obtained for all samples (parallel straight lines) but with different pre-exponential factors. The values of N_t and H_0 were obtained separately for each sample from the visible and infrared absorption spectra, respectively. In Section 12.3.4, we discussed the theoretical expression (12.24) for the hologram lifetime in which the dependencies on the grating period K, the temperature T, the effective trap N_t, and proton H_0 explicitely appeared. The accordance between theory and experiment was excellent. In fact, even the dependencies with N_t and H_0 were experimentally confirmed by the data of Fig. 12.4 because when calculating the factors $\tau[(H_0/N_t) + 1] = 1/(D_H K^2)$, all values for different samples appear ordered in a single straight line. On the other hand, from this analysis, the activation energy and pre-exponential factor of the diffusion coefficient of hydrogen in lithium niobate were obtained: $D_H^0 = (1.4 \pm 0.5) \times 10^{-3}$ cm^2 s^{-1} and $E_a = (0.95 \pm 0.02)$eV.

It is worthwhile remarking that, on one side, the absorption stretching band of OH^- was used to obtain the factors to convert the decay times to diffusion

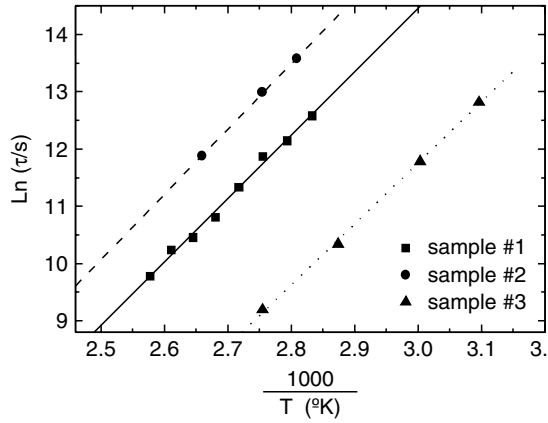

FIGURE 12.4. Arrhenius-like plot of the temperature dependence of decay time constants of fixed holograms, for three different $LiNbO_3$: Fe samples, after [14].

coefficient values according to Eq. (12.24), and on the other side, these values follow a single straight line independently of the sample. Therefore, this constitutes the proof that the hydrogen is responsible for thermal fixing of holograms in lithium niobate, at least within the range of hydrogen doping and oxidation levels used in the experiment.

The extrapolation to room temperature, using the values obtained, allowed these authors [14] to plot expected curves of lifetimes versus the hydrogen density in the crystals. In Fig. 12.5, the curves corresponding to grating spacings of 1 μm and 0.35 μm at 20°C are presented. The spacing of 0.35 μm corresponds to a grating that produces back reflection of light of 1.55 μm. As it can be seen in the

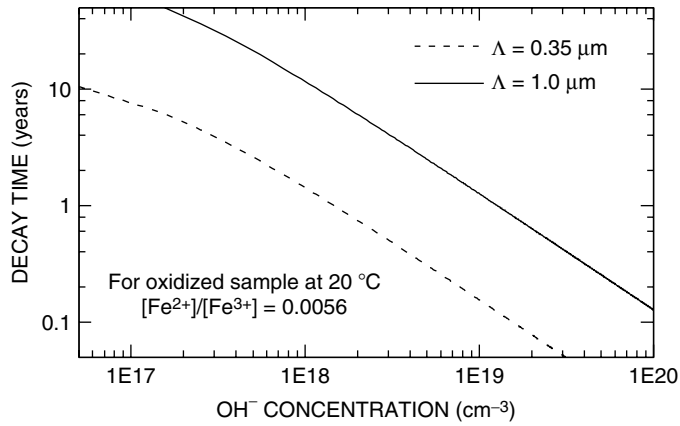

FIGURE 12.5. Extrapolated lifetime values at 20°C for fixed holograms as function of the density of hydrogen impurity in the sample, for two different grating spacings [14].

figure, lifetimes are longer as the hydrogen density is lower. Lifetimes longer than ten years could be produced in samples with less than $10^{17}\,cm^{-3}$ of these ions. The amount of hydrogen can be easily controlled and altered by thermal treatments at very high temperatures (800°C–1000°C) in the proper atmosphere.

Dark decays of diffraction efficiency during fixing. Dark decays of the difraction efficiency at a constant temperature in the range 144°C–168°C were measured for several different grating periods by *Müller et al.* [51]. These decays presented a three-exponential time dependence with very similar activation energies but differing in the pre-exponential factors. The activation energies ranged from 1.0 to 1.3 eV. Those components where interpreted as due to different proton sites in the lithium niobate gratings. After the theoretical work of Sturman et al. [17], we know that one has to take also into account the thermal excitation of electronic charges, and these activation energies cannot be assigned purely to proton diffusion.

In the holographic scattering decay technique followed by Ellabban et al. [52] with Mn-doped $LiNbO_3$ crystals, light scattering was produced by a single laser beam at room temperature, leading to a transmission decrease down to a steady state level. After that, the sample is heated to a temperature in the range 60–115°C for fixing. Then the transmission of a weak beam is measured as a function of time at each constant temperature. Between individual measured points, the sample is kept in the dark. As a result of field screening by the mobile ions, the scattering decreases with time, i.e., the beam transmission increases up to a maximum constant value. These scattering decays were observed to be single exponential and from them, time constants were extracted. These time constants were dependent on the fixing temperature, and an Arrhenius-like plot of them resulted in an activation energy of 1.06 ± 0.03 eV. Regarding the determination of hydrogen parameters the same criticism expressed above to the results of Müller et al. [51] can be applied to this work. Additionally, one has to take into account that in the last experiment, there is an undetermined distribution of spatial frequencies of gratings recorded in the crystal. This distribution does not affect the fast relaxation process, i.e., the screening of the space charge field controlled by Γ_f. However, it should markedly influence the slow decay determined by Γ_s that corresponds to the real decay of the trapped electronic pattern origin of the light scattering.

Lengyel et al. [53] studied variations of the OH absorption components bands at different temperatures. In fact, the components of the stretching absorption band of OH near $3460\,cm^{-1}$ are more resolved in stoichiometric crystals even at room temperature. This has been used to observe and measure changes of spectra with time at a given temperature, after equilibrium at a temperature of 250°C was reached. The analysis of changes of four different absorption bands resulted in activation energies from 0.9 eV up to 1.34 eV. This could mean that OH ions in different lattice positions actually present different activation energies. These authors also measured the decay of stored gratings in the dark at different constant temperatures. They found for these decays an activation energy of 1.14 ± 0.02 eV, for the same crystals used in the

infrared absorption experiments. The value obtained is in the range of those derived from absorption measurements, but is also slightly higher than that reported in Ref. [14]. Nevertheless, in the results presented in Ref. [53], the two simultaneous processes commented before should be involved in the decays measured at a given temperature, the decay of the electronic grating due to thermal excitation of electrons from traps and the ionic screening of the spatial charge field. Both processes could have different activation energies and then the result could be a somehow intermediate value.

12.4.3 Fixing of Multiple Holograms

Superposition of multiple fixed holograms could be of great interest for information storage applications, optical correlation, and communications wavelength demultiplexing. From the early times of thermal fixing in lithium niobate, the fixing of multiple holograms with individual high diffraction efficiencies was demonstrated by Staebler et al. [54]. In this first experiment, the image bearing holograms were recorded and fixed simultaneously at 160°C.

The Bragg mismatch produced when those holograms were read at room temperature was not important for those simple analog images. But for high capacity digital data storage, the holograms must be recorded at RT and fixed with a post-recording heating procedure. Heanue et al. [55] recorded and fixed successfully 530 holograms containing digital information. These authors observed that the bit error rate decreased in more than two orders of magnitude with the fixing process, mainly due to the lower diffraction efficiency obtained after fixing and developing. More recently, An et al. [56] recorded and fixed 10,000 digital holograms, using an incremental fixing schedule to obtain equal diffraction efficiency for all of them. After recording each group of 1000 holograms the crystal was heated for fixing, and only at the end of all the process the crystal was illuminated for developing. Limeres et al. [57] studied the effect of different recording-fixing-developing schedules in the formation of combinational spurious gratings that can highly contribute to the optical noise in a memory. These authors observed that a key factor in the formation of a combinational grating, a grating with sum grating vector for example, is the presence of the modulated space electric field of a former hologram during recording of a second one. The amplitude of the combinational gratings is much reduced if each holograms is fixed but not developed before recording the next one. In this case, the recording of a new hologram is not affected by the spatial electric field of the former hologram because it is still compensated. This should be taken into account to improve signal to noise ratio in multiple fixed hologram systems.

12.4.4 Thermal Fixing in Other Materials

Thermal fixing of holograms has been also experienced in many other photorefractive materials. However, there are important differences in the fixing temperatures, activation energies, and lifetimes. The fixed diffraction efficiency

ratios also depend strongly on the material. Developing is much more efficient for photovoltaic samples. In nonphotovoltaic samples, an external electric field is used to increase the diffraction efficiency. Table 12.1 presents a summary of the main properties of fixed holograms in different photorefractive crystals.

It can be seen in this table that thermal fixing has been attributed to protons in almost all cases. The determined RT lifetimes are, in general, in the range of several hours to hundreds of days. This is well below the lifetimes of years found for lithium niobate, and of course below the minimum lifetime necessary for practical fixed devices. The activation energies for thermal decay of ionic fixed gratings ranged from about 0.7 eV up to 1.44 eV, but for many materials, the value was close to 1 eV. In general, the diffraction efficiency is quite lower than that observed in holograms fixed in lithium niobate for the same crystal thickness. This could be attributed to the important role of the photovoltaic field in the developing ratio [18, 19].

12.5 Fixing in Photorefractive Waveguides

Photorefractive effects were soon noticed and studied in optical waveguides and they are reviewed in Chapter 9 of this book as well as in previous review articles [73] and [74]. A major reason for this fact is the relevant role played by the photorefractive effect in many optical communication designs, either for reducing the optical damage or for applications in useful devices. A variety of photorefractive experiments and some devices have been performed in the guiding geometry, soon after they were reported in bulk material. The fixing process in photorefractive waveguides is particularly relevant because the gratings recorded in the guiding configuration generally show much shorter lifetimes than those of the bulk case.

Holographic gratings have been recorded and fixed in planar [75] and channel [76] $LiNbO_3$: Ti: Fe waveguides. The amplitudes of either recorded or fixed gratings are found to decrease near the guide surface, probably because of a greater surface value of the ratio Fe^{2+}/Fe^{3+} [75]. In channel $LiNbO_3$: Ti guides, a lifetime for dark decay of a few days has been reported for fixed gratings [77], whereas longer lifetimes are obtained under continuous illumination. Moreover, the peak wavelength for Bragg diffraction has been tuned between 1557.85 nm and 1558.08 nm within the temperature range 294 K–328 K [77]. Quasi-permanent holograms with diffraction efficiency above 90% have been obtained by thermal fixing in $LiNbO_3$: Ti: Cu waveguides. Fixed holograms last unchanged for at least one year in the dark. They partially decay under homogeneous illumination and recover again in the dark (dark developing). Then, they do not require any optical developing at all and are attributed to migration of Cu ions instead of protons [44].

In the case of soft proton-exchanged (SPE) $LiNbO_3$ guides (α-phase), recorded holograms show a short lifetime (a few hours). Two main contributions appear to be responsible for this behavior [78]: A much greater electron

TABLE 12.1.

Material	Fixing temp. °C	Activation energy, eV	Lifetime at RT	Diff. eff. % (thickness:)	Attrib. to:	Authors and ref.
$BaTiO_3$	80			10 % of initial		Kirillov and Feinberg [58]
	95	1.05	150 d	10 %	H^+	Tomita et al. [59, 60]
$Ba_{0.23}Ca_{0.77}TiO_3$	65		few h	12% (1.8 mm) after optical + dc field developing		Korneev et al. [61]
$Bi_{12}SiO_{20}$	200	1.44		0.1%	H^+	Arizmendi [62]
$Bi_{12}TiO_{20}$	90 + ac field			13% (4 mm) after optical + ac field developing		McCahon et al. [63]
$La_3Ga_5SiO_{14}$: Pr^{3+}	63	0.89	35 h	20% of the initial		Nikolajsen and Johansen [64]
$KNbO_3$	70–100	1.04 (pure)	1 d		H^+ or V_o	Montemezzani and Günter [65, 66]
		0.81 (Fe doped)	20 min			
		0.98 (Li, Na, Fe doped)	20 d			
		0.79 (pure)	100 d	16% (6 mm)	H^+	Tong et al. [67]
		0.81 (Fe doped)	39 d			
$K_{1-y}Li_yTa_{1-x}Nb_xO_3$	70 + dc field	0.67 (Cu, V, Ti doped)		25% (5.4 mm)		Leyva et al. [68]
	70 + dc field	0.76 (Co, V, Ti doped)			H^+	Tong et al. [69]
	0	0.27			domain inversion	
		0.85 – 1.0 depending on H^+ conc.	depend on H^+ conc.		H^+	Imai et al. [70]
$Pb_{0.5}Ba_{0.5}Nb_2O_6$	110		30 h	0.5% (20% of initial)		Liu et al. [71]
	125	0.95	10 h		H^+	Lee et al. [72]

thermal excitation probability S_T (about five orders of magnitude greater than in bulk) and likely a much greater mobility of certain ion carriers located at the sample surface (about nine orders of magnitude greater than in bulk). On the other hand, high temperature photorefractive phenomena, closely related to thermal fixing, which are not commonly observed in bulk $LiNbO_3$ have been recently reported. Let us comment some specific results.

As a first example, recording at temperatures above 80°C in SPE-guides exhibits a transient peak, i.e., a quick growth of the diffraction efficiency up to a maximum, followed by a slower decrease down to zero [79]. Fig. 12.6 shows the normalized diffraction efficiency as a function of time during recording at several temperatures (actual maximum values decrease on increasing the temperature). A similar effect has been reported during recording in bulk $LiNbO_3$ [28]. This behavior is predicted by the model discussed in Section 12.3.3 when the recording temperature is above the critical temperature given by expression (12.20). Thus, the critical temperature T_C in SPE-guides, if there exists, appears to be well below 100°C whereas in bulk, material is around 200°C. The reason for that change seems to be the higher thermal electron excitation probability [78]. A second example is dark developing observed at room temperature in SPE-guides [78], although the grating lifetimes are rather short in this case. In addition, the last paper has provided values for most photorefractive parameters in SPE-guides. These values appear very similar to those of bulk crystals, except for those mentioned above (the thermal ionization probability S_T and the ion mobility). Finally, developing after fixing at high temperature have been also carried out obtaining a diffraction efficiency of

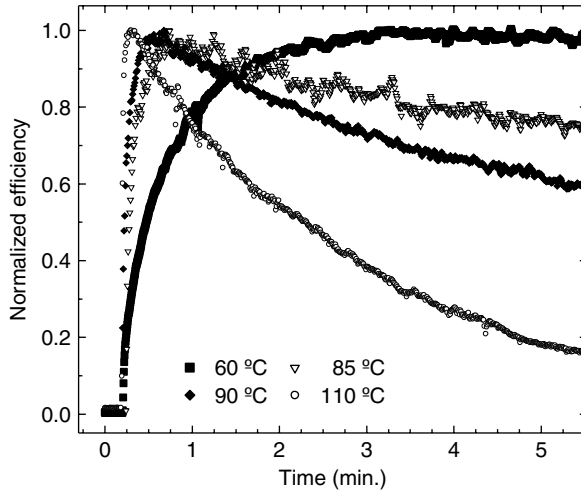

FIGURE 12.6. Recording behavior in a SPE $LiNbO_3$ waveguide at different temperatures. The normalized diffraction efficiency during recording has been plotted as a function of time; the peak value tends to decrease on increasing the temperature.

about 15%. The developed grating decays to zero in dark but can be recovered by further developing as illustrated in Fig. 12.7.

12.6 Photorefractive Applications Using Thermal Fixing

12.6.1 Volume Holographic Devices

Several narrow band holographic optical filter devices based in bulk thermally fixed holograms in Fe-doped $LiNbO_3$ have been reported. The early prototype of Rakuljic and Leyva [80] had a reflection peak of 12% at 656.45 nm with a bandwidth as narrow as 0.0125 nm. These authors mentioned the possibility of thermal fixing but they did not fix their filter. The fixed filter produced by Müller et al. [9] had a measured reflection peak of 32.5% at 518.45 nm with a bandwidth of 0.05 nm. This filter was recorded using reflection geometry and fixed after recording. The reflection peak position could be elected prior to recording by adjusting the recording beam angle or wavelength for the required grating spacing. Fine tuning could be obtained by application of an electric field or by changing the working temperature [81]. Using a configuration of transmission geometry for recording and a sample of 10 mm long in the

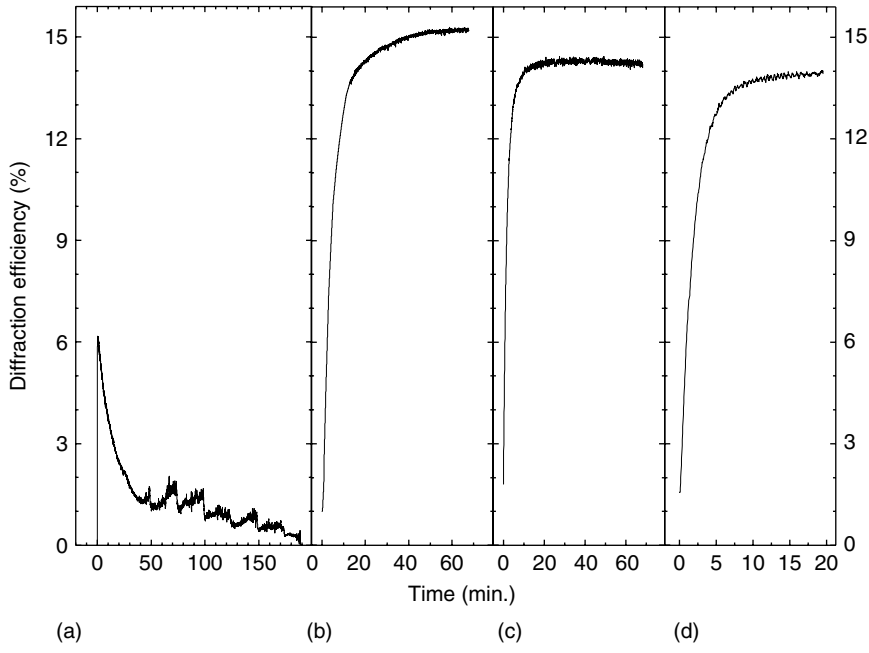

FIGURE 12.7. Diffraction efficiency η as a function of time (a) during recording at 90°, (b) during the first developing at RT, (c) during the second developing after a decay to zero in dark, (d) during the third developing after the second one decayed.

direction of reflection, Leyva et al. [8] produced a reflection filter for a wavelength of 1548 nm with a bandwidth of 0.18 nm and a peak reflection of 98%, in a fixed device. Superposition of several reflection gratings in a single filter device can be applied as wavelength demultiplexer for DWDM communication systems. This extension of the holographic filters has been also developed with fixed holograms in $LiNbO_3$: Fe by An et al. [82]. The demonstration device was produced by recording 16 gratings using a 90° geometry, and a Bragg reflection geometry. The result was a 16 channel device of 0.16 nm bandwidth separated 0.5 nm, in the region of 670 nm. This device diffracted the light of each of channel wavelength in a different angle. Very recently Nee et al. [83] presented a demultiplexer device with 16 channels of 0.1 nm bandwidth and separated 0.4 nm for the communication band of 1550 nm. The device was produced by angular multiplexing of holograms recorded in the transmission geometry. The device was used in Bragg reflection geometry and had fixed reflection efficiencies of about 20%. An holographic fixed optical correlator with very interesting properties has been also demonstrated [84]. A photorefractive fixed volume hologram of high diffraction efficiency can be used in confocal scanning microscopes in order to produce spatial filtering in advantageous substitution of a pinhole [85]. The technique of optical phase encryption [86] can take advantage of thermal fixing for storage and portability of the holographic phase keys. Finally, optical holographic memories formed by or containing fixed holograms have similar features as the computer ROM (read-only memory) but improved with parallel reading properties. An example of such a memory is that demonstrated by An et al. [56].

12.6.2 Waveguide Devices

In an early work [87], a large-angle electro-optical switch/deflector was demonstrated by recording and fixing a photorefractive grating in a Fe-indiffused $LiNbO_3$ guide. A strong reduction of the optical damage was also reported for a Ti-indiffused $LiNbO_3$ channel guide after submitting the sample to a "thermal fixing" process [88]. More recently, interesting devices have been reported with fixed gratings in photorefractive Ti: $LiNbO_3$ waveguides. In a similar way as that described in Section 12.6.1, integrated narrow-bandwidth Bragg reflectors have been fabricated by fixing in planar [75] and channel [76] waveguides of Ti: Fe: $LiNbO_3$. A two-step method has been used to fix the photorefractive holograms obtaining a reflectivity of 60% and a spectral line width of 110 pm. Additionally, the Bragg reflector appears almost insensitive to the light polarization. Moreover, thermal tuning has been also demonstrated in these waveguides inside a range of 0.2 nm [77]. Fixed Bragg reflectors have been used as mirrors in an integrated Ti: Er: $LiNbO_3$ laser emitting 5 mW power at 1531.7 nm and pumped with 110 mW at 1480 nm [89, 90, 91]. Very recently, a similar device has been fabricated in a Ti: Er: Fe: $LiNbO_3$ waveguide [92].

All these devices can take benefit of the fixing technique developed in Cu-doped Ti: $LiNbO_3$ waveguides [44], which apparently gives rise to much longer lifetimes

than the conventional one based on protons. After high temperature recording with green light, refractive index changes exceeding $\Delta n \simeq 8 \times 10^{-5}$ for 1550 nm IR light have been achieved in channel waveguides [93, 94].

12.7 Summary

This Chapter has reviewed our present understanding of thermal fixing phenomena, the updated theoretical model, relevant experimental data and techniques, and applications in photorefractive crystals, particularly $LiNbO_3$. After describing the physical model for thermal fixing, the recent mathematical formulation of the model has been presented. This has emerged as a coherent and clear picture from which particular models can be reliably developed to explain and predict most experimental results, as well as to design long lifetime photorefractive devices. Common experimental methods and techniques have been discussed in detail, emphasizing their advantages and drawbacks. Relevant experimental data are presented and discussed to the light of the theoretical model, including those referred to photorefractive waveguides. Finally, applications of the thermal fixing technique to practical devices have been presented for both bulk and waveguide geometries. Many of them exhibit excellent performances with $LiNbO_3$ and they are very close to the market. On the other hand, further improvements are needed with other materials before they can be applied to real devices.

Acknowledgments

This work was partially supported by the Spanish Ministerio de Ciencia y Tecnología under grants (TIC2001-0605) and (MAT2002-03220).

References

1. A. Ashkin, G.D. Boyd, J.M. Dziedzic, R.G. Smith, A.A. Ballmann, H.J. Levinstein, K. Nassau, *Appl. Phys. Lett*. **9**, 72 (1966).
2. P. Günter, J.P. Huignard, Editors, *Photorefractive Materials and Their Applications* Vol. I (1988) and Vol. II (1989). Springer-Verlag, Berlin.
3. F. Agulló-López, Editor, *Photorefractive Materials, MRS Bulletin* **XIX** (March 1994).
4. L. Solymar, D.J. Webb, A. Grunnet-Jepsen, *The Physics and Applications of Photorefractive Materials*, Clarendon Press, Oxford (1996).
5. F.T.S. Yu and F.H. Yin, Eds. *Photorefractive Optics*, Academic Press, San Diego (2000).
6. J.J. Amodei, D.L. Staebler, *RCA Rev*. **33**, 71 (1972).

7. D.L. Staebler, J.J. Amodei, *Ferroelectrics* **3**, 107 (1972).
8. V. Leyva, G.A. Rakuljic, B. O'Conner, *Appl. Phys. Lett*. **65**, 1079 (1994).
9. R. Müller, M.T. Santos, L. Arizmendi, J.M. Cabrera, *Opt. Lett*. **28**, (2003).
10. H. Vormann, G. Weber, S. Kapphan, E. Krätzig, *Sol. Stat. Commun*. **40**, 543 (1981).
11. N. Schmidt, K. Betzler, M. Grabs, S. Kapphan, F. Klose, *J. Appl. Phys*. **65**, 1253 (1989).
12. J.M. Cabrera, J. Olivares, M. Carrascosa, J. Rams, R. Müller, E. Diéguez, *Advances in Physics* **45**, 349 (1996).
13. K. Buse, S. Breer, K. Peithmann, S. Kapphan, M. Gao, E. Kratzig *Phys. Rev*. **B 56**, 1225 (1997).
14. E.M. de Miguel-Sanz, M. Carrascosa, L. Arizmendi, *Phys. Rev. B* **65**, 165101 (2002).
15. Y. Ohmori, M. Yamaguchi, K. Yoshina, Y. Inuishi, *Jpn. J. Appl. Phys*. **15**, 2263 (1976).
16. M. Carrascosa, F. Agulló-López, *J. Opt. Soc. Am*. B **7**, 2317 (1990).
17. B.I. Sturman, M. Carrascosa, F. Agulló-López, J. Limeres, *Phys. Rev. B (Cond. Matt.)* **57**, 12792 (1998).
18. M. Carrascosa, F. Agulló-López, *Opt. Commun*. **126**, 240 (1996).
19. E.M. de Miguel, J. Limeres, M. Carrascosa, L. Arizmendi, *J. Opt. Soc. Am*. **B 17**, 1140 (2000).
20. I. Oliveira, J. Frejlich, L. Arizmendi, M. Carrascosa, *Opt. Lett*. **28**, 1040 (2003).
21. R. Matull, R.A. Rupp, *J. Phys. D: Appl. Phys*. **21**, 1556 (1988).
22. M. Carrascosa, F. Agulló-López, *Opt. Commun*. **151**, 257 (1998).
23. W. Meyer, P. Würfel, R. Munser, G. Müller-Vogt, *phys. stat. sol*. (a) **53**, 171 (1979).
24. V.V. Kulikov, S.I. Stepanov, *Sou. Phys. Solid State* **21**, 1849 (1979).
25. M. Jeganathan, L. Hesselink, *J. Opt. Soc. Am*. **B 11**, 1791 (1994).
26. P. Hertel, K.H. Ringhofer, H. Sommerfeldt, *phys. stat. sol*. (a) **104**, 855 (1987).
27. A. Yariv, S. Orlov, G. Rakuljic, V. Leyva, *Opt. Lett*. **20**, 1334 (1995).
28. M. Carrascosa, L. Arizmendi, *J. Appl. Phys*. **73**, 2709 (1993).
29. B.I. Sturman, M. Carrascosa, F. Agulló-López, J. Limeres, *J. Opt. Soc. B* **15**, 148 (1998).
30. L. Arizmendi, E.M. de Miguel-Sanz, M. Carrascosa, *Opt. Lett*. **23**, 960 (1998).
31. L. Arizmendi, A. Méndez, J. V. Alvarez-Bravo, *Appl. Phys. Lett*. **70**, 571 (1997).
32. J. Limeres, M. Carrascosa, E. García de la Cera, E.M. de Miguel-Sanz, L. Arizmendi, *OSA Trends in Opt. and Photon*. **62**, 180 (2001).
33. E. Serrano, V. López, M. Carrascosa, F. Agulló-López, *IEEE J. Quant. Electron*. **30**, 875 (1994).
34. O.F. Schirmer, O. Thiemann, M. Wöhlecke, *J. Phys. Chem. Solids* **52**, 185 (1991).
35. T. Volk, N. Rubinina, M. Wohlecke, *J. Opt. Soc. Am*. **B 11**, 1681 (1994).
36. M. Simon, St. Wevering, K. Buse, E. Krätzig, *J. Phys. D* **30**, 144 (1997).
37. G. De la Paliza, O. Caballero, A. García-Cabañes, M. Carrascosa, J.M. Cabrera, *Appl. Phys. B* **76**, 555 (2003).
38. S. Breer, K. Buse, F. Rickermann, *Opt. Lett*. **23**, 73 (1998).
39. D.H. Jundt, M.M. Fejer, R. G. Norwood, P.F. Bordui, *J. Appl. Phys*. **72**, 3468 (1992).
40. A. Yariv, S.S. Orlov, G.A. Rakuljic, *J. Opt. Soc. Am*. **B 13**, 2513 (1996).
41. S.S. Orlov, W. Phillips in *Holographic Data Storage*, Eds. H.J. Coufal, D. Psaltis, G.T. Sincerbox. Springer, Berlin (2000).
42. L. Kovacs, M. Wöhlecke, A. Jovanovic, K. Polgar, S. Kapphan, *J. Phys. Chem. Sol*. **52**, 797 (1991).

43. S. Kapphan, A. Breithopf, *phys. stat. solidi* **A133**, 159 (1992).
44. J. Hukriede, D. Kip, E. Krätzig, *Appl. Phys.* **B 72**, 749 (2001).
45. R. Müller, L. Arizmendi, M. Carrascosa, J. M. Cabrera, *Appl. Phys. Lett*. **60**, 3212 (1992).
46. P.M. García, K. Buse, D. Kip, J. Frejlich, *Opt. Commun*. **117**, 235 (1995).
47. S. Breer, K. Buse, K. Peithmann, H. Vogt, E. Krätzig, *Rev. Sci. Intrum*. **69**, 1591, (1998).
48. B. Liu, L. Liu, L. Xu, J. Ma, S. H. Lee, *Appl. Opt*. **37**, 1342 (1998).
49. A. Méndez, L. Arizmendi, *Opt. Mater*. **10**, 55 (1998).
50. I. Nee, M. Müller, K. Buse, *Appl. Phys. B* **72**, 195 (2001).
51. R. Müller, M. Carrascosa, L. Arizmendi, J.M. Cabrera, *J. Appl. Phys*. **77**, 308 (1995).
52. M.A. Ellabban, G. Mandula, M. Fally, R. A. Rupp, L. Kovacs, *Appl. Phys. Lett*. **78**, 844 (2001).
53. K. Lengyel, L. Kovács, G. Mandula, R. Rupp, *Ferroelec*. **257**, 255 (2001).
54. D.L. Staebler, W.J. Burke, W. Phillips, J. J. Amodei, *Appl. Phys. Lett*. **26**, 182 (1975).
55. J.F. Heanue, M.C. Bashaw, A.J. Daiber, R. Snyder, L. Hesselink, *Opt. Lett*. **19**, 1615 (1996).
56. X. An, D. Psaltis, G.W. Burr, *Appl. Opt*. **38**, 286 (1999).
57. J. Limeres, E.M. de Miguel-Sanz, A. Suchocki, L. Arizmendi, M. Carrascosa, *Opt. Mat*. **18**, 115, (2001).
58. D. Kirillov, J. Feinberg, *Opt. Lett*. **16**, 1520 (1991).
59. Y. Tomita, S. Matsushima, *J. Opt. Soc. Am. B* **14**, 2877 (1997).
60. Y. Tomita, *Jpn. J. Appl. Phys*. **38**, L440 (1999).
61. N. Korneev, H. Veenhuis, K. Buse, E. Krätzig, *J. Opt. Soc. Am. B* **18**, 1570 (2001).
62. L. Arizmendi, *J. Appl. Phys*. **65**, 423 (1989).
63. S.W. McCahon, D. Rytz, G.C. Valley, M.B. Klein, B.A. Echsler, *Appl. Opt*. **28**, 1967 (1989).
64. T. Nikolajsen, P.M. Johansen, *Opt. Lett*. **24**, 1419 (1999).
65. G. Montemezzani, P. Gunter, *J. Opt. Soc. Am*. **B 7**, 2323 (1990).
66. G. Montemezzani, M. Zgonik, P. Gunter, *J. Opt. Soc. Am*. **B 10**, 171 (1993).
67. X. Tong, M. Zhang, A. Yariv, A. Agranat, *Appl. Phys. Lett*. **69**, 3966, (1996).
68. V. Leyva, D. Engin, Tong Oxiaolin, Tong Min, A. Yariv, A. Agranat, *Opt. Lett*. **20**, 1319 (1995).
69. X. Tong, R. Hofmeister, M. Zhang, A. Yariv, A. Agranat, V. Leyva, *Opt. Lett*. **21**, 1860 (1996).
70. T. Imai, S. Yagi, H. Yamazaki, *J. Opt. Soc. Am. B* **13**, 2524, (1996).
71. A.Y. Liu, M.C. Bashaw, L. Hesselink, M. Lee, R.S. Feigelson, *Opt. Lett*. **22**, 187 (1997).
72. M. Lee, R.S. Feigelson, A. Liu, L. Hesselink, R. Route, *Phys. Rev. B* **56**, 7898, (1997).
73. V.E. Wood, P.J. Cressman, R.L. Holman, C.M. Verber, *Photorefractive Materials and Their Applications II*, Ed. by P. Günter and J. P. Huignard, Chapter 3, Springer-Verlag, Berlin, (1989).
74. D. Kip, *Appl. Phys*. **B 67**, 131 (1998).
75. J. Hukriede, D. Kip, E. Krätzig, *Appl. Phys*. **B66**, 333 (1998).
76. J. Hukriede, I. Nee, D. Kip, E. Krätzig, *Opt. Lett*. **23**, 1405 (1998).
77. J. Hukriede, D. Kip, E. Krätzig, *Appl. Phys*. **B 70**, 73 (2000).

78. A. Méndez, A. García-Cabañes, M. Carrascosa, J. M. Cabrera, *J. Opt. Soc. Am.* **B 17**, 1412 (2000).
79. G. De la Paliza, A. García-Cabañes, M. Carrascosa, J.M. Cabrera, *OSA Trends in Opt. and Photon.* **87**, 172 (2003).
80. G.A. Rakuljic, V. Leyva, *Optics Lett.* **18**, 459 (1993).
81. R. Müller, J.V. Alvarez-Bravo, L. Arizmendi, J.M. Cabrera, *J. Phys. D: Appl. Phys.* **27**, 1628 (1994).
82. J.W. An, N. Kim, K.W. Lee, *Opt. Commun.* **197**, 247 (2001).
83. I. Nee, O. Beyer, M. Müller, K. Buse, *J. Opt. Soc. Am. B* **20**, 1593, (2003).
84. E.M. de Miguel, M. Tebaldi, S. Granieri, N. Bolognini, L. Arizmendi, *Appl. Phys.* **B 70**, 379 (2000).
85. G. Barbastathis, M. Balberg, D.J. Brady, *Opt. Lett.*, **24**, 811, (1999).
86. O. Matoba, B. Javidi, *Opt. Lett.* **24**, 762 (1999).
87. C.M. Verber, V.E. Wood, R.P. Kenan N.F. Hartman, *Ferroelec.* **10**, 253 (1976).
88. R.A. Becker, *Appl. Phys. Lett.* **45**, 121 (1984); *Proceedings of the SPIE. The Intern. Soc. for Opt. Eng*, Vol. **517**, 194 (1985).
89. C. Becker, A. Greiner, Th. Oesselke, A. Pape, W. Sohler, H. Suche, *Opt. Lett.* **23**, 1194 (1998).
90. C. Becker, Th. Oesselke, J. Pandavenes, R. Ricken, K. Rochhausen, G. Schreiber, W. Sohler, H. Suche, R. Wessel, S. Balsamo, I. Montrosset, D. Sciancalepore, *IEEE J. Sel. Top. Quant. Electron.* **45**, 101 (2000).
91. B.K. Das, H. Suche, W. Sohler, *Appl. Phys.* **B73**, 439 (2001).
92. B.K. Das, R. Ricken, W. Sohler, *Appl. Phys. Lett.* **82**, 1515 (2003).
93. J. Hukriede, D. Kip, E. Krätzig, *J. Opt. A: Pure Appl. Opt.* **2**, 481 (2000).
94. K. Pecthmann, J. Hukriede, K. Buse, E. Krätzig, *Phys. Rev.* **B61**, 4615 (2000).

13

Electrical Fixing of Photoinduced Gratings

R.S. Cudney[1] and J. Fousek[2]

[1] Centro de Investigación Científica y de Educación Superior de Ensenada, Mexico
rcudney@cicese.mx
[2] Faculty of Mechatronics, Technical University of Liberec, Czech Republic.
fousek@fzu.cz

13.1 Introduction

Perhaps the most important feature of the photorefractive effect is that it can be used to perform real-time holography, in the sense that the photorefractive medium can adapt instantly, or almost instantly, to changes of the light intensity pattern produced by the optical interference of two or more waves. This feature is vital to several applications of the photorefractive effect, such as adaptive interferometry, laser beam clean-up, phase conjugation, to name a few. As a rule of thumb, for a given intensity and wavelength, it takes essentially the same time to write a photorefractive grating than to erase it.

However, there are applications where this feature is more of a nuisance than an advantage. Holographic data storage is one of these applications: It is desirable to be able to record a hologram very quickly with very little power, and once recorded, the diffraction efficiency and fidelity of the hologram should not degrade over time, even under the presence of an intense light beam. Ideally, there should also be a mechanism to erase the contents of the hologram. Several schemes to "fix" holograms have been proposed, such as thermal fixing, which is discussed in detail in Chapter 12 of this book, two-wavelength recording, also discussed in this book in Chapter 8, and electrical fixing. In this chapter, we shall discuss the electrical fixing in ferroelectric photorefractive materials.

In 1972, Micheron and Bismuth [1] observed that photorefractive gratings could be fixed in crystals that were also ferroelectric, i.e., crystals that have a spontaneous polarization $\mathbf{P}_s$ that can be reversed when an electric field exceeding a certain threshold (coercive field) is applied against $\mathbf{P}_s$, without changing the spontaneous strain. The method they used to fix the gratings consisted in applying an electric field against $\mathbf{P}_s$ after a photorefractive grating had been recorded. Once the electric field was applied, the sample could diffract a properly Bragg-matched beam for an indefinite time without an appreciable decay of the diffraction efficiency. This phenomenon was explained the following way: The light interference pattern created by the beams produces a space-charge field which, together with the biasing, externally applied electric

field, reverses the spontaneous polarization wherever the total field exceeds the coercive field. By adjusting the magnitude of the applied field to be slightly lower than the coercive field, a spatially oscillating pattern of head-to-head 180° ferroelectric domains is formed. The resulting "ferroelectric domain grating" was considered to be responsible for the nondecaying diffraction of light incident on the sample. This effect was initially observed in barium titanate [1], and subsequently in $Sr_{0.75}Ba_{0.25}Nb_2O_6$ [2, 3, 4].

The field of electrical fixing in ferroelectric photorefractives remained somewhat dormant till the beginning of the 90s. Qiao et al. [5] and Orlov et al. [6, 7] fixed low-diffraction efficiency gratings in $Sr_{0.75}Ba_{0.25}Nb_2O_6$ using a similar procedure. However, by repoling the crystal, that is, by reversing the ferroelectric domains back to their original orientation, the diffraction efficiency increased substantially and subsequently decayed. Using a similar (but not identical) technique, Horowitz et al. [8] fixed both images and holograms in $Sr_{0.75}Ba_{0.25}Nb_2O_6$. Kewitsch et al. [9, 10, 11] found evidence that the light induced space-charge fields themselves were sufficient to produce spontaneous polarization reversal and therefore fixing in $Sr_{0.75}Ba_{0.25}Nb_2O_6$. Cudney et al. [12] fixed gratings in top-seeded solution grown $BaTiO_3$ by simultaneously recording gratings and depoling the sample in which they were recorded. Unlike the previous cases, the fixed grating did not diffract light until the crystal was repoled by an electric field. A following publication by the same authors showed that photorefractive gratings could be fixed in a barium titanate sample if it was depoled *prior* to their recording [13]; this method of fixing holograms led to an increase of over a factor of 20 of the diffraction efficiency of the gratings. Ma et al. [14, 15] found that both the diffraction efficiency and lifetime of multiplexed holograms recorded in cerium-doped $Sr_{0.75}Ba_{0.25}Nb_2O_6$ increased by several orders of magnitude if the holograms were recorded in a depoled crystal; using this technique, they were able to record 1000 distinct holograms in the same sample and read them out with a diffraction efficiency exceeding 0.005%. Similar results were obtained in $Sr_{0.61}Ba_{0.39}Nb_2O_6$ [16]. Photorefractive hologram fixing using ferroelectric domains has also been observed in $KNbO_3$ [17], although the diffraction efficiency reported for holograms fixed in this crystal was low. There are other forms of ferroelectric domain fixing techniques that have been reported. Tong et al. [18, 19] reported hologram fixing in $K_{1-x}Li_xTa_{1-y}Nb_yO_3$, although the fixing mechanism is not clear. Fixing of waveguide channels in $Sr_{0.61}Ba_{0.39}Nb_2O_6$ has also been reported by Wesner et al. [20].

13.2 Basic Properties of Ferroelectric Crystals

13.2.1 Electrical Properties

As mentioned in 13.1, ferroelectric crystals posess a permanent polarization, known as the spontaneous polarization $\mathbf{P}_s$. In an ideal ferroelectric crystal, the direction of the spontaneous polarization of the entire crystal will be inverted if

an electric field with a magnitude equal to or higher than a threshold value E_c, known as the coercive field, is applied [21, 22, 23]. Once $\mathbf{P}_s$ is inverted by the applied field, it will remain in the new orientation until it is reversed by another applied field, also with a magnitude equal to or higher than E_c, but of the opposite sign. Suppose a perfectly insulating ferroelectric sample of thickness d that has some form of electrodes on the surfaces perpendicular to $\mathbf{P}_s$ is placed in a circuit like the one shown in Fig. 13.1a. For applied electric fields $E_{applied} = V/d < E_c$, where V is the voltage, the ammeter will not detect a current since the crystal is an insulator. However, when $E_{applied} = E_c$, the polarization reversal process begins and creates a displacement current that is detected by the ammeter; ideally, the direction of $\mathbf{P}_s$ is inverted at the same time throughout the entire crystal, producing a high but short-lived current spike, as shown in Fig. 13.1b. If the sign of the voltage is inverted, the same process occurs but with the opposite sign. By integrating the current $I(t)$ with respect to time, we obtain the total amount of charge Q inverted,

$$Q = \int I(t)dt. \tag{13.1}$$

If the spontaneous polarization of the entire crystal is flipped, it can be shown that $Q = 2P_sA$, where A is the area of each electrode [24]. The corresponding hysteresis curve for the spontaneous polarization of this sample, shown in Fig. 13.1c, can therefore be determined by measuring the displacement current. In fact, this is the most widely used method to determine the spontaneous polarization of a material, and the circuit employed in this technique is known as the Sawyer-Tower circuit [25].

In reality, the spontaneous polarization of the entire sample does not flip at the same time; instead, it begins to flip on small regions of the surface, creating

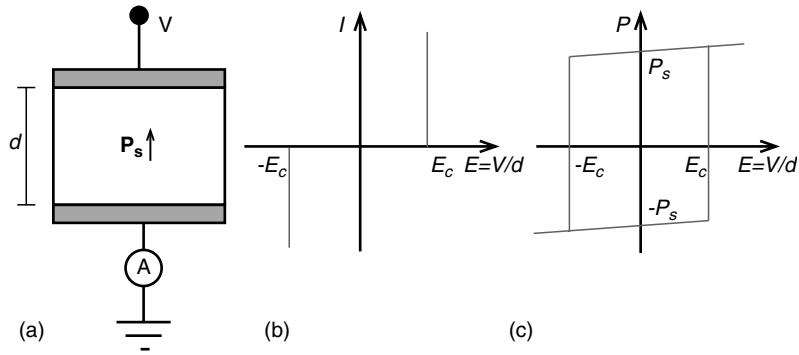

FIGURE 13.1. Ferroelectric hysteresis loop. (a) Sawyer-Tower circuit; (b) current vs. applied field, (c) spontaneous polarization vs. applied field. The slant of the top and bottom lines is due to the induced polarization present in any dielectric material, $P = \epsilon\epsilon_0 E$.

small domains (regions where the spontaneous polarization has the same direction). This process is called nucleation. Then these small domains grow both longitudinally (along the direction of the spontaneous polarization) and laterally; it is generally accepted that the longitudinal rate of growth is orders of magnitude larger than the lateral rate. In addition, the voltage at which domain reversal occurs may not be the same at different locations throughout the crystal, due to inhomogeneities of the electrodes, inhomogeneities of the crystal, or simply because the coercive field itself may not be well defined, as occurs with relaxor or soft ferroelectric crystals such as $Sr_xBa_{1-x}Nb_2O_6$ [26]. A real measurement performed by the Sawyer-Tower circuit actually shows broadened current spikes, and the edges of the hysteresis loop are smoothed out. By varying the magnitude of the field and the time it is applied, we can adjust the degree of polarization g of the sample, defined here as

$$g = \frac{V^+ - V^-}{V^+ + V^-}, \tag{13.2}$$

where V^+ and V^- are the total volumes of the domains where the spontaneous polarization points in the + and − directions, respectively. For a plane-parallel slab of area A, and assuming the crystal is initially well-poled along the + direction, the degree of polarization can be determined from the switched charge Q by

$$g = \frac{P_s A - Q}{P_s A}. \tag{13.3}$$

In general, the regions separating two adjacent 180° domains (domains where the spontaneous polarization of one domain is antiparallel to the spontaneous polarization of the other), are charged due to the discontinuity of the spontaneous polarization. From Maxwell's equations, it can be shown that the surface charge density σ_b that arises at the domain walls is given by

$$\sigma_b = 2\mathbf{P}_s \cdot \hat{\mathbf{n}}, \tag{13.4}$$

where $\hat{\mathbf{n}}$ is a unitary vector normal to the domain wall. Fig. 13.2 shows the surface charge density in three different situations. In Fig. 13.2a the domains are side-by-side and the bound charge at the domain wall is zero. In Fig. 13.2b the domains are head-to-head and the bound charge is maximum, $\sigma_b = 2P_s$; this configuration is energetically unstable and requires a compensating free charge of the opposite sign to make it stable. A theoretical analysis of requirements for an internal space-charge distribution to induce and maintain a stable configuration of head-to-head domains throughout the bulk of a ferroelectric crystal was given in [27]. Finally, Fig. 13.2c shows an intermediate configuration in which $\sigma_b = 2P_s \sin\alpha$, where α is the angle between the domain wall and $\mathbf{P}_s$.

In general, ferroelectric domain configurations are not restricted to the 180° domains discussed above. The possible orientations that $\mathbf{P}_s$ may take depends on the symmetry of the crystal. For example, at room temperature lithium

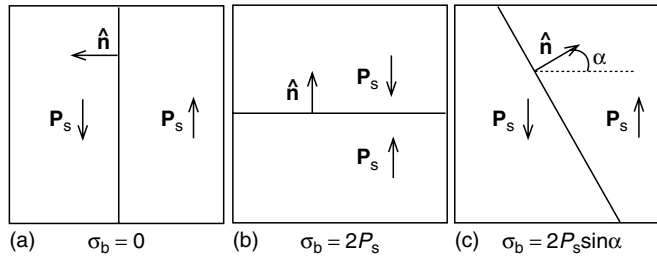

FIGURE 13.2. Bound charge surface density at domain walls. (a) Adjacent 180° domains; (b) head-to-head 180° domains; (c) 180° domains separated by a slanted domain wall.

niobate belongs to the 3m point group in which $\mathbf{P}_s$ can only be parallel or antiparallel to the crystal's 3-fold symmetry rotation axis. Therefore, this crystal can only have 180° domains. On the other hand, barium titanate in the paraelectric phase (above ≈ 130°C) has cubic symmetry, and as it is cooled below this temperature, the unit cell becomes tetragonal (4mm point group) in which $\mathbf{P}_s$ can be oriented along any of the 3 pairs of anti-parallel orientations corresponding to the normals of the original cubic cell. In addition to 180° domains, this crystal can also have domains in which the spontaneous polarization rotates 90° from one domain to the other (90° domains). If the symmetry of the crystal is even lower, such as is the case of potassium niobate, which is orthorhombic at room temperature, the number of possible orientations of $\mathbf{P}_s$ increases, allowing 180°, 90°, 120°, and 60° domains.

Finally, if instead of well-defined domains in which $\mathbf{P}_s$ varies discontinuously from one domain to another the spontaneous polarization varies continuously, the bound charge *volume* density that arises is given by

$$\rho_b = -\nabla \cdot \mathbf{P}_s. \tag{13.5}$$

13.2.2 Optical Properties

The refractive index of a ferroelectric crystal remains the same if the spontaneous polarization is flipped by 180° [23]; therefore, in principle, 180° domains should not be visible, at least if only linear optics is used to detect them. However, all third-rank, second-order nonlinear susceptibility tensors $\chi^{(2)}(\omega_3;\omega_1,\ \omega_2)$, which relate the induced polarization $P(\omega_3)$ of the medium at a frequency ω_3 to the driving electric fields $\mathbf{E}(\omega_1)$ and $\mathbf{E}(\omega_2)$ at frequencies ω_1 and ω_2 by

$$P(\omega_3) = \epsilon_0 \chi^{(2)}(\omega_3;\ \omega_1,\ \omega_2) : E(\omega_1)E(\omega_2), \tag{13.6}$$

are in turn functions of the spontaneous polarization [23, 28]. In (13.6), ϵ_0 is the permittivity of vacuum and $\omega_3 = \omega_1 + \omega_2$. The electro-optic effect is a special case of (13.6), in which $\omega_2 = 0$ and $\omega_3 = \omega_1$. The elements r_{ijk} of the

electro-optic tensor, which describes the linear electro-optic effect, can be shown to be of the form [28, 29, 30]

$$r_{ijk} \propto \sum_{l=1}^{l=3} g_{ijkl} P_{s,l}, \tag{13.7}$$

where g_{ijkl} are the components of the quadratic electro-optic tensor and $P_{s,l}$ are the components of the spontaneous polarization vector. Consequently, a static electric field of amplitude E will induce a change $\Delta n(E)$ of the refractive index that will depend on the orientation of $\mathbf{P}_s$; in particular, if it is rotated by 180°, the sign of $\Delta n(E)$ will change while its magnitude will remain the same. Since the direction of energy transfer in photorefractive two-beam coupling depends on the sign $\Delta n(E)$, a reversal of the direction of $P_{s,l}$ will bring about a reversal of the direction of energy transfer.

13.3 Domain Fixing Mechanisms

The main idea behind photorefractive grating fixing is to create a space-charge distribution that does not decay under illumination. Normally, this is accomplished by first recording a normal photorefractive grating; that is, by letting a light interference pattern optically excite charges, creating a spatially-varying free-charge distribution $\rho_{free}(\mathbf{r})$ among the trap sites, and then creating a replica of $\rho_{free}(\mathbf{r})$ with another source of electric charge that is not easily moved. In thermal fixing, this source is ions, mostly single protons, which become mobile once the crystal is heated to a certain temperature. By recording the grating at high temperature, the ions move to electrically compensate the charge distributed among the traps, forming a space-charge replica but of the opposite sign of the original space-charge distribution; in other words, a charge density distribution $\rho_{ion}(\mathbf{r}) \propto -\rho_{free}(\mathbf{r})$ is formed. Once the temperature of the crystal is lowered the mobility of the ions is significantly reduced, so that $\rho_{ion}(\mathbf{r})$ can no longer be altered. If $\rho_{free}(\mathbf{r})$ is removed by some means, for example, uniform optical illumination, $\rho_{ion}(\mathbf{r})$ is left behind, producing an electric field given by

$$\nabla \cdot \mathbf{E}(\mathbf{r}) = \frac{\rho_{ion}(\mathbf{r})}{\epsilon_0} \propto -\frac{\rho_{free}(\mathbf{r})}{\epsilon_0}. \tag{13.8}$$

In ferroelectric domain fixing, the principle is essentially the same; the difference is that the compensating charge is provided by the bound charge of the domain walls, or more in general, by ρ_b given in (13.5). Exactly how and where this bound charge is produced depends on the material and the experimental procedure used to fix the grating. In the simplest model, such as that proposed in 1973 by Micheron et al. [1, 2], one might think that the spontaneous polarization is reversed in slab-shaped domains wherever the sum of the applied and the internally developed fields exceeds the coercive field. However, the discontinuity of the polarization between these head-to-head slabs is quite large; for barium

titanate at room temperature $2P_s \approx 56\,\mu C/cm^2$, whereas the typical value of the space charge density of a photorefractive grating, integrated over half a period (1 μm), is only around $5 \times 10^{-2}\,\mu C/cm^2$. The bound charge of the slabs would largely overcompensate the free space charge, making this model highly improbable. In addition, this arrangement by itself would not produce a refractive index grating, since the linear optical properties are the same for both orientations of $\mathbf{P}_s$. An externally applied field would be needed to reveal the domain grating, or a strong change of the index of refraction at the domain walls.

As far as we know, it was not until 20 years later, in 1993, that publications in this field appeared once again. As mentioned in 13.1, Qiao et al. [5] reported domain fixing in $Sr_{0.75}Ba_{0.25}Nb_2O_6$, and during the same year Cudney et al. independently performed similar experiments in $BaTiO_3$ [12]. The domain fixing techniques used in both cases followed basically the same procedure:

a) Grating recording. A photorefractive grating is recorded the usual way by two interfering beams inside a single-domain photorefractive crystal.
b) Fixing. An electric field is applied to the crystal against the direction of the spontaneous polarization. The magnitude of this field is above the coercive field of the crystal, so it presumably depoles the sample, at least partially.
c) Erasure of the original grating. Once the fixing field is applied, an intense light beam erases the original grating. During this period, the diffraction efficiency of the grating is monitored by a probe beam, possibly one of the original recording beams or another beam of a different wavelength, which is incident at the correct angle to ensure Bragg matching.
d) Revealing. This step was not included in Micheron's original work. An electric field of the opposite polarity of the field used in the fixing step is applied, which repoles the crystal. As we shall discuss below, this step dramatically increases the diffraction efficiency of the grating.

The basic experimental setup for these experiments is described in Fig. 13.3. Two mutually coherent beams (*light gray lines*) overlap inside a photorefractive crystal, producing the interference pattern that creates the photorefractive grating. A third beam (*dark gray*) is used to monitor the diffraction efficiency of the gratings. For the specific case of experiments perfomed in top-seeded, solution grown barium titanate [12], an ammeter was introduced to record the displacement current produced by the reversal of the spontaneous polarization, which was monitored to measure the degree of depolarization. Electrodes were evaporated onto the c-faces of the sample, which were used to apply electric fields and to monitor the current produced by polarization reversal. Previous experiments with this crystal showed that $P_s = 28\mu C/cm^2$ and that, at very low frequencies, it had a well-defined coercive field $E_c = 480\,V/cm$ at which the switching process begins. Two $\lambda = 488\,nm$ laser beams of equal intensity were used as the recording beams. The diffraction efficiencies of the gratings were monitored by a weak He-Ne laser.

Figure 13.4 shows data obtained from a typical domain-fixing sequence performed in a nominally undoped top-seeded solution grown $BaTiO_3$ sample.

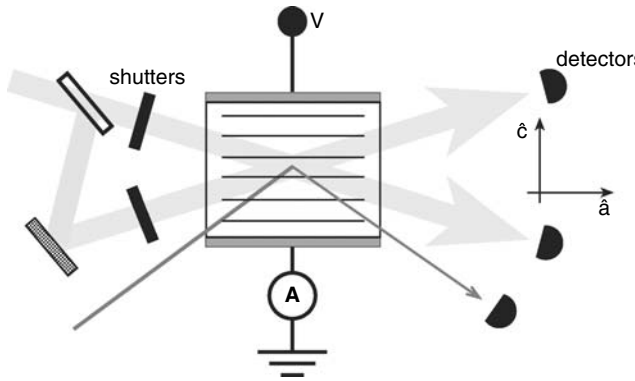

FIGURE 13.3. Experimental setup for domain fixing.

First the crystal is poled by applying a high (much larger than the coercive field), positive electric field along its c-axis for over a minute, as shown in the upper graph of Fig. 13.4, to ensure that the crystal is well-poled (without 180° domains) before the grating is recorded. At the same time, one of the recording beams illuminates the crystal to help the poling process by optically exciting charge that might be pinning some 180° domains [31]. Then a photorefractive grating of a large spatial periodicity is recorded (both recording beams now illuminate the crystal) while a negative field is simultaneously applied. This field serves two purposes. For $|E_{applied}| > |E_c|$, this field depoles the crystal, forming 180° domains that will provide the bound charge to fix the grating. In addition, for $|E_{applied}| < |E_c|$, it enhances the diffraction efficiency of the grating. If the photogalvanic effect is neglected and the effective trap density is very large, the steady-state amplitude E_{sc} of the photorefractive space-charge field is the sum of a diffusion-driven field and a drift-driven field, i.e.,

$$E_{sc} \approx im\left(\frac{k_B T}{e} k_g + iE_{applied}\right), \tag{13.9}$$

where m is the complex modulation of the interference pattern, $k_B T/e$ is the thermal energy per charge carrier, $k_g = 2\pi/\Lambda$ is the magnitude of the grating wavevector. Λ is the grating spacing, and $E_{applied}$ is the amplitude of the applied electric field. For the grating spacing used in this experiment, $\Lambda = 23\,\mu$m, the diffusion-driven field is negligible. However, once $|E_{applied}| > |E_c|$, the diffraction efficiency is reduced. This is due to two reasons. First, the effective electro-optic seen by the beams is reduced by the presence of 180° domains [29, 30, 32, 33]. For light propagating perpendicular to c-axis of the crystal, the average electro-optic coefficient is given by [33]

$$\langle r \rangle = r\frac{V^+ - V^+}{V^+ + V^+} = gr, \tag{13.10}$$

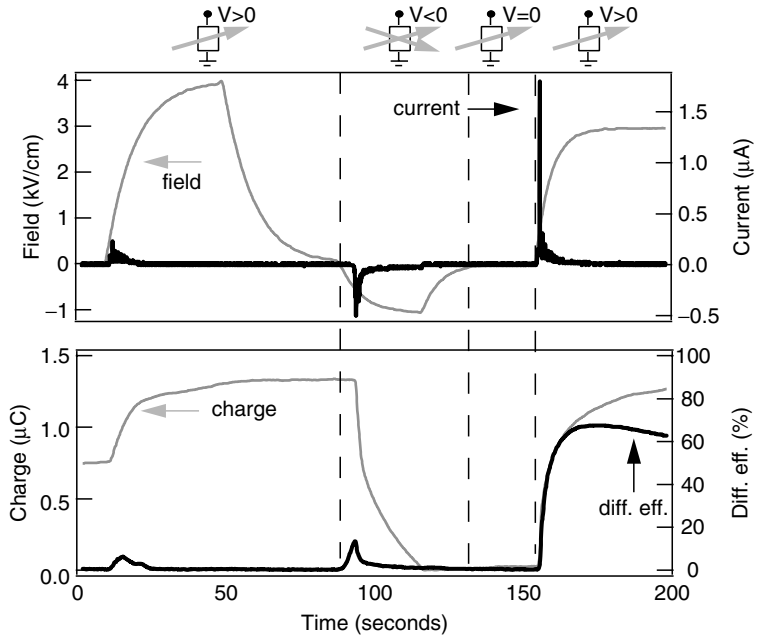

FIGURE 13.4. Fixing sequence. The upper graph shows the applied field and the resulting current vs. time; the lower graph shows the charge, obtained by integrating the current shown in the upper graph, and the diffraction efficiency of the probe beam. The icons on top of the upper graph depict the status of the recording beams. Recording beams: $\lambda = 488\,\text{nm}$, o-polarized. Probe beam wavelength: $\lambda = 633\,\text{nm}$, e-polarized. Grating spacing: $23\,\mu\text{m}$. (Adapted from [12].)

where r is the appropriate effective electro-optic coefficient for a single-domain crystal that depends on the orientation of the grating wavevector and on the polarization of the beams. For a completely depoled crystal, that is $V^+ = V^-$, $\langle r \rangle = 0$. Second, assuming the domain walls somehow produce a bound charge distribution similar to the original free charge distribution but of the opposite sign, the total charge and therefore the space-charge field is reduced.

After the grating is recorded and fixed, one of the recording beams is blocked; the other beam is left on to erase the grating. As can be seen in the lower graph of Fig. 13.4, the diffraction efficiency is negligible until the 180° domains are removed by a field applied along the same direction as the original poling field. This repoling process, which is confirmed by the presence of the positive current spike shown in the upper graph of Fig. 13.4, reveals a grating that diffracts the probe beam. As can be seen in the lower graph of Fig. 13.4, the diffraction efficiency reaches 70% and then decays like a normal photorefractive grating. Again, the diffraction efficiency suddenly increases once the 180° domains are removed because the effective electrooptic coefficient is

restored to its full value and because the bound charge density that screens the free charge is removed.

Figure 13.5 shows proof-beyond-reasonable-doubt that 180° domains are involved in the fixing process described above. Two grating recording and fixing procedures were performed, one with $E_{applied} = 450\,\mathrm{V/cm}$ and another with $E_{applied} = 530\,\mathrm{V/cm}$, which are values slightly below and above the coercive field, respectively. When $E_{applied} = 450\,\mathrm{V/cm}$ the current is zero during the fixing stage and no diffraction occurs during the revealing stage, whereas when $E_{applied} = 530\,\mathrm{V/cm}$ domain reversal occurs in both the fixing and revealing stages, and an unambiguous diffracted signal is detected during the revealing stage.

The diffraction efficiency of the revealed grating should depend on how well the bound charge can compensate the free charge, which in turn should depend on the density of domain walls available to provide bound charge; therefore, one can expect the maximum diffraction efficiency of the revealed grating to occur when the fixing is performed in a completely depoled crystal [34]. Fig. 13.6 shows the diffraction efficiency of the revealed grating as a function of the degree of depoling g of the crystal during the fixing stage. Each data point was

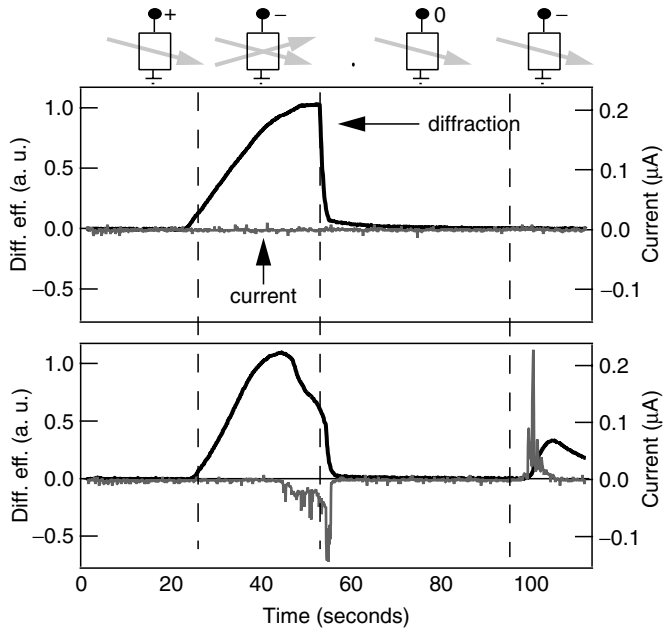

FIGURE 13.5. Relation between diffraction efficiency and displacement current. In the upper graph, $E_{applied} = 450\,\mathrm{V/cm} < E_c$ and in the bottom graph, $E_{applied} = 530\,\mathrm{V/cm} > E_c$. A grating is only revealed if depoling occurred during the fixing stage. The icons on top of the upper graph depict the status of the recording beams and the applied voltage. Recording beams: $\lambda = 488\,\mathrm{nm}$, o-polarized. Probe beam: $\lambda = 633\,\mathrm{nm}$, e-polarized. Grating spacing: $23\,\mu\mathrm{m}$. (Adapted from [12].)

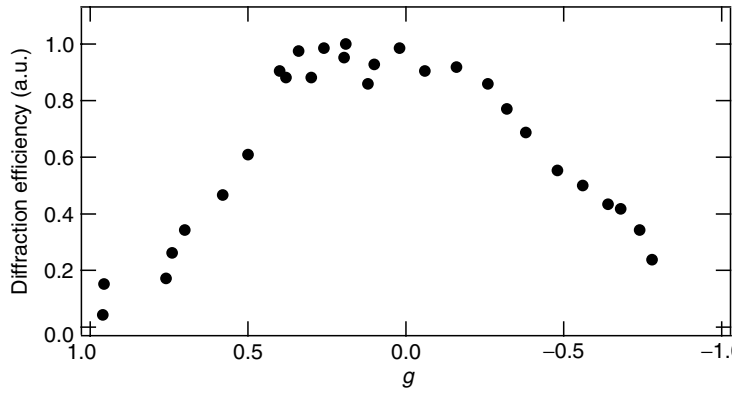

FIGURE 13.6. Diffraction efficiency of the revealed grating vs. degree of polarization of the sample during the fixing stage. (Adapted from [34].)

obtained by first poling the crystal, then depoling it a certain amount, which could be varied by changing the magnitude of the applied voltage and the time it was applied, then erasing the original grating with an intense light beam, and finally revealing the grating by repoling the crystal with an applied field. As expected, the diffraction efficiency is high when $g \approx 0$; in other words, when the grating is fixed in a completely or close to completely depoled crystal.

The diffraction efficiency of the fixed gratings in barium titanate depends strongly on the periodicity of the grating [35]. Fig 13.7 shows the diffraction efficiency vs. the grating periodicity; all other experimental parameters, such as the degree of depoling g and the applied fields, were kept constant. In these experiments, only the two recording beams were used; the probing of the

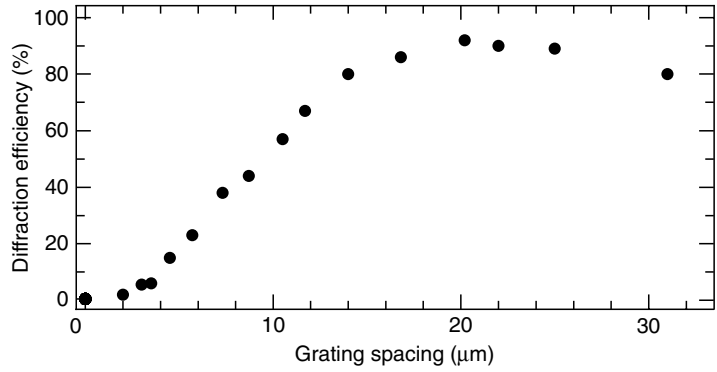

FIGURE 13.7. Diffraction efficiency of the revealed grating vs. grating spacing. One of the recording beams (488 nm, e-polarized) was used as the probe beam. Power per beam: 48 mW. (Adapted from [35].)

diffraction efficiency of the revealed grating was accomplished by simply blocking one of the recording beams and using the other as the probe beam. The diffraction efficiency was calculated as the percentage of the total power emerging from the crystal diffracted into the direction of the blocked beam. As can be seen in the figure, the diffraction efficiency reaches its maximum, over 92%, at $\Lambda \approx 20\,\mu$m. Experiments performed in other nominally-undoped barium titanate samples and with different experimental parameters showed similar results: The maximum diffraction efficiency was always obtained using large grating spacings, between 20 and 25 μm.

It was also found that the lifetimes of these gratings depend strongly on the grating spacing, where by lifetime we do not mean the time it takes for a *revealed* grating to decay; instead, we mean the time it takes for a fixed but dormant grating to decay under illumination. To measure this decay rate, the gratings were fixed and revealed with the process described above, and the only parameter that was varied was the time between the end of the fixing and revealing processes, which we shall call the *latency time*. During this time, the grating was illuminated by one of the recording beams. The lifetime for each grating spacing was determined by fitting the revealed diffraction efficiency $\eta(t)$ to an exponential decay, $\eta(t) = \eta_0 \exp(-t/\tau)$. Figure 13.8 shows the fitted values of the decay constant τ vs. the grating spacing; the solid line in the figure is an empirical fit to $\tau(\Lambda) = \tau_0 \exp(\Lambda/\Lambda_0)$. Assuming this empirical formula to be valid at $\Lambda \approx 20\,\mu$m, the expected lifetime of the fixed gratings even under intense illumination would be of the order of days. It is clear that the grating fixing process in barium titanate requires very large periodicities, of the order of 20 μm or more, for both the diffraction efficiency and the lifetime to be large.

Similar results were obtained with $Sr_{0.75}Ba_{0.25}Nb_2O_6$ using essentially the same technique; the diffraction efficiency of the revealed grating and the decay

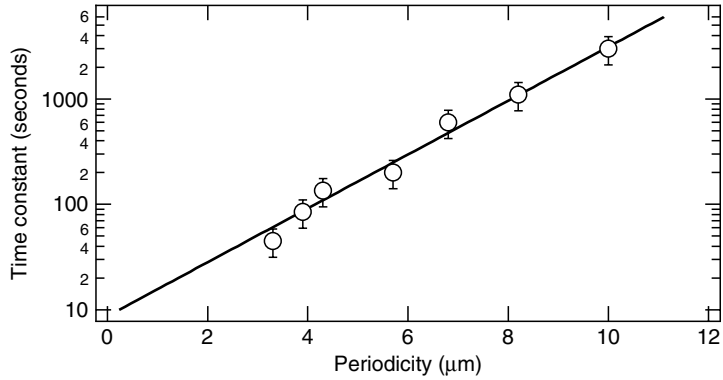

FIGURE 13.8. Decay time constant of the fixed gratings vs. grating periodicity. Solid line: Empirical fit to $\tau(\Lambda) = \tau_0 \exp(\Lambda/\Lambda_0)$, where $\Lambda_0 = 1.7\,\mu$m and $\tau_0 = 8.7$ s. Power per beam: 60 mW.

constant of the fixed grating increased with grating period [5, 6, 7]. However, in contrast with $BaTiO_3$, it was not necessary to reveal the fixed grating to obtain a beam diffracted by the fixed grating, although the diffraction efficiency of this grating was low, of the order of 1%.

We have not specified exactly what configuration domain walls take to compensate the space-charge distribution and several models have been proposed. One model invokes local switching of $\mathbf{P}_s$ wherever the total field exceeds the coercive field [1, 2]; however, for reasons discussed above, this model is unsatisfactory. A related model proposes that many small, ellipsoidally shaped domains, of the order of microns or smaller, are formed throughout the bulk of the material by the space-charge field produced by the interference pattern, without requiring an additional electric field. This model stems from evidence of fixing in $Sr_{0.75}Ba_{0.25}Nb_2O_6$ in which no external field was applied; all that was required was to dramatically increase the time and light intensity used to record the grating in the sample [9, 10, 11]. Another model proposes that needle-shaped domains nucleated at one electrode propagate toward the other electrode until they are stopped by the space-charge distribution [12]. Finally, deformation of the domain walls by the space-charge field such that this field is screened has also been proposed as the source of the compensating bound charge [13, 34]. Figure 13.9 gives a graphic explanation of this proposed mechanism. In 13.9a, there is no free charge and the wall separating two domains is parallel to $\mathbf{P}_s$. In 13.9b, the light interference pattern gives rise to free charge (*circles*). In 13.9c, the field produced by the free charges warps the domain wall, producing a bound surface charge density (*squares*) given by (13.4) which electrically compensates the free charge. This rippled domain model implies that it may be possible to record and simultaneously compensate an optically induced space-charge pattern in a ferroelectric crystal by depoling it *before* the grating is created. This is indeed possible, as was shown in [13].

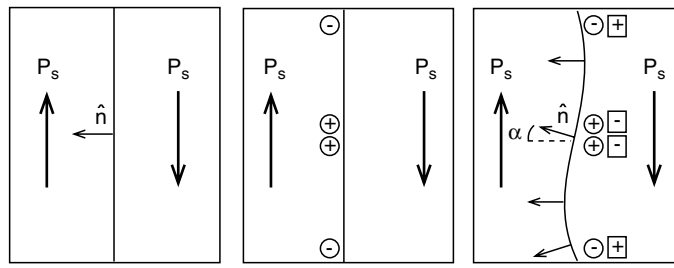

FIGURE 13.9. Space-charge screening by domain wall deformation. (a) The wall separating two domains is initially parallel to $\mathbf{P}_s$; (b) The light interference pattern redistributes free charge among the trap sites (*circles*); (c) The field produced by the free charges warps the domain wall, in turn creating a bound charge surface density (*squares*) that electrically compensates the free charge.

The experimental procedure was the following. First a top-seeded solution-grown $BaTiO_3$ sample was poled and then depoled to a certain degree by applying electric fields along its c-axis. A grating was then recorded in this multi-domain crystal by two interfering light beams. Since the grating spacing in these experiments was quite large, an auxiliary electric field was applied during the recording stage to enhance the charge transport; the magnitude E_{aux} of this field was low enough to avoid any further depoling (verified by the absence of current during this stage). After some time τ_R (recording time), the field was turned off and one of the beams was blocked. The diffraction of the other beam off the grating decayed in a few seconds. The crystal could be illuminated for a long time during the latency period and the diffracted beam would not reappear. However, if the crystal was repoled by applying a field in the original poling direction the diffracted beam reappeared, indicating that a latent grating that could not be erased by light had been revealed. The crystal could be illuminated with an intense beam for hours during the latency period without significantly affecting the diffraction efficiency of the grating revealed afterward. An example of the time development of the applied field and the detected current is given in Fig. 13.10.

The diffraction efficiency of the revealed grating depended on the recording time and the grating spacing, as shown in Fig. 13.11. For comparison, the diffraction efficiencies of gratings recorded in a single-domain crystal (without fixing) are also shown. Notice that the diffraction efficiency is about 20 times higher when the grating is recorded in a multidomain crystal and then revealed.

The explanation given in [13] for these results is as follows. The light interference pattern that has the form $I = I_0(1 + \cos k_g z)$ produces a spatially

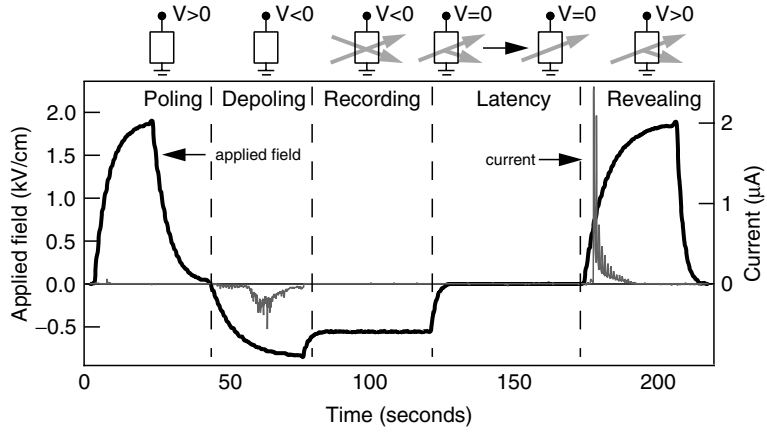

FIGURE 13.10. Fixing in depoled barium titanate: Applied field and detected current vs. time. The icons on top of the graph depict the status of the recording beams. (Adapted from [13].)

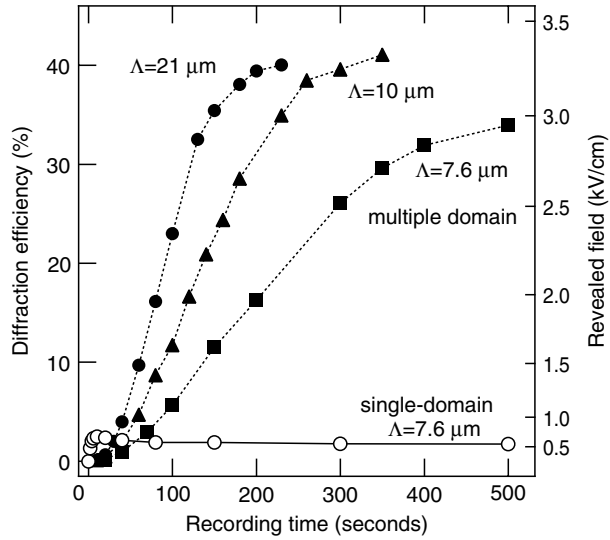

FIGURE 13.11. Fixing in depoled barium titanate: Diffraction efficiency of the revealed grating vs. recording time for three different grating spacings. The inferred value of the amplitude of the space-charge field is shown on the right-hand axis. $\lambda = 488\,nm$, o-polarized; intensity per beam: 2.3 W/cm2; auxiliary field during the recording stage: 600 V/cm. (Adapted from [13].)

periodic excitation of charge carriers located in trap sites. These charges migrate through drift and diffusion currents to other places in the crystal and then recombine into other trap sites, producing a nonuniform charge density distribution ρ_{free}. This charge density is related to the space-charge field E_{sc} that it produces and to the spontaneous polarization by

$$\rho_{free} = \epsilon_0 \epsilon \boldsymbol{\nabla} \cdot \mathbf{E}_{sc} + \boldsymbol{\nabla} \cdot \mathbf{P}_s \tag{13.11}$$

where ϵ is the dielectric constant of the medium. In a single-domain crystal, $\mathbf{P}_s$ is constant so $\boldsymbol{\nabla} \cdot \mathbf{P}_s = 0$. In multidomain crystals, $\mathbf{P}_s$ changes discontinuously across domain walls producing a bound charge density given by (13.4). The orientation of the walls depends on the domain structure configuration the crystal acquires after partial switching and on the interaction between the space-charge field and the domain structure. Suppose that the domain walls existing before the space-charge grating is recorded have the ability to distort themselves such that induced bound charge locally compensates the free charge as it develops during the recording process. Let $E_{sc}(k_g)$, $\rho_{free}(k_g)$, and $\rho_b(k_g)$ be the amplitudes of the Fourier components of E_{sc}, ρ_{free} and ρ_b that have the spatial periodicity of the light pattern. Although the bound charge located at the domain walls is actually a surface charge density, we assume that it can be described macroscopically by a volume charge density given by (13.5). We

assume that at steady-state the bound charge spatially follows the free charge to a certain extent, so that in a multidomain crystal,

$$\rho_{\mathrm{b}}^{recording}(k_{\mathrm{g}}) = -\gamma \rho_{free}^{recording}(k_{\mathrm{g}}). \tag{13.12}$$

We have added the superscript "recording" to specify that $\rho_{\mathrm{b}}^{recording}$ and $\rho_{free}^{recording}$ refer to the charge densities during the recording stage. The proportionality constant γ describes the degree of the compensation and therefore must satisfy $0 < \gamma < 1$, i.e., we assume that the bound charge cannot overcompensate the free charge. From (13.5), (13.11) and (13.12), during the recording stage $\rho_{free}(k_{\mathrm{g}})$ and $E_{\mathrm{sc}}(k_{\mathrm{g}})$ are related by

$$\rho_{free}^{recording}(k_g) = \frac{k_{\mathrm{g}} \boldsymbol{\epsilon} \epsilon_0}{1-\gamma} E_{\mathrm{sc}}^{recording}(k_g). \tag{13.13}$$

Since the grating decays very slowly during the latency time, the interaction between $\rho_{free}(k_{\mathrm{g}})$ and $\rho_b(k_{\mathrm{g}})$ must be strong enough such that any optical re-excitation of charge is followed by the trapping of another charge at nearly the same location. Therefore when the crystal is illuminated by homogeneous illumination during the latency period, the fraction γ of $\rho_{free}(k_{\mathrm{g}})$ that was compensated is not erased. When the crystal is repoled, the compensating $\rho_{\mathrm{b}}(k_{\mathrm{g}})$ provided by the domain walls is removed, leaving behind the previously compensated free charge density. The revealed charge density is then given by

$$\rho_{free}^{revealed}(k_{\mathrm{g}}) = \gamma \rho_{free}^{recording}(k_{\mathrm{g}}), \tag{13.14}$$

so that from (13.5), (13.11), (13.13), and (13.14), the final revealed space-charge field responsible for the revealed diffraction efficiency is

$$E_{\mathrm{sc}}^{revealed}(k_g) = \frac{\gamma}{1-\gamma} E_{\mathrm{sc}}^{recording}(k_{\mathrm{g}}), \tag{13.15}$$

i.e., the revealing process enhances (or diminishes) the space-charge field created during the recording stage by $\gamma/(1-\gamma)$.

We compare the revealed space-charge field achieved in a multidomain crystal with that obtained in a single-domain crystal. The steady-state is reached once the drift current produced by the space-charge field balances the drift current induced by the externally applied field E_{aux} plus the diffusion current. For unity modulation of the interference pattern, if the density of charges and trap sites is large enough such that at steady-state $E_{\mathrm{sc}}(k_{\mathrm{g}})$ is not limited by its finite value, then according to the standard band conduction model of photorefractives [36]

$$E_{\mathrm{sc}}^{recording}(k_{\mathrm{g}}) = 2\sqrt{\left(\frac{k_{\mathrm{B}}T}{e}k_{\mathrm{g}}\right)^2 + (E_{\mathrm{aux}})^2}. \tag{13.16}$$

In (13.16), the contribution from the photogalvanic effect has been neglected. Notice that $E_{\mathrm{sc}}(k_{\mathrm{g}})$ does not depend on the value of the dielectric constant nor

on any other form of field screening, such as that provided by the bound charge. This is because the electric field, not the electric displacement, is the source of the drift currents. Therefore the steady-state value of $E_{sc}(k_g)$ does not depend on whether the grating is recorded in a single or multidomain crystal. From this we conclude that the revealed space-charge field of a grating recorded in a multidomain crystal is $\gamma/(1-\gamma)$ times that of a grating recorded in a single domain crystal. For the data shown in Fig. 13.11, the steady-state field amplification is around 5, so that $\gamma \approx 0.83$.

We now consider how the domain structure responds to the light-induced charge distribution. On the basis of experiments performed with $BaTiO_3$ using different techniques [37, 38, 39, 40], it can be assumed that a partially depoled crystal contains predominantly many needle-like domains with a square or rectangular cross-section, with a width r_0 of the order of 10 μm; most of these domains start at one electrode and reach the opposite one, and only a few end in the bulk. From (13.4), the walls between neighboring domains have a bound surface charge density given by

$$\sigma_b = 2P_s \sin\alpha. \tag{13.17}$$

It is this surface charge density which, averaged over a volume enclosing many domain walls, provides the compensating charge $\rho_b(k_g)$. Let us assume that the space-charge field modulates the width r of the domains so that $r(z) = r_0 + \Delta r \sin(k_g z)$. For $k_g \Delta r << 1$, the surface charge density at the domain walls is given by

$$\sigma_b(z) = 2P_s k_g \Delta r \cos(k_g z). \tag{13.18}$$

Assuming the crystal is completely depoled, i.e., $g \approx 0$, from (13.12), (13.13) and (13.16), it can be shown that the bending of the domain walls necessary to provide the bound charge for the fixing process is given by

$$\frac{\Delta r}{r_0} \approx \frac{\epsilon_0 \epsilon E aux}{2P_s} \frac{\gamma}{1-\gamma}. \tag{13.19}$$

Using $\epsilon = 135$, $P_s = 0.26\,\mathrm{C/m^2}$, $E_{aux} = 500\,\mathrm{V/cm}$, and $\gamma = 0.8$ we obtain $\Delta r/r_0 \approx 5 \times 10^{-4}$. For an average domain width $r_0 \approx 10\,\mu$m [38], the ripple of the wall is of the order of 5 nm; only a small ripple of the domain walls is needed to fix the gratings.

13.4 Fidelity of Fixed Holograms

In order for domain fixing to be of any practical use, it is necessary to be able to fix photorefractive *holograms*, not just plane wave gratings. It is not obvious if this technique can be used to fix holograms of complex wavefronts, since the size and distribution of the domains may greatly affect the quality of the reconstructed wavefront. Photorefractive holograms of complex wavefronts

have been fixed in $Sr_{0.75}Ba_{0.25}Nb_2O_6$ [5, 8, 9, 14, 15]; furthermore, angular-multiplexing of over 1000 holograms fixed in depoled $Sr_{0.75}Ba_{0.25}Nb_2O_6$ has been reported [14, 15]. As far as we know, the fidelity the reconstructed wavefronts diffracted by fixed gratings has only been studied in $BaTiO_3$ [41].

Fig. 13.12 shows the results of holograms fixed in depoled $BaTiO_3$. An image-plane. (1:1 amplification) hologram was recorded in a depoled $BaTiO_3$ sample. Fig. 13.12a shows the image of a resolution chart focused into the barium titanate sample obtained by imaging the object beam, i.e., no holograms are involved. The resolution of this picture, about 4 μm, was limited by the imaging lens employed and by the imperfect homogeneity of the sample. Fig. 13.12b shows an image of the same portion of the resolution chart as in (a), but obtained from the reconstruction of the object beam produced by a non-fixed photorefractive hologram. The resolution is essentially the same as in (a), indicating that the holographic recording process by itself did not significantly degrade the resolution. Fig. 13.12c shows the image obtained from the fixed-and-then-revealed hologram. Notice that the resolution is slightly degraded, especially for the horizontal lines: The minimum thickness of the resolvable vertical lines (resolution along the c-axis) is about 8 μm, whereas for horizontal lines (resolution perpendicular to the c-axis), it is about 18 μm. The loss of horizontal resolution is clearly due to striations along the c-axis. These horizontal striations are due to the long 180° domains, which extend throughout the whole region imaged. The average thickness of these striations is in very good agreement with the average thickness of 180° domains obtained from other experiments. Head-to-head domains would be revealed by vertical striations, which do not appear in 13.12c. These experiments show that holograms of complex wavefronts can be fixed in $BaTiO_3$ with a fidelity close to what can be obtained with a perishable photorefractive grating. In addition, the absence of vertical striations give additional support to the rippled-domain wall model ferroelectric domain fixing, at least for $BaTiO_3$.

FIGURE 13.12. Fidelity of holograms fixed in depoled $BaTiO_3$. (a) Image of the object beam; (b) image of the reconstructed object beam produced by a perishable (nonfixed) hologram; (c) image of the reconstructed object beam produced by the revealed hologram. Average grating spacing: 7.8 μm. (Adapted from [41].)

References

1. F. Micheron, G. Bismuth: Appl. Phys. Lett. **20**, 79 (1972).
2. F. Micheron, G. Bismuth: Appl. Phys. Lett **23**, 71 (1973).
3. J.B. Thaxter, M. Kestigian: Appl. Opt. **13**, 913 (1974).
4. F. Micheron, C. Mayeux, J.C. Trotier: Appl. Opt. **13**, 784 (1974).
5. Y. Qiao, S. Orlov, D. Psaltis, R.R. Neurgaonkar: Opt. Lett. **18**, 1004 (1993).
6. S. Orlov, D. Psaltis, R.R. Neurgaonkar: Appl. Phys. Lett. **64**, 824 (1994).
7. S. Orlov, D. Psaltis, R.R. Neurgaonkar: Appl. Phys. Lett. **63**, 2466 (1993).
8. M. Horowitz, A. Bekker, and B. Fischer: Opt. Lett. **18**, 1964 (1993).
9. A. Kewitsch, M. Segev, A. Yariv, R. Neurgaonkar: Opt. Lett. **18**, 1262 (1993).
10. A. Kewitsch, M. Segev, A. Yariv, G.J. Salamo, T.W. Towe, E.J. Sharp, R.R. Neurgaonkar: Phys. Rev. Lett. **73**, 1174 (1994).
11. A.S. Kewitsch, A. Saito, A. Yariv, M. Segev, R.R. Neurgaonkar: J. Opt. Soc. Am. B **12**, 1460 (1995).
12. R.S. Cudney, J. Fousek, M. Zgonik, P. Günter, M.H. Garrett and D. Rytz: Appl. Phys. Lett. **63**, 3399 (1993).
13. R.S. Cudney, J. Fousek, M. Zgonik, P. Günter, M.H. Garrett, D. Rytz: Phys. Rev. Lett. **72**, 3883 (1994).
14. J. Ma, T.Y. Chang, J.H. Hong, R.R. Neurgaonkar: Phys. Rev. Lett. **78**, 2960 (1997).
15. J. Ma, T.Y. Chang, J.H. Hong, R.R. Neurgaonkar, G. Barbastathis, D. Psaltis: Opt. Lett. **22**, 1116 (1997).
16. M.H. Garrett, J.P. Wilde, "Angular multiplexing using ferroectric domain screening in strontium barium niobate for holographic data storage," in *Proceedings from the Topical Meeting on Photorefractive Materials, Effects and Devices*, Chiba, Japan (1997).
17. R.S. Cudney, P. Bernasconi, M. Zgonik, J. Fousek, P. Günter: Appl. Phys. Lett. **70**, 1339 (1997).
18. X. Tong, R. Hofmeister, M. Zhang, A. Yariv, A. Agranat, V. Leyva: Opt. Lett. **21**, 1860 (1996).
19. X.L. Tong, A. Yariv, M. Zhang, A.J. Agranat, R. Hofmeister, V. Leyva: Appl. Phys. Lett. **70**, 2241 (1997).
20. M. Wesner, C. Herden, D. Kip: Appl. Phys. B **72**, 733 (2001).
21. W. Känzig, *Ferroelectrics and Antiferroelectrics*, Academic Press (1957).
22. E. Fatuzzo, W. Merz, *Ferroelectricity*, North-Holland Publishing Company (1967).
23. M.E. Lines, A.M. Glass, *Principles and Applications of Ferroelectrics and Related Materials*, (Clarendon Press (1977).
24. R. Landauer: J. Appl. Phys. **28**, 227 (1957).
25. C.B. Sawyer, C.H. Tower: Phys. Rev. **35**, 269 (1930).
26. S.M. Emelyanov, F.I. Savenko, Y.A. Trusov, V.I. Torgashev, P.N. Timonin: Phase Transitions **45**, 251 (1993).
27. J. Fousek, M. Marvan, R.S. Cudney: Appl. Phys. Lett. **72**, 26 (1998).
28. M. DiDomenico, Jr., S.H. Wemple: J. Appl. Phys. **40**, 720 (1969).
29. F. Kahmann, R. Matull, R.A. Rupp, J. Seglins: Phase Transitions **40**, 171 (1992).
30. F. Kahmann, R. Matull, R.A. Rupp, J. Seglins: Europhys. Lett. **13**, 405 (1990).
31. A. Hadni, R. Thomas: Ferroelectrics **6**, 241 (1974).
32. A.A. Grabar, R.I. Muzhikash, A.D. Kostyuk, Y.M. Vysochanskii: Sov. Phys. Solid State **33**, 1314 (1992).

33. R.S. Cudney, J. Fousek, M. Zgonik, P. Günter, M.H. Garrett, D. Rytz: Ferroelectrics **157**, 45 (1994).
34. J. Fousek, R.S. Cudney, M. Zgonik, P. Günter: Ferroelectrics **172**, 85 (1995).
35. M. Friedrich: Gitterkonstantenabhängigkeit der Beugungseffizienz bei elektrisch fixiertem photorefraktivem Gitter. Thesis, ETH-Zurich, Zurich (1993).
36. P. Günter and J.-P. Huignard, in Photorefractive Materials and their applications I, edited by P. Günter and J.-P. Huignard, Springer Verlag, Berlin (1988).
37. V. Grubsky, S. MacCormack, J. Feinberg: Opt. Lett. **21**, 6 (1996).
38. R.S. Cudney, V. Garcés-Chávez, P. Negrete-Regagnon: Opt. Lett. **22**, 439 (1997).
39. P. Mathey, P. Jullien, P. Lompré, D. Rytz: Appl. Phys. A **66**, 511 (1998).
40. R.S. Cudney, M. Kaczmarek: Optics Express **7**, 327 (2002).
41. R.S. Cudney, "Fidelity of ferroelectrically fixed holograms in barium titanate," in *Proceedings from the Topical Meeting on Photorefractive Materials, Effects and Devices*, Chiba, Japan (1997).

Index

absorption constant 84
absorption grating 91, 92
active stabilization 164
active stabilization system 381
anisotropic diffraction 99
anisotropic media. 96
anisotropic wave mixing 299
anisotropy of the photoexcitation 85
anisotropy parameter 107
antisite defects 237
attenuated total reflection 294
attractors 166
average electro-optic coefficient 404

band grating 213
band-gap 203
barium titanate 303, 398, 403, 407, 408, 414
$BaTiO_3$ 87, 90, 104, 111, 113, 260, 305, 398, 403, 410, 413, 414
beam coupling 2
beam coupling direction 305
beam fanning
bipolar transport 66
birefringence 9, 23
bound surface charge density 413
Bragg angle 213
Bragg condition 33
Bragg conditions 94
Bragg matching 98
Bragg mismatch 97
Bragg selectivity 101
bright solitons

carrier diffusion. 26
carrier drift mobility 90
carrier mobilities 209
channel waveguides 301
charge density 209
clamped static dielectric tensor 86
codirectional two-wave mixing 38
coercive field 398, 399, 409
coherence 16
coherent oscillation' 263
combinational gratings 387
complex refractive index 22
(complex) modulation index 86
congruent $LiTaO_3$ 217
counterpropagating beams 255
counterpropagating pattern formation 262
coupled first order equations: relaxation modes 374
coupled wave model 91
coupled-wave equation 35, 93
coupled-wave theory 91
coupling coefficient 39
coupling constant 36
coupling strength 165
cross-talk effects 60
Curie temperature 295

dark conductivity 218
dark decays of diffraction efficiency 386
dark electronic conductivity 373
dark intensity I_d 218
dark solitons
DAST 99
Debye screening length 57
developing 377
developing process 382
development without light 383

dichroic materials 83
dichroism 23, 84
dielectric gratings 91
dielectric relaxation time 56, 111
dielectric tensor 85
difference frequency 19
diffraction efficiency 34, 37, 95, 96, 97, 101, 293
diffusion 29
diffusion coefficient of hydrogen in lithium niobate 384
diffusion field 104, 207
diffusion length 56
diffusion time 209
direct recombination constant 205
dispersion law 126
dispersion relation 125
displacement vector field 87
domain fixing 402, 413
domain walls 400, 409, 413
drift 29
drift length 56
dynamic grating 7, 102
dynamic holograms 1, 204

effective amplitude absorption constants 96
effective dielectric constant 84, 86, 104, 110, 112, 205
effective electro-optical coefficient 84, 112
effective mobility 216
effective third-rank electro-optic tensor 89
efficient diffraction without developing 383
Einstein summation convention 86
elastic stiffness tensor 86
electric displacement vector 86
electrical fixing 397, 398
electro-optic coefficients 267, 299
electro-optic effect 30
electro-optic tensor 89
electrochemical reduction 303
electron density 205
electron tunneling 231
electron-hole competition factor 66
electronic feedbacks 163
energy density 12
energy transfer 2
excitation time 203
exponential gain 103, 107

feedback condition 164, 165, 166, 195
feedback equation 168, 169
feedback loop 168
feedback loop response time 169
feedback setup 168
feedback signal 171
feedback-controlled beam coupling 163, 167
feedback-controlled grating recording 170
feedback-controlled steady states 177
Fermi function 25
ferroelectric domains 398
ferroelectrics 122
fiber Bragg gratings 308
fidelity 413, 414
filamentation 258
final developed ratio 382
fixed gratings 414
fixing after recording 378
fixing in photorefractive waveguides 388
flat-top hat beam *73*
four-wave mixing 1
Fourier control is 281
Fourier transform 34
frame rate 223, 223
Franz-Keldysh effect 204
free charge limiting field 211
free-carrier absorption 28

gain media 93
gain-length product 106
Gaussian 77
Gaussian beam 8, 10
Gaussian beams 70
general equations 372
generation of subharmonics 61
Ginzburg-Landau 273
graded-index waveguide 291
grating anisotropy 100
grating coupler 292
grating enhancement 57
grating instabilities 61

grating 34
grating period 12

Helmholtz equation 34
hexagonal structure 260
high-contrast effects 145
hole density 205
hologram lifetime 231, 377
holographic memory 223
holographic sensitivity 298
hysteresis loop 400

ideal conditions 170
ideal feedback 180
incoherent-to-coherent conversion 204, 221
inertial feedback 181
inertial feedback conditions 166
integrated optics 290
interband absorption 26
interband photorefractive effect 203
interference tensor 13
intrinsic levels 203
ion implantation 302
ionic conductivity 231
isotropic wave mixing 299

JFT correlator 223

$\mathbf{K}_{1-x}Li_xTa_{1-y}Nb_yO_3$ 398
Kerr medium 255
$KNbO_3$ 90, 104, 111, 113, 206, 212, 213, 260, 398
Kogelnik [1] 91
Kogelnik's expression 99, 100
Kramers–Kronig relation 27

large-angle electro-optical switch/deflector 392
level population 23
lifetime of the holograms 244
light domains 190
light fanning 113
light induced domain switching 225
light induced waveguides 225
light intensities 107
light-matter interaction 31
linear electro-optic effect 88
linear excitation 131
linear polarization 15
linear stability analysis 269
liquid crystals 100
$LiTaO_3$ 212
lithium niobate 297
lithium tantalate ($LiTaO_3$) 217, 301
local response 172
local thermal fixing 382
localized optical beams 67
long-term fixing 4
longitudinal geometry 212
low-frequency peculiarities 145

material excitation 19, 21
maximization of the diffraction efficiency 167
Maxwell dielectric time 90, 203
mechanical deformation fields 84
Mg doped $LiTaO_3$ 217
mixed transmission gratings 95
mobile charge carriers 85
mobility 84
mobility tensor 84, 90, 111
modified elasto-optic tensor 89
modified intensity ralio 107
modulation depth 53
modulation technique 168
modulational instability 256
molecular beam epitaxy 295
multiple active centers 65
multiple pattern region 274
multiple quantum-well 204

Nb_{Li}^{4+} defects as electron donors 379
near-stoichiometric $LiTaO_3$ 217
nondestructive readout 231
nonlinear optics 1
nonlinear stability analysis 272
nonlocal response 172, 179
nonreciprocal behavior of light-diffraction 96
nucleation 400

one-photon processes 204
optical correlation 204, 223
optical damage 289, 298, 301

optical indicatrix 88, 92
optical interconnections 307
optical path difference 32
optical tunneling 302
optical waveguides 289
oxide crystals 289

parallel processing 204
parametric instability 137
parametric processes 63
pattern control 253
pattern formation 253
periodic state 166, 180
permittivity 9
phase conjugate 2
phase coupling factor 103
phase fluctuations 163
phase grating 92
phase-matching conditions 135
photoconductivity 206, 218, 298
photoexcitation 84, 203
photoexcitation anisotropy 104, 113
photoexcitation constant 205
photoexcitation tensor 107
photogalvanic effect 104, 217
photorefractive effects 1
photorefractive materials 119
photorefractive nonlinearity 43
photorefractive space-charge electric field 85
photovoltaic current 299
photovoltaic drift 48
photovoltaic effect 300, 373
photovoltaic length 57
photovoltaic solitons
physical model for thermal fixing 371
piezoelectric stress tensor 86
planar waveguide 291
plane hologram 92
Pockels electro-optic coefficients 46
polarization 11
polarization conversion 300
polarons 237
polymer-dispersed liquid crystals 100
population gratings 20
potassium niobate 213, 304
Poynting vector 8, 94, 105
prism coupler 291
proton exchange 295, 296
pulsed lasers 1
pulses 10
pump depletion 106
pump wave amplitude 95
pyroelectric 231
pyroelectric field 241

quality factor 120
quantum efficiency 85
quantum-confined Stark effect 204

rate equations 47
recombination fields 207
recombination time 56
reconfigurable optical interconnects 226
recording at high temperature 375
reflection filters 308
reflection gratings 100, 109, 226
reflection volume grating 33, 36
refractive index 91
refractive index change 292
refractive index profiles 294
resolution 221
resonant response 179
resonant wave effects 119
response speed 203
response time 303
rippled domain 409
rippled-domain wall 414
rocking curve 213

Sagnac interferometer 309
Sawyer-Tower 400
Sawyer-Tower circuit 399
SBN 259
scalar coupling constants 94
scalar effective electro-optic coefficient 90, 94
scaling relations 183
screening nonlinearity
screening solitons 72
second harmonic generation 301
self-consistency 290
self-focusing 225
self-organizing phenomena 254
semiconductor 24, 204
separatrix 176

shallow levels 231
shallow trap 217
sillenites 307
singularities 76
slowly varying envelope amplitude approximation 255
$Sn_2P_2S_6$, (SPS) 212, 219
soft proton-exchanged (SPE) $LiNbO_3$ guides 388
soliton-induced waveguiding
space charge field 29, 48, 103, 107
space-charge field amplitude 89
space-charge waves 64, 119
spatial coherenc 18
spatial light modulator 223
spatial solitons 4
spatio-temporal structures 253
spontaneous polarization P_s 397, 398, 402
sputtering 295
$Sr_{0.61}Ba_{0.39}Nb_2O_6$ 398, 408, 409, 414,
steady state 175
stop band 101
strain tensor 86
strain-optic effect 306
strontium-barium niobate 305
subharmonic generation 119
surface charge density 400
symmetry breaking bifurcation 257

telecommunication applications 231
temporal coherence 16
tensor gratings 22
thermal fixing 309, 369, 370
thick gratings 33, 91
Ti: $LiNbO_3$ waveguides 392
thin dynamic hologram 223
thin gratings 31
third-rank effective electro-optic tensor 94
three-step method 372, 378
three-valence model 235
tin hypothiodiphosphate 219
titanium diffusion 295
transmission gratings 94, 106
transmission volume grating 33, 36
transverse effects 254
transverse geometry 212
transverse instabilities 253
transverse nonlinear optics 255
trap grating 213
trap-free model 205
trap-limited field 104
tunable Bragg filters 226
two-beam interference 11
two-center model 234
two-level models 234
two-photon processes 204
two-photon recording 370
two-step excitation 231
two-step method 372
two-step recording 4
two-wave mixing 102, 258, 260
two-wave mixing gain 214
two-wavelength technique 370

unclamped (free) dielectric tensor 88
unclamped electro-optic tensor 112
undepleted pump approximation 103
usefully dissipated energy 85
"usefully dissipated energy" 85

vapor-phase proton exchange 297

walkoff angle 99
wave equation 91
wave-mixing 299
waveguide devices 392
waveguides 204
wavelength division multiplexing 308
wavelength filters 101
wavelength-demultiplexer 247
wavevectors 84
wavevector diagram 93
wavevector mismatch 94
Wiener–Khintchine theorem 17
WKB method 294
writing beams 14

Springer Series in

OPTICAL SCIENCES

Volume 1

1 **Solid-State Laser Engineering**
By W. Koechner, 5th revised and updated ed. 1999, 472 figs., 55 tabs., XII, 746 pages

Published titles since volume 90

90/1 **Raman Amplifiers for Telecommunications 1**
Physical Principles
By M.N. Islam (Ed.), 2004, 488 figs., XXVIII, 328 pages

90/2 **Raman Amplifiers for Telecommunications 2**
Sub-Systems and Systems
By M.N. Islam (Ed.), 2004, 278 figs., XXVIII, 420 pages

91 **Optical Super Resolution**
By Z. Zalevsky, D. Mendlovic, 2004, 164 figs., XVIII, 232 pages

92 **UV-Visible Reflection Spectroscopy of Liquids**
By J.A. Räty, K.-E. Peiponen, T. Asakura, 2004, 131 figs., XII, 219 pages

93 **Fundamentals of Semiconductor Lasers**
By T. Numai, 2004, 166 figs., XII, 264 pages

94 **Photonic Crystals**
Physics, Fabrication and Applications
By K. Inoue, K. Ohtaka (Eds.), 2004, 209 figs., XV, 320 pages

95 **Ultrafast Optics IV**
Selected Contributions to the 4th International Conference on Ultrafast Optics, Vienna, Austria
By F. Krausz, G. Korn, P. Corkum, I.A. Walmsley (Eds.), 2004, 281 figs., XIV, 506 pages

96 **Progress in Nano-Electro Optics III**
Industrial Applications and Dynamics of the Nano-Optical System
By M. Ohtsu (Ed.), 2004, 186 figs., 8 tabs., XIV, 224 pages

97 **Microoptics**
From Technology to Applications
By J. Jahns, K.-H. Brenner, 2004, 303 figs., XI, 335 pages

98 **X-Ray Optics**
High-Energy-Resolution Applications
By Y. Shvyd'ko, 2004, 181 figs., XIV, 404 pages

99 **Mono-Cycle Photonics and Optical Scanning Tunneling Microscopy**
Route to Femtosecond Ångstrom Technology
By M. Yamashita, H. Shigekawa, R. Morita (Eds.) 2005, 241 figs., XX, 393 pages

100 **Quantum Interference and Coherence**
Theory and Experiments
By Z. Ficek and S. Swain, 2005, 178 figs., XV, 418 pages

101 **Polarization Optics in Telecommunications**
By J. Damask, 2005, 110 figs., XVI, 528 pages

102 **Lidar**
Range-Resolved Optical Remote Sensing of the Atmosphere
By C. Weitkamp (Ed.), 161 figs., XX, 416 pages

103 **Optical Fiber Fusion Splicing**
By A.D. Yablon, 2005, 137 figs., XIII, 306 pages

Springer Series in

OPTICAL SCIENCES

104 **Optoelectronics of Molecules and Polymers**
By A. Moliton, 2005, 200 figs., approx. 460 pages

105 **Solid-State Random Lasers**
By M. Noginov, 2005, 149 figs., approx. XII, 380 pages

106 **Coherent Sources of XUV Radiation**
Soft X-Ray Lasers and High-Order Harmonic Generation
By P. Jaeglé, 2005, 150 figs., approx. 264 pages

107 **Optical Frequency-Modulated Continuous-Wave (FMCW) Interferometry**
By J. Zheng, 2005, 137 figs., XVIII, 254 pages

108 **Laser Resonators and Beam Propagation**
Fundamentals, Advanced Concepts and Applications
By N. Hodgson and H. Weber, 2005, 497 figs., approx. 790 pages

109 **Progress in Nano-Electro Optics IV**
Characterization of Nano-Optical Materials and Optical Near-Field Interactions
By M. Ohtsu (Ed.), 2005, 123 figs., XIV, 206 pages

110 **Kramers-Kronig Relations in Optical Materials Research**
By V. Lucarini, J.J. Saarinen, K.-E. Peiponen, E.M. Vartiainen, 2005, 37 figs., X, 162 pages

111 **Semiconductor Lasers**
Stability, Instability and Chaos
By J. Ohtsubo, 2005, 169 figs., XII, 438 pages

112 **Photovoltaic Solar Energy Generation**
By A. Goetzberger and V.U. Hoffmann, 2005, 139 figs., XII, 234 pages

113 **Photorefractive Materials and Their Applications 1**
Basic Effects
By P. Günter and J.P. Huignard, 2005, 169 figs., approx. XII, 300 pages

114 **Photorefractive Materials and Their Applications 2**
Materials
By P. Günter and J.P. Huignard, 2006, 100 figs., approx. XII, 300 pages

115 **Photorefractive Materials and Their Applications 3**
Applications
By P. Günter and J.P. Huignard, 2006, 100 figs., approx. XII, 300 pages